

2nd Central European Symposium on Plasma Chemistry

Organized by

*Department of Physical Electronics
Faculty of Science
Masaryk University*

and by

Union of Czech Mathematicians and Physicists

**31st August – 4th September 2008
Brno, Czech Republic**

Honorary Symposium Chair

J. Janča, Czech Republic

Symposium Chair

A. Brablec, Czech Republic

Secretary

P. Vašina, Czech Republic

Scientific Committee

Yu. Akishev, Russia

L. Bárdos, Sweden

J. Bretagne, France

V. Čech, Czech Republic

M. Černák, Slovakia

S. Debenedictis, Italy

N. Gherardi, France

V. Guerra, Portugal

J. Janča, Czech Republic

F. Krčma, Czech Republic

H. Kersten, Germany

U. Kogelschatz, Switzerland

M. Kuraica, Serbia

J. Paillol, France

J. Skalný, Slovakia

M. Šimek, Czech Republic

D. Trunec, Czech Republic

P. Veis, Slovakia

R. Vladioiu, Romania

L. Zajíčková, Czech Republic

Contact Address

Department of Physical Electronics

Faculty of Science

Masaryk University

Kotlářská 2

61137 Brno

Czech Republic

e-mail: cespc@physics.muni.cz

<http://cespc.physics.muni.cz>

Editors

A. Brablec, P. Vašina, O. Jašek, D. Trunec

Supported by

Central European Initiative (CEI Cooperation Fund)

Masaryk University

Union of Czech Mathematicians and Physicists

The Second Central European Symposium on Plasma Chemistry is a natural development of the First Central European Symposium on Plasma Chemistry, which was held in Gdańsk, Poland, 27 – 31 May, 2006 and series of seven Polish Symposiums on Plasma Chemistry originated in 1971. The first symposium, as well as the mentioned symposiums, has brought together scientists and engineers studying the plasma chemistry and its applications, in particular for environmental issues. Nowadays, it seems to be obvious to continue the formula of the international symposium founded in Gdansk, 2006. The Symposium provides the possibility to scientists from Central Europe to meet each others, exchange knowledge and ideas in plasma based applications.

The First Central European Symposium on Plasma Chemistry was supported by the CEI Cooperation Fund, which supports this symposium again. This activity was very successful and so we expect that the Symposium in Brno will have the similar exciting impact. The topics of the Second Central European Symposium on Plasma Chemistry cover both chemical and technological aspects of the plasma processing of gases, liquids and solids.

The Central European Symposium is focused on exchanging new experience and ideas in the plasma applications for materials processing, surface modifications, medicine, environment protection and other fields related to the plasma chemistry. The aim of the symposium is to accelerate development of plasma-based technologies, dedicated in particular to environmental protection and improvement of quality of life. Moreover, due to broad symposium scope we enable and welcome participation of researches from related branches. The four-day format of the symposium provides excellent opportunities for both formal presentations and informal discussions in between more than 100 participants. Each day starts with topical lecture provided by an invited speaker selected by International Scientific Committee of the Symposium. After that several oral presentations follows; the authors of the best submitted abstracts were nominated for oral presentations. Two evenings are dedicated to the poster session, where participants will present results and discuss informally. The Symposium covers up-to-date topics and so the meeting is open for researchers from Universities and R/D institutions as well as for people responsible for innovations in the industry. We intend to ensure friendly environment for valuable exchange of ideas.

The Second Central European Symposium on Plasma Chemistry held in Brno 31th August - 4th September, 2008 provided excellent opportunity for approximately 100 participants from 11 European countries. More than 50 participants took advantage of submitting the results presented at the Symposium for consideration as regular paper in special issue of Chemické listy journal. This CD contains those papers, which were accepted for publication.

The Local Organizing Committee and Editors

PLASMA SOURCES, PLASMA REACTORS

ODORS CONTROL WITH NON-THERMAL PLASMA REACTOR

**TOMASZ CZAPKA^{a*}, WITOLD MIELCAREK^b,
JOANNA WARYCHA^b, KRYSZYNA PROCIOW^b
and BOLESŁAW MAZUREK^{a,b}**

^a Institute of Electrical Engineering Fundamentals (I-7), Wrocław University of Technology, Wybrzeże Wyspińskiego 27, 50370 Wrocław, Poland, ^b Electrotechnical Institute, Division of Electrotechnology and Materials Science, M. Curie-Skłodowskiej 55/61, 50369 Wrocław, Poland
tomasz.czapka@pwr.wroc.pl

Key words: non-thermal plasma reactors, back corona discharges mechanism, odors removal

1. Introduction

Recent public concern about air pollution from production units has prompted more research to develop methods to reduce and control odors. Masking chemicals, oxidation processes, air scrubbers, biofilters and ventilation systems have been studied. Many new techniques for gaseous pollutants removal have been developed recently. In general, there are several industrial applications used to clean gaseous streams containing VOCs. The most common are activated carbon filters¹, photocatalytic oxidation² and non-thermal plasma systems³. Nowadays the third way is very promising because of the economic reasons and low power consumption. Non-thermal plasma processes have been investigated a lot during the past decade by many researchers for volatile organic compounds (VOCs) control in air. Many different types of low-temperature reactors have been developed⁴. In all reactors plasma is generated and maintained by electrical discharge.

In this research, the prototype non-thermal plasma reactor was proposed and its efficiency in removal of odors was calculated. The back corona discharge phenomenon was used for promoting the rise of the density of plasma in the reactor.

2. Non-thermal plasma reactors

In general, plasma reactors are devices which generate plasma. Typically plasma is an ionized gas and could be divided into two categories: thermal and non-thermal. In the thermal plasma all the particles (electrons, positive ions, neutral atoms) are in thermodynamic equilibrium, whereas in low-temperature plasma, there is a significant difference in kinetic energy i.e. temperature of electrons and ambient gas particles. Electrons with very high self-energy (1–10 eV)

collide and interact with molecules of pollutant. It leads to the cleavage of bonds. There are two major methods of the cold plasma generation: the electron accelerators and plasma reactors.

Non-thermal plasma reactors usually are built as a planar or cylindrical construction employing high voltage discharge electrodes system (needles, wires). The most common types of cold plasma reactors are: corona discharge reactor, dielectric barrier discharge (DBD) reactor and packed-bed discharge reactor. The power supply, plasma density and pressure drop of the gas passing through the reactors are completely different in these reactors. Corona discharge reactor is characterized by low discharge intensity what is not desirable from the point of view of pollutant removal. The goal is to get the plasma density as high as possible. The key to enhance the plasma density is in using the back corona discharge phenomenon.

3. Back corona discharge mechanism

The back corona discharge is a special type of the partial discharge. In the electrostatic precipitators being used in industry for removal of solid phase particles from gases this phenomenon was observed⁵. The dust particles were charged electrically and then gathered on the collecting electrodes by electrostatic forces (Coulomb forces). In case of dust particles with volume resistivity above $\rho_v \geq 5 \cdot 10^8 \Omega\text{m}$ the back corona discharge was generated. The schematic diagram depicting the stages in the process of back ionization is shown in Fig. 1.

The mechanism proceeds as follows. At first dielectric layer on the grounded electrode is charged by the corona electrode. If the electric field in the dielectric layer exceeds the critical value the back corona occurs in the channels of the layer. As the result, the great amount of charge of opposite polarity to corona electrode is injected to the space between

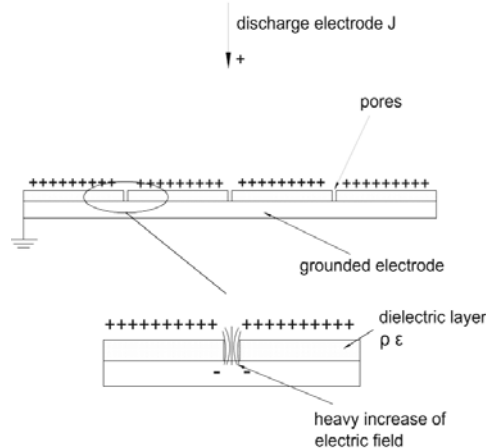


Fig. 1. Schematic diagram of back corona discharge phenomenon

the electrodes and the discharge current significantly increase⁶. For the electrostatic precipitator it is a very undesirable effect because its collection efficiency lessens. However this effect is desirable in plasma reactors.

Using perforated dielectric layer with proper volume resistivity on the grounded electrode it is possible to obtain the low-temperature plasma with the proper intensity under the atmospheric pressure. The plasma channels are distributed at a uniform rate in the dielectric layer and the glow is observed.

4. The laboratory-scale plasma reactors

The laboratory-scale plasma reactors were designed and executed. The frontal views of the constructed reactors are shown in Fig. 2. The two different designs were suggested, one with planar electrodes and the other with cylindrical electrodes system.

The main difference in reactors was the realization of low-field electrode. The reactors shown in the Fig. 2a, 2b had a polystyrene as a dielectric layer on the grounded electrodes and discharge electrodes were made of copper wire, \varnothing 0.35 mm. The volume resistivity of this aromatic polymer (about $10^{12} \Omega\text{m}$) allowed the back ionization. The phenomenon occurred in pores of polystyrene layer. The reactor shown in the Figure 2c was equipped with the low field metallic electrode covered with a high quartz glass fabric (volume resistivity about $10^{10} \Omega\text{m}$) as the dielectric. Furthermore co-

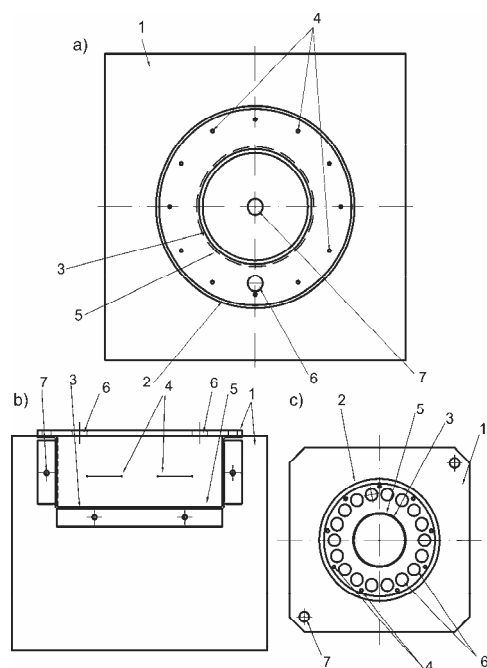


Fig. 2. The scheme of the non-thermal plasma reactors with cylindrical (a, c) and planar (b) electrodes system: 1 – dielectric walls made of plexiglass, 2 – cylindrical housing made of epoxy resin with glass fibre (Figure 2a) or of glass (Figure 2c), 3 – metallic grounded electrode, 4 – corona discharge electrodes, 5 – perforated dielectric layer, 6 – gas inlet (outlet), 7 – holes for screws

rona electrodes were made of Cu-Ni alloy wire, \varnothing 0.30 mm.

The construction of this particular non-thermal plasma reactor allow the gas to cross the plasma chamber perpendicularly to the electric field direction. Also all the reactors were featured by a low drop of pressure between their inlets and outlets. The volumes of the reactors equaled to 2500 cm^3 (Fig. 2a), 900 cm^3 (Fig. 2b) and 1500 cm^3 (Fig. 2c).

5. Electrical measurements

The corona discharge electrodes were connected with dc high voltage power supply. During measurements the voltage was risen up to 20 kV. The current – voltage characteristics of the reactors with the back corona discharges occurring in the pores of the dielectric layer are shown in Fig. 3. The power consumption in the reactors as a function of the applied negative dc voltage are presented in Fig. 4.

It was estimated, that reactor with a glass fabric covered grounded electrode generated the highest discharge current

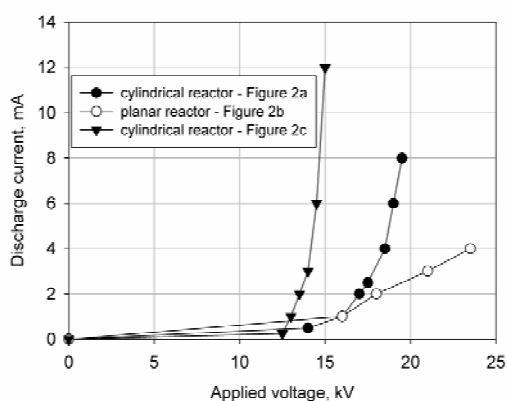


Fig. 3. Current – voltage characteristics of plasma reactors shown in Fig. 2, under the atmospheric pressure and at room temperature for negative polarization of discharge electrodes

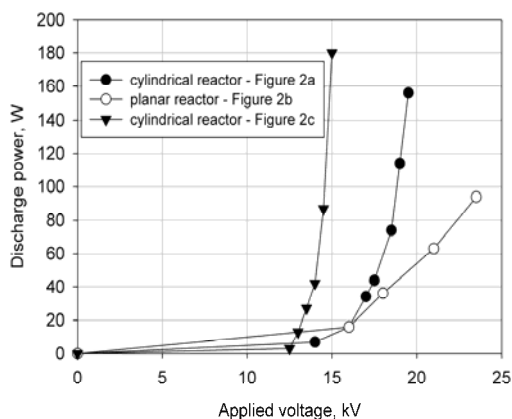


Fig. 4. Discharge power as a function of the applied negative dc voltage

12 mA, with density of $24 \mu\text{A cm}^{-2}$. In other reactors with polystyrene as dielectric layer these values were much lower. For planar reactor they were 4 mA and $11 \mu\text{A cm}^{-2}$ respectively, while for the last cylindrical reactor they were 8 mA, $10 \mu\text{A cm}^{-2}$. It was estimated, that non-thermal systems used in this experimental were low power-consuming. In any case the discharge power did not exceed 200 W and was on the level of 180 W in the case of reactor in Fig. 2c, 160 W for the reactor in Fig. 2a and 100 W for the reactor in Fig. 2b. The influence of the temperature on corona discharge process was noticeable. The plasma reactor was heated up.

On the basis of the above mentioned results the cylindrical reactor equipped with glass fabric as perforated dielectric layer was selected to the further investigations.

6. Odors removal in the plasma reactor

A schematic diagram of laboratory apparatus for the investigations of gaseous pollutants removal by plasma reactor with back discharges is shown in Fig. 5. The apparatus composes of plasma reactor, odors generator and gas analyzer. The quantitative analysis of gaseous samples was carried out using vapor-phase chromatography (HP 5890II Hewlett Packard) and odors conversion rate was analyzed using mass spectrometer (HP 5973).

The investigations were carried out as follows. Odors in liquid or gaseous phase were injected into the odors generator where they were warmed and mixed to obtain a uniform compound. Then the compound was pumped to the flow regulator. The second flow regulator was coupled with the air compressor. This apparatus allowed to adjust the operating flow during the experiments from 29 to 214 l h^{-1} . The concentration of odors in air was controlled over the wide (1.3–104 ppm) range. The odors from the mixer flowed through the plasma reactor which was supplied with sufficiently high voltage to get the back discharges but to avoid sparks between

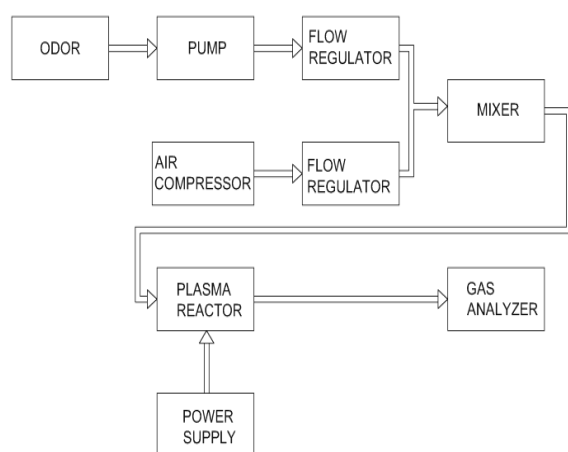


Fig. 5. Schematic diagram of apparatus for odors removal using the non-thermal plasma reactor

the electrodes.

The experiments were realized at room temperature and under atmospheric pressure. The negative polarity was set at corona electrodes during the experiments, as this application led to the higher rate of VOC's decomposition. It was proved in the previous paper⁷.

Alcohols, ketones, alkenes, cycloalkenes, aromatic hydrocarbons and their mixture were used as odorous compounds. The energetic electrons in the non-thermal plasma reactor with back ionization produced free radicals which led to the removal process take place. Dependencies of the compounds decomposition on the power input and current discharge are shown in the Fig. 6, 7. The gas mixtures with cyclopentene, pentene and cyclohexane content equal to 1.3 ppm and the flow rate equal to 214 l h^{-1} were subjected to the action of plasma. It was estimated, that the increase of the discharge current and power input led to the higher efficiency in odors decomposition. The maximum removal rate was 90 % as above some saturation due to electrical properties of the plasma reactor and flow properties took place.

The influence of the flow rate and the initial odors concentration on their conversion efficiency was also checked and verified. The flow rates were adjusted at 180 l h^{-1} for the mixture acetone – toluene (Fig. 8), 120 l h^{-1} for the ethyl ether – acetone – benzene – toluene mixture (Fig. 9) and at 29 l h^{-1} for the mixture ethyl ether – benzene (Fig. 10). In all the cases the corona electrodes were supplied with the constant dc voltage value of 12 kV (negative polarity). The conversion rate of the odors depended strongly on their concentration in air stream and its flow rate. The influence of the flow rate and odors content on the decomposition rate was following. For the mixture of gaseous compounds flowing at a rate of 180 l h^{-1} containing 1 ppm of toluene and acetone their removal ratios were at 75 % and 63 %, whereas for 7.5 ppm these ratios were at 34 % and 17 % respectively. In the case of toluene and acetone mixture (3 ppm) at the flow rate of 180 l h^{-1} , the removal efficiency was 38 % and 25 % for toluene and acetone respectively (Fig. 8). When ethyl ether, acetone, benzene and toluene were mixed so as the concentrations of the particular component at the flow rate of 120 l h^{-1} and the rate of toluene removal was 40 % and acetone 5 % (Fig. 9). Therefore it was

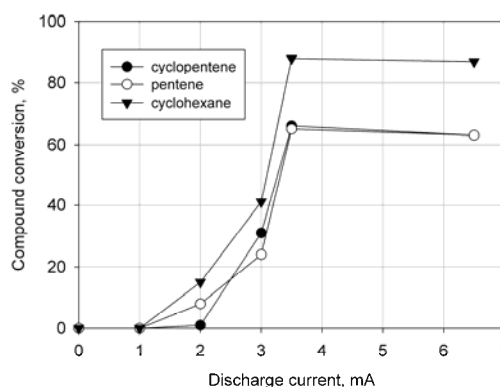


Fig. 6. Conversion efficiency as a function of discharge current in the plasma reactor for compounds content equal to 1.3 ppm and flow rate equal to 214 l h^{-1}

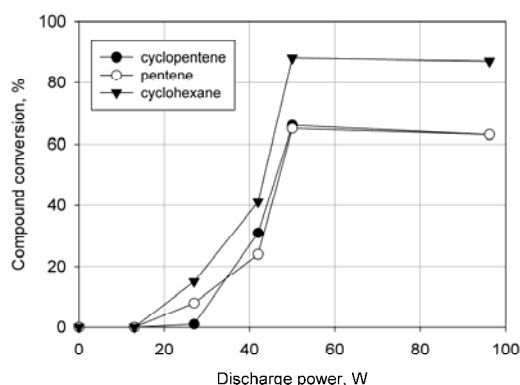


Fig. 7. Conversion efficiency as a function of power input in the plasma reactor for compounds content equal to 1.3 ppm and flow rate equal to 214 l h⁻¹

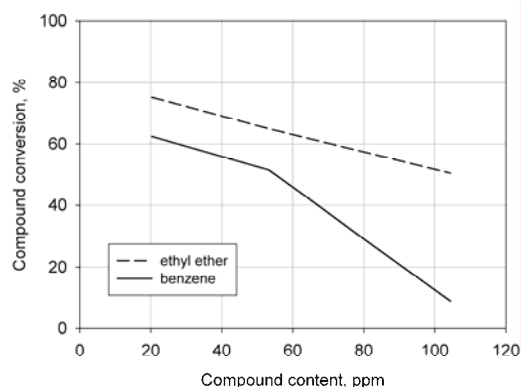


Fig. 10. Dependence of the conversion ratio of ethyl ether and benzene on their initial content for flow rate equal to 29 l h⁻¹

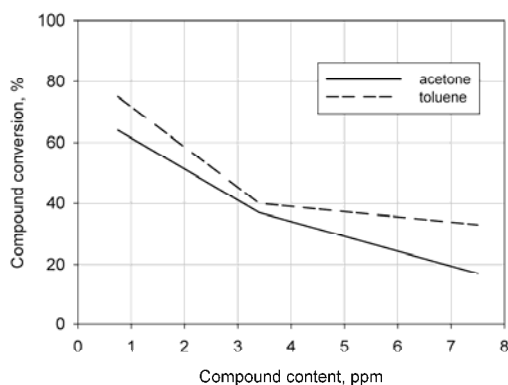


Fig. 9. Dependence of the removal ratio of ethyl ether, acetone, benzene, toluene on their initial concentration for flow rate equal to 120 l h⁻¹

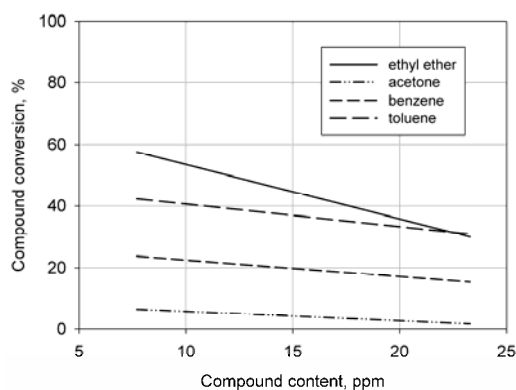


Fig. 8. Dependence of the conversion ratio of acetone and toluene on their initial content for flow rate equal to 180 l h⁻¹

concluded, that the process of odors conversion depend also on the type of the mixture. For flow rate of 29 l h⁻¹ it was found out, that the plasma control was very sensitive on the component content in the mixture. The conversion rate of

ethyl ether changed from 75 % to 50 % while the conversion rate of benzene was 62 % and 8.9 % (Fig. 10) while their concentrations in mixture increase from 20 to 100 ppm.

7. Conclusions

Non-thermal plasma reactor described in this paper is an alternate proposition to be applied for air odors control under atmospheric pressure. The back discharge phenomenon was used for promoting the rise of the density of the excited species.

The power consumption in conversion process was at low level. This was an important advantage from the view point of the energy savings.

The reactor applicability to odors control was proven. The significant dependence of the decomposition efficiency on the flow rate of air containing odors and on their content in gas mixture was estimated. The rate of the particular compound removal was varied. To rise the conversion efficiency of the gaseous compounds the reactor electrical properties have to be modified.

Authors gratefully acknowledge the support from Polish State Committee for Scientific research KBN under grant No PBZ-MeiN-5/2/2006.

REFERENCES

1. Ao C. H., Lee S. C.: Chem. Eng. Sci. 60, 103 (2005).
2. Noguchi T., Fujishima A.: Environ. Sci. Technol. 32, 3831 (1998).
3. Oda T., Kumada A., Tanaka K., Takahashi T., Maruda S.: J. Electrostat. 35, 93 (1995).
4. Penetrante B. M., Hsiao M. C., Merritt B. T., Vogtlin G. E., Wallman P. H.: IEEE Plasma Sci. 23, 679 (1995).
5. Masuda S., Mizuno A.: J. Electrostat. 2, 375 (1976).
6. Mizuno A.: IEEE T. Dielec. El. In. 7, 615 (2000).
7. Kacprzyk R., Miśta W., Czapka T.: III International Conference on Advance In Processing Testing and Application of Dielectric Materials APATDM '2007, Wrocław, 26 – 28. 09. 2007, 65. Wrocław 2007.

ELECTRICAL DISCHARGE IN HONEYCOMB MONOLITH

KAROL HENSEL*, SATOSHI SATO,
and AKIRA MIZUNO

*Department of Astronomy, Earth Physics and Meteorology,
Comenius University, Bratislava, 842-48 Slovakia, Department
of Ecological Engineering, Toyohashi University of
Technology, Toyohashi 441-8580, Japan
hensel@fmph.uniba.sk*

Keywords: microplasmas, sliding discharge, honeycomb catalyst, flue gas treatment, emission spectroscopy

1. Introduction

Tree-way catalysts of honeycomb structure are used in gasoline automobiles for the exhaust gas cleaning. The performance of the catalysts strongly depends on the composition and the temperature of the exhaust gas. The catalysts can be ineffective, if the temperature of the exhaust gases is low or in case of an excess of oxygen. One of the possibilities, how to improve the performance is to combine the catalyst with a non-thermal plasma. It is well-known that the combination of such plasma and catalyst in a hybrid system usually results in an improvement of gas treatment efficiency, carbon balance and reduction of suspended particles in the gas. In the past, there have been several attempts to generate the discharges inside the ceramic honeycomb monoliths^{1,2}. Various cuts and slices of honeycomb monolith integrated with a system of electrodes of assorted geometries were applied to generate the plasma inside the channels of these catalysts. Despite the promising results obtained for NO_x and VOC treatment several serious problems has been reported. One of them is a stability of the discharge and plasma generated inside thin and long channels of honeycomb monolith. The stability can be very much affected by the walls confining the discharge. Due to the loss of the charged particles on the walls of the capillaries, the onset and operating voltages is higher compared to non-confined system. A stable streamer discharge is very difficult to obtain, instead of that rather unstable sparking occur. When operating the discharge for a certain period of time in sparking mode, the mechanical breakdown of the ceramic walls and ultimate failure of the catalyst may occur. Therefore the generation of homogenous and stable plasma inside thin channels of honeycomb catalysts was found so far rather difficult.

In this paper we present a new method for the generation of the stable discharge plasma inside the honeycomb monolith. The idea behind this method is that instead of generating the discharge directly inside the channel, the discharge is generated outside the channels and subsequently extended into the channels. It is done by the generation of auxiliary discharge at one of the ends of the honeycomb monolith and application of the additional electric field across the monolith. This method is in fact a utilization of a technique used in the

past for a sliding discharge generation^{3,4}. The sliding discharge is a discharge generated on flat dielectrics by e.g. combination of AC and DC powers in three-electrode geometry. It is particularly important in aeronautics for active wing flow control by the electric wind produced by the discharge. We used the concept of the sliding discharge to generate the discharge inside the honeycomb monolith along the dielectric walls of the thin channel. The paper present basic characteristics of the sliding discharge inside the capillary channels, addressing the effects of the diameter, length of the channels and the applied voltage.

2. Experimental System

The simplified scheme of the experimental reactor equipped with relevant measuring systems is depicted on Fig. 1.

The reactor consisted of a cylindrical quartz tube of 26 mm diameter. The tube was filled with a bundle of quartz capillaries of 1–3 mm diameter and lengths of 2 or 3 cm. The capillaries were placed on the top of γ -Al₂O₃ pellet bed located at the bottom part of the tube. The bundle of transparent capillaries was used instead of ceramic honeycomb monolith in order to visually observe the discharges inside and to be able to apply the optical emission spectroscopy. The set of three electrodes consisted of a rod plugged in the middle of the pellet bed, aluminum foil wrapped around the quartz tube and a mesh electrode placed on the top of the capillaries. The rod was powered by AC high voltage of 50 Hz, the mesh by negative DC high voltage, and the foil was grounded. Negative DC was chosen to ensure discharge operation up to higher voltages without sparking. The amplitude and waveform of the applied voltages was measured by high voltage probes Tektronix P644A connected to the digital oscilloscope Tektronix TDS2014. The pellet bed discharge power was evaluated from Lissajous figures and the power of the discharge in capillaries as a product of DC voltage and a mean current. Optical measurements were performed by an emission spectrometer Ocean Optics SD2000 and the images were recorded by a digital camera Nikon D40x.

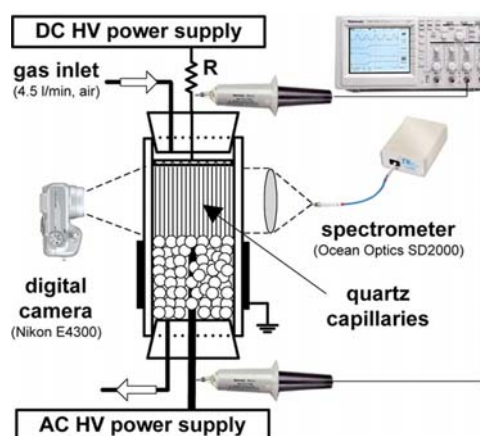


Fig. 1. Experimental setup depicting discharge reactor and electric and optical measuring systems

3. Results and Discussion

When AC voltage was applied on the rod electrode, the barrier discharge inside the pellet bed was formed. The discharge current waveform of the barrier discharge was typical by the current pulses of amplitudes of several tens of milliamperes, which were superposed on the capacitive current bias component. The barrier discharge produced the plasma which served as a kind of ionizer. It produced charged particles and ionic space charges at the bottom of the bundle of glass capillaries. Upon the application of DC voltage on the mesh electrode the charges were accelerated through the capillaries toward the mesh electrode finally forming a sliding discharge. As a result, stable and homogenous plasma formation was observed inside the capillary channels.

Fig. 2 shows the typical voltage and current waveforms of the sliding discharge when negative DC was used. Compared to waveform of the barrier discharge, additional negative pulses can be recognized during the positive maximum of the applied voltage. They are the result of the sliding discharge propagation inside the capillaries. The discharge occurred only when the polarity of the rod and mesh electrode were opposite as result of the high potential difference across the capillaries. When the rod and the mesh were of the same polarity no sliding discharge was observed.

Fig. 3 present the images of the discharges taken by the digital camera for various amplitudes of the applied voltage. The images show the sliding discharge inside glass capillaries formed only when both AC and DC were applied. With AC only barrier discharge inside the pellet bed was formed, while with DC only a corona discharge at the mesh could be observed. The images also show the distribution of the discharge and the emission inside the capillaries was relatively homogenous. The stable sliding discharge operation was possible within a wide interval of both DC and AC applied voltages. The transition of the sliding discharge into a spark discharge was observed when too high applied voltages were used. The DC sparking voltage decreased with increasing the AC applied voltage and vice versa.

Excessive sparking was also observed when dry gas

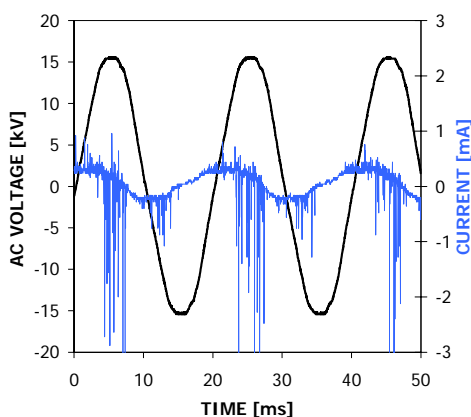


Fig. 2. Waveforms of the applied voltage and discharge current of sliding discharge [$U_{AC} = 15$ kV, $U_{DC} = -16$ kV]



Fig. 3. Images of the discharge in capillaries [diameter 2 mm, length 3 mm] at different AC and DC applied voltages in ambient air: (top left) the reactor, (top right) barrier discharge [$U_{AC} = 16$ kV, $U_{DC} = 0$ kV], (bottom left) corona discharge [$U_{AC} = 0$ kV, $U_{DC} = -20$ kV], (bottom right) sliding discharge [$U_{AC} = 15$ kV, $U_{DC} = -16$ kV]

mixtures were used. Fig. 4 shows the images of the discharge in dry nitrogen and ambient air, showing higher operational AC and DC applied voltages could be reached without sparking if moisture was present in the system. The origin of the effect is not fully understood, but it is assumed to be connected with the formation of water clusters which stabilize the discharge. The transition of the sliding discharge into a spark could also be suppressed by ballasting the DC line with the appropriate resistor, thus limiting the amplitude of the discharge current

Fig. 5 shows the power of the sliding discharge as a function of the DC applied voltage for various lengths of the capillaries and the AC voltages. The discharge power increased with both DC and AC applied voltages. The effect of AC voltage was however negligible since the power of the pellet bed discharge was one order of magnitude less than that of the sliding discharge. With extending the length of capillaries at a given DC voltage, the discharge current and power decreased. In contrast, a diameter of the capillary had marginal effect on the discharge power.

Emission spectroscopy is a method that provides valuable information on excited atomic and molecular states, enables the determination of the temperatures of the plasma and thus the level of non-equilibrium, and the gas temperature. Fig. 6 shows the emission intensity of the sliding discharge

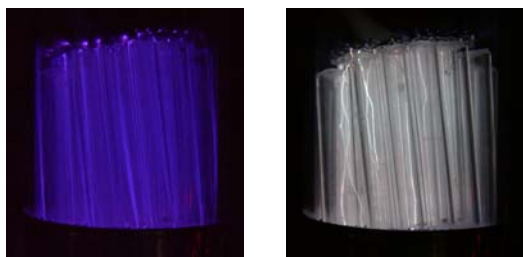


Fig. 4. Images of the discharge in capillaries [diameter 2 mm, length 2 mm] at different AC and DC applied voltages in: (left) ambient air [$U_{AC} = 15$ kV, $U_{DC} = -16$ kV], (right) dry nitrogen [$U_{AC} = 15$ kV, $U_{DC} = -10$ kV]

based on the 0-0 spectral band (337 nm) of 2nd positive system of N_2 ($C_3\Pi_u-B_3\Pi_g$) as a function of the DC voltage. The intensity increased with both DC and AC applied voltages. In contrast to the negligible effect of AC voltage on the discharge power, its effect on the discharge emission was significant. The intensity also reflects a concentration of active species generated by the discharge. To minimize the power consumption but keep the same intensity, it seems appropriate to maximize AC and minimize DC applied voltage. The figure also shows the intensity decreased for longer capillaries as a result of decreasing discharge current.

Fig. 7 shows the emission intensity of the sliding discharge depending on the DC applied voltage for various diameters of capillaries. On contrary to the effect of the length of capillaries, the effect of the diameter was found negligible, especially at low DC applied voltage.

By using Specair software from N_2 ($C_3\Pi_u-B_3\Pi_g$) spectral bands we determined rotational and vibrational temperatures found the typical values 300 ± 30 K and 1800 ± 300 K, respectively. Rotational temperature was found independent of the applied voltages. The plasma generated by the sliding discharge is cold with a high level of non-equilibrium.

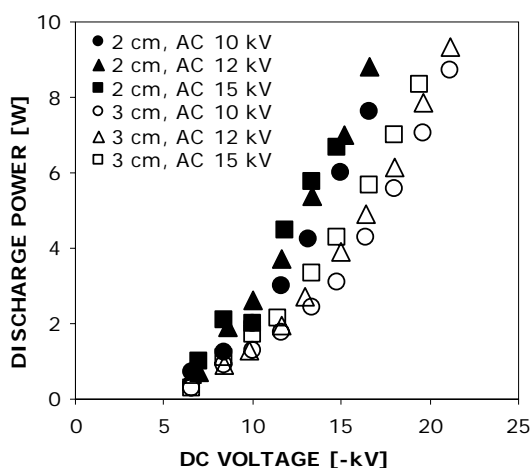


Fig. 5. Discharge power as functions of negative DC applied voltage for various AC applied voltage and the length of capillaries [diameter 2 mm, ambient air]

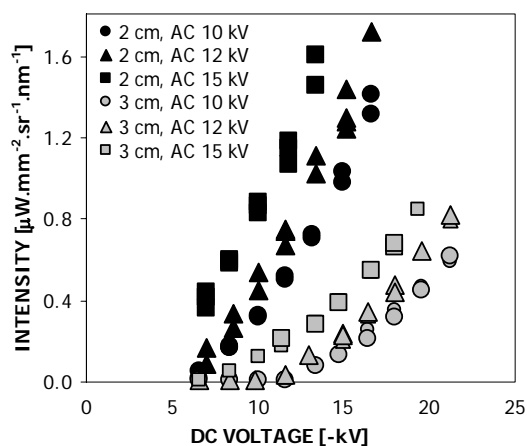


Fig. 6. Discharge emission intensity as functions of negative DC applied voltage for various AC voltage and the length of capillaries [diameter 2 mm, ambient air]

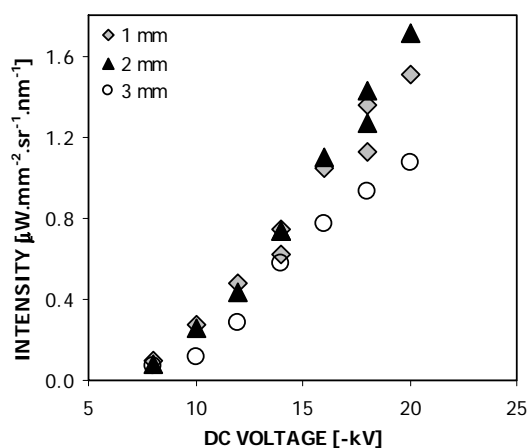


Fig. 7. Emission intensity as functions of negative DC applied voltage for various diameters of capillaries [length 20 mm, AC 10 kV]

4. Conclusions

Generation of microplasmas inside spatially confined geometry of bundle of glass capillaries (simulating honeycomb monolith structure) by using sliding discharge was presented. The paper introduced the fundamental physical properties of the discharge based on electrical and optical measurements. Sliding discharge inside honeycomb was generated by a superposition of AC barrier discharge in series with DC powered honeycomb monolith. The homogeneity and the stability of the discharge can be controlled by amplitude and polarity of the applied voltage and contents of moisture. The discharge generates relatively cold plasma with a high level of non-equilibrium.

Work was supported by Slovak Research and Development Agency grants APVT 20-032404, SK-FR-00506 and by Slovak Grant Agency grant 1/3041/06.

3. Moreau E., Louste C., Touchard G.: *J. Electrostat.* 66, 107 (2008).
4. Sosa R., Kelly H., Grondona D.: *J. Phys. D: Appl. Phys.* 41, 035202 (2008).

REFERENCES

1. Kim H. H.: *PhD Thesis*, Toyohashi University of Technology, Toyohashi (2000).
2. Blin-Simiand N., Tardiveau P., Risacher A., Jorand F., Pasquiers S.: *Plasma Proc. Polym.* 2, 256 (2005).

ATMOSPHERIC PRESSURE MICRO-WAVE MICROPLASMA SOURCES

MARIUSZ JASIŃSKI^{a*}, ŁUKASZ KROPLEWSKI^{a*}, ZENON ZAKRZEWSKI^a, and JERZY MIZERACZYK^{a,b}

^a Centre for Plasma and Laser Engineering, The Szevalski Institute of Fluid-Flow Machinery, Polish Academy of Sciences, Fiszera 14, 80-952 Gdańsk, ^b Dept. of Marine Electronics, Gdynia Maritime University, Morska 83, 81-225 Gdynia, Poland
mj@imp.gda.pl

1. Introduction

Nowadays, there is a growing interest in atmospheric pressure microwave microplasma sources (MMSs)^{1–11}. They are needed for gas cleaning, microwelding, surface modification, light sources, and atomic spectroscopy system. They can be also used in the biomedical applications such as sterilization of medical instruments, high-precision surgery, cells treatment and deactivation of bacteria and viruses^{1–11}.

We present a new MMSs based on a coaxial line. The main advantage of the presented MMSs is its simplicity and low cost. Our first model of MMS was described in¹². Here we present its advanced two versions. First version of the MMS (see chapter 2.1) is oriented for microplasma generation in noble gases. The second version of the MMS (see chapter 2.2) is oriented for operation in nitrogen.

2. Experimental procedure and results

The scheme of the experimental setup is shown in Fig. 1. It consists of a microwave magnetron generator (2.45 GHz), microwave power measuring system (directional coupler, power meters with thermistor mounts), gas flow control system (Mass flow controller) and microwave microplasma source (MMS). The whole arrangement was connected via coaxial cable (50 Ω).

The absorbed microwave power P_A , i.e. microwave power delivered to the discharge was calculated as $P_I - P_R$, where P_I and P_R are the incident and reflected microwave powers, respectively. The incident and reflected microwave powers P_I and P_R were directly measured using directional coupler equipped with bolometric heads and HP power meters (Fig. 1). The ferrite isolator protected the magnetron head from the reflected microwave power.

2.1. Microwave microplasma source operated in argon at atmospheric pressure

In this investigation argon at atmospheric pressure was used as a working gas. The argon flow rates varied from 1 to 20 l min⁻¹. The microwave power was from 10 to 80 W.

The structure of the presented MMS is based on the

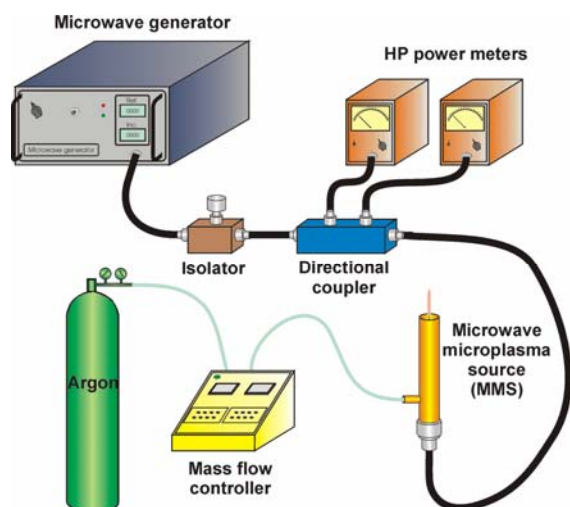


Fig. 1. Experimental setup

transmission coaxial line. The sketch of the transmission coaxial line is shown in Fig. 2.

The important parameter of the transmission coaxial line is its characteristic impedance Z_0 , described as follows:

$$Z_0 = \frac{138}{\sqrt{\epsilon_r}} \log \frac{D}{d} \quad (1)$$

where ϵ_r – dielectric constant (for air – 1.0, for Teflon – 2.1), D – inner diameter of the outer conductor, d – outer diameter of the inner conductor.

The cross-sectional view of the MMS used in this investigation is shown in Fig. 3 and 4.

The centering Teflon nozzle with narrow gas channel ($\phi = 3$ mm) ensures operation at relatively low flow rate of argon.

Important part of the MMS is an impedance matching circuit in the form of the quarter-wave transformer $\lambda/4$. This circuit is based on the coaxial line filled with Teflon.

The length of the used quarter-wave transformer in the MMS is 21 mm.

The best impedance matching of the MMS (i.e. the lowest reflected microwave power) was realized by optimizing the following dimensions (see Fig. 4):

- L_c – length of the inner conductor above the outer conductor,
- L_e – length of the outer conductor measured from the quarter-wave transformer,

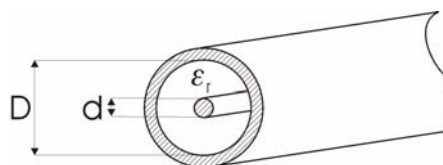


Fig. 2. Sketch of the transmission coaxial line

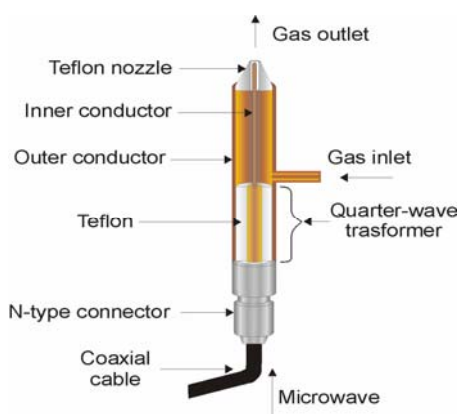


Fig. 3. Coaxial MMS operated in argon at atmospheric pressure

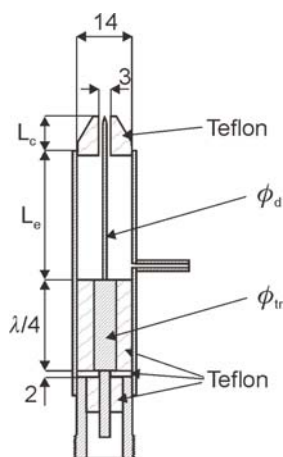


Fig. 4. Draft of the coaxial MMS operated in argon at atmospheric pressure

- ϕ_d – diameter of the inner conductor,
- ϕ_{tr} – diameter of the conductor inside the quarter-wave transformer.

Dependences on the reflection coefficient P_R/P_I versus the length of the outer conductor L_c for different diameters of the conductor inside the quarter-wave transformer ϕ_{tr} are shown in Fig. 5–9. The length above the outer conductor of the inner conductor L_c was fixed (15 mm). Fig. 5–9 shows that at lower diameter of the conductor inside the quarter-wave transformer ϕ_{tr} , the better impedance matching was achieved.

The influence of the incident microwave power P_I ($P_I = 30$ W and $P_I = 60$ W) on the reflection coefficient P_R/P_I was very low.

The influence of length L_c above the outer conductor of the inner conductor on the reflection coefficient P_R/P_I for chosen $L_c = 30$ mm is shown in Fig. 10. As seen, the impedance matching was better for lower values of L_c . This is also confirmed in Fig. 11, where the influence of length L_c on the

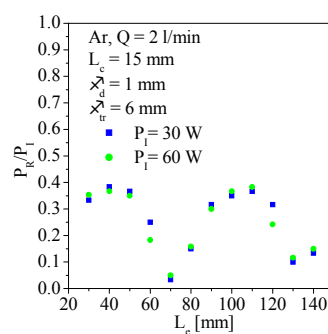


Fig. 5. Influence of length L_c on the reflection coefficient P_R/P_I for different incident microwave powers $P_I = 30$ W and $P_I = 60$ W. The diameter of the wire inside the quarter-wave transformer $\phi_{tr} = 6$ mm. The length above the outer conductor of the inner conductor $L_c = 15$ mm

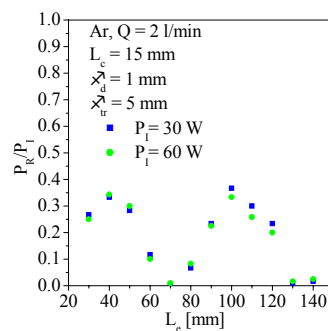


Fig. 6. Influence of length L_c on the reflection coefficient P_R/P_I for different incident microwave powers $P_I = 30$ W and $P_I = 60$ W. The diameter of the wire inside the quarter-wave transformer $\phi_{tr} = 5$ mm. The length above the outer conductor of the inner conductor $L_c = 15$ mm

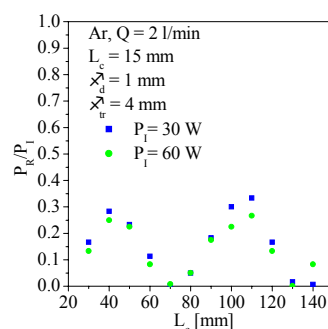


Fig. 7. Influence of length L_c on the reflection coefficient P_R/P_I for different incident microwave powers $P_I = 30$ W and $P_I = 60$ W. The diameter of the wire inside the quarter-wave transformer $\phi_{tr} = 4$ mm. The length above the outer conductor of the inner conductor $L_c = 15$ mm

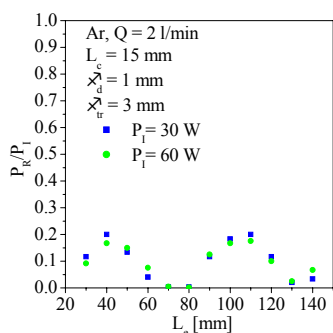


Fig. 8. Influence of length L_c on the reflection coefficient P_R/P_I for different incident microwave powers $P_1 = 30$ W and $P_1 = 60$ W. The diameter of the wire inside the quarter-wave transformer $\phi_{tr} = 3$ mm. The length above the outer conductor of the inner conductor $L_c = 15$ mm

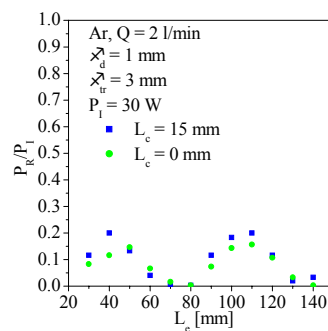


Fig. 11. Influence of length L_c on the reflection coefficient P_R/P_I for different lengths L_c ($L_c = 15$ mm and $L_c = 0$ mm). The diameter of the wire inside the quarter-wave transformer $\phi_{tr} = 3$ mm. Microwave power $P_1 = 30$ W

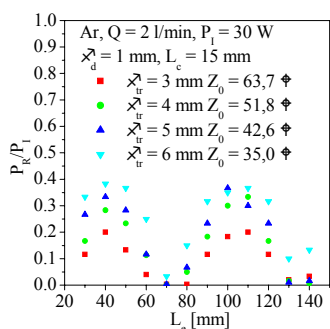


Fig. 9. Influence of length L_c on the reflection coefficient P_R/P_I for different diameters of the wire inside the quarter-wave transformer ϕ_{tr} . The microwave power $P_1 = 30$ W. The length above the outer conductor of the inner conductor $L_c = 15$ mm. The diameter of the inner conductor $\phi_d = 1$ mm

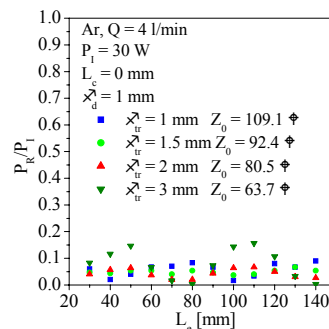


Fig. 12. Influence of length L_c on the reflection coefficient P_R/P_I for different diameters of the wire inside the quarter-wave transformer ϕ_{tr} . The length $L_c = 0$ mm. The diameter of the inner conductor $\phi_d = 1$ mm. Microwave power $P_1 = 30$ W

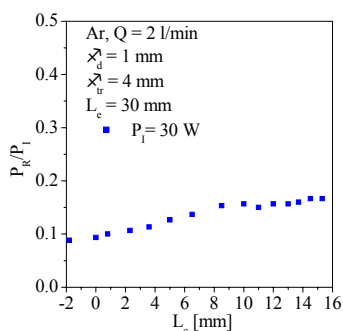


Fig. 10. Influence of the length above the outer conductor of the inner conductor L_c on the reflection coefficient P_R/P_I . The diameter of the wire inside the quarter-wave transformer $\phi_{tr} = 4$ mm. Microwave power $P_1 = 30$ W

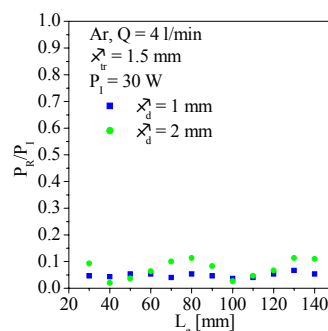


Fig. 13. Influence of length L_c on the reflection coefficient P_R/P_I for different diameters of the inner conductor ϕ_d . ($\phi_d = 1$ mm and $\phi_d = 2$ mm). The length $L_c = 0$ mm. Microwave power $P_1 = 30$ W

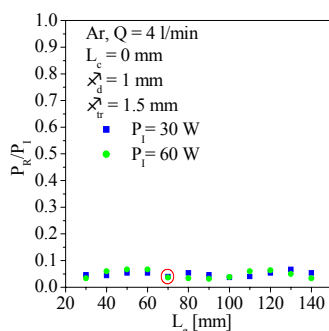


Fig. 14. Influence of length L_c on the reflection coefficient P_R/P_I for different incident powers ($P_I = 30$ W and $P_I = 60$ W) The diameters of the inner conductor $\phi_d = 1$ mm. The diameter of the wire inside the quarter-wave transformer $\phi_{tr} = 1.5$ mm. The length $L_c = 0$ mm.

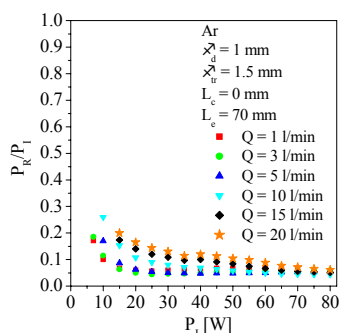


Fig. 15. The reflection coefficient P_R/P_I versus incident microwave power for different argon flow rates Q for optimized $\phi_d = 1$ mm, $\phi_{tr} = 1.5$ mm and $L_c = 0$ mm

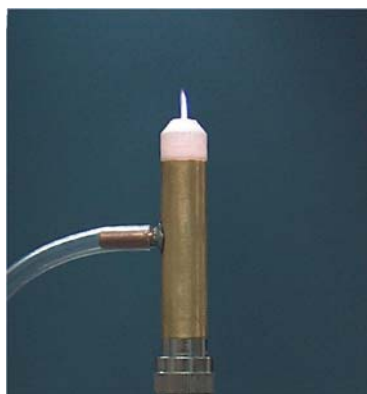


Fig. 16. Photo of the optimized coaxial MMS with atmospheric pressure argon microplasma

reflection coefficient P_R/P_I for two values of L_c ($L_c = 15$ mm and $L_c = 0$ mm) was shown.

Basing on the results presented in Fig. 10 and 11, we chose a length $L_c = 0$ as optimum.

Fig. 12 shows the influence of length L_c on the reflection coefficient P_R/P_I for different diameters of the wire inside the quarter-wave transformer ϕ_{tr} for the fixed length $L_c = 0$ and diameter $\phi_d = 1$ mm.

As seen, the best impedance matching was achieved when the diameter of the wire inside the quarter-wave transformer ϕ_{tr} was equal to 1.5 mm.

The dependence of reflection coefficient P_R/P_I on length L_c , shown in Fig. 13, indicates that the optimum diameter of the inner conductor ϕ_d is 1 mm.

Fig. 14 shows the influence of length L_c on the reflection coefficient P_R/P_I for different incident powers P_I ($P_I = 30$ W and $P_I = 60$ W) for the optimum diameter of the inner conductor ϕ_d ($\phi_d = 1$ mm), diameter of the wire inside the quarter-wave transformer ϕ_{tr} ($\phi_{tr} = 1.5$ mm) and the length L_c above the outer conductor of the inner conductor ($L_c = 0$ mm).

As seen, characteristics are almost independent on the incident microwave power P_I and the length of the outer conductor L_c . It is very important advantage when industrial applications are considered.

Fig. 15 shows the reflection coefficient P_R/P_I versus the incident microwave power P_I for different argon flow rates Q for optimized ϕ_d , ϕ_{tr} and L_c . As seen, the better matching was achieved at lower argon flow rates.

Fig. 16 shows the photo of the optimized coaxial MMS with atmospheric pressure argon microplasma.

Anti-bacteria UVB radiation emitted by the argon microplasma was from 10 to 45 mW m⁻², depending on the discharge conditions (UVB probe was located 7 cm from the plasma region).

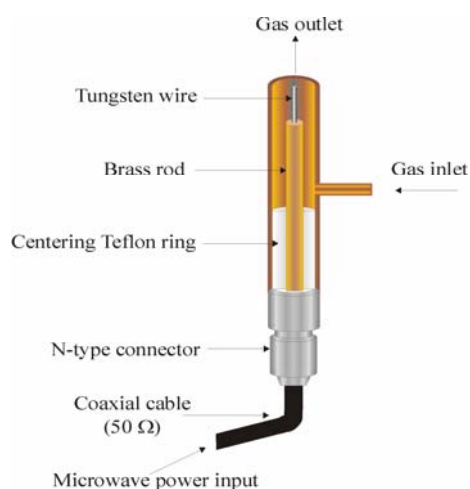


Fig. 17. Coaxial MMS operated in nitrogen at atmospheric pressure

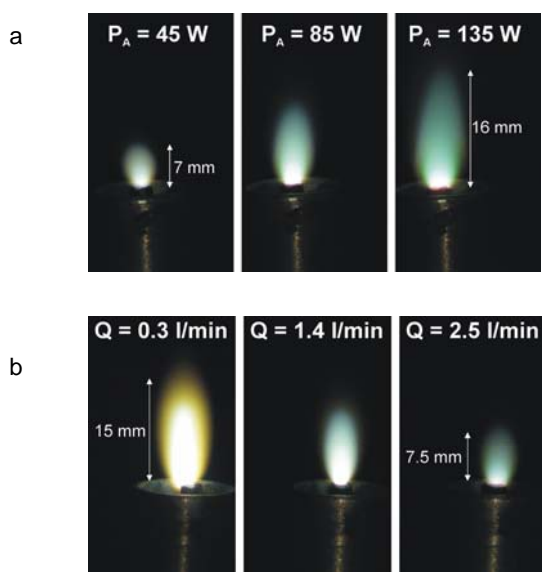


Fig. 18. The photos of N_2 microplasmas for different absorbed microwave powers (a) and N_2 flow rates (b)

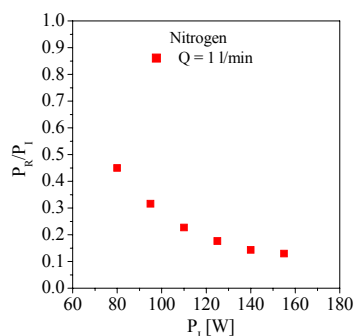


Fig. 19. The reflection coefficient P_R/P_I versus incident microwave power at N_2 flow rates $Q = 1 \text{ l min}^{-1}$

2.2. Microwave microplasma source operated in nitrogen at atmospheric pressure

In this investigation nitrogen at atmospheric pressure was used as a working gas. The nitrogen flow rates varied from 0.3 to 3 l min^{-1} . The absorbed microwave power was from 40 to 140 W .

The sketch of the nitrogen MMS and the photos of N_2 microplasmas are shown in Fig. 17 and 18, respectively.

Anti-bacteria UVB radiation emitted by the N_2 microplasma was from 20 to 2000 mW m^{-2} , depending on the discharge conditions (UVB probe was located 7 cm from the plasma region).

The reflection coefficient P_R/P_I was relatively high, i.e. from 15 to 45% (Fig. 19), depending on the discharge conditions, so geometry of the presented MMS should be optimized for operation in nitrogen.

3. Conclusions

The simplicity of the MMSs, operation stability and parameters of the microplasma allows the conclusion that the presented MMSs can find practical applications in various fields. The anti-bacteria UVB radiation measured close to the microplasmas proves that microplasma can indeed be used for tissue and material treatment.

This research was supported by the Ministry of Science and Higher Education (MNiSW) under the programme 0895/B/T02/2007/33.

REFERENCES

- Kim J., Terashima K.: Proc. APSPT 4, 324 (2005).
- Yoshiki H.: Jpn. J. Appl. Phys. 45, 5618 (2006).
- Iza F., Hopwood J.: Plasma Sources Sci. Technol. 14, 397 (2005).
- Kikuchi T., Hasegawa Y., Shirai H.: J. Phys. D: Appl. Phys. 37, 1537 (2004).
- Stonies R., Schermer S., Voges E., Broekaert J. A. C.: Plasma Sources Sci. Technol. 13, 604 (2004).
- Bilgic A. M., Engel U., Voges E., Kuckelheim M., Broekaert J. A. C.: Plasma Sources Sci. Technol. 9, 1 (2000).
- Iza F., Hopwood J. A.: IEEE Trans. Plasma Sci. 32, 2 (2004).
- Iza F., Hopwood J. A.: IEEE Trans. Plasma Sci. 31, 4 (2003).
- Stalder K. R., McMillen D. F., Woloszko J.: J. Phys. D: Appl. Phys. 38, 1728 (2005).
- Sladek R. E. J., Stoffels E.: J. Phys. D: Appl. Phys. 38, 1716 (2005).
- Becker K. H., Kogelschatz U., Schoenbach K. H., Barker R. J., ed.: *Non-Equilibrium Air Plasmas at Atmospheric Pressure*, chapter 9. IOP Published Ltd, Bristol 2004.
- Goch M., Jasiński M., Zakrzewski Z., Mizeraczyk J.: Czech. J. Phys. 56, 795 (2006).

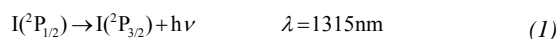
PLASMACHEMICAL GENERATION OF ATOMIC IODINE FOR IODINE LASERS PUMPED BY SINGLET OXYGEN

VÍT JIRÁSEK*, JOSEF SCHMIEDBERGER, MIROSLAV ČENSKÝ, IRENA PICKOVÁ, JARMILA KODYMOVÁ, and OTOMAR ŠPALEK

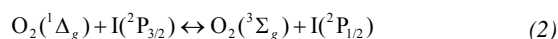
*Institute of Physics, Academy of Sciences CR, Na Slovance 2, 182 21 Prague 8, Czech Republic
jirasek@fzu.cz*

1. Introduction

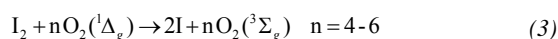
The oxygen-iodine laser is a promising candidate for future challenging technologies, like the decommissioning and dismantling of closed nuclear facilities, raw materials mining and military applications¹. The laser radiates on the magnetic dipole transition of iodine atom between the first electronically excited state and ground state



The excited iodine atom (the upper laser level) is populated by a nearly resonant energy transfer from the electronically excited molecular oxygen in the singlet delta state $O_2(^1\Delta_g)$ to iodine atom



The atomic iodine is usually produced by the dissociation of molecular iodine which consumes energy of several $O_2(^1\Delta_g)$ molecules



An alternative way of atomic iodine generation may save $O_2(^1\Delta_g)$ for significant enhancement of the laser efficiency. The operation of oxygen-iodine laser requires the following properties of iodine generator: high yield of atomic iodine, low temperature and sufficiently high pressure to inject produced iodine into the laser cavity. The reactants and reaction products also must not quench excited oxygen or iodine.

The chemical methods and electric discharge methods have been investigated for atomic iodine production without the need of singlet oxygen. The chemical methods yielded sufficient amount of iodine but they suffered from chemicals seriously quenching singlet oxygen or from very high reaction temperature². The survey of hitherto studied discharge dissociation of iodine donors was given in ref³. The fulfillment of all above mentioned requirements has not been achieved till now. The enhancement of laser performance using the dis-

charge dissociation of I_2 was achieved only at conditions far from optimal for the efficient laser operation³.

We suggested a generation of atomic iodine by the RF discharge dissociation of iodine donors directly inside a cooled iodine injector with a subsequent immediate supersonic injection into the laser cavity. The experimental study of the first version of the proposed discharge generator is a subject of this paper.

2. Experimental

The scheme of the apparatus is shown in Fig. 1. The injector is made of pure aluminum (99.5% Al, A1050).

A middle channel of inner diameter 9 mm is the discharge chamber and simultaneously the iodine injector. Axially inserted RF wolfram electrode has 2 mm in diameter. The left and right holes (channels) of inner diameter 5 mm serve for introducing cooling water. The injector shape was calculated by means of 2-D and 3-D modeling to form the supersonic double-slit nozzle.

Alkyl iodides CH_3I (>99 %, Fluka) and CF_3I (99 %, Sigma Aldrich) were used as the iodine donors. The iodide was mixed with He (99.996 %) and Ar (99.998 %) and then introduced to the injector. The flow rate of iodide was measured by a calibrated sonic orifice. The flow rates of buffer gases were determined by measurement of pressure prior and behind a needle valve. The needle valve (Swagelok comp.) has precisely defined opening by a screw micrometer which enables to change the range of measured flow rates. Each needle valve – flow meter for particular buffer gas was calibrated by means of an appropriate mass flow meter.

The RF power source (PEARL KOGYO Co., Ltd, Osaka, Japan, model CF-500-20/100M) is a wideband tunable cw/pulse radiofrequency generator with oscillating frequency

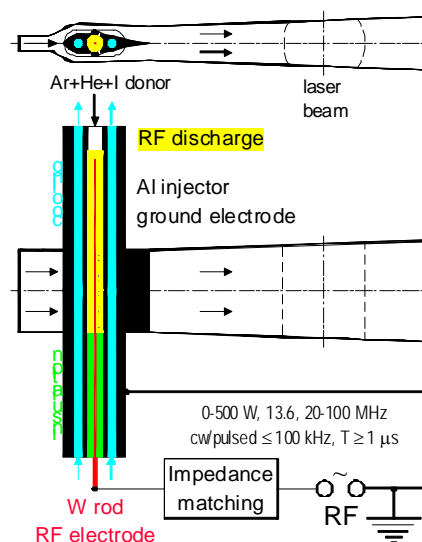


Fig. 1. Scheme of the experimental set-up

20–100 MHz, output power ≤ 500 W and a possibility of repetitively pulsed mode with the repetition rate of 100–99 kHz and pulse duty ratio of 5–95 %.

The Iodine Scan Diagnostics (ISD, Physical Science Inc., USA) based on a narrow band tunable diode probe laser was used for determination of atomic iodine concentration and temperature⁴ in the cavity by measuring the absorption for the $I(^2P_{1/2}) - I(^2P_{3/2})$ transition at 1315 nm. The ISD probe beam emitter/detector unit was mounted on the assembly of motorized linear positioning equipment controlled by PC. Atomic iodine concentration and temperature measured in the expansion cavity perpendicularly or along the injector were used to evaluate the partial pressure of atomic iodine using the formula:

$$p_I = \frac{1}{y_2 - y_1} \int_{y_1}^{y_2} c_I(y) RT(y) dy \quad (5)$$

where $c_I(y)$, $T(y)$ are evaluated number density and temperature and y is the position in direction perpendicular of along the injector. Then the dissociation fraction is

$$\eta_{diss} = \frac{p_I}{p_{cav}} \frac{\dot{n}}{n_{CH_3I}} \quad (6)$$

where $\dot{n} = \dot{n}_{Ar} + \dot{n}_{He} + \dot{n}_{N_2} + \dot{n}_{CH_3I}$ is the total gas flow rate and p_{cav} is the pressure in the detection cavity.

3. Continuous-wave discharge mode

In a continuous-wave operation, 40 MHz RF power in the range of 50–250 W was used to dissociate the iodides. The discharge was stable in this power range and at pressure inside the injector of 2–3 kPa. The gas flow leaving the discharge was injected into the flow of 10–37 mmol s⁻¹ of N₂. Although the future laser operation will require supersonic flow, most of the experiments were done under higher, sub-

sonic pressures, in order to increase the signal from the absorption measurement. In Fig. 2, the dependence of the dissociation fraction on the absorbed power and CH₃I flow rate is shown.

The linear dependence of η_{diss} on the power indicates that the energetic efficiency was constant with increasing power. This efficiency was evaluated as a fraction of the ab-

$$fP_{diss} = \frac{P_{diss}}{P_{abs}} = \frac{eN_I E_{bond}}{P_{abs}} \quad (7)$$

sorbed power consumed on the dissociation

where E_{bond} is the dissociation energy of C-I bond (2.47 eV/molec for CH₃I, and 2.34 eV/molec for CF₃I), N_I is the evaluated flow rate of generated iodine atoms (in at/s) and e is the electric charge of electron. The fP_{diss} value was 5–7 % for flow rates 0.2–0.5 mmol s⁻¹ but increased to 10 % at 0.73 mmol s⁻¹ of CH₃I. The analogous dependence for CF₃I dissociation is shown in Fig. 3.

The dissociation fraction was a bit lower than for CH₃I at similar conditions, but increased significantly (from 8 % to 15 % at 0.5 mmol s⁻¹ CF₃I) when 3.1 mmol s⁻¹ of Ar was used instead of the mixture of 1.9 Ar + 1.9 He. At higher flow rates of CF₃I, a sparking instability destroyed the discharge at RF power > 150 W.

The optimization of Ar and He flow rates was done with 0.51 mmol s⁻¹ of CH₃I and 138 W of RF power. A slight maximum is apparent in Fig. 4 at the ratio Ar : CH₃I = 3.5 : 1. The dissociation fraction also slightly decreased with increasing He flow rate at constant Ar flow rate – see Fig. 5. These results were achieved at relatively high pressure in the expansion cavity (700–800 Pa in case of CH₃I and 500–600 Pa in case of CF₃I). However, strong pressure dependence was obtained for CF₃I, as can be seen in Fig. 6. The dissociation fraction strongly increased with decreasing cavity pressure.

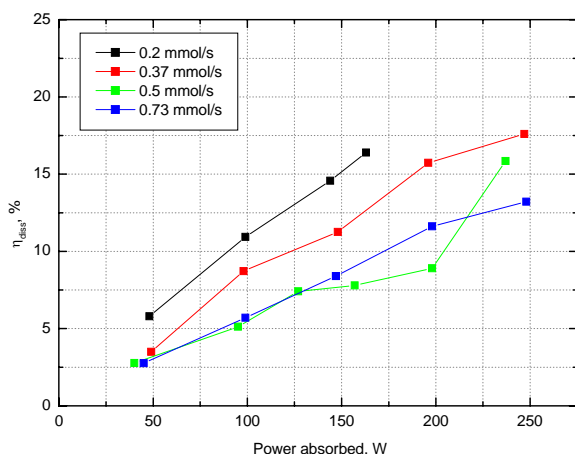


Fig. 2. Dependence of CH₃I dissociation fraction on the absorbed RF power and CH₃I flow rate, measured 137 mm downstream the injector outlet. $p_{cav} = 560\text{--}780$ Pa; 1.9 mmol s⁻¹ Ar, 1.9 mmol s⁻¹ He

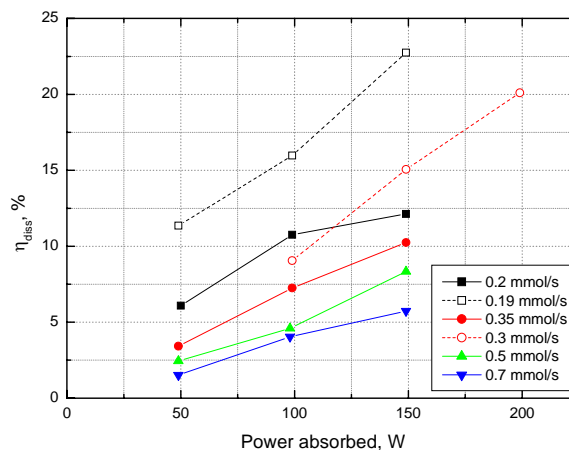


Fig. 3. Dependence of CF₃I dissociation fraction on the absorbed RF power and CH₃I flow rate, measured 137 mm downstream the injector outlet. $p_{cav} = 480\text{--}540$ Pa; flow rates (mmol/s): 1.9 Ar (solid lines) or 3.1 Ar (dashed line); 1.9 He (solid) or 0 He (dashed)

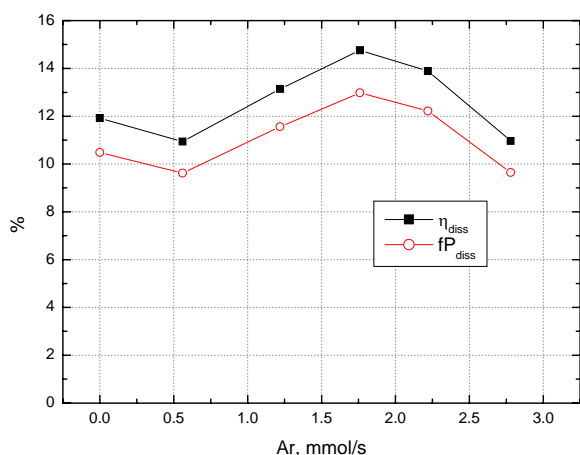


Fig. 4. Dependence of CH_3I dissociation fraction (η_{diss}) and the fraction of power consumed on the dissociation (fP_{diss}) on the Ar flow rate in the absence of He, measured 87 mm downstream the injector outlet. $p_{cav} = 600\text{--}650$ Pa; 0.51 mmol s^{-1} CH_3I , 138 W

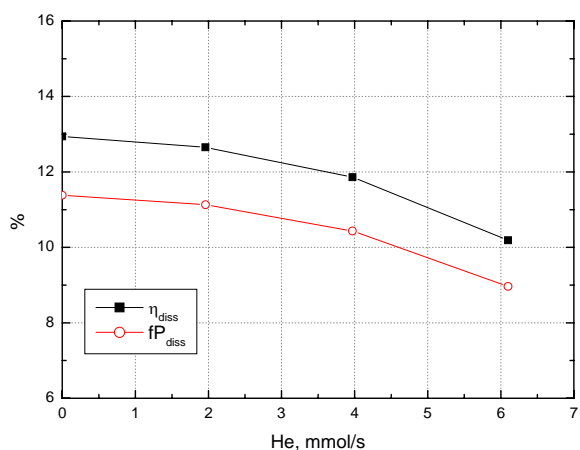


Fig. 5. Dependence of CH_3I dissociation fraction (η_{diss}) and the fraction of power consumed on the dissociation (fP_{diss}) on the He flow rate, measured 87 mm downstream the injector outlet. $p_{cav} = 560\text{--}670$ Pa; 0.51 mmol s^{-1} CH_3I , 1.15 mmol s^{-1} Ar, 138 W

This effect was attributed to the three-body recombination reaction:



which is highly accelerated at elevated pressure. The rate constant reported for the reaction (7) is very large⁵, $k = 1.3 \cdot 10^{-28}$ cm⁶ s⁻². Similar rate constant for CH_3I was not found in the literature, but no significant dependence of CH_3I dissociation fraction on pressure or distance from the injector was observed in our measurement. Therefore, we believe that the best obtained value of 17 % at 0.37 mmol s^{-1} of CH_3I and at the power of 250 W corresponds to the atomic iodine produced in the discharge region itself.

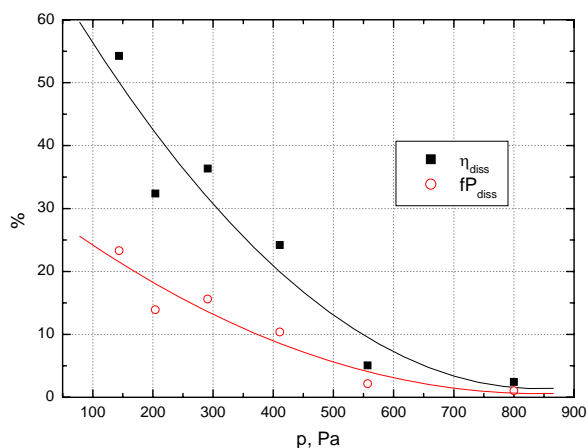


Fig. 6. Dependence of CF_3I dissociation fraction (η_{diss}) and the fraction of power consumed on the dissociation (fP_{diss}) on the cavity pressure, measured 102 mm downstream the injector outlet. 0.28 mmol s^{-1} CF_3I , 3.1 mmol s^{-1} Ar, 21 mmol s^{-1} N_2 , 147 W

The integral cross-section for the dissociative electron attachment on CH_3I is 4 times smaller than for CF_3I ^{6,7}. This is probably one reason for its worse dissociation fraction in the discharge.

Temperatures evaluated from the ISD measurement were in the range of $320\text{--}420$ K in most of the experiments. However, it was found that the higher the dissociation fraction, the higher temperature. Thus at low pressure in case of CF_3I , where the η_{diss} is large, temperature is also high despite the supersonic cooling effect. The temperature dependence on the generated iodine may be explained by the exothermic recombination reactions:



The reaction heat is -375.2 kJ mol⁻¹ for reaction (8) and -402 kJ mol⁻¹ for reaction (9) and the corresponding rate constants are $4 \cdot 10^{-11}\text{--}6 \cdot 10^{-11}$ cm³ s⁻¹ and $3 \cdot 10^{-11}\text{--}10^{-10}$ cm³ s⁻¹, respectively⁸.

Table I illustrates an influence of different parameters on the generation of iodine atoms.

4. Repetitively pulsed discharge mode

In the experiments with a repetitively pulsed mode, a 40 MHz RF power supply was periodically switched on and off with a repetition rate from 0.7 kHz to 99 kHz. A pulse duty ratio (ratio between “on” time and “off” time in the period) was changed from 10 to 100 %. A systematic study of the influence of the repetition rate and pulse duty ratio on the atomic iodine number density at the cavity center, 47 mm from the injector, was done. The dependence on the repetition

Table I

Influence of different parameters on the generation of iodine atoms. x_{inj} is a distance of the detection point from the injector outlet

x_{inj} [mm]	CH ₃ I	Ar	He	N ₂	p_{cav} [Pa]	P_{abs} [W]	η_{diss} [%]	fP_{diss} [%]	T [k]
137	0.76	1.95	1.92	37.7	140	252	12.5	9.1	240
137	0.74	1.98	1.90	20.7	808	250	13.2	9.4	375
87	0.51	1.15	0.00	21.5	578	150	12.9	11.4	411
87	0.51	1.15	6.10	21.5	693	150	10.2	9.0	338
87	0.51	1.76	0.00	21.5	599	150	14.8	13.0	401
87	0.51	0.00	0.00	21.5	550	150	11.9	10.5	422
x_{inj}	CF ₃ I	Ar	He	N ₂	p_{cav}	P_{abs}	η_{diss}	fP_{diss}	T
57	0.58	2.17	0.00	21.3	604	148	9.8	8.7	418
87	0.58	2.17	0.00	21.3	604	148	4.4	3.9	367
102	0.28	3.10	0.00	21.1	411	147	24.2	10.4	481
102	0.28	3.10	0.00	21.1	557	147	5.1	2.2	267
102	0.28	3.10	0.00	21.1	800	147	2.5	1.1	280
137	0.31	3.09	0.00	20.5	505	149	15.1	7.0	353

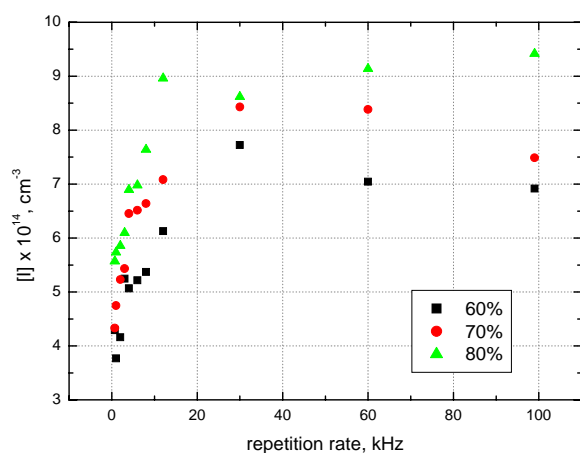


Fig. 7. Dependence of I number density on the repetition rate for 3 values of pulse duty ratio, measured 47 mm downstream the injector outlet. $p_{cav} = 960$ Pa, 0.72 mmol s⁻¹ CH₃I, 2.3 mmol s⁻¹ Ar, 237 W

frequency for three values of the pulse duty ratio is shown in Fig. 7 in the case of CH₃I dissociation.

There is a very weak maximum around 30 kHz and the number density strongly falls at rate < 4 kHz. Such low rates correspond in an order of magnitude with the gas residence time in the injector, which is around 1 ms. In the case of CF₃I, the repetition rates higher than 10 kHz were used only, since the discharge was unstable at lower rates. The dependence is non-trivial and is shown in Fig. 8.

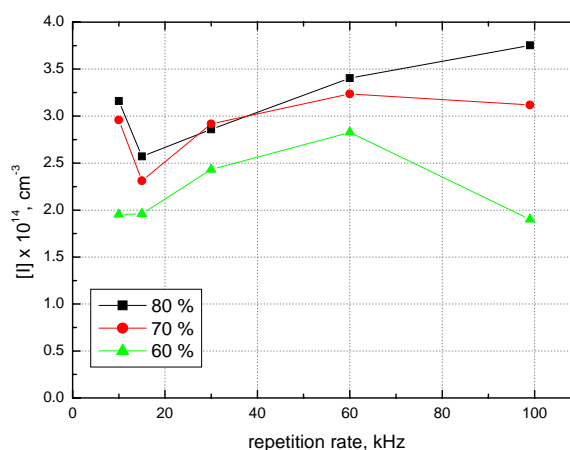


Fig. 8. Dependence of I number density on the repetition rate for 3 values of pulse duty ratio, measured 47 mm downstream the injector outlet. $p_{cav} = 930$ Pa, 0.5 mmol s⁻¹ CF₃I, 2.2 mmol s⁻¹ Ar, 197 W

In several cases, the iodine atom number densities and temperatures along the injector were measured and the dissociation fraction and efficiency fP_{diss} were evaluated. These quantities were not higher than in the experiments with CW mode. The fP_{diss} value was evaluated using the mean absorbed power $P_{mean} = P_{abs}/\text{pulse duty ratio}$. This quantity was nearly independent on the pulse duty ratio in the range 50–90 %, but it strongly decreased at p.d. < 40 % for both iodine donors and independently on the repetition rate.

It was found that the discharge in CF₃I could be operated without sparking effects up to 350 W, contrary to the CW

mode, where the upper limit was 150 W. The sparking instability had not sufficient build-up time in the pulsed mode and the discharge appeared stable.

5. Conclusions

The RF discharge dissociation of CH_3I and CF_3I was studied experimentally. This work was aimed at developing an alternative method of atomic iodine generation for the oxygen-iodine laser. The discharge was ignited in the mixture of alkyl iodide and $\text{Ar} + \text{He}$ at 2–3 kPa, which was then injected to the low pressure flow of nitrogen. A maximum dissociation fraction of CH_3I was 17 % at the flow rate of 0.72 mmol s^{-1} . A maximum dissociation fraction of CF_3I was 54 % at the flow rate of 0.28 mmol s^{-1} and lowered pressure. The discharge was more stable in a repetitively pulsed mode than in the CW mode, but the iodine generation efficiency was similar in both modes.

This work has been supported by the US Air Force European Office of Aerospace Research and Development (EOARD) under the Grant # FA8655-06-1-3034.

REFERENCES

1. Kodymová J.: Proc. SPIE 6346, 634609 (2006).
2. Jirásek V., Špalek O., Čenský M., Picková I., Kodymová J., Jakubec I.: Chem. Phys. 334, 167 (2007).
3. Schmiedberger J., Jirásek V., Kodymová J., Rohlena K.: CD Proc. AIAA Plasmadynamics and Lasers Conference, Miami FL, 2007, (ed. American Institute of Aeronautics and Astronautics), AIAA Paper 2007–4239. Miami 2007.
4. Tate R. F., Hunt B. S., Helms C. A., Truesdell K. A., Hager G. D.: IEEE J. Quant. Electronics 31, 1632 (1995).
5. Velichko A. M., Gordon E. B., Nadelkin A. A., Nikitin A. I., Tal'roze V. L.: High Energy Chem. 19, 138 (1985).
6. Nagesha K., Marathe V. R., Krishnakumar E.: Int. J. Mass Spectrom. Ion Processes 145, 89 (1995).
7. Christophorou L. G., Olthoff J. K.: J. Phys. Chem. Ref. Data 29(4), 553 (2000)
8. NIST Chemical Kinetics Database on The Web, <http://kinetics.nist.gov/>

HYDROGEN PRODUCTION VIA METHANE REFORMING USING VARIOUS MICROWAVE PLASMA SOURCES

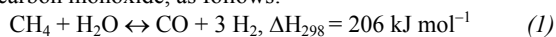
MARIUSZ JASIŃSKI^{a,*}, MIROSLAW DORS^a,
HELENA NOWAKOWSKA^a, and JERZY
MIZERACZYK^{a,b}

^a Centre for Plasma and Laser Engineering, The Szwedzki Institute of Fluid-Flow Machinery, Polish Academy of Sciences, Fiszera 14, 80-952 Gdańsk, ^b Dept. of Marine Electronics, Gdynia Maritime University, Morska 83, 81-225 Gdynia, Poland
mj@imp.gda.pl

1. Introduction

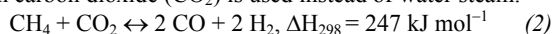
Methane or natural gas reforming is widely used in industry to obtain hydrogen or synthesis gas (H₂+CO), which are utilized in industry, for example as source materials for the production of raw chemicals (e.g. methanol and ammonia), as well as hydrogenation agents in oil refinery and reducing gases in steel industry. Recently hydrogen gains in importance as fuel in fuel cell applications, combustion engines or gas turbines with the goal to achieve more efficient exploitation of energy sources and to reduce noxious emissions¹.

The conventional reforming of methane is carried out thermally using water steam and oxygen. In this process, oxidation of methane provides heat that is necessary for performing the endothermic methane reforming reaction using steam. The steam methane reforming yields a mixture of hydrogen and carbon monoxide, as follows:

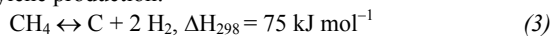


where ΔH_{298} is a standard reaction enthalpy.

Similar process, named the partial oxidation, occurs when carbon dioxide (CO₂) is used instead of water steam:



Hydrogen may be also produced in the process of methane pyrolysis, which is, however, often accompanied with acetylene production:



Since reactions (1) and (2) are highly endothermic, to decrease the activation energy, a catalyst (usually Ni/Al₂O₃ working at temperature 1100–1150 K) is used. This methane reforming method is sensible to impurities in substrates which deactivate the catalyst.

The other conventional technologies of hydrogen production, i.e. coal gasification, hydrocarbon reforming and water electrolysis, are too expensive or not applicable for specific applications (e.g. for fuel cells) due to technical reasons. Thus, new methods for hydrogen production are under development, such as water photolysis, and biological and plasma methods.

One of attracting methods for reforming hydrocarbons to produce hydrogen is the use of plasmas^{1–10}. The plasma con-

tains reactive radicals, ions and high-energetic electrons. High reactivity shown by these species enhances the chemical reaction rates whereby expensive and impurity vulnerable catalysts can be avoided. This plasma capability as well as its high energy density ensure the compactness of the plasma system. Besides, the plasma system can be adapted for reforming various hydrocarbons, such as natural gas, gasoline, heavy oils and biofuels. Another advantage is the fast response time that can be achieved because the plasma is operated by electricity. When water steam is used as the plasma supporting gas, reductive and oxidative radicals such as H, OH, and O, are produced in the plasma, enabling the plasma to be effective for reforming different hydrocarbons.

Recently developed microwave plasma sources (MPSs) operated at atmospheric pressure^{5,10–14} seem to have a high potential for hydrogen production via hydrocarbon reforming. The microwave plasma at atmospheric pressure is one of the plasma techniques providing the electron temperature of 4000–10 000 K, and the heavy particle temperature of 2000–6000 K (ref.^{12–14}). Such properties of microwave plasma provide proper conditions for methane reforming.

In this paper results of investigations on the usefulness of several microwave plasma methods for hydrogen production via methane reforming are presented. The microwave plasma methods employed are:

- steam reforming of methane using a low flow rate nozzle-type MPS;
- reforming of methane using high flow rate coaxial-type MPSs (three versions A, B, and C) supplied through either a rectangular waveguide WR 284 or rectangular waveguide WR 430. In both high flow rate coaxial-type MPSs an additional swirl flow, N₂ or CO₂, was used;
- reforming of methane using high flow rate cylinder-type MPS supplied through a rectangular waveguide WR 430. The only gas used in this MPS was methane delivered as a swirl.

2. Experimental set-up

The main components of the experimental setup were 2.45 GHz magnetron generator (operated in a continuous mode), waveguide based microwave plasma source (MPS), plasma reactor in the form of quartz tube, microwave power supplying and measuring systems, gas supplying and flow control systems, Fourier Transform Infrared (FTIR) spectrophotometer for gas analysis and gas chromatograph for hydrogen concentration measurement.

2.1. Low flow rate nozzle-type MPS

When steam reforming of methane using a low flow rate nozzle-type MPS was carried out, a MPS was based on a TI-AGO (Torche a Injection Axiale sur Guide d'Ondes) concept disclosed by Moisan et al¹¹ (Fig. 1). The microwave power (200–750 W) was fed to the plasma generator directly by a standard rectangular waveguide. The other end of the waveguide was terminated with a movable plunger, used for the impedance matching. The plasma was generated in the form of a „plasma flame“ at the end of the nozzle, that protruded from the waveguide directly into the reactor. The

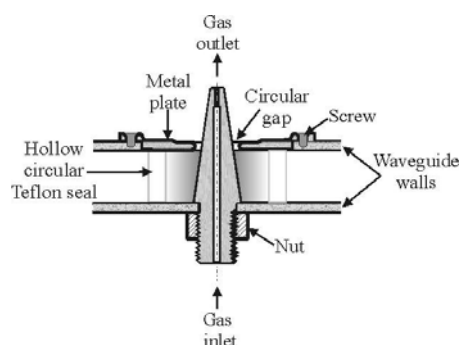


Fig. 1. Sketch of the nozzle-type MPS operated at low gas flow rate

working gas [Ar (97–96 %) + CH₄ (1–2 %) + H₂O (2 %)] at atmospheric pressure flowed through the nozzle at a flow rate of 2–4 l min⁻¹ and 25 l min⁻¹, forming the plasma flame above the nozzle.

2.2. High flow rate coaxial-type MPSs – versions A, B, and C

When methane reforming using high flow rate coaxial-type MPSs was performed then three versions (A, B, and C) of coaxial-type MPS were tested. In these MPSs, on contrary to previous MPSs operating at atmospheric pressure, there was not any nozzle. Instead, the plasma was generated straightforward inside a quartz cylinder. The plasma generation was stabilized by forming an additional gas swirl flow (up to 100 l min⁻¹) in the quartz cylinder. The gas swirl held the plasma in the centre of the cylinder, protecting the cylinder wall from overheating.

In the first version (called version A), rectangular waveguide WR 284 was used to deliver microwave power to a coaxial microwave module, where the plasma was generated

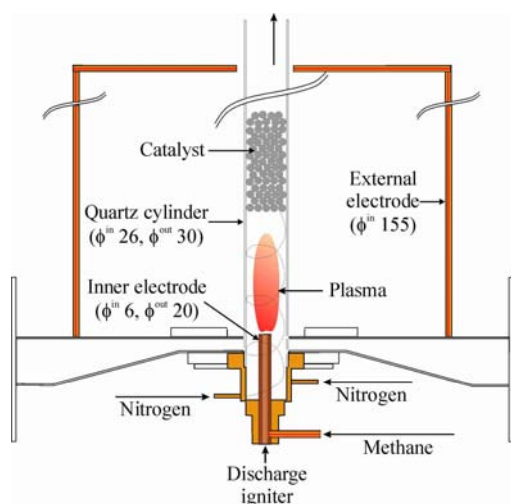


Fig. 2. Sketch of the high flow rate waveguide-based coaxial-type MPS (with a wide external electrode). Version A

(Fig. 2). The coaxial module had a wide external electrode with an inner diameter of 155 mm. The flow rate of methane (axial flow) and nitrogen (swirl flow) were up to 175 l min⁻¹ and 50 or 100 l min⁻¹, respectively. The microwave power absorbed was up to 5000 W. Version A of the high flow rate coaxial-type MPS was used for hydrogen production via methane reforming both without catalyst and with catalyst.

In the version of high flow rate coaxial-type MPS called version B, the coaxial microwave module was supplied with microwave power through a rectangular waveguide WR 430. (the design similar to version A shown in Fig. 2). This high flow coaxial-type MPS was equipped with a wide external electrode (wider than version A) with an inner diameter of 180 mm. In version B, the plasma generation was stabilized by an additional nitrogen swirl flow (50 or 100 l min⁻¹). The methane flow rate was up to 175 l min⁻¹. The absorbed microwave power was changed from 3000 W to 5000 W. In this

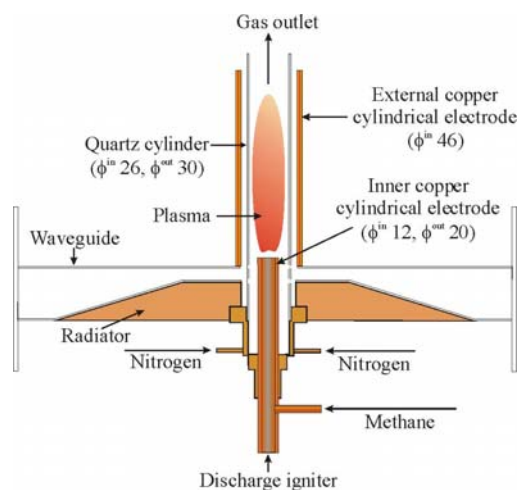


Fig. 3. Sketch of the high flow rate waveguide-based coaxial-type MPS with narrow external electrode. Version C

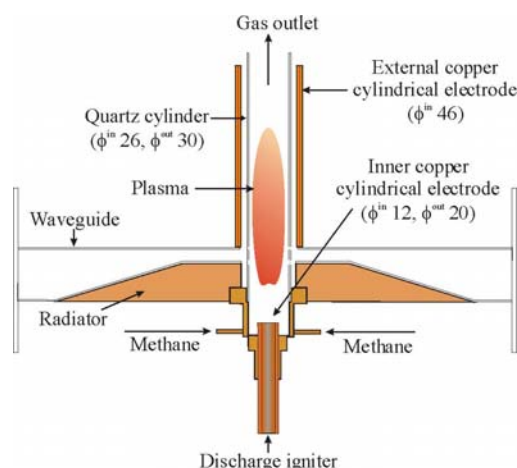


Fig. 4. Sketch of the high flow rate waveguide-based cylinder-type MPS

Table I
Parameters and results of experiments on hydrogen production via methane conversion using MPSs at atmospheric pressure

MPS TYPE	Initial gas composition	Methane flow rate Q_{met} [l min ⁻¹]	Swirl flow rate Q_{swirl} [l min ⁻¹]	Hydrogen mass yield rate [gH ₂ h ⁻¹]	Energetic hydrogen mass yield [gH ₂ kWh ⁻¹]	Methane conversion degree [%]	Selectivity to H ₂ [%]
Low flow rate waveguide-based nozzle-type MPS	CH ₄ + H ₂ O + N ₂	2*	–	0.31	1.56	98.5	91.4
High flow rate coaxial-type MPS, waveguide WR 284, external electrode 155mm, inner electrode 6mm, N ₂ swirl, without catalyst. Version A.	CH ₄ + N ₂	152	100	284	67.6		
High flow rate coaxial-type MPS, waveguide WR 284, external electrode 155mm, inner electrode 6mm, N ₂ swirl, with catalyst. Version A.	CH ₄ + N ₂	152	100	311	76.5		
High flow rate coaxial-type MPS, waveguide WR 430, external electrode 180mm, inner electrode 6mm, N ₂ swirl, without catalyst. Version B.	CH ₄ + N ₂	175	50	222	74	13.2	96.7
High flow rate coaxial-type MPS, waveguide WR 430, external electrode 180mm, inner electrode 6mm, N ₂ swirl, with catalyst. Version B.	CH ₄ + N ₂	175	50	255	85	20.2	97.5
High flow rate coaxial-type MPS, waveguide WR 430, external electrode 46mm, inner electrode 12mm, N ₂ swirl. Version C	CH ₄ + N ₂	175	50	432	280**	25.5	99.2
High flow rate coaxial-type MPS, waveguide WR 430, external electrode 46mm, inner electrode 12mm, CO ₂ swirl, without catalyst. Version C	CH ₄ + CO ₂	175	50	943	605**	58.0	93.6
High flow rate cylinder-type MPS, waveguide WR 430, CH ₄ swirl.	CH ₄	–	87.5	866	381**	99.9	100

* total gas flow rate, initial methane concentration 1 %, ** total electric energy used (the plug efficiency of the microwave magnetron generator was higher than 66 %)

experiment the influence of catalyst was also studied.

Later, we modified the geometry of coaxial microwave module by narrowing its external electrode (to 46 mm in diameter) and increasing the inner diameter of the internal electrode (to 12 mm) (Fig. 3). In this version, called version C, the plasma generation was stabilized by an additional nitrogen swirl (50 l min⁻¹). The methane flow rate was 175 l min⁻¹. The absorbed microwave power could be changed from 1000 W to 5000 W. No catalyst was used when reforming CH₄ using version C.

Also, in version C we used CO₂ to produce the swirl, instead of nitrogen. CO₂ swirl had a flow rate of 50 l min⁻¹. The methane flow rate was 175 l min⁻¹. The absorbed micro-

wave power was 3000 W. No catalyst was used in this experiment.

2.3. High flow rate cylinder-type MPS

Finally, we tested methane reforming using high flow rate cylinder-type MPS. In this MPS only methane was used as the operating gas. The methane was introduced to the plasma in the form of a swirl (87.5 l min⁻¹ or 175 l min⁻¹). The cylindrical microwave module was supplied with microwave power through a rectangular waveguide WR 430 (Fig. 4).

3. Results

Main results of all our experiments on hydrogen production via methane reforming using various MPSs are summarized in Table I.

3.1. Low flow rate nozzle-type MPS

The results of the investigation of hydrogen production via steam reforming of methane using the low flow rate nozzle-type MPS showed that energetic parameters (mass and energetic yields) of hydrogen production are relatively low ($0.31 \text{ g[H}_2\text{]} \text{ h}^{-1}$ and $1.56 \text{ g[H}_2\text{]} \text{ kWh}^{-1}$). Moreover, analysis of the gas composition after the plasma processing showed that methane is converted not only into H_2 but also to CO , CO_2 , H_2O and C_2H_2 . Concentrations of CH_4 and its conversion products (H_2 , CO , and C_2H_2) are presented in Fig. 5. Fig. 5a shows that CH_4 conversion increases with increasing microwave power and decreasing gas flow rate. At a high flow rate of 25 l min^{-1} CH_4 conversion rate is relatively low. Increasing the gas flow rate results in shorter residence time of CH_4 in the plasma, and consequently in a lower conversion of CH_4 . Production of H_2 and CO corresponds to the CH_4 conversion and increase with increasing microwave power and residence time in the plasma (Fig. 5b and c). The highest concentrations

of H_2 (1.8 %) and CO (0.52 %) were measured at 2 l min^{-1} and 400 W.

According to the reaction (1), the amount of CH_4 decomposed in the plasma should be equal to the concentration of CO and to one third of the H_2 concentration. However, our results show that concentrations of CO and H_2 are lower. One of the reasons is production of acetylene (C_2H_2) in the reaction (4). In such a case CO concentration should correspond to the two third of decomposed CH_4 . Indeed, concentrations of CO obtained at gas flow rate of 25 l min^{-1} prove this hypothesis. However, at low gas flow rates, i.e. $2\text{--}4 \text{ l min}^{-1}$, concentrations of H_2 and CO are much lower than expected. Since no soot or other hydrocarbons were found after the plasma processing, we assume that low concentrations of H_2 and CO result from their oxidation to CO_2 and H_2O . Unfortunately, quantitative determination of CO_2 and H_2O concentrations could not be carried out in the experiment.

Concentration of acetylene (C_2H_2), which is produced during CH_4 conversion, is presented in Fig. 5d. At gas flow rate of 2 l min^{-1} and 3 l min^{-1} no C_2H_2 was found regardless the microwave power delivered to the MPS. Detectable production of acetylene starts from 4 l min^{-1} and 300 W and increase with gas flow rate and microwave power. The highest C_2H_2 concentration of 0.038 % was measured at gas flow rate of 25 l min^{-1} and 450 W of microwave power and corre-

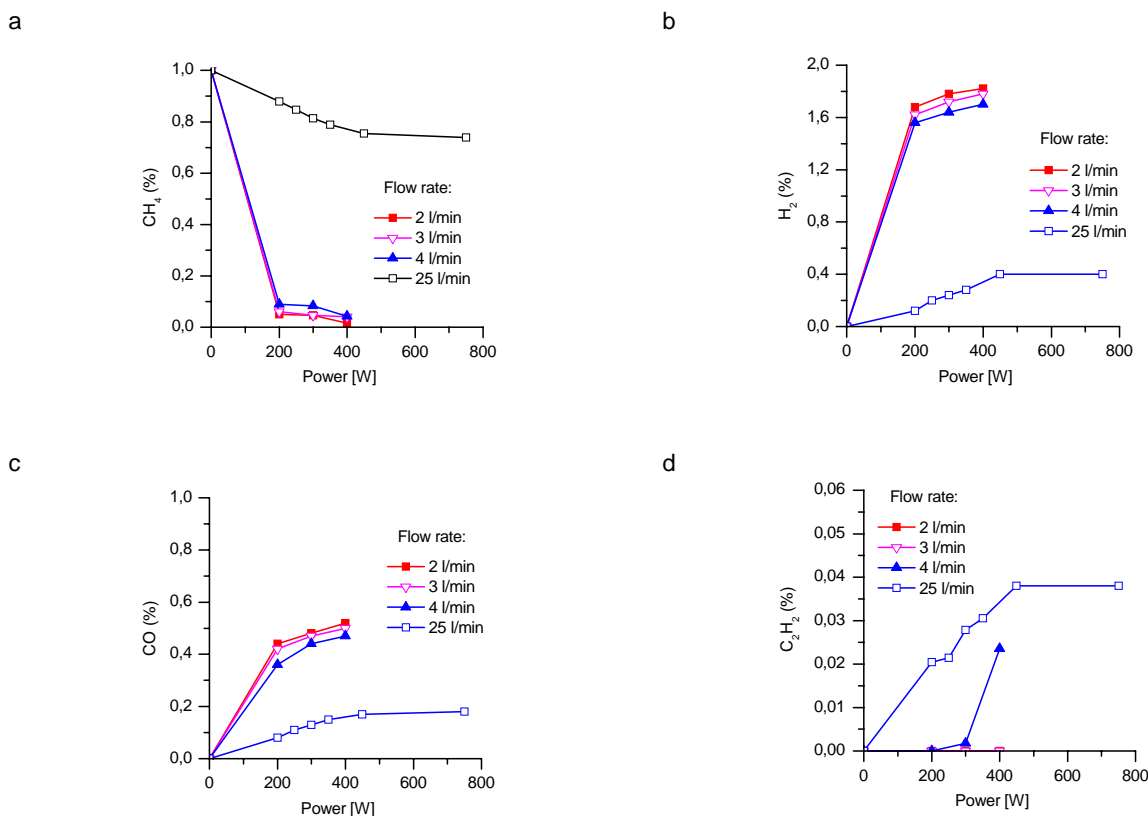


Fig. 5. Low flow rate waveguide-based nozzle-type MPS. Concentrations of CH_4 (a), H_2 (b), CO (c), and C_2H_2 (d) in the outlet gas as a function of microwave power. Initial CH_4 concentration 1 %. Initial $\text{CH}_4\text{:H}_2\text{O}$ ratio 1:2

sponds to the one third of CH_4 decomposed in the reaction (4).

Since the gas exiting the system of low flow rate nozzle-type MPS is a mixture of several compounds, hydrogen must be extracted from the other compounds using a membrane or PSA (Pressure Swing Adsorption) filter. This may be a disadvantage. On the other hand, steam reforming of CH_4 provides high methane conversion degree (98.5 %) and no soot as a solid by-product.

3.2. High flow rate coaxial-type MPSs – version A

When reforming methane into hydrogen using version A of the high flow rate coaxial-type MPS without catalyst, the hydrogen mass yield rate and the corresponding energetic hydrogen mass yield were $284 \text{ g}[\text{H}_2] \text{ h}^{-1}$ and $68 \text{ g}[\text{H}_2] \text{ kWh}^{-1}$, respectively (Tab. I). Catalyst placed in the plasma reactor increased those parameters to $311 \text{ g}[\text{H}_2] \text{ h}^{-1}$ and $77 \text{ g}[\text{H}_2] \text{ kWh}^{-1}$, respectively. Due to the absence of any oxygen in the system no oxides were detected in the exit gas. The only by-products of methane conversion to hydrogen were acetylene (< 1 %) and carbon (soot). The soot deposit could be easily noticed on the reactor walls.

3.3. High flow rate coaxial-type MPSs – version B

The hydrogen mass yield rate and the corresponding energetic hydrogen mass yield when reforming methane using version B of the high flow rate coaxial-type MPS were respectively up to $255 \text{ g}[\text{H}_2] \text{ h}^{-1}$ and $85 \text{ g}[\text{H}_2] \text{ kWh}^{-1}$ (Tab. I). These results correspond to the case with catalyst and are better than those obtained without catalyst. Detailed results are presented in ref.¹⁰.

3.4. High flow rate coaxial-type MPSs – version C

The hydrogen mass yield rate and the corresponding energetic hydrogen mass yield when methane reforming using version C of the high flow rate coaxial-type MPS with N_2 swirl were up to $432 \text{ g}[\text{H}_2] \text{ h}^{-1}$ and $418 \text{ g}[\text{H}_2] \text{ kWh}^{-1}$, respectively.

Energetic parameters of hydrogen production in version C of the MPS with CO_2 swirl were $943 \text{ g}[\text{H}_2] \text{ h}^{-1}$ and $919 \text{ g}[\text{H}_2] \text{ kWh}^{-1}$, respectively. In our experiment, the plug efficiency of the microwave magnetron generator was higher than 66 %, so taking into account this efficiency, the energetic hydrogen mass yield is $605 \text{ g}[\text{H}_2]$ per kWh of electrical energy used (Tab. I). These parameters are better than previous results when nitrogen was used as the swirl gas and much better than those typical of other plasma methods of hydrogen production (e.g. plasmatron², gliding arc⁴, electron beam⁹). However, using CO_2 seems unpractical because of a problem with separation of H_2 from CO_2 and CO (produced in the reforming process) in the off-gas.

As can be seen in Table I methane conversion degree was relatively low when the high flow coaxial-type MPS of version C with N_2 or CO_2 swirl was used. In the case of N_2 swirl it was not higher than 25.5 %. Replacing N_2 with CO_2 increased methane conversion over twice. Such an increase results probably from a lower heat loss since thermal conduc-

tivity of CO_2 is 1.6 times lower than nitrogen. Thus, there was no mixing of CO_2 swirl with methane introduced to the plasma by the central duct of the MPS. This hypothesis is confirmed by the low concentration of CO in the exit gas (0.9 %) showing that reaction of methane partial oxidation (2) had small contribution to the methane conversion into hydrogen. From the significant production of soot one may conclude that methane pyrolysis (reaction 3) was the main process of hydrogen production.

Presence of swirl gas as well as methane conversion by-products, i.e. acetylene and unconverted methane, necessitate to separate hydrogen from other gaseous components using a pressure swing adsorbent (PSA) unit or membrane filter unit. In order to avoid separation process we propose in our last experiment presented in this paper to use methane as the only gas entering the plasma generator.

3.5. High flow rate cylindrical-type MPS

Diagnostics of gas exiting high flow rate coaxial-type MPS supplied with CH_4 swirl only showed that unprocessed methane was found as the only gaseous by-products resulting from methane conversion. The methane decomposed to hydrogen H_2 and carbon (soot). At the power of 1.5 kW and methane flow rate of 87.5 l min^{-1} concentrations of hydrogen and methane were 99.88 % and 0.12 %, respectively, whereas at the power of 5 kW they were 99.94 % and 0.06 %, respectively. Thus, the total methane decomposition degree was 99.76–99.88 %. When methane flow rate was doubled then only half of CH_4 was converted (Fig. 6).

The selectivity of methane conversion to hydrogen was 100%. Such a high selectivity as well as lack of other gaseous by-products and significant production of soot show that reaction of methane pyrolysis (3) was the main path of methane conversion.

The energetic parameters of the hydrogen production via the methane pyrolysis were up to $866 \text{ g}[\text{H}_2] \text{ h}^{-1}$ and $577 \text{ g}[\text{H}_2]$ per kWh of microwave energy absorbed by the plasma, respectively (Fig. 7). When conversion of methane was 100 %

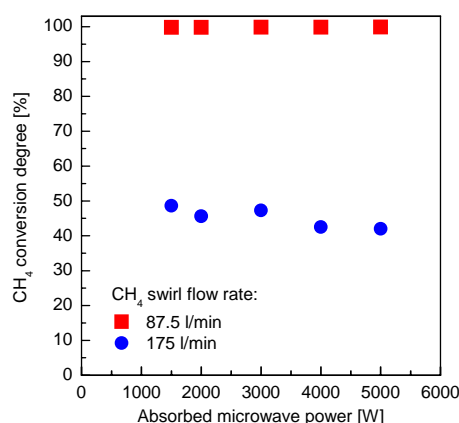


Fig. 6. High flow rate coaxial-type MPS, version C. Methane conversion degree as a function of absorbed microwave power at different methane swirl flow rate

then the hydrogen mass yield rate did not depend on the microwave power. Lower CH_4 conversion degree observed at CH_4 flow rate of 175 l min^{-1} resulted in decreasing hydrogen mass yield rate. On the other hand, energetic hydrogen mass yield was the same for both methane flow rates.

4. Conclusions

Our investigation of methane reforming using MPS operated at atmospheric pressure show a progress in improving the hydrogen mass and energetic yields. The high energetic hydrogen mass yield obtained in the final experiments using the high flow rate cylindrical-type MPS with CH_4 swirl is better than that obtained in other plasma methods even if we take into account the energy losses in the microwave power supply used in our experiment. Then, the energetic hydrogen mass yield is $381 \text{ g[H}_2\text{]} \text{ kWh}^{-1}$ (~ 33 % lower than $577 \text{ g[H}_2\text{]} \text{ kWh}^{-1}$ presented above, Tab. I). The absence of other compounds (CO , CO_2 , C_2H_2) as by-products in the off-gas is additional benefit of methane reforming using the high

flow rate cylinder-type MPS.

Comparison of energetic parameters of hydrogen production by microwave plasma, which is a laboratory scale at the moment, with industrial scale conventional steam methane reforming is difficult. Only comparison with water electrolysis, where the only kind of energy used is electricity similarly as in our method, is possible. The best available commercial electrolyzers produce hydrogen with energetic hydrogen mass yield up to $21 \text{ g[H}_2\text{]} \text{ kWh}^{-1}$ (ref.¹⁵). This value is much lower than that obtained using plasma methane reforming. However, energetic hydrogen mass yield is not good parameter for comparing plasma reforming with electrolysis since both methods use different substrates. One of the way for comparing those both methods is calculating of costs of methane and electricity. Assuming that water cost in electrolysis is negligible the cost of 1 kg of hydrogen produced by plasma method is about 2 times lower than that obtained via electrolysis.

The high flow rate cylinder-type MPS for H_2 production via methane reforming tested by us as the last MPS design is expected to be of low cost and effective, and thus promising for applications in the distributed hydrogen production.

These studies were supported by the Ministry of Science and Higher Education (MNiSW) under the program PB 3020/T02/2006/31.

REFERENCES

- Petitpas G., Rollier J.-D., Darmon A., Gonzalez-Aguilar J., Metkemeijer R., Fulcheri L.: *Int. J. Hydrogen Energy* 32, 2848 (2007).
- Bromberg L., Cohn D. R., Rabinovich A., Alexeev N., Samokhin A., Ramprasad R., Tamhankar S.: *Int. J. Hydrogen Energy* 25, 1157 (2000).
- Bromberg L., Cohn D. R., Rabinovich A., Alexeev N.: *Int. J. Hydrogen Energy* 24, 1131 (1999).
- Cormie J. M., Rusu I.: *J. Phys. D: Appl. Phys.* 34, 2798 (2001).
- Sekiguchi H., Mori Y.: *Thin Solid Films* 435, 44 (2003).
- Kabashima H., Einaga H., Futamura S.: *IEEE Trans. Ind. Appl.* 39, 340 (2003).
- Pietruszka B., Anklam K., Heintze M.: *Appl. Catal., A* 261, 19 (2004).
- Mutaf-Yardimci O., Saveliev A. V., Fridman A. A., Kennedy L. A.: *Int. J. Hydrogen Energy* 23, 1109 (1998).
- Kappes T., Hammer T., in: *Proc. 4th Int. Symp. on Non-thermal Plasma Technology, Panama City Beach, Florida, USA*, p. 206, 2004.
- Jasiński M., Dors M., Mizeraczyk J.: *J. Power Sources* 181, 41 (2008).
- Moisan M., Sauve G., Zakrzewski Z., Hubert J.: *Plasma Sources Sci. Technol.* 3, 584 (1994).
- Jasiński M., Mizeraczyk J., Zakrzewski Z., Ohkubo T., Chang J. S.: *J. Phys. D: Appl. Phys.* 35, 2274 (2002).
- Green K. M., Borrás M. C., Woskow P. P., Flores G. J., Hadidi K., Thomas P.: *IEEE Trans. Plasma Sci.* 29, 399 (2001).
- Uhm H. S., Hong Y. C., Shin D. H.: *Plasma Sources Sci. Technol.* 15, S26 (2006).
- <http://www.loim.vrn.ru/index.php?m=63&page=58&nm=74&p=.2.3.56.64.70.71.72.73.74>

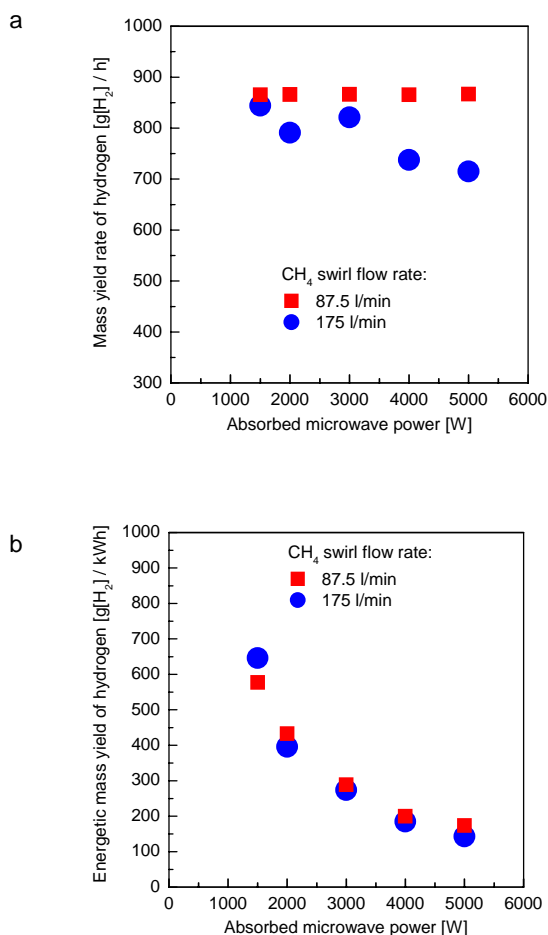


Fig. 7. High flow rate coaxial-type MPS, version C. The hydrogen mass yield rate (a) and the energetic hydrogen mass yield (b) versus absorbed microwave power for different methane swirl flow rate

RF DISCHARGE AT ATMOSPHERIC PRESSURE – DIAGNOSTICS AND APPLICATIONS

PAVEL SLAVICEK^{*a}, MILOS KLIMA^a, DANA SKACELOVA^a, EVA KEDRONOVA^a, ANTONIN BRABLEC^a, and VLADIMIR AUBRECHT^b

^a Department of Physical Electronics, Faculty of Science, Masaryk University, Kotlarska 2, 611 37 Brno, ^b Department of power electrical and electronic engineering, Brno University of Technology, Technicka 8, budova A3, 61600, Brno, Czech Republic
ps94@sci.muni.cz

1. Introduction

Low temperature plasmas are extensively used for the plasma processing¹, light sources, various plasma technologies² etc. During several last years different plasma discharges with nozzle and powered by rf generator driven at frequency 13,56 MHz have been investigated. Plasma pencil is a special type of plasma nozzle working at atmospheric pressure, which is interesting for possible applications^{6,8} such as local treatment of surface, deposition of thin films, change surface energy, cutting in surgery, etc. Through this nozzle, which is made from quartz tube with typical inner diameter 2 mm, flows working gas (argon with water vapour). The powered electrode is connected through the matching unit to the rf generator.

In the contribution, we present diagnostics of unipolar discharge channel generated by the plasma pencil at atmospheric pressure. For different electrical parameters and various construction design of the plasma pencil the parameters of the plasma channel are estimated from optical emission spectra in the spectral range 200–900 nm: rotation temperature from OH rotational lines, vibrational temperature from nitrogen bands as well as concentration of electrons and temperature of neutral gas from Stark and Doppler broadening of hydrogen lines, resp.



Fig. 1. Photograph of plasma pencil

2. Experimental setup

The plasma pencil is shown in Fig. 1. The powered electrode of was separated by the dielectric quartz tube, nozzle

with the inner diameter 2 mm and the outer diameter 4 mm and 50 mm length. As an active medium flowing through the hollow electrode of the plasma pencil argon with purity 99.996 % was used. Note, that the working gas flowing from the nozzle stabilises the discharge. The hollow electrode was connected through the matching network to the rf generator Cesar – 1310 by Dresler driven at frequency 13,56 MHz^{5–7}.

Optical emission spectroscopy was accomplished by means of the monochromator FHR 1000 by Jobin-Yvon-Horiba supplied with CCD detector and ICCD (Intensified Charge Couple Device) system. CCD detector in “continual” regime was used, ICCD system in pulse regime was chosen whereas square pulse modulation frequency of 27 kHz by means of external triggering generator Agilent 33220A was adjusted.

The spectra was recorded perpendicularly to the plasma channel for different discharge parameters.

The rotational temperature from rotational lines of OH, the electron temperature from Ar lines in the plasma channel at different conditions of discharge (power supply, frequency, length) were determined. Rotational and electron temperature were calculated from Boltzmann plot^{3,4}.

The most frequently used technique for determination of electron concentration N_e is based on the half-width and shape of the hydrogen Balmer beta ($H_\beta = 486.13$ nm) spectral line.

Electron concentration was estimated by approximate formula e.g.() by Weise et al^{9,10,12}.

$$N_e [m^{-3}] = 10^{22} \left[\frac{W_s}{4 \cdot 7333} \right]^{1.49}$$

W_s is the Stark halfwidth at half maximum (HWHM) of line. In case when Stark width, W_s , is small and comparable

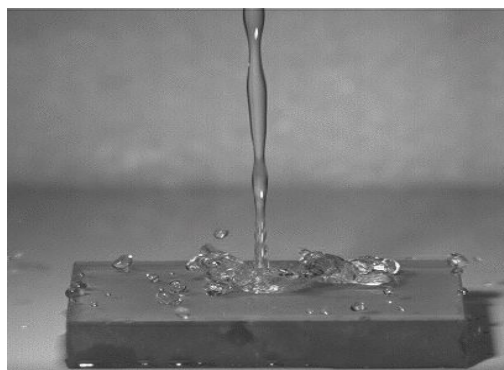


Fig. 2. Thin hydrophobic layer on glass

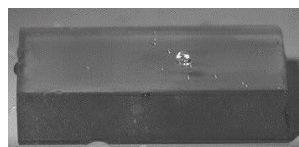


Fig. 3. Drop of water on thin hydrophobic layer surface. This layer was deposited by plasma pencil at atmospheric pressure

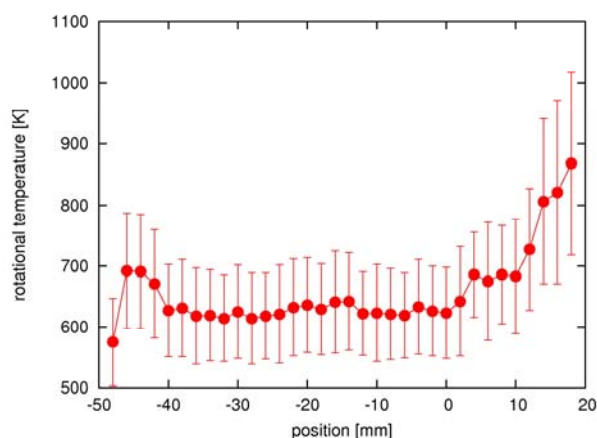


Fig. 4. Rotational temperature estimated from OH lines as a function of the distance from the end of the nozzle for fixed gas flow of 1 l min^{-1} and fixed hf power input of 125 W. The negative distance was taken in the nozzle while the positive values were taken out of the nozzle.

with Doppler and/or instrumental broadening it may be determined by using an approximate deconvolution formula¹¹.

In calculation of electron concentration other broadening mechanism such as resonance and Van der Waals broadening were ignored, because Stark broadening was dominant.

3. Results and discussion

A typical distribution of rotational temperature estimated from OH lines as a function of the distance from the end of the nozzle for fixed gas flow of 1 l min^{-1} and fixed hf power input of 125 W is shown in Fig. 4. The negative distance was taken in the nozzle while the positive values were taken out of the nozzle and the length of nozzle was 50 mm.

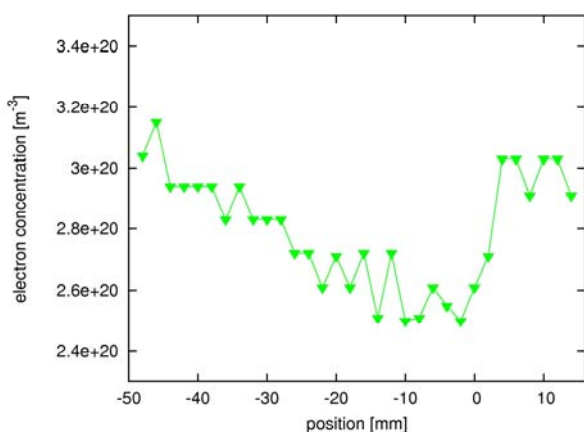


Fig. 5. Concentration of electrons as function of the distance from the end of the nozzle for fixed gas flow of 1 l min^{-1} and fixed hf power input of 125 W. The negative distance was taken in the nozzle while the positive values were taken out of the nozzle

The rotational temperature is approximately constant along the nozzle. In side the nozzle rotational temperature increases fast.

Fig. 5 shown a distribution of concentration of electrons as function of the distance from the end of the nozzle for fixed gas flow of 1 l min^{-1} and fixed hf power input of 125 W. The negative distance was taken in the nozzle while the positive values were taken out of the nozzle. Concentration of electrons, calculated from the half-width and shape of the hydrogen Balmer beta line $H_{\beta} = 486,13 \text{ nm}$, decreases along the nozzle from electrode to the end of the nozzle.

A typical distribution of electron temperature and rotational temperature as a function of the delay while using ICCD system in pulse regime, square pulse modulation frequency of 27 kHz and duty cycle 50 % is shown in Fig. 6. and Fig. 8. Gas flow of 1 l min^{-1} and hf power input of 135 W in the end of the nozzle. Is evidently, that the temperature is measurable only in the range of modulation pulse.

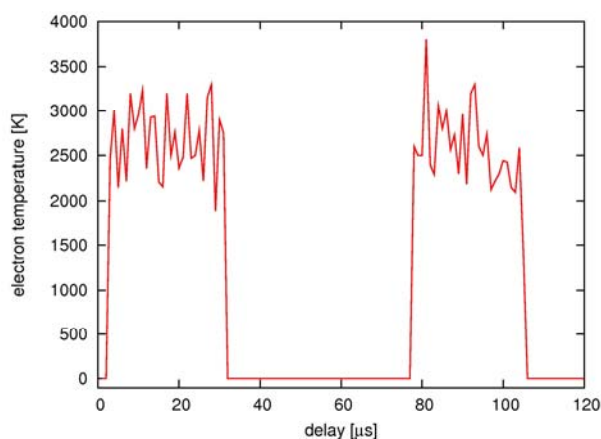


Fig. 6. Electron temperature calculated from Ar lines as a function of the delay while using ICCD detector for fixed gas flow of 1 l min^{-1} and fixed hf power input of 135 W in the end of the nozzle. Pulse modulation frequency of 27 kHz was adjusted

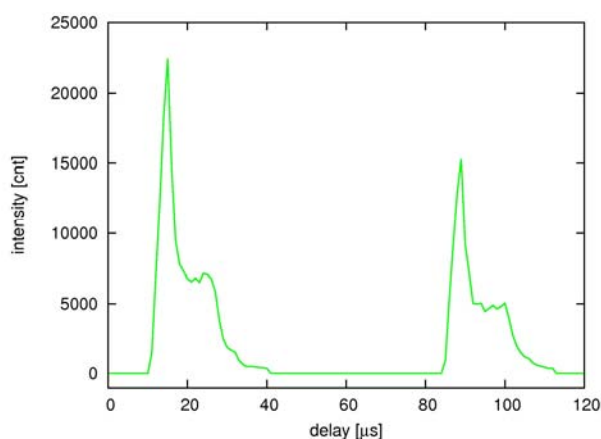


Fig. 7. Intensity of OH lines as a function of the delay while using ICCD detector for fixed gas flow of 1 l min^{-1} and fixed hf power input of 135 W in the end of the nozzle. Pulse modulation frequency of 27 kHz was adjusted

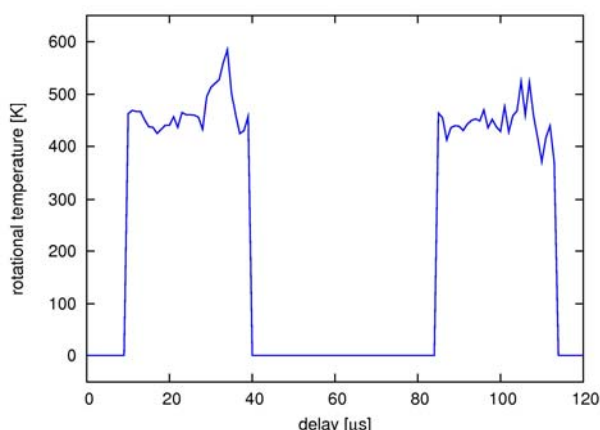


Fig. 8. Rotational temperature calculated from OH lines as a function of the delay while using ICCD detector for fixed gas flow of 1 l min^{-1} and fixed hf power input of 135 W in the end of the nozzle. Pulse modulation frequency of 27 kHz was adjusted

Fig. 7 shows a distribution of intensity of one rotational line of OH molecule as a function of delay in pulse regime of discharge.

Pulse regime of discharges are perspective for deposition of thin layer on thermal sensitive materials and for other applications.

This discharge in „continual“ regime was used for deposition thin layers on glass substrates. For this deposition mixture of Ar and hexamethyldisiloxane (HMDSO) was used as working gas.

High speed camera Olympus i-SPEED-2 was used for demonstration of properties of this thin films. Record speed 1000 frames per second was used. Fig. 2 and Fig. 3 show pictures accomplished by this camera. Pictures show drops of water on hydrophobic thin films deposited on glass substrates. This are first hydrophobic films deposited by this plasma device at atmospheric pressure.

4. Conclusion

In this article results of electron concentration, rotational and electron temperature in discharge generated by plasma pencil at atmospheric pressure were presented for „continual“ and pulse regime.

First results of deposition of hydrophobic thin films on glass substrates by plasma pencil were presented too.

In this contribution the single nozzle was used, but several nozzles can be applied simultaneously in one device, which is more convenient for practical application.

This research has been supported by the grant 202/07/1207, by the Czech Science Foundation and by the research intent MSM:0021622411 funding by the Ministry of Education of the Czech republic and Grant Agency of Academy of Science of Czech Republic contract No. KAN101630651.

REFERENCES

1. Rahel J., Simor M., Cernak M., Stefecka M., Imahori Y., Kando M.: *Surf. Coat. Technol.* 169-170, 604 (2003).
2. Sira M., Trunec D., Stahel P., Bursikova V., Navratil J.: *Phys. D* 41, 015205 (2008).
3. Griem H. R.: *Principles of Plasma Spectroscopy*. Academic Cambridge Univ. Press, New York 1997.
4. Lochte-Holtgreven Ed W.: *Plasma Diagnostics*. American Institute of Physics, New York 1995.
5. Cada M., Hubicka Z., Sicha M., Churpita A., Jastrabik L., Soukup L., Tichy M.: *Surf. Coat. Technol.* 174-175, 530 (2003).
6. Slavicek P., Klima M., Janca J., Brablec A., Kadlecova J., Smekal P.: *Czech. J. Phys.*, B 56 (2006).
7. Slavicek P., Bursikova V., Brablec A., Kapicka V., Klima M.: *Czech. J. Phys.* 54, C586 (2004).
8. Hubicka Z.: *Plasma Sources Sci. Technol.* 11, 195 (2002).
9. Zikic R., Gigisos M. A., Ivkovic M., Gonzales M. A., Konjevic N.: *Spectrochim. Acta, Part B* 57, 987 (2002).
10. Kelleher D. E.: *J. Quant. Spectrosc. Radiat. Transfer* 25, 191 (1981).
11. Ivkovic M., Jovicevic S., Konjevic N.: *Spectrochim. Acta, Part B* 59, 591 (2004).
12. Zikic R., Gigisos M. A., Ivkovic M., Gonzales M. A., Konjevic N.: *Spectrochim. Acta, Part B* 57, 987 (2002).

DIAGNOSTICS OF PLASMA PROCESSES AND MODELLING

APPROXIMATE CALCULATIONS OF CONTINUOUS SPECTRA OF DIATOMIC MOLECULES

MILADA BARTLOVA* and VLADIMIR AUBRECHT

Faculty of Electrical Engineering and Communication, Brno University of Technology, Technická 8, 616 00 Brno, Czech Republic
bartlova@feec.vutbr.cz

1. Introduction

Radiative transport of energy plays an important role in many plasma processing devices. Jets of thermal plasma are produced in plasma generators with electric arcs. The experimental observation of radiation transfer is very difficult due to extreme experimental conditions. In such cases, the mathematical modeling is of great importance. However, the non-linearity of equations describing the radiation field and strong dependency of input parameters on the radiative frequency and properties of the medium make mathematical plasma models very complicated. Exact calculations are hardly possible, even with modern computers, due to the large computation times required; therefore, several approximate methods have been developed (method of partial characteristics, net emission coefficient, etc.).

Any quantitative study of the radiative transport of energy requires knowledge of the frequency-dependent absorption properties of the arc plasma. Theoretical calculations of radiation field are based on the knowledge of the plasma composition and subsequently absorption coefficients. The total spectral absorption coefficient (spectral absorptivity) needs to be calculated as a function of wavelength, temperature and pressure with radiation wavelengths spanning from the infrared to the far ultraviolet region of the spectrum.

Intensive radiation is irradiated from the hot central part of the arc and reabsorbed in cold edge of the plasma. Therefore, besides of continuous and discrete radiation of atoms and atomic ions the influence of molecular species on the absorption properties of the plasma has to be taken into account. Recently, we have studied discrete band spectra of diatomic molecules¹. In this paper two radiation processes leading to the continuous absorption molecular spectra are studied. Simple approximate formulas for photodissociation and photoionization cross sections of diatomic molecules are presented. Results obtained for selected diatomic molecules are compared with available experimental and other theoretical data from literature.

2. Absorption coefficients

A light beam traveling through a participating gas layer of thickness dx loses energy by absorption and by scattering away from the direction of travel. The attenuation of radiation in non-scattering medium is proportional to the magnitude of the incident energy (intensity I_n) and to the length of the path

$$dI_\nu = -\kappa_\nu I_\nu dx \quad (1)$$

The proportionality constant κ_n is known as an absorption coefficient. When a photon interacts with a gas molecule, atom, or ion, it may be absorbed raising the particle's energy level. Conversely, a gas particle may spontaneously lower its energy level by the emission of an appropriate photon. Three different types of radiative transitions can be distinguished: *i*) transition between bound atomic or molecular states, called bound-bound transitions (*bb*), *ii*) transitions from a bound state to a "free" (dissociated) one (absorption) or from "free" to bound (emission), called bound-free transitions (*bf*), and *iii*) transitions between two different "free" states, free-free transitions (*ff*).

Total absorption coefficient is given as a linear sum of all three processes

$$\kappa(\nu, T, p) = \kappa^{bb} + \kappa^{bf} + \kappa^{ff} \quad (2)$$

The spectral absorption coefficient of any process is related to the photo-absorption cross section $s_n(T)$ by

$$\kappa_{\nu,i}^a(T, p) = \sigma_{\nu,i}^a(T) N_i^a(T, p) \quad (3)$$

where N_i^a is the population density of the i -th electronic state E_i^a of the absorbing species "a". Thus, at a given spectral frequency, plasma temperature and pressure, the total spectral absorption coefficient is

$$\kappa_\nu = \sum_a \sum_i \sigma_{\nu,i}^a N_i^a \quad (4)$$

Calculation of absorption coefficients represents a complex task, since the radial wave functions of all free and bound atomic and molecular states must be known. However, simplifications can be made by using various semi-empirical methods.

3. Photodissociation

The process of photodissociation can proceed in various ways. Photodissociation can occur by line and by continuous absorption. The most important case of dissociation absorption continua is the direct photodissociation, in which a transition takes place from a stable lower state to a

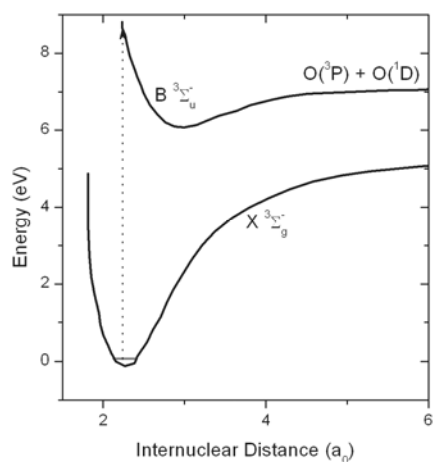


Fig. 1. Relevant potential curves for O_2 illustrating direct photo-dissociation (Schumann-Runge continuum) from Jarman at all²

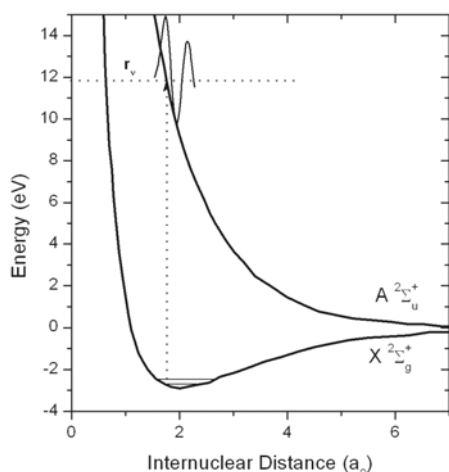


Fig. 2. Relevant potential curves for H_2^+ illustrating direct photo-dissociation from Dunn³. Also shown are a typical continuum wave function and turning radius r_c .

continuous upper state.

Continuous spectra join onto the series of vibrational levels of the upper electronic state (see Fig. 1 for Schumann-Runge continuum of molecule O_2), and are the only feature present if the electronic state under consideration has no discrete vibrational levels at all (unstable state – see Fig. 2 for molecule H_2^+).

According to the Franck-Condon principle, the most probable transition in absorption is that going vertically upward (see Fig. 1 and Fig. 2). The probability of the transition between two states ψ' and ψ'' is proportional to the square of

the dipole transition moment

$$\left| \int \psi'^* D \psi'' d\tau \right|^2 \quad (5)$$

where D is the vector of electric dipole moment and $d\tau$ is the element of volume of the space of nuclear and electronic coordinates. Neglecting the molecular rotation we obtain

$$\left| \int \psi_E R_e(r) \psi_{v'} dr \right|^2 \quad (6)$$

where $\psi_{v'}$ and ψ_E are the vibrational wave function for the lower bound molecular state and the repulsive wave function of continuum state, respectively, and

$$R_e(r) = \int \psi_e(r, \tau_e) D \psi_e(r, \tau_e) d\tau_e \quad (7)$$

is the electronic transition moment. The variation of R_e with internuclear distance r is slow and R_e may be replaced by an average value \bar{R}_e . With this assumption we obtain

$$\bar{R}_e^2 \left| \int \psi_{v'} \psi_E dr \right|^2 \quad (8)$$

The overlap integral

$$q_{v'E} = \int \psi_{v'} \psi_E dr \quad (9)$$

is the Franck-Condon density. It has a maximum value when the broad maximum of the repulsive function lies approximately above the maximum of the vibrational wave function of the lower state.

In first approximation, very simple form of repulsive wave function can be used⁴: it is replaced by a d -function, which is different from zero only at the classical turning point r_n (see Fig. 2).

Then the overlap integral for a given energy of the repulsive state is simply equal to the value $|\psi_{v'}(r)|^2$, where $\psi_{v'}$ is to be taken for the r value that corresponds to the frequency ν considered. Supposing $\psi_{v'}(r)$ are harmonic oscillator wave functions

$$|\psi_{v'}(r)|^2 = \sqrt{\frac{\alpha}{\pi}} \frac{\exp(-\alpha x^2)}{2^{v'} v'!} [H_{v'}(\sqrt{\alpha} x)]^2 \quad (10)$$

where $x = r - r_e$, $\alpha = \frac{4\pi^2 \mu \nu_{osc}}{h}$, $\nu_{osc} = \frac{1}{2\pi} \sqrt{\frac{k}{\mu}}$, $H_{v'}(\sqrt{\alpha} x)$ are Hermitean polynomials.

The continuous spectrum corresponding to transition from the lower vibrational state $v''=0$ has one maximum, transitions from the vibrational state $v''=1$ show two intensity maxima, since the probability density distribution curve has two maxima. Similarly, three maxima are to be expected for transitions from $v''=2$, etc. In absorption at high temperatures the continua corresponding to $v''=0,1,2,\dots$ are superimposed, and in general only a single maximum arrives which is broader and less high than at low

temperature.

Absorption coefficients for dissociative transition from a bound vibrational level v'' of a lower state to the vibrational continuum of an upper state is given by

$$\kappa^{v''} = N_{v''} \sigma_{v''} \quad (11)$$

where $N_{v''}$ is the number density of molecules in the lower vibrational state v'' , and the cross section according Herzberg⁴

$$\sigma_{v''} = \frac{16\pi^3 \nu}{3hc} \sqrt{2\mu R_e^2} |\psi_{v''}(r_v)|^2 \quad (12)$$

The classical turning point r_n is the solution of equation

$$h\nu = V(r) - hc\omega_{v''} \quad (13)$$

Here $V(r)$ is the potential energy curve of upper molecular state, $hc\omega_{v''}$ is the energy of the lower vibrational term. Total spectral absorption coefficient is given by

$$\kappa_{\nu} = \sum_{v''} \kappa^{v''} = \frac{N}{Q(T)} \frac{\sigma_{v,0}}{\nu_0} \sqrt{\frac{\pi}{\alpha}} \nu \sum_{v''=0}^6 \exp\left(-\frac{hc\omega_{v''}}{kT}\right) |\psi_{v''}(r_v)|^2 \quad (14)$$

Only first 7 vibrational levels of the lower electronic state were taken into account. N is the total number density of absorbing molecules, $Q(T)$ denotes the partition function

$$Q(T) = \sum_{v''=0}^{\infty} \exp\left(-\frac{hc\omega_{v''}}{kT}\right) = \frac{1}{1 - \exp\left(-\frac{hc\omega_e}{kT}\right)} \quad (15)$$

$\sigma_{v,0}$ and ν_0 are empirical data – photodissociation cross section at low temperature and corresponding radiation frequency of absorbed photon.

3.1. Photodissociation of O₂

The most important photodissociation transition of O₂ molecule is the convergence limit of $X^3\Sigma_g^- \rightarrow B^3\Sigma_u^-$ (Schumann-Runge continuum). It corresponds to dissociation O₂ → O(³P) + O(¹D) (Fig. 1).

The potential curve of the upper state was approximated by Morse potential

$$V(r) = T_e + D_e \left(1 - e^{-\beta(r-r_e)}\right)^2 \quad (16)$$

where $\beta = \sqrt{\frac{2\pi^2 c\mu}{D_e h}} \omega_e$, T_e is the electronic term energy, D_e denotes dissociation energy from the ground vibrational state $v = 0$, r_e is the equilibrium internuclear distance, ω_e is the vibrational constant, and μ the reduced mass. Values of molecular parameters are given in Tab. I.

The value of empirical data was determined from Baulch at all⁶

$$\frac{\sigma_{v,0}}{\nu_0} = 6.55 \times 10^{-33} \text{ cm}^2 \cdot \text{s}$$

Table I

Molecular parameters of O₂ (α is parameter in wave function of lower state) from Herzberg at all⁵

State	T_e [cm ⁻¹]	ω_e [cm ⁻¹]	r_e [10 ⁻¹⁰ m]	
$B^3\Sigma_u^-$	49793	709.3	1.604	$D_e = 0.95$ [eV]
$X^3\Sigma_g^-$	0	1580.2	1.207	$\alpha = 7.5e18$ (cm ⁻²)

Photodissociation cross section of Schumann-Runge continua for different temperatures is shown in Fig. 3. Comparison is made with the calculations of Mnacakanjan⁷, good agreement was achieved.

3.2. Photodissociation of H₂⁺

The transition $X^2\Sigma_g^+ \rightarrow A^2\Sigma_u^+$ of H₂⁺ ion provides the clearest example of direct photodissociation (Fig. 2). The upper potential curve was approximated by exponential decay

$$V(r) = V_0 + A \exp\left(-\frac{r}{t}\right) \quad (17)$$

where V_0 , A , and t are fit parameters. Their values are given in Tab. II, together with molecular parameters for the lower state. The value of empirical data was determined from Van Dishoeck⁸

$$\frac{\sigma_{v,0}}{\nu_0} = 2.795 \times 10^{-33} \text{ cm}^2 \cdot \text{s}$$

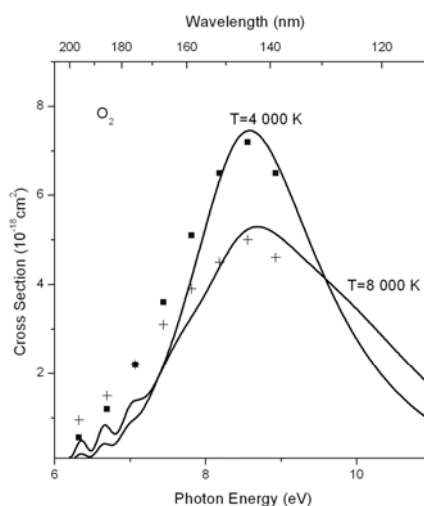


Fig. 3. The photodissociation cross sections for Schumann-Runge continuum of molecule O₂ at different temperatures. Solid lines: present work; squares and crosses: calculations from Mnacakanjan⁷ for 4000 K and 8000 K, resp.

Table II
Molecular parameters of H_2^+ and OH from Herzberg at all⁵

Molecule	State	ω_e [cm^{-1}]	r_e [10^{-10}m]	α [cm^{-2}]
H_2^+	$X^2\Sigma_g^+$	2321.7	1.052	3.345e17
OH	$X^2\Pi$	3737.8	0.969	1.027e18
Molecule	State	V_0 [eV]	A [eV]	t [10^{-10}m]
H_2^+	$A^2\Sigma_u^+$	0.546	66.261	0.546
OH	$1^2\Sigma^-$	4.353	27.57	0.492
OH	$1^2\Delta$	6.883	138.42	0.253
OH	$B^2\Sigma^+$	8.497	82.123	0.283

The photodissociation cross sections are presented in Fig. 4. Calculation was performed for first 7 vibrational levels (solid curve) and for transition from the vibrational level $v'' = 0$ only (dashed curve). Comparison with Dunn³ (dotted curve) and Van Dishoeck⁸ (dash-dot curve) shows good agreement.

3.3. Photodissociation of OH

Direct photodissociation from the ground $X^2\Pi$ state may take place by absorption into three higher states, the $1^2\Sigma^-$, $1^2\Delta$, and $B^2\Sigma^+$ state. The three states are repulsive in the Franck-Condon region of the ground state (Fig. 5). Data for repulsive potential curves were taken over from paper of Van Dishoeck at all⁹; curves can be approximated by exponential

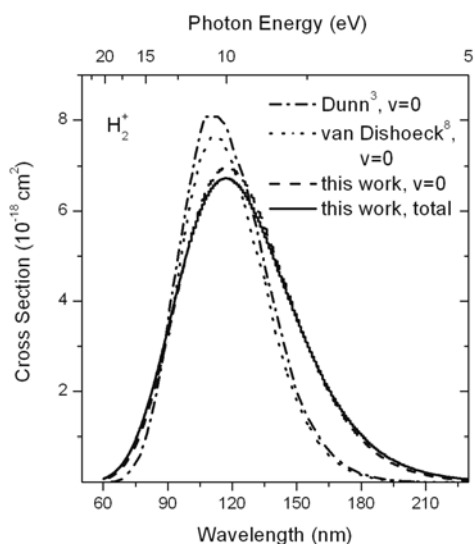


Fig. 4. The photodissociation cross section for transition $X^2\Sigma_g^+ \rightarrow A^2\Sigma_u^+$ of molecule H_2^+ . Solid line: present work for first 7 vibrational levels of lower state; dashed line: present work for transition from only basic vibration lower state $v = 0$; dotted and dash-dot line: data from Van Dishoeck⁸ and Dunn³, resp.

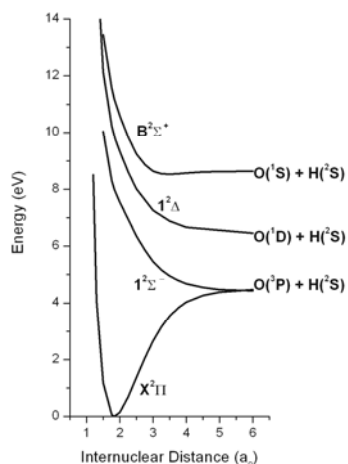


Fig. 5. Relevant potential energy curves for direct photodissociation of OH from Van Dishoeck at all⁹

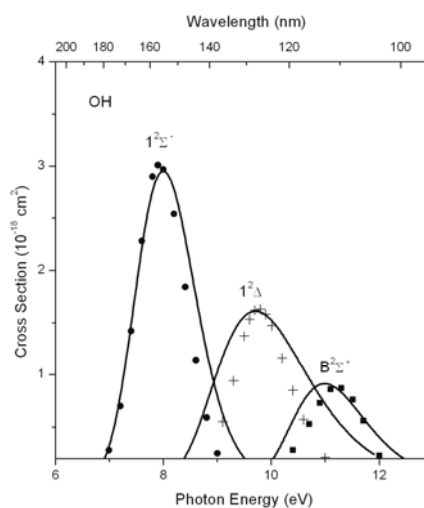


Fig. 6. The calculated photodissociation cross sections as functions of incident photon energy for the $1^2\Sigma^-$, $1^2\Delta$, and $B^2\Sigma^+$ states starting from the $X^2\Pi$. Solid line: present work; circles, crosses, squares: calculations from Van Dishoeck at all⁹

decay (17). Values of molecular and fit parameters are given in Tab. II.

The photodissociation cross sections for absorption into the $1^2\Sigma^-$, $1^2\Delta$, and $B^2\Sigma^+$ states are presented in Fig. 6. Comparison is made with the calculations of Van Dishoeck at all⁹ where configuration-interaction method was used for obtaining approximate electronic wave functions. Very good agreement shows that the simple calculations presented in this work give reliable results.

4. Photoionization

For atoms, a continuous range joins onto each series of discrete electronic states and corresponds to the removal of an electron (ionization) with more or less relative kinetic energy or, conversely, to the capture of an electron by the ion (recombination). Such continuous ranges of energy levels, corresponding to ionization, are possible also for molecules. Ionization potentials of most diatomic molecules are greater than 10 eV and therefore the ionization continua lie in the far ultraviolet.

The processes of interest here are one-photon, single ionization events; they can be written for a prototype molecule AB in the form



where $h\nu$ is the incident photon energy, AB is the target molecule in the ground electronic state, $[AB^+]^j$ is the molecular ion in the electronic excited state j , and e^- is the ejected electron carrying off kinetic energy.

In the Born-Oppenheimer and Franck-Condon approximation the photoionization cross section of the process (18) can be expressed in the form

$$\sigma(\nu, T) = \sum_{v''} w_{v''}(T) \sigma_{v''}(\nu) \quad (19)$$

where $w_{v''}$ is the Boltzmann probability of occupation of the vibration level v'' of the ground electronic state of the neutral molecule and the partial cross section $\sigma_{v''}$ is from Mnacakanjan⁷

$$\sigma_{v''}(\nu) = \frac{\pi r_0}{3R_\infty^2} \frac{\nu}{c} q_{v''} Re^2 \phi(\nu - \nu_{v''}) \quad (20)$$

In (20) n is the photon frequency, r_0 is the Bohr radius, R_∞ is the Rydberg constant, c is speed of light, $q_{v''}$ are Franck-Condon factors for transitions between vibronic levels of the neutral molecule and the ion, and $Re^2 \phi(\nu - \nu_{v''})$ represents the electronic part of the transition dipole moment. Both the constant part Re^2 and the frequency variation $\phi(\nu - \nu_{v''})$ can be determined from experimental results in cold gas. Three different types of frequency variation $\phi(\nu - \nu_{v''})$ were used:

$$\begin{aligned} \phi_1(\nu - \nu_{v''}) &= \begin{cases} 0 & \nu < \nu_{v''} \\ (\nu_{v''}/\nu)^4 & \nu > \nu_{v''} \end{cases} \\ \phi_2(\nu - \nu_{v''}) &= \begin{cases} 0 & \nu < \nu_{v''} \\ (\nu_{v''}/\nu)^3 & \nu > \nu_{v''} \end{cases} \\ \phi_3(\nu - \nu_{v''}) &= \begin{cases} 0 & \nu < \nu_{v''} \\ (\nu_{v''}/\nu)^2 & \nu > \nu_{v''} \end{cases} \end{aligned} \quad (21)$$

4.1. Examples of Photoionization

Calculations were performed for molecules O₂, N₂, NO, and H₂. The molecules were in their ground electronic states. Following partial photoionization cross sections were computed: for the production of O₂⁺ in the states X²Π_g⁺, b⁴Σ_g⁻, and a⁴Π_u + A²Π_u; for the production of N₂⁺ in the states X²Σ_g⁺, A²Π_u and B²Σ_u⁺; for the production of NO⁺ in the states X¹Σ⁺ and A¹Π; and for the production of H₂⁺ in the state

Table III

Recommended data for Franck-Condon factors, Re^2 , and $\phi(\nu - \nu_{v''})$ for photoionization of O₂, N₂, NO, and H₂

O ₂	O ₂ ⁺	FC factors	Re^2	$\phi(\nu - \nu_{v''})$
X ³ Σ _g ⁻	X ² Π _g ⁺	Ref ¹¹	1	φ ₂
	a ⁴ Π _u + A ² Π _u	Ref ¹¹	0.4	φ ₂
	b ⁴ Σ _g ⁻	Ref ¹¹	1	φ ₁
N ₂	N ₂ ⁺	FC factors	Re^2	$\phi(\nu - \nu_{v''})$
X ¹ Σ _g ⁺	X ² Σ _u ⁺	Ref ¹²	3.7	φ ₃
	A ² Π _u	Ref ¹²	5	φ ₃
	B ² Σ _u ⁺	Ref ¹²	1	φ ₂
NO	NO ⁺	FC factors	Re^2	$\phi(\nu - \nu_{v''})$
X ² Π	X ¹ Σ ⁺	Ref ¹³	1.25	φ ₃
	A ¹ Π	Ref ¹³	1.25	φ ₂
H ₂	H ₂ ⁺	FC factors	Re^2	$\phi(\nu - \nu_{v''})$
X ¹ Σ _g ⁺	X ² Σ _g ⁺	Ref ¹⁴	2	φ ₁

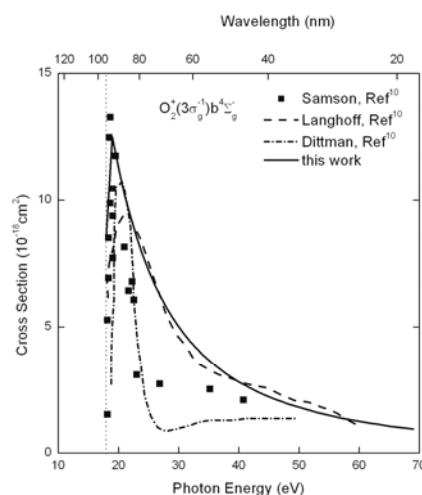


Fig. 7. Partial photoionization cross section for O₂ (X³Σ_g⁻) → O₂⁺(b⁴Σ_g⁻) as a function of photon energy. Comparison is made with data available in Gallagher at all¹⁰

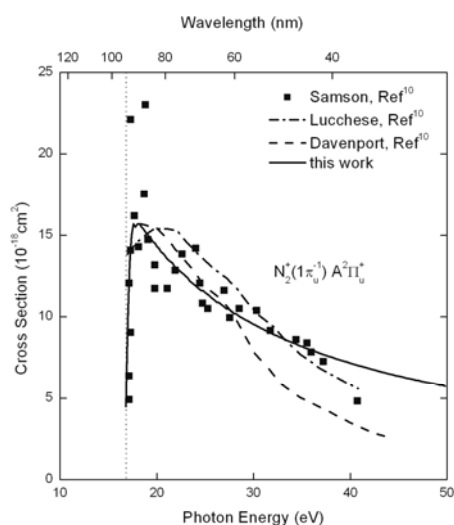


Fig. 8. Partial photoionization cross section for $N_2 (X^1\Sigma_g^+) \rightarrow N_2^+ (A^2\Pi_u^+)$ as a function of photon energy. Comparison is made with data available in Gallagher at all¹⁰

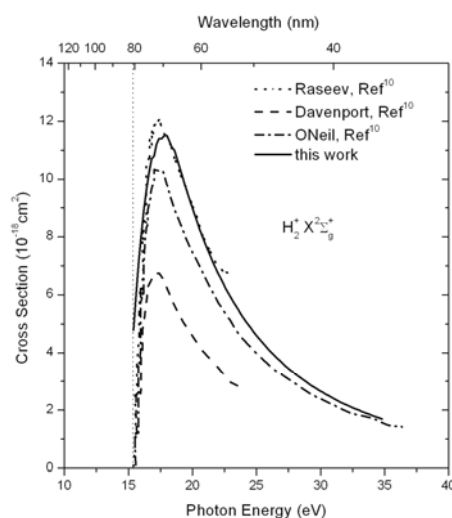


Fig. 10. Partial photoionization cross section for $H_2 (X^1\Sigma_g^+) \rightarrow H_2^+ (X^2\Sigma_g^+)$ as a function of photon energy. Comparison is made with data available in Gallagher at all¹⁰

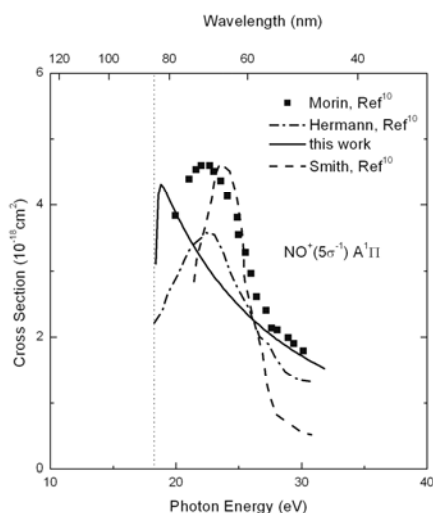


Fig. 9. Partial photoionization cross section for $NO (X^2\Pi) \rightarrow NO^+ (A^1\Pi)$ as a function of photon energy. Comparison is made with data available in Gallagher at all¹⁰

$X^2\Sigma_g^+$. Molecular data for all electronic states under consideration were taken from Herzberg at all⁵. Sources of Franck-Condon factors, and recommended values of Re^2 and the frequency variation $\varphi(\nu - \nu_{v,v'})$ obtained by means of comparison with available experimental data in literature are presented in Tab.3. Results of calculation for transitions $O_2 (X^3\Sigma_g^-) \rightarrow O_2^+ (b^4\Sigma_g^-)$, $N_2 (X^1\Sigma_g^+) \rightarrow N_2^+ (A^2\Pi_u^+)$, $NO (X^2\Pi) \rightarrow NO^+ (A^1\Pi)$, and $H_2 (X^1\Sigma_g^+) \rightarrow H_2^+ (X^2\Sigma_g^+)$ are shown in Fig. 7, Fig. 8, Fig. 9, and Fig. 10, respectively.

Cross sections are plotted on individual figures as functions of the incident photon energy. Comparison was made with data published in review paper of Gallagher at all¹⁰ where many experimental and theoretical data are compiled. Cross sections were extracted using standard digitization techniques. The threshold energy for the relevant photoionization process is indicated by a vertical dotted line on each figure.

Discrepancies between measured values and theoretical calculations appear particularly in threshold regions where polarization effects and possible non-Franck-Condon behavior are important.

5. Conclusions

Calculations have been made of the cross sections of direct photodissociation and photoionization of some diatomic molecules. General agreement with other sources of similar data has been reached. The presented simple formulas for cross sections will be used in improved calculation of total spectral absorption coefficients of air and water vapour plasmas. These coefficients are necessary input data for computation of tables of partial characteristics and net emission coefficients of radiation which are widely used for a prediction of the radiation heat transfer in arc plasma.

Authors gratefully acknowledge financial support from Grant Agency of Czech Republic under project No. GA 202/06/0898 and from Ministry of education under project No. MSM 0021630503.

REFERENCES

1. Bartlová M., Aubrecht V.: Czech. J. of Phys. 26, B632 (2006).

2. Jarman W. R., Nicholls R. W.: Proc. Phys. Soc. 84, 417 (1964).
3. Dunn G. H.: Phys. Rev. 172, 172 (1968).
4. Herzberg G.: *Molecular Spectra and Molecular Structure. I. Spectra of Diatomic Molecules*. D. Van Nostrand Co., NY 1950.
5. Herzberg G., Huber K. P.: *Molecular Spectra and Molecular Structure, IV. Constants of Diatomic Molecules*. D. Van Nostrand Co., NY 1979.
6. Baulch D. L., Cox R. A., Hampson R. F., Kerr J. A., Troe J., Watson R. T.: J. Phys. Chem. Ref. Data 9, 295 (1980).
7. Mnacakanjan A.C.: TVT 6, 236 (1968).
8. Van Dishoeck E. F., in: *Rate Coefficients in Astrochemistry*, (Miller T. J., Williams D. A., ed.), p. 49. Kluwer Academia Publisher, 1988.
9. Van Dishoeck E. F., Dalgarno A.: J. Chem. Phys. 79, 873 (1983).
10. Gallagher J. W., Brion C. E., Samson J. A. R., Langhoff P. W.: J. Phys. Chem. Ref. Data 17, 9 (1988).
11. Krupenie P. H.: J. Phys. Chem. Ref. Data 1, 423 (1972).
12. Lofthus A., Krupenie P. H.: J. Phys. Chem. Ref. Data 6, 113 (1977).
13. Wacks M. E.: J. Chem. Phys. 41, 930 (1964).
14. O'Neil S. V., Reinhardt W. P.: J. Chem. Phys. 69, 2162 (1978).

SPACE AND TIME RESOLVED OPTICAL EMISSION SPECTROSCOPY OF DIFFUSE COPLANAR BARRIER DISCHARGE IN NITROGEN

JAN ČECH^{*a}, PAVEL ŠTAHEL^a, ZDENĚK NAVRÁTIL^a, and MIRKO ČERNÁK^{a,b}

^a Dept. of Physical Electronics, F. of Science, Masaryk University, Kotlářská 2, 611 37, Brno, Czech Republic, ^b Dept. of Experimental Physics, Faculty of Mathematics, Physics and Informatics, Comenius University, Mlynská Dolina, 842 48 Bratislava, Slovakia
cech@physics.muni.cz

1. Introduction

Atmospheric pressure dielectric barrier discharges (DBD)¹ are used in the industry for in-line plasma treatment of fabrics or large area substrates. The utilization of different types of DBD for these applications has been made with different success. The main problem of processing of movable substrates in DBD stands is the inhomogeneity of DBD at atmospheric pressure (formation of plasma microchannels). This results in inhomogeneous treatment of the substrates and unintentional pin-holing of the substrates at high power densities necessary for rapid treatment. This disadvantage is not presented at atmospheric pressure glow discharge (APGD), but on the other hand the glow regime of this discharge is sensitive to the gas impurities and the discharge power.

The diffuse surface coplanar barrier discharge (DSCBD) plasma is generated in thin layer above the surface of dielectric. The plasma microchannels are oriented parallel to dielectric surface. Due to small distance between electrodes the microchannel part of the discharge can be suppressed in order to increase the homogeneity of the treatment and suppress the pin-hole effects. Furthermore, the plasma microchannels of DSCBD move rapidly along the surface, which improves the homogeneity of the treatment^{2,3}.

For better utilization of the DSCBD for industrial purposes⁴⁻⁶ the influence of the outer physical conditions on the discharge parameters has to be studied. In this paper the influence of electrode temperature and total input power is presented. Using spatially resolved spectroscopy spatial profiles of vibrational and rotational temperature calculated from the second positive system of nitrogen was determined and correlated with profile of intensity of the second positive system of nitrogen. Time-space maps of integrated intensities of second positive system of nitrogen (SPS – 377.1 nm) and first negative system of nitrogen (FNS – 391.5 nm) were also estimated.

2. Experimental setup

The scheme of experimental setup is shown in Fig. 1. It consisted of coplanar discharge cell with discharge chamber and cooling/heating unit, power supply unit and diagnostic instruments.

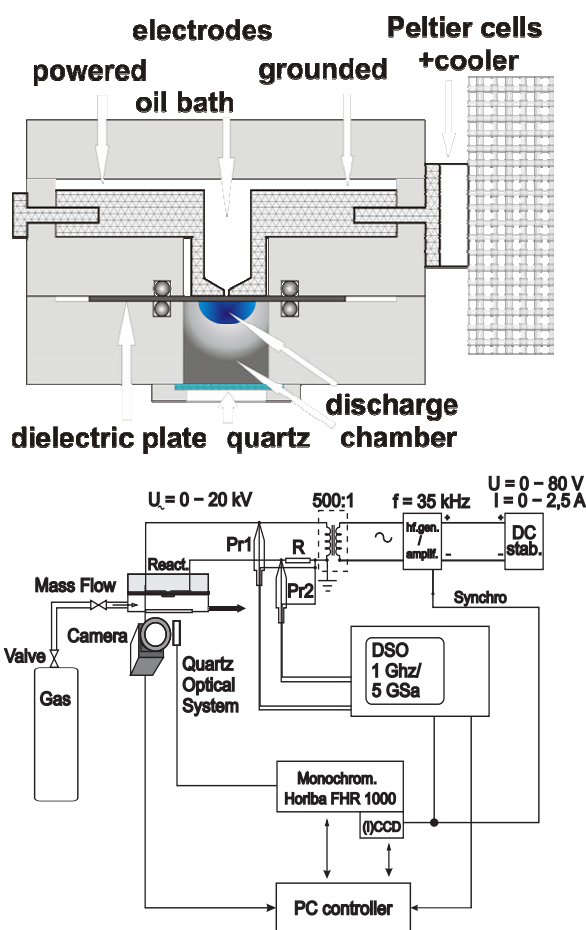


Fig. 1. Scheme of experimental setup with discharge cell and supporting and diagnostic unit (top). Detail of the discharge cell with coplanar electrode system (bottom). The dielectric plate, electrodes, discharge chamber and Peltier cells with cooler are labeled

The discharge cell (see also Fig. 1 – bottom) was composed of two brass electrodes overlaid by dielectric plate (96 % Al₂O₃ with the thickness of 0.5 mm). The electrodes had form of semi-circle. Gap between electrodes had length of 30 mm and width of 0.7 ± 0.1 mm in all cases. This coplanar electrode system was dipped in insulating oil bath. The grounded electrode was controllably heated/cooled using cascade of Peltier cells attached eventually to external cooler. The electrode system consisted of only one electrode pair, contrary to large area DCSBD.

The open space below the dielectric (in Fig. 1 – bottom) was covered with cylindrical discharge chamber. The diameter of the chamber was 30 mm and its height was 30 mm. The chamber enables us to control the discharge atmosphere. In this work 99.996 % pure nitrogen was flown through the chamber with constant rate of 3 slpm controlled with Vögtlin Instruments red-y GCR mass flow meter. The emission spectra and discharge pictures were taken through the quartz window on the chamber.

The discharge was powered by LIFETECH high voltage power supply unit with sinusoidal output of 35 kHz frequency. The voltage amplitude was changed in the range 12

to 18 kV. This corresponds to discharge power of 16 to 42 W. TTL triggering signal for time resolved spectroscopy was taken from the power supply frequency generator.

Electrical parameters were measured by LeCroy WaveRunner 6100A digital storage oscilloscope (1 GHz / 5 GSa). Input voltage was measured by Tektronix P6015A high voltage probe (1000:1). The discharge current was measured using HP 1160A (10:1) probe by the voltage drop on the 330 Ω resistor placed in the circuit. Dissipated discharge power was then calculated from the time evolution of input voltage and discharge current.

Optical emission spectra were recorded with Horiba Jobin-Yvon FHR 1000 monochromator equipped with two gratings (2400 gr mm^{-1} and 3600 gr mm^{-1}). The optical signal was detected by Symphony CCD camera and i-Spectrum ICCD camera that was externally synchronized by TTL signal. Both of them were cooled by means of cascaded Peltier cells.

The discharge emission pattern was projected by quartz lens on the adjustable slit. The light passing through the slit was guided by the quartz optical fiber to the monochromator. The 1D spatial profile of discharge emission was obtained by moving the slit in direction across the electrode gap. The optical resolution in the direction of scanning was set to 1 mm and the optical signal was gathered from the total area of approx. 5 mm^2 of the discharge in all cases.

3. Experimental results and discussion

3.1. Visual appearance of the discharge and the electrical parameters

The visual appearance of the discharge is presented in Fig. 2 (top). The distinct pictures show discharge operated at different conditions. The horizontal axis represents increase of the temperature of grounded electrode from 10 $^{\circ}\text{C}$ to 80 $^{\circ}\text{C}$. The vertical axis represents increase of input voltage amplitude from 12 kV to 17 kV.

The planar structure of the discharge pattern can be recognized, both on the discharge pictures and on the corresponding intensity profiles of the SPS given in Fig. 2 (bottom). The first region is formed by microchannels – filaments crossing the gap in-between of the electrodes (the distance of -1 mm to 1 mm on the intensity profile). The second region is represented by the bright violet areas above the edge of electrodes. These bright areas propagate above the electrodes with increasing input voltage (power). The outer edge of this region can be recognized on the intensity profile as well (at the distance of -5 mm). Third region, that is most clearly visible for the pictures with input voltage of 15 kV, appears as the diffuse blue light that is extended up to the outer edge of the electrodes. There is a slight asymmetry of the luminosity towards powered electrode, which is visible both in the discharge pattern and on the intensity profile.

It can be seen that electrode temperature influences, even in very narrow range, the discharge pattern and the corresponding intensity profiles. Most pronounced is the change of the second region above the powered electrode. The equilibrium temperature of the powered electrode was in the range of 40 $^{\circ}\text{C}$ to 50 $^{\circ}\text{C}$ (measured after several tens of minutes of discharge operation).

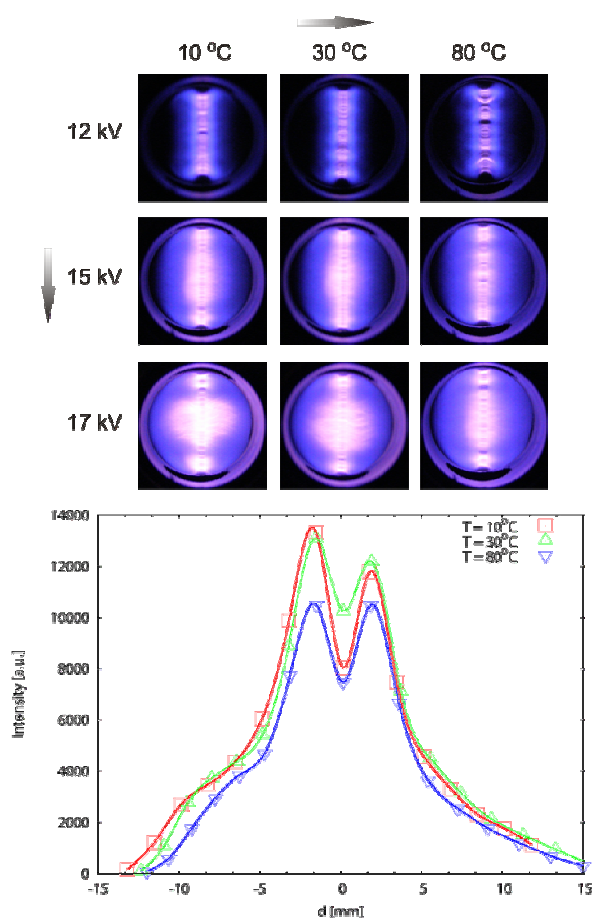


Fig. 2. Set of characteristic discharge images ($\tau = 1/50$ s). The powered electrode is on left side, grounded on right side. The actual size of the square picture is 35 mm. The changing character of the DCSBD with the input power and electrode temperature is presented (top), corresponding spatial profiles of SPS intensity for different electrode temperatures for applied voltage of 15 kV (bottom)

3.2. Rotational and vibrational temperature spatial profiles

The spatial profiles of rotational and vibrational temperature are useful characteristics for deducing the effects of plasma treatment of materials in DCSBD. The distribution of vibrational temperature (comparing with the intensity profiles) can give us the information about the “active area” involved in plasma treatment and the efficiency of this treatment. The distribution and the absolute values of the rotational temperature is on the other hand very important parameter in the case of plasma treatment of temperature sensitive materials. The rotational temperature of SPS can be used as a measure of the neutral gas temperature, thus the rotational temperature profile can be used for the estimation of the temperature stress of treated materials.

The evolution of spatial profiles of rotational temperature, with respect to the input power as well as the electrode temperature, is given in Fig. 3. For the estimation of rotational temperature rotational lines R_1 (22–21) to R_1 (17–16) of fully

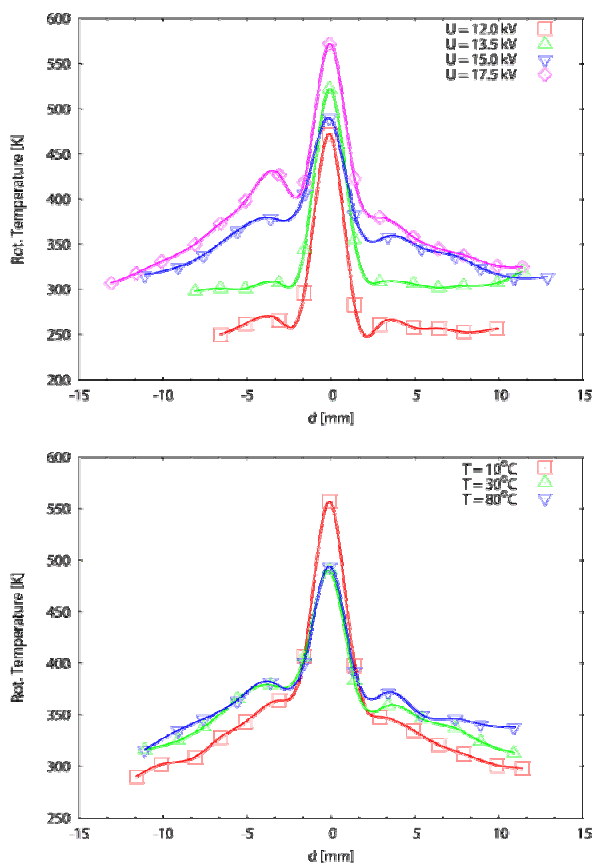


Fig. 3. Spatial profiles of rotational temperature across the inter-electrode gap: input voltage varied, electrode temperature kept at 30 °C (top), grounded electrode temperature varied, input voltage kept at 15 kV (bottom). The errorbars for both temperature and distance is not shown for better clarity of the figures

resolved rotational spectrum of second positive system of nitrogen $C^3\Pi_u \rightarrow B^3\Pi_g$ (band 0–0 at 337.1 nm) were used.

In the filamentary region of the discharge the rotational temperature raises up to 600 K, whereas the rotational temperature in the second region of the discharge, the bright one, has substantially lower values around 350 K. The rotational temperature increases proportionally with the input voltage.

The estimated error of the rotational temperature is about 50 K for the 12 kV and about 20 K for the rest of the profiles. This was caused by low signal to noise ratio for the signal of the discharge operated at 12 kV.

The changes of the rotational temperature profile due to electrode heating/cooling are apparent too (Fig. 3, bottom). It can be observed, that the rotational temperature of the filamentary region is the highest in case of electrode temperature of 10 °C. Rotational temperature above electrodes increase with increasing electrode temperature, as can be expected.

The evolution of spatial profiles of vibrational temperature, with respect to the input power as well as the electrode temperature is given in Fig. 4. The vibrational temperature was estimated from the bands of SPS ($\Delta v = -2$, heads 0–2, 1–3, 2–4 starting at 380 nm).

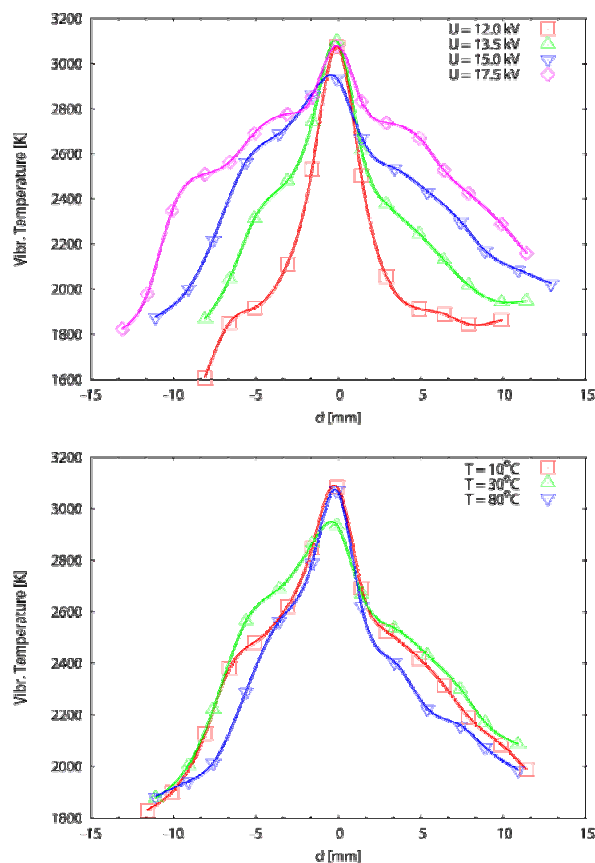


Fig. 4. Spatial profiles of vibrational temperature across the inter-electrode gap: input voltage varied, electrode temperature kept at 30 °C (left), grounded electrode temperature varied, input voltage kept at 15 kV (right). The errorbars for both temperature and distance are not shown for better clarity of the figures

The vibrational temperature of the filamentary region of the discharge peaks at approx. 3000 K. In the second region of the discharge there is still high vibrational temperature with the values about 2800 K. Thus, it can be seen that the DCSBD creates highly non-equilibrium plasma with low rotational and high vibrational temperature and high emission intensity in UV region. The estimated error of the vibrational temperature is about 200 K.

These results are in good agreement with our observation, that the results of plasma treatment of materials above the luminous (second) region are better than above the filamentary (first) region.

In Fig. 5 the time-space map of the SPS is given. This map represents the accumulated time and space distributed luminosity of the SPS over thousands of discharge periods, representing the average exposure of the treated samples during the potential plasma treatment.

The results are qualitatively in agreement with cross-correlation spectroscopy measurements of Hoder et al.⁷, carried on one-filament coplanar discharge with pin-to-pin electrode configuration. The luminous regions can be distinguished above the anode in both semi-periods of the dis-

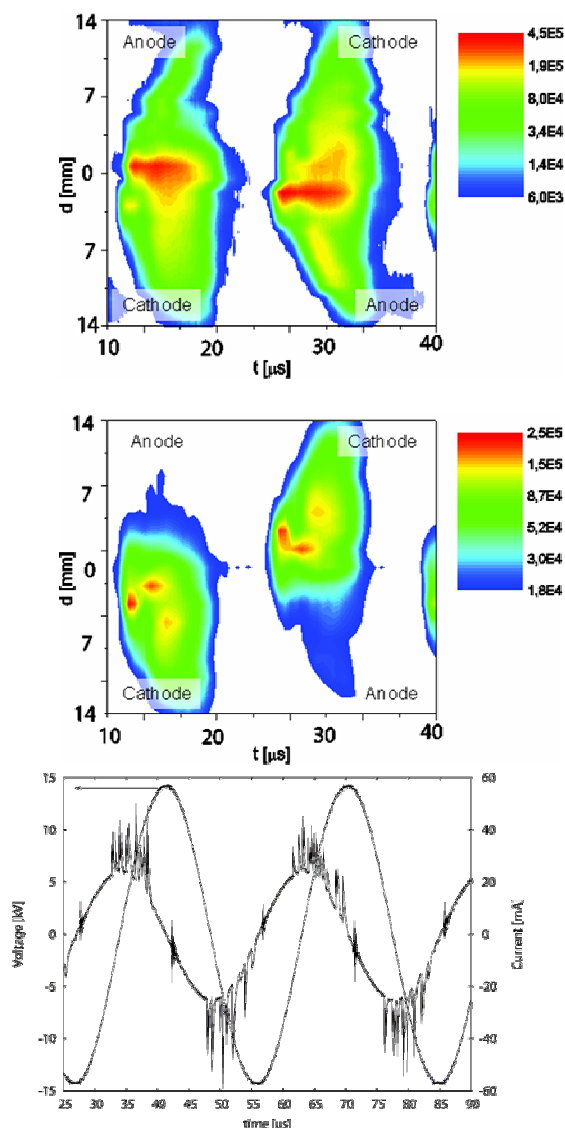


Fig. 5. Time-space map of SPS intensity (top) and FNS intensity (middle) interpolated from the time and space resolved spectra. Time scale represents time from the beginning of positive voltage period. The cathode (C) and anode (A) parts of the discharge is labeled (left). The typical time evolution of applied voltage and discharge current (bottom). These two figures do not represent the same measurements

charge.

It can be observed that the large area of the electrodes is effectively irradiated during the voltage period.

4. Conclusion

Experimental apparatus for the space and time resolved spectroscopy of DSCBD was successfully developed. The spatial profiles of intensities of SPS and the rotational and vibrational temperatures of SPS were obtained. The results

show the significant influence of the input voltage and electrode temperature on the plasma parameters of coplanar barrier discharge, especially in the spatial distribution of the intensities and temperatures. The time-space maps of the SPS intensities were also obtained. The results are in agreement with the DSCBD plasma treatment experiments.

This research has been supported by the grant No. 202/05/0777 of Czech Science Foundation, Grant of Academy of Science CR KAN101630651 and the Long-term intent project No. MSM0021622411, Ministry of Education, Czech Republic and by Slovak grants APVV No. 0485-06 and AV 4/2033/08.

REFERENCES

1. Becker K. H., Kogelschatz W., Schvenbach K. H., Bacher R. J.: *Non/Equilibrium Air Plasmas at Atmospheric Pressure, Series in Plasma Physics*, IOP, Bristol 2005.
2. Šimor M., Rahel J., Vojtek P., Brablec A., Černák M.: *Appl. Phys. Lett.* 81, 2716 (2002).
3. Černák M., Ráhel J., Kováčik D., Šimor M., Brablec A., Slaviček P.: *Contrib. Plasma Phys.* 44, 504 (2004).
4. Kováčik D., Zahoranová A., Buček A., Černák M.: *HA-KONE XI, Proceedings: Contributed Papers, Vol. 2, p. 493-497, Oléron Island, France, September 7-12, 2008.*
5. Kováčik D., Zahoranová A., Buček A., Ráhel J., Černáková, E., Černák M.: *17th Symposium on Physics of Switching Arc, Proceedings: Contributed Papers, Vol. I., pp. 129-132, Nové Město na Moravě, Czech Republic, September 10-13, 2007.*
6. Kováčik D., Brablec A., Ráhel J., Šťáhel P., Slaviček P., Chorvát D., Buček A., Zahoranová A., Zábudlá Z., Šimor M., Černák M.: *Contributed Papers and Invited Lectures, Physics of Switching Arc: Symposium, Nové Město na Moravě, Czech Republic, September 5-9, 2005.*
7. Hoder T., Šíra M., Kozlov K. V., Wagner H.-E.: *J. Phys. D: Appl. Phys.* 41, 035212 (2008).

J. Čech^a, P. Šťáhel^a, Z. Navrátil^a, and M. Černák^{a,b}

^(a)Dept. of Physical Electronics, F. of Science, Masaryk University, Brno, Czech Republic, ^(b)Dept. of Experimental Physics, Faculty of Mathematics, Physics and Informatics, Comenius University, Bratislava, Slovakia): **Space and Time Resolved Optical Emission Spectroscopy of Diffuse Coplanar Barrier Discharge in Nitrogen**

In this work we have studied the influence of electrode temperature and input power on plasma properties of the surface diffuse coplanar barrier discharge. Properties of the discharge can be affected by outer conditions and discharge configuration and better understanding of these effects can lead to optimization of the discharge parameters for industrial applications. The discharge was operated in nitrogen at atmospheric pressure. The power input and electrode temperatures were changed and plasma parameters were studied by the means of time and space resolved optical emission spectroscopy. These measurements gave us time and space distribution of discharge luminosity (e.g. intensity of second positive system of nitrogen) and spatial profiles of rotational and vibrational temperatures.

DOUBLE MONOCHROME SIGNAL (DOUBLE M-EFFECT) IN PULSED Ne-Ar-H₂ MIXTURE DISCHARGES

RODICA VLADOIU*, MIRELA CONTULOV,
and GEAVIT MUSA

Department of Plasma Physics, Faculty of Physics Chemistry
Electronics and Oil Technology, Ovidius University, Mamaia
124, Constanta, 900527, Romania

1. Introduction

The M-effect (mono-chromatization effect) is a physical phenomena defined by the emission of specific monochromatic line spectra in certain gas mixture plasmas¹⁻³.

Previous studies carried out in the case of the mixture of one electropositive gas and one electronegative gas – the main requirement for obtaining the M-effect – provided a clear 585.3 nm emission monochromatic line for Ne and H₂ mixture and 750.4 nm respectively for Ar and H₂ mixture at values of total pressure ranging between 10–100 torr (ref.⁴⁻¹¹).

Recent experiments revealed that the M-effect can be extended on two or more lines simultaneously just by adding more electropositive gases in the same reaction chamber¹².

The M-effect may be useful for explaining processes in known lasers and may also be important in developing of the new monochromatic light sources and also sources for standard references spectral lines, etc.¹⁴⁻¹⁷.

The aim of this paper is to put in evidence the emission spectral lines that present M-effect in pulsed discharges in Ne-Ar-H₂ mixtures. Also, the influence of the optical emission spectra at different percentages of hydrogen added in pulsed Ne-Ar mixture discharges from the total pressure is reported.

2. Experimental arrangement

A view of the experimental arrangement used for the study of the double M-effect is presented in the Fig. 1. The experimental set up consists from the following parts:

- The discharge tube,
- Power Supply,
- Vacuum system,
- Gas filling system.

The discharge tube is made from quartz with an inside diameter of 20 mm and an active length (maximum value) of 200 mm, the narrow-gap being 10 mm (Fig. 2). Just on the axes of this quartz tube there were two metallic electrodes mounted axially, which are movable along the axes of the quartz tube in order to have the possibility to establish various discharge spaces.

In order to help the ignition and also to ensure a stable discharge, the electrodes – made from tungsten wires with a diameter $\Phi = 1.5$ mm – are needle-like sharpened using the electrocorrosion technology.

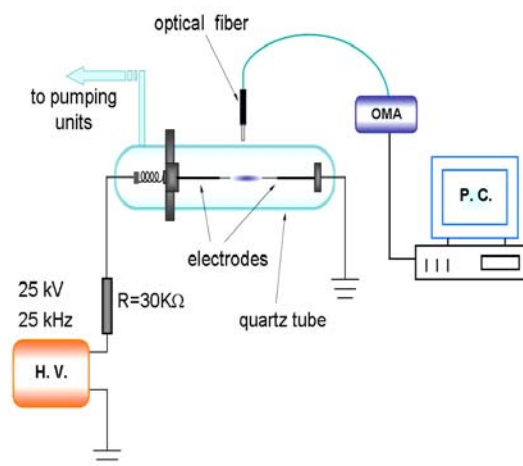


Fig. 1. Schematic diagram of the experimental arrangement

The tungsten wires – except the active electrode parts – are covered with glass or quartz tubing (except the discharge space) tightly bounded to the tungsten wire.

The uses of an adequate electrical source (power supply of 25 kV and a frequency of 25 kHz) to generate plasma ensure an increased efficiency of the emitted radiation. We find out that a high voltage pulsed sources is an optimum one because the source temperature is kept low (cooling between pulsed discharges) but delivering enough power due to 25 kV pulses of 25 kHz frequencies.

To ignite a discharge in the interelectrode space, the discharge device is filled with a gas mixture of an established composition of the used filling gas mixtures. A pulsed high voltage is applied across the electrodes. A bright light in the gas mixtures is established in the interelectrode space, due to the short and powerful applied voltage pulses.

Firstly a vacuum of $8.7 \cdot 10^{-3}$ mbar was created in the installation, after which Argon was allowed to enter until it reached a pressure of 90 Torr. After the pressure was dropped

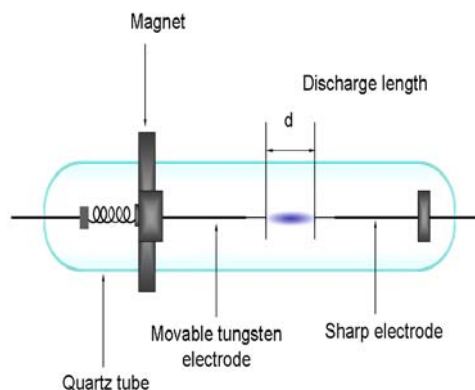


Fig. 2. The discharge device used for study of the double monochrome signal

down to 45 Torr in steps of 10 and then 5 Torr, and each time measuring the respective spectra, neon was pumped until the 90 Torr pressure was restored, thus having the conditions for the following measurements.

The following ones were taken by dropping the total pressure in steps of 10 Torr, until a pressure of only 40 Torr was reached. At that point Argon and Neon were pumped in the installation again in equal proportions, plus 10 percent hydrogen until the pressure raised back up to 90 Torr, and the measurements were taken as previously.

The following sets of measurements were made using higher proportions of hydrogen, raising the pressure in steps of 5 percent.

Measurements were taken with a total pressure ranging from 40 to 90 torr, in 10 by 10 steps. For each value of the total pressure, the partial pressure of the hydrogen in the mixture was raised respectively: 10 %, 15 %, 20 %, 25 %, 28 %, 30 %, 35 %, while the partial pressure of Ne and Ar were maintained permanently equal ($p_{Ar} = p_{Ne}$).

An Optical Multichannel Analyzer (OMA) is mounted transversally on quartz glass tubing and also on the discharge volume. Using OMA, with a cross-section of the optically active signal of 2 mm the discharge spectra is easily recorded.

The emission spectra were acquired using a PC-controlled Optical Multichannel Analyzer (OMA), Spectral Products SM 242. with the resolution of 0,9 nm over an intervals from 200 to 850 nm.

Usually, it is necessary to calibrate the OMA before use but in the case of M-effect the studied emission spectral lines are well known and can be easily identified.

3. Results and discussion

An interesting influence of the percentage of H_2 on the double M-effect was noticed at total pressure ranged from 40–80 torr.

The spectral lines for Ar-Ne mixture at 50 torr's total pressure are given in Fig. 3 as reference spectrum ($p_{Ar} = p_{Ne}$) compared to emission spectra in the Ne-Ar- H_2 mixture

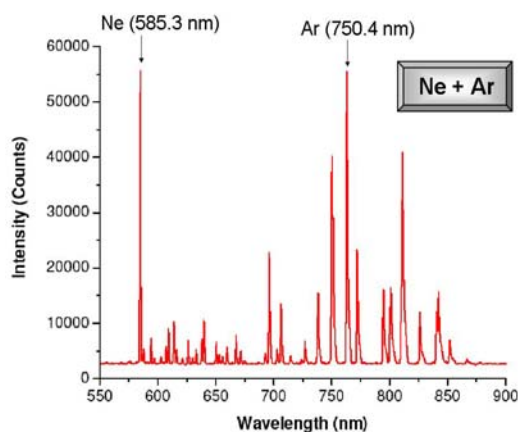


Fig. 3. Emission spectra of Ne-Ar mixture at 50 Torr's total pressure

Table I

The values of relative intensity for Ne-Ar- H_2 mixture discharge at 20 % H_2 from total pressure

H_2 percentage [%]	Total pressure [torr]	Relative intensity I_{Ne} [a.u.]	Relative intensity I_{Ar} [a.u.]
20	40	22146	65535
	50	20093	52812
	60	26415	61034
	70	29701	57944
	80	45486	64500
	90	62338	56676

discharges at 20 and 28 % H_2 respectively from total pressure.

At percentage of $H_2 < 20$ % the intensity line corresponding to M-effect for Ne (585.3 nm) was higher than the intensity line corresponding to the M-effect for Ar (750.4 nm), as well as for percentages greater or equal to 28 %, for all the total mentioned pressures above as it can be seen in the Fig. 4.a, b.

Table I gives the experimental values of the line intensities taken for Ne-Ar- H_2 mixture discharge at 20 % H_2 from total pressure given in Fig. 4a.

But, in the case of $p_{H_2} = 20$ %, the coupling of these two line was inverted, the intensity line corresponding to M-effect for Ar (750.4 nm) was higher than the intensity line corresponding to the M-effect for Ne (585.3 nm).

In Table II are presented the values obtained in the case of Ne-Ar- H_2 mixture discharge at 28 % H_2 from total pressure shows in Fig. 5b.

It has to be underlined the fact that only in the case of the 90 Torr total pressure the coupling remains accordingly to the previous behavior.

As can be seen in these figures, on additional of hydrogen, a drastic change of the emission spectrum of Ne takes place.

Figures 5a,b shows the intensity results of Ne and Ar lines for different values at 20 and 28 % H_2 respectively from total pressure.

This interesting feature can be attributed to the following elementary processes: three body collisions and also other

Table II

The values of Ne-Ar- H_2 mixture discharge at 28 % H_2 from total pressure

H_2 percentage [%]	Total pressure [torr]	Relative intensity I_{Ne} [a.u.]	Relative intensity I_{Ar} [a.u.]
28	40	65098	10025
	50	56928	8961
	60	60520	10595
	70	64082	12547
	80	61100	13416
	90	62112	17169

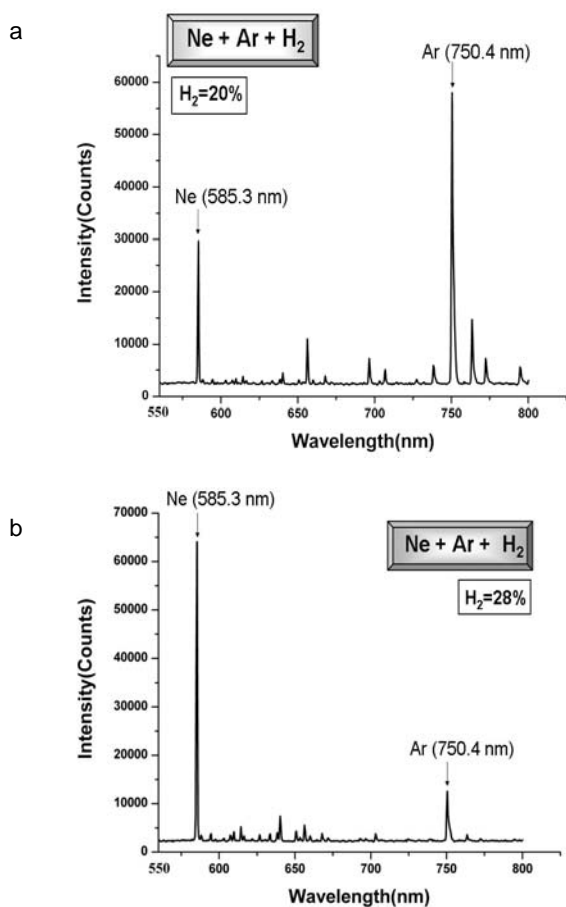


Fig. 4. a) Emission spectra of Ne-Ar-H₂ mixture discharge at 20 % H₂ from total pressure, b) Emission spectra of Ne-Ar-H₂ mixture discharge at 28 % H₂ from total pressure

processes with high rate of efficiency as additional effects for explaining the M-effect like trapped resonant radiation or metastable capture.

The distance between electrodes can be changed at will using permanent magnets. Usually in the present experiment most of the data was taken using a distance between the electrodes of 10 mm, but other distances could be used as well, the quality of the measurements not being affected by this factor. Fig. 6 shows the photo image for the Ne-Ar-H₂ mixture discharge at 28 % H₂ from total pressure.

The conditions for M-effect appearance are the following ones:

- nearly zero electric field in plasma region where the negative ions are generated;
- high density of electrons;
- low electron temperature in order to ensure the electron attachment to electronegative atoms or molecules;
- high partial pressure of the gas mixture atomic and molecular partners from the total pressure;
- high total pressure of the gas mixture (toward atmospheric pressure) in order to sustain triple particle collisions;

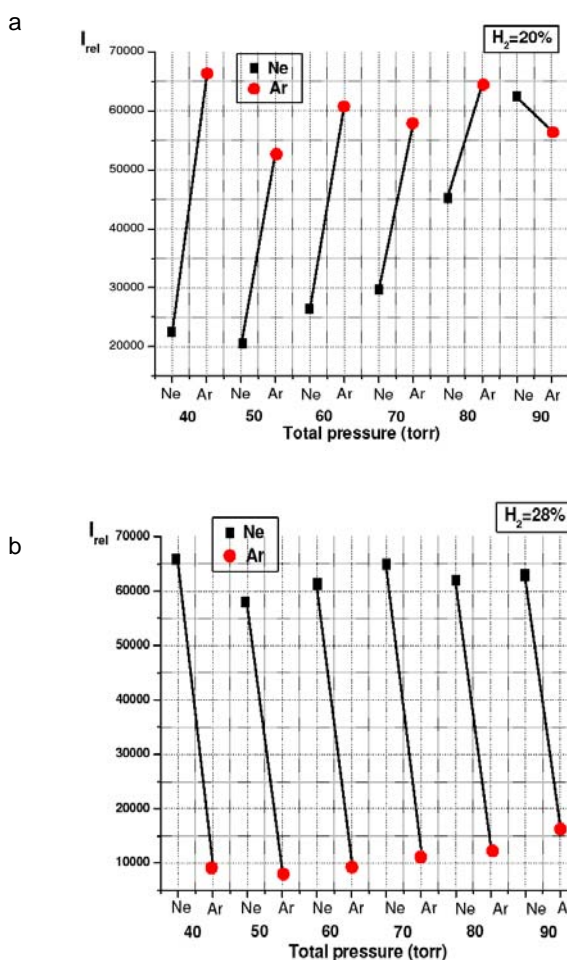


Fig. 5. a) Results of relative intensity of Ne and Ar lines for different values at 20 % H₂ from total pressure, b) Results of relative intensity of Ne and Ar lines for different values at 28 % H₂ from total pressure

- low temperature of the gas mixture in order to reduce the collisional quenching of the reacting triple particle compound.

It can be underlined that two processes are responsible for the appearance of this effect: ion-ion recombination, a process with high cross-section and resonant three body collision reaction of heavy particles. Moreover, another possible explanation for this could be the gas temperature of the plasma in which M-effect was generated because one of the conditions to appear the effect is that the gas temperature must be low in order to avoid the quenching processes in the ion-ion recombination.

4. Conclusions

The current paper reports on new research on the simultaneous appearance of two M-effect in a discharge tube containing two rare gases and an electronegative gas, the hydrogen.

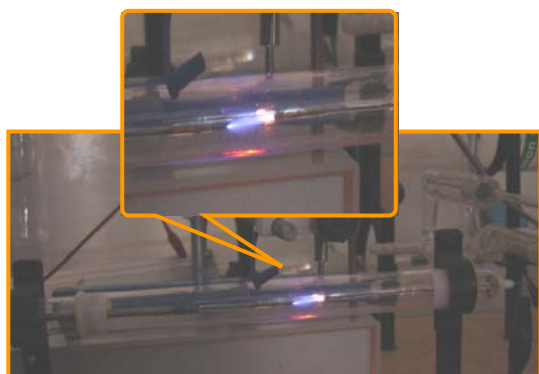


Fig. 6. Digital photo image of the Ne-Ar-H₂ mixture discharge

The M-effect is a powerful effect which gives monochromatic line spectra of wavelengths dependent on the type of gas used.

The mechanism responsible for the generation of the monochrome radiation is based on elementary process of three body collision. This behavior was explained by ion-ion recombination.

New experiments revealed that this effect can be obtained simultaneously for two different electropositive gases, in the same plasma.

In this paper a mixture of Ne-Ar with H₂ was used to demonstrate the existence of this multiple M-effect signal.

The influence of percentages of hydrogen added in Ne-Ar discharges reveals a very interesting feature of the emission spectra due to the physical processes involved in the double M-effect.

These results have opened a new research area, with tremendous applications involving custom wavelength emission line sources.

REFERENCES

1. Musa G., Popescu A., Baltog A., Mustata I., Niculescu N., Lungu C. P.: *Revue Roumaine de Physique* 26, 125 (1981).
2. Musa G., Popescu A., Baltog A., Lungu C. P.: *Romanian Reports in Physics* 45, 287 (1993).
3. Lieberman M. A., Lichtenberg A. J.: *Principle of plasma discharges and Material Processing*, John Willey & Sons, N. Y. 1995.
4. Musa G., Popescu A., Baltog A., Mustata I.: *J. Phys. Appl. Phys.* 18, 2119 (1985).
5. Musa G., Baltog A., Bajeu G., Lungu C. P., Raiciu R., Borcoman I., Ricard A.: *Eur. Phys. J. Applied Physics* 4, 165 (1998).
6. Byoung-Kulk Min, Lee S.-H., Park Hun-Gun: *J. Vac. Sci. Technol.* 18, 349 (2000).
7. Curran N. P., Hopkins M. B., Vender D., James B. W.: *Plasma Sources Sci. Technol.* 9, 169 (2000).
8. Musa G., Baltog A.: *Contrib. Plasma Phys.* 43, 216 (2003).
9. Musa G., Ciobotaru L. C., Baltog A., Chiru P.: *Eur. Phys. J. Applied Physics* 28, 339 (2004).
10. Musa G., Ciobotaru C. I., Chiru P., Baltog A.: *J. Optoelectron. Adv. Mater.* 6, 459 (2004).
11. Musa G., Baltog A.: *Rom. Reports Phys.* 54, 79 (2002).
12. Musa G., Surdu-Bob C., Vladioiu R.: *J. Optoelectron. Adv. Mater. – Rapid Communications* 1, 305 (2007).
13. Musa G., Surdu-Bob C., Vladioiu R.: *J. Optoelectron. Adv. Mater.* 9, 2653 (2007).
14. Olson R. E., Peterson J. R., Moseley J.: *J. Chem. Phys.* 53, 3391 (1970).
15. Musa G., Surdu-Bob C. C., Chiru P.: *Rom. J. Phys.* 50, 749 (2005).
16. Curran N. P., Hopkins M. B., Vender D., James B. W.: *Plasma Sources Sci. Technol.* 9, 169 (2000).
17. Katsch H.-M., Quandt E.: *J. Phys. D.: Appl. Phys.* 25, 430 (1992).

DEPENDENCE OF HIGHER HARMONIC FREQUENCIES MEASURED IN CAPACITIVELY COUPLED PLASMA ON THE MATCHING UNIT PARAMETERS

PAVEL DVOŘÁK* and ZDENĚK MORAVEC

Masaryk University, Faculty of Science, Kotlářská 2,
611 37 Brno, Czech republic
pdvorak@physics.muni.cz

Introduction

Nonlinear behaviour of sheaths in capacitively coupled discharges gives rise to higher harmonic frequencies of RF voltage and current^{1,2}. The higher harmonics influence the plasma parameters^{3,4}, especially at low pressures. Moreover, they can be used for diagnostics purposes^{5,6}. However, the higher harmonics show a complicated dependence on both the plasma and the reactor parameters including the parameters of the matching unit. Since the matching unit parameters are not constant during numerous plasma measurements or processes, it is useful to understand the influence of the matching unit parameters on the higher harmonics behaviour. Therefore, this article deals with measurements of the influence of the matching unit parameters on the higher harmonic amplitudes. Since the higher harmonics are strong especially inside the plasma, they were measured by means of an uncompensated probe immersed directly into the plasma between the electrodes.

Experimental

The experiments were carried out in a spherical (i.d. ca 33 cm) stainless steel grounded reactor with two horizontally mounted, parallel, stainless steel electrodes of 80 mm diameter. The upper electrode, embedded in a grounded ring, was driven at the frequency of 13.56 MHz. The bottom electrode was grounded. Their distance was 40 mm. The reactor was exhausted by a turbomolecular pump with a membrane pump. The pressure varied within the range 4–32 Pa. The presented

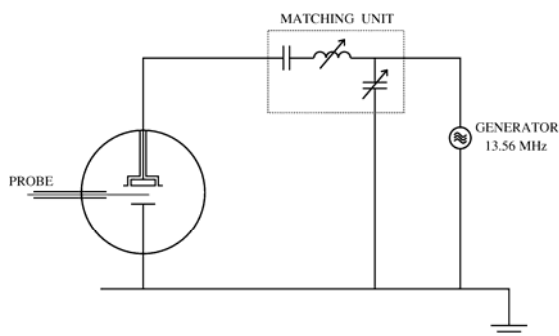


Fig. 1. Schema of the experimental apparatus

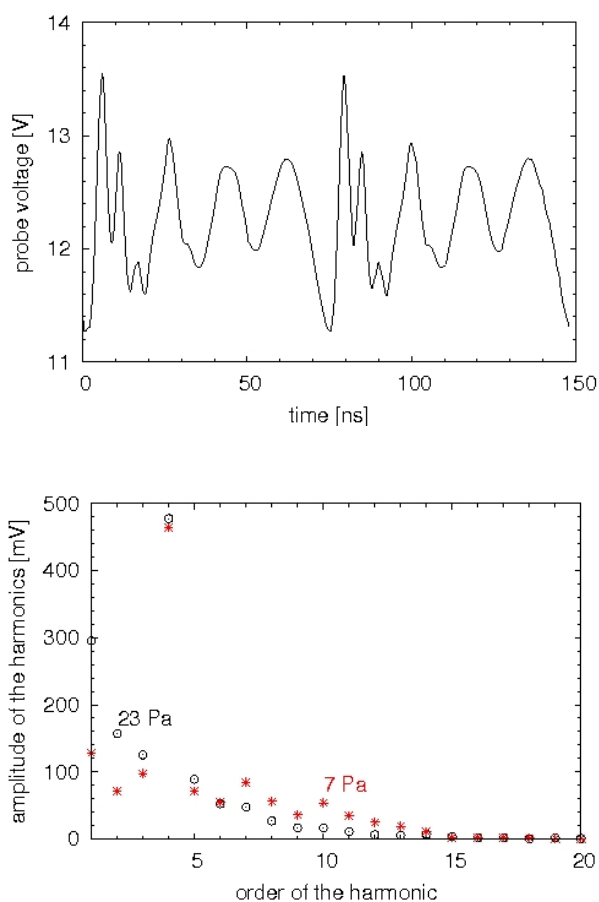


Fig. 2. Two periods of a typical waveform measured by means of an uncompensated probe immersed into the plasma (upper graph) and two examples of the Fourier transformation of the probe waveform (bottom graph). The stars and circles represent measurements at 7 Pa and 23 Pa, respectively

experiments were carried out in argon.

The matching unit, which was placed between the RF generator and the powered electrode, consisted from two capacitors (one from them was tunable) and a tunable coil. The schema of the electric circuit is shown in the fig. 1. The RF power varied within the range 10–45 W. The DC self-bias was measured on the coaxial cable between the matching unit and the reactor.

The higher harmonic frequencies were measured by means of an uncompensated probe consisting of a metallic wire connected via a coaxial cable to the oscilloscope. Since the wire was immersed directly into the plasma, it was a sensitive sensor of higher harmonics. The amplitudes of the harmonics were calculated by Fourier transformation.

Results and discussion

Whereas the current and voltage waveforms measured on the coaxial cable between the matching unit and the reac-

tor showed only small deviations from a monofrequency sinusoidal behaviour, the uncompensated probe voltage was superposed by a number of strong harmonic frequencies. A typical waveform measured by means of the probe and its Fourier transformation are shown in the fig. 2. The waveform consists from more than ten harmonic frequencies whose amplitude generally decreases with increasing order (frequency) of the harmonic. It is worth to mention that higher harmonics are stronger at low pressure since they are less damped by the electron-neutral collisions and they can eventually reach the series plasma-sheath resonance⁷. The relationship between the measured probe voltage waveform and the time dependence of the plasma potential is quite complex, since the measured waveforms are affected by the probe electric parameters and by the thin nonlinear sheath around the probe. However, proper understanding of this relationship is not necessary for the plasma monitoring based on the uncompensated probe. Consequently, simply the amplitudes measured by the probe were used for the purpose of this article without an complicated calculation of the amplitudes of the plasma potential harmonics.

Firstly, the uncompensated probe voltage waveforms

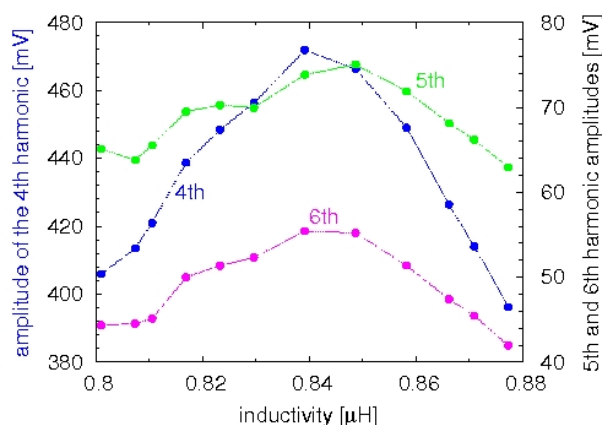
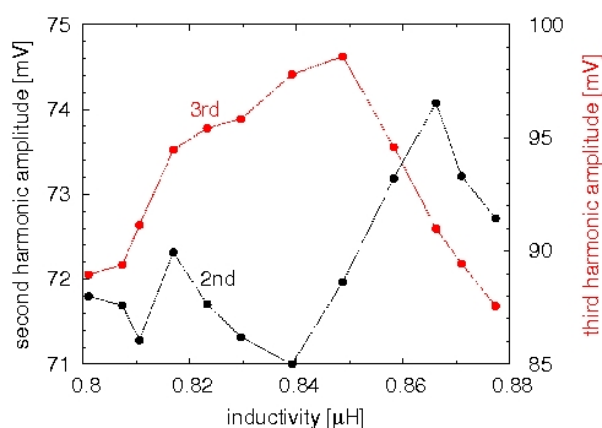


Fig. 3. The dependence of the amplitude of second and third (upper graph) and fourth to sixth (bottom graph) harmonic frequencies on the inductivity of the coil in the matching unit. The power produced by the RF generator was kept at 30 W during this measurement

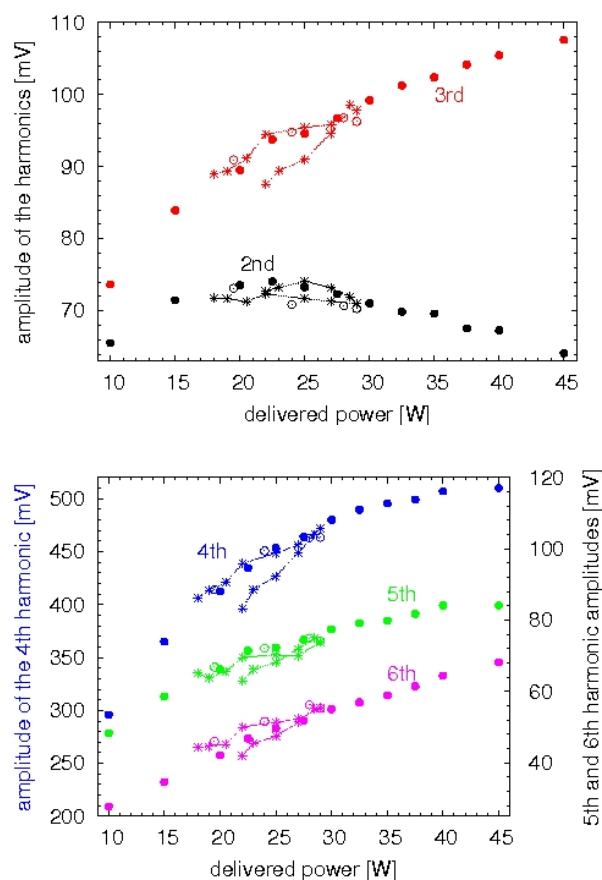


Fig. 4. The dependence of the amplitude of second and third (upper graph) and fourth to sixth (bottom graph) harmonic frequencies on the (non-reflected) power delivered to the discharge. The closed circles represent the power dependence measured at constant matching unit parameters, the stars represent the dependence measured at various coil inductances (see fig. 3) and the open circles are measurements with various capacitances of the capacitor

were measured at various matching unit parameters and the higher harmonic amplitudes were calculated from the recorded data. The power produced by the RF generator was kept constant during these measurements. An example of the dependence of higher harmonic amplitudes on the matching unit parameters is shown in the fig. 3. This figure depicts the dependence of the harmonic amplitudes on the matching unit coil inductivity at argon pressure of 7 Pa. The picture shows behaviour of only five harmonic frequencies (second to sixth) because the other harmonics with higher order show very similar behaviour to the five depicted harmonics. Most of the harmonic amplitudes reach their maxima at the inductivity of approximately 0.84 μH , which corresponds to an ideal tuning of the matching unit. At this inductivity the RF power delivered to the discharge reaches its maxima resulting in the highest harmonic amplitudes.

The measurements shown in the fig. 3 evoke a question whether the only reason for the depicted behaviour of higher harmonics is the change of the RF power delivered to the discharge. In order to test this hypothesis power dependences

of the higher harmonic amplitudes were measured at constant matching unit parameters. The parameters related to the best matching were chosen. These power dependences of the second to sixth harmonic amplitudes measured at 7 Pa are shown in the fig. 4. The same picture shows the dependences of the harmonic amplitudes measured at constant generator power but at varying inductivity of the matching unit coil (the dependences depicted in the fig. 3) or at varying capacity of the matching unit capacitor. In spite of the fact that the power produced by the RF generator was constant in these two measurements, the power delivered to the discharge varied due to the reflections caused by the unideal matching. Therefore, both these dependences of the harmonic amplitudes can be shown in the fig. 4 as functions of the RF power delivered to the discharge. Since the three dependences shown in the fig. 4 (which are represented by closed circles, stars and open circles) do not coincide, the change of the higher harmonic amplitudes induced by the change of the matching unit parameters is not caused only by the change of power delivered to the discharge. In other words, any change of process parameters followed by a change of matching unit parameters can cause a change of higher harmonics even if the power

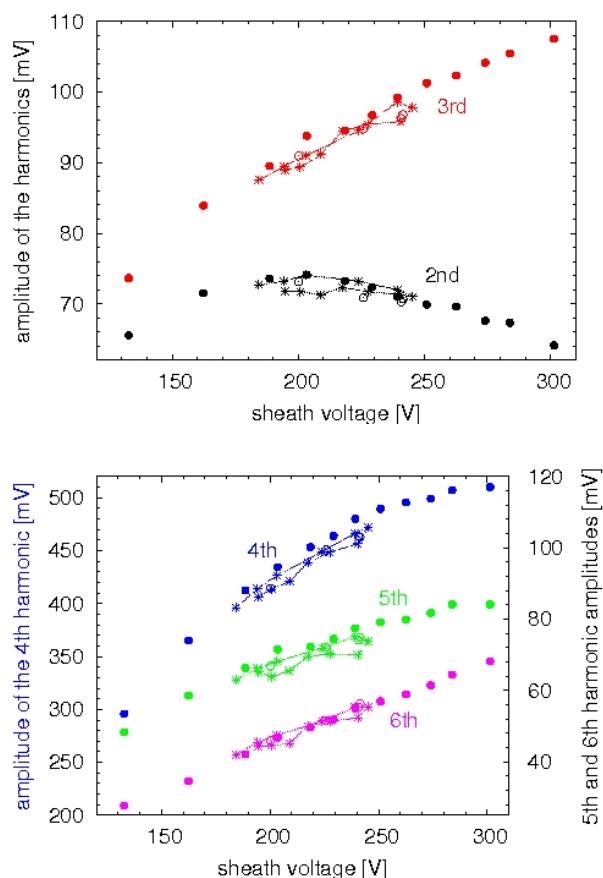


Fig. 5. The dependence of the amplitude of second and third (upper graph) and fourth to sixth (bottom graph) harmonic frequencies on the sheath voltage. The symbols and their meanings are the same as in the fig. 4

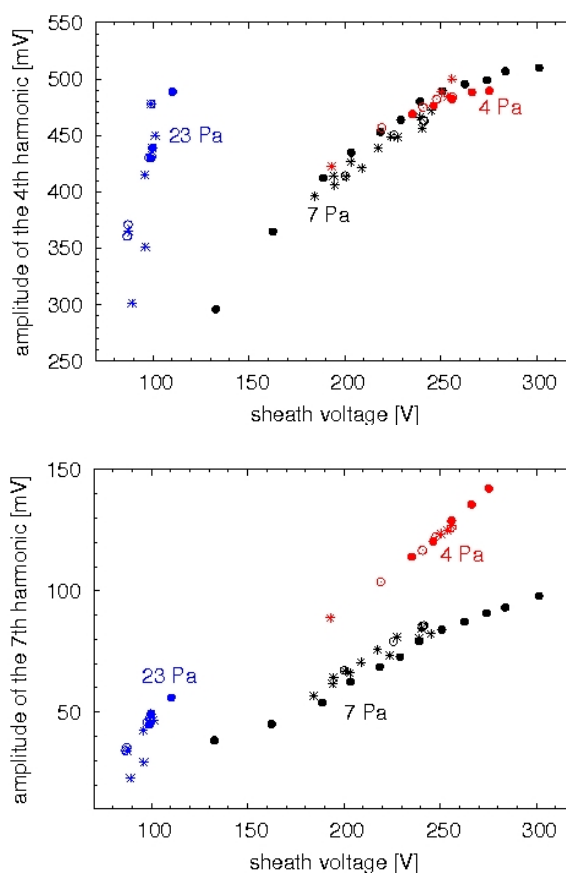


Fig. 6. The dependence of the amplitude of the fourth (upper graph) and the seventh (bottom graph) harmonic frequency on the sheath voltage for three different argon pressures. The symbols and their meanings are the same as in the fig. 4

delivered to the discharge remains constant.

Since higher harmonics are produced by the nonlinearity of sheaths, all the measurements that were depicted in the fig. 4 are shown in the fig. 5 as functions of the DC voltage of the sheath at the powered electrode. The value of the sheath voltage was estimated as a difference between the probe floating potential and the DC self-bias measured at the powered electrode. This estimation neglects the difference between the floating potential of the uncompensated probe and the plasma potential, which is sufficiently small when compared with the sheath voltage. Since the discharge was strongly asymmetric at the pressure of 7 Pa, the sheath voltage at the grounded electrode was negligible when compared to the sheath voltage at the powered electrode. In this case, all the three depicted dependences coincide well. As a result, at our particular experimental conditions the behaviour of the higher harmonics induced by the change of the matching unit parameters was entirely controlled by the behaviour of the sheath voltage.

The above described dependences were measured at the pressure of 7 Pa. The same measurements were carried out also at different pressures and examples of the measurements are shown in the fig. 6. The harmonic amplitudes changed

significantly when the pressure was changed since the harmonics are sensitive to many pressure dependent plasma parameters like electron concentration, electron collisional frequency, discharge asymmetry etc. However, the fact that the change of the harmonic amplitude induced by the change of matching unit parameters can be explained by the change of the sheath voltage remained approximatively valid. Certain deviation from this rule can be seen in the case of the pressure 23 Pa. At this pressure the discharge was not longer asymmetric enough to enable the neglect of the sheath at the grounded electrode and the influence of this sheath should be taken into account.

Conclusion

The dependence of amplitudes of higher harmonic frequencies on the matching unit parameters was measured in asymmetric capacitively coupled discharge by means of an uncompensated probe immersed into the plasma. Most of the harmonics reached their maxima in the case of optimal matching, i.e. when the RF power delivered to the discharge was maximal. However, the decrease of the power delivered to the discharge due to the power reflection caused by a change of matching unit parameters did not explain the behaviour of higher harmonics sufficiently. It was shown that the behaviour of higher harmonics was at our experimental conditions determined by the sheath voltage.

This research was supported by the MSM, contract 0021622411.

REFERENCES

1. Lieberman M. A.: IEEE Transactions on Plasma Science 16, 638 (1988).
2. Mussenbrock T., Ziegler D., Brinkmann R. P.: Phys. Plasmas 13, 083501 (2006).
3. Rauf S., Kushner M. J.: J. Appl. Phys. 83, 5087 (1998).
4. Mussenbrock T., Brinkmann R. P.: Appl. Phys. Lett. 88, 151503 (2006).
5. Law V. J., Kenyon A. J., Thornhill N. F., Srigengan V., Batty I.: Vacuum 57, 351 (2000).
6. Klick M., Rehak A., Kammeyer M.: Jpn. J. Appl. Phys. 36, 4625 (1997).
7. Ku V. P. T., Annaratone B. M., Allen J. E.: J. Appl. Phys. 84, 6536 (1998).

P. Dvořák* and Z. Moravec (*Masaryk University, Faculty of Science, Brno, Czech republic*): **Dependence of Higher Harmonic Frequencies Measured in Capacitively Coupled Plasma on the Matching Unit Parameters**

Higher harmonic frequencies of electric voltage and current are significant features of low-pressure capacitively coupled discharges. Their behaviour is quite complex since it is a function of many plasma and reactor parameters. This article deals with the influence of matching unit parameters on amplitudes of higher harmonics, which were measured by means of an uncompensated probe immersed into the plasma of an asymmetric capacitive discharge. Most of the harmonics reached their maxima in the case of optimal matching, i.e. when the RF power delivered to the discharge was maximal. However, the amount of the power delivered to the discharge did not explain the behaviour of higher harmonics sufficiently. It was shown that at our experimental conditions the behaviour of higher harmonics was determined by the sheath voltage.

POPULATION STATISTICS OF ELECTRON AVALANCHES AND STREAMERS

TOMÁŠ FICKER

Department of Physics, Faculty of Civil Engineering, Brno
University of Technology, Žižkova 17, 602 00 Brno
ficker.t@fce.vutbr.cz

So far the exponential distribution of charge populations of electron avalanches has been considered as a regular distribution describing avalanches regardless of their average carrier populations \bar{n} . The distributions of avalanches with high populations ($\bar{n} > 10^5$) that exhibit peculiar convex shapes, deviated from that of exponential, have been considered as experimental artefacts¹. On the basis of our refined experiments^{2–4} we argue for a new interpretation of these peculiar distribution curves. The new interpretation is based on the Pareto distribution^{2,4}. The basic physics underlying „deviated“ statistical distributions is intimately related to the inner space charges formed inside the avalanches with higher carrier populations. The formation of space charges inside avalanches is accompanied by the transition from collisional ionisation to photoionisation and this leads to manifestation of a new statistical behaviour.

The microdischarges (high populated avalanches and streamers) have been detected by the classical RC-circuit where the capacitor has been formed by the flat bronze electrodes between which the polyethyleneterephthalate foil of 0.18 mm thick has been inserted. The electrodes have been loaded with the constant high voltages ranging from 2 kV to 8 kV. The whole electrode system has been embedded into the Faraday cage. All experiments have been carried out under normal atmospheric conditions. Avalanches and streamers have been detected across the measuring resistance $R = 100 \text{ k}\Omega$ as short voltage pulses $u(t)$ with random amplitudes $U \sim n$.

Collecting a large statistical ensemble of pulses (50–60 thousand pulses) a common histogrammic technique has allowed to form the probability density function $w(U)$. This function shows different behaviours when following the exponential or Pareto statistics. The exponential probability density function is given as follows

$$w(U) \approx \frac{1}{\bar{U}} \exp\left(-\frac{U}{\bar{U}}\right) \quad (1)$$

whereas the Pareto probability density function reads

$$w(U) \approx c_0 \cdot U^{-(D+1)} \quad (2)$$

where c_0 is a constant and D fractal dimension.

Extensive experimental work has shown that the Pareto distribution is definitely a more convenient distribution for high populated avalanches and streamers as compared with that of exponential. The following illustrations (Fig. 1 and 2) offer an example where it can be seen how well the Pareto

function follows the measured experimental data whereas the exponential fit shows an essential discrepancy.

Numerous experiments performed in our laboratory have unambiguously supported the Pareto distribution function as a reasonable choice which fulfils requirements for a successful description of the statistical behaviour of Townsend's high populated avalanches and streamers. The main difference between the Pareto statistics of Townsend's avalanches and the Pareto statistics of streamers consists in their D -values. High populated Townsend's avalanches show smaller D , i.e. $0 < D < 1$, whereas streamers possess $D \geq 1$.

Although in the past some researchers¹ tried to explain the ‘peculiar’ statistical behaviour of high populated avalanches and streamers by an experimental artefact, today it is clear that the Pareto distribution is, at least, a very convenient approximation if not an exact statistical law governing populations of saturated electron avalanches and streamers. However, so far no theory has been developed for this peculiar statistical behaviour. To tackle successfully the problem, it is necessary to find a corresponding physical process underlying

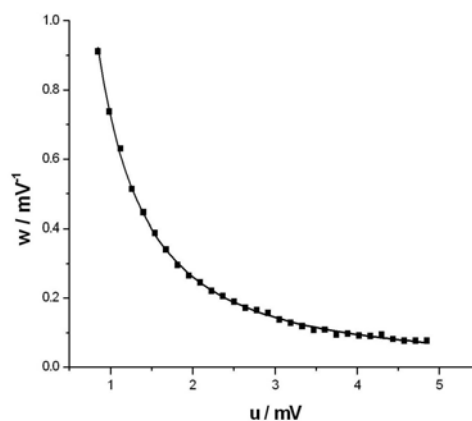


Fig. 1. Pareto's power function fit (2) of experimental data; $E/p = 52 \text{ V Pa}^{-1} \text{ m}^{-1}$; Fitting constants: $c_0 = 0.724$ and $D = 0.471$

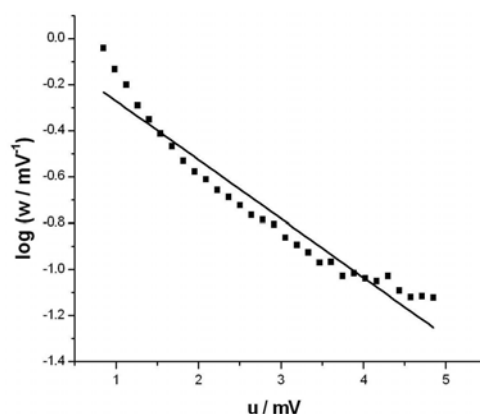


Fig. 2. Exponential fit (solid line) of experimental data; $E/p = 52 \text{ V Pa}^{-1} \text{ m}^{-1}$; Fitting constant $\bar{U} = 1 \text{ mV}$

the phenomenon. There are three important points that should be taken into account when forming a theoretical concept explaining the mentioned cross-over of the exponential statistics to the Pareto one:

- The change of statistical behaviour occurs simultaneously with the change of electron multiplication, i.e. when photoionisation starts dominating over collisional ionisation and, as a consequence, high populated avalanches appear ($\bar{n} > 10^5$).
- Since all fractal objects are governed by the Pareto statistics, the electron multiplication mechanism that forms the Pareto set of avalanches has to be of fractal nature, too.
- The fractal photoionisation multiplication should be based on creating additional smaller avalanches accompanying the initial (parent) avalanche because an increase of electron populations within parent avalanches leads only to an increase of average populations \bar{n} which does not change the character of the exponential distribution itself (I).

A proposal of a convenient fractal mechanism of electron multiplication, capable to create the Pareto set of electron avalanches, is formulated in the following paragraphs.

On the basis of the experimental observations and deductions mentioned above it is clear that the multiplication mechanism of high populated avalanches, whose populations follow Pareto's distribution, may be governed by a fractal scenario with the following properties.

- Besides a parent avalanche a series of additional smaller avalanches arise inside the discharge gap. These smaller avalanches are generated in a hierarchical manner with different mean populations \bar{n}_d

$$\{\bar{n}_d\}_{j=0}^J = \left\{ e^{\alpha(d-j\bar{\Delta})} \right\}_{j=0}^J, \quad J \leq \frac{d}{\bar{\Delta}} - 1 \quad (3)$$

In this way the number of less populated avalanches increases and, as a consequence, deviations from the exponential distribution may occur.

- Multiplication of high populated avalanches with mean populations $\{\bar{n}_d\}_{j=0}^J$ must be generated according to a fractal scenario based on branching or partitioning like most fractals when going to smaller scales. Therefore, some type of fractal avalanche branching should be explored. The branching should originate with a parent avalanche possessing a mean population $n_{d,0} = e^{\alpha d}$ (fractal initiator). After having passed a certain distance $\bar{\Delta} > 0$ and gathered a certain number of energetic electrons $\bar{N} = e^{\alpha \bar{\Delta}} \geq 1$, which are capable of creating a group of UV photons, a photoionisation process may start and a swarm of $\bar{K} \geq 1$ smaller avalanches with mean populations $\bar{n}_{d,1} = e^{\alpha(d-\bar{\Delta})}$ may appear beside the parent avalanche. Let us call them the "side avalanches of the first generation". The side avalanches of the first generation actually represent the so-called fractal generator given by the multiplicity \bar{K} . The side avalanches, once created, become parent avalanches for the next generation of new side avalanches. So, the side avalanches of the

first generation become parent avalanches for the side avalanches of the second fractal generation with the mean population $\bar{n}_{d,2} = e^{\alpha(d-2\bar{\Delta})}$. This process of avalanche multiplication may or may not continue up to the last possible generation $J = d/\bar{\Delta} - 1$ with the mean population $\bar{n}_{d,J} = e^{\alpha(d-J\bar{\Delta})}$. Provided the multiplicative process reaches the j th generation, the mean (average) total number of side avalanches is just \bar{K}^j . The multiplicative process described yields a hierarchy of avalanches and when extended to infinity ($J \rightarrow \infty$), it yields an infinite set of avalanches that is similar to the well-known fractal object called the Cantor fractal set. By using the mentioned similarity a relation between avalanche characteristics and properties of the fractal set can be easily found

$$\bar{K}^j = \left(\frac{L_0}{l_j} \right)^D = \left(\frac{\bar{n}_{d,0}}{\bar{n}_{d,j}} \right)^D \Rightarrow \bar{K}^j = (\bar{N}^j)^D \Rightarrow D = \frac{\ln \bar{K}}{\ln \bar{N}} \quad (4)$$

Since all fractal objects obey the Pareto statistics with the probability density in the form of the power law (2), the studied avalanche set, being of fractal nature, will also follow this statistical law

$$w(n) = c_o \cdot n^{-(1+D)} = c_o \cdot n^{-\left(1 + \frac{\ln \bar{K}}{\ln \bar{N}}\right)} \quad (5)$$

Such a strictly deterministic mechanism, which has already been described, might hardly be expected in a real situation. Instead, a strongly stochastic mechanism is more probable with certain distributions of detectable quantities Δ , K and N . However, using their average values $\bar{\Delta}$, \bar{K} and \bar{N} makes the treatment more realistic and partly advocates the deterministic view of the problem.

- The described fractal mechanism of multiplication of high populated avalanches anticipates that the most probable place where a parent avalanche initiates side avalanches is in some of the first $\bar{\Delta}$ -intervals because due to diffusion at a larger distance the parent avalanche is broadened enough to integrate the side avalanches.

The foregoing paragraphs have summarised the main properties of the concept of fractal multiplication of high populated avalanches.

Taking into account all the foregoing considerations and summarising the exponential probability density functions for all avalanche generations, one can obtain⁴ the following general expression that contains both the exponential and Pareto distributions as special asymptotic cases

$$F(n, d) \approx \frac{G}{\bar{n}_d} \sum_{j=0}^J (\bar{K} \cdot \bar{N})^j \cdot \exp\left(-\frac{n \cdot \bar{N}^j}{\bar{n}_d}\right) \quad (6)$$

where G is a normalisation constant.

At first sight the probability density (6) seem not to be likely to follow the Pareto power law (2) but the opposite is true. When this function is plotted with convenient parameters

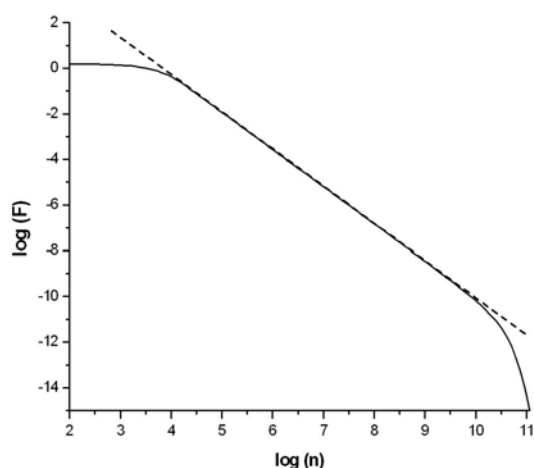


Fig. 3. **Fractal fit (6) (solid line).** Fitting constants: $\bar{K}=2$, $\bar{N}=3$, $\bar{n}_d=10^0$, $D=0.631$, $J=12$, $G=1$

\bar{n}_d , \bar{K} and \bar{N} within bilogarithmic co-ordinate systems, their graphs indeed show linear sections (power behaviours) spanning over many orders of magnitudes of electron populations. In Fig. 3 there is an example of such a plot showing a perfect linear section.

To illustrate the capability of the generalised statistical pattern (6) to fit faithfully the experimental data of population statistics, the data from Fig. 1 have been fitted by the pattern (6) – see Fig. 4. As far as the fractal dimensions are concerned, they are in excellent agreement (≈ 0.471 in Fig. 1 versus ≈ 0.473 in Fig. 4). At this point we would like to mention that all other data measured in our laboratory during the last 13 years have been processed in the same way. They have confirmed the same fact, namely that the generalised distribution function (6) is capable to reproduce faithfully the statistical data of high populated electron avalanches and streamers. Shortly speaking, the generalised statistical pattern (6) seems

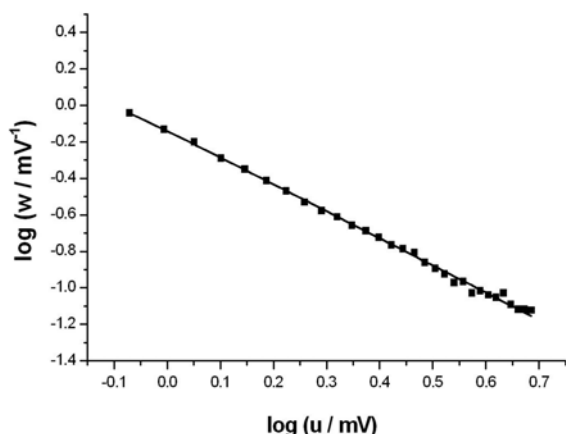


Fig. 4. **Fractal fit (solid line) of experimental data** ($E/p = 52 \text{ V Pa}^{-1} \text{ m}^{-1}$; Fitting constants: $\bar{K}=1.3882$, $\bar{N}=2$, $\bar{n}_d \rightarrow u_d = 10^{555}$, $D=0.473$, $J=7$, $G=0.105$)

to be a very convenient probability density function capable to incorporate all the main specific features of fractal avalanche multiplication.

The fractal population distribution functions of the Pareto type have also been confirmed⁵ by spot statistics. Under the term „spot statistics“ it is understood the following: streamers, when impinging on a suitable sensibilised photographic film (dielectric barrier), leave light spots with dark centres on its surface (see Fig. 5).

From the photographic point of view the explanation of the spot structures is clear: the places of dark islands had to be screened from light at the moment of exposition. Nevertheless, from the physical point of view it seems to be a problem to suppose that mass particles reach the surface of the film sooner than the light they emit during their movement. Taking into account the whole mechanism of the streamer development and propagation, especially in its final stages when streamers are converted into sparks, the situation becomes much clearer. During streamer propagation back to the film barrier (which is the cathode in this case) the light emission is insufficient to expose the photographic emulsion due to its very low sensitivity (5 DIN). When the positive head of a streamer impacts on the surface of the polymeric cathode, an effective screening is created. The gap is then bridged with a thin channel of high conductive plasma and a mass of electrons having been liberated from the cathode by an intense UV radiation of the streamer head can quickly propagate to the anode. This concluding stage of streamer development is often termed as a ‘backward ionizing wave of potential’ or shortly ‘return stroke’ and represents the spark process which is accompanied by a very sharp flash of light which is actually responsible for the exposition of our photographic emulsion. This last spark stage of streamer development is almost immediately quenched by the field of the charges trapped on the surface of the polymeric barrier. This is why the carrier population of sparks running in the vicinity of a dielectric barrier does not reach the carrier population of those sparks spanning two metallic electrodes.

To summarize the process underlying the inner structure of the microdischarge spots studied, it is necessary to name the succession of two main phenomena:

- (i) A permanent immobilization of charges from a streamer head on the dielectric barrier, i.e., formation of an almost non-transparent optical shielding and a counterproductive field which quenches the microdischarge.

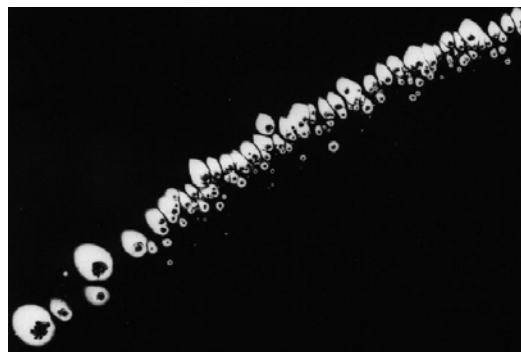


Fig. 5. **Streamer spots on the dielectric barrier**

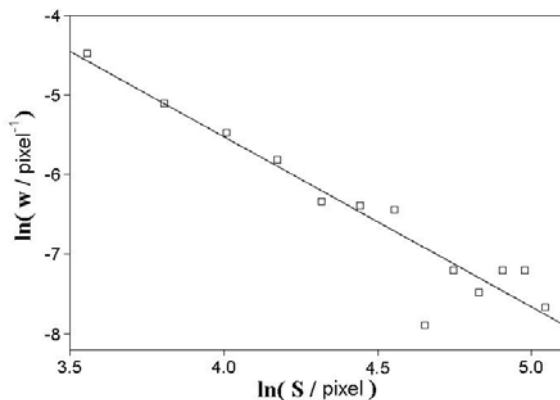


Fig. 6. Statistics of streamer spots

- (ii) A sharp light flash (photographic exposition) in the last stadium of the degenerate spark.

Shortly speaking, the dark centres of streamer spots are sites where charge carriers have impacted when a plasma channel has connected both electrode sides and afterwards a flash of visible light exposes the vicinity of the site of the charge impact. The area of a dark centre is proportional to the charge transferred, i.e. to streamer population n . Therefore, probability density created from all the set of the dark centres corresponds to population statistics of streamers. More details on this phenomenon and its analysis can be found elsewhere^{3,5}.

In Fig. 6 there is one of the typical spot statistics plotted in the bilogarithmic co-ordinates, respectively. The statistics in log-log plot shows linear behaviour similarly as in Fig. 4 which is further evidence of fractal population statistics with streamers.

In conclusion we would like to underline several main points:

- A new concept of the fractal multiplication of high populated avalanches and streamers has been proposed. The concept is based on a generalised photoionisation mechanism leading to side branching of avalanches.
- The proposed concept might be considered as a new supplement to the classical theory of avalanche and streamer multiplications.

- Instead of the simple photoionisation that acts solely within the primary (parent) avalanche, the new concept of side branching allows for photoionisation going beyond the parent avalanche and creating side avalanches that accompany the parent avalanches with a certain delay (incubation time).
- The branching may propagate to higher generations of side avalanches. This process is inherently stochastic and requires introducing the *average* multiplicity \bar{K} and the *average* number \bar{N} of initiating electrons to describe analytically the branching procedure.
- The generalised probability density function (6) has been verified as a function that faithfully describes the statistical behaviour of avalanche and streamer high populations.

All the results lead us to the conclusion that the „deviated“ population statistics of big electron avalanches are not artefacts, as has been suggested in the past¹, but rather a manifestation of a real physical process that is well described by the fractal side branching of avalanches.

The fractal population statistics in the form of the general pattern (6) shed new light not only on the photoionisation multiplication of high populated electron avalanches and streamers but they also provide a practical tool for the expert systems of high voltage technology since population statistics, known as the height statistics in this field, are frequently used as recognition patterns assessing degradation stages and the lifetime of high voltage insulation components and systems.

This work was supported by the Grant Agency of the Czech Republic under the grant no. 202/07/1207.

REFERENCES

1. Raether H.: *Electron Avalanches and Breakdown in Gases*. Butterworths, London 1964.
2. Ficker T.: IEEE Trans. Diel. El. Insul. *10*, 689 (2003).
3. Ficker T.: IEEE Trans. Diel. El. Insul. *10*, 700 (2003).
4. Ficker T.: J. Phys. D: Appl. Phys. *40*, 7720 (2007).
5. Ficker T.: IEEE Trans. Diel. El. Insul. *11*, 137 (2004).

STRUCTURE OF HOT MIXTURE FREE JET AT THE ARC-HEATER OUTPUT

JAN GREGOR, IVANA JAKUBOVÁ*, TOMÁŠ MENDL, and JOSEF ŠENK

Faculty of Electrical Engg. and Communication Technology,
Brno Univ. of Technology, Purkynova 118, 612 00 Brno,
Czech Republic
jakubova@feec.vutbr.cz

Introduction

The final properties of the coating sprayed by thermal plasma are substantially influenced by heat and momentum transfer between the flowing plasma and injected particles. For this reason it is necessary to know the main parameters of the plasma jet along the whole path of the particles. Because of great changes in plasma parameters, different measuring techniques must be used for the parts close to plasma generator output and in the regions far from it. In this paper, attention is focused to the character of flow and to the diffusion of the components of the hot gas mixture in the area near the output nozzle.

Experiments have been carried out on a hybrid water/argon plasma torch in the Institute of Plasma Physics, Academy of Sciences of the Czech Republic, Prague¹. DC electric arc in it is stabilized by tangential argon flow in the vicinity of the cathode, and mainly by water vortex in the prevailing part downstream. The anode is formed by an external rotating water-cooled disc situated several millimetres downstream of the torch exit orifice (see Figure 1). The plasma jet flows out into the surrounding air of atmospheric pressure. Typical operational parameters of the torch are: arc current between 150 and 500 amperes, voltage between 160 and 270 volts, argon flow rate between 12 and 28 slm. The share of argon and water vapour in the plasma jet outputting the exit nozzle varies not only in dependence on the argon flow, but also according to the input power which influences the evaporation rate of the stabilizing water. This fact must be taken into account in the following computations.

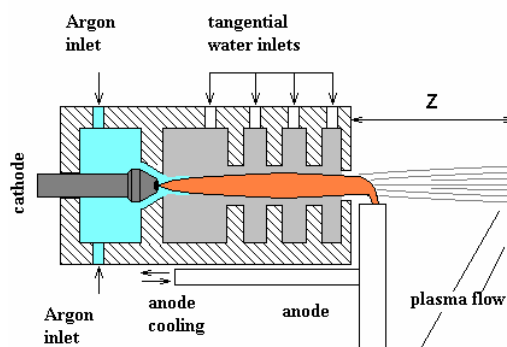


Fig. 1. Experimental set-up

The paper deals with the investigation of the character of flow of the plasma jet near the exit nozzle using radial temperature profiles obtained by spectroscopic measurement and velocities measured by enthalpy probe^{1,2}.

Parameters of plasma leaving the output

The analysed experiment is characterised by the following values: the output orifice diameter 5.6 mm, the arc current $I = 300$ A, the arc voltage $U = 220$ V, the input power $P = 66$ kW, the efficiency $\eta = 0.55$, the output power $P_{\text{net}} = 36.3$ kW, and the net flow-rate of argon $G_{\text{Ar}} = 0.4126 \cdot 10^{-3}$ kgs⁻¹. The determination of the flow rate of water vapour at the output G_{WV} is very difficult. Of course, the total flow rate of water is measured but the water evaporated from the water swirl is only a negligible portion of it. Thus, the flow rate G_{WV} must be computed indirectly using the continuity and energy equation.

The following values of the output quantities have been determined from the measured parameters by the method described in³: the ratio of components $G_{\text{WV}}/G_{\text{Ar}} = 0.64$, Mach number $M = 0.64$, the total flow-rate $G(0) = 6.36 \cdot 10^{-4}$ kgs⁻¹, and the total moment of the momentum of the mixture for $z = 0$ $J(0) = 0.36$ kgms⁻².

The centreline temperatures at the region close to the plasma generator exit nozzle have been measured using spectroscopy. They range between 16900 and 8500 K for z between 0.035 m and 0.050 m. The corresponding measured velocities are between 800 and 200 ms⁻¹. The measured axial dependencies of centreline temperature and axial component of velocity have been approximated by parabolic functions.

The radial dependencies of both temperature (Fig. 2) and axial component of velocity are approximated by exponential (Gaussian) functions

$$T(r, z) = [T(0, z) - T_{\infty}] \exp \left[- \ln 2 \frac{r^2}{b_T^2(z)} \right] + T_{\infty}$$

$$v_z(r, z) = v(0, z) \exp \left[- \ln 2 \frac{r^2}{\sigma(z) b_T^2(z)} \right]$$

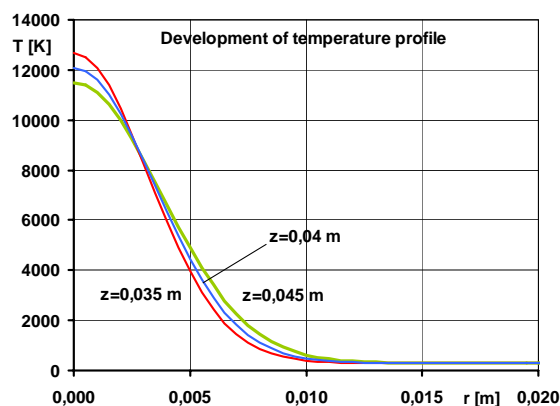


Fig. 2. Approximated radial temperature profile near the output

$\sigma(z) = b_{vz}^2(z) / b_{Tz}^2(z)$ is the ratio of the squared half-width of the radial profile of the axial component of velocity to the squared half-width of the temperature radial profile and is determined during the calculation.

Investigation of free jet near the output

The radial component of the velocity $v_r(r, z)$ complying with the measured axial velocity was computed by the equation system consisting of the continuity equation

$$\frac{\partial v_z(r, z)}{\partial z} + \frac{\partial v_r(r, z)}{\partial r} + \frac{v_r(r, z)}{r} = 0 \quad (1)$$

and the axial component of the momentum equation in kinematic expression

$$v_z(r, z) \frac{\partial v_z(r, z)}{\partial z} + v_r(r, z) \frac{\partial v_z(r, z)}{\partial r} = v(r, z) \frac{1}{r} \frac{\partial}{\partial r} \left[r \frac{\partial v_z(r, z)}{\partial r} \right] \quad (2)$$

In the centreline, the radial component of velocity must be equal to zero. Using the momentum equation, the relation between $\sigma(z)$ and the dimensionless parameter c_t characterizing the turbulent component of viscosity can be written as follows

$$\sqrt{\sigma(z)} = \frac{4 \ln 2 v(0, z)}{b_r(z) \frac{\partial v(0, z)}{\partial z}} c_t(z) \left[1 + \frac{1}{v_i(z)} \sum_i x_i(0, z) v_{ii}(0, z) \right] \quad (3)$$

where subscript $i=1$ stands for air, 2 for argon, and 3 for water vapour. The turbulent component of the kinematic viscosity follows from Prandtl's theory of the mixing length

$$v_i(z) = c_t(z) \sqrt{\sigma(z)} b_r(z) v(0, z) \quad (4)$$

The total kinematic viscosity includes the turbulent (common for all species of the mixture) and the laminar component as follows

$$v(r, z) = v_i(z) \left[1 + \sum_i x_i(r, z) \cdot \varepsilon_{vi}(r, z) \right] \quad (5)$$

$$\varepsilon_{vi}(r, z) = \frac{\mu_i(r, z)}{\rho_i(r, z)} = \frac{v_{li}(r, z)}{v_i(z)}$$

The radial component of velocity $v_r(r, z)$ can be expressed from the continuity equation and from the axial component of the momentum equation. From the equality of the two relations it follows

$$v_r(r, z) = -\frac{2v(0, z) v_z(r, z)}{\frac{\partial v(0, z)}{\partial z} r} \left\{ \left[\frac{1}{v(0, z)} \frac{\partial v(0, z)}{\partial z} + \frac{2}{b_r(z)} \frac{\partial b_r(z)}{\partial z} \right] \left[1 - \exp\left(\ln 2 \frac{r^2}{\sigma(z)} \right) \right] + \frac{2}{\sigma(z) b_r^3} \frac{\partial b_r(z)}{\partial z} r^2 \right\} \quad (6)$$

The quantities $\sigma(z)$ and c_t and their possible dependencies on the variable z are determined by iterative computation.

The following relation can be used for the specific mass of the gas mixture in LTE

$$\rho(r, z) = \sum_i x_i(r, z) \rho_i(r, z); \quad \sum_i x_i(r, z) = 1 \quad (7)$$

The continuity equation including the diffusion member for each of the individual components leaving the exit nozzle ($i = 2$ (Ar), 3 (water vapour)) was used for investigating the diffusion of gas mixture components by means of the measured and computed temperature and velocity fields

$$\nabla \cdot (\rho x_i \vec{v}) + \nabla \cdot (\rho D_{mi} \nabla x_i) = 0 \quad (8)$$

Solving this differential equation, we obtain the relation for the distribution of concentrations of individual species of the gas mixture as follows

$$\frac{x_i(r, z)}{x_i(0, z)} = \exp[-B_{ci}(r, z)] \quad (9)$$

$$B_{ci}(r, z) = \int_0^r \frac{v_z(r, z)}{D_{mi}(r, z)} \frac{2 \frac{dr}{dz}(r, z)}{1 + \left(\frac{dr}{dz}(r, z) \right)^2} dr$$

where the total diffusion coefficient of the i -th component is

$$\rho D_{mi}(r, z) = \rho(0, z) b_{vz}(z) v(0, z) \left[\frac{c_t}{Sc(z)} + \varepsilon_{vri}(r, z) \right] \quad (10)$$

$$\varepsilon_{vri}(r, z) = \frac{k_\mu}{b_{vz}(z) v(0, z)} \frac{\mu_{li}(r, z)}{\rho_i(r, z)}$$

and the ratio $dz/dr(r, z)$ is

$$\frac{dz}{dr} = \frac{v_z(r, z)}{v_r(r, z)} \quad (11)$$

From the condition of constant mass flow-rate along the jet axis⁴ it follows

$$v(0, z) [x_2(0, z) B_{G2}(z) + x_3(0, z) B_{G3}(z)] = G(0) = G_2 + G_3 \quad (12)$$

where

$$B_{Gi}(z) = \int_0^\infty \rho_i [T(r, z)] \exp[-b_{Gi}(r, z)] 2\pi r dr \quad (13)$$

$$b_{Gi}(r, z) = \ln 2 \frac{r^2}{b_{vz}^2(z)} + B_{ci}(r, z)$$

The last condition to be fulfilled by the results of the iterative computation is the constant moment of momentum along the axis of the flow⁵

$$J(0) = \int_0^{\infty} \rho(r, z) v_z^2(r, z) 2\pi r dr. \quad (14)$$

$J(0)$ is the moment of momentum of the components (argon and water vapour) at the output of the plasma generator. Using relation (7), the condition of constant momentum can be written as follows

$$v^2(0, z) \int_0^{\infty} \left\{ \begin{aligned} &1 + \\ &x_{Ar}(0, z) \left[\frac{\rho_{Ar}[T(r, z)]}{\rho_{Air}[T(r, z)]} - 1 \right] \exp[-B_{cAr}(r, z)] + \\ &+ x_{wv}(0, z) \left[\frac{\rho_{wv}[T(r, z)]}{\rho_{Air}[T(r, z)]} - 1 \right] \exp[-B_{cWV}(r, z)] \end{aligned} \right\} \rho_{Air}(r, z) \exp \left[2 \ln 2 - \frac{r^2}{\sigma(z) b_r^2(z)} \right] 2\pi r dr = J(0) \quad (15)$$

The previous computations⁴ have proved extremely low value of the laminar component of the diffusion coefficient compared to its turbulent component. Its influence on the iteration procedure is negligible. Thus, the coefficient $Sc(z)$ is used to fit the leading turbulent component.

The iterative computation starts with the chosen coefficient $Sc(z)$ in the relation for diffusion (10) and $\sigma(z)$. Using (3), (6), and (12), the turbulent coefficient c_t , radial velocity $v_r(r, z)$, and concentrations $x_i(r, z)$ are computed until the above mentioned conditions are met. Finally, the condition (15) is tested, and if not fulfilled, the computation is repeated with a different value of Sc .

Results and discussion

In Fig. 3 to 5, the results of the computations are given when the recommended and in literature commonly used value of coefficient $Sc=1$ has been applied. During these first calculations the momentum conservation condition (15) has not been tested yet. Fig. 3 shows the computed radial profiles of the axial and radial component of velocity as an example for the distance of 0.045 m from the plasma generator exit orifice. The dependencies were computed for several positions near the output (between 0.035 to 0.050 m). Naturally, both velocity components are decreasing with the increasing distance. Simultaneously with the increasing distance from the output, the maximum value of the radial component of velocity shifts from the axis of the jet. The maximum value of the axial component of velocity is about ten to twenty times higher than the maximum value of the radial component of velocity.

An example of the computed radial dependency of mass concentration of the components of the gas mixture for the

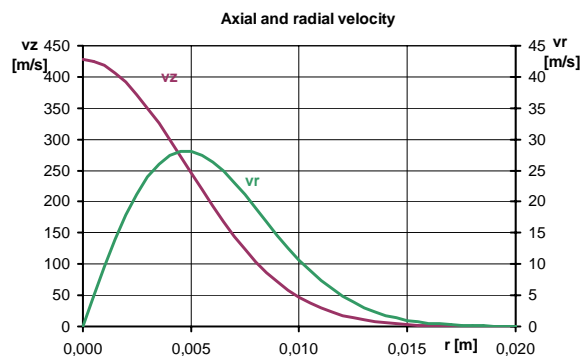


Fig. 3. The computed development of axial and radial velocity of free jet near the plasma generator exit nozzle; $z = 0.045$ m, (15) not tested

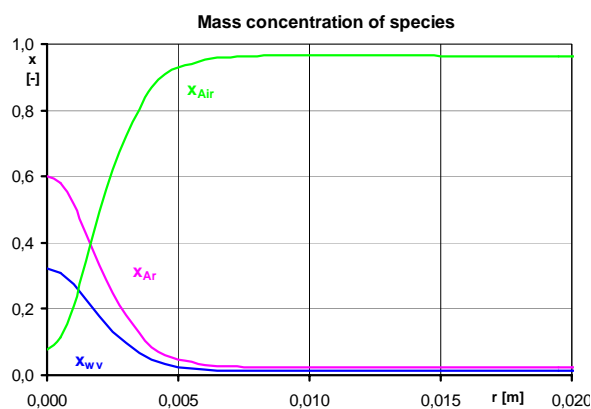


Fig. 4. The computed concentration of species at the distance 0.045 m from the plasma generator output

distance of 0.045 m from the output is given in Fig. 4. The concentration of argon and water vapour steeply decrease with radius.

Fig. 5 demonstrates a low share of the laminar component of viscosity (at $z = 0.045$ m from the output again). Due to this weak influence of the laminar component, parameter

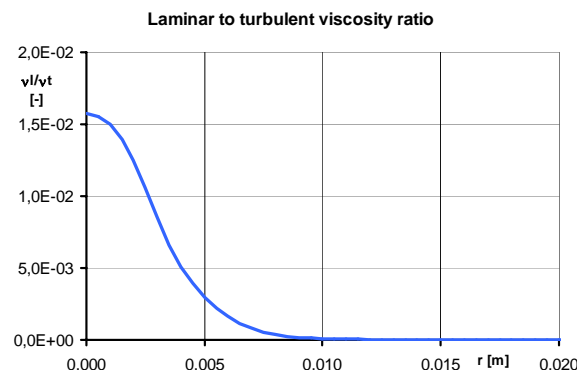


Fig. 5. The ratio of laminar to turbulent component of viscosity

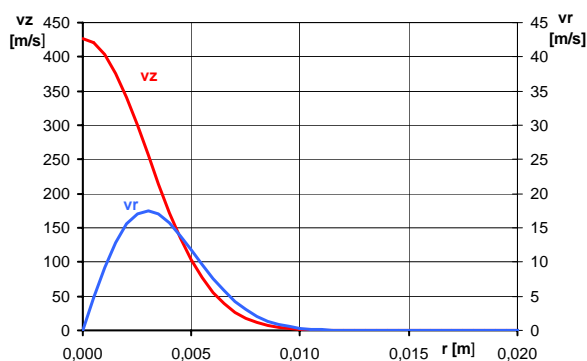


Fig. 6. The example of the computed velocity profiles at the distance 0.045 m from the plasma generator output – the momentum conservation condition fulfilled

Sc concerning the turbulent component has been taken as another free parameter for the iterative computation in order to meet the momentum conservation condition.

The condition (15) has been fulfilled with Sc significantly lower than 1 (e. g. for $z = 0.045$ m with $Sc = 0.18$). It results in a steeper decrease of both velocities with the increasing radius and a higher ratio of maximum values of the axial and radial component of velocity (see Fig. 6).

The lower value of parameter Sc causes a higher value of the diffusion coefficient Dm (see relation (10)) and a lower value of exponent $B_{C_i}(r,z)$ in relation (9). This leads to substantially slower decrease of the concentrations of individual species compared to the computation with $Sc = 1$. The ratio of laminar to turbulent component of viscosity with $Sc = 0.18$ has been computed almost three times higher than with $Sc = 1$ but it remains of order of several hundredths.

Conclusions

The computation enabling to estimate the parameters describing the hot gas mixture jet behaviour and development from the measured quantities near the arc heater output has been designed and tested on real measured data. The radial dependencies of velocity components, concentrations of species and laminar to turbulent viscosity ratio have been determined. Very weak influence of laminar viscosity even in the area close to the arc heater output has been found.

The change in parameter Sc has influenced the computed dependencies strongly which points to the necessity of deeper investigation of diffusion. The momentum conservation condition should be considered again with respect to radiation and radial heat convection losses which have not been taken into account yet.

The research has been supported by the Ministry of Youth, Education and Sports of the Czech Republic under the projects no. MSM002163516 and MSM0021630513.

REFERENCES

1. Sember V., Kavka T., Kopecký V., Hrabovský M.: In Proc. of 16th Int. Symp. on Plasma Chemistry in Taormina /Abstracts and Full-Papers CD (pub.) Department of Chemistry, University of Bari, 2003.
2. Sember V.: Czech. J. Phys. 52, D643 (2002).
3. Gregor J., Jakubová I., Mendl T., Šenk J., Konrád M.: High Temperature Material Processes 11, 181 (2007).
4. Gregor J., Jakubová I., Mendl T., Šenk J., Kavka T.: High Temperature Material Processes (in press).
5. Schlichting H.: Theory of Boundary Layer. Nauka, Moscow, 1969 (in Russian).

INTERACTION OF ELECTRICAL DISCHARGE WITH WATER SOLUTIONS OF HUMIC MATTERS

IVANA HALAMOVA*, ZDENKA STARA,
and FRANTISEK KRCMA

Institute of Physical and Applied Chemistry, Faculty of Chemistry, Brno University of Technology, Purkynova 118, 612 00 Brno, Czech Republic
xchalamova@fch.vutbr.cz

Introduction

Electrical discharges generated in liquids have been in a worldwide focus from the viewpoint of water treatment during the last few decades. Many scientists deal with various types of discharge configuration and several kinds of applied high voltage. The most frequent electrode geometry used for discharge creation is point-to-plane or coaxial^{1–3} together with the application of DC pulsed voltage of about 20 kV. Other experiments in liquids have been carried out with capillary⁴ or diaphragm discharge⁵. Discharge generation using AC⁶ or RF⁷ voltage is also possible as well as a hybrid system with one electrode above water surface⁸.

High energy transformed from plasma generated by various voltage sources (DC, AC, MW, etc.) into the liquid initiates both physical and chemical processes important for subsequent destruction of organic pollutants. Reactive species produced by the discharge in water (hydroxyl and hydrogen radicals, hydrogen peroxide or ozone) have a high oxidation potential and thus they can rapidly attack other molecules. Strong oxidation ability of plasma in water has been widely studied on model organic compounds such as phenol⁹ or organic dyes². Influence of electrical discharge on solutions containing humic substances has been investigated, too¹⁰, however, the detail study describing overall effects on humic solutions is still missing.

Presented work extends previous knowledge by the influence of input power, electrolyte contents, solution conductivity and pH on humic acids (HA) in the solutions before and after plasma treatment using DC diaphragm discharge.

Experimental

Diaphragm discharge studied in this work was generated in a batch reactor¹⁰ (Fig. 1) using constant high voltage from the DC source that gave the input power up to 250 W. Two planar electrodes made of stainless steel were separated by the dielectric barrier. Both electrode spaces were connected by only a small pin-hole (initial diameter of 0.25 mm) in this diaphragm. Discharge breakdown appeared just in this orifice and plasma channels propagated from this spot towards electrodes. Due to the application of DC voltage, two different kinds of plasma streamers appeared on the opposite sides of the diaphragm¹¹. On the side with the positive electrode, shorter plasma channels fill a spherical volume around the orifice. In the other reactor part containing the cathode, longer

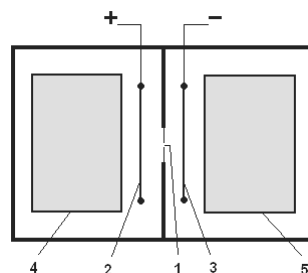


Fig. 1. Scheme of the discharge reactor: 1 – diaphragm with pin-hole, 2, 3 – electrodes, 4, 5 – cooling boxes

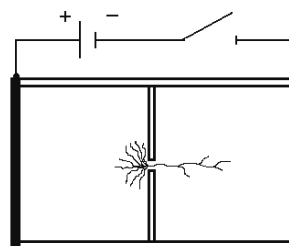


Fig. 2. Simplified model of plasma streamer propagation on both sides of the diaphragm when the DC discharge is generated

plasma channels propagated from the pin-hole towards the negative electrode (see Fig. 2).

Each part of the reactor contained 2 litres of treated solution. Water solutions contained a commercial mixture of humic acids (HUMIN S-775, concentration of 35 mg l⁻¹) and a definite amount of supported electrolyte providing particular solution conductivity (initially of 400 μS cm⁻¹). Three model electrolytes were selected for the experiments (NaCl, Na₂SO₄ and Na₂HPO₄ · 2 H₂O). Solution pH was primary adjusted by the electrolyte kind. As pH significantly changed during all experiments, its value was either modified by acid/base adding or it was let without any correction. Analyses of quality changes in humic solutions were carried out by spectroscopic methods (UV-VIS and fluorescence spectroscopy).

Results and discussion

Water solutions of humic acids were treated by the DC diaphragm discharge for 40 minutes. Decrease of absorption intensity around 300 nm was observed in both electrode spaces however, changes were more remarkable in the anode space¹⁰.

Influence of three different inorganic electrolytes (NaCl, Na₂SO₄ and Na₂HPO₄ · 2 H₂O) on the HA decomposition by the discharge was investigated. Evaluations of the maximal absorbance intensity at 288 nm during the treatment of selected solutions are compared in Fig. 3. It is obvious that NaCl electrolyte stimulated the degradation process with the highest efficiency, probably due to the formation of chlorine radicals. Moreover, pH of the solution significantly decreased

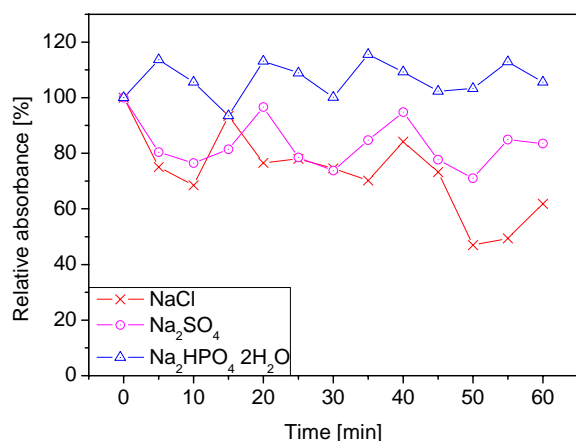


Fig. 3. Evaluation of HA absorbance intensity at 288 nm during the diaphragm discharge treatment in anode space in selected electrolyte solutions: NaCl, Na₂SO₄ and Na₂HPO₄ · 2 H₂O (input power: 190 W, initial conductivity: 400 μS cm⁻¹)

in the anode space and increased by the cathode¹². On the other hand, sodium hydrogenphosphate electrolyte almost disabled the process. In this case, buffer properties of phosphate solution could play an important role.

For determination of the input power influence on humic acid decomposition by the diaphragm discharge treatment three experiments were performed in the 4 mM NaCl solution. At first the lowest power possible for the discharge ignition was adjusted. Such conditions required the energy input of 30 W to the system. However, it wasn't recorded any removal of humic acid at this setting. It is possible that such energy is too weak to produce a sufficient quantity of reactive particles that decompose molecules of humic acid. Next higher power of 75 W was applied. Results showed a slight improvement of degradation. A subsequent power increase up to 195 W resulted in the confirmation of the decreasing amount of humic acid (Fig. 4).

Next very important parameter that significantly influenced the discharge creation in liquid itself was the conductivity of the treated solution. It had been already mentioned in some previous works¹² that the diaphragm discharge generation required a specific adjustment of the solution conductivity in a convenient range (between 100 and 1000 μS cm⁻¹ for the NaCl solution). Low conductivity adjusted by low concentration of electrolyte induced relatively high resistance of the system and disabled the discharge breakdown. On the other hand, too high conductivity values caused such low resistance that it was also insufficient for the breakdown appearance. The appropriate conductivity value of the dye solution in our experiment was adjusted by the addition of a specific amount of selected electrolyte (NaCl, Na₂SO₄ and Na₂HPO₄ · 2 H₂O).

To observe the effect of initial solution conductivity on the humic acid mixture during the diaphragm discharge treatment a series of experiments with Na₂SO₄ as an supporting electrolyte was different conductivity values (300, 500, 800 and 1200 μS cm⁻¹). Presented results are demonstrated as a relative absorption decrease (at 288 nm) during the discharge

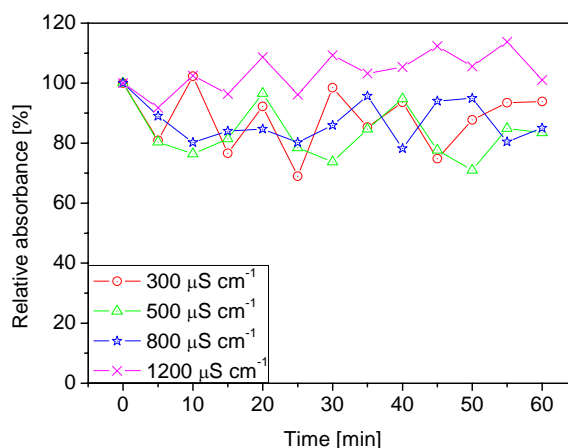


Fig. 4. Effect of input power value on humic acid decomposition by the diaphragm discharge (initial HA concentration: 35 mg l⁻¹, electrolyte: 4 mM NaCl, initial conductivity: 500 μS cm⁻¹)

treatment. It was observed that experiments carried out at conductivities from 300 to 800 μS cm⁻¹ led to more or less similar results. The final decomposition reached approximately 20 % after the one hour experiment (i.e. final relative absorption stopped on 80 %). The highest decrease was observed at conductivity of 500 μS cm⁻¹, however the difference with the other results obtained up to 800 μS cm⁻¹ was almost negligible. In experiment carried out at 1200 μS cm⁻¹ the discharge burned irregularly and the decomposition process disappeared. Therefore the optimal conductivity for the degradation process was assumed to be around 500 μS cm⁻¹.

Similar results of conductivity influence on the process have been already obtained during hydrogen peroxide generation by the same diaphragm discharge¹³.

Previous attempts with humic acid decomposition by DC diaphragm discharge have already revealed a remarkably higher HA destruction in the anode space of the reactor¹⁰. Moreover, a significant decrease of pH value in the anode space and an increase of pH value in the cathode space were detected during the diaphragm discharge treatment (a significant effect of electrolysis took place in the reactor if constant DC voltage is applied on the electrodes)¹². Therefore our next investigation was focused on the pH influence on HA treatment.

As the use of various electrolyte kinds provided different initial pH value (NaCl and Na₂SO₄ almost neutral, Na₂HPO₄ base), we had expected its influence on the decomposition process (the comparison of HA removal in various electrolytes has been already given above in Fig. 3). Consequently, we came up to attempts focused on pH value maintenance at a neutral value by the method of dropping the definite amount of surfactant (acid or base) to the both parts of the discharge reactor during the reaction.

At first it was detected how pH value changed during the decomposition in the dependence on the used electrolyte kind. Changes of pH value for sodium sulfate and sodium chloride were almost coincident. It decreased from the value

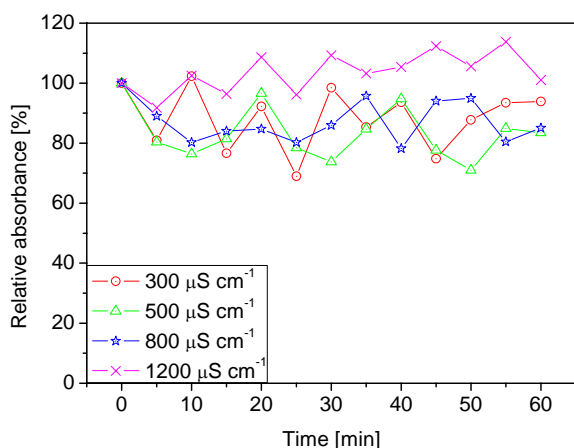


Fig. 5. Effect of initial conductivity on humic acid decomposition by the diaphragm discharge (initial HA concentration: 35 mg l^{-1} , electrolyte: Na_2SO_4 , input power: 170 W)

of approximately 6.7 to 3.6 in the anode space and increased to 9.8 in the cathode space after 20 minutes of the discharge treatment. Further, 1 M H_2SO_4 , 1M HCl and 1M NaOH solutions were used as surfactants because of their ion identity with the used electrolytes (Na_2SO_4 and NaCl, respectively). Injection step of surfactant was determined on every 2 minute so that the main pH value remained more or less constant at neutral level during the whole experiment. Solution of the third electrolyte Na_2HPO_4 was not examined by this experimental procedure because its influence on the degradation process was strongly negative due to its base initial character.

Results obtained during the discharge treatment of humic acid solution with NaCl as a supported electrolyte are presented in Fig. 6. Both pH-corrected and pH-uncorrected data determined in two electrode spaces of the reactor are compared in this figure. As we had expected, observed degradation efficiency of humic acid in the anode space was a little

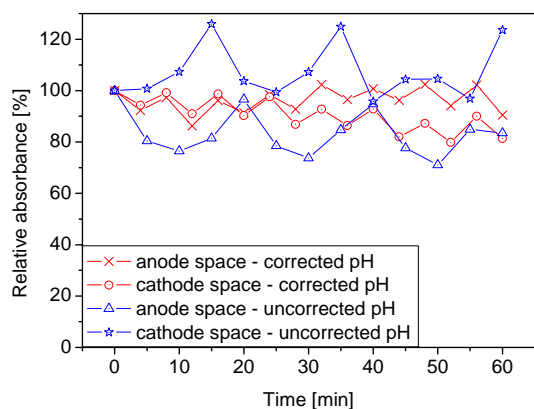


Fig. 6. Effect of pH value correction on HA decomposition by the diaphragm discharge (initial HA concentration: 35 mg l^{-1} , input power: 200 W, electrolyte: 4 mM NaCl, corrected pH 6.7, initial conductivity: $500 \mu\text{S cm}^{-1}$)

bit worse at the pH-corrected conditions, while in the cathode space a slight degradation improvement was determined in comparison with experiments without pH value correction. The same effect of pH correction was also observed in the Na_2SO_4 electrolyte. In the part with the anode (where pH spontaneously changed from the neutral value to acidic conditions), maintenance of neutral pH value decreased the degradation process. On the other side of the diaphragm with the cathode (where pH spontaneously changed from the neutral value to base conditions), neutral pH slightly improved the decomposition. Based on these results, it could be assumed that the maintenance of neutral pH value during discharge treatment was inconvenient because it generally led to lower degradation. On the other hand, it was possible to assume that the low pH value stimulated the degradation process.

Initial and final samples of humic solution obtained before and after diaphragm discharge treatment were also analysed by the fluorescence emission spectrometry, where the exciting wavelength was adjusted on 280 nm (Fig. 7 and 8). It is obvious that the intensity of fluorescence significantly decreased during the discharge treatment and this decrease was remarkably higher in the anode space than in the cathode one. Comparing the results achieved in the pH-corrected NaCl solution (Fig. 7) and pH-uncorrected NaCl solution (Fig. 8), it is evident that the fluorescence intensity of final samples with modified pH reached higher values than in the uncorrected solution. However, fluorescence intensity itself represented only a hint directed to the confirmation of decomposition processes in humic solutions. More exact was the estimation of so-called humification index (HIX, see below).

From the ratio of the emission intensity values obtained from the fluorescence spectra at 470 and 400 nm, the humification index (HIX) was calculated (Table I). This parameter indicated the mutual content of aromatic and aliphatic components in the humic mixture. Indices, given in Table I for the NaCl solution before and after diaphragm discharge treatment, are compared for pH corrected and uncorrected experiments. Decrease of aromatic part in final samples was determined in both electrode spaces. Thus a partial decomposition

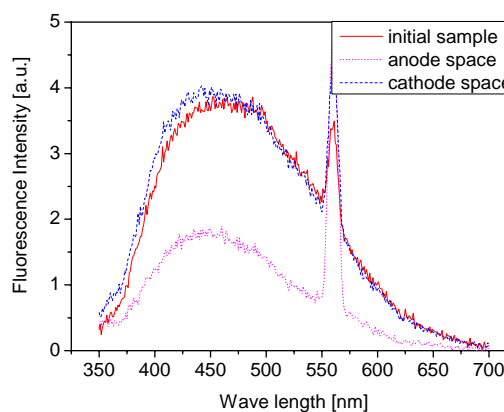


Fig. 7. Fluorescence emission spectra of humic samples before and after treatment in the NaCl solution with pH correction (excitation wavelength at 280 nm)

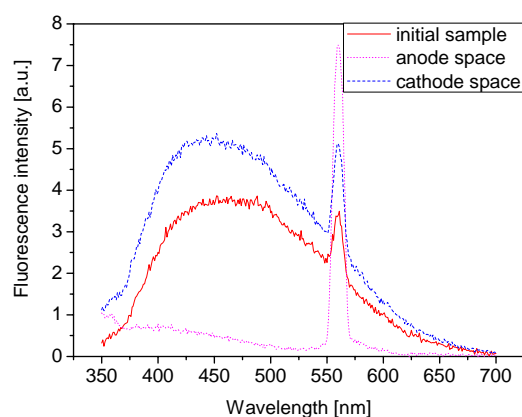


Fig. 8. Fluorescence emission spectra of humic samples before and after treatment in the NaCl solution without pH correction (excitation wavelength at 280 nm)

of humic acids in the mixture leading to the increase of aliphatic components could be assumed. Comparing the experiments with the modified and uncorrected pH we can observe that the acidic conditions created in the anode space during the diaphragm discharge without pH correction significantly stimulate the decomposition process (the lowest final humification index was achieved).

Table I
Humification index (HIX) obtained in the NaCl solution

Samples-corrected pH	HIX	Samples-uncorrected pH	HIX
initial	1.47	initial	1.47
final – anode	1.28	final – anode	0.55
final – cathode	1.31	final – cathode	1.27

Conclusion

Commercial humic acids dissolved in water solution were treated by the DC diaphragm discharge. The changes of quality were observed by the absorption spectroscopy and fluorescence spectroscopy.

The NaCl electrolyte stimulated the degradation process with the highest efficiency. Moreover, pH of the solution significantly decreased in the anode space and increased by the cathode. On the other hand, sodium hydrogenphosphate electrolyte almost disabled the process. In this case, buffer properties of phosphate solution could play an important role. Generally, degradation processes became more efficient at lower pH values (acidic medium). Optimal conductivity for degradation process was estimated to $500 \mu\text{S cm}^{-1}$ because the highest decomposition was observed near this conductivity value.

Fluorescence analysis provided not so misrepresenting results than absorption analysis (UV-VIS). Humification indices calculated from the fluorescence spectra determined the decrease of the aromatic content and the increase of aliphatic

substances in humic mixture during the discharge treatment. Detail analyses of final degradation products will be an object of our further study.

This work has been supported by the Czech Science Foundation, project No. 202/07/P371 and by the Czech Ministry of Education, Youths and Sports, Research Plan No. MSM0021630501.

REFERENCES

- Sun B., Sato M., Clements J.S.: *Environ. Sci. Technol.* **34**, 509 (2000).
- Sugiarto A.T., Ito S., Ohshima T., Sato M., Skalný J.D.: *J. Electrostatics* **58**, 135 (2003).
- Sunka P., Babický V., Clupek M., Lukes P., Simek M., Schmidt J., Cernak M.: *Plasma Sources Sci. Technol.* **8**, 258 (1999).
- De Baerdemaeker F., Simek M., Schmidt J., Leys C.: *Plasma Sources Sci. Technol.* **16**, 341 (2007).
- Monte M., De Baerdemaeker F., Leys C., Maximov A.I.: *Czech. J. Phys.* **52**, D724 (2002).
- Manojlovic D., Ostojic D.R., Obradovic B.M., Kuraica M.M., Krsmanovic V.D., Puric J.: *Desalination* **213**, 116 (2007).
- Schaper L., Deilmann M., Graham W.G., Stalder K.R.: *Proc. 19th ESCAMPIG, Granada, 15-19 July 2008*, poster 2-01.
- Lukes P., Locke B.R.: *J. Phys. D: Appl. Phys.* **38**, 4074 (2005).
- Lukes P., Clupek M., Sunka P.: *Res. Chem. Intermed.* **31**, 285 (2005).
- Stara Z., Krcma F.: *Czech. J. Phys.* **56**, B1351 (2006).
- Kuzhekin I.P.: *Proc. 9th Int. Symp. High Voltage Eng., Graz, 28 August - 1 September 1995*, 8073-1.
- Stara Z., Krcma F.: *Proc. XVIth Symp. Phys. Switch. Arc, Nove Mesto na Morave, 5-9 September 2005*, 178.
- Stara Z., Krcma F.: *Czech. J. Phys.* **54**, C1050 (2004).

I. Halamova*, Z. Stara, and F. Krcma (*Institute of Physical and Applied Chemistry, Faculty of Chemistry, Brno University of Technology, Brno, Czech Republic*): **Interaction of Electrical Discharge with Water Solutions of Humic Matters**

Preliminary results of our research focused on the application of constant DC diaphragm discharge in water solutions containing humic substances are presented in this paper. It has been found out that character of humic acid solution remarkably changes from aromatic to aliphatic, especially in the anode space of the reactor. Presented work extends our knowledge about decomposition of humic substances by the electric discharge in the dependence of solution properties and discharge conditions. Parameters such as initial solution conductivity, electrolyte kind or input power have been investigated. Moreover, substantial effect of pH on humic acid decomposition has been observed. Absorption spectroscopy in UV-VIS region together with fluorescence spectroscopy has been used for the detection of changes in humic solutions.

**SPATIALLY RESOLVED LASER
INDUCED BREAKDOWN
SPECTROSCOPY IN ORTHOGONAL
DOUBLE PULSE CONFIGURATION
AND LASER ABLATION INDUCTIVELY
COUPLED PLASMA MASS
SPECTROMETRY
OF ARCHAEOLOGICAL FINDINGS**

**ALEŠ HRDLIČKA*, LUBOMÍR PROKEŠ*,
KAREL NOVOTNÝ, VERONIKA KONEČNÁ,
VIKTOR KANICKÝ, and VÍTĚZSLAV OTRUBA**

*Masaryk University, Faculty of Science, Dep. Chemistry: Lab.
Atomic Spectrochemistry, Kotlářská 2, CZ 611 37 Brno
ahrdlicka@chemi.muni.cz, prokes@chemi.muni.cz*

Keywords: laser ablation, inductively coupled, plasma, mass spectrometry, laser induced, breakdown spectrometry, orthogonal, double pulse, archaeological, tooth

1. Introduction

Local analysis of dental calcified tissues plays important role in medicine, toxicology, environmental science, paleontology and anthropology. In these fields of action a bulk analysis of a mineralized material from a defined and well-localized volume belongs to a marginal stream. On the other hand, spatially resolved analyses of calcified tissues as teeth or bones without any previous decomposition have been routinely performed with laser ablation inductively coupled plasma mass spectrometry (LA-ICP-MS)^{1–10}, X-ray fluorescence (XRF)^{11–13}, particle (proton) induced X-ray emission spectroscopy (PIXE)^{14,15}, secondary ions mass spectrometry (SIMS)^{16,17} or even formerly electron microprobe analysis (EMP)^{18,19}.

Nowadays, Laser Induced Breakdown Spectroscopy (LIBS) becomes a widely employable technique in analytical chemistry. It can be used for elemental analyses of samples of any state (i.e. gas, solid and liquid)²⁰. In last ten years the double pulse configuration (DP) became a great importance due to some advantages as intensity enhancement of emission lines²¹. Up to now, several combinations were tested. The four basic are: *i*) two consequent coaxial laser pulses (but perpendicularly to the sample) – the first one ablates the sample and the second one even more feeds the microplasma induced by the first one, *ii*) the first one ablates the sample and the second one feeds the plasma perpendicularly, *iii*) the first pulse is collinear with the sample and induces a plasma by a breakdown of the atmosphere and the second one strikes the sample perpendicularly through the breakdown plasma, *iv*) any other spatial non-orthogonal configuration. The typical time gap between the pulses is 1–10 μ s.

Due to a transient behaviour of the microplasma some non-linear effects occur at analytical measurements with

LIBS and finally demonstrate themselves as nonlinear calibration curves (intensity vs. element content). These phenomena are matrix-dependent and limit the use of LIBS to mostly semi-quantitative precision. Nevertheless, it is commonly used for *in situ* analysis of cultural heritage objects²². For spatially resolved analysis of bones and teeth it has been still rarely used²³.

The main advantage of the DPLIBS is a substantial enhancement of the sensitivity against the single pulse LIBS. This approach is still rarely applied to analysis of artifacts²². To the best knowledge of the authors the DP variant has been never used for the analysis of calcified tissues.

Thus, one can expect that a valuable comparison of LA-ICP-MS with DPLIBS will be to some extent feasible. This is also the main goal of this work. It aims to compare whether the spatial distributions of some major and minor elements in a reindeer tooth section yielded by both the methods are equivalent.

2. Experimental

2.1. LA-ICP-MS Instrumentation

The measurements were realized using an ICP-MS Agilent 7500ce. It was operated under standard conditions with forwarded rf power of 1350 W without the collision cell. A New Wave Research (Laser Ablation Systems, USA, UK) UP 213 facility was used for laser ablation. The basic source was a Nd: YAG laser emitting the fundamental wavelength 1064 nm which is consequently frequency quintupled to the 213 nm one and the lasing beam is homogenized to a flat-top energy cross section profile. The impact laser pulse fluence 12 J cm⁻² at the beam diameter of 100 μ m was selected with respect to yield an appropriate signal levels for both major and minor elements. The produced aerosol was transported into the ICP-MS with 1 l min⁻¹ helium carrier gas through a Tygon tubing (i.d. 4 mm, length about 1.5 m) and behind the ablation cell it was mixed with 0.6 l min⁻¹ argon make-up gas. The flow rate was stabilized with a Brooks mass flow controller.

With the LA-ICP-MS, three rows of craters were ablated in a single-spot mode with repetition frequency of 10 Hz during 45 s so that 450 pulses were executed on each spot. The mutual distance of crater centres was 0.15 mm which was controlled with an x, y translation stage (a sub-component of the UP 213 facility). The sum signal for each crater was processed and depicted in a graph as one point (all Figs.).

2.2. Double pulse LIBS Instrumentation

The first (ablation) pulse was executed with a UP 266 Macro laser (New Wave, 266 nm flat top beam) with 8 mJ and the second one with a Quantel Brilliant (1064 nm) laser with 125 mJ pulse energy. The triggering signal from the UP 266 laser flash lamp was led to an external delay generator DG 535 to control the gap between the pulses (0.1 μ s) and between the flashlamp ignition and the Q-switch of the Quantel laser to control its pulse energy. Between the pulse generator and the final destination of the delayed signal a pulse repetition rate divider was placed and each 20th pulse was used. The delay between the 2nd pulse and the spectra

measurement (1 μ s) was controlled with an in-built delay generator of a Triax 320 spectrometer.

The microplasma emission was delivered with an optical bundle to the Triax 320 monochromator (Horiba JY, ICCD, entrance slit 50 and 100 μ m, grating 2400 mm^{-1}). The spectral range in the used setting was about 19 nm for simultaneous measurements.

The sample was ablated vertically and the very small primary microplasma was excited horizontally (orthogonal configuration) using a quartz lens with 80 mm focal length. The produced craters were also about 0.1 mm in diameter and spaced 0.15 mm. 4 pulses per crater were executed and the sum signal processed and depicted in graphs (all Figs.). After one crater line was finished the measured spectral interval was changed and the same crater line was ablated again. As a result, each crater was made by 4 \times 7 pulses because 7 spectral intervals were necessary to cover all the requested spectral lines.

2.3. Sample

A reindeer tooth (right 2nd upper molar, era: upper paleolithic, 29-21 000 BP) from Moravany-Lopata, Western Slovakia, was chosen due to a well-defined structure with several lamellas. It was embedded with a polyester resin, cut lengthways and polished (all Figs. background).

3. Results and discussion

Spatial distributions of four key elements are presented: Ca, Mg, Sr, Zn. They are biologically very important. Some isotope ratios: Ca 44/Mg 25, Ca 44/P 31 and Sr 88/Ca 44 were calculated from the LA-ICP-MS calibration measurement using a NIST 1486 bone meal standard pressed in a pellet (Fig. 1).

The other Figs. 2–4 depict maximum-normalized intensities in order to highlight relative changes in an appropriate scale. All the scans are fitted to the structure of the analyzed tooth (Figs. 1–4). The structural description of the tooth is marked in Fig. 1.

3.1. Calcium and strontium

The major element is calcium. It is a component of hydroxyapatite which is a main constituent of any calcified tissue. It is also a main matrix element which can be used as an internal standard.

In the tooth structure, a slight increase of strontium is observable from the outer part of the enamel towards the dentine. In the dentine, its content gradually decreases towards the pulp^{24–26}. These facts are confirmed by the results of our analysis except for the pulp which was out of the scanned area (Figs. 1, 3, 4). Strontium is not an essential element and has no specific biochemical or physiological function in organisms. Its metabolism is analogical to the calcium one. More than 90 % of calcium is accumulated in calcified tissues. In contrast to the calcium its content in a body is not under a homeostatic control⁷. Strontium may substitute calcium and thus the ratio Sr/Ca increases in case of calcium deficiency. The ratio Sr/Ca in bone reflects the Sr/Ca in consumed food

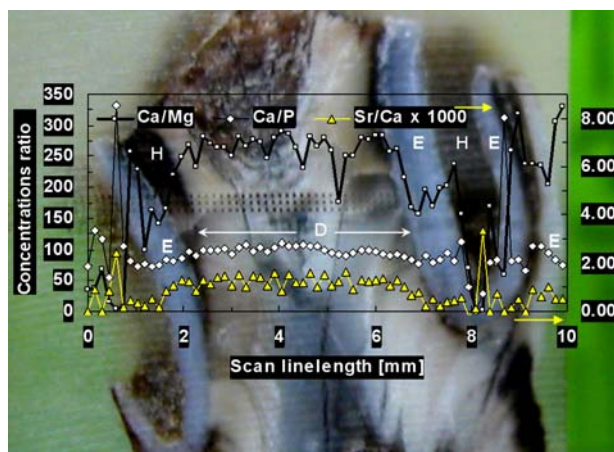


Fig. 1. LA-ICP-MS line scan. Concentration ratios of selected elements are depicted. The Sr/Ca ratio refers to the right axis. Additionally, the tooth structure is marked: E...enamel; H...hole, empty area with resin; D...dentine. The depicted scans refer to the upper crater line

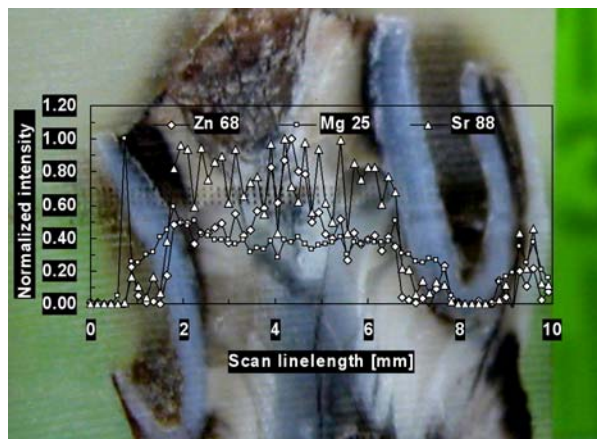


Fig. 2. LA-ICP-MS line scan. Maximum normalized intensities of the selected elements are depicted

and consequently the bone Sr/Ca ratio is higher for herbivores than for carnivores.

3.2. Magnesium

The magnesium content is substantially higher in the dentine than in the enamel^{17–19,29,30} which is also in accordance with the presented results (Figs. 1–3). Possible significant increase of magnesium at the beginning of the scan can indicate the presence of the tartar (Fig. 2). This increase is commonly not observable, e.g. in the DPLIBS profile (Fig. 3) it is absent. This fact probably signalizes some local differences in the tartar presence. Magnesium is an important constituent of calcified tissues and plays a key role in the early phase of the development of the mineral component^{27,28}. Its content slightly increases from the enamel surface and the increase continues also in the dentine.

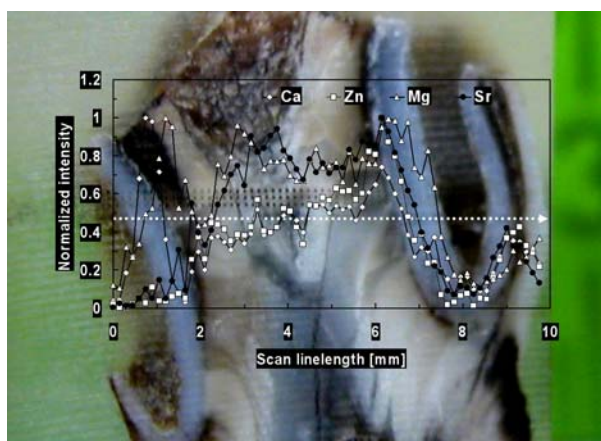


Fig. 3. **DPLIBS line scan.** The crater line is marked with the dotted arrow. The craters are not very deep and thus they are invisible. Maximum normalized intensities of the selected elements are depicted. Used spectral lines [nm]: Ca I 335.020, 335.035; Mg I 285.21; Sr II 407.77; Zn I 330.29

3.3. Zinc

The initial increase of zinc is well observable in the LA-ICP-MS profile (Fig. 2) while the DPLIBS scan yielded a substantially weaker and nearly negligible peak (Fig. 3). Again, this fact can be attributed to the different position of the LA-ICP-MS and DPLIBS scans (see and compare the calcium distributions by LA-ICP-MS and DPLIBS in Figs. 1 and 4). The initial zinc increase is, however, significantly lower in comparison with the magnesium maximum (Fig. 2). Zinc is an essential element which is extremely important for the growth and the mineralization of bones and teeth^{32,33} and may be also related to sanative processes. It is preferentially accumulated in surface layers of the enamel^{7,9,12,24,25,26,34}, as well as in the dentine⁹. Besides, the zinc content increases from the boundary enamel-dentine towards the pulp^{8,24}.

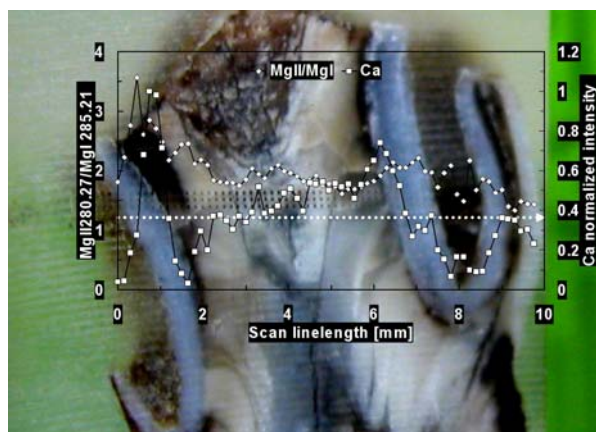


Fig. 4. **DPLIBS line scan.** Tooth hardness local changes across the ablated path

3.4. Tooth hardness monitoring

Both these methods are based on LA sampling and thus they may suffer from some matrix effects. The scan line crosses all parts of the tooth and these have various hardnesses. In this aspect the leader is the enamel, the second is the dentine and the softest is the pulp. The ablation can then be more efficient in the dentin thus delivering more material into the excitation source. The consequent precise quantification of the elemental contents in various parts of the tooth would be quite problematic. This difficulty can be partially solved by use of the Mg II 280.26 nm / Mg I 285.22 nm ratio or by a calcium ionic to atomic line ratio³⁵. This ratio increases with the hardness of the tissue. In our case it is applicable only to the DPLIBS method. It really shows that the highest ratio well corresponds with the enamel position (Fig. 4). The other variations are not so much significant.

4. Conclusion

The presented comparison of DPLIBS with LA-ICP-MS and with already published results showed that the DPLIBS method in the presented particular orthogonal configuration can be successfully used for the mapping of the spatial distributions of biologically important elements as Ca, Mg, Sr, Zn. It can be applied as a suitable alternative to the routinely used LA-ICP-MS method due to the sufficient spatial resolution and sensitivity to the minor elements. These properties are not obtainable for single pulse LIBS.

The authors wish to thank Miriam Fišáková from the Institute of Archaeology Brno for samples and the Czech Ministry of Education, Youths and Sports for the projects MSM0021622411 and ME08002.

REFERENCES

- Bellis D. J., Hetter K. M., Joines J., Aamarasiriwardena D., Parsons P. J.: *Environ. Res.* 106, 34 (2008).
- Budd P., Montgomery J., Cox A., Krause P., Barreiro B., Thomas R. G.: *Sci. Total Environ.* 220, 121 (1998).
- Cox A., Keenan F., Cooke M., Appleton J.: *Fresenius' J. Anal. Chem.* 354, 254 (1996).
- Dolphin A. E., Goodman A. H., Aamarasiriwardena D. D.: *Am. J. Phy. Anthropol.* 128, 878 (2005).
- Evans R. D., Richner P., Outridge P. M.: *Arch. Environ. Contam. Toxicol.* 28, 55 (1995).
- Humphrey L. T., Dirks W., Dean M. Ch., Jeffries T. E.: *Folia Primatol.* 79, 197 (2008).
- Humphrey L. T., Jeffries T. E., Dean M. C., in: *Technique and Application in Dental Anthropology* (Irish J. D., Nelson G. C., ed.), p.87. Cambridge University Press, Cambridge 2008.
- Kang D., Aamarasiriwardena D., Goodman A. H.: *Anal. Bioanal. Chem.* 378, 1608 (2004).
- Lee K. M., Appleton J., Cooke M., Keenan F., Sawicka-Kapusta K.: *Anal. Chim. Acta* 395, 179 (1999).
- Lochner F., Appleton J., Keenan F., Cooke M.: *Anal. Chim. Acta* 401, 299 (1999).
- Carvalho M. L., Casaca C., Pinheiro T., Marques J. P.,

- Chevallier P., Cunha A. S.: Nucl. Instr. Meth. Phys. Res., B 168, 559 (2000).
12. Martin R. R., Naftel S. J., Nelson A. J., Feilen A. B., Narvaez A.: J. Archaeol. Sci. 34, 936 (2007).
 13. Brenn R., Haug Ch., Klar U., Zander S., Alt K. W., Jamieson D. N., Lee K. K., Schutkowski H.: Nucl. Instr. Meth. Phys. Res., B 158, 270 (1999).
 14. Rodríguez-Fernández L., Ruvalcaba-Sil J. L., Ontalba-Salamanca M. A., Román-Berrelleza J. A., Gallardo M. L., Grimaldi D. M., de Lucio O. G., Miranda J.: Nucl. Instr. Meth. Phys. Res., B 150, 663 (1999).
 15. Jälevik B., Odelius H., Dietz W., Norén J. G.: Arch. Oral Biol. 46, 239 (2001).
 16. Stermer E. M., Risnes S., Fischer P. M.: Eur. J. Oral Sci. 104, 253 (1996).
 17. Besic F. C., Knowles C. R., Wiemann M. R. Jr., Keller O.: J. Dental Res. 48, 131 (1969).
 18. Grman D., Andrik P.: Čs. Stomatologie 78, 63 (1978).
 19. Johnson A. R.: J. Dental Res. 51, 115 (1972).
 20. De Giacomo A., Dell'Aglio M., De Pascale O., Capitelli M.: Spectrochim. Acta, B 62, 721 (2007).
 21. Babushok V. I., DeLucia F. C. Jr., Gottfried J. L., Munson C. A., Miziolek A. W.: Spectrochim. Acta, B 61, 999 (2006).
 22. Giakoumaki A., Melessanaki K., Anglos D.: Anal. Bioanal. Chem. 387, 749 (2007).
 23. Samek O., Beddows D. C. S., Telle H. H., Kaiser J., Liška M., Cáceres J. O., González Ureña A.: Spectrochim. Acta, B 56, 865 (2001).
 24. Frank R. M., Sargentini-Maier M. L., Turlot J. C., Leroy M. J. F.: Arch. Oral Biol. 34, 593 (1989).
 25. Molleson T. in: *Trace Elements in Environmental History* (Grupe G., Herrmann B. ed.), p. 67. Springer, Berlin – New York 1988.
 26. Reitznerová E., Aamarasiriwardena D., Kopčáková M., Barnes R. M.: Fresenius' J. Anal. Chem. 367, 748 (2000).
 27. Aoba T., Shimoda S., Moreno E. C.: J. Dental Res. 71, 1826 (1992).
 28. Kirkham J., Robinson C., Weatherell J. A., Richards A., Fejerskov O., Josephsen K.: J. Dental Res. 67, 1156 (1988).
 29. Shaw J. H., Yen P. K.-J.: J. Dental Res. 51, 95 (1972).
 30. Steinfors J., Driessens F. C. M., Heijligers H. J. M., Beertsen W.: J. Dental Res. 70, 187 (1991).
 31. Hayashizaki J., Ban S., Nakagaki H., Okumura A., Yoshii S., Robinson C.: Arch. Oral Biol. 53, 168 (2008).
 32. Brandão-Neto J., Stefan V., Medonca B. B., Bloise W., Castro A. V. B.: Nutr. Res. 15, 335 (1995).
 33. Kirsch T., Harrison G., Worch K. P., Golub E. E.: J. Bone Miner. Res. 15, 261 (2000).
 34. Nixon G. S., Livingston H. D., Smith H.: Arch. Oral Biol. 12, 411 (1967).
 35. Abdel-Salam Z. A., Galmed A. H., Tognoni E., Harith M. A.: Spectrochim. Acta, B 62, 1343 (2007).

ADVANCED MODELING OF REACTIVE SPUTTERING PROCESS WITH NON-LINEAR DISCHARGE CURRENT DENSITY

TEREZA HYTKOVÁ, PETR VAŠINA*,
and MAREK ELIÁŠ

Department of Physical Electronics, Faculty of Science, Masaryk University, Kotlářská 2, 611 37 Brno, Czech Republic
vasina@physics.muni.cz

Key words: reactive sputtering, modeling, hysteresis behavior

Introduction

A deposition of thin films by magnetron sputtering is a widely used technique. When a reactive gas is added to the deposition chamber, the process of the sputtering becomes different and it is referred to as the reactive sputtering. The main advantage of the reactive sputtering is its ability to deposit complex films, for example nitride or oxide films. To set working conditions during the deposition itself, it is easier to use the flow of the reactive gas rather than its partial pressure. However, the process controlled by the reactive gas flow exhibits a hysteresis behaviour.

At a certain flow of the reactive gas, the system transits from the metallic to the compound mode and vice versa depending on whether the flow of the reactive gas is increased or decreased. This transition is caused by the fact that when increasing the reactive gas flow the growing thin film reaches its gettering capability and the partial pressure of the reactive gas suddenly increases. As a consequence the reactive gas gettering to the target rises resulting in a compound formation at the target. The process of the target coverage by the compound layer is called the target poisoning. The inverse process is called the target cleaning. The compound sputtering yield is however usually lower than the metal sputtering yield, so the poisoned target is more difficult to sputter. Thus to ensure always the same conditions for growing of thin films during depositions are very different.

For better understanding of the reactive sputtering process a reliable model is needed. The model well describing the observed behaviour was developed by S. Berg and his colleagues¹⁻⁴ during past two decades. Nevertheless Berg's model postulates the uniform discharge current density over the magnetron cathode. But the discharge current density is very non-uniform in the magnetron configuration due to the presence of the magnetic field. In front of the magnetron cathode high dense toroidal plasma is formed. Thus the racetrack part is significantly more sputtered than the central part of the target and its edges. We have modified the original Berg's model in order to accommodate the non-uniformity of the discharge current density. Here we present results for various profiles of the discharge current density over the magnetron cathode.

Model enhancement

Berg's model is described by sets of fundamental equations that represent main processes occurring during the deposition. The model assumes that the discharge current density is uniform, that the reactive gas does not contribute to the sputtering, that the compound layer is formed on the magnetron cathode only in a form of a monolayer and that the density of the reactive gas is the same in the whole deposition chamber. Following stoichiometry is assumed – the compound molecule contains always one metallic atom and one atom of the reactive gas and the reactive gas molecule is composed of two atoms. The model¹ assumes that the vacuum chamber contains the target of the area A_t which is placed in front of the collecting area A_c including the substrate. The chamber is pumped by a vacuum pump of constant pumping speed S . Presence of the reactive gas in the deposition chamber causes a fraction θ_t (θ_c) of the target (substrate) to be covered by compound molecules. Since the target is intensively sputtered by impacts of ions originating from the plasma (discharge current density J) θ_t is always lower than θ_c . The total supply of the reactive gas Q_{tot} is either consumed at the target (Q_t) or at the substrate (Q_c) or escape from the deposition chamber via the pumping system (Q_p). The resulting partial pressure of the reactive gas is denoted P . At the steady state conditions, number of compound molecules out-sputtered from the target must be the same as twice the number of reaction between neutral reactive gas molecules and not-reacted target material.

The briefly described Berg's model¹ has been extended in order to accommodate the non-uniformity of the discharge current. The target has been artificially divided into N annuli. Each of the annuli is so small, that the discharge current density can be assumed to be constant within. Thus each of target annuli is treated in the same way as the whole magnetron target is treated by Berg's model. For each of them, a balance equation is written and total fluxes of sputtered metals and compound molecules are given as the summary of contributions from all annuli.

Previously such approach has been already applied as-

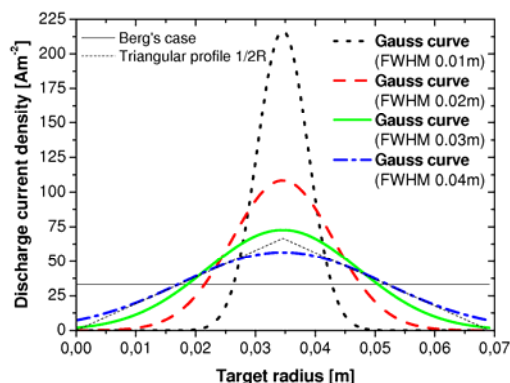


Fig. 1. Various profiles of the discharge current density. All of assumed shapes were constructed to have the maximum at the half radius of the target and the total current value of 0.5 A

suming triangular shapes of the discharge current density⁵. In this particular paper, we are going to present mainly results for Gaussian current density profiles and their comparison to Berg's model with the uniform current density. Various shapes of discharge current density profiles have been assumed (see Fig. 1). These profiles of the discharge current density were constructed to acquire the same total discharge current 0.5 A as in the Berg's case. Four Gaussian profiles with different values of the full width at half maximum and one triangular profile have been created. All of them have the maximum of the total discharge current density at the half radius of the target.

For clear comparison of Berg's model and our results from the modified model we kept input parameters such as sputtering yields, areas of the target and the substrate, the total discharge current etc. the same as in the original Berg's model¹.

Results and discussion

Assuming the non-linear profile of the discharge current density it is obvious that target parts with lower discharge current density are less sputtered than parts with higher density and the general behaviour of the sputtering process is mainly ruled by the condition at the racetrack. The less-sputtered parts of the target are also more covered by the compound. However, to quantify this statement, the calculation has to be performed. Since the sputtering rate of the metallic atoms from the poisoned parts of the target is lower than from the clean surface, during the reactive deposition the target changes its sputtering capability due to the formation of the compound at the target surface. At a certain flow of the reactive gas, the growing thin film can attain its gettering capability and the partial pressure of the reactive gas leaps up and causes the target to become more and more poisoned. This situation is the transition from the metallic to the compound mode of the sputtering process (M-C transition). In

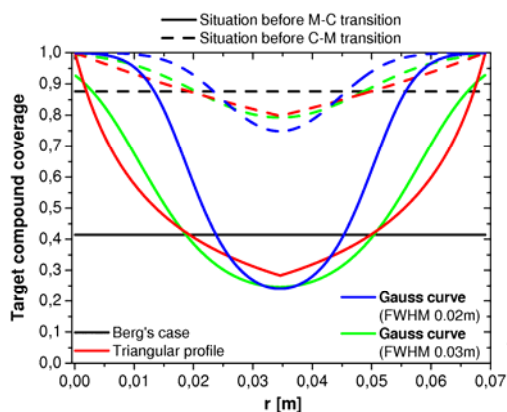


Fig. 2. Target compound composition for various discharge current density profiles. Dashed lines represent situation before M-C transition and continuous lines represent situation before C-M transition

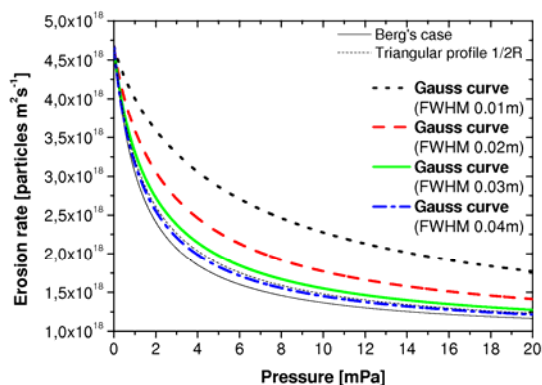


Fig. 3. The target erosion rate as a function of the partial pressure of the reactive gas modelled for the uniform, the triangular and four Gaussian discharge current density profiles

Fig. 2 there is calculated target compound coverage for these two modes of operations. Generally the target in the compound mode is by 50 % more covered by the compound layer than in the metallic mode. Recently, similar evolution has been measured experimentally⁶. Steeper profiles better restrict the racetrack and because it plays dominant role during the sputtering process thus the target erosion rate should be subsequently higher.

As it was concluded above the erosion rate is highest for the steepest profile. The target erosion rate as a function of the partial pressure of the reactive gas is plotted in Fig. 3. The target erosion rate varies mainly at higher partial pressures of the reactive gas. In the case for 20 mPa the difference between erosion rates for the uniform and the Gaussian profile with FWHM 0.01 m is up to $5 \cdot 10^{17}$ particles per square meter per second i.e. almost 25 percent. It can be also noted that the outputs for the Gaussian profile with FWHM 0.04 m and

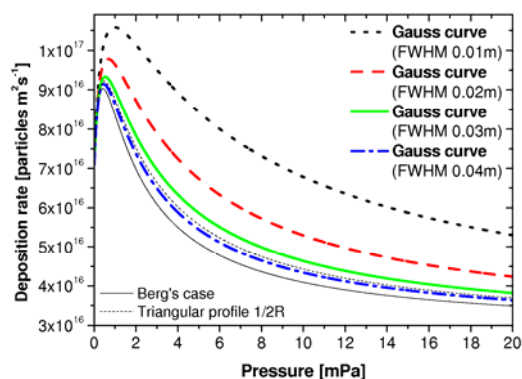


Fig. 4. Modelled deposition rate as a function of the partial pressure of the reactive gas for four Gaussian profiles with different full width at the half maximum, the triangular profile and the uniform Berg's case. All sharp profiles have the maximum at the half radius of the target and they were constructed in order to obtain

previously studied triangular profile are very similar. This reflects the fact that the profiles themselves are alike.

In practice it is desirable to obtain high deposition rates during the growing of thin films. In Fig. 4, we present the deposition rate as a function of the partial pressure of the reactive gas for all studied models in order to settle if there is any considerable difference. Comparing to Berg's case, higher deposition rates have been achieved for any of assumed non-uniform profiles of the cathode load. The situation for the triangular profile and the Gaussian profile with FWHM 0.4 m is almost the same. But if a steeper Gaussian profiles is used higher deposition rate can be reached. The explanation is following. If a very pointy steep shape is used, fluxes of metal and compound particles from the racetrack of the target will be much higher even though a great part of the target will be completely covered by the compound. This is because so called

poisoned parts of the target are practically not sputtered for there is very low or almost negligible discharge current density.

If the sputtering process is controlled by the flow of the reactive gas the whole process exhibits the hysteresis behaviour. In Fig. 5 the relation between the partial pressure of the reactive gas and the total reactive gas supply rate is shown. The hysteresis behaviour is clearly distinguishable. If the reactive gas flow is continuously increased the abrupt jump towards higher partial pressures of the reactive gas occurs. This is the transition from the metallic to the compound mode. When decreasing the flow of the reactive gas it is necessary to decrease the flow even lower to clear the target. The clearing of the target represents the C-M transition.

Modelling with non-linear profiles of the discharge current density there are different conditions for the transitions between two modes of operation. For steeper profiles the whole hysteresis region is shifted towards higher total reactive gas supply rates. This comes from the fact that if the target is more sputtered as it is for cases with non-uniform discharge current density profiles, higher reactive gas flow is needed to poison the target in that scale that it would switch from the

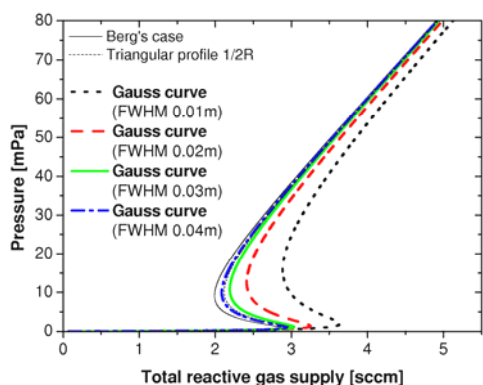


Fig. 5. Modelled dependency of the partial pressure of the reactive gas on the total supply rate of the reactive gas. The relation is shown for various profiles of the discharge current density, for four Gaussian curves and for the triangular profile and the uniform Berg's case

metallic mode to the compound one and vice versa. The difference in amount of the total reactive gas supply needed for the M-C transition for the target exposed to the uniform discharge current and to the Gaussian profile (FWHM 0.01 m) reaches non-negligible 0.8 sccm. Not only the point of the transition is shifted, there is also a pressure shift, in heights of transitions. The target in Berg's case in the M-C transition jumps over 35 mPa whereas the Gaussian profile (FWHM 0.01 m) undergoes the jump over 42 mPa. In closer look at the Fig. 3, the slight difference can be noticed even in the width of the hysteresis region. This difference is not more than 5 % for models with non-uniform discharge current density profiles compared to Berg's case, with one exception which corresponds to the most extreme Gaussian profile (FWHM 0.01 m). The hysteresis width is about 15 % narrower then in the Berg's case.

The results using steep Gaussian profiles are very similar to situation when smaller targets are used. The effective area of the target is narrowed to the racetrack part. The advantage of these Gaussian profiles is that the discharge current density at edges and at the centre of the target is not zero as in the experiment.

Conclusion

We have presented an enhanced model for the reactive magnetron sputtering which takes into account the non-homogeneity of the discharge current density. Instead of previously artificially used triangular shapes of the discharge current density, more realistic Gaussian profiles were assumed. If a steeper profile is used higher target erosion and deposition rate can be achieved. The hysteresis region is generally shifted towards higher reactive gas supply rates for steeper profiles. However the hysteresis region itself does not significantly differ.

The general behaviour of processes with steep discharge currents densities is similar to processes that use small targets⁴. It is like the target effectively decreases its area. But when using Gaussian profiles the discharge current density at the edges and at the centre of the target is not zero but is very low.

This research has been supported by the MSM contract 0021622411 and by GACR contract 202/08/P038.

REFERENCES

1. Berg S., Nyberg T.: *Thin Solid Films* 476, 215 (2005).
2. Berg S., Blom H.-O., Larsson T., Nender C.: *J. Vac. Sci. Technol., A* 5, 202 (1987).
3. Kubart T., Kappertz O., Nyberg T., Berg S.: *Thin Solid Films* 515, 421 (2006).
4. Nyberg T., Berg S., Helmersson U., Hartig K.: *Appl. Phys. Lett.* 86, 164106 (2005).
5. Vašina P., Hytková T., Eliáš M.: submitted to *Plasma Source Sci. Technol.* (2008).
6. Güttler D., Grötzschel R., Möller W.: *Appl. Phys. Lett.* 90, 263502 (2007).

T. Hytková, P. Vašina*, and M. Eliáš (*Department of Physical Electronics, Faculty of Science, Masaryk University, 602 00 Brno, Czech Republic*): **Advanced Modeling of Reactive Sputtering Process with Non-Linear Discharge Current Density**

In the classical magnetron configuration, the non-uniform magnetic field is applied in order to enhance the target sputtering at a given applied voltage. As a consequence, the cathode load is non-uniform, too. There is a clearly defined part of the target which is intensively sputtered, so called racetrack. This fact is not taken into account in well known Berg's model that assumes a uniform current density over the target. Thus the target in the Berg's case is sputtered homogeneously. We present a modification of the classical model when the Gaussian current density profile that should better describe the real situation is assumed. The deposition rate, the target erosion rate and the hysteresis region are compared to previously studied model with a triangular profile and to the original Berg's model.

DETERMINATION OF $N_2(A)$ POPULATION FROM OPTICAL EMISSION SPECTRA

M. MEŠKO, P. VAŠINA*, J. MUÑOZ ESPADERO^a, V. KUDRLE, A. TÁLSKÝ, and J. JANČA

Department of Physical Electronics, Faculty of Science, Masaryk University, Kotlářská 2, CZ-611 37 Brno, Czech Republic, ^a on leave from Facultad de Ciencias, Universidad de Cordoba, Campus Rabanales, 14071 Cordoba, Spain
vasina@physics.muni.cz

Key words: nitrogen metastables, high power microwaves, pulsed discharge, optical emission spectroscopy

Introduction

Microwave discharges containing nitrogen are commonly used both in the research and the technology. Often it is advantageous for the given function (deposition, etching, plasma treatment, etc.) to exploit the processes in the afterglow rather than those in the active discharge. In most published works the authors used relatively low peak power in the range of hundreds of watts. However, in our apparatus we use very short pulses with peak power around 10^5 W, which is challenging from both theoretical and experimental point of view.

Interferometer diagnostics and spectroscopic measurements of pulse excited plasmas may give interesting results, concerning the loss, excitation and deexcitation processes as we have shown in our previous papers^{1–4}. However, in many common experimental setups the interaction between the plasma and the walls is very difficult to account for. Therefore we carried out our experiments in the device with suppressed influence of surface processes. The processes involving nitrogen molecules in $A^3\Sigma_u^+$ metastable state are studied using time resolved optical emission spectroscopy of decaying plasma. The paper proposes a way to determine the absolute density of nitrogen metastable molecules at the end of the discharge pulse from relative intensity of second positive system ($N_2(C^3\Pi_u-B^3\Pi_g)$) emission in the afterglow.

Experimental set-up

We have developed the apparatus, where the volume processes are significant and the interaction of the plasma with the walls can be neglected. Plasma is produced in spherical glass vessel with inner diameter of 0.5 m, on one side covered by reflection foil, which reflects and focuses the microwaves radiated on another side by horn antenna. Microwaves (10 GHz, X-band) are generated by pulse magnetron. The 100 kW pulses have duration 2.5 μ s and are repeated 400 times per second.

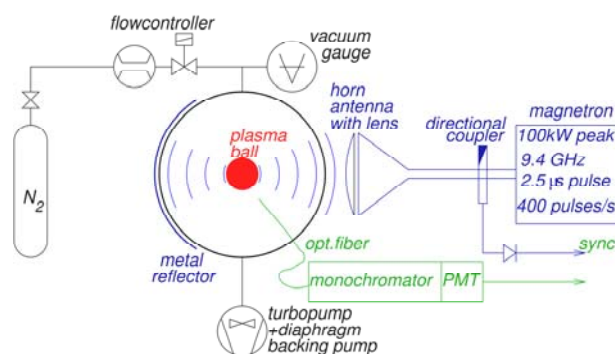


Fig. 1. Experimental set-up

The electric field is just in front of the horn antenna not high enough to produce a breakdown at reduced gas pressure. Only after focusing, the field has a maximum in the centre of the glass vessel and therefore a plasma ball is formed there. A pressure is measured by a Pirani/Penning full-range gauge and controlled by a gas flow meter and by varying rotation speed of a turbo pump. We use nitrogen as working gas and the operating pressure is in the range 20–2000 Pa.

The light emitted from plasma was collected into the optical fiber made from fused silica (see Fig. 1). Spectral analysis was made by Zeiss SPM2 monochromator equipped with EMI 6255B photomultiplier tube. Output signals from photomultiplier are digitalized via 50 Ω inputs by HP Infinium 500 MHz digital oscilloscope. Relatively large buffers of this device permitted us to record data points during the whole pulse with a time step of 10 ns. The synchronization pulses are taken from the 70 dB directional coupler. To perform sensitive measurements was quite a challenge and careful shielding, wiring and grounding had to be employed.

Results and discussion

In discharges containing nitrogen, $N_2(A)$ metastables are of relatively high population and therefore they strongly influence the plasma kinetics. In order to determine the concentration of $A^3\Sigma_u^+$ metastable state of N_2 we should discuss the processes relevant for their production and loss.

Regarding the literature we can find that it is possible to generate nitrogen neutral metastables by electronic collisions, radiative cascade, electronic ionic recombination and neutral atomic recombination. As we follow the evolution of spectral intensity in the afterglow, the collisions with electrons are not important due to their rapid cooling⁵. As the intermediary states in radiative cascade have permitted transitions, the process is very fast and need not to be accounted for in the afterglow. Using the NO titration experiment⁶ we found that $[N]$ is under our detection limit, i.e. lower than 10^{13} cm^{-3} . Considering this low atomic density and low rate constant for volume atom reassociation, we neglect this process, too. Using the values of electron density and recombination coefficient from¹ we conclude that contribution of electron – ion recombination on population of nitrogen metastables is low. Therefore, all production processes taken into account may be successfully neglected and we should deal only with the loss

processes.

In literature⁷ we can find many sources of destruction for the $N_2(A^3\Sigma_u^+)$ metastables, such as

- quenching by N_2 ($l_1 = 3 \cdot 10^{-16} \text{ cm}^3 \text{ s}^{-1}$),
- quenching by N ($l_2 = 4 \cdot 10^{-11} (300/T)^{2/3} \text{ cm}^3 \text{ s}^{-1}$),
- energy pooling to B and C states ($l_3 + l_4 = 2.6 \cdot 10^{-10} \text{ cm}^3 \text{ s}^{-1}$),
- quenching by N_2^+ (l_5 unknown).

It is possible to write the following kinetic equation for our problem

$$\frac{d[N_2(A)]}{dt} = -(l_1[N_2(X)] + l_2[N(^4S)] + l_5[N_2^+]) [N_2(A)] - (l_3 + l_4) [N_2(A)]^2 - D\nabla^2 [N_2(A)]$$

where the reaction coefficients l are explained above, D is the diffusion coefficient for nitrogen metastables and $[N_2(A)]$ is the $N_2(A^3\Sigma_u^+)$ metastable concentration.

We can make following assumptions:

- It is possible to neglect the effect of diffusion since the times we are dealing with in our experiment are on the microsecond scale.
- It is possible to neglect the quenching by N_2 and by N because their rates are low compared with energy pooling reactions and the concentration of $N(^4S)$ is relatively low compared with the concentration of $N_2(A)$
- Since the l_5 coefficient is not known (we could not find it in any publication), we will solve this matter later demonstrating that it is possible to neglect the quenching by ions, too. Let us work now with the hypothesis that l_5 is low enough to be neglected.

Neglecting the above mentioned, it reduces the previous equation to following

$$\frac{d[N_2(A)]}{dt} = -(l_3 + l_4) [N_2(A)]^2 = -I [N_2(A)]^2$$

which can be easily solved, giving us the following solution:

$$[N_2(A)](t) = \frac{[N_2(A)]_{t=0}}{1 + I [N_2(A)]_{t=0} t}$$

where $t = 0$ corresponds to the end of the discharge pulse, i.e. the beginning of the afterglow. Then we can apply this to the temporal evolution profiles we have found experimentally for the second positive system of N_2 . Assuming that the $N_2(C)$ state is populated by the energy pooling reaction only, the intensity of the second positive system is proportional to the squared concentration of $N_2(A)$ metastables

$$I(2^{nd} \text{ positive}) \approx \frac{([N_2(A)]_{t=0})^2}{(1 + I [N_2(A)]_{t=0} t)^2} \quad (I)$$

We measured the intensities of the electronic-vibrational transitions 0–2, 1–3 and 2–4 from $N_2(C^3\Pi_u)$ to $N_2(B^3\Pi_g)$ for several pressures. Typical curve is presented in Fig. 2, which also demonstrates excellent agreement between experimental data and the theoretical curve (Eq. (I)). For each pressure the nonlinear fitting of experimental data to Eq. (I) was per-

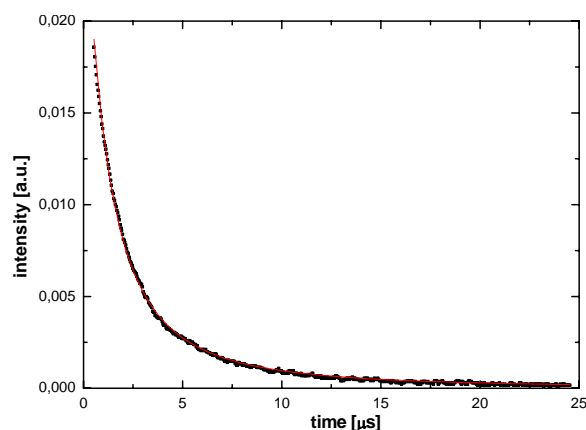


Fig. 2. Measured data of the 0–2 2nd positive system evolution in afterglow (points) and fit by Eq. (I) (line)

formed and as a result, the value of initial $N_2(A)$ metastables concentration was found.

The dependence of the initial value (i.e. the concentration at the end of the microwave pulse and at the beginning of the afterglow) is plotted in Fig. 3. The error bars were calculated from the three independent values obtained from 0–2, 1–3 and 2–4 transitions measured for each pressure.

Now, if we have not neglected the ion quenching (which we assume is also responsible for production of excited molecular ions), it would be possible to find an expression for intensity of the 1st negative system of nitrogen

$$I(1^{st} \text{ negative}) \approx \frac{[N_2(A)]_{t=0}}{(1 + I [N_2(A)]_{t=0} t)} \frac{[N_2^+]_{t=0}}{(1 + r [N_2^+]_{t=0} t)}$$

since the intensity of the ionic band is proportional to the metastable concentration and to the ground state ion concentration. The constant r corresponds to the electron-ion recombination coefficient.

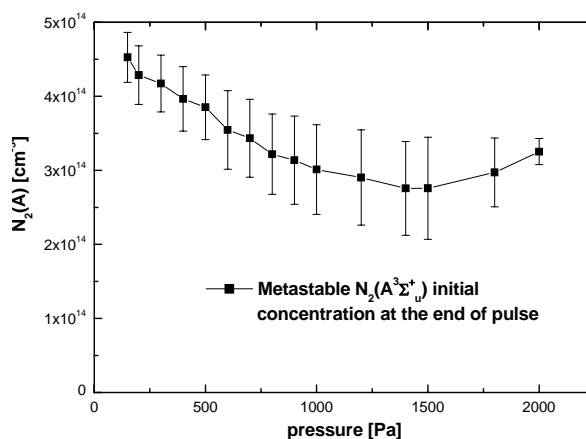


Fig. 3. Density of $N_2(A^3\Sigma_u^+)$ metastable molecules produced by the microwave pulse

Let us now demonstrate that we can neglect the quenching by the ions. We normalize the intensities of $I(2^{\text{nd}} \text{ positive})$ and $I(1^{\text{st}} \text{ negative})$ by their initial values (at $t = 0$). In such way we can follow the evolution of both band intensities in the same plot (Fig. 4). For pressures increasing up to 1500 Pa the metastable initial concentration decreases (see Fig. 3) and so our normalized intensity of second positive system must increase at any time in the afterglow, as normalized $I(2^{\text{nd}} \text{ positive})$ is

$$\frac{I(2^{\text{nd}} \text{ positive})}{([N_2(A)]_{t=0})^2} \approx \frac{1}{(1 + I[N_2(A)]_{t=0}t)^2}$$

In our previous paper¹ we found that electron concentration at the beginning of the afterglow also decreases with pressure. Due to plasma neutrality, the ion density should also decrease. From the similar reasoning as above we can see that normalized $I(1^{\text{st}} \text{ negative})$

$$\frac{I(1^{\text{st}} \text{ negative})}{[N_2(A)]_{t=0} \cdot [N_2^+]_{t=0}} \approx \frac{1}{(1 + I[N_2(A)]_{t=0}t)} \frac{1}{(1 + r[N_2^+]_{t=0}t)}$$

must also increase with the increasing pressure, as both the initial metastable concentration and initial ion concentration decrease with pressure. In Fig. 4 we can see that the behavior of the neutral lines is the one expected, but the ion lines behave in the opposite manner. This means that the excitation of ions by collision with metastables molecules is not the main process responsible for 1^{st} negative system.

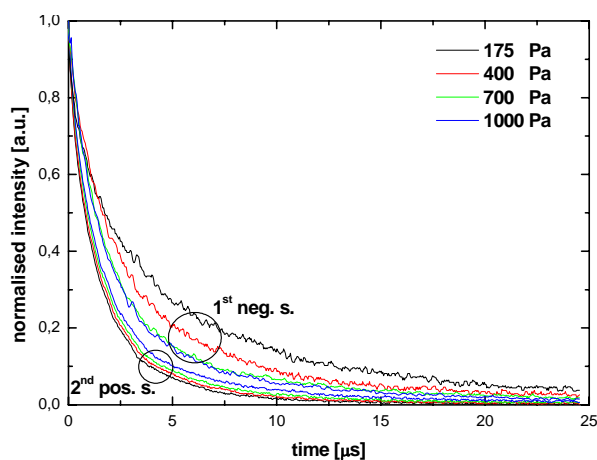


Fig. 4. Time evolution of 2^{nd} positive and 1^{st} negative systems in the afterglow. All intensities have been normalized by the initial value

Consequently, this process should not be important for the quenching of metastables molecules.

Conclusion

We carried out complex diagnostics of the afterglow of short pulse high power low pressure nitrogen discharge. From the temporal evolution of the second positive system of nitrogen we calculated concentration of nitrogen molecules in $A^3\Sigma_u^+$ metastable state.

This research has been supported by the contracts MŠMT 0021622411 and GAČR 202/08/1106.

REFERENCES

1. Meško M., Bonaventura Z., Vašina P., Tálský A., Frgala Z., Kudrle V., Janča J.: Plasma Sources Sci. Tech. 13, 562 (2004).
2. Bonaventura Z., Trunec, D., Meško M., Vašina P., Kudrle V.: Plasma Sources Sci. Tech. 14, 751 (2005).
3. Meško M., Bonaventura Z., Vašina P., Kudrle V., Tálský A., Trunec, D., Frgala, Z., Janča J.: Plasma Sources Sci. Tech. 15, 574 (2006).
4. Bonaventura Z., Trunec, D., Meško M., Vašina P., Kudrle V.: J. Phys. D: Appl. Phys. 41, 015210 (2008).
5. Guerra V., Dias F. M., Loureiro J., Sa P. A., Supiot P., Dupret C., Popov T.: IEEE Trans. Plasma Sci. 31, 542 (2003).
6. Vašina P., Kudrle V., Tálský A., Botoš P., Mrázková M., Meško M.: Plasma Sources Sci. Tech. 13, 668 (2004).
7. Nahorny J.: Étude de la cinétique d'une décharge électrique dans des mélanges Azote-Oxygène, Thesis. Université Paris-Sud, France 1994.

M. Meško, P. Vašina*, J. Muñoz Espadero^a, V. Kudrle, A. Tálský, and J. Janča (Department of Physical Electronics, Faculty of Science, Masaryk University, 611 37 Brno, Czech Republic, ^a on leave from Facultad de Ciencias, Universidad de Córdoba, Campus Rabanales, 14071 Córdoba, Spain): **Determination of $N_2(A)$ Population From Optical Emission Spectra**

We studied the low pressure high power pulsed microwave discharge produced in the experimental device with suppressed influence of wall reactions. This work is focused on the afterglow. Using the experimental results, the elementary plasma processes in such type of discharge are discussed, mainly the kinetics of metastable states. It enables us to derive absolute density of nitrogen metastable molecules from relative evolution of emission of second positive system of N_2 .

DIAGNOSTIC OF PLASMA NEEDLE PROPERTIES BY USING MASS SPECTROMETRY

SAŠA LAZOVIĆ*, NEVENA PUAC̃, GORDANA MALOVIĆ, ANTONIJE ĐORĐEVIĆ, and Z. LJ. PETROVIĆ

*Institute of Physics, Pregrevica 118, 11080 Belgrade, Serbia
lazovic@phy.bg.ac.yu*

1. Introduction

Interest in the non-thermal atmospheric pressure plasmas began to grow rapidly in the late 1980s. Such discharges have drawn considerable attention due to their enormous potential for technological applications mostly in surface modifications especially for materials or living tissues that may not allow putting it into vacuum chambers.

Different kinds of atmospheric pressure plasma sources have been developed for various types of applications^{1,2}. Advantages of working at atmospheric pressures are that expensive pumping systems are not needed, it is possible to treat samples that are sensitive to low pressures and plasma can be easily put in contact with samples. If one achieves operation free from spark and if gas temperature is not increased it may allow application to sensitive surfaces.

Because of its mild plasma and geometry, plasma needle is especially convenient for medical applications. Non contact disinfection of dental cavities and wounds and minimum-destructive precise treatment and removal of diseased tissue can be done by a plasma needle³. The treatment can be done with less than 0.1 mm accuracy. The goal is to separate the cells without causing the necrosis of the cells or in some situations to induce apoptosis. Biological samples like plant tissue can also be easily treated⁴.

For the purpose of successful treatment and comparison of different samples by plasma needle it is necessary to characterize the plasma itself the best way possible. The standard parameters for treatment of samples are duration of treatment, power transmitted to the plasma and distance of the sample to the tip of the needle. For the power measurements the derivative probes were used. The percentage of the total power distributed to plasma itself was determined from the recorded voltage and current waveforms.

In order to understand the chemistry in the gas phase and at the surface of the sample a knowledge of the composition of plasma, i.e. of the active species, is needed. Mass spectrometry (MS) is a popular method to analyse chemical composition of gases and plasmas. The results are particularly relevant for surface treatment, because the mass spectrometer samples the species which arrive at and potentially interact with the surface.

The advance of the differential pumping/evacuating has been already used for mass spectrometric study of atmospheric plasma operated in mixture of helium, nitrogen and oxygen. Stoffels and coworkers investigated various short living nitrogen and oxygen species and their threshold ioniza-

tion⁵ as well as nitric oxide generation by the plasma needle⁶. As the pumping of the mass analyzer affected (turned off) their standard plasma needle these authors have used a significantly larger model of the plasma needle.

Mass spectrometry (HIDEN HPR60) was also used for detection of ions produced both in positive and negative point-to-plane corona discharges in nitrous oxide containing traces of water vapor at atmospheric pressure⁷. A point-to-plane negative corona fed by ambient air under static conditions was analyzed using the Hiden HPR60 MBMS spectrometer operating at atmospheric pressure⁸.

In this paper we will present some of the properties of our low temperature atmospheric pressure discharge (plasma needle). We have achieved mass analysis with the standard geometry albeit with a somewhat increased gas flow rate.

2. Experimental set up

Plasma needle is atmospheric pressure plasma source powered by 13.56 MHz RF generator that operates in a mixture of air and helium. The needle consist of central tungsten wire (0.5 mm in diameter) placed into a ceramic tube with slightly larger diameter and both placed into the glass tube with 6 mm diameter (see Fig. 1). We have used configuration with the grounded copper ring placed at the tip of the glass tube. The central wire represents the powered electrode and the grounded electrode is the surface in the vicinity of the plasma needle tip.

The rest of the electrical circuit is the same that we have already used⁴ and is shown in Fig. 1. Low-temperature RF discharge at 13.56 MHz is generated using a Dressler Caesar 1010 power supply, in combination with Variomatch matching network. In order to increase the peak-to-peak voltage, we have used a custom-made transformer and inserted it between the plasma needle and the RF matching network. We have implemented a dummy load to make the discharge more stable and to be sure that only a small part of the power supplied by the RF power supply is transmitted to the discharge. In this configuration the dummy load serves as a 'power divider'.

Instantaneous voltage and current are monitored using two derivative probes⁹ somewhat different from the probes already proposed in the literature. Both probes were placed inside a stainless steel box opposite to each other. The box was placed as close as possible to the plasma needle. The output of the probes was connected to a digital oscilloscope (Tektronix TDS220) with the cables of equal length. All waveforms were collected by the computer for further manipulation.

The MBMS (Molecular Beam Mass Spectrum) system incorporates a Hiden EQP mass/energy analyzer. This system consists of two parts: pumping section that has three different pumping stages which makes it possible to work at atmospheric pressures and the detector section which itself works at low pressures. The sampling orifice is the entrance to the first pumping stage and plasma needle is positioned against the orifice. Species created in the discharge are sampled using a triple stage differentially pumped molecular beam inlet system. The sampling orifices are carefully aligned to produce a molecular beam which minimizes the collisions of the sam-

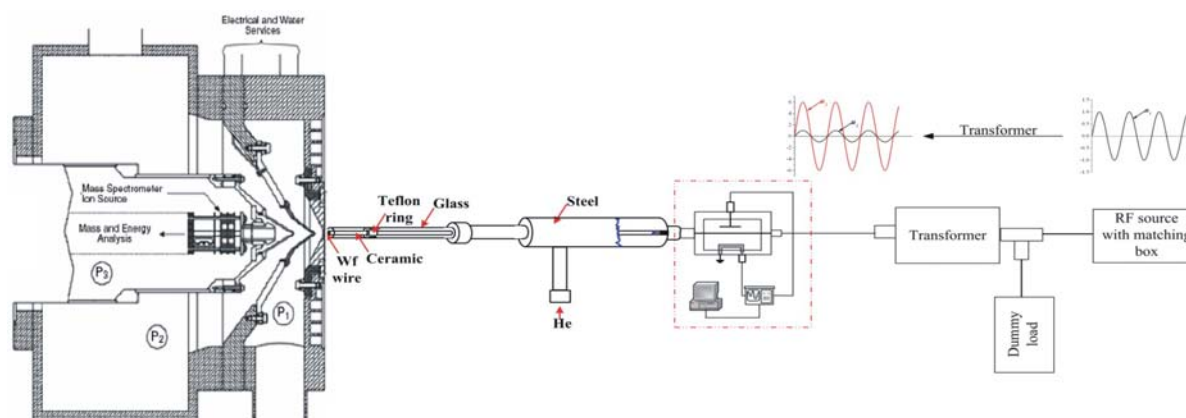


Fig. 1. Experimental setup of plasma needle with mass spectrometer head on the left

pled particles with each other and with surfaces.

Between the second and the third stage of the MBMS there is an Open/Close valve (Swagelock) which is used to detect background signal of the MBMS. In all measurements this valve is open so the SEM (Secondary Electron Multiplier) counts that we are measuring are actually foreground signal plus the background signal from the detector. In order to see how big the background signal is one has to close this valve.

The mass spectrometer is equipped with an internal electron source with variable electron energy, which allows ionization of species (positive RGA) as well as electron attachment (negative RGA or EAMS, electron attachment mass spectrometry). We have made our measurements of plasma needle discharge in RGA positive mode. The recorded positive ion signal in this case is directly proportional to the radical number density.

While similar work of Stoffels et al. has been done on what appears to be the same system they had to use somewhat larger dimensions and flow because pumping of the mass analyzer perturbed and even turned off the discharge⁶. The plasma source used by them in the experiment has been described as a 'robust' version of the plasma needle: it generates an elongated jet of 4 mm length, and the power consumption is from 1 to 10 W. Naturally, this type of plasma needle is developed only for mass spectrometric diagnostics and has not been to our knowledge used for medical treatment with tissue in direct contact with the plasma.

These authors found that atmospheric plasma operated in air and helium is a good source of active oxygen and nitrogen radicals. This could explain the efficiency of such plasma (among others) in bacterial inactivation.

Our measurements were performed on a standard size plasma needle. After some efforts it was possible to operate the mass analyzer under conditions that would not greatly affect the discharge itself. However, we had to increase the gas flow from several 100 sccm to more than 1000 sccm.

3. Results and discussion

Electrical measurements

In the standard configuration the plasma needle uses the target surface as the grounded electrode. In that respect the properties of the plasma change depending on the proximity of the target surface. In configuration that we have used in these experiments a grounded stainless steel cylinder (copper ring) was added at the tip of the glass tube. With the grounding cylinder the glow of plasma was wider in area and we

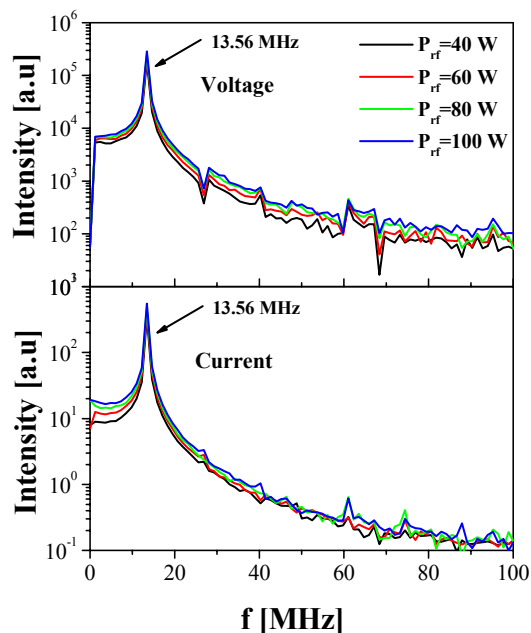


Fig. 2. Voltage and current signals in frequency domain

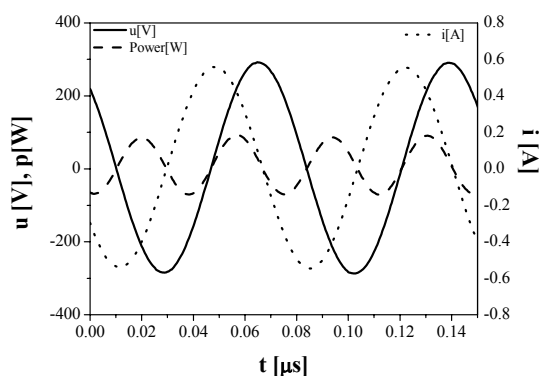


Fig. 3. Current, voltage and power signals

were able to ignite plasma for smaller powers given by the RF power supply. In addition, operation appeared to be stable and mostly independent on the proximity of the target surface.

One of the parameters important for the diagnostic of the discharge is the power transmitted to the plasma. Due to a large number of the components in electrical circuit and in particular the presence of the 'power divider', the power transmitted to the plasma differs significantly from the power given by the RF power supply. Thus we have determined the current and voltage waveforms and the related U-I characteristics of the discharge under different conditions.

Instantaneous current and voltage waveforms were recorded for a range of powers (10–150 W) given by the RF power supply. After that all these signals were transferred to the frequency domain (see Fig. 2). We can see that both for voltage and current only basic harmonic are significant, i.e. that there are practically no higher harmonics.

Signals were then transferred back to the time domain and instantaneous power was calculated. In Fig. 3 instantaneous signals for current, voltage and powers signals are shown.

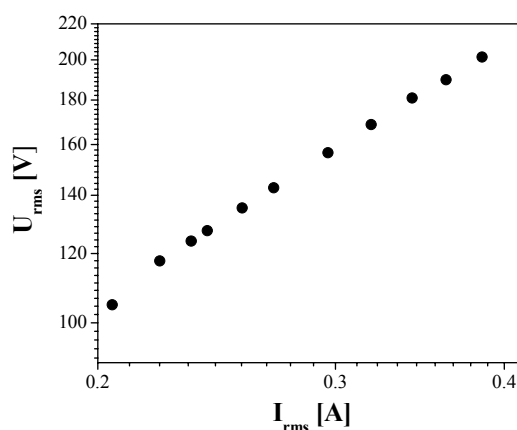


Fig. 4. Voltage-Current characteristics

Peak to peak values for voltage lie between 300 and 600 V, while current peak to peak values are between 0.5 and 1 A. By calculating root-mean-square values of current and voltage we were able to obtain U-I characteristics (see Fig. 4). As we can see, from linearity of the obtained U-I characteristics, our discharge works in α mode.

Mass spectrometry

We were able to obtain stable plasmas in air-helium atmospheres containing down to 10 % of helium. However, we had to increase the gas flow from several 100 sccm to more than 1000 sccm in order to sustain plasma in the close vicinity of mass spectrometer. Data were collected for different values of plasma parameters such as power, various distances between the needle and the QMS and flow.

In Fig. 5 one of the recorded mass spectrum is shown. When presenting results we have used yields of specific masses (relative contribution to the total signal) instead of counts per second obtained directly from the MBMS to reduce noise induced by temporal variations of the plasma. The yield was calculated as:

$$Y = \frac{Y_{mass}^i}{\sum_i Y_{mass}^i} [\%]$$

where Y_{mass}^i is the count due to the specific positive ion (like N^+ , O^+ , etc.) and this was divided by sum of counts for all recorded masses (1–100 amu).

We can see He^+ signal as the highest peak. Percentage of He in the overall mixture increases with the increase of the He flow. In our experiments we did not use the mixture of He, N_2 and O_2 as the feeding gas. We used pure He with different flow rates (1–3 slm) in surrounding air. Besides the He^+ peak we can see intensive peaks for N_2^+ and O_2^+ , H_2O^+ , OH^+ , N^+ , O^+ , NO^+ etc. Sometimes quantitative analysis is difficult because some of the detected compounds have the same mass to

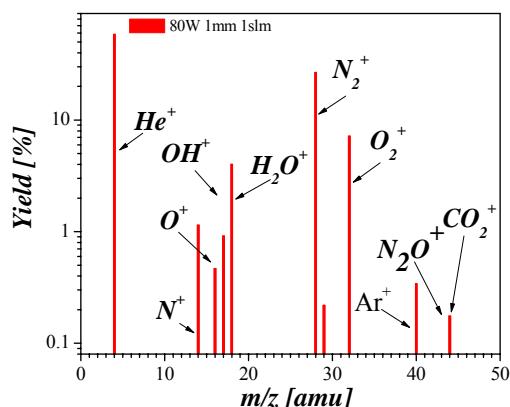


Fig. 5. Mass spectra

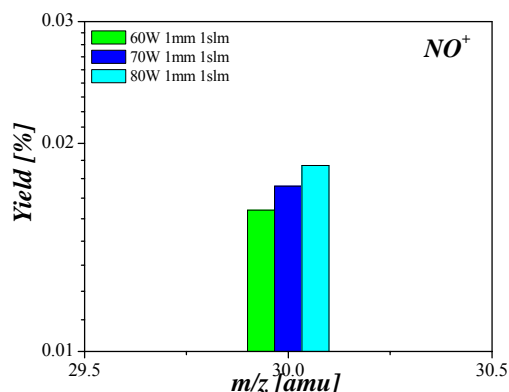


Fig. 6. Yields of NO^+ ions for powers of 60 W, 70 W and 80 W given by the RF source. Distance between tip of the needle and orifice of mass spectrometer was 1 mm and He flow rate was 1 slm

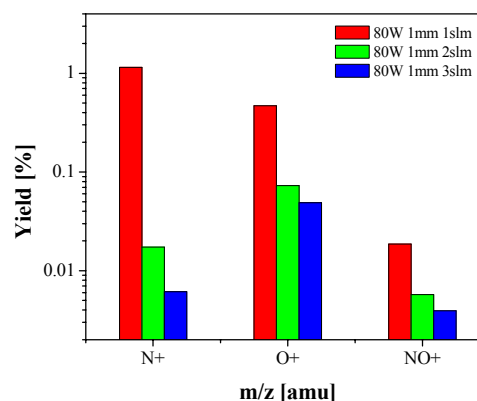


Fig. 7. Yields of N^+ , O^+ and NO^+ ions for He flow rates of 1 slm, 2 slm and 3 slm and power of 80 W. Distance between tip of the needle and orifice of mass spectrometer was 1 mm

charge ratio. For example, N_2O^+ has mass of 44 amu, but its signal coincides with the persistent CO_2^+ peak and this causes problems in analysis of recorded spectra.

Main species of our interest were N^+ , O^+ and NO^+ ions. In Fig. 6 we show yields for NO^+ ion for three different powers given by the RF power supply. We can see that with the increase of the power the yields for NO^+ increase. We have not produced detailed explanation but our observations are in agreement with the discussion in the work of Stoffels and coworkers⁶.

In case of nitrogen monoxide (NO) one of the possible reactions is forming of NO by the three-body recombination



The recombination rate at temperatures close to the ambient temperature for this reaction is about $10^{-45} \text{ m}^6 \text{ s}^{-1}$ (ref.¹⁰).

Another possibility for the creation of NO radicals is the 2nd order reaction



which has a rate coefficient of $1.56 \cdot 10^{-21} \text{ m}^3 \text{ s}^{-1}$ at 400 K (ref.¹¹).

With the increase of the flow rate of the feeding gas (He) from 1 slm (standard liter per minute) to 3 slm one can observe a decrease in yields for all three ions (see Fig. 7). This may be explained by dilution of the atmospheric gases by the buffer gas which is supported by the increased yield of He^+ .

Thus we have to use small flow rates of helium in order to gain more active species. During our previous work on the treatments of plant cells the flow rate of helium was around 100 sccm so we can assume that even larger amount of active species was created if electron temperatures are not reduced by molecular species for that range of mixtures.

Of the chemically active molecular species the dominant molecules are NO (see Fig. 8) which while toxic at high abundances may be useful for numerous processes. Surprisingly, little ozone has been found. With an increase of the flow rate, yields for all three compounds decrease. Of course, one should be careful when choosing the optimal conditions for

desired treatment because with the increase of the flow we eliminate undesirable species, but, also, at the same time we reduce amounts of species which are important for treatment.

Plasma needle can operate in two different modes. Stoffels and coworkers labeled them as: a bipolar mode, when the nearby surface affects the shape of the plasma and unipolar mode when the surface does not affect very much the shape of the plasma^{6,12}. This was also confirmed in simulations done by Sakiyama and coworkers^{13,14}.

In Fig. 9 measurements for the distance of 1.5 mm are shown. We can see that with the increase of the power there is a general increase in the yields which becomes greater after the sudden transition to the bipolar mode which occurs at the highest power. This sudden transition is also observable with bare eyes. In unipolar mode one can see discharge at the tip of the needle and after transition it spreads towards the surface of

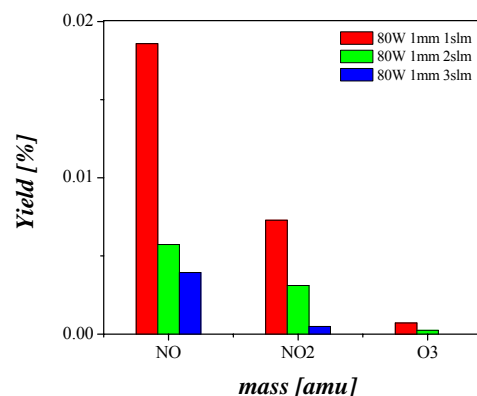


Fig. 8. Yields of NO, NO_2 and O_3 for He flow rates of 1 slm, 2 slm and 3 slm and power of 80 W. Distance between tip of the needle and orifice of mass spectrometer was 1 mm

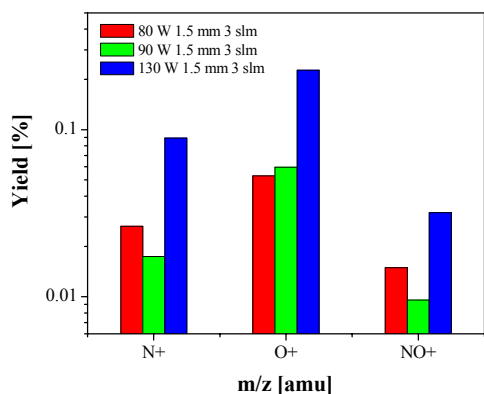


Fig. 9. Yields of N^+ , O^+ and NO^+ ions for powers of 80 W, 90 W and 130 W given by the RF source. Distance between tip of the needle and orifice of mass spectrometer was 1.5 mm and flow rate of He was 3 slm

the mass spectrometer covering it in the area of 1–2 mm².

4. Conclusion

In this paper we have shown some of the characteristics of plasma needle obtained by using mass spectrometry. Mass spectrometric measurements show significant conversion of feed gases (nitrogen and oxygen) into radicals N and O, and NO molecule which is found to be the dominant reaction product of these reactions.

Measurements were made for the range of powers (0.1 to 1 W) and two distances (1 and 1.5 mm) in order to determine optimal conditions for plasma treatment of samples. We needed to increase the flow of the feeding gas from 100 sccm up to several standard liters per minute in order to be able to sustain the discharge in the close vicinity of the working mass spectrometer.

Transition from unipolar to bipolar mode was observed through sudden increase in the yields of the measured species. Also, dominant species was NO radical and surprisingly, little

ozone has been found.

This research has been supported by the Ministry of Science Serbia under the contract number 141025 of the project Physics Fundamentals of Applications of Non-Equilibrium Plasmas in Nanotechnologies and Treatment of Materials.

REFERENCES

- Kunhart E. E.: IEEE Trans. Plasma Sci. 28, 189 (2000).
- Fridman A., Chirokov A. and Gutsol A.: J. Phys. D: Appl. Phys. 38, R1 (2005).
- Sladek R. E. J., Stoffels E.: J. Phys. D: Appl. Phys. 38, 1716 (2005).
- Puač N., Petrović Z. Lj., Malović G., Đorđević A., Živković S., Giba Z. and Grubišić D.: J. Phys. D: Appl. Phys. 39, 3514 (2006).
- Stoffels E., Aranda Gonzalvo Y., Whitmore T. D., Seymour D. L. and Rees J. A.: Plasma Sources Sci. Technol. 16, 549 (2007).
- Stoffels E., Aranda-Gonzalvo Y., Whitmore T. D., Seymour D. L. and Rees J. A.: Plasma Sources Sci. Technol. 15, 501 (2006).
- Skalny J. D., Orszagh J., Mason N. J., Rees J. A., Aranda-Gonzalvo Y. and Whitmore T. D.: J. Phys. D: Appl. Phys. 41, 085202 (2008).
- Skalny J. D., Orszagh J., Mason N. J., Rees J. A., Aranda-Gonzalvo Y., Whitmore T. D.: Int. J. Mass Spectrom. 272, 12 (2008).
- Puač N., Petrović Z. Lj., Živković S., Giba Z., Grubišić D. and Đorđević A. R., in: *Plasma Processes and Polymers*, Chap. 15, p. 193. John Wiley, NY 2005.
- <http://kinetics.nist.gov>
- Hewson J. C. and Williams F. A.: Combust. Flame 117, 441 (1999).
- Stoffels E., Kieft I. E., Sladek R. E. J., van den Bedem L. J. M., van der Laan E. P., Steinbuch M.: Plasma Sources Sci. Technol. 15, S169 (2006).
- Sakiyama Y. and Graves D. B.: J. Phys. D: Appl. Phys. 39, 3451 (2006).
- Sakiyama Y., Graves D. B., Stoffels E.: J. Phys. D: Appl. Phys. 41, 095204 (2008).

INFLUENCE OF OXYGEN TRACES ON RECOMBINATION PROCESSES IN NITROGEN POST-DISCHARGE

VĚRA MAZÁNKOVÁ and FRANTIŠEK KRČMA

Institute of Physical and Applied Chemistry, Faculty of Chemistry, Brno University of Technology, Purkyňova 118, Brno 612 00, Czech Republic
mazankova@fch.vutbr.cz

Introduction

Kinetic processes in nitrogen post-discharges have been a subject of many studies because nitrogen and nitrogen based plasmas are used in a huge number of applications like hard films deposition¹ or plasma sterilization². Besides the use of an active discharge nowadays the post-discharge is one of the most favorite research directions because it can be applied for the treatment of various temperature sensitive materials³.

The neutral nitrogen molecule can form many electronic states. Due to its symmetry, all vibrational levels of the ground state and also the first eight levels of the first electronically excited state are metastables. Besides them, there are some other strongly metastable highly excited states. All these states conserve the excitation energy for a long time. The excitation energy transfer during collisions among these species as well as atomic recombination processes lead to the formation of some radiative states and the visible light emission can be observed up to one second after switching off an active discharge depending on the experimental conditions, mainly on pressure. Kinetic modeling of pure nitrogen was given for example in *Guerra's* work⁴. It is interesting that oxygen concentration has strong influence on kinetic processes. This study extends our recent experiments by the changes in nitrogen post-discharge kinetics caused by oxygen impurity. Paper compares the influences of reactor wall material and its temperature on the post-discharge kinetics with respect to the three body recombination of nitrogen ground state atoms. This process populates mainly the $N_2(B^3\Pi_g)$ state⁵ at its vibrational levels 10–12 but all the kinetics is much more complex and thus some other observations are also briefly described in this paper.

Experimental set up

The DC flowing post-discharge was used for the experimental study. The schematic drawing of the experimental set up is given in Fig. 1. The active discharge was created in Pyrex or Quartz discharge tube with a 120 mm electrode distance at current of 200 mA and pressure of 1000 Pa. Hollow molybdenum electrodes were placed in the side arms of the main discharge tube to minimize their sputtering and also to suppress the light emitted in the electrode regions. Nitrogen was of 99.999 % purity and it was further cleaned by Oxy-clear and LN_2 traps. No oxygen or carbon traces were detectable in the pure nitrogen discharge and post-discharge

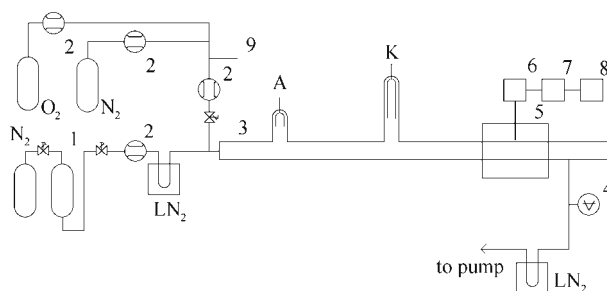


Fig. 1. Scheme of the experimental set up. 1 – catalyzer BASF R-3-11; 2 – mass flow controller; 3 – Pyrex discharge tube (900 mm long, inner diameter 13 mm); 4 – capacitance gauge; 5 – quartz optical fiber; 6 – monochromator Jobin Yvon Triax 550; 7 – CCD; 8 – PC; 9 – outlet of synthetic air

(concentrations under 1 ppm or 0.01 ppm, resp.⁶). The reactor system was pumped continuously by a rotary oil pump separated from the discharge tube by another LN_2 trap.

The oxygen traces were added into the main pure nitrogen flow just before the active discharge using the low range mass flow controller (MFC). To reach concentrations less than 1000 ppm synthetic air was prepared continuously using another set of MFCs. Also in this case, nitrogen of 99.999 % purity was used and the purity of oxygen was the same. Thus concentrations of other impurities, containing mainly carbon, were kept low enough to have no disturbing effect on the studied processes.

The post-discharge optical emission spectra were measured by Jobin Yvon monochromator TRIAX 550 with the 1200 grooves per mm grating coupled with CCD detector. The emitted light was lead to the entrance slit of the monochromator by the multimode quartz optical fiber movable along the discharge tube. The optical fiber holder (length of 6 cm with optical fiber mounted at its center) had to be filled by liquid nitrogen. Thus the reactor wall temperature was kept at 300 K or 77 K around (± 3 cm) the optical spectra observation point. Temperature of decaying plasma at 77 K wall temperature was calculated at about 100 K (ref.⁷) using the simulated nitrogen 1st positive ($N_2(B^3\Pi_g) \rightarrow (A^3\Sigma_u^+)$) 2–0 band spectrum. Nitrogen 1st ($N_2(B^3\Pi_g) \rightarrow (A^3\Sigma_u^+)$) and 2nd ($N_2(C^3\Pi_u) \rightarrow (B^3\Pi_g)$) positive and nitrogen 1st negative ($N_2^+(B^2\Sigma_u^+) \rightarrow (X^2\Sigma_g^+)$) systems were recorded in all spectra. The bands of NO^+ system ($NO(B^2\Pi) \rightarrow NO(A^2\Sigma^+)$) dominantly originating from vibrational level 0 were observed, too. The bands of NO^+ system dominantly originating also from vibrational level 0 were observed only in the Quartz tube. No other molecular emissions were observed. The relative vibrational populations at the selected nitrogen levels were calculated using all measurable emission band intensities. The transition probabilities and wavelengths of the transitions were taken from *Gilmore's* tables⁸.

Results and discussion

The examples of measured spectra are shown in the Figs. 1 and 2 in Pyrex and Quartz discharge tube at the decay time of 42 ms and for two wall temperatures mentioned

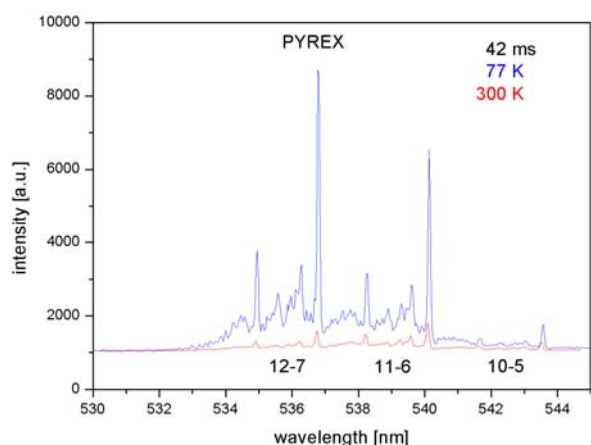


Fig. 2. Example of nitrogen recombination spectrum in Pyrex tube at decay time of 42 ms and wall temperatures of 77 K and 300 K. Concentration of oxygen traces was 1 871 ppm

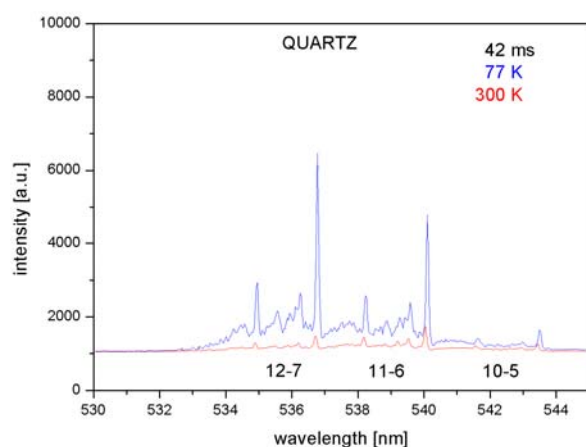


Fig. 3. Example of nitrogen recombination spectrum in Quartz tube at decay time of 42 ms and wall temperatures of 77 K and 300 K. Concentration of oxygen traces was 1 871 ppm.

above. The shown bands are dominantly populated by the three body recombination of nitrogen ground state atoms. It can be seen that at the given decay time there is no great difference between observation in Pyrex and Quartz but there is a strong effect of the wall temperature. At the lower wall temperature, the 12–7 band is much more intensive than at ambient wall temperature and its maximal intensity is even higher than the intensity of 11–6 band. The same effect was observed more times before⁹ and it reflects the recombination mechanism that was reported in *Partridge's* work⁵ and that is briefly described below.

The post-discharge in Pyrex tube is shown in Fig. 4. The relatively strong light is emitted at all oxygen concentrations. In pure nitrogen a pink afterglow effect (a part of the post-discharge where the pink light emission is dominant) is well visible and this effect is quenched by oxygen traces as it is shown in Fig. 4 and as it was reported in details recently¹⁰. The pink afterglow effect in pure nitrogen is also well observ-

able in Quartz discharge tube but the light emission outside this region is significantly lower in comparison to the post-discharge in Pyrex. The light emission in Quartz significantly increases with the increase of oxygen concentration and at oxygen concentrations higher than 1000 ppm the post-discharge in Quartz looks visually as post-discharge in Pyrex.

This visual observation is described more exactly in Figs. 5 and 6 where the relative populations of $N_2(B^3\Pi_g)$ state at levels 10–12 are shown and compared at different conditions. It can be seen from these figures that the populations at all these three levels are significantly lower in pure nitrogen in Quartz discharge tube than in Pyrex one at all post-discharge times. Oxygen added into the discharge in low concentration up to about 500 ppm enhances all the populations and the difference given by the wall material is nearly negligible at higher oxygen concentrations. This well corresponds to the direct visual observation, as it was shown before. It should be also pointed out that the oxygen increase over 500 ppm has nearly no effect on the populations at given vibrational levels.

There are two main processes populating vibrational levels of $N_2(B^3\Pi_g)$ state. Besides the ground state atoms recombination, the pooling of lower energy metastables can play a significant role in the population of the studied levels. To verify the significance of pooling contribution to the populations the ratio of band head intensities of 11–7 band and 2–0 band from the nitrogen first positive system ($N_2(B^3\Pi_g) \rightarrow (A^3\Sigma_u^+)$) was calculated. We can suppose that the $N_2(B^3\Pi_g, v=2)$ level is populated mainly by the pooling and the contribution of recombination can be neglected at this level. Thus the I_{11-7}/I_{2-0} ratio can reflect the effectiveness of the recombination process.

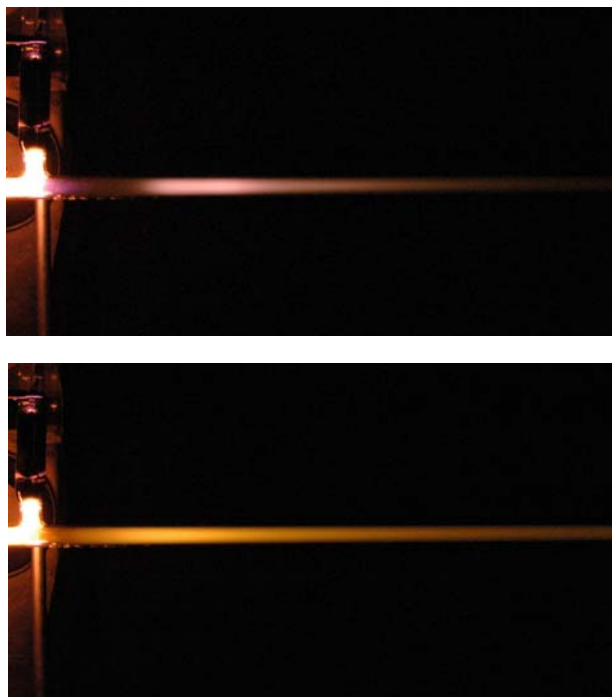


Fig. 4. Post-discharge in pure nitrogen (top) and in nitrogen containing 1 870 ppm of oxygen (bottom) in Pyrex discharge tube at the ambient wall temperature

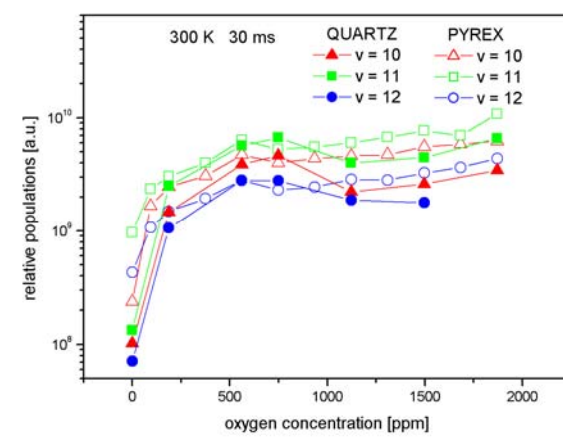
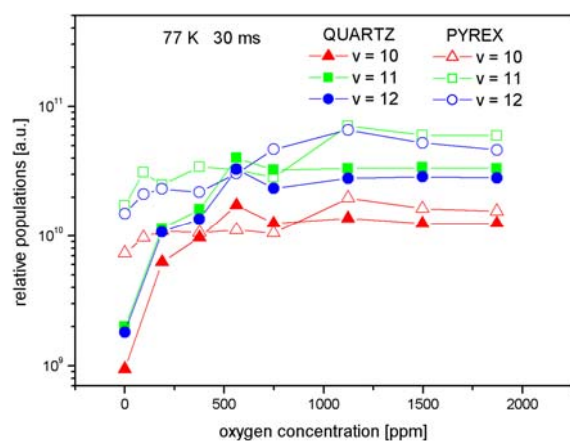
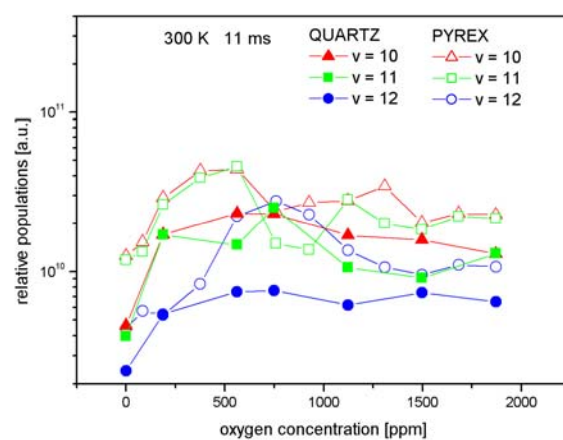
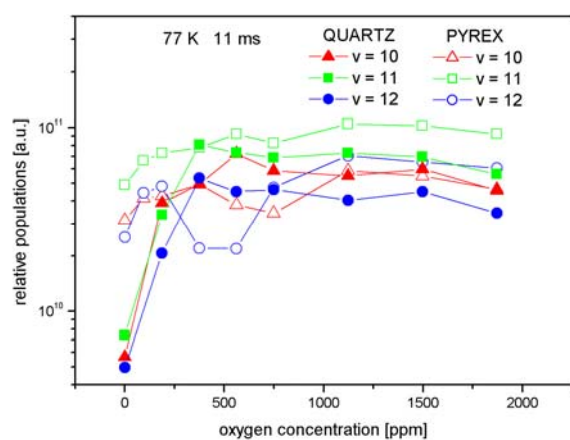
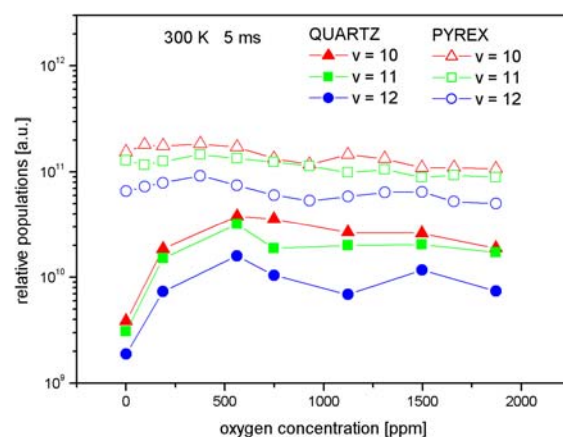
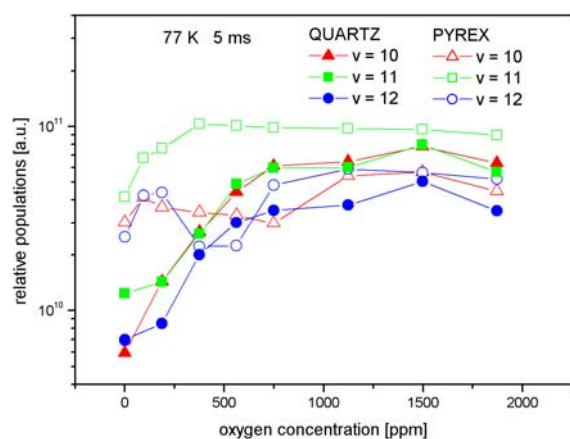


Fig. 5. Dependencies of $N_2(B^3\Pi_g, v=10-12)$ relative populations on oxygen concentration at selected decay times and at wall temperature of 77 K

Fig. 6. Dependencies of $N_2(B^3\Pi_g, v=10-12)$ relative populations on oxygen concentration at selected decay times and at wall temperature of 300 K

The experimental results are shown in Figs. 7–10 during the post-discharge in dependencies on wall material and wall temperature at selected oxygen concentrations. The nearly linear increase of the ratio can be seen during the post discharge at decay times later than 10 ms. This time corresponds

to the maximum emission of pink afterglow effect (see Fig. 4 and details in references¹⁰).

The figures also demonstrate the increase of intensity ratio with the increase of oxygen concentration. This effect is observable in all cases but it is more visible in Quartz tube,

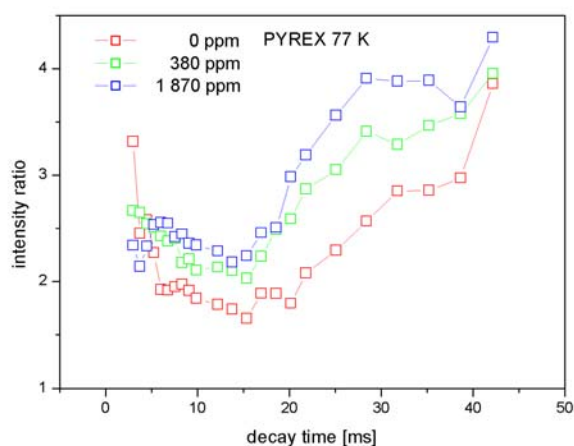


Fig. 7. Band head intensities ratio of 11-7 and 2-0 bands of nitrogen 1st positive system during the post-discharge in Pyrex tube at wall temperature of 77 K

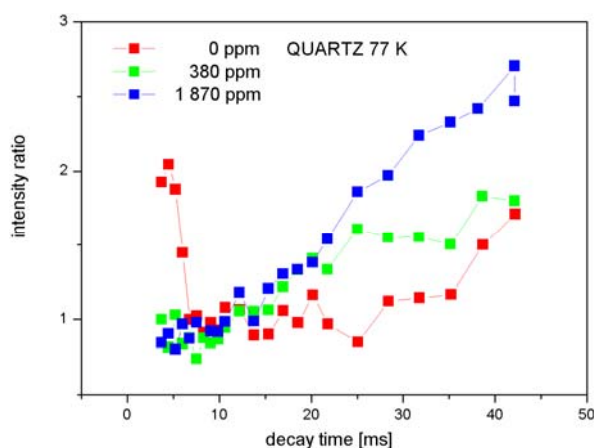


Fig. 9. Band head intensities ratio of 11-7 and 2-0 bands of nitrogen 1st positive system during the post-discharge in Quartz tube at wall temperature of 77 K

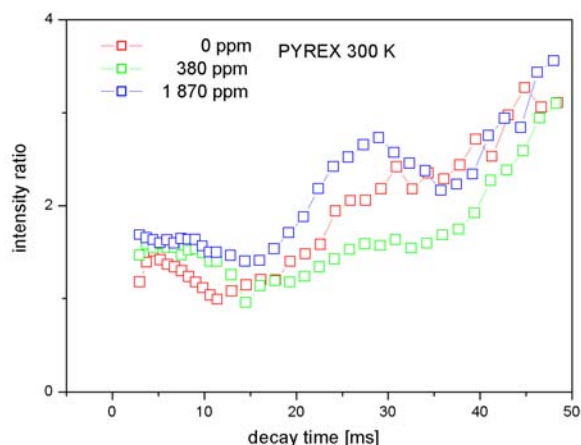


Fig. 8. Band head intensities ratio of 11-7 and 2-0 bands of nitrogen 1st positive system during the post-discharge in Pyrex tube at wall temperature of 300 K

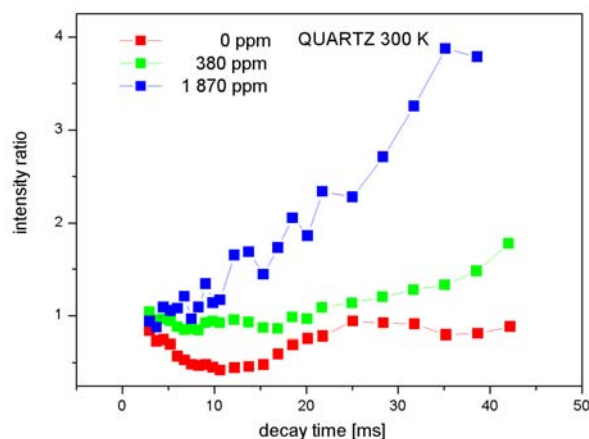


Fig. 10. Band head intensities ratio of 11-7 and 2-0 bands of nitrogen 1st positive system during the post-discharge in Quartz tube at wall temperature of 300 K

especially at the ambient wall temperature.

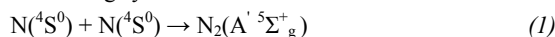
It is known that the recombination is the main process at the later decay times (during so called Lewis-Rayleigh afterglow¹¹) and thus the pooling efficiency is decreasing and the I_{11-7}/I_{2-0} ratio increases. To describe the oxygen influence in more detail, the I_{11-7}/I_{2-0} ratio is shown in Figs. 11 and 12 as a function of oxygen concentration at two selected decay times at all reactor wall conditions. It can be seen the ratio of intensities increases with the increase of oxygen concentration at all wall conditions at shorter decay time (Fig. 11). The situation at later decay time is not such simple. There is no clear dependence in the Pyrex. The ratio of intensities strongly increases in the Quartz at the ambient wall temperature but its dependence on oxygen concentration at wall temperature of 77 K shows different behavior but generally it is also increasing.

The last experimental results that must be mentioned before the kinetic description of the observed processes are

the following. The pink afterglow effect is strongly quenched by oxygen and it disappears at oxygen concentrations over about 1000 ppm¹⁰. The NO^β and NO^γ emission is directly proportional to the oxygen concentration and it is nearly directly proportional to the decay time at given oxygen concentration. Based on these all experimental results the following kinetic description can be proposed.

Kinetic processes

Atomic recombination in nitrogen is known for a long time¹¹. A detailed theory of the three body recombination of two nitrogen ground state atoms was presented in Partridge's work⁵. The mechanism of the recombination can be described by the following system of reactions



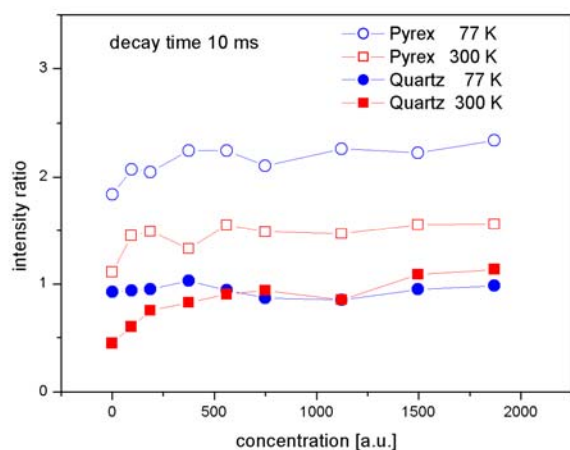


Fig. 11. Band head intensities ratio of 11-7 and 2-0 bands of nitrogen 1st positive system as a function of oxygen concentration at decay time of 10 ms

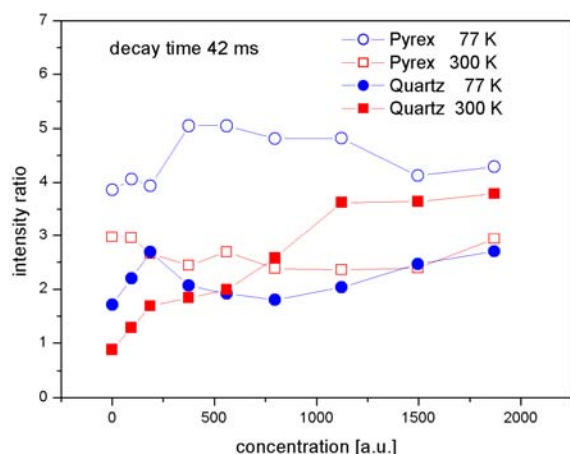
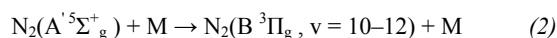
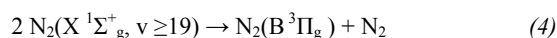
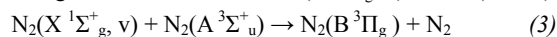


Fig. 12. Band head intensities ratio of 11-7 and 2-0 bands of nitrogen 1st positive system as a function of oxygen concentration at decay time of 42 ms



where M is the third body, mainly any nitrogen molecule. The first of these reactions represented the equilibrium between concentrations of nitrogen atoms and weakly bonded molecules. Usually it is presented in complex with the second reaction. Thus this recombination has a three body form. The rate coefficient of this process is $8.3 \cdot 10^{-34} \exp(500/T) \text{ cm}^6 \text{ s}^{-1}$ as it was reported in ref.¹². As it has a negative temperature dependence, the recombination increases with decreasing temperature as it was presented in the Results.

Other process that contributes to $\text{N}_2(\text{B}^3\Pi_g)$ population is the pooling of lower metastables $\text{N}_2(\text{X}^1\Sigma_g^+, v)$ and $\text{N}_2(\text{A}^3\Sigma_u^+)$.

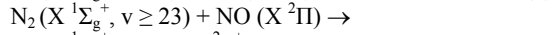
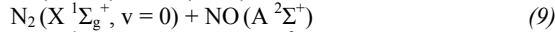
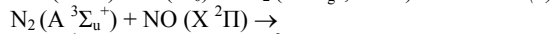
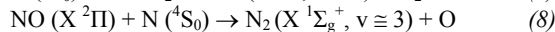
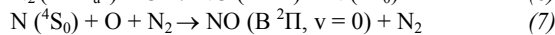
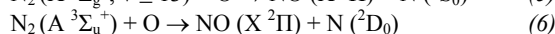
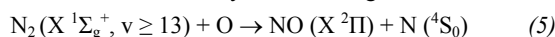


The $\text{N}_2(\text{A}^3\Sigma_u^+)$ state is again created by the pooling of

ground state molecules (the process similar to the reaction 4). Vibrationally excited ground state molecules are created during the post-discharge period mainly by a well known v-v process⁴. As the $\text{N}_2(\text{A}^3\Sigma_u^+)$ state concentration at the end of an active discharge is low¹³, the main energy source in the afterglow besides the atoms is vibrationally excited nitrogen ground state molecules.

The same molecules that are precursors for the $\text{N}_2(\text{B}^3\Pi_g)$ state creation are also the precursors for molecular ion creation. This process is known as a step-wise ionization¹⁴. The highly excited neutral metastable molecules (excited both electronically and vibrationally) can have energy sufficient for the ionization during their mutual collisions. After molecular ion creation, the excitation to the radiative $\text{N}_2^+(\text{B}^2\Sigma_u^+)$ state is done by the collisionally induced energy transfer from the vibrationally excited neutral ground state molecules, namely $\text{N}_2(\text{X}^1\Sigma_g^+, v \geq 12)$ ^{6,10}. This mechanism is responsible for the pink afterglow creation.

If some other species are added the reaction scheme become more complicated and it is significantly different. Small addition of oxygen traces lead to form NO. The oxygen influence can be described by the following main reactions



The reactions 5 and 10 have a strong influence on the v-v process in nitrogen ground state. Highly excited molecular states are thus formed with a lower probability and the pooling creation of electronically excited states is strongly decreased. Moreover, the concentration of $\text{N}_2(\text{A}^3\Sigma_u^+)$ state is quenched by atomic oxygen as it is described by the reactions 6 and 9. On the other hand, these processes increase the populations at lower vibrationally excited ground state levels and thus the pooling processes involving only these levels are more efficient. Reactions 7 and 8 describe the NO species formation and backward dissociation. The reactions 6 and 7 lead also to the increase of atomic nitrogen concentration. This description itself is not sufficient for the experimental results explanation. Thus the nitrogen molecular ion must be included in the model.

The formation of nitrogen molecular ion is strongly dependent on the oxygen concentration. Its formation by the step-wise ionization process is strongly decreased because the reactions 5 and 6 strongly decrease the production of high energetic metastables. Thus the ion formation efficiency is significantly lower and there are not enough ionic species that could be populated by energy transfer from the vibrationally excited nitrogen ground state. That reaction has a high rate coefficient and at low temperature, it has a strongly resonant character^{6,10}. Thus if the molecular ion is created, the strong depopulation of $\text{N}_2(\text{X}^1\Sigma_g^+, v \geq 12)$ vibrational levels is observed.

When oxygen is added, the process of the step-wise ionization creating molecular ion is blocked and thus higher ground state vibrational levels can be significantly populated.

Besides the higher electronic states creation by pooling of these states, the dissociation can be observed, too. It means the concentration of nitrogen ground state atoms can be increased in the afterglow if the oxygen traces are added. Similar effect was recently directly observed in Vašina's work¹⁵. This process has a reflection in the increase of populations at $N_2(B^3\Pi_g, v=10-12)$ levels as it was observed. The same process is also reflected in the observed dependences of NO emission bands.

High vibrationally excited ground state nitrogen molecules (over $v=22$) play a minor role in the direct formation of electronically excited states. Thus the reaction (10) has only the slight effect, mainly on the population of $N_2(B^3\Pi_g)$ levels laying above the predissociation limit.

Conclusions

The recombination of nitrogen ground state atoms was observed through the emission of nitrogen first positive system spectral bands in pure nitrogen containing the traces of oxygen. The observations were carried out in Pyrex and Quartz discharge tubes at wall temperatures of 300 and 77 K. The significant increase of the bands originating at level $N_2(B^3\Pi_g, v=12)$ was observed at decreased wall temperature. The oxygen traces increased the light emission during the post-discharge period; this effect was significantly stronger in Quartz tube. Simultaneously, the nitrogen pink afterglow effect was strongly quenched by oxygen. The detail study showed that low oxygen concentration up to 500 ppm significantly increased the populations at $N_2(B^3\Pi_g, v=10-12)$ levels and this effect was higher in the Quartz tube. The kinetic model showed that oxygen traces were responsible for the NO creation that consequently decreased the populations of highly excited nitrogen molecular metastables. Thus the step-wise ionization was quenched and finally this influence resulted in the increase of atomic nitrogen concentration in the afterglow. To verify this model experimentally the NO titration during the post-discharge in nitrogen-oxygen mixtures will be carried out.

This work was supported by the Czech Science Foundation under projects No. 202/05/0111 and No. 202/08/1106.

REFERENCES

- Pierson J. F., Belmonte T., Michel H.: *Appl. Surf. Sci.* **172**, 285 (2001).
- Pintassilgo C. D., Loureiro J., Guerra V.: *J. Phys. D: Appl. Phys.* **38**, 417 (2005).
- Mezerette D., Belmonte T., Hugon R., Czerwiec T., Henrion G., Michel H.: *Surf. Coat. Technol.* **142-144**, 761 (2001).
- Guerra V., Sa P. A., Loureiro J.: *Eur. Phys. J. – Appl. Phys.* **28**, 125 (2004).
- Partridge H., Langhoff S. R., Bauschlicher C. W., Schwenke D. W.: *J. Chem. Phys.* **84**, 6901 (1986).
- Krčma F., Protasevich E. T.: *Post-discharges in Pure Nitrogen and Nitrogen Containing Halogenated Hydrocarbon Traces*, Tomsk Polytechnic University 2003.
- Krčma F., Mazánková V., Soral I., Šimek M.: *Proceedings of ICPIG XXVIII, 1722 Praha 2007*.
- Gilmore F. R., Laher R. R., Espy P. J.: *J. Phys. Chem. Ref. Data* **21**, 1005 (1992).
- Kumar V., Kumar A.: *Physica* **132 C**, 273 (1985).
- Krčma F., Mazánková V., Soral I.: *Publ. Astronom. Observatory of Belgrade* **82**, 133 (2007).
- Kistiakowski G. B., Warneck P.: *J. Chem. Phys.* **27**, 417(1957).
- Klopovsky K. S., Mukhovatova A. V., Popov A. M., Popov N. A., Popovicheva O. B., Rakhimova T. V.: *J. Phys. D: Appl. Phys.* **27**, 1399 (1994).
- Sadeghi N., Foissac C., Supiot P.: *J. Phys. D: Appl. Phys.* **34**, 1779 (2001).
- Paniccia F., Gorse C., Cacciatore M., Capitteli M.: *J. Phys.* **61**, 3123 (1987).
- Vašina P., Kudrle V., Tálský A., Botoš P., Mrázková M., Meško M.: *Plasma Source Sci. Technol.* **13**, 668 (2005).

THE CHEMISTRY OF GOLD CLUSTERS IN PLASMA GENERATED WITH MALDI, LASER DESORPTION IONISATION AND LASER ABLATION FROM VARIOUS PRECURSORS

E. M. PEÑA-MÉNDEZ^{a*},
J. R. HERNÁNDEZ-FERNAUD^b,
R. NAGENDER^c, J. HOUŠKA^c,
and J. HAVEL^{c,d}

^a Department of Analytical Chemistry, Nutrition and Food Chemistry. Faculty of Chemistry, University of La Laguna, Campus de Anchieta, 38071 – La Laguna, Tenerife, Spain,

^b Servicio de Proteómica, Unidad de Investigación Mixta ULL-HUC, Edificio de Enfermería, Campus de Ofra, s/n La Cuesta 38320, Tenerife, Spain, ^c Department of Chemistry, Faculty of Science, Masaryk University, Kotlarska 2, 61137 Brno, Czech Republic, ^d Department of Physical Electronics, Faculty of Science, Masaryk University, Kotlarska 2, 61137 Brno, Czech Republic

1. Introduction

Nanotechnology is a rapidly growing science of producing and utilizing among others nano-sized particles. Their unique size-dependent properties make them superior and indispensable as they show unusual physical, chemical and biological properties. Nanomaterials are already having a huge impact on nanotechnology and nanomedicine¹. Nanomaterials are present in toothpaste, sunscreens, sanitary ware coatings, medicaments, and even in food products but they can also represent health risks, like for example silver².

Generally, the behavior of metal particles with well-defined nanostructures has become one of the most active research areas. The inorganic nanoparticles exhibit significantly distinct physical, chemical and biological properties from their bulk counterparts. Discoveries in the past decade have demonstrated that the electromagnetic, optical and catalytic properties of noble-metal nanoparticles are strongly influenced by shape and size. Nanogold represents a tiny particle from a few gold atoms up to hundreds/thousands of atoms. This has motivated an upsurge in research on the synthesis routes that allow better control of shape and size for various nano-biotechnological applications^{3,4}.

Gold nanoparticles (GNP) are quite important in electronics, bio-analytics and in nano-medicine. They are produced by various technologies, mostly by chemical methods but also by laser ablation.

1.1. Short historical overview

GNP have been known for a long time but they were called colloidal gold. The history of GNP goes back to ancient times, for example, the so-called „Elixir of Life“, searched by alchemists, was a potion made of gold. Colloidal gold was used since Roman times to colour glass in yellow or red and

famous bohemian ruby glass is also based on nano-gold. Paracelsus in the 16th century created a potion called *Aurum Potabile*, Herschel in 1842 used colloidal gold to record images on paper, etc. but Faraday in 1857 was perhaps the first one to understand that the colour of gold solutions was due to the small size of gold particles.

1.2. Applications of GNP in medicine

As nano gold is quite reactive, the gold particles are usually covered with a suitable layer of inorganic⁵ and organic material (Fig. 1), e.g. with thiols, sugars, etc.^{6,7}. Such functionalized GNP are stable and are used in bioanalytics and biomedicine.

Most recently gold colloids have gained significant attention in the field of biomedicine. Due to their several exclusive properties, metallic gold acquired an excellent profile for use in these biomedical applications. Gold nanoparticles have a great impact in the medical society and they were used in cancer diagnosis, treatment and as a drug delivery vector for biological or pharmacological agents^{8–14}.

GNP have been applied as a drug carrier in diagnostic and medical fields as they comprise some explicit properties such as i) they are easily fabricated ii) they have a very good capacity to bind to target cancer cells, carbohydrates, antibodies, proteins, pharmacological agents rather than other nanoparticles^{15–19}.

It was recently reported that GNP can be used to detect some toxic metals like mercury in human body and in environmental bodies such as rivers, streams, lakes and oceans. When mercury contaminated fish and shell fish are ingested by children and women, it is dangerous to their health. Even if there are several conventional methods²⁰, a sensitive and accurate colorimetric method was developed which can detect mercury at nano-molar level by using DNA-functionalized gold nanoparticles.

During the last decade, fluorescence based assays have gained a prior position in immunochemistry-based *in vitro* diagnosis and *in vivo* imaging assays. In this field, radio chemical labels and chromophores have several advantages such as high sensitivity and potential for easy multiplexing. But these traditional radio chemical labels and organometallic chromophores were replaced by Au-QDs, where QDs are quantum dots, because of their exclusive characteristics including size dependent controllable emission spectra, narrow band width, broad excitation, high extinction coefficient and potential stability against photobleaching²¹.

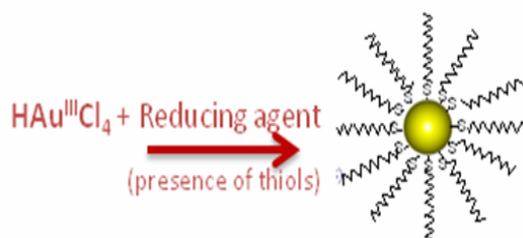


Fig. 1. Schema of nano gold formation from Au(III) salt

The combination of GNP and poly-amidoamine (PAMAM) dendrimers as capping ligands to biomolecules has recently been reported²². So these AuQDs are suitable for biological applications. These dendrimers can be covalently or electrostatically conjugated to DNA^{23–24}, RNA²⁵, carbohydrates²⁶ and proteins^{27–28}. PAMAM dendrimers have been proven as excellent cell transfection agents as they contain hydroxyl or amino groups at their end groups. So with the combination of a biologically inert material such as gold, along with good biological compatibility, the dendrimers penetrate into the cell membranes easily. PAMAM could efficiently conjugate with various biomolecules like DNA, proteins, RNA and carbohydrates.

1.3. Mass spectrometry of GNP

Among various methods used to study and characterize GNP, mass spectrometry is quite important. However, the ionization of GNP represents the major problem. It was reported²⁹ that GNP are mostly decomposed during the ionization process and to obtain correct information about the size and the molecular weight of GNP is quite difficult. Recently, it was shown in MALDI that using 2-(4-hydroxyphenylazo) benzoic acid (HABA) matrix³⁰ the real size of even very high Au clusters can be detected. Another technique to be considered is electrospray ionization mass spectrometry³¹ or visible-MALDI with tunable laser³².

Successful MALDI analysis of GNP with HABA concerning chemically covered GNP, such as in Fig. 1 has been reported^{33,34}. Mass spectrometric analysis of gold nanoclusters has also been reported in the literature³⁵.

In this paper we are studying “naked” GNP, not covered with any ligand, and trying to develop a reliable approach to analyze such particles. We are studying the possibilities of TOF to characterize GNP in plasma and, to understand their plasma chemistry. Gold clusters are generated either by the use of matrices (MALDI) or by laser desorption ionization or ablation.

2. Experimental

2.1. Chemicals

Gold (III) chloride trihydrate, gallic acid, 2-(4-hydroxyphenylazo) benzoic acid (HABA), citric acid and nanodiamond powder (< 10 nm, purity 95 %) were purchased from Sigma-Aldrich (Stenheim, Germany). Sodium azide and sodium hydroxide were from Merck (Darmstadt, Germany). The matrices α -cyano-4-hydroxycinnamic acid (CHCA), 2,5-dihydroxybenzoic acid (DHB), sinapinic acid (SPA) and peptide mixture (Pepmix) for calibration were purchased from Bruker Daltonics (Bremen, Germany). Calmix (mixture of bradikinin, angiotensin I, renin, and adrenocorticotrophic hormone) from Sigma Aldrich (Steinheim, Germany) was used in an AXIMA for external calibration. All other reagents were of analytical grade purity.

Water used to prepare all solutions was double distilled from the quartz apparatus by Heraeus Quarzschmelze (Hanau, Germany).

2.2. Instrumentation

Mass spectra were obtained either using a MALDI-TOF Auto-flex mass spectrometer (Bruker Daltonics, Bremen, Germany) or an AXIMA Shimadzu of Kratos (Manchester, U.K.). Mass spectrometers were equipped with delayed extraction, 337 nm nitrogen laser. Bruker spectrometer was provided with a hydrophobic coating target (Anchor Chip 600/384, Bruker Daltonics, Bremen, Germany). The accelerating voltage was set to 20 kV and laser repetition rate to 16 Hz. Mass spectra were obtained using linear positive or negative ion modes with delayed extraction. The mass spectra were accumulated for approximately 50–100 shots per preparation in total.

2.3. Synthesis of GNP

We have produced GNP from HAuCl₄ salt using various reducing agents like hydrogen peroxide, azide, citric^{36,37}, gallic or humic acids. The synthesis of GNP from citric acid was done in the following way: an aqueous solution of citric acid (2 ml 1 % solution) was mixed with 2 ml of acetone. The resulting mixture (2 ml) was diluted up to 4 ml with water. A solution of 0.25 mM Au(III) chloride (40 ml) was transferred to a clean 60 ml baker and heated in a water bath. When the temperature reached 80 °C, 4 ml of the reducing mixture (0.25 % citric acid in 25 % acetone) was added (pH of the mixture was 3) and stirred vigorously. After 10 min of continuous heating and stirring, the color of solution turned to wine red. It was the clear indication of gold nanoparticles formation. GNP were also synthesized by the reduction of Au (III) by gallic acid and the details are given elsewhere³⁸.

2.4. Samples preparation

The matrix solutions were prepared in the following way: CHCA (0.3 mg ml⁻¹ in acetone-ethanol 2:1); DHB (0.16 mg ml⁻¹ in acetonitrile); SPA (1 mg ml⁻¹ in 70 % aqueous acetonitrile); and HABA (1 mg ml⁻¹ in 70 % aqueous acetonitrile).

On the MALDI target plate 0.5–1 μ l of matrix solution followed by 0.5–1 μ l of sample was deposited. In LDI and LA modes, no matrices were used.

3. Mass spectrometry of gold clusters

3.1. Analysis of gold clusters with laser desorption ionization and TOF MS

GNP produced in aqueous solution were then ionized using a nitrogen laser 337 nm either (i) with the help of a matrix (MALDI mode) or (ii) via laser desorption ionization. Under linear and reflectron modes and dependent on the laser energy, single charged gold clusters Au_{*n*} (*n* = 1–55) were observed both in positive and negative ion modes. In addition, depending on the precursors used, various gold clusters like Au_{*m*}Na⁺ (*m* = 1–6) adducts, AuH⁺, Au₃H₂⁺, AuH₃O⁺, Au₄H⁺, AuK⁺, AuCa⁺ etc. were identified in the plasma (Fig. 2).

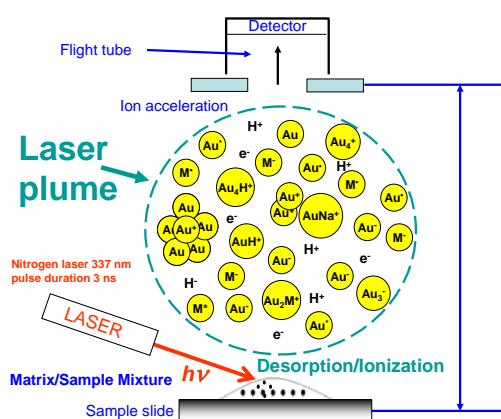


Fig. 2. Experimental set up and schema of gold clusters formation in a plasma plume (* signs excited species, M means matrix molecule)

Using common matrices, like dihydroxybenzoic acid (DHB), α -cyano-4-hydroxycinnamic acid (CHCA) and sinapinic acid for MALDI, no high clusters known from the literature were observed. Most probably high Au_m clusters are broken down by the action of the laser.

An example of LDI mass spectrum is given in Fig. 3, where GNP are synthesized by the reduction of $HAuCl_4$ and citric acid. The results in negative ion mode were similar to those obtained in the positive one.

A part of the mass spectrum is given in Fig. 4, where GNP were synthesized by the reduction of $HAuCl_4$ by gallic acid. The highest cluster we have detected here was Au_{55} . Negative ion mode results were similar to the results of positive mode.

3.2. Examination of matrices to ionize GNP

Different matrices to ionize GNP were examined. When DHB matrix was applied and using a laser pulse intensity threshold approach, we have been able to suppress, to some extent, nanoparticles fragmentation. Good results were also obtained by using DHB matrix. Additionally, the use of ND as a matrix for analysis of GNP was examined. Only several

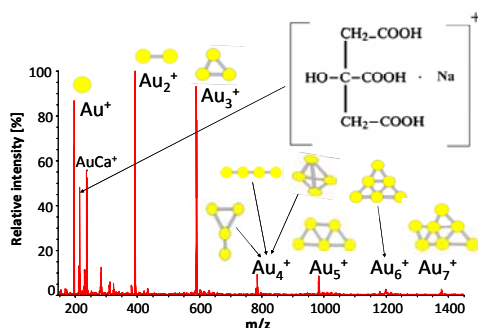


Fig. 3. Part of LDI TOF mass spectrum showing the formation of gold clusters Au_n^+ ($n = 4-25$). Conditions: Bruker MALDI TOF MS, positive ion mode, laser energy 100 A.U.

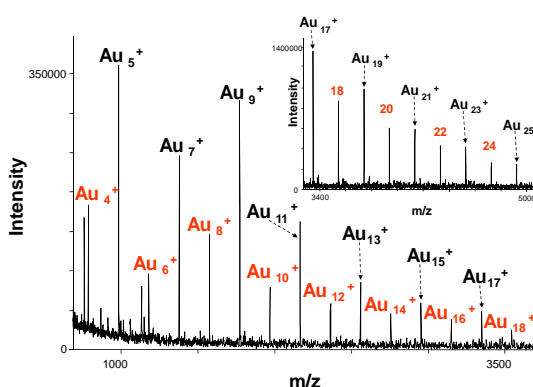


Fig. 4. LDI mass spectrum showing the formation of high gold clusters Au_n^+ ($n = 4-25$). Conditions: Autoflex mass spectrometer Bruker MALDI TOF MS, positive ion mode

low gold clusters ($n = 1-5$) were observed. However the formation of several mixed Au-C clusters such as $C_{11}Au$, CAu_2 , $C_{17}AuH_2$, $C_{18}Au$, CAu_2Na , C_2Au_2Na , $C_{22}Au_2$, $C_{17}AuNa_4$ and $C_{31}Au$ were detected.

A part of LDI mass spectrum measured in the positive ion mode is given in Fig. 5. The spectrum is showing the formation of carbon-gold mixed clusters with good resolution and intensity.

Good agreement between model and experimental spectra was found (Fig. 6).

3.3. The use of GNP as a matrix for MALDI analysis

The use of GNP as a matrix was tested near the limit of the MALDI TOF MS detection (1 fmol) for the ionization of the organic molecule Huperzine A³⁹ (Hup A), known as anti-Alzheimer drug. It was observed that the use of the GNP as a matrix increases the signal of Huperzine A 100 times. The formation of adducts like $Au_m(Hup A)_n$ in the plasma phase

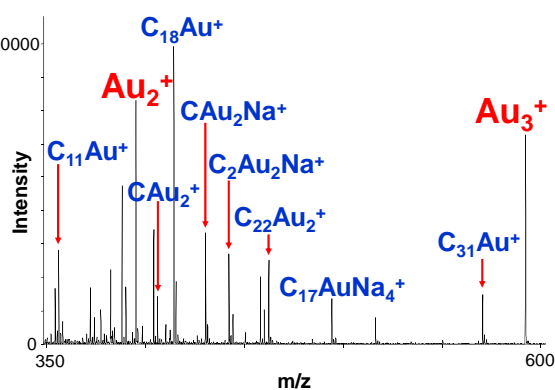


Fig. 5. Part of mass spectrum concerning the formation of mixed carbon-gold clusters. Conditions: Bruker MALDI TOF MS, LDI, positive ion mode. Precursors: mixture of nanodiamonds and GNP produced using gallic acid as a reducing agent. (All clusters are single positively charged)

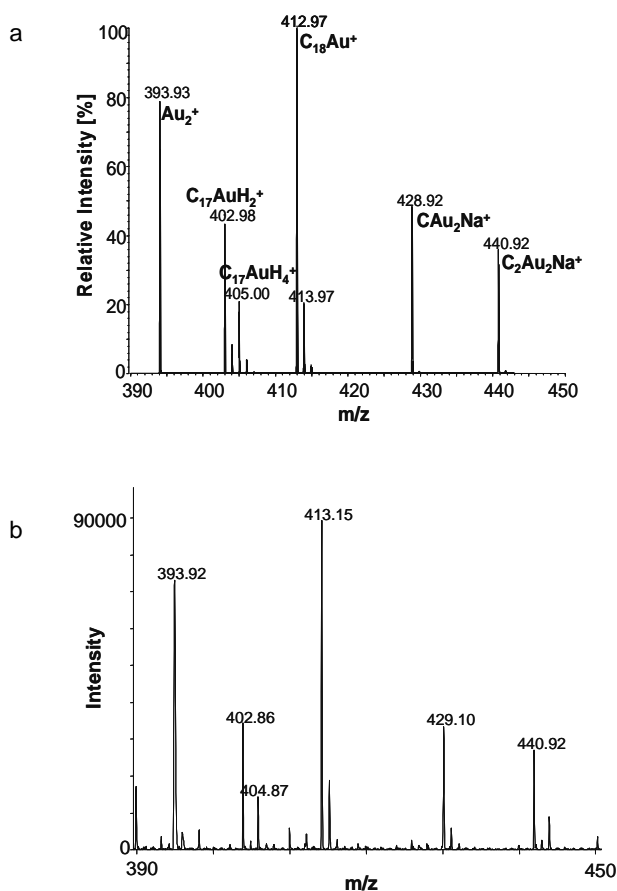


Fig. 6. a) Model of the part of the mass spectrum concerning the formation of Au_2 , C_{18}Au , CAu_2Na and $\text{C}_2\text{Au}_2\text{Na}$; b) Experimental MALDI spectrum of GNP using nano-diamonds as a matrix. Conditions: same as Fig. 5. (All clusters are single positively charged)

was also detected. GNP were also examined as a matrix for ionization of mycotoxins (deoxynivalenol). However, the sensitivity was low and the procedure needs optimization.

4. Structure of gold clusters

Gold clusters show different structures. Low clusters are planar (Fig. 3). High clusters are either compact or hollow gold cages. Recently, both compact and hollow gold cages which are fullerene like structures were reported^{40,41}. An example of compact and hollow cage structures is given in Fig. 7.

Gold cluster cations have planar structures for $n = 3-7$ and starting from $n = 8$, they form slightly distorted 3-dimensional structures⁴². On the basis of quantum-chemical calculations, it has been reported that medium-sized gold clusters, such as Au_n with $n = 32-35$, 42 and 50 also have cage-like structures⁴³. Gold, having special properties, is the only metal which can form hollow cages⁴³. Even though it has some unusual structural characteristics, gold clusters have become particularly attractive due to their diverse catalytic

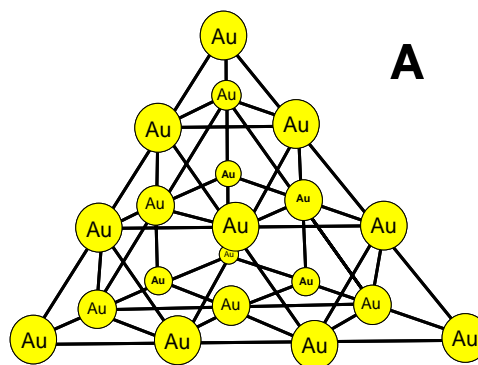


Fig. 7. Structure of compact magic gold cluster Au_{20} (A, adapted from⁴⁰) and hollow golden cage Au_{16} (B, adapted from⁴¹)

properties. In the case of hollow gold cages, clusters with 16–18 atoms have been experimentally observed and larger clusters, such as icosahedral Au_{72} were theoretically predicted⁴⁴.

5. Conclusions

Common MALDI TOF MS instrumentation can be used to analyze gold species ionized in plasma by laser from GNP synthesized by chemical procedures.

Gold is forming in plasma positively and negatively single charged clusters Au_m^+ or Au_m^- which are also reacting with the other ions and mixed Au_mNa_n , AuCa , AuK , etc. clusters were also observed. The formation of gold hydrides, such as AuH , Au_3H , and hydroxide AuOH and peroxides Au-HOOH , were also observed here for the first time.

When GNP were used as a matrix for ionization of nanodiamonds, carbon-gold mixed clusters which includes C_{18}Au , CAu_2Na and $\text{C}_2\text{Au}_2\text{Na}$, and others were detected.

Grant Agency of the Czech Republic, project no. 525/06/0663 and 202/07/1669. Academy of Sciences of the Czech Republic, project KAN 101630651. E.M.P-M and J.H. acknowledge the partial support from University of La Laguna, La Laguna, Tenerife, Spain. JRF acknowledges Ministry of Science and from La Laguna University grant E-38-2006-0289614.

REFERENCES

- Zharov P. V., Kim J. W., Curiel D. T., Everts M.: *Nanomed. Nanotechnol. Biol. Med.* 1, 326 (2005).
- Panyala N. R., Peña-Méndez E. M., Havel J.: *J. Appl. Biomed.* 6, 47 (2008).
- Sukdeb P., Yu K. T., Joon M. S.: *Appl. Environ. Microbiol.* 73, 1712 (2007).
- Chen Y., Gu X., Nie C. G., Jiang Z. Y., Xie Z. X., Lin C. J.: *Chem. Commun. (Camb)* 33, 4181 (2005).
- Wang Q., Shantz D. F.: *J. Solid State Chem.* 181, 1659 (2008).
- Guodong L., Yuehe L.: *Talanta* 74, 308 (2007).
- Larsen K., Thygesen M. B., Guillaumie F., Willats W. G. T., Jensen K. J.: *Carbohydr. Res.* 341, 1209 (2006).
- Brigger I., Dubernet C., Couvreur P.: *Adv. Drug Deliv.*

- Rev. 54, 631 (2002).
- Cuenca A. G., Jiang H., Hochwald S. N., Delano M., Cance W. G., Grobmyer S. R.: *Cancer* 107, 459 (2006).
 - Jain K. K.: *Technol. Cancer Res. Treat.* 4, 407 (2005).
 - Zhang Z., Yang X., Zhang Y., Zeng B., Wang S., Zhu T., Roden R. B., Chen Y., Yang R.: *Clin. Cancer Res.* 12, 4933 (2006).
 - Bhattacharya R., Senbanerjee S., Lin Z., Mir S., Hamik A., Wang P., Mukherjee P., Mukhopadhyay D., Jain M. K.: *J. Biol. Chem.* 280, 28848 (2005).
 - Mukherjee P., Bhattacharya R., Wang P., Wang L., Basu S., Nagy J. A., Atala A., Mukhopadhyay D., Soker S.: *Clin. Cancer Res.* 11, 3530 (2005).
 - Paciotti G. F., Myer L., Weinreich D., Goia D., Pavel N., McLaughlin R. E., Tamarkin L.: *Drug Deliv.* 11, 169 (2004).
 - Ganon C. J., Patra C. R., Bhattacharya R., Mukherjee P., Curley S. A.: *J. Nanobiotechnol.* 6, 2 (2008).
 - Huang S. H.: *Clin. Chim. Acta* 373, 139 (2006).
 - Mukherjee P., Bhattacharya R., Bone N., Lee Y. K., Patra C. R., Wang S., Lu L., Charla S., Banerjee P. C., Yaszemski M. J., Kay N. E., Mukhopadhyay D.: *J. Nanobiotechnol.* 5, 4 (2007).
 - Niidome T., Yamagata M., Okamoto Y., Akiyama Y., Takahashi H., Kawano T., Katayama Y., Niidome Y.: *J. Controlled Release* 114, 343 (2006).
 - Hirsch L. R., Halas N. J., West J. L.: *Methods Mol. Biol.* 303, 101 (2005).
 - Lee J. S., Han M. S., Mirkin C. A.: *Angew. Chem.* 46, 4093 (2007).
 - He H., Xie C., Ren J.: *Anal. Chem.* 80, 5951 (2008).
 - Triulzi R. C., Micic M., Orbulescu J., Giordani S., Mueller B., Leblanc R. M.: *Analyst* 133, 667 (2008).
 - Choi Y., Thomas T., Kotlyar A., Islam M. T., Baker J. R.: *Chem. Biol.* 12, 35 (2005).
 - Choi Y., Mecke A., Orr B. G., Holl M. M. B., Baker J. R.: *Nano Lett.* 4, 391 (2004).
 - Kang H., DeLong R., Fisher M. H., Juliano R. L.: *Pharm. Res.* 22, 2099 (2005).
 - Tsvetkov D. E., Cheshev P. E., Tuzikov A. B., Chinarev A. A., Pazyynina G. V., Sablina M. A., Gambaryan A. S., Bovin N. V., Rieben R., Shashkov A. S., Nifant'ev N. E.: *Russ. J. Bioorg. Chem.* 28, 470 (2002).
 - Wang X., Inapagolla R., Kannan S., Lieh-Lai M., Kannan R. M.: *Bioconjugate Chem.* 18, 791 (2007).
 - Lee S. C., Parthasarathy R., Botwin K., Kunneman D., Rowold E., Lange G., Klover J., Abegg A., Zobel J., Beck T., Millar T., Hood W., Monahan J., Mckearn J. P., Jansson R., Voliva C. F.: *Biomed. Microdev.* 6, 191 (2004).
 - Dass A., Stevenson A., Dubay G. R., Tracyst J. B., Murray R. W.: *J. Am. Chem. Soc.* 130, 5940 (2008).
 - Keki S., Nagy L., Deak G., Zsuga M.: *J. Am. Soc. Mass Spectrom.* 15, 1455 (2004).
 - Tracy J. B., Crowe M. C., Parker J. F., Hampe O., Fields-Zinna C. A., Dass A., Murray R. W.: *J. Am. Chem. Soc.* 129, 16209 (2007).
 - Spencer M. T., Furutani H., Oldenburg S. J., Darlington T. K., K. A.: *J. Phys. Chem., C* 112, 4083 (2008).
 - Keki S., Nagy L., Deak G., Zsuga M.: *J. Am. Soc. Mass Spectrom.* 15, 1455 (2004).
 - Subramaniam C., Tom R. T., Pradeep T.: *J. Nanopart. Res.* 7, 209 (2005).
 - Maya L., Chen C. H., Stevenson K. A., Kenik E. A., Allman S. L., Thundat T. G.: *J. Nanopart. Res.* 4, 417 (2002).
 - Turkevich J., Stevenson P. C., Hillier J.: *Discuss. Faraday Soc.* 11, 55 (1951).
 - Kumar S., Gandhi K. S., Kumar R.: *Ind. Eng. Chem. Res.* 46, 3128 (2007).
 - Wang W., Chen Q., Jiang C., Yang D., Liu X., Xu S.: *Colloids Surf.* 301, 73 (2006).
 - Ben Hamed A., Taborský P., Peña-Méndez E. M., Havel J.: *Talanta* 72, 780 (2007).
 - Kryachko E. S., Remacle F.: *Int. J. Quant. Chem.* 107, 2922 (2007).
 - Bulusu S., Li X., Wang L. S., Zeng X. C.: *PNAS* 103, 8326 (2006).
 - Gilb S., Weis P., Furche F., Ahlrichs R., Kappes M. M.: *J. Chem. Phys.* 116, 4094 (2006).
 - Lechtken A., Detlef S., Stairs J. R., Blom M. N., Furche F., Morgner N., Kostko O., Issendorff B. V., Kappes M. M.: *Angew. Chem.* 46, 2944 (2007).
 - Karttunen A. J., Linnolahti M., Pakkanen T. A., Pyykko P.: *Chem. Commun. (Camb)* 4, 465 (2008).

DOUBLE PULSE LASER ABLATION AND PLASMA: TIME RESOLVED SPECTRAL MEASUREMENTS

KAREL NOVOTNÝ^{a*}, FILIP LUTZKÝ^b,
MICHAELA GALIOVÁ^a, JOZEF KAISER^c,
RADOMÍR MALINA^c, VIKTOR KANICKÝ^a,
and VÍTĚZSLAV OTRUBA^a

^a Dep. of Chemistry, Faculty of Science, Masaryk University, Kotlářská 2, 61137 Brno, Czech Republic, ^b Gymnasium of T. G. Masaryk, Dukelské náměstí 7, 693 31 Hustopeče, ^c Institute of Physical Engineering, Faculty of Mechanical Engineering, Brno University of Technology, Technická 2896/2, 616 69 Brno, Czech Republic
codl@sci.muni.cz

Keywords: laser induced breakdown spectroscopy, LIBS, double pulse LIBS, plasma characterization, time resolved measurement, ICCD, photomultiplier

Introduction

Due to the relative experimental simplicity and immediate analyte response, laser-induced breakdown spectroscopy (LIBS) has gained popularity among researchers interested in real-time or in situ material detection and analysis for a wide range of sample forms. The elemental concentrations in the material are determined by spectrally analyzing the optical emission from the laser-produced plasma¹. Although well suited for rapid in situ analysis, the LIBS technique possesses a lower sensitivity and precision than other methods of elemental analysis². For several applications of LIBS, it is important to enhance the detection of atomic spectral lines by increasing the analyte signal while minimizing the background continuous emission (i.e. by improving the sensitivity and detection limits).

It was recently demonstrated that double pulse LIBS represents a very effective approach for improvement of analytical capabilities of the LIBS technique^{3–8}. The use of double pulse LIBS can provide enhanced emission intensities, lower detection limits and longer sustained emission^{9,10}. Two main beam geometries were suggested for realization of double pulse LIBS: orthogonal and collinear. For the orthogonal re-heating mode, the first pulse irradiates the sample and the second re-heating pulse propagates parallel to the target surface. In the collinear mode the second laser pulse is incident both on the surface and the plasma formed by the first pulse. A review of recent results of the studies of double pulse plasma and ablation for laser induced breakdown spectroscopy applications was reported by Babushok *et al* in 2006 (ref.¹¹).

In the recent years, there has been increasing interest in the characterization of plasmas formed in laser ablation, a necessity for understanding the physical processes involved

and improving the results of the diverse applications^{12–16}.

Most of the studies on double-pulse LIBS have been performed using an intensified CCD (ICCD) detection. Using ICCD, spectral information over wide range can be recorded on each laser pulse^{17–19}. Besides ICCD, also photomultipliers (PMT) can be used to monitor single emission lines^{20–22}. The output of the PMT is a current proportional to the intensity of the incident light. PMT's are not integrating devices as they provide a signal simultaneous in time with the incident light intensity. The combination of ICCD and PMT can be useful to determine both, the spectral and time resolved plasma emission.

In this study, we present orthogonal re-heating double pulse experimental system equipped with both ICCD and PMT detection and preliminary measurements of temperatures of plasmas generated on an iron sample.

Experimental setup

The experimental double pulse system was designed to reach high sensitivity maintaining high spatial resolution and possibilities of line or raster scanning. This paper presents for the first time double pulse LIBS system utilizing modified commercially available laser ablation system (New Wave, UP 266 MACRO). This UV Nd-YAG laser ablation system was specifically designed for ICP-OES and ICP-MS solid sampling analysis. For these purposes, the laser ablation device incorporates a 30 µm to 750 µm expandable, aperture imaged beam delivery system. The control software offers a wide variety of ablation methods such as spot ablation for depth profiling, line scanning for lateral analysis and raster scanning for bulk or surface analysis. The laser ablation software program controls all laser parameters, sample viewing and stage positioning. It also offers the possibility of external triggering.

For double pulse LIBS experiments the ablation chamber used for connection UP 266 MACRO to ICP spectrometry, was replaced with a sample holder, which was equipped with inclination alignment (Fig. 1).



Fig. 1. UP 266 MACRO Laser Ablation System modified for double-pulse LIBS measurements. The ablation chamber was replaced with sample holder; the second laser pulse was focused by side glass lens and the laser induced plasma emission was collected by fiber placed in the front part

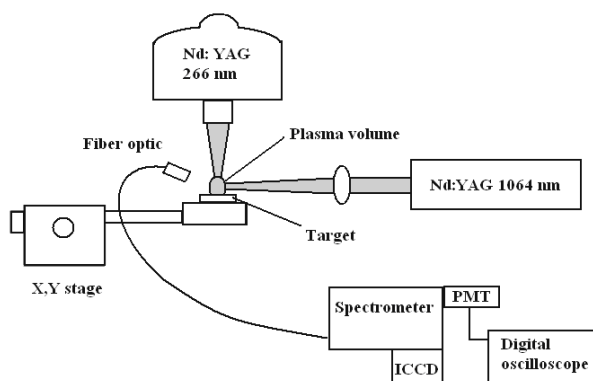


Fig. 2. Schematic drawing of the experimental set-up

The radiation of the second Nd:YAG laser (Quantel, Brilliant) with fundamental wavelength 1064 nm was focused parallel to the sample surface by 80 mm focal length glass lens. The two lasers were aligned such that their intersecting beam path resulted in a coincident spark just 0.5 mm above the sample surface. A schematic of the optical configuration is shown in Fig. 2.

Both lasers were externally triggered using a digital delay generator (Stanford Research Systems, DG 535) which was initialized by starting pulses from UP 266 MACRO laser module. Hence the starting of measurement, sample position and parameters of first laser pulse was controlled by UP 266 MACRO software. The ablation repetition rate had to be reduced to 1 Hz in order to transfer all data from the ICCD camera for each investigated spot. This was achieved by fixing the repetition rate of both laser's flashlamp to 10 Hz, and triggering the Q-switch for every tenths pulse by laboratory made pulse counter/divider. The laser-induced plasma radiation was transported by a fiber optic system onto the entrance slit of a monochromator (Jobin Yvon TRIAX 320). ICCD detector (Jobin Yvon Horiba) or a photomultiplier (R928 Hamamatsu) gated by a laboratory-built control unit were employed as detectors. For the gate-time delay monitoring and time-resolved signal recording, a digital storage oscilloscope Tektronix TDS 1012 was used. The double pulse LIBS system control block scheme with ICCD and PMT detection is shown in Fig. 3.

Results and discussion

The oldest and simplest method to determine the plasma temperature by emission spectroscopy is based on the measurement of the relative intensities of two lines from the same element and ionization stage. If E is the energy of the upper level and defining for each line $y \equiv \varepsilon\lambda/(gA)$, where ε is the line emissivity ($\text{Wm}^{-3} \text{sr}^{-1}$) integrated over the line profile, λ is the transition wavelength, g is the statistical weight of the upper level and A is the transition probability, the temperature results from the Boltzman equation: $\ln(y_1/y_2) = -1/kT(E_2 - E_1)$.

Control block diagram

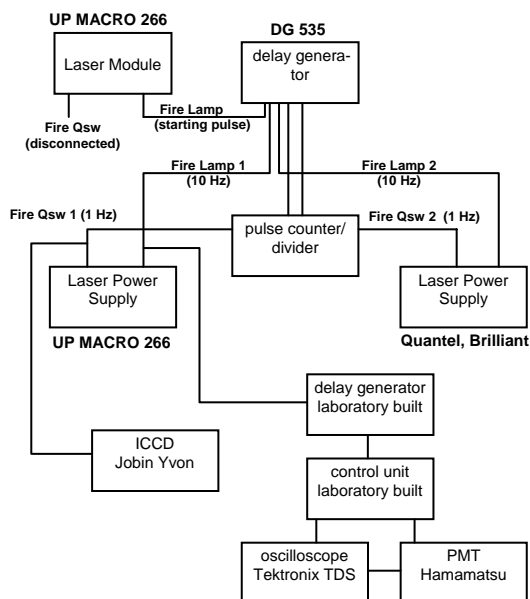


Fig. 3. The double pulse LIBS system control block scheme with ICCD and PMT detection

This temperature has sometimes been called excitation temperature although, in conditions of local thermodynamic equilibrium (LTE) assumed for LIBS analysis, it should be equal to the electron kinetic temperature. The main disadvantage of the Boltzmann two-line method is that it may lead to considerable uncertainties of the determined temperatures. The accuracy of temperature determination may be improved by measuring a number of different lines. Moreover, to increase the accuracy, the range of upper level energies of the so-called Boltzmann plot should be as large as possible¹⁶.

In this study the temperatures have been obtained from the intensity of eight iron atomic lines which are shown in Tab. I.

Table I
Series of iron atomic emission lines selected for temperature determination

Wavelength [nm]	Upper level energy [J]
371.993	$5.34 \cdot 10^{-19}$
373.486	$6.69 \cdot 10^{-19}$
373.713	$5.40 \cdot 10^{-19}$
374.826	$5.47 \cdot 10^{-19}$
374.948	$6.76 \cdot 10^{-19}$
375.823	$6.82 \cdot 10^{-19}$
376.379	$6.86 \cdot 10^{-19}$
376.719	$6.89 \cdot 10^{-19}$

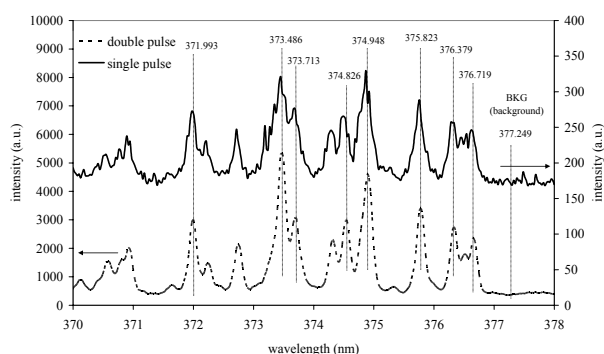


Fig. 4. Comparison of the single and double-pulse signals in spectral region of selected iron lines and neighboring background

The selected spectral lines fulfill several criteria, important to obtain reasonable results. They do not have any spectral interferences and their atomic parameters are known. Moreover, the selected spectral lines are grouped in close wavelengths in order to allow using single ICCD spectral detection window. All the measurements in single or double pulse mode were performed using high purity Fe target (high purity iron S11 – 2theta Czech Republic). The energy of first laser pulse was set to 10 mJ corresponding to irradiance on the target of 25 GW cm^{-1} with a spot size of $100 \mu\text{m}$ in diameter. The second laser pulse had energy of 100 mJ, with interpulse delay of 500 ns. The ICCD delay time between the first laser pulse and detection was of $1.5 \mu\text{s}$ and the acquisition time was $5 \mu\text{s}$. These values were found in preliminary measurements as optimal for the investigated sample. The spectral data acquired for single and double-pulse are compared in Fig. 4.

From Fig. 4 is evident that the double pulse signal is more than 10 times enhanced in comparison to the signal obtained in single pulse mode. The wavelengths of iron emission lines (Tab. I) and the background position that were sub-

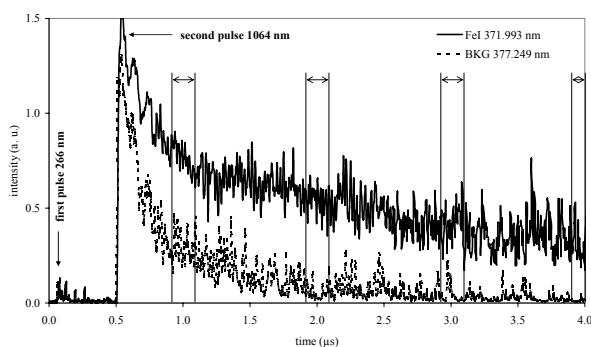


Fig. 5. Comparison of temporal emission signal of double pulse laser induced microplasma on iron atomic emission line at 371.993 nm and background at 377.249 nm. The marked time intervals (200 ns width) were averaged and used for calculation of plasma temperature

Table II

Temperatures of plasmas calculated from time dependent emission signal of eight iron atomic lines measured by gated PMT

Delay time [μs]	Temperature [K]
0.9–1.1	8920
1.9–2.1	8690
2.9–3.1	7580
3.9–4.1	7310

sequently used for time resolved measurement by PMT are marked.

Fig. 5 show the time resolved intensity signal of the FeI 371.993 nm line and corresponding time dependent signal of background (at 377.249 nm) measured by gated PMT. The noisy signal is caused by the fact, that only single double-shot signal was recorded.

For the rest of above indicated iron atomic lines (Tab. I) the time dependent emission signal was measured in the same way as it is presented on Fig. 5. The Boltzmann plots were constructed after the background subtraction from the averaged intensity signals in marked regions (Fig. 5). The plasma temperatures derived from these plots for delay time intervals (1.0 ± 0.1 , 2 ± 0.1 , 3 ± 0.1 and $4 \pm 0.1 \mu\text{s}$) after the first laser pulse are summarized in Tab 2. These values are comparable with values formerly obtained at similar experimental conditions (see for example ref¹⁶ and reference therein).

Conclusion

In this work, we present a double pulse LIBS system utilizing modified commercially available Laser Ablation System (New Wave, UP 266 MACRO), second Nd:YAG laser (Quantel, Brilliant) and a unique combination of ICCD and PMT detection. It was shown that combination of these two detectors in one experimental setup can be useful to determine both, the spectral and time resolved plasma emission. Preliminary measurements with this setup were focused on determination of the plasma temperature in different time intervals after the first laser pulse reaches the target. The plasma temperatures calculated from time dependent signals of iron atomic emission lines series demonstrate the advantages of this system for such type of measurements. The temporal emission signal measured by gated PMT can be useful not only for direct plasma diagnostic, but also for selecting the best ablation conditions including the optimum delay time between the two laser pulses and the delay and duration of ICCD acquisition. Moreover, in case of complicated samples the gated PMT can help to discover the matrix effect or spectral interferences. The aim of this reliability study was to proof the potentialities of the developed instrumentation. On the frame of the ongoing work more detailed study of the influence of double pulse conditions on the laser induced plasma properties and application of this technique for different samples are planned.

Authors acknowledge support from the Ministry of Education, Czech Republic (grant MSM0021622411, grant MSM0021630508 and grant ME08002).

REFERENCES

1. Cremers D. A., Radziemski L. J., in *Handbook of Laser-Induced Breakdown Spectroscopy*. John Wiley & Sons, West Sussex 2006.
2. Radziemski L. J., Cremers D. A., in: *Laser-Induced Plasmas and Applications*. Marcel Dekker, New York 1989.
3. Sattman R., Sturm V., Noll R.: *J. Phys. D.: Appl. Phys.* 28, 2181 (1995).
4. St-Onge L., Sabsabi M., Cielo P.: *Spectrochim. Acta, Part B* 53, 407 (1998).
5. Stratis D. N., Eland K. L., Angel S. M.: *Appl. Spectrosc.* 54(9), 1270 (2000).
6. Coloa F., Lazic V., Fantoni R., Pershin S.: *Spectrochim. Acta, Part B* 57, 1167 (2002).
7. Corsi M., Cristoforetti G., Giuffrida M., Hildago M., Legnaioli S., Palleschi V., Salvetti A., Tognoni E., Vallebona C.: *Spectrochim. Acta, Part B* 59, 723 (2004).
8. Hohreiter V., Hahn D. W.: *Spectrochim. Acta, Part B* 60, 968 (2005).
9. Scaffidi J., Angel S. M., Cremers D. A.: *Anal. Chem.* 78, 24 (2006).
10. Gautier C., Fichet P., Menut D., Lacour J. L., L'Hermite D., Dubessy J.: *Spectrochim. Acta, Part B* 60, 265 (2005).
11. Babushok V. I., DeLucia Jr. F. C., Gottfried J. L., Munson C. A., Miziolek A. W.: *Spectrochim. Acta, Part B* 61, 999 (2006).
12. Aguilera J. A., Aragón C.: *Appl. Phys., A* 69, S475 (1999).
13. Aguilera J. A., Aragón C.: *Appl. Surf. Sci.* 197–198, 273 (2002).
14. Aguilera J. A., Aragón C.: *Spectrochim. Acta, Part B* 62, 378 (2007).
15. Aydin U., Roth P., Gehlen C. D., Noll R.: *Spectrochim. Acta, Part B* doi: 10.1016/j.sab.2008.08.003, (2008).
16. Aragón C., Aguilera J. A.: *Spectrochim. Acta, Part B* 63, 893 (2008).
17. Bauer H. E., Leis F., Niemax K.: *Spectrochim. Acta, Part B* 53, 1815 (1998).
18. Taschuk M. T., Godwal Y., Tsui Y. Y., Fedosejevs R., Tripathi M., Kearton B.: *Spectrochim. Acta, Part B* 63, 525 (2008).
19. Goode S. R., Morgan S. L., Hoskins R., Oxsher A.: *J. Anal. At. Spectrom.* 15, 1133 (2000).
20. Bette H., Noll R.: *J. Phys. D.: Appl. Phys.* 37, 1281 (2004).
21. Novotný K., Vaculovič T., Galiová M., Otruba V., Kanický V., Kaiser J., Liška M., Samek O., Malina R., Páleníková K.: *Appl. Surf. Sci.* 253, 3834 (2007).
22. Novotný K., Staňková A., Hakkanen H., Korppi-Tommola J., Otruba V., Kanický V.: *Spectrochim. Acta, Part B* 62, 1567 (2007).

PLAS-MA PROPERTIES OF TRANSVERSE BLOWING ARC UNDER ATMOSPHERIC PRESSURE

IRYNA PRYSIAZHNEVYCH*, VALERIY
CHERNYAK, SERGEY OLZEWSKI,
and VITALIY YUKHYMENKO

National Taras Shevchenko University, Prospect Glushkova
2/5, Kyiv 03022, Ukraine
priv@ukr.net

Introduction

It is well known that for solving of different applied tasks plasmachemistry needs the sources of nonequilibrium atmospheric pressure plasmas with controllable level of non-isothermality. The most interesting from this point of view are dynamic plasma systems with transversal gas flows of atmospheric pressure: gliding arc $GA^{1,2}$, gliding arc in tornado $GAT^{3,4}$, transverse DC glow discharge⁵, arc discharge in the transversal blowing gas flow (transverse arc TA)^{6–8}. A transversal gas ventilation of the discharge increases efficiency of heat- and mass- exchange between plasma and environment. It is possible to influence on the plasma properties due to the choosing gas flow rate and discharge parameters (current, voltage). The results of researching of plasma properties of the transverse arc in airflow at atmospheric pressure are presented in this work.

Experimental setup

Transverse arc TA differs from the non-stationary GA of Czernichowski type^{1,2} by the fixed arc length. It has also a convective cooling of the plasma column by the airflow but without conductive heat losses at walls since it is a free arc jet. The scheme of the TA discharge in gas flow is shown on Fig. 1.

The atmospheric airflow was directed from the nozzle across two horizontal opposite electrodes and formed a bright crescent-shaped electric arc. The rod copper electrodes with

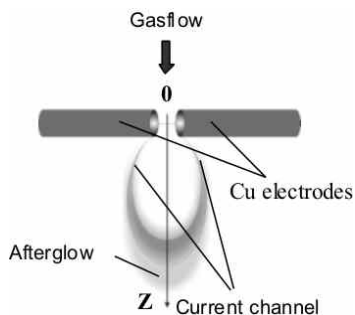


Fig. 1. Experimental sketch of the transverse arc

diameter $d = 6$ mm and nominal gap between them $\delta \approx 1.5$ mm were used. Axially symmetrical nozzle, with inner diameter $\varnothing = 1$ mm made from stainless steel was maintained vertically perpendicular to the electrode axis at the length $L = 20$ mm and centered strictly between the electrodes. The arc discharge was powered by the DC source at the ballast resistance $R = 2$ k Ω in the circuit. To regulate the airflow rate G a standard dry air system supplied with the flow meters was used. There was enough high gas-dynamic pressure in the flow to blow out the electric arc downstream. The gas flow rates $G = 0$ –110 cm³s⁻¹ and discharge current I_d (330–660 mA) were kept constant.

Current-voltage characteristics of TA discharge in airflow are shown on Fig. 2.

Diagnostics of plasma parameters was made by optical emission spectroscopy (OES). Computer operated CCD-based spectrometer SL40-2-3648USB with spectral resolution ~ 0.73 nm was used for spectra registration in the range of 210–1100 nm. Temperatures, which correspond to the population distribution of the excited electronic states of atoms (electronic temperature T_e^*), vibration and rotational levels of molecules (vibration T_v^* and rotation T_r^* temperatures) in investigated plasmas, were determined.

Methodology

Determination of mole fractions of the radiating components of nonequilibrium plasma at atmospheric pressure in the case of weakly known composition of plasmaforming gas is very interesting and actual problem. Method of evaluation of relative concentration of neutral and ionic components in generated plasma by using SPECAIR⁹ was suggested in this work.

SPECAIR code allows modeling the absolute intensity of spectral radiation emitted by gases and plasmas of various compositions (N, O, C, NO, N₂, N₂⁺, OH, NH, C₂, CN, CO) in the wide spectral range for different pressures. Traditionally

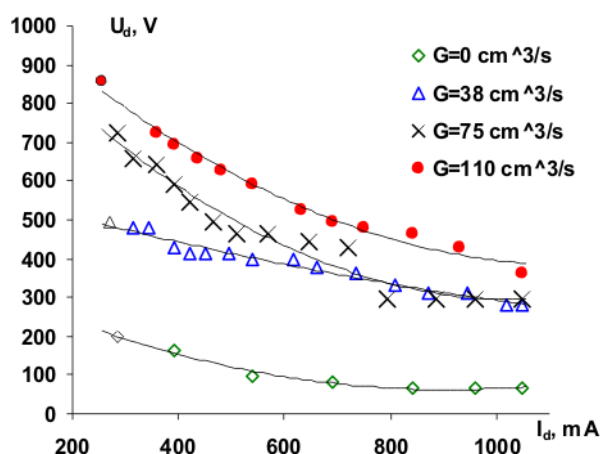


Fig. 2. Volt-ampere characteristics of the TA discharge for different rates of airflow G

SPECAIR uses database of an initial LTE species distribution in air at various temperatures (electronic, vibrational, rotational and translation) in the range $T = 1000\text{--}14\,000\text{ K}$.

So far as using known methods of working with SPECAIR for determining relative concentrations of radiating species¹⁰ is not possible in the case of weakly known compound of plasmaforming gas, we suggested to use the following procedure.

At the first stage the identification of emission spectra was made and T_v^* and T_r^* temperatures were determined by fitting experimental spectrum of the 2nd positive system of N_2 with results of SPECAIR simulation¹⁰. It is possible to determine electronic temperature T_e^* from Boltzmann plot by using relative intensities of spectral atomic lines (emission of blowing gas or electrodes material atoms)⁷. Besides T_e^* can be evaluated from the best fit of the relative intensities of N_2 (C-B) and NO (A-X) in experimental spectrum with simulated one (after having T_v^* and T_r^* already determined) in the case of LTE for discharges with low rates of blowing gasflow or without any blowing¹¹.

At the next step the intensity (signal) of each radiating species $I_{exp}(A_i)$ was determined from experimental spectrum and corresponding to them wavelengths λ_i were fixed. It is better to carry out this procedure of signal determination in the range free from overlapping spectral bands and lines. After that we simulated emission spectrum of each radiating compound separately by using SPECAIR at previously determined T_e^* , T_v^* , T_r^* temperatures. The absolute intensities of calculated spectrum $I_{cal}(A_i)$ at wavelength (where the corresponding experimental signals $I_{exp}(A_i)$ were estimated) were determined.

Then the concentration ratio of two radiating species A and B can be evaluated by following formula:

$$\frac{[A_1]}{[A_2]} = \frac{I_{exp}(A_1) \cdot I_{cal}(A_2)}{I_{exp}(A_2) \cdot I_{cal}(A_1)} \quad (1)$$

That makes possible to determine relative concentration of each component in the investigated plasma:

$$[A_1]^* = \frac{[A_1]}{\sum_i [A_i]} \quad (2)$$

Results

Emission of N_2 2nd positive system ($C^3\Pi_u - B^3\Pi_g$), 1st negative system of N_2^+ ($B^2\Sigma_u^+ - X^2\Sigma_g^+$), of NH ($A^3\Pi^+ - X^3\Sigma^-$), NO g system ($A^2\Sigma^+ - X^2\Pi$), weak OH bands ($A^2\Sigma^+ - X^2\Pi$), O lines ($\lambda = 777.2; 844.6; 926.6\text{ nm}$), Cu lines (electrode's material) ($\lambda = 324.75; 327.4; 465.1; 510.5; 515.3; 521.8; 578.2\text{ nm}$) was observed in plasma of the transverse arc in air. T_e^* was determined from Boltzmann plots by using intensities of oxygen spectral lines O ($\lambda = 777.2; 844.6; 926.6\text{ nm}$) and copper (electrode's material) lines Cu ($\lambda = 465.1; 510.5; 515.3; 521.8; 578.2\text{ nm}$) Fig. 3.

To verify Boltzmann population distribution of the ex-

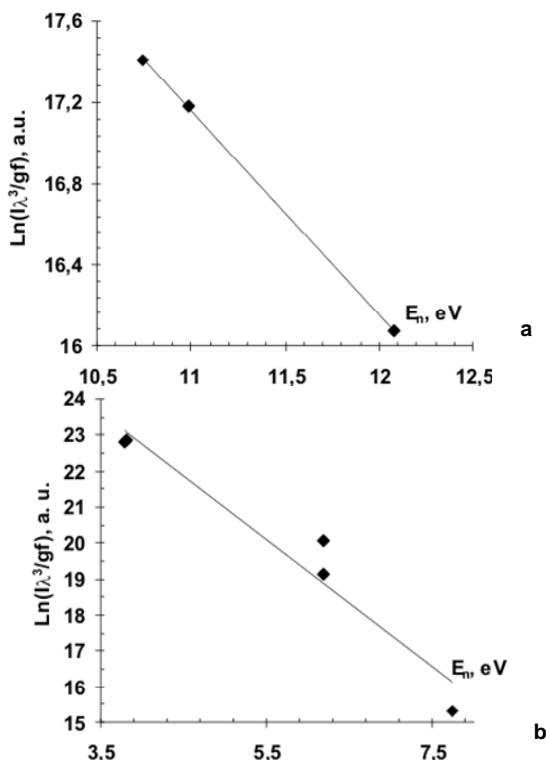


Fig. 3. Characters of population distributions of the excited electronic states of O (a) and Cu (b) atoms in plasma of TA in air (airflow rate $G = 75\text{ cm}^3\text{ s}^{-1}$, discharge current $I_d = 480\text{ mA}$) at the distance from electrodes $z = 7.2\text{ mm}$

cited vibrational levels of molecules in generated transverse arc plasma the relative intensities of nitrogen molecular bands of the 2nd positive system ($\lambda = 337.1; 371; 375.5; 380.5; 399.8\text{ nm}$) were measured. It was shown that population distribution character of the excited vibration levels of N_2 molecule in the investigated plasma is close to Boltzmann Fig. 4. Thus T_v^* can

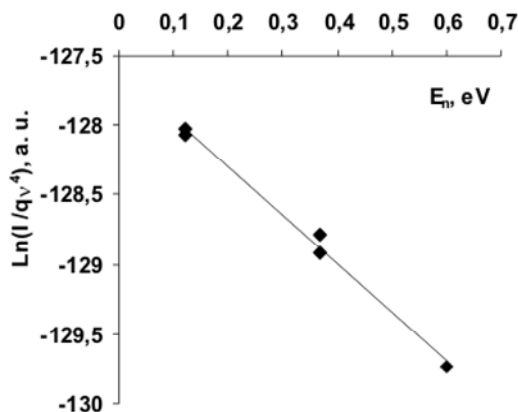


Figure 4. Character of the population distribution of the excited vibrational levels of the N_2 molecule in TA plasma ($G=75\text{ cm}^3/\text{s}$, $I_d=480\text{ mA}$, $z=1.6\text{ mm}$). $T_v^*=3400\text{ K}$ was obtained from this Boltzmann plot.

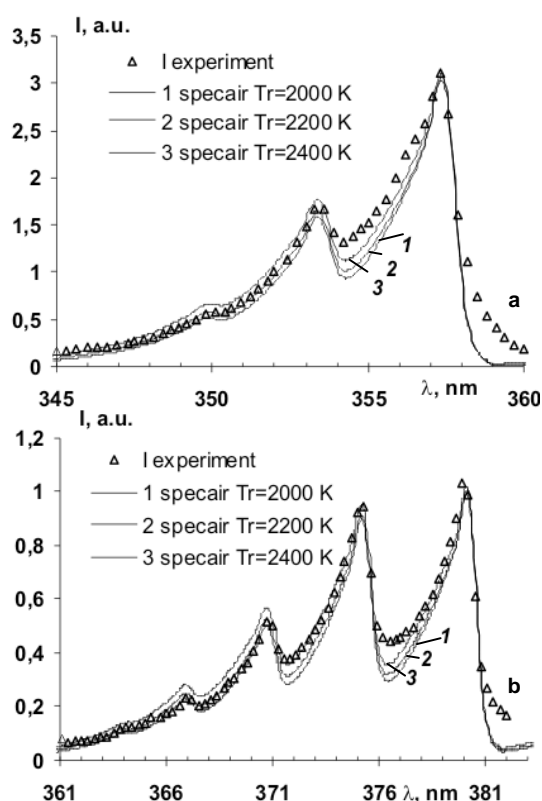


Figure 5. Fitting experimental spectral bands of N_2 (C-B) ($z=1.6$ mm, $G=75$ cm³/s, $I_s=480$ mA) and results of modelling by SPECAIR for different T_r . The best-obtained accuracy of this technique is ± 200 for T_r , and ± 500 for T_v , temperature correspondingly.

be determined from Boltzmann plot⁷ or by using SPECAIR program, which calculations are valid in LTE case.

In this work $T_v \approx 4000$ – 4600 K and $T_r \approx 2000$ – 2800 K were estimated from 2nd positive system of nitrogen by fitting the experimental spectra with the simulated ones Fig. 5. For determining rotational temperature by the 2nd positive system of N_2 it is better to use spectral bands in the region 360–385 nm since it is free from overlapping with other lines and bands. As we can see from Fig. 5a, a noticeable discrepancy between experimental spectrum and calculated one in the region 354–360 can be explained by overlapping with some of the bands of the 1st negative system of N_2^+ ($\lambda = 354.8, 356.2, 358$ nm).

Fitting of experimental spectrum of the transverse arc plasma with calculated one is shown on Fig. 6.

From Fig. 6 can be seen that a good fit was obtained. Discrepancy between spectra in the region of 325 nm can be dealt with presence of *Cu* lines ($\lambda = 324.75$ and 327.4 nm) and not identified bands (at $\lambda = 282.5$ and $\lambda = 296$ nm), which were not taken into account by SPECAIR calculations.

Temperature distribution in plasma of *TA* along gas flow z is shown on Fig. 7.

Since the basic ions in low-current arc are ions of electrode material, an additional mechanism of populating the excited electronic levels in copper atoms, besides the excitation by electrons, can appear owing to electron-ion recombination; this mechanism is inactive for the atoms of a blowing

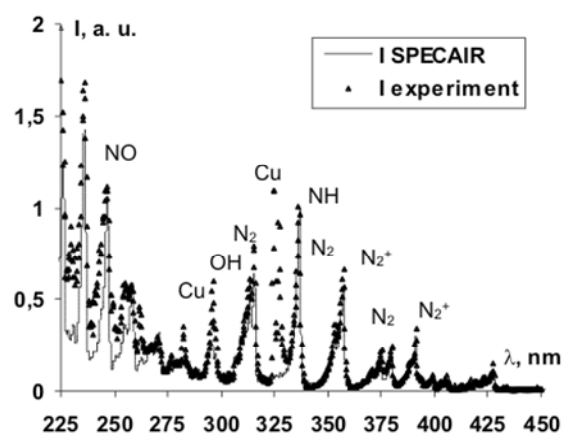


Figure 6. Emission spectrum of *TA* air plasma at atmospheric pressure ($G=75$ cm³/s $I_s=480$ mA at the distance $z=1.6$ mm from electrode axis) and spectrum simulated by SPECAIR at $T_e^*=4600$ K, $T_v^*=4200$ K, $T_r^*=2200$ K.

Table I

Relative concentrations of radiating species in generated plasma of the transverse arc in air flow

z , mm	$[NH]/[N_2] \times 10^{-8}$	$[OH]/[N_2] \times 10^{-7}$	$[N_2^+]/[N_2] \times 10^{-9}$	$[NO]/[N_2] \times 10^{-4}$	$[NO]/[N_2] \times 10^{-2}$ Database SPECAIR
1,6	6,3	4,9	6,8	1,2	1,7
3,2	4,4	5,8	3,3	1,0	2,5
4,8	6,3	13,0	2,8	1,7	3,5
6,4	7,5	10,9	1,1	1,3	4,6

gas. In our opinion it can explain the revealed difference between the values $T_e^*(O) \approx 4200$ – 4600 K and $T_e^*(Cu) \approx 6800$ – 8200 K.

At atmospheric pressure, rotational temperature equilibrates with the gas temperature ($T_g \approx T_r$) owing to fast collisional relaxation. The increasing character of rotational tem-

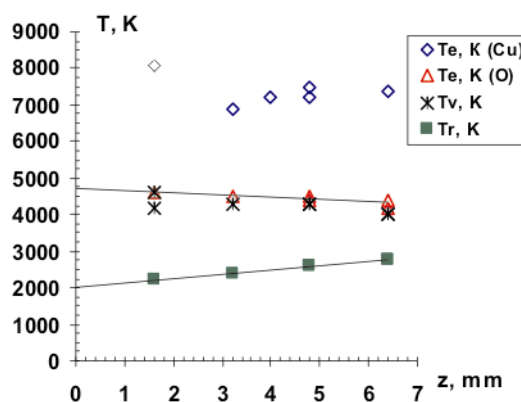


Figure 7. Temperature distributions along air flow z ($z=0$ – point at electrode axis) in plasma of *TA* at atmospheric pressure ($G=75$ cm³/s, $I_s=480$ mA).

Table II
Parameters of non-equilibrium atmospheric pressure plasma sources

Type	Electric power, W	Gas flow rate $G, \text{cm}^3 \text{s}^{-1}$	T_{es}^*, eV	T_{vs}^*, eV	T_{rs}^*, eV
$GA^{1,2}$	200–1000	$(2-50) \times 10^3$	$T^*: 0.52$ $**NT: 0.86$	$T^*: 0.27-0.34$ $**NT: 0.17-0.26$	$T^*: 0.2-0.34$ $**NT: 0.07-0.18$
GAT^3	90–300	$(0.5-2.5) \times 10^3$	> 0.9		0.17–0.34
$DGCLW^8$	260–300	$0.11 \cdot 10^3$	(Cu) 0.6 (O) 0.35 (H) 0.35	(N_2) 0.3–0.35	(OH) 0.35–0.4
$TA^{7,8}$	220–330	$(0.04-0.2) \times 10^3$	<i>in air:</i> (Cu) 0.6 (O) 0.35 (H) 0.35	(N_2) 0.35	(N_2) 0.1–0.2

*T – thermal regime of GA, **NT – non-thermal regime of GA^2

perature distribution along gasflow may testify that the gas heating occurs owing to the convective heat exchange between gas particles and the current channel at the periphery of the transverse arc. Plasma at the periphery of the discharge tends to isothermality.

Relative concentrations of radiating plasma components of the investigated TA in airflow ($G = 75 \text{ cm}^3 \text{ s}^{-1}$ and $I_s = 480 \text{ mA}$) were calculated by using suggested method of working with SPECAIR and their values are presented in the table I.

Calculated relative concentrations should be taken as a very rough estimate, just indicating the order of magnitude.

Distribution of the relative mole fractions of radiating species in the investigated plasma along gasflow is represented on Fig. 8.

Decreasing of $[N_2^+]$ concentration with increasing of distance from electrodes is in good correlation with excitation temperature distributions. It is clear that ionization processes

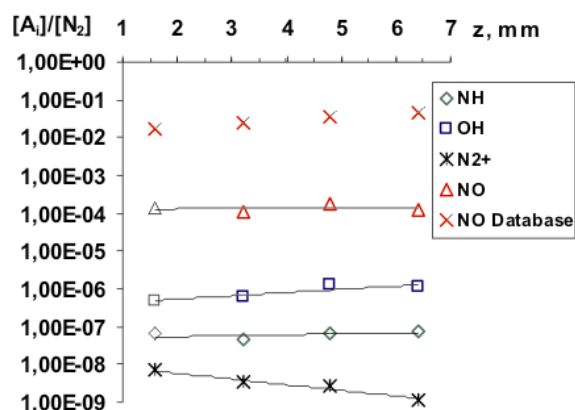


Figure 8. Distributions of relative concentrations of radiating plasma components in TA discharge along the gasflow z .

($I_s=480 \text{ mA}$, $G=75 \text{ cm}^3/\text{s}$, z - distance from electrode's axis)

decreases at the periphery of the discharge.

As can be seen from Fig. 8, amount of NO radicals in plasma of the transverse arc is much lower than corresponding values in SPECAIR database for air at the same temperatures. We supposed that it could be explained by the following: the characteristic time of NO producing reaction is larger than transit time of initial components (N_2^* , O_2^* and etc.) through plasma column.

Regime of the arc in air (under the same geometry but without of gasflow $G = 0 \text{ cm}^3 \text{ s}^{-1}$) with discharge current $I_d=660 \text{ mA}$ was investigated and the excitation temperatures were determined ($T_{es}^* \approx T_{vs}^* \approx 6950 \text{ K}$ and $T_{rs}^* \approx 1750 \text{ K}$). Relative concentration of the NO radicals ($[NO] / [N_2] \approx 4.5 \cdot 10^{-3}$) in generated plasma was evaluated in this case. Obtained value is comparable with $4.38 \cdot 10^{-3}$ represented in SPECAIR database under similar temperature $T \approx 1800 \text{ K}$. It can be considered like one more confirmation of our assumption.

The comparative analysis of plasma parameters of investigated TA discharge in airflow with other known sources of non-equilibrium atmospheric pressure plasma was made and the main results are presented in table II.

Conclusions

- Transverse arc generates non-thermal plasma $T_r^*(N_2) < T_v^*(N_2) \approx T_e^*(O, H) < T_e^*(Cu)$ with noticeable increasing of rotational temperature along the gas flow.
- Obtained T_e^* of blowing gas atoms (O and H) are smaller than corresponding values of Cu atoms (material of electrodes) due to the additional electron-ion recombination mechanism of excited electronic states population of copper atoms, which is almost absent for atoms of a blowing gas.
- The relative concentrations of radiating plasma species (N_2 , N_2^+ , NO , OH , NH) in the transverse arc were estimated by using SPECAIR. It was shown that relative

concentration of [NO] evaluated from experimental spectra is significantly lower than data in SPECAIR database for air at the same temperatures.

This work was supported by Kyiv National Taras Shevchenko University.

REFERENCES

1. Czernichowski A.: *J. Pure & Appl. Chem.* 66, 1301 (1994).
2. Mutaf-Yardimci O., Saveliev A., Fridman A.: *J. Appl. Phys.* 87, 1632 (2000).
3. Karla C., Matveev I., Gutsol A., Fridman A.: *Elec. Proc. of 2004 Technical Meeting, Central States Section, 21-23 March 2004, Texas*, A34.pdf, 2004.
4. Karla C., Kossitsyn M., Ishenderova K.: *Elec. Proc. of 16th International Symposium on Plasma Chemistry, Taormina, Italy, June 22-27, 2003*. ISPC-565.pdf, 2003.
5. Machala Z., Laux C., Kruger C.: *IEEE Trans. Plasma Sci.* 33, 320 (2005).
6. Chernyak V., Kernazhitsky L., Naumov V.: *J. Mol. Struct.* 744-747, 871 (2005).
7. Prysiazhnevych I., Chernyak V., Yukhymenko V.: *Ukr. J. Phys.* 52, 1061 (2007).
8. Prysiazhnevych I., Chernyak V., Skalny J.: *Ukr. J. Phys.* 53, 472 (2008).
9. SPECAIR is available: <http://www.specair-radiation.net>
10. Laux C., Spence T., Kruger C., Zare R.: *Plasma Sources Sci. Technol.* 12, 125 (2003).
11. Machala Z., Janda M., Hensel K.: *J. Mol. Spectrosc.* 243, 194 (2007).

ANALYSIS OF ENERGY AND MASS FLOWS IN AN ARC HEATER WITH INTENSIVELY BLOWN ELECTRIC ARC

JAN GREGOR, IVANA JAKUBOVÁ*,
and JOSEF ŠENK

Faculty of Electrical Engg. and Communication Technology,
Brno Univ. of Technology, Purkynova 118, 61200 Brno,
Czech Republic
jakubova@feec.vutbr.cz

Introduction

The paper focuses on energy flows inside the anode channel of an arc heater with electric arc stabilized by flowing working gas. The analysis is based on numerous experiments the measured results of which have served as input data of a designed mathematical model.

The mentioned experiments have been carried out on a laboratory model of an arc heater a modular construction of which makes it possible to measure energy loss of individual parts of the device, namely of the cathode, the parts of the anode channel, the extended anode, and the reaction chamber. Energy losses have been determined from cooling water flow rate and temperature. Simultaneously, other integral quantities characterizing arc heater operating conditions have been measured (the arc current and voltage, the flow rate of the working gas, its pressure, etc.). Pure argon and nitrogen and their mixtures have been used as working medium. In this paper, experimental data measured on the arc heater with the anode channel of 80 millimetres in length and 8 millimetres in radius, with argon flow rate of 22.5 grams per second, and with the electric power about 14 kilowatts are analyzed¹.

Sets of experiments have been carried out with the same geometrical and electrical operational parameters but with a different segmentation of the arc heater. The measured results show the previously used assumption concerning a negligible influence of phenomena near the electrodes on the arc inside the anode channel may be invalid. Thus, a procedure is designed making it possible to correct the previously obtained measured and computed data with respect to the cathode and anode loss.

The paper is organised as follows. First, the mathematical model of electric arc in the anode channel is shortly described. Then, the influence of phenomena near the electrodes and the correction of the voltage distribution is dealt with. An iterative procedure for correction of characteristic parameters of the model without complicated time-consuming computations is introduced. The next section gives typical results and compares the original and corrected dependencies of selected quantities. The last section suggests further possibilities of more precise evaluation of measured integral data.

Mathematical model

The mathematical model of the electric arc inside the arc heater anode channel is described in details in the previous papers¹. Here, only its basics are shortly mentioned. The mathematical model of the electric arc inside the arc heater anode channel is based on the continuity equation, the energy equation, and the Ohm's law. Naturally, some simplifying presumptions are used. The arc plasma is assumed to be in LTE and its kinetic energy to be small compared with its enthalpy. In the continuity equation, the Mach number is considered to be constant across the channel cross-section. The energy equation contains four terms: the electric power on the input side, and terms relative to conduction, radiation and enthalpy flow on the output side. Only the radial components of conductive and radiation energy flow, and the axial component of enthalpy flow are taken into account. The volume of the arc heater anode channel and the extended anode is divided into two regions: the arc zone and the remaining volume including the zone of heated and cold gas (see Fig. 1). The expected axial symmetry enables to solve only 1D problem instead of 2D task. In the arc zone, the radial temperature profile is approximated by a generalized parabola the exponent n of which is the computed parameter. In the heated zone, Gaussian approximation of the radial temperature dependency is used, both segments having the same values of temperature and its first derivative at the boundary of the arc zone ($T = 6000$ K). Also the axial dependency of the arc radius is defined and its exponent n_r is another calculated parameter.

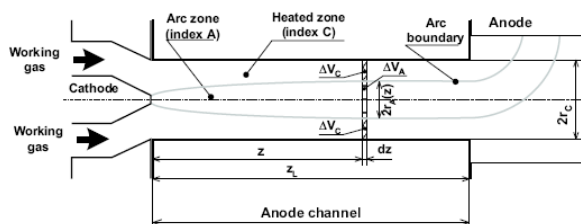


Fig. 1. Experimental device

The boundary conditions of the model are given by the measured integral quantities: the voltage U , the energy loss P_{ch} absorbed by the arc heater anode channel wall, and the energy balance of the whole channel. In previous experiments, the total voltage was used for computation presuming the voltage drops on regions near the electrodes to be negligible. New experiments with a segmented arc heater make it possible to estimate these voltage drops and to correct the voltage on the part of the arc inside the anode channel. The difference is found to be reasonable. Thus, an iterative procedure is designed in order to make the computation more precise and simultaneously to use the results of numerous previous measurement and computations.

Corrected voltage and power loss distribution

Originally, the near-electrode phenomena and the corresponding voltage drops have been omitted. The anode channel loss P_{ch} have been taken as a part of the total input power and characterised by coefficient ε in the relation $P_{ch} = \varepsilon UI$. The more precise corrected relations for the distribution of the arc heater input power and anode channel power loss can be derived using the new measured data

$$UI = P_{cat} + P_{as} + (U_{ch} + U_a)I \quad (1)$$

$$P_t = P_{cat} + P_{as} + \varepsilon_{ch}(U_{ch} + U_a)I \quad (2)$$

where P_t is the total power loss, U is the total voltage, I is the current, U_{ch} is the corrected voltage on the arc in the anode channel, U_a is the voltage on the part of the arc in the anode segment, P_{cat} and P_{as} is the power loss of the cathode and anode spot, respectively, and ε_{ch} is the corrected coefficient. The measured loss of the anode segment $P_a = P_{as} + \varepsilon_{ch}U_aI$ includes the loss of the anode spot and the loss of the part of the arc in the anode. For further calculation, the losses of the cathode and anode spots are presumed to be the same. Then, the loss of the anode spot is put equal to the separately measured loss of the cathode spot $P_{cat} \approx P_{as}$. The corrected loss coefficient can be expressed as follows

$$\varepsilon_{ch} = \frac{P_t - 2P_{cat}}{UI - 2P_{cat}} \quad (3)$$

The corrected values of the voltage on the arc in the anode channel is

$$U_{ch} = \frac{P_{ch}}{\varepsilon_{ch}I} \quad (4)$$

Correction of the computed dependencies

Using the above mentioned modified values, the parameters and axial dependencies, namely axial dependency of the centreline temperature $T_A(0,z)$, Mach number $M(z)$, arc radius $r_A(z)$, and the exponents n , n_r , calculated by the original mathematical model must be corrected. The following equations (5) to (9) define the main relations valid both for the original values from the mathematical model, and the corrected values derived from the designed modification.

The temperature distribution in the arc zone is approximated by a generalized parabolic function

$$\frac{T_A(r,z)^{1/n} - T_{AA}^{1/n}}{T_A(0,z)^{1/n} - T_{AA}^{1/n}} = 1 - \left(\frac{r}{r_A(z)}\right)^2 \quad (5)$$

The temperature T_{AA} corresponds to zero electric conductivity of the working gas and thus represents the boundary temperature of the arc zone $T_{AA} = T_A(r_A, z)$. For argon, T_{AA} is equal to 6000 K. In the heated zone, the radial

temperature dependency is approximated by the exponential function as follows

$$T_C(r,z) = T_{AA} \cdot \exp\left(\frac{r_A^2(z) - r^2}{b_C^2(z)}\right) \quad (6)$$

The parameter b_C is determined from the requirement of the equality of the first derivative of (5) and (6) at the boundary temperature

$$b_C^2(z) = r_A^2(z) \left\{ n \cdot \left[\left(\frac{T_A(0,z)}{T_{AA}} \right)^{1/n} - 1 \right] \right\}^{-1} \quad (7)$$

because the conduction heat flow must be the same on both sides of the arc boundary.

Cylindrical symmetry of the arc is supposed. The axial trend of the arc radius is given by the following relation²

$$r_A(z) = r_0 \left[1 + \left(\frac{z}{r_0} \right)^{1/n_r} \right] \quad (8)$$

r_0 is the radius of the arc at the cathode, defined by the arc current and by the cathode current density (10^8 A m^{-2} for current up to 2.16 kA^2), and n_r is a calculation parameter which influences the shape of the arc.

Utilization of approximation (5) enables to convert integration over the arc radius to integration over the arc axial temperature in the arc zone as follows:

$$\int_0^{r_A(z)} f[T_A(r,z)] 2\pi r dr = \pi r_A^2(z) F[T_A(0,z), n] \quad (9)$$

$$F[T_A(0,z), n] = \frac{1}{n \left[T_A^n(0,z) - T_{AA}^n \right]} \int_{T_{AA}}^{T_A(0,z)} f(T) T^{\frac{1-n}{n}} dT$$

This simplifies the calculation and saves much computing time because for a given working medium the function $F[T_A(0,z), n]$ can be determined in advance.

The designed correcting procedure uses the parameters computed by the original mathematical model and introduces three conditions based on the Ohm's law, continuity and energy equations in order to fulfil the modified boundary conditions. The calculation is iterative (indices i , j indicate iteration steps) and starts with the data computed by the original model from the original (less precise) input data. The corrected exponents are calculated for the cross-section z_l at the end of the anode channel and finally applied for the whole channel.

The first condition follows from the Ohm's law and uses the measured loss of the anode channel. Electric field intensity $E(z)$ can be obtained from the Ohm's law by integration of the current density over the arc cross-section

$$I = \int_{A_A(z)} \vec{j} d\vec{A} = E(z) \int_0^{r_A(z)} \sigma[T_A(r,z)] \pi r^2(z) E(z) \mathbb{E}[T_A(0,z), n]$$

where

$$\Sigma[T_A(0, z), n] = \frac{1}{n \left[\frac{1}{T_A^n(0, z)} - \frac{1}{T_{AA}^n} \right]} \int_{T_{AA}}^{T_A(0, z)} \sigma(T) T^{\frac{1-n}{n}} dT$$

is the application of the general relation (9) for conductivity of argon $\sigma(T)$. Electric field intensity $E(z)$ can be expressed as

$$E(z) = \frac{1}{\pi r_A^2(z) \Sigma[T_A(0, z), n]} \quad (10)$$

or from the increment of Joule loss $\Delta P_{ch}(z)$ of the segment Δz of the arc in the anode channel

$$E(z) = \frac{\Delta P_{ch}(z)}{\varepsilon_{ch} I \Delta z} \quad (11)$$

From the equality of (10) and (11) the first condition defining the relation between the arc radius and centreline temperature along the axis follows

$$r_{Ai}^2(z) \Sigma[T_{Ai+1}(0, z), n] = \frac{\varepsilon_{ch} I^2 \Delta z}{\pi \Delta P_{ch}(z)} = \text{const}(z) \quad (12)$$

The corrected value of Mach number $M(z_i)$ can be obtained from the continuity equation

$$M(z_i) \left\{ \int_0^{r_A(z)} \rho [T_A(r, z_i)] a [T_A(r, z_i)] 2\pi r dr + \int_{r_A(z)}^{r_{cc}(z)} \rho [T_C(r, z_i)] a [T_C(r, z_i)] 2\pi r dr + \rho(T_0) a(T_0) \int_{r_{cc}(z)}^{r_c(z)} 2\pi r dr \right\} = G \quad (13)$$

the three members of which represent the mass flow through the arc, the heated, and the cold zone.

Using (9), the integration variable is transformed as follows

$$RA [T_A(0, z_i), n] = \frac{1}{n \left[\frac{1}{T_A^n(0, z_i)} - \frac{1}{T_{AA}^n} \right]} \int_{T_{AA}}^{T_A(0, z_i)} \rho(T) a(T) T^{\frac{1-n}{n}} dT$$

and the precalculated values of RA can be used. The radius of the heated zone can be expressed as

$$r_{cc}^2(z) = r_A^2(z) \left[1 - \frac{\ln \frac{T_0}{T_{AA}}}{n \left\{ \left[\frac{T_A(0, z)}{T_{AA}} \right]^{1/n} - 1 \right\}} \right] \quad (14)$$

Further simplification can be reached using the relations for the mass density and sound velocity of argon in the temperature interval in the cold and heated zone, i. e. between 300 K and 6000 K.

$$\rho [T_C(r, z)] = \frac{p M_\rho}{R T_C(r, z)}, \quad a [T_C(r, z)] = \frac{\kappa R}{M_\rho T_C(r, z)}$$

where p is the gas pressure, κ is Poisson constant, M_ρ is the molar mass of argon, and R is the universal gas constant.

The second condition to fulfil is then

$$M_{i+1}(z_i) \pi \psi_{Ai}^2(z_i) RA [T_{Ai+1}(0, z_i), n] + 2p \sqrt{\frac{\kappa M_\rho}{R}} \left(\frac{1}{\sqrt{T_0}} - \frac{1}{\sqrt{T_{AA}}} \right) \frac{r_{Ai}^2(z_i)}{n \left\{ \left[\frac{T_{Ai+1}(0, z_i)}{T_{AA}} \right]^{1/n} - 1 \right\}} + [r_c^2 - r_{CCi}^2(z_i)] \rho(T_0) a(T_0) = G \quad (15)$$

The corrected value of the arc radius at the anode channel output $r_A(z_i)$ can be obtained from the energy equation

$$M(z_i) \left\{ \int_0^{r_A(z_i)} \rho [T_A(r, z_i)] a [T_A(r, z_i)] h [T_A(r, z_i)] 2\pi r dr + \int_{r_A(z_i)}^{r_{cc}(z_i)} \rho [T_C(r, z_i)] a [T_C(r, z_i)] h [T_C(r, z_i)] 2\pi r dr + \rho(T_0) a(T_0) h(T_0) \int_{r_{cc}(z_i)}^{r_c} 2\pi r dr \right\} = U_{ch} I - P_{ch} \quad (16)$$

where the first member on the left-hand side is the enthalpy flow through the arc zone, the second member is the enthalpy flow through the heated zone, and the third member is the enthalpy flow through the cold zone. The right-hand side of the equation represents the input power of the arc in the anode channel decreased by the measured anode channel loss.

Using (9), the pre-calculated quantity RAH is introduced

$$RAH [T_A(0, z), n] = \frac{1}{n \left[\frac{1}{T_A^n(0, z)} - \frac{1}{T_{AA}^n} \right]} \int_{T_{AA}}^{T_A(0, z)} \rho(T) a(T) h(T) T^{\frac{1-n}{n}} dT$$

Besides the above mentioned simplifying relations for mass density and sound velocity of argon, also the relation for argon enthalpy $h(T_0) = c_p T_0$ is applied. Then after integration, the corrected arc radius at the anode channel end can be determined from the following relation

(17)

$$\begin{aligned}
& r_{Ai+1}^2(z_l) \pi M_{i+1}(z_l) \{ RAH [T_{Ai+1}(0, z_l), n_j] [1 - RM_i(z_l)] + \\
& + 2pC_p \sqrt{\frac{\kappa M_\rho}{R}} \sqrt{T_{AA}} \left[1 - \sqrt{\frac{T_0}{T_{AA}}} \left(2 - \sqrt{\frac{T_0}{T_{AA}}} \right) \right] \frac{T_{AA}^{1/n_j}}{n_j [T_{Ai+1}^{1/n_j}(0, z_l)]} + \\
& + \frac{r_C^2 - r_{CCi}^2(z_l)}{r_{Ai}^2(z_l)} \rho(T_0) a(T_0) C_p T_0 \left[1 - \frac{M(0)}{M_{i+1}(z_l)} \right] \} = \\
& = (1 - \varepsilon_{ch}) U_{ch} I
\end{aligned}$$

where

$$RM_i(z_l) = \frac{r_0^2 M(0) RAH [T_A(0, 0), n]}{r_{Ai}^2(z_l) M(z_l) RAH [T_{Ai+1}(0, z_l), n]}$$

As mentioned above, the procedure starts with the parameters computed by the original model n , n_r and stops if the change of the computed arc radius is negligible $r_{Ai+1} - r_{Ai} \rightarrow 0$.

The computation can be checked according to the condition

$$\sum_{k=1}^l \frac{I}{\pi r_{Ai}^2(z_k) \Sigma [T_{Ai}(0, z_k), n_j]} \Delta z = U_{ch}$$

where the values of the arc radius $r_A(z_k)$ and of the centreline temperature $T_A(0, z_k)$ for individual points of the computation net are obtained from (8) and (12).

Results

From the model, information on the distribution of basic quantities, especially of the temperature $T(0, z)$ and velocity $v(0, z)$ at the arc centreline, of the electric intensity $E(z)$ and the arc radius $r_A(z)$ on the axial position z along the anode channel, can be obtained for the measured arc current. The described correcting procedure with more precise measured input data results in changes of these dependencies. As an example, the distributions computed by the original model and those corrected by the designed iterative procedure are given for one point of the arc heater voltage-current characteristic ($I = 122$ A).

The original model has found the exponents $n = 1$, $n_r = 3.2$. The correction respecting near-electrode voltage drops has led to a significantly different exponent $n = 0.1$. The substantially lower value of exponent n causes the radial temperature profile to be almost rectangular. This finding is in accordance with the fact that intensively blown electric arc is used to be modelled by a rectangular radial temperature profile by many authors (see e.g.³). A comparison of the original and modified radial temperature profiles for the position in the middle of the anode channel length ($z = 0.040$ m) is shown in Fig. 2.

In consequence of the substantial decrease of exponent n , the heated zone almost disappears after correction and the corrected radius of the jet (r_{CC} for $T = 300$ K) is nearly the same as the radius of the arc (r_A for $T = 6000$ K). This fact is clearly seen in Fig. 3, which compares the dependencies of

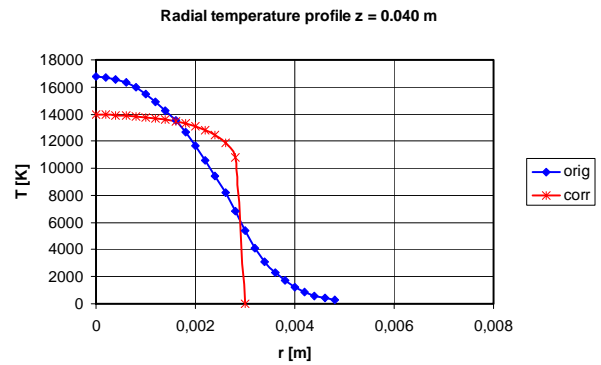


Fig. 2. The original and corrected radial temperature profiles

the original and modified radii of the arc and the heated zone on the axial position z . While the axial dependency of the original and corrected arc radius is the same the radii of the heated zone differ significantly in both cases. The original computation leads to the relatively broad heated zone but in the case of the corrected very flat radial temperature profile the heated zone is extinguished.

As it can be seen in Fig. 3 the heated zone radius never reaches the channel wall. Thus, the leading role in the radial energy exchange is supposed to be played by radiation. Energy irradiated by central parts of the arc is absorbed in outer parts of the plasma column which contributes to flatter radial temperature profile. The development of the radial temperature profile along the anode channel axis is depicted in Fig. 4 for the original computation and in Fig. 5 for the corrected case.

Although the radial temperature profiles are substantially influenced by the correction the original and corrected axial dependencies of the centreline temperature $T_A(0, z)$, electric field intensity $E(z)$ (Fig. 6), and Mach number $M(z)$ (Fig. 7) are similar in shape. After correcting the arc voltage for electrode voltage drops ($U < U_{ch}$) the input power of the arc inside the anode channel is lower. Naturally, also the corrected values are expected to decrease.

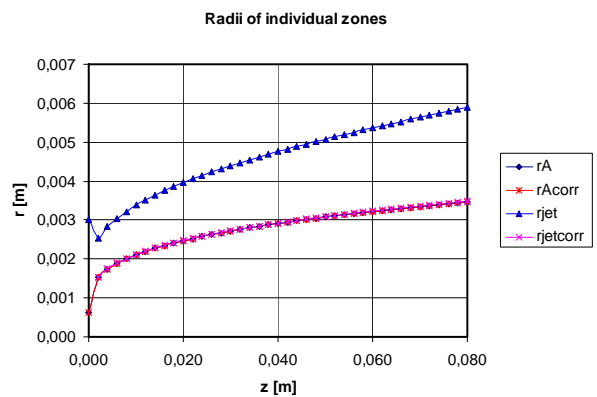


Fig. 3. The original and corrected radii of the arc and the heated zone

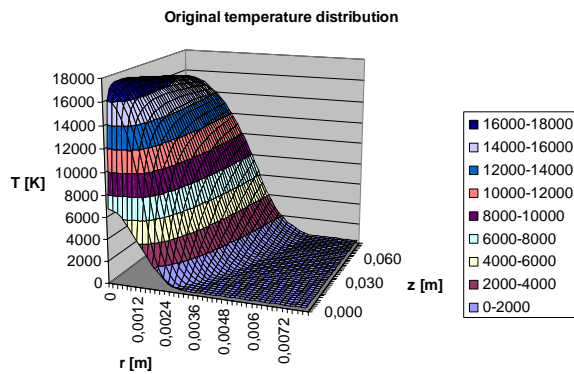


Fig. 4. The development of the temperature profile (original)

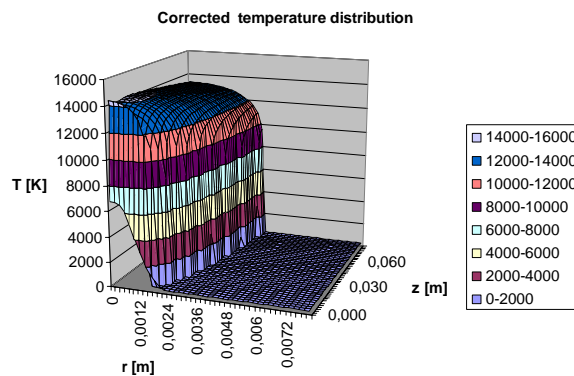
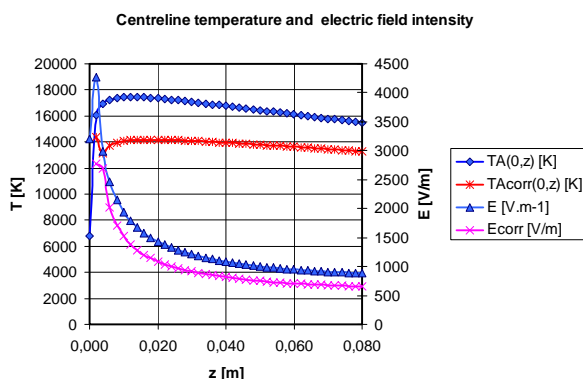
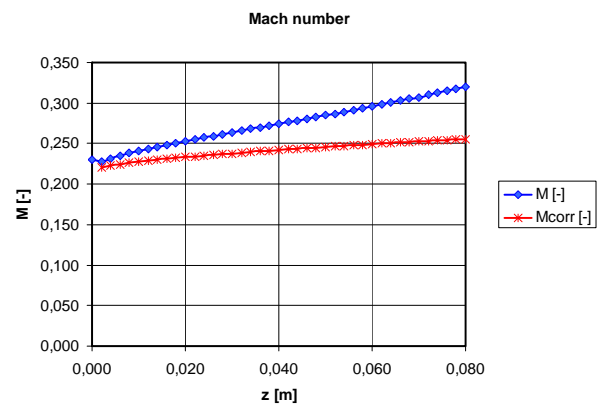


Fig. 5. The development of the temperature profile (corrected)

Fig. 6. Axial dependencies of the centreline temperature $T_A(0,z)$ and electric field intensity $E(z)$ Fig. 7. Axial dependencies of Mach number $M(z)$

Consequences important for practical applications of the arc heater can be seen in Fig. 8 and 9. Fig. 8 shows the distribution of relative mass flows G_x/G through the arc, heated, and cold zone along the anode channel axis. From the practical point of view, the distribution of mass flows (and similarly, of enthalpy flows, too) at the end of the channel ($z = z_1$) is the most important one. As it can be seen in Fig. 8, almost the whole mass flow goes through the cold zone (97 per cent). The arc zone transports only a little part of mass (about 2.8 per cent), and the contribution of the heated zone after correction is negligible.

With enthalpy flows (Fig. 9), the situation is opposite: the prevailing part of energy is transported via enthalpy flow of the arc zone (about 95 per cent at the anode channel end) while the enthalpy flow through the cold zone is low (about 5 per cent at the channel output).

The original evaluation, in which the influence of near-electrode phenomena has been completely ignored, has led to the following distribution of mass and enthalpy flows at the end of the anode channel: the mass flow through the arc zone about 4 per cent, through the heated zone about 28 per cent, through the cold zone about 68 per cent, and enthalpy flow through the arc zone about 67 per cent, through the heated zone about 23 per cent, through the cold zone about 10 per cent. The influence of the correction of the radial temperature profile here is obvious. The non-corrected evaluation results in an overestimated contribution of the heated zone to the total energy transport.

As mentioned above, the results show radiation to be the main mechanism of energy exchange in the radial direction. The fact that the computed gas temperature near the channel wall does not exceed the temperature of the cold gas at the input proves the total measured power loss absorbed by the channel wall originates in the plasma column radiation. Under these conditions, the radiation coefficient of argon at atmospheric pressure can be roughly estimated using the computed values of ϵ_{ch} , $E(z)$, $T_A(0,z)$ (for details see⁴). Fig. 10 gives the values of the radiation coefficient of argon at atmospheric pressure estimated for the centreline temperatures in the region towards the anode channel output

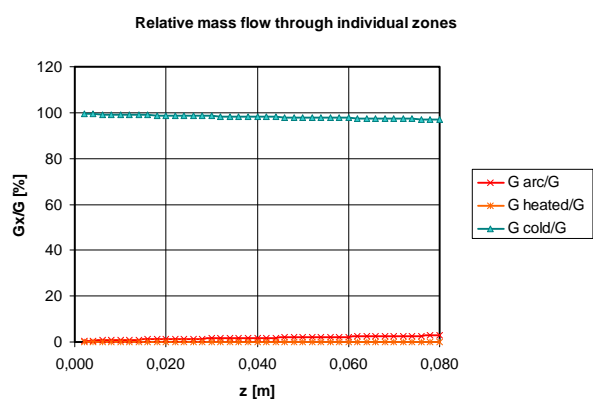


Fig. 8. Corrected relative mass flow distribution

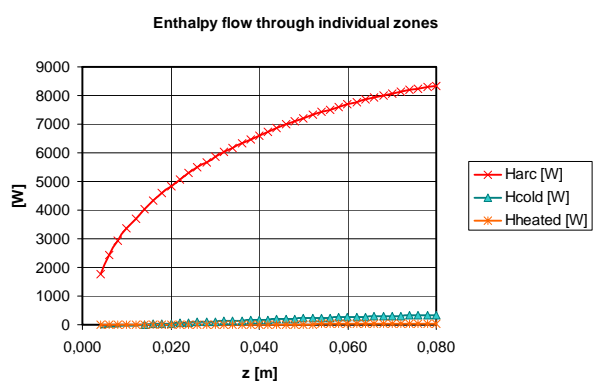
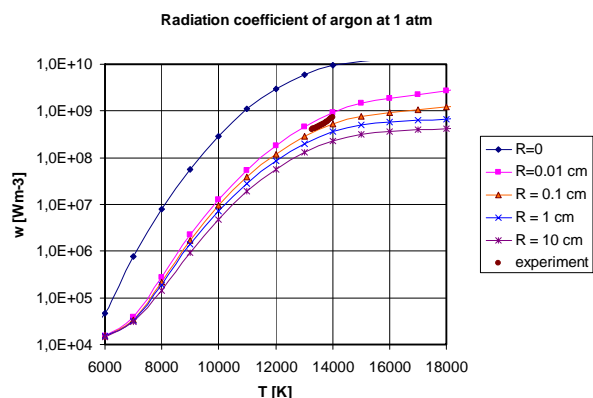


Fig. 9. Corrected enthalpy flow distribution

Fig. 10. Estimated and theoretically computed radiation⁵ coefficient of argon at atmospheric pressure

($z > 0.040$ m) together with the values of the radiation coefficient of argon at atmospheric pressure computed theoretically by Aubrecht and Bartlova⁵. Considering the used simplifications during the computation and the different real and theoretical conditions, the agreement of the estimated and theoretical data can be judged as satisfactory.

Conclusion

The modified set-up of the arc heater has made it possible to distinguish the influence of the phenomena near the electrodes. The designed iterative procedure has been used for quick correction of the results obtained by the original mathematical model. The consequences of the correction have been demonstrated for a set of real experimental data and have been discussed. The most surprising finding of much lower corrected exponent n confirms the validity of application of almost rectangular radial temperature profile for informative analysis of intensively blown electric arc. The main practical conclusions concerning the mass and energy distribution at the end of the anode channel have not changed substantially after the correction. On the other hand, some simplifications used in the original mathematical model should be re-considered.

The research has been supported by the Ministry of Youth, Education and Sports of the Czech Republic under the projects no. MSM002163516 and MSM0021630513.

REFERENCES

1. Heinz J., Šenk J.: Czech. J. Phys. C54, 702 (2004).
2. Ramakrishnan S., Stokes A. D., Lowke J. J.: J. Phys. D: Appl. Phys. 11, 2267 (1978).
3. Frost L. S., Liebermann R. W.: Proc. IEEE 59, 474 (1971).
4. Gregor J., Jakubová I., Šenk J.: Eur. J. Phys. D, in press.
5. Aubrecht V., Bartlová M.: Czech. J. Phys. D52, 522 (2002).

ION MOBILITY SPECTROMETRY STUDY OF NEGATIVE CORONA DISCHARGE IN OXYGEN/NITROGEN MIXTURES

MICHAL STANO^{a*}, EUGENE SAFONOV^b,
MAREK KUČERA^a, and ŠTEFAN MATEJČÍK^a

^a Faculty of Mathematics, Physics and Informatics, Mlynska dolina F2, 84248 Bratislava, Slovak republic, ^b Radiophysical Faculty, National Taras Shevchenko University, Glushkova 2, 03122 Kyiv, Ukraine
stano@fmph.uniba.sk

Introduction

The Ion Mobility Spectrometry (IMS) is an ion separation method based on the phenomenon that different ions have different drift velocities in a drift gas and homogeneous electric field. The IMS technique has been developed and introduced in 1970 under the name plasma chromatography¹. Since then a variety of different devices working on this principle were developed, mainly for detection of trace organic compounds in air^{2,3}. In the 80's a huge progress was achieved on the field of the ion – molecule reactions at atmospheric pressure and the IMS was rediscovered as a powerful analytical method^{3,4}.

Generally, the IMS consists of the ionization source, the reaction region, the shutter grid and the drift tube. The most common ionization source is ⁶³Ni (β-radiation) radioactive source, which is suitable for many applications because of its stability, low cost and low weight. Unfortunately, this source is radioactive and there is tendency to replace the radioactive source from environmental reasons. Several ionization sources using UV ionization, multi-photon laser ionization, electrospray ionization or corona discharge^{2,3} were tested in the past. The ionization efficiency of corona discharge is very high and it can be used for production of both positive and negative ions⁵. The ions formed in the ion source are called primary ions. These ions react with the sample gas which is introduced into reaction region of the spectrometer. The sample molecules are ionized by ion-molecular reactions with primary ions. In the case of positive ions the reaction involved is mainly proton transfer and as a result the proton will stick to the compounds with the highest proton affinity. High electron affinity and charge transfer reactions are usually decisive for negative ions formation. In both polarities the ionization processes are very selective and as a result the ion mobility spectrometry is very sensitive technique for detection of certain compounds.

The ions are separated at ambient pressure as they drift in weak electric field through a gas (oxygen in this case). The velocity v of a drifting ion is proportional to electric field E and a constant K called the mobility:

$$v = K \cdot E \quad (1)$$

The mobility of certain ion in a drift gas depends on several parameters and can be expressed as

$$K = \frac{3q}{16n} \sqrt{\frac{2\pi}{k_b T}} \sqrt{\frac{m_g + m_i}{m_g \cdot m_i}} \frac{1}{\sigma} \quad (2)$$

where q is charge of an ion, n neutral gas density, T temperature of the gas, m_g and m_i the mass of gas molecules and ions respectively and σ is the collisional cross-section. As the mobility depends on the collisions of the ion with the drift gas it depends also on the density of the drift gas. Therefore a correction to the standard conditions ($T_0 = 273$ K, $p_0 = 101.3$ kPa) is made and resulting value is reported as reduced mobility K_0 given by the formula:

$$K_0 = K \frac{T_0}{T} \frac{p}{p_0} \quad (3)$$

The most common gas which is used in the commercial IMS instruments as a drift gas is dry purified air. The same gas is usually used in the ion source where primary ions are formed. Formation of negative ions in air by corona discharge has been studied using mass spectrometry by several authors.

Skalny et al.⁶ studied negative ions formed in a negative corona discharge using both dry and 'wet' air at pressures between 5 and 27 kPa. In dry air the dominant ion was CO_3^- . In presence of water this was converted to cluster ions containing one or more water molecules. If ozone and nitrogen oxides were added, or were produced in discharge in sufficient concentrations, NO_3^- ions and NO_3^- hydrated clusters were formed.

Nagato et al.⁷ studied ions in negative corona in air at ambient pressure at different reaction times, 1 ms and 10 ms. They observed that after 10 ms the number of ions is significantly reduced and the only significant intensity appears at masses 62, 124 and 125 amu. They attributed these masses to NO_3^- , HCO_3^- - HNO_3 and NO_3^- - HNO_3 ions. When the humidity was limited to 25 ppm of H_2O the only ion observed was the NO_3^- .

Gravendeel and Hogg⁸ studied mass spectrometrically negative corona in N_2/O_2 mixture with ratio 5 to 1. Although they used high purity gases with less than 5 ppm H_2O and 0.1 ppm CO_2 they observed numerous negative ions with O_3^- , OH^- , NO_3^- and CO_3^- being the most intense ones. In this case however the time between formation of ions and their entrance to vacuum was in order of 10 μs and the reactions might not have been completed.

As we can see the types and relative intensity of the ions observed in these studies differ significantly. The results are very sensitive to many parameters. This includes humidity, concentration of O_3 , NO_x and other molecules. It depends also on the reaction time for which the ions are present in gaseous environment before they enter vacuum to be mass analysed.

In the present work we have applied the IMS technique to study the ion formation in the negative corona discharge in the pure O_2 and N_2/O_2 mixtures. One of the major advantages of the IMS technique is that in contrast to the mass spectroscopic techniques it avoids the generation of the high vacuum. The transport of the ions from ambient pressure into vacuum is associated with negative effects which may change the nature of the ions (clustering, collision induced dissociation). One of the main drawbacks of the IMS technique is the lack

of data concerning the ion mobilities in the particular drift gases and thus the difficulties with the identification of ions.

In the present experiment we used the O₂ drift gas in the IMS. There are several works^{9–12} dealing with ion mobilities of the negative ions in O₂ drift gas, however, also in this case there is relatively large uncertainty in the values of the ion mobilities.

Experiment

The work was performed on a home made ion mobility spectrometer schematically shown on Fig. 1. The ions are formed in negative corona discharge in a point to plane geometry. The point electrode is made of a thin tungsten wire with 100 μm diameter. It is situated 14 mm from a brass aperture with 5 mm diameter which serves as a plane electrode. The discharge chamber is made of PTFE and it has a gas inlet in the proximity of coronating electrode.

The reaction region is located between the ion source and the drift tube. It is equipped with an independent gas inlet. The molecules introduced to this region react with primary ions formed in the ion source. The reaction region is separated from the drift tube by an aperture with 5 mm diameter. The aperture is necessary to maintain high purity of gas in the drift tube. The reaction region contains also gas outlet from the spectrometer.

The ions in the drift tube are separated according to their individual mobilities. The ions enter the drift tube in short 150 μs pulses controlled by a shutter grid (SG). The shutter grid is built according to Bradbury-Nielsen design¹³.

The drift tube consists of identical brass rings separated by the PTFE teflon rings. The inner diameter of the brass ring is 50 mm and the length is 9 mm. The distance between two rings is 1 mm. The brass rings are connected to a voltage divider. The drift tube length (shutter to collector) is 110 mm and electric field along the drift tube is 278 V cm⁻¹. The field strength corresponds to reduced electric field $E/N = 1.1$ Td. The drift tube is terminated with an ion collector. The ion collector consists of aperture grid, collector and shielding. The collector is made of stainless steel and its diameter is 16 mm. The collector is shielded from the front side by an aperture grid and from other sides by a brass body. The aperture grid is made of a fine Ni mesh. The distance from the collector to the aperture grid is 1 mm. The ion current is amplified by a home made current/voltage amplifier with amplification

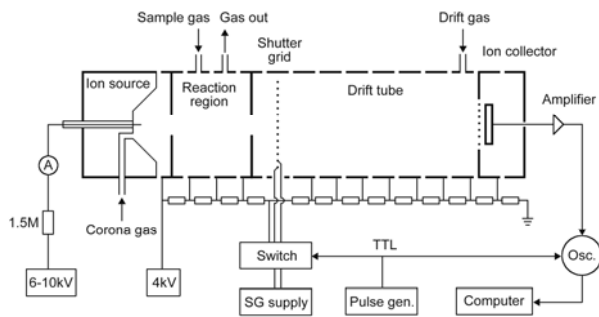


Fig. 1. Schematic view of the ion mobility spectrometer

10⁸ and is averaged and recorded by a Tektronix TDS 220 oscilloscope.

The gas flows were measured by flowmeters and were kept constant in present measurements. The drift tube was fed by pure oxygen with flow 400 ml min⁻¹. The ion source was fed by pure oxygen or by nitrogen/oxygen mixture with total flow of 200 ml min⁻¹. The purity of both oxygen and nitrogen gas was 5.0. The measurements were performed at ambient temperature and pressure. The mobility of ions is calculated using the formula:

$$K = \frac{l_d}{t_d \cdot E} \quad (4)$$

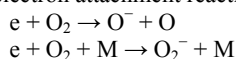
where l_d is the length of the drift tube and t_d is the drift time of the ions. The reduced mobility K_0 is calculated using the equation 3. The uncertainty in calculated K_0 values is believed to be ± 4 %.

Results

Pure O₂

The IMS spectrum of negative ions formed in the negative corona discharge in pure O₂ is shown on the Fig. 2. The spectrum shows one peak at 14.75 ms drift time which corresponds to reduced mobility 2.55 cm² V⁻¹ s⁻¹.

In previous mass spectrometric studies⁸ it was reported that dominant ion in negative corona in O₂ is the O₃⁻. The O₃⁻ ions are effectively formed by several reaction channels. The negative corona discharge in O₂ is source of neutral O₃ molecule¹⁴. Additionally, to the neutral products, primary negative ions O⁻ and O₂⁻ are formed in the corona discharge via electron attachment reactions to the O₂:



These primary ions may further undergo binary reactions with O₃ forming O₃⁻ ions¹⁴:

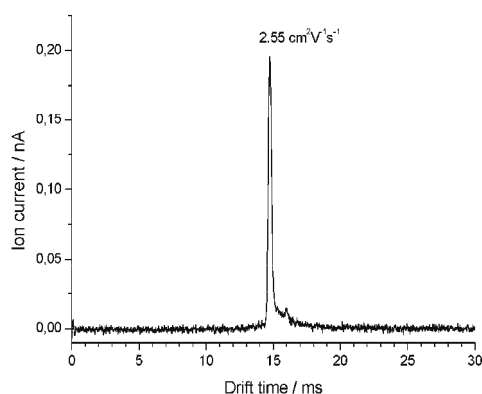
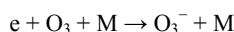
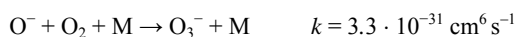


Fig. 2. Ion mobility spectrum of the ions formed in the negative corona discharge in O₂

As the electron affinity of O_3 (2.10 eV) exceeds those of O (1.46 eV) and O_2 (0.45 eV) both reactions are exothermic. Formation of the O_3^- is possible also via three body reactions:



which represent the electron attachment reaction of the thermal electrons and



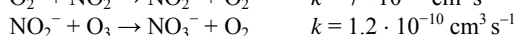
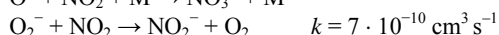
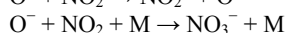
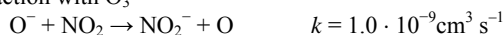
three body formation of the O_3^- via association reaction.

The reduced mobility of O_3^- in O_2 has been measured by Snuggs et al.¹⁰ to be $2.55 \pm 0.08 \text{ cm}^2 \text{ V}^{-1} \text{ s}^{-1}$. This is in agreement with present value $2.55 \text{ cm}^2 \text{ V}^{-1} \text{ s}^{-1}$ determined for the dominant ion. We therefore assign O_3^- to this ion.

The earlier IMS/MS studies^{9, 10} showed formation of O_3^- , O_2^- and O^- ions in pure O_2 . These experiments, however, were carried at lower pressures. In present experiment carried out at ambient pressure we are not able to see O^- and O_2^- ions in the IMS spectrum. Additional structures at the feet of the dominant peak we associate with trace gases present in the O_2 .

N_2/O_2 mixture

The negative corona discharge in the mixture of N_2 with O_2 results in formation of nitrogen oxides N_xO_y . Many of these molecules possess a positive electron affinity. The electrons and the primary negative ions O^- and O_2^- react with NO_2 and form NO_2^- which may be converted to NO_3^- by a reaction with O_3



The electron affinity of both NO_2 (2.27 eV) and NO_3 (3.93 eV) exceeds that of O_3 (2.10 eV). The NO_3^- has also been observed to be the terminal negative ion in dry air⁷.

In the present study the corona discharge was fed by the mixtures of N_2 with O_2 while drift gas was still pure O_2 . The concentration of N_2 in mixture varied from 10 % to 90 %. Fig. 3 shows the ion mobility spectra with 10 % and 80 % concentration of N_2 in the corona discharge. The spectrum obtained in the pure O_2 is also shown as a reference. In addition to $2.55 \text{ cm}^2 \text{ V}^{-1} \text{ s}^{-1}$ peak which was present also in the pure O_2 we have observed additional ions with reduced mobility 2.45, 2.23 and $2.14 \text{ cm}^2 \text{ V}^{-1} \text{ s}^{-1}$. The intensity of produced ions as a function of N_2 concentration is plotted on the Fig. 4. We see that with increasing concentration of N_2 the intensity of the ion with reduced mobility $2.55 \text{ cm}^2 \text{ V}^{-1} \text{ s}^{-1}$ significantly decreases. When concentration of N_2 exceeds 50 % this ion has only 10 to 15 % of its initial intensity. The ion with $K_0 = 2.45 \text{ cm}^2 \text{ V}^{-1} \text{ s}^{-1}$ has maximum intensity in mixture with 30 % N_2 concentration. Above this N_2 concentration its intensity is slightly decreasing. The ion with $K_0 = 2.14 \text{ cm}^2 \text{ V}^{-1} \text{ s}^{-1}$ is dominant at N_2 concentration exceeding 30 %. The intensity of the $2.23 \text{ cm}^2 \text{ V}^{-1} \text{ s}^{-1}$ ion was too low to be determined with reasonable precision. The structure at $2.35 \text{ cm}^2 \text{ V}^{-1} \text{ s}^{-1}$ has also been observed in the pure O_2 and therefore it is not clear if it is related to presence of N_2 .

Clear identification of the observed ions is problematic due to lack of data concerning ion mobilities. The mobility of negative ions in O_2 has been measured previously by several authors^{10–12}. The measurements were performed at low pres-

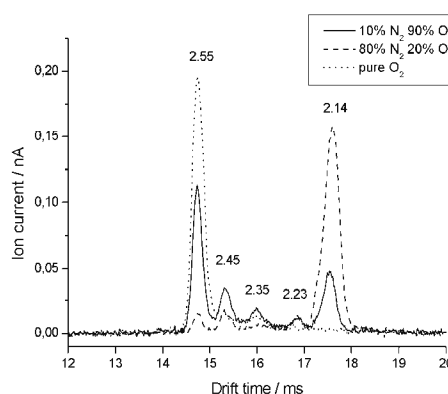


Fig. 3. Mobility spectra of negative ions formed in corona discharge in N_2/O_2 mixture with 10 % and 80 % concentration of N_2 . Ions formed in pure O_2 are shown as reference. Mobility values are in $\text{cm}^2 \text{ V}^{-1} \text{ s}^{-1}$

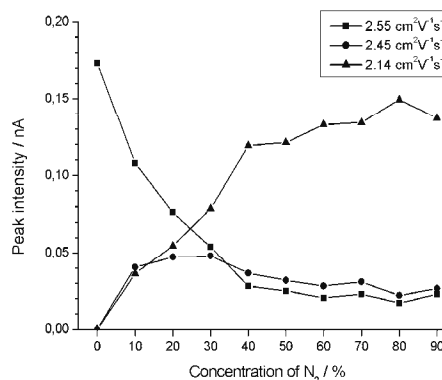


Fig. 4. Intensity of observed ions as a function of N_2 concentration in the corona discharge

sure and low reduced electric field (E/N). Low values of E/N are necessary to maintain the ions in thermodynamical equilibrium with the drift gas. Under such condition the reduced mobility K_0 is constant and it does not depend on field intensity and pressure and it has a characteristic value for every combination of ion and a drift gas. We can therefore directly compare K_0 values obtained in previous studies at low pressure with our values obtained at ambient pressure.

Snuggs and coworkers¹⁰ performed measurements at low pressure 0.02 to 10 Torr and low E/N values. The ions were identified using mass spectrometry. They determined the reduced mobilities of O^- , O_2^- , O_3^- and O_4^- in O_2 to be 3.20, 2.16, 2.55 and $2.14 \text{ cm}^2 \text{ V}^{-1} \text{ s}^{-1}$. Perkins et al.¹¹ measured temperature dependency of reduced mobility of negative ions in O_2 in the pressure range 27 to 42 Torr and E/N 2 to 4 Td. At 300 K they obtained the mobility values for NO_2^- and NO_3^- 2.6 and $2.4 \text{ cm}^2 \text{ V}^{-1} \text{ s}^{-1}$.

In the pure oxygen we have assigned the ion with mobility $2.55 \text{ cm}^2 \text{ V}^{-1} \text{ s}^{-1}$ to O_3^- . Virtually same mobility has

been measured in N_2/O_2 mixture. In this case also formation of NO_2^- with very similar mass and mobility is possible. The electron affinity of NO_2 is larger than the electron affinity of O_3 and thus the collision of the O_3^- ion with NO_2 may result in electron transfer to NO_2 . The mobility of NO_2^- has been reported¹¹ to be close to that of O_3^- , it is therefore possible that the peak at $2.55 \text{ cm}^2 \text{ V}^{-1} \text{ s}^{-1}$ now exhibits both O_3^- and NO_2^- ions.

The reduced mobility corresponding to the second peak in the spectra in Fig. 3 is $2.45 \text{ cm}^2 \text{ V}^{-1} \text{ s}^{-1}$. This value is close to the value $2.4 \text{ cm}^2 \text{ V}^{-1} \text{ s}^{-1}$ which was measured by Perkins et al. for NO_3^- . Therefore most probably the ion with mobility $2.45 \text{ cm}^2 \text{ V}^{-1} \text{ s}^{-1}$ is NO_3^- .

For ions with reduced mobility 2.23 and $2.14 \text{ cm}^2 \text{ V}^{-1} \text{ s}^{-1}$ which were observed in the present study we do not find any reference in the literature.

It has been shown that the collisional cross-section s in the equation (2) for small molecules is given by polarizability of drift gas molecules and that geometric size of ions can be neglected⁸. This approximation is also known as the polarization limit model. If we assume that s is constant we obtain the relation between the ion mass and the mobility of the ion

$$K_0 \propto \sqrt{\frac{m_g + m_i}{m_g \cdot m_i}} \quad (5)$$

This dependence is plotted by a solid curve in the Fig. 5. The curve was set to pass through mass 48 amu and mobility $2.55 \text{ cm}^2 \text{ V}^{-1} \text{ s}^{-1}$ measured for the O_3^- . In the Fig. 5 are also indicated mobilities of the negative ions in O_2 obtained in previous studies which are scattered around the curve. The main exception is the O_2^- ion which has significantly lower mobility. This is well known effect. The mobility of the ion is reduced due to resonant charge transfer reactions between the O_2^- ion and the O_2 molecules. It is very unlikely that formation of O_2^- with mobility $2.16 \text{ cm}^2 \text{ V}^{-1} \text{ s}^{-1}$ might be enhanced by presence of N_2 . It is more reasonable to expect formation of other nitrogen oxides or their clusters.

In the case of large ions the polarization limit model does not work, as the size and geometry of the ions can not be neglected. The mobility of heavy ions will therefore fall below the curve. The dash line represents mobility $2.14 \text{ cm}^2 \text{ V}^{-1} \text{ s}^{-1}$ obtained for dominant ion at high N_2 concentration. According to equation (5) this mobility is reached at about 160 amu. Although polarization limit model does not have clear limit we do not consider 160 amu to be low ion mass in the O_2 drift gas. It is likely that ions in this mass range have already lower mobility as is given by the equation (5). We therefore consider 160 amu to be the upper mass limit for ion with $2.14 \text{ cm}^2 \text{ V}^{-1} \text{ s}^{-1}$ mobility. Most probably we are dealing with a large cluster ion.

Summary

Formation of negative ions in the negative corona in N_2/O_2 mixtures has been investigated using ion mobility spectrometry in the oxygen drift gas. Negative corona in the pure O_2 results in formation of single anionic product with reduced mobility $2.55 \text{ cm}^2 \text{ V}^{-1} \text{ s}^{-1}$ which was identified as the

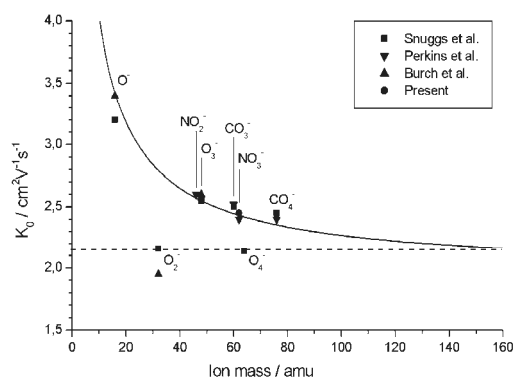


Fig. 5. Mobilities of negative ions in oxygen obtained in previous studies⁹⁻¹¹ and present

O_3^- . Negative corona discharge in N_2/O_2 mixtures results in formation of several negative ions. The ion with mobility $2.45 \text{ cm}^2 \text{ V}^{-1} \text{ s}^{-1}$ was identified as the NO_3^- . The nature of other products including the most intense with reduced mobility $2.14 \text{ cm}^2 \text{ V}^{-1} \text{ s}^{-1}$ remains unclear.

This work was supported by the Slovak VEGA grant No.1/0051/08.

REFERENCES

1. Karasek F. W.: Res.Dev. 21, 34 (1970).
2. Eiceman G. A., Karpas Z.: *Ion Mobility Spectrometry*. CRC Press, 2005.
3. Borsdorf H., Eiceman G. A.: Appl. Spectroscopy Rev. 41, 323 (2006).
4. Baumbach J. I., Eiceman G. A.: Appl. Spectr. 53, 338 (1999).
5. Tabrizchi M., Khayamian T., Taj N.: Rev. Sci. Instrum. 71, 2321 (2000).
5. Skalny J. D., Mikoviny T., Matejcik S., Mason N. J.: Int. J. Mass Spectrom. 233, 317 (2004).
6. Nagato K., Matsui Y., Miyata T., Yamauchi T.: Int. J. Mass Spectrom. 248, 142 (2006).
7. Gravendeel B., Hoog F. J.: J. Phys. B: At. Mol. Phys. 20, 6337 (1987).
8. McDaniel E. W., McDowell M. R. C.: Phys. Rev. 114, 1028 (1959).
9. Snuggs R. M., Volz D. J., Schummers J. H., Martin D. W., McDaniel E. W.: Phys. Rev., A 3, 477 (1971).
10. Perkins M. D., Eisele F. L., McDaniel E. W.: J. Chem. Phys. 74, 4206 (1981).
11. Burch D. S., Geballe R.: Phys. Rev. 106, 183 (1957).
12. Bradbury N. E., Nielson R. A.: Phys. Rev. 49, 388 (1936).
13. Skalny J. D., Mikoviny T., Mason N. J., Sobek V.: Ozone Sci. Eng. 23, 29 (2001).
14. Eliasson B.: *Electrical Discharge in Oxygen*. Part 1. Basic Data, Rate Coefficients and Cross Sections, Report KLR 83/40 C, Brown Boveri Forschungszentrum, Baden-Dättwil 1985.

PLASMA IN MEDICINE, BIOLOGY AND ENVIRONMENTAL PROTECTION

ENVIRONMENTALLY FRIENDLY METHOD OF WATER DECONTAMINATION

ENGLÉN AZIZOV, ALEXEY EMELYANOV*,
NIKOLAY RODIONOV, and VLADIMIR
YAGNOV

Federal State Unitary Enterprise State Research Center of Russian Federation "Troitsk Institute for Innovation and Fusion Research", Troitsk, Moscow reg., Pushkov Str., possession 12, 142190
emelyan@triniti.ru

Annotation

Possibilities of bactericidal effect of phenomena which are following electric discharges in liquid initiated by a different ways are analyzed. Methodology, based on application of discharges in still liquid and electrical discharges with a large surface of radiation, formed in a zone of viscous mixing of a submerged stream during one operating cycle of decontamination is discussed.

Introduction

Voluminous literature covers the investigations in electrical discharges in liquid^{1,2}. To a considerable extent it is connected with application of such discharges for switching currents³, decontamination and cleaning liquid (partially, water) from pollutions⁴, and also for production of nanomaterials.

One of the first propositions for application of pulse electric discharges in liquid was method of use of its bactericidal characteristics. It is considered that for the complete water decontamination is necessary energy $W = 3\text{--}4 \text{ MJ m}^{-3}$ during periodically-pulsed discharges with energy in pulse approx. $1\text{--}10 \text{ J}$ (ref.^{8–10}). For reduction of energy consumption to $0.02\text{--}0.04 \text{ kW h m}^{-3}$ it is necessary to considerably increase energy of pulse (to 21.5 kJ)¹¹. In ref.⁸ is reported that among phenomena, which are following pulse electric discharge in water, UV radiation and shock wave having maximal bactericidal effect. Moreover, short-wave radiation assumes 80 % of exterminated pathogenic cells in conditions of liquid mixing. In ref.^{10,12} is also mentioned that water decontamination occurs in close proximity to interelectrode space (IS). At a distance from discharge channel $r > 3\text{--}4 h$, where h – interelectrode gap, bactericidal effect is insignificant¹². That's why such devices are often multielectrode¹³ and works under high voltages in frequency regime, which defines specific requirements for power supply.

Though, coefficient of efficiency of such devices is low,

because bulk of the inserted electric energy turns into the energy of shock wave. Also, the prebreakdown losses are high. So, according to the estimations that were made in monograph¹, on the part of UV radiation goes only 10 % of the energy.

In addition, formation of shock waves of high intensity (pressure drop on a shock wave front $\geq 50 \text{ MPa}$, ref.¹¹) makes high demands of mechanical strength of devices.

1. Electric discharges with a large surface of radiation, as a tool for liquid decontamination.

In ref.^{15,16} for the first time was shown, that electric discharge in flowing liquid is essentially easier, without qualitative changes of its progress process in a broad interval of liquid electrical conduction. In ref.¹⁷ are given the results of initiation and formation of electric discharge in a zone of a viscous turbulent mixing of a submerged water stream, flowing across the electrode system. First stimulus for such experiments was a problem of commutators creation for feed systems, based on a inductive energy storages¹⁸ (Fig. 1).

Capacitive energy capacitor with a capacitance $C_0 = 88 \text{ mF}$ served as an energy source. When a discharger P_0 was switched on, a battery discharge through the inductance $L_0 = 0.3 \text{ mH}$ and mechanical commutator has occurred. Break of the contacts was carried out at a current maximum. Divergence of the contacts, ignition of an arc and formation of a submerged liquid stream occurred under the pulse increase of the pressure to $30\text{--}60 \text{ MPa}$ in inside volume of contact block. Then, current commutated directly in ohmic load or through the second stage – electrically blowing conductor or thyristor key. As an arc-suppressing environment was used condensed insulating gas (sulfur hexafluoride SF_6 under the temperature of $t = 4 \text{ }^\circ\text{C}$, saturated vapors pressure $p = 1.8 \text{ MPa}$) and service water with conductivity $\sigma_0 = 2.8 \cdot 10^{-2} \text{ cm m}^{-1}$ ($t = 20 \text{ }^\circ\text{C}$, nitrogen supercharge N_2 , $p = 1.8 \text{ MPa}$). The speed of the fan-shape submerged stream, which forms during a cylindrical electrodes break reached $30\text{--}120 \text{ m s}^{-1}$ (depending on realizing power of commutation switch drive). On a fig. 2 is shown an arc shape in a submerged liquid stream. In such conditions, arc looks like a sail, which repeats a liquid stream shape. The arc thickness at front of a stream is δ approx. $3\text{--}4 \text{ mm}$, its

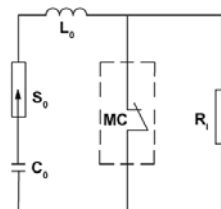


Fig. 1. Electrical circuit of the plant for high-current high-voltage commutation processes researches. C_0 – capacitive energy capacitor, $C_0 = 88 \text{ mF}$, S_0 – switching tube, L_0 – inductive energy storage, $L_0 = 0.3 \text{ mH}$, MC – mechanical commutator, R_1 – ohmic load, $R_1 = 0.1\text{--}0.8 \text{ } \Omega$, discharge cycle, $T = 32 \text{ ms}$

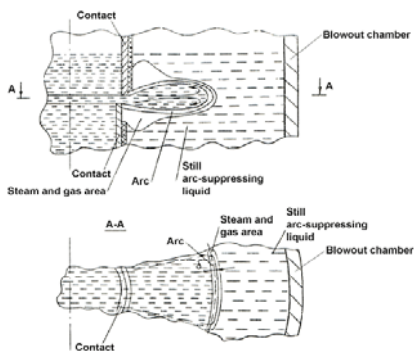


Fig. 2. Shape of the arc in a submerged liquid stream

azimutal width is b approx. 25 mm.

The current and voltage oscillograms of the electric and a shadow photos, made by streak cameras during its quenching and recovery of electric strength of interelectrode gap are given on the fig. 3 and 4.

On a final commutation phase the voltage on interelectrode gap have reached $U = 5\text{--}15$ kV (in various experiments). At the same time a liquid flow through the nozzle-like interelectrode gap has went on. The plant, which principal scheme is given on figure 5 was made for the electric

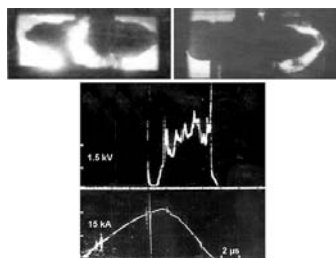


Fig. 3. Current and voltage oscillograms of the electric arc in a submerged service water stream. Shadow photos of the arc, made synchronously by two photochronographs. $t = 550$ μs – time, after the divergence of the contacts, stream speed – 50 m s^{-1} , frame exposure time – 25 μs

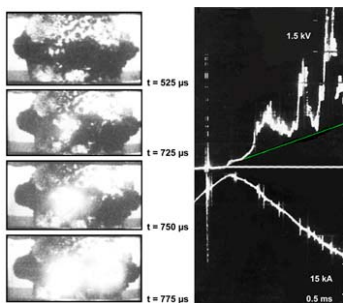


Fig. 4. High-current electric discharge submerged service water stream. t – time, after the divergence of the contacts, stream speed – 100 m s^{-1} , frame exposure time – 25 μs . Current and voltage oscillograms of the electric arc

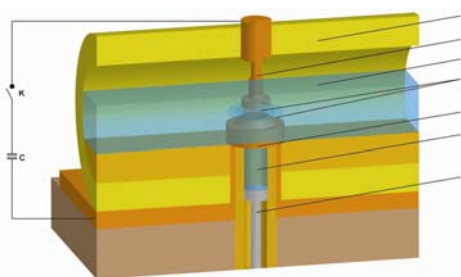


Fig. 5. Scheme of the experiment and model of the camera for water electrical breakdown study. 1 – camera, 2 – electrode, 3 – undisturbed liquid, 4 – dynamics of the disturbed zone in still liquid during the submerged stream flow, 5 – electrode, 6 – working cylinder, 7 – plunger

strength study of the interelectrode gap, which was situated in a still water and in conditions of submerged streams of various intensity. Studies on water decontamination were carried out at the same plant¹⁹.

Hollow vertically oriented cylindrical electrodes 2 and 5 made of copper M1 were placed at a fixed distance of $h = 5$ mm from each other in a cylindrical dielectric chamber 1 (Fig. 5) with diameter and length of 250 mm and 300 mm, respectively.

The external electrode diameter is $D = 50$ mm and the internal is $d = 47$ mm. The electric circuit consisted of a switch K and a capacitive energy capacitor with capacitance $C = 16$ μF was connected in parallel to the electrodes. Circuit inductivity has estimated basically by inductivity of leading-in cables and totaled $L_c = 5.7$ μH .

The resistance is approximately equal to a basic resistance of interelectrode gap R_c approx. = R_{EG0} . The period of circuit discharge under short-circuited interelectrode gap is $T = 60$ μs . Ends of the camera 1 were capped by flanges, made from quartz (on a figure 5 they are absent). Approximately 4.5 liters of water were flooded into the camera 1. During this, the interelectrode gap was not less than 50 mm lower than the water level. The liquid volume, which flooded the cavity of the bottom electrode 5 and working cylinder 6 was 54 cm^3 . During the plunger move, water was displaced from the hollow bottom electrode 5, and a fan-shape liquid stream in the interelectrode gap has occurred. Its velocity was kept at approximately the same level during the $t_s = 3$ ms. The voltage pulse $U = 7\text{--}20$ kV ($dU/dt = 1$ kV/ μ) was given with a delay of approx. 0.5–2 ms relatively to a plunger 7 start in order to have by that time a submerged water stream, flowing from an interelectrode gap (Fig. 5).

During the studies, were used the following liquids: distilled water with a conductivity of $\sigma_0 = 1.5 \cdot 10^{-4}$ S m^{-1} , service water with $\sigma_0 = 2.8 \cdot 10^{-2}$ S m^{-1} and a 5 % NaCl solution in water with $\sigma_0 = 1.7$ S m^{-1} . The basic resistance of was $R_{EG0} = 47 \cdot 10^3$ Ω , 250 Ω , 4.1 Ω respectively. The circuit wave impedance $\rho_c = \sqrt{L/C}$ approx. 0.59 Ω . If $R_{EG} > 2\rho_c$ – the capacitive capacitor discharge is aperiodic (prebreakdown stage). If $R_{EG} < 2\rho_c$ – the discharge is oscillatory (after the interelectrode gap breakdown).

The interelectrode gap breakdown expands not by a shortest distance between the electrodes, but by the stream envelope in the border area, which becomes an area of the

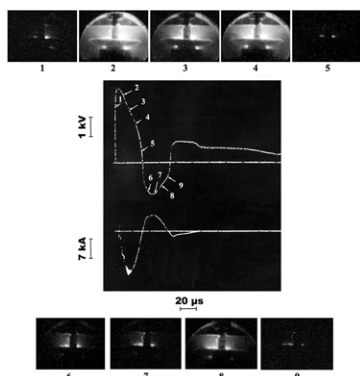


Fig. 6. Current and voltage oscillograms on interelectrode gap and self-light photos of the discharge in a submerged service water stream. Frame exposure time – 8 μ s

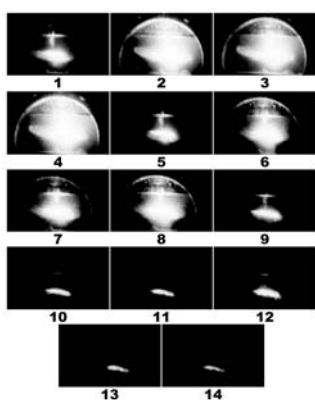


Fig. 7. Self-light photos of the discharge in a submerged service water stream. Frame exposure time – 8 μ s. Interval between the frames – 8 μ s

discharge ignition (Fig. 6, 7).

The disturbed area dynamics in still liquid during a submerged stream flow become well-visible (Fig. 6), when stream velocity reached 20–30 m s^{-1} , because of the light scattering on cavitation bubbles. The transmittance for a layer of thickness $Z = 1$ cm with optically heterogeneous inclusions (bubbles) was approximately equal to $K_{tr} = 5 \cdot 10^{-2}$. No spectral dependence of the transmittance was observed, which meant that the sizes of light-scattering heterogeneous inclusions should be $S > 10\lambda = 5.0 \mu\text{m}$ (λ – wavelength of the transmitted light). The volume density of these inclusions N was determined from the known relationship $K_{tr} = \exp(-2\pi NS^2Z)$, which, for $K_{tr} = 5 \cdot 10^{-2}$, gave $N \leq (10^6 - 10^7) \text{cm}^{-3}$. The bubbles appear behind the electrode edges, where the liquid pressure falls and the number of cavitation $K = 2(P_0 - P_{sat})/\rho v^2 \leq K_{cr}$ (ref.²⁰), where P_{sat} is the pressure of saturated vapor of liquid, K_{cr} corresponds to the initiation of cavitation and r is the liquid density, v is the flow velocity. Cavitation caverns initiate the release of the dissolved gas. The cavitation bubbles which size remains larger than the critical value of $S > S_{cr} = 1.4 \mu\text{m}$ during their compression can be saturated with gas and grow. On the other hand, the growth of bubbles in liquid

streams is limited by their crushing, which occurs at the Weber number $We > 10$. Therefore, in the zone of viscous turbulent mixing, bubbles with sizes $1.4 \mu\text{m} < S < 10 \mu\text{m}$ can accumulate, and a two-phase medium may form. Estimates indicate that the multiplication of electrons (avalanche) takes place primarily inside the gas bubbles. At the pressures of $P_0 = 0.1 - 2$ MPa, micro bubbles reach the sizes when the conditions of discharge self-maintenance near the minimum of the Paschen curve are fulfilled.

The discharge ignition starts already on the front of rising voltage pulse, $U = 1.5 - 3$ kV (Fig. 6). The breakdown channel leaves the region of a strong electric field between electrodes, where $E = 3 - 6$ kV cm^{-1} , and grows at an angle direction to the lines of external electric field. Apparently, the conditions are developed for strengthening local fields along the stream profiles, so that the ionization processes started at an early stage inside collapsing cavitation bubbles at the stream front simultaneously take place in a number of its boundary regions. The mean value of the electric field over the discharge length $l_d = 4 - 16$ cm is $E_m = 0.45 - 0.7$ kV cm^{-1} . The characteristic feature of the discharge in the presence of stream is that the current rises simultaneously with voltage. Therefore, when a thick grid of brightly glowing channels flashes at the stream leading edge, the magnitude of discharge current reaches several kilo amperes. The moment of electrodes shorting and the formation of a conducting channel along the stream profile corresponds to the turn point of the voltage curve. The breakdown voltage $U_b = 1.9 - 6$ kV between electrodes is always lower than the initial voltage of the capacitor $U_0 = 10 - 20$ kV. The current and voltage oscillograms show no kinks typical of breakdown in undisturbed water. The current varies sinusoidally with the period of $T = 60 \mu\text{s}$, similarly to the short-circuited electrode gap. The formation of a high-conductivity channel is completed within 5 μs after the start of voltage pulse, which is indicated by a sharp fall of the resistance in the electrode gap (Fig. 8). The $W = 200 - 250$ J cm^{-3} energy is consumed, which is two orders of magnitude less than in the case of ordinary linear discharge.

The electric discharges influence on water has significantly decreased its hardness. Disposition of sediments on the bottom of a camera corresponded to a horizontal projection of a stream at the moment of discharge ignition.

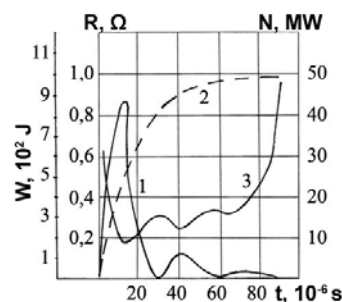


Fig. 8. Time changes of the discharge electric characteristics in a submerged service water stream. For the zero scale mark is taken a moment, when a voltage pulse was given on interelectrode gap. Stream length $l_s = 3.5$ cm, discharge length $l_d = 8.6$ cm. 1 – power, 2 – energy, 3 – resistance

Measurements showed that the energy of plasma channel radiation is almost proportional to that introduced into the discharge and equals approx. 80 % of stored energy. As it was determined with the help of the filters, near the wave-length $\lambda = 210$ nm the spectral density of radiation has a maximum, and then with the increase of wave-length it is smoothly decreases.

The formation of the glow-ing shell several centimeters wide is seen to take place at the mean velocity V approx. $5 \cdot 10^4$ m s⁻¹. The greatest intensity of discharge glow is close in time to the maxima of discharge current. The pressure in the plasma channel, measured by a piezoelectric pickup, is governed by the stream velocity and is close to the calculated stagnation pressure of the stream $P = \rho v^2/2 + P_0$.

When a fall in the current amplitude during the second period is appreciable, the discharge dies out over the time t approx. 10 μ s, although the voltage up to approx. 1 kV remains across the capacitor (Fig. 6).

In a liquid in an external strong electric field, there can be a formation of discharge channels (zones of ionization), extending on a direction of a field. It is known, that directly at the metal surface, contacting to water, the dense bed of positive charged ions of water and an impurity with concentration of ions of 10^{21} cm⁻³ (ref.²¹) carries out. In other words, contact electrode – water acts as a generator of ions.

In case of movement of a liquid through an interelectrode space, a contact layer of ions continuously carries away by the jet and takes away from an interelectrode space. We assume, that at the flow of a jet, from ions ionic drop-alike structures which under action of electrostatic repulsion collect on periphery of the disturbed area (area of mixture) are formed. Cavitation phenomena can promote formation of such “drops”, that leads the occurrence on periphery of a jet a thin layer of drop-alike structures (ions of water, an impurity, cavitation bubbles) and formation of area of the increased conductivity. It causes the fast formation of extended discharge channels and development of electric breakdown on bending around area of viscous hashing of the submerged liquid stream. With the help of such model it is possible to try to explain the decrease of discharge ionization voltage at the presence of a liquid jet and formation of the film discharge with a large surface of radiation.

It is known²² that bactericidal effect of UV radiation depends on: wavelength, intensity and exposure. Also, it is quite selective. Radiation with the same characteristics can be fatal for some microorganisms, but at the same time it can only depress the others. Intensity, which is lower than certain level can even stimulate the growth of bacteria. That's why for the effective liquid decontamination, characteristics of device should optimal for each specific task. In particular, in ref.²³ has underlined, that for preliminary estimate of bactericidal effect of discharge, should be taken into account, not only the energy, stored in capacitive energy storage, but also correctly choose the voltage, capacity and interelectrode gap. It is recommended to increase the number of pulses, capacity of capacitor and interelectrode gap. Voltage should be medium. In device¹⁹ discharge in a submerged liquid stream allows accomplishing all these requirements.

For the discharge in a submerged stream of service water breakdown voltage is U_b approx. 4.5 kV. Size of the interelectrode gap is not important here, because the length of the

discharge l_d approx. 10 cm \gg h (interelectrode gap). Also, during a shift to a greater capacity of capacitors there is no shock wave occurred, but radiating surface is increasing. With a help of iodineometric method was also detected an ozone formation, which is one of the most powerful and environmentally friendly antiseptics.

Extra power inputs, connected with initiation of high-speed liquid stream and occurrence electromechanical block are the main disadvantage of such device.

2. Application of electric discharge in still liquid for initiation of submerged stream and decontamination of environment.

On the figure 10 are shown current and voltage oscillograms and self-light photos of the discharge in a still service water. The experimentally observed breakdown and discharge characteristics in undisturbed water are typical of breakdown in water with the initial conductivity $\sigma = 1-10^{-3}$ S m⁻¹ (ref.^{1,2,7}). Thus, a relatively long pre-breakdown stage $t_{b,d}$ approx. $10^{-5}-10^{-3}$ s takes place when actually constant pre-breakdown resistive current $I_{p,b} = 150-450$ A flows through the electrode gap; the current value is dictated by the initial water conductivity, and the voltage falls slowly.

At the beginning of the prebreakdown stage on an edge of the electrode 5, which was under ground potential (Fig. 5, 10 (frame 1) and 11 (frames 3 and 4) has occurred a glow in a point, randomly placed on its circle. It has a shape of diffuse radiating sphere, which has expanded in a radial direction with velocity of 100–150 m s⁻¹.

Gradually, the glow has deformed in a direction of cathode 2 and a central area of the glow become brighter. At the moment when glowing area has reached the opposite electrode, an interelectrode breakdown has taken place (Fig. 10 frame 2, Fig. 11 frame 5).

During breakdown, the current, I , sharply increases with time t (dI/dt approx. $6 \cdot 10^8$ A s⁻¹) and the discharge transits to the oscillation mode with a period of $T = 60$ μ s.

The discharge is localized in interelectrode gap and shapes a hemisphere $r_d \sim h$ at the arc stage (Fig. 12).

Electric discharge causes a shock wave, which in turn, initiates converging wave of unloading after its exit on a free liquid surface. It leads to a cavitation bubbles formation in

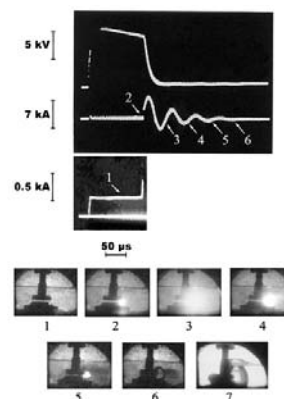


Fig. 10. Current and voltage oscillograms on interelectrode gap and self-light photos of the discharge in a still service water. Frame exposure time – 25 μ s. Interval between frames 6 and 7 – 375 μ s. Light filter density at frame 7 is two times less, then at the others



Fig. 11. Shadow photos of the discharge in a still service water. Frame exposure time – 25 μ s. Time interval between frames 1 – 7, 24 – 33 is 50 μ s. Between the others – 25 μ s. Frames 1 – 7, 9, 11, 13, 15, 17, 19, 21 and 23 were taken with a help of blue light filter

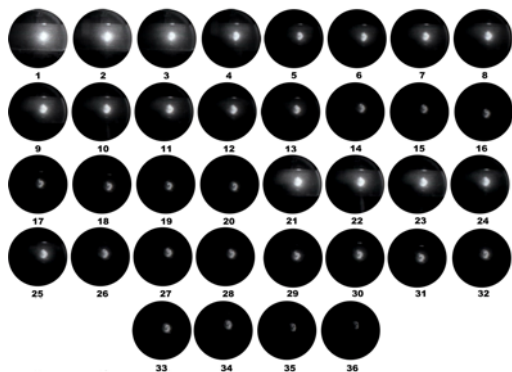


Fig. 12. Self-light photos of the discharge in a still service water. Frame exposure time – 4 μ s. Time interval between frames – 8 μ s

near-surface liquid layer (Fig. 11, frame 7). These bubbles are then clapping under the atmospheric pressure, which stimulates further liquid decontamination in volume, which considerably exceeds the volume of liquid layer that directly surrounds the electric discharge channel. After the complete run down of capacitive energy storage, electric discharge quenches and on its place appears a steam and gas bubble, which expands in direction of free liquid surface (Fig. 10, frame 6). It causes a bell-shaped blowout on liquid surface, like an explosion at a small depth. It increases an amount of air, dissolved in liquid. Therefore, it stimulates cavitation processes and leads to an ozone formation from the air oxygen under UV radiation of electric discharge. Electric discharge in liquid is following by optical radiation, shock wave generation, pulsations of steam and gas bubble at postbreakdown period and other factors, which are fatal for pathogenic microorganisms. Simultaneously with steam and gas bubble expansion, starts submerged liquid stream outflow in interelectrode gap (Fig. 10, frame 7 and Fig. 13).

On the fig. 14 is presented longitudinal shear of one of the possible liquid decontamination constructions.

On a platform-float 1, made as a disc with a hole in centre in alignment are placed with a help of holders 2 and 3

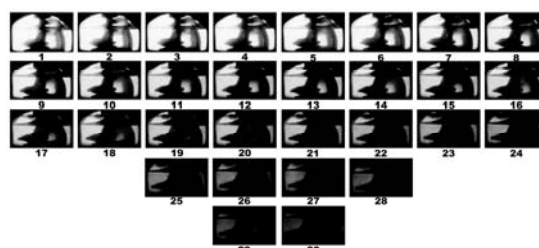


Fig. 13. Shadow photos of the discharge in still service water. Exposure time – 25 μ s. Interval between frames – 50 μ s. Frame 1 was made 1600 μ s after the moment of pulse voltage application on the electrodes

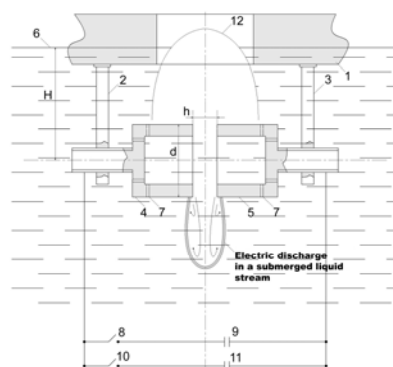


Fig. 14. Device for liquid decontamination

hollow cylindrical electrodes 4 and 5. Their common axis subtends with a free liquid surface 6 an angle of $\varphi = 0^\circ$. Angle φ can be changed from 0° to 90° with a help of holders 2 and 3 or other motion block. Electrode cavities 4 and 5 are filled with liquid. Electric circuit, which consists from commutator 8 and capacitive energy storage 9 and electric circuit, which consists from commutator 10 and capacitive energy storage 11 are parallel connected with electrodes 4 and 5. Capacitive energy storages 9 and 11 are charging. Then capacitive energy storage 9 is connecting with a help of commutator 8 to electrodes 4 and 5. Decontamination, connected with bactericidal effect electric discharge occurs. Also, submerged stream is forming. When common axis of hollow cylindrical electrodes 4 and 5 subtends with a liquid surface an angle of $\varphi = 0^\circ$, stream axis independently from a place of circular interelectrode gap where discharge have occurred, is always perpendicular to a free liquid surface and turned into opposite part. On the fig. 15 are shown the electrodes. We can see prints of a series of discharges in submerged liquid streams on the nozzles made from plexiglass. These electrodes were placed in camera according to a fig. 14, but only one of the electrodes was hollow.

If $\varphi = 90^\circ$ (Fig. 5, fig. 13), direction of the stream flow is diametrically opposite to a place of circular interelectrode gap where discharge have occurred. That's why it is possible to use the stream for a mechanical cleaning of surfaces, such as swimming pool walls, or flushing of medical instrument, placed in wire containers, which were installed along the



Fig. 15. Electrodes with a nozzles made from plexiglass

stream flow. When the stream length reaches an optimal size, capacitive energy storage 11 is connecting with a help of commutator 10 to electrodes 4 and 5. In the presence of liquid stream, discharge ionization voltage decrease and discharge with a large surface of radiation formation is taken place. Processes of liquid flow and filling of the electrode cavities 4 and 5 with a liquid through the holes 7 and the interelectrode gap area, which are abut on stream flow sector are simultaneous. Capacitive energy storage 11 runs down and the discharge is quenching. Capacitive energy storages 9 and 11 are charging. During the charging complete recovery of electric strength of interelectrode gap has happen. After the end of charging the device is ready for the next operating cycle. Such devices can work with the frequency from 1 to 100 Hz.

Conclusion

For the complete water decontamination by means of discharges in still liquid and electric discharges with a large surface of radiation, formed in a zone of viscous mixing of a submerged stream has consumed an energy W approx. 0.2 MJ m^{-3} (according to a test, made by generally accepted Koch method). This method has more effective and widely targeted effect because of cavitation phenomena initiation in a large liquid volume and application of two types of electric discharges with different characteristics (for example, emission wavelength) during one operating cycle.

Studies have shown a possibility in principle and reasonability of application of this methodology for effective pathogenic microorganism decontamination, including their stable spore forms.

Supported by Russian Foundation for Basic Research under Grant 08-02-08563-z.

REFERENCES

1. Naugolnikh K. A., Roj N. A.: Electrical discharges in water. M.: Nauka, 1971. – 155.
2. Ushakov V. J., Klimkin V. F., Korabeinikov S. M., Lopatin V. V.: The discharge during a pulse voltage. Tomsk: NTL, 2005. – 488.
3. Schoenbach Karl H., Xiao Shu, Kolb Juergen F., Joshi Ravindra P.: *Proc. XXVIII-th International Conference*

on Phenomena in Ionized Gases. ICPIG 2007. Prague, Czech Republic, July 15-20, 2007. P. 57.

4. Masayuki Sato: *Plasma Sources Sci. Technol.* 17, 024021 (7pp) (2008).
5. Burakov V., Savastenko N., Tarasenko N., Misakov P., Nevar A.: *Proc. 3rd International Workshop on Microplasmas. IWM 2006. Greifswald, Germany. May 9 – 11, 2006.* P. 74.
6. Boguslavsky L. Z., Kuskova N. I., Smalko A. A., Zubenko A. A.: *Proc. The 13-th International scientific school-seminar (August 21-st – 25-th 2007).* Physics of pulse discharges in condensed matters. Nikolaev: 2007. P. 21–24.
7. Guly G. A., Malushevsky P. P.: High-voltage electrical discharge in power pulse systems. Kiev: Naukova Dumka, 1977. P. 5.
8. Zhuk E. G.: *Electrical Электронная treatment of materials.* 1978. № 4. P. 80.
9. Jutkin L. A., Goltsova L. I.: Way of purification of drinkable and waste waters. Certificate of authorship USSR № 196632. Bulletin of inventions 1983. № 18. P. 211.
10. Bogomaz A. A., Gorjachev V. L., Remenni A. S., Rutberg F. G.: Letters to ZhTF. 1991. part 17. Issue 12. P. 65.
11. Vilkov K. V., Grigorjev A. L., Nagel U. A., Uvarova I. V.: Decontamination effect of the powerful electric discharge in water. II. Experimental results. Letters to ZhTF. 2004. part 30. Issue. 7. P. 48 – 53.
12. Vishnevitsky I. I., Rjazanov N. D., Semkin B. V.: Plant for water decontamination with a help of electric discharges. Certificate of authorship USSR № 861332. Bulletin of inventions 1981. № 33. P. 110.
13. Blokhin V. I., Visikailo F. I., Dmitriev K. I., Efremov N. M.: TVT 1999. part 37. № 6. P. 998.
14. Grekhov I. V., Korotkov S. V., Andreev A. G.: PTE 1997. № 5. P. 128.
15. Azizov E. A., Godonyuk V. A., Emel'yanov A. I., Nastoyashchii A. F.: "Effect of High-Velocity Breakdown Characteristics and Formation of Electrical Discharge in Water", *High Temperature*, vol. 32, N 5, pp.643–646, 1994.
16. Azizov E. A., Godonyuk V. A., Emel'yanov A. I., Nastoyashchii A. F.: "Method of initiating and forming electric discharge" (in Russian), Patent RF № 1828353, *Byulleten' izobreteniy* N 32, P. 282, 1995.
17. Azizov E. A., Emel'yanov A. I., Yagnov V. A.: *IEEE Trans. Dielectrics Electrical Insulation* 14, 1291 (2007).
18. Azizov E. A., Godonyuk V. A., Emel'yanov A. I.: *Proc. of The 3-rd all-USSR conference on engineering problems of thermonuclear reactors. Leningrad, 1984.* Part 3. P. 119–126.
19. Azizov E. A., Emel'yanov A. I., Yagnov V. A.: *Appl. Phys.* 2003. № 2. P. 26–31. Available: <http://www.vimi.ru/applphys/2003/2/f25.htm>
20. Pearsall I. S.: *Cavitation.* Mills&Boon Limited, London 1972.
21. Arthur W. Adamson: *Physical Chemistry of Surfaces,* NY 1976.
22. Galanin N.F.: *Medicine* 1969.
23. Bubentsov V. I., Zhuk E. G., Jakunin U. V.: *Electron. Treatment Mater.* 5 (1983).

VOC DECOMPOSITION IN SURFACE DISCHARGE

FRANTIŠEK KRČMA, JANA VYHNALÍKOVÁ,
LUCIE POLÁCHOVÁ, HANA GROSSMANNOVÁ
and ZDENKA STARÁ

*Institute of Physical and Applied Chemistry, Faculty of Chemistry, Brno University of Technology, Purkyňova 118, Brno 612 00, Czech Republic
krcma@fch.vutbr.cz*

Introduction

VOCs (volatile organic compounds) are organic chemical compounds that have vapor pressures under normal conditions high enough to significantly evaporate and enter the atmosphere. They are sometimes accidentally released from the industrial processes into the environment, where they can damage soil and groundwater. Vapors of VOCs escaping into the air contribute significantly to the air pollution (e.g. they cause photochemical smog and also contribute to the global warming). In recent years, their influence on the quality of indoor environment has started to be a serious task, too. Common artificial sources of VOCs include paint thinners, wood preservatives or cleaning solvents. Regarding the medical risks, it is known that many VOCs are toxic, several of them are known as human carcinogens¹.

Conventional techniques for the abatement of VOCs, such as thermal and catalytic oxidation, are able to completely decompose the VOCs, but they suffer from the low energy efficiency given by the high operating temperature. The biological degradability of VOCs is also very problematic due to low concentration of VOCs in the gas phase. This degradation way is also impossible for many VOCs based on aromatic ring that could not be biologically destroyed. Technologies based on non-thermal plasmas could offer an alternative and they are capable to remove various pollutants in the gas phase². The plasma decomposition process of VOC is rather complex and the hydrocarbons are attacked in several ways. In the plasma reactor, the hydrocarbons are partly transformed into oxygenated compounds and into CO and CO₂. Unfortunately, undesirable toxic by-products can be formed.

Various non-thermal atmospheric plasma sources have been studied with respect to VOC destruction^{2–4}. This study presents the first results obtained using recently developed surface discharge that is nowadays widely used mainly in the surface treatment processes⁵.

Experimental set up

The schematic draw of the experimental device is shown in Fig. 1. The discharge reactor consisted of a surface discharge electrode 10×10 cm² connected to the HF power supply. The Al₂O₃ plate in the distance of 2 mm above the electrode was installed. The reactor side walls were made from Teflon with one fused silica window oriented in parallel to the gas flow through the reactor. The gas inlet into the reactor was realized by the system of equidistant holes (distance of

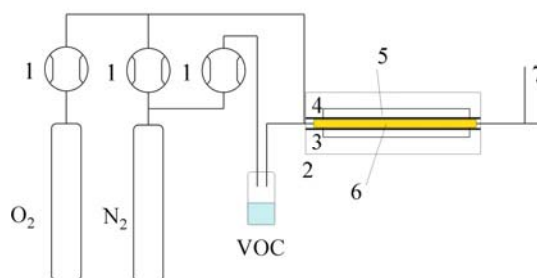


Fig. 1. Scheme of the experimental set up; 1 – mass flow controllers; 2 – Teflon discharge reactor; 3 – surface discharge electrode; 4 – Al₂O₃ plate; 5 – Quartz window; 6 – discharge; 7 – sampling point for the chemical analyzes

5 mm, i.d. 1 mm); the outlet was possible through the open electrode gap on the opposite side. This system guaranteed nearly homogeneous flow of the reacting gas mixture through the discharge.

The synthetic dry air was used as the carrier gas and it was enriched by the VOC (hexane, cyclohexane or xylen) just in front of the reactor. VOC concentration in the reactor was constant at about 1 %.

The exhaust gas analyses were carried out by three different ways. The simple gas analyzer Testo 350 XL was used for the detection of low molecular weight discharge products as CO, NO₂, NO, H₂, etc. The analyses of high molecular weight products were made by *ex-situ* GC-MS. Samples of exhaust gas for these analyses were taken by active carbon sorption tubes or by solid phase micro extraction (SPME) technique using Divinylbenzene/CarboxenTM/polydimethylsiloxane (DVB/CARTM/PDMS) fibers⁶. The GC-MS analysis was done using spectrometer GC 8000 with the quadrupole mass spectrometer MS TRIO 1000 (both made by Fision Instruments Ltd.). Quartz capillary (30 m long) with polydimethylsiloxane stationary phase (0.25 μm) was used for the separation.

The optical emission spectroscopy using Jobin Yvon TRIAX 550 spectrometer was applied to characterize the surface discharge plasma. The molecular bands of nitrogen (1st and 2nd positive and 1st negative systems) were observed with high intensities, some bands of CO were recognized, too. The rotational temperature of about (850 ± 100) K was calculated from the rotational structure of nitrogen second positive 0–2 band. Vibrational temperature of about (1900 ± 150) K was calculated using nitrogen second positive –2 sequence bands. Both rotational and vibrational temperatures were more or less independent on the VOC compound and also the dependence on discharge power was negligible. The discharge reactor construction allowed also partial space resolution of spectroscopic observations. However, no significant changes in the plasma parameters were determined along the whole reactor.

Results and discussion

The results of the laboratory experiments are presented in this part. The implicit concentrations of low molecular inorganic products as CO, NO₂, NO or H₂ and relative con-

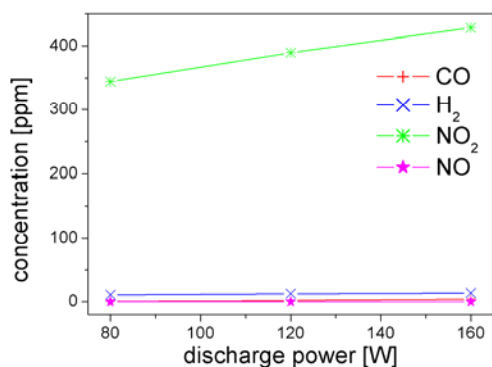


Fig. 2. Concentrations of low molecular products generated by surface discharge in synthetic air without VOC

concentrations of combustion high molecular products of hexane, cyclohexane or xylene are displayed. The resulting concentrations depended on energy input and gas composition as it is shown on following figures and tables. Only nitrogen dioxide was generated in the discharge without VOC and its concentration was directly proportional to the discharge power. Fig. 3–5 show the results obtained during the selected VOCs destruction. The concentrations of CO and H₂ resulting from combustion were again directly proportional to the applied discharge power and their concentrations depended on the VOC. NO₂ was generated in the significant amount in all cases; in contrary, no measurable value of NO species was observed.

According to the results and the mechanism of VOC oxidation studied in the literature⁷, benzene rings of cyclohexane and xylene in the collisions with active species (mainly O and OH radicals) are firstly oxidized to dihydroxybenzenes and subsequently to quinones. Both continue to yield ring-cleavage products (i.e. aldehydes and carboxylic acid groups). Finally, carboxylic acids such as formic and acetic acids are mineralized to CO and CO₂. Though mixture of nitrogen and

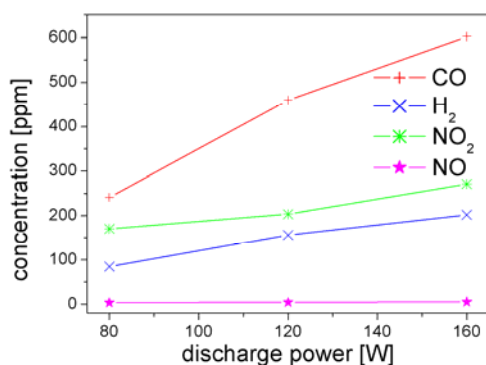


Fig. 3. Concentrations of low molecular products generated by surface discharge in synthetic air with hexane

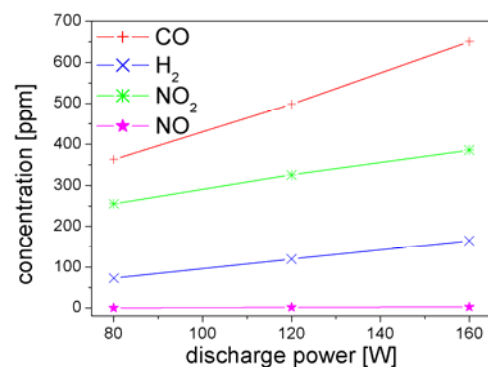


Fig. 4. Concentrations of low molecular products generated by surface discharge in synthetic air with cyclohexane

oxygen are used as the carrier gas, no nitrogen compounds were detected in the treated gas samples.

Electrons produced in surface discharge in atmospheric air initiate gas phase reactions to produce remarkable quantity of ozone and nitrogen oxides. As it can be seen from Fig. 2, production of significant amount of NO₂ is higher when input power is increased. Destruction and resulting very low concentration of NO is primarily due to the oxidative properties of ozone molecules. The influence of an admixture of a VOC on the production of NO₂ was studied as well. Fig. 3–5 show the behavior of NO₂ production for three different admixtures. Xylene admixture leads to an increase in the NO₂ concentration, on the other hand cyclohexane and hexane admixtures lead to slight decrease with the increasing discharge power. Therefore we can't conclude the existence of negative or positive effect of the VOC admixture to the NO₂ formation. The large occurrence of CO is detected during the plasma treatment of VOC as well. Increasing energy input is leading to higher efficiency of VOC decomposition resulting in higher concentration of CO, which is up to 700 ppm for treated amount of VOC (initial concentration of about 1 %).

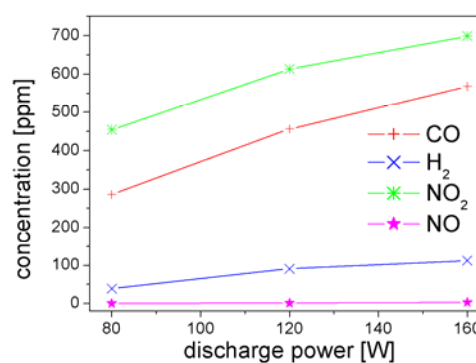


Fig. 5. Concentrations of low molecular products generated by surface discharge in synthetic air with xylene

Table I

Chromatographic peak areas of selected products identified in the exhaust gas during the decomposition of hexane at two different discharge powers and ratio of peak areas A_{160}/A_{120}

Specie	120 W	160 W	<i>F</i>
Nox	9110000	8480000	0.93
Hexane	3550000	4430000	1.25
2,5-dihydro-2,5-dimethyl-furanone	1930000	1890000	0.98
2-hexene	1180000	253000	0.21
2-hexanol	726000	785000	1.08
2-pentanone	710000	638000	0.90
2-hexanone	668000	692000	1.04
3-methyl-2,4-pentadione	668000	663000	0.99
2-hexene-1-ol	456000	434000	0.95

Table II

Chromatographic peak areas of selected products identified in the exhaust gas during the decomposition of cyclohexane at two different discharge powers and ratio of peak areas A_{160}/A_{80}

Specie	80 W	160 W	<i>F</i>
Nox	9750000	2800000	0.29
2-hydroxy-cyclohexanone	2640000	238000	0.09
3-hydroxy-cyclohexanone	607000	663000	1.09
1,5-pentandiol	470000	62000	0.13
2-cyclohexene-1-one	505000	264000	0.52
1,6-hexandiol	323000	113000	0.35
1,2-cyclohexandiol	182000	199000	1.09
cyclopentandiol	56000	56000	1.01

Table III

Chromatographic peak areas of selected products identified in the exhaust gas during the decomposition of xylene at two different discharge powers and ratio of peak areas A_{160}/A_{80}

Specie	80 W	160 W	<i>F</i>
NOx	11900000	8600000	0.73
1,3-dimethylbenzene	21300000	7850000	0.37
2-hexanol	9660000	559000	0.06
ethylbenzene	6290000	2720000	0.43
4-methylbenzaldehyde	996000	627000	0.63
benzaldehyde	694000	465000	0.67
methylbenzene	658000	340000	0.52
cyclohexanol	449000	317000	0.71

Tables I–III provide a summary of the most significant high molecular weight combustion products analyzed by GC/MS system. Many different especially oxygenated compounds

originated from the added VOC were detected. When oxygen reacts with nitrogen it is possible to form different nitrogen oxides: N_2O , NO , N_2O_3 , NO_2 , N_2O_4 , N_2O_5 . The summation of all of these oxides is marked as NO_x in the tables. Third columns show the correlation factor *F* between concentrations of products at the highest and the lowest value of input power. It can be clearly seen that this factor is mostly lower than 1. This means that higher input energy would lead to the shift in the product distribution towards low molecular inorganic compounds.

Influence of oxygen content

The oxidation properties of plasma are related to the occurrence of highly reactive species. Of course, generation of these species is highly dependent on the gas composition. In order to investigate the effect of different synthetic gases on the decomposition of VOC, oxygen and nitrogen can be used separately as a carrier gases. Some experiments were carried out when oxygen was added in the gas stream up to 30%. The examples of chromatograms obtained at these conditions are shown in Figs. 6–9. The results presented in Tables IV–VI show that the oxygen addition led to a slight increase of oxygen compounds generation, only.

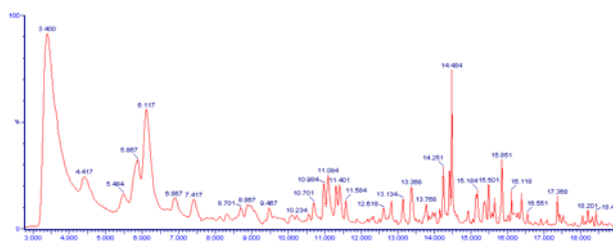


Fig. 6. Chromatogram of exhaust gas sampled by SPME technique during hexane decomposition in nitrogen with 30% of oxygen at discharge power of 160 W

Table IV

Comparison of chromatographic peak areas of selected compounds identified in the exhaust gas during the hexane decomposition at two different oxygen concentrations at discharge power of 160 W

Peak time [s]	Specie	10 % O_2	30 % O_2
3.3	NOx	10200000	16000000
4.3	2-hexanol	2350000	2880000
6.867	2-hexene	638000	783000
8.867	2,5-dihydro-2,5-dimethyl-furan	610000	746000
9.467	4-methyl-3-pentanal	446000	632000
11.084	2-hexanone	490000	588000
13.368	1,3-dimethylbenzene	202000	455000
14.484	2,5-hexanedione	1310000	1220000
16.385	3-methylpentanal	266000	192000
17.368	5-ethylidihydro-2(3H) furanone	212000	173000

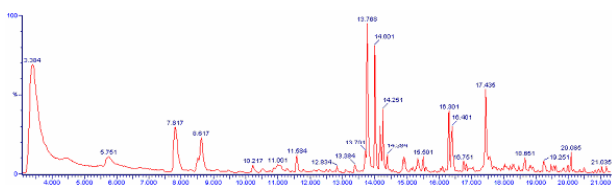


Fig. 7. Chromatogram of exhaust gas sampled by SPME technique during cyclohexane decomposition in nitrogen with 30 % of oxygen at discharge power of 160 W

Conclusion

This article gave some results relevant to the surface discharge environmental application. The objects of research were hexane, cyclohexane and xylene decomposition at the atmospheric pressure. The dependences of low molecular products concentration versus discharge power were studied. GC/MS analyses allowed the better understanding of high molecular products formation.

The role of oxygen content in the carrier gas for the VOC removal process was also investigated. The presented result indicated that the most of carbon in the decomposition of VOC was converted to carbon oxides rather than to hydrocarbons. The main problem of VOC removal in a plasma system is the by-product formation. Unfortunately, the surface discharge plasma generates high concentrations of carbon monoxide and nitrogen dioxide. This main disadvantage can be successfully (but not completely) solved by the additional application of catalytic system.

Table V

Comparison of chromatographic peak areas of selected compounds identified in the exhaust gas during the cyclohexane decomposition at two different oxygen concentrations at discharge power of 160 W

Peak time [s]	Specie	10 % O ₂	30 % O ₂
3.367	NOx	14600000	15100000
5.734	2-butenal	1430000	996000
6.734	2-hexanol	390000	319000
7.817	cyclohexane	2150000	2030000
8.617	3-methylbutanal	1470000	1340000
13.768	cyclohexanol	2650000	2160000
14.001	2-methyl-cyclopentanol	1950000	1520000
16.301	2-hydroxy-cyclohexanone	838000	728000
17.435	dihydro-4-methyl-2(3H)furanone	1570000	1350000
18.651	3-hydroxy-cyclohexanone	298000	266000
19.668	cyclobutanol	365000	586000

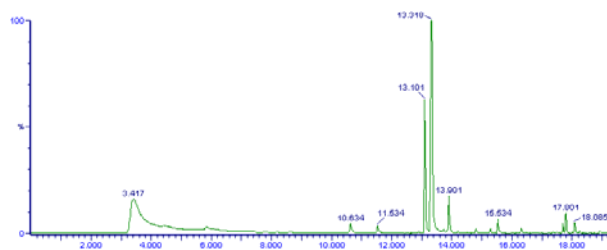


Fig. 8. Chromatogram of exhaust gas sampled by SPME technique during xylene decomposition in nitrogen with 30 % of oxygen at discharge power of 160 W

Table VI

Comparison of chromatographic peak areas of selected compounds identified in the exhaust gas during the xylene decomposition at two different oxygen concentrations at discharge power of 160 W

Peak time [s]	Specie	10 % O ₂	30 % O ₂
3.417	NOx	11300000	13200000
5.851	2-hexanol	2100000	2580000
10.634	methylbenzene	461000	438000
13.101	ethylbenzene	3490000	3410000
13.318	1,3-dimethylbenzene	10500000	10500000
13.901	1,4-dimethylbenzene	954000	1000000
14.801	dihydro-3-methyl-2,5-furandione	180000	186000
15.534	benzaldehyde	433000	393000
17.801	4-methylbenzaldehyde	454000	451000
19.568	ethylbenzaldehyde	37000	68800
19.935	3-fenyl-2-propenal	490000	356000

This work was supported by the Czech Ministry of Education, Youth and Sports, research project MSM 0021630501 and by the Czech Science Foundation, project No. 202/03/H162.

REFERENCES

- Jones S. P.: *Atm. Envir.* 33, 4533 (1999).
- Kim H. H.: *Plasma Proces. Polymers* 2, 91 (2004).
- Mutaf-Yardimci Ö., Savaliev A., Fridman A., Kennedy L. A.: *J. Appl. Phys.* 87, 1632 (2000).
- Fridman A., Gutsol A., Cho Y. I.: *Adv. Heat Transf.* 40, 1 (2007).
- Šimor M., Ráhel' J., Černák M., Imahori Y., Štefečka M., Kando M.: *Surf. Coat. Technol.* 172, 1 (2003).
- Grossmannová H., Cigánek M., Krčma F.: *J. Phys.: Conf. Series* 63, Article No. 012011 (2007).
- Yan J., Du Ch., Li X., Sun X., Ni M., Cen K, Cheron B.: *Plasma Sources Sci. Technol.* 14, 637 (2005).

ATMOSPHERIC PRESSURE MW PLASMA FOR WASTE CARBON TREATMENT

L. LEŠTINSKÁ^{a*}, V. MARTIŠOVIČ^a,
M. ZAHORAN^b, and Z. MACHALA^a

^a Division of Environmental Physics, Department of Astronomy, Earth Physics and Meteorology, ^b Department of Experimental Physics, Comenius University, Mlynská dolina, 842 48 Bratislava, Slovakia
lestinska@gmail.com

Introduction

The disposal of waste tyres represents a great problem throughout the world, as it is causing many environmental and economic problems in most countries. Pyrolysis seems to be a good way of waste tyre disposal, because it does not only reduce the volume of the waste significantly, but also allows recovering of valuable materials¹. Additional treatment is sometimes needed to improve their qualities^{2–3}. In our case, the MW plasma beneficiation of the pyrolytic carbon is applied to get rid of the volatile components causing its bad smell, and to make it reusable for other processes, e.g. it could be used as a colouring agent for plastic materials or as an adsorbent.

We use Litmas Red MW torch (2.45 GHz, 3 kW), which is able to generate plasma in a state close to Local Thermodynamic Equilibrium (LTE) in temperature range of 1000–5000 K at atmospheric pressure in various gases. In our previous works^{4,5} we investigated the basic characteristics of atmospheric MW nitrogen plasma torch. Here we present the first tests of its application for thermal treatment of waste carbon.

Experimental setup

Atmospheric pressure MW plasma is generated by a Litmas Red plasma torch (2.45 GHz, 3 kW) in N₂. Experimental setup and the basic torch characteristics are described in more detail in ref.⁴.

Contrary to the typical MW torch systems, in our case the gas is inserted downstream and tangentially through the two holes of the nozzle into the cylindrical plasma chamber, made of Al₂O₃. This is causing the swirl flow in the cylinder and generated swirling plasma is consequently blown out upstream through the central orifice of the nozzle. Blown-out plasma is then analyzed by optical emission spectroscopy. We identified emission of N₂ molecules, N₂⁺ ions and NO and CN radicals in the emission spectra (Fig. 1). CN comes from a minor carbon-containing impurity from the feeding gas, which reacts with N₂ and forms CN radical.

Generated MW plasma was used for waste carbon treatment. In the first approach, the carbon sample was placed on a stainless steel plate in the plasma plume about 1 cm above the nozzle (Fig. 2).

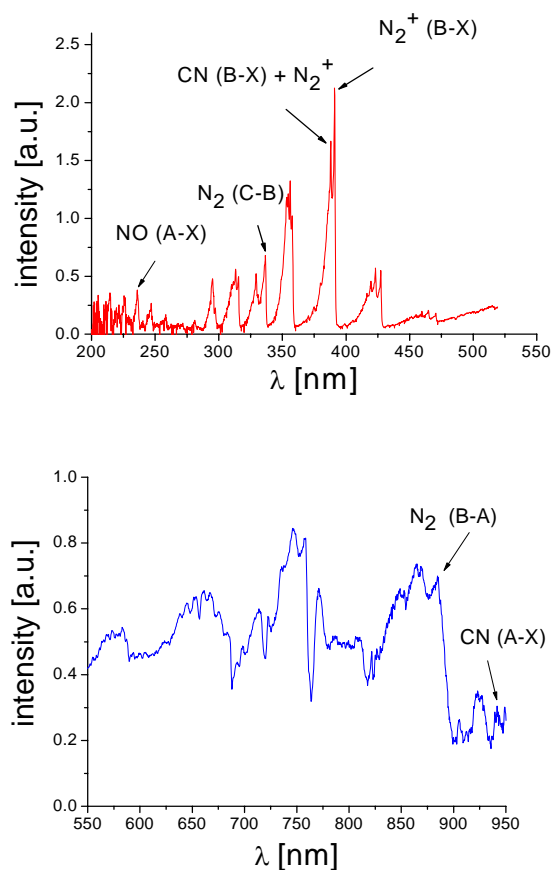


Fig. 1. UV (up) and visible (down) emission spectra of generated nitrogen plasma

Approximate temperature of the plate, measured by a pyrometer, was 1500 K. The system was closed and exhausted because of possibly dangerous gases being emitted from polluted carbon samples. The carbon samples were heated for 5 or 10 minutes in nitrogen plasma of 13 l min⁻¹ flow rate and 1.4 kW generator power. After plasma being switched off, the sample was cooled at a low N₂ flow 2 l min⁻¹ to avoid oxidation. The diagnostics of carbon samples was performed directly by a scanning electron microscope (SEM) Tescan TS5136MM equipped with wavelength dispersive X-ray (WDX) INCA Wave analyzer, and on KBr pellets analyzed by Fourier-transform infrared (FTIR) spectrometer Perkin Elmer Spectrum BX. KBr powder to the sample ratio was 1:100.

In the second approach (Fig. 3), which is still being developed, the waste carbon samples are continuously inserted directly into the plasma chamber, where the temperature is considerably higher compared to the first approach. The plasma temperature, determined as the rotational temperature by comparing experimental and simulated (LIFBASE⁶) CN spectra, was 4500 ± 250 K and 1.78 kW magnetron power and 4000 ± 250 K at 1.46 kW, both at 15 l min⁻¹ gas flow rate⁴.

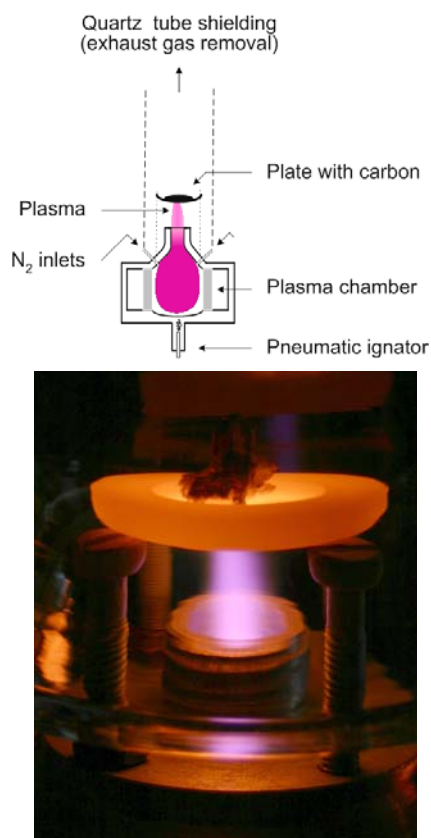


Fig. 2. Treatment of carbon samples on the supporting stainless steel plate

In this arrangement, the treated carbon is also in a direct contact with radicals and active species generated in the plasma. The whole system, including the plasma plume, is turned upside down to enable the collection of the treated carbon powder below the plasma chamber. The carbon collection chamber is water-cooled. It also enables on-line emission spectroscopic analysis, which is performed by portable spectroscope Ocean Optics SD 2000 through the quartz window.

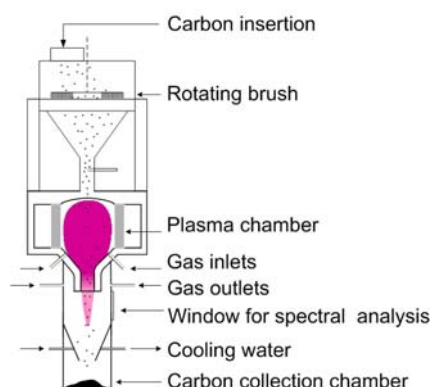


Fig. 3. Treatment of carbon samples passing through the plasma chamber

Results and discussion

After plasma heating of the carbon samples, we first observed that the sample did not smell anymore and its mass decreased (by 27 % for 5 min and 48 % for 10 min heating). We assume that some volatile substances, most likely aliphatic and aromatic hydrocarbons and their $-OH$ and ether derivatives were released from the carbon, which was confirmed by FTIR spectra (Fig. 4). An apparent reduction of CH_2 , $C-O-C$, $-OH$, and aromatic $C-H$ functional groups was observed. On the other hand, new compounds were created. We assume them to be metal oxides of trace elements found by WDX analysis. Detailed interpretation of the measured FTIR spectra requires further investigation.

WDX analysis (Fig. 5–6) of all samples demonstrated C as a dominant element. Trace amounts of S, Ca and Zn were found in the original carbon sample and decreased after the heating, but new elements, such as Fe, Al, Si, K, Mg were found. We assume that some of these metals were released

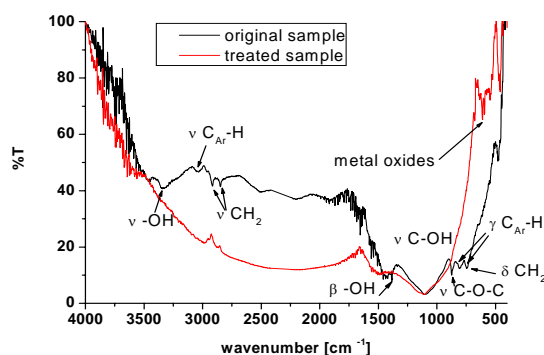


Fig. 4. FTIR spectra of carbon samples

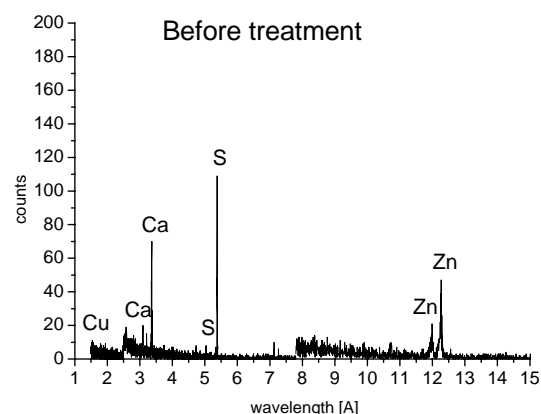


Fig. 5. WDX analysis of carbon samples before treatment

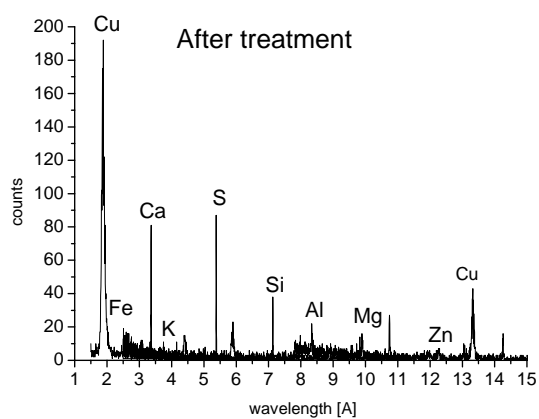


Fig. 6. WDX analysis of carbon samples after treatment

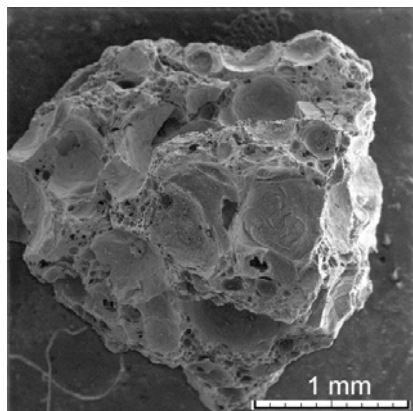


Fig. 7. SEM picture of carbon sample before treatment

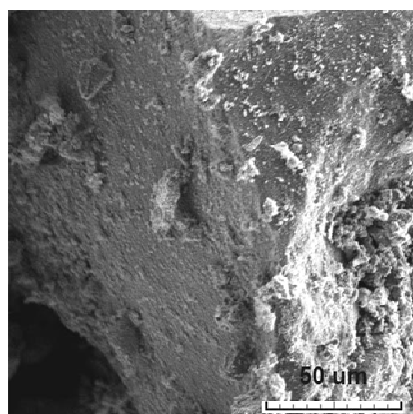


Fig. 8. SEM picture of carbon sample after treatment

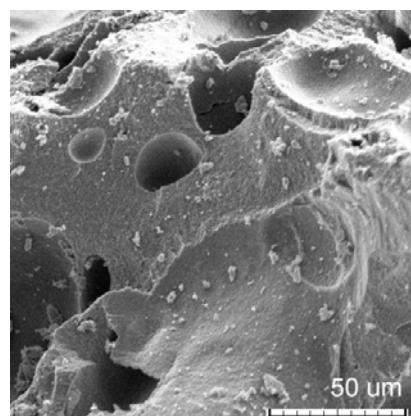


Fig. 9. SEM picture of the cleaving area before treatment

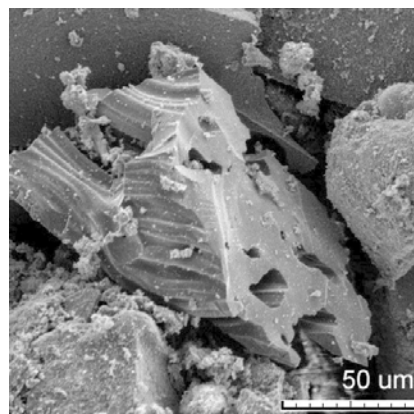


Fig. 10. SEM picture of the cleaving area after treatment

from the stainless steel plate during the heating (Fe, Si). Cu is from the supporting tape used during SEM analysis.

Despite the conductivity of the carbon samples being weak, it was good enough for SEM analysis at low magnifications. Microscopic pictures showed that the carbon has an amorphous structure with pores (Fig. 7–8). Pictures of the treated samples revealed the steps-like shaped cleaving area (Fig. 10), which compared to the smooth shape in the original sample (Fig. 9) shows that material became more compact.

Summary and perspectives

Atmospheric pressure nitrogen microwave plasma was used as a heat source for used tyre waste carbon beneficiation. The plasma heat treatment removed the smell and caused a mass loss, a composition change and a structure change of the waste carbon. The treated carbon could be potentially used as a colouring agent. We are currently testing the adapted microwave torch system in which the carbon powder is inserted directly into the plasma chamber. This provides higher temperatures compared to when the sample is heated on the

supporting metal plate. In the new setup, the plasma chamber is turned upside down to enable the collection of the treated carbon powder in the cooled collection chamber. Because of the presence of pores in the treated carbon we also plan its further investigations, such as measuring its adsorption capacity. This could be interesting for its potential use as an active carbon.

This work was carried out under the support of the Slovak Grant Agency VEGA 1/0293/08 and 1/3043/06, EOARD FA8655-08-1-3061 and APVV 0267-06 grants. We gratefully thank Sencera, Ltd. for loaning us the MW torch, KFS Stavstroj Delta Ltd. for waste carbon samples and Dr. V. Foltin for technical assistance.

REFERENCES

1. Sharma V. K., Fortuna F., Mincarini M., Berillo M., Cornacchia G.: *Appl. Energy* 65, 381 (2000).
2. Helleur R., Popovic N., Ikura M., Stanciulescu M., Liu D.: *J. Anal. Appl. Pyrolysis* 58, 813 (2001).
3. Zabaniotou A. A., Stavropoulos G.: *J. Anal. Appl. Pyrolysis* 70, 711 (2003).
4. Foltin V., Leštinská L., Machala Z.: *Czech. J. Phys.* 56, B712 (2006).
5. Leštinská L., Foltin V., Machala Z.: *IEEE Trans. Plasma Sci.* 36, (2008) – in press.
6. Luque J., Crosley D. R.: *SRI Report MP 99-009*, 1999.

L. Leštinská^{a*}, V. Martišovič^a, M. Zahoran^b, and Z. Machala^a (^a*Division of Environmental Physics, Department of Astronomy, Earth Physics and Meteorology,* ^b*Department of Experimental Physics, Comenius University, Mlynská dolina, Bratislava, Slovakia*): **Atmospheric Pressure MW Plasma for Waste Carbon Treatment**

The first tests of beneficiation of waste carbon from used tyre pyrolysis are presented. The treatment of carbon samples is performed by microwave (MW) plasma generated by Litmas Red MW torch (2.45 GHz, 3 kW) in nitrogen at atmospheric pressure. We employ two ways of waste carbon treatment – heating the samples on the supporting plate and direct treatment inside the plasma chamber. The diagnostics of carbon samples was performed by gravimetry, SEM equipped with WDX element analyzer and FTIR spectroscopy. The plasma heat treatment causes a mass loss, a composition change and a structure change of the waste carbon.

REMOVAL OF COPPER METAL IONS FROM AQUEOUS SOLUTIONS BY PLASMA MADE CHITOSAN FILTER

JOZEF RÁHEL^{a,b,*}, VOJTĚCH PROCHÁZKA^a, MIROSLAV ZAHORAN^b, and DAN ERBEN^a

^a Department of Physical Electronics, Masaryk University, Kotlářská 2, 611 37 Brno, Czech Republic, ^b Department of Experimental Physics, Comenius University, Mlynská dolina F2, 842 48 Bratislava, Slovakia
rahel@mail.muni.cz

1. Introduction

Copper is found in the industrial wastewater mainly due to the printed circuit board manufacturing, electronics plating, plating, wire drawing, copper polishing, paint manufacturing, wood preservatives and printing operations.

The most common treatment for copper removal is its precipitation. After adjusting the wastewater pH by NaOH (caustic soda) to the precipitation region, the coagulant is added, and coagulated metal hydroxide particles are extracted by the combination of sedimentation – filtration processes. Final copper containing sludge is then recovered for Cu metal or disposed to a landfill¹. The necessity for several unit operations, costly reagents, low flow rate, existence of limits given by the minimum metal solubility, and finally the toxic sludge output drives the current need for looking some more economic alternatives for heavy metal uptake. One of the promising alternatives is the copper removal by a suitable abundant in nature adsorbent².

The most widely used adsorbent in wastewater treatment applications is the activated carbon. However its selectivity towards metallic ions is low; therefore activated carbon requires complexing agents to improve its removal performance.

A substantially higher (10× and more)³ metal-binding capacity is offered by *chitosan*, a polymer made from chitin, which is the second only to cellulose in terms of abundance in nature. When used for the water decontamination in its natural flake form, chitosan suffers from gelling and associated hydrodynamic flow problems. Moreover the specific binding sites are not readily available for sorption in the natural form. A chitosan structure thinly coated on a suitable support, such as glass beads, sand or filter fabric is therefore desirable⁴.

The use of filter fabric is favored by its large surface area, excellent control on flow transfer characteristics and the low-cost – especially when nonwoven fabrics such as PP or PET are adopted. A principal obstacle hampering the use of these low-cost carriers is their generally poor wettability, which adversely affects the adhesion of chitosan coating. A conventional organic solvent methods used for imparting the desired adhesive properties presents both health and environmental concerns. In addition, this surface modification method increases cost considerably, thus negating the possible advantages of the use of low-cost fabrics.

Plasma oxidation of polymer materials at atmospheric

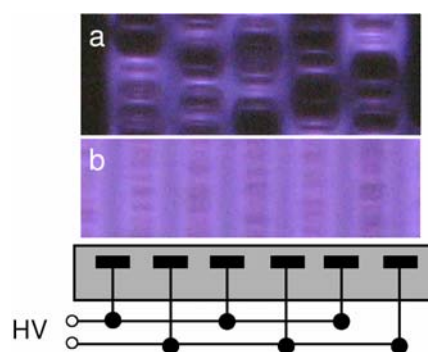


Fig. 1. DCSBD electrode geometry (side view) and the plane view of the discharge appearance: a) low applied power; b) fully energized electrode at 15 kHz, 400 Watt

pressure proved to an effective (and environmentally attractive) tool for creating substantial amount of radical and polar carboxylic and carbonyl groups on their surface. Created polar groups are capable to permanently improve the wettability of polyolefin nonwoven fabrics, which may be used then as a support for suitable adsorbing medium. Created radicals are initiating the graft polymerization, which positively alter the support-coating adhesion strength.

A suitable source of atmospheric pressure plasma for low-added value materials treatment was developed in joint effort of Masaryk University Brno (Czech republic) and Comenius University Bratislava (Slovakia). The plasma source (Diffuse Coplanar Surface Barrier Discharge – DCSBD) creates a thin layer of highly energetic plasma ($\sim 100 \text{ W cm}^{-3}$) above the ceramic panel (Fig. 1). The DCSBD proved to be highly efficient in increasing the wettability of various low-cost materials (PP and PET nonwovens, wood, paper, plastic foils)⁵.

Cernakova et al.⁶ have already reported a successful immobilization of chitosan on a DCSBD plasma activated nonwoven fabric. Nitrogen atmosphere and stationary (batch) treatment condition were used in their case. Nevertheless for the practical purposes a continuous (roll-to-roll) treatment and the air gas plasma operating conditions are more desirable. We have therefore decided to set-up the experimental apparatus enabling the continuous fabric treatment in air. The aim of our work was to prepare the chitosan thinly coated on the plasma-activated fabric and to evaluate its copper adsorption performance.

2. Experimental

2.1. Plasma treatment

Polypropylene spunbond nonwoven fabrics of 17 gsm, supplied PEGAS a.s., Czech Rep., was activated by atmospheric pressure air plasma generated by means of DCSBD⁵. The primary role of plasma treatment was to improve the wettability of PP fabrics, so the chitosan coating solution can penetrate inside the bulk of fabric and interacts with individual fibers. The DCSBD electrode consisted of 11 pairs of silver strip electrode embedded 0.5 mm below the surface of

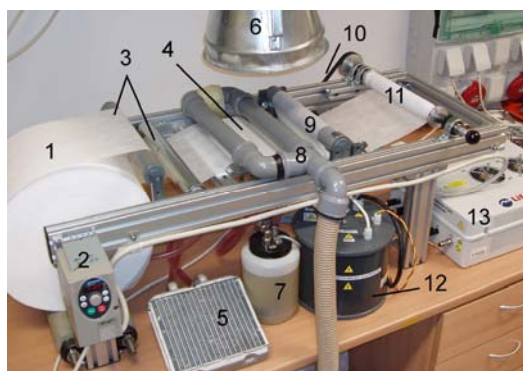


Fig. 2. The DCSBD reactor for continuous textile treatment CONTIONE: 1 – feed roll; 2 – frequency converter; 3 – guiding rolls; 4 – DCSBD electrode; 5 – radiator; 6 – fume hood; 7 – oil pump; 8 – air blower; 9 – stretching roll; 10 – motor unit; 11 – take up roll; 12 – HV transformer; 13 – power voltage generator

96 % Al_2O_3 ceramics. The mutual distance of the 200 mm long and 3 mm wide silver strip electrodes was 1.5 mm. The electrode was energized by 14 kHz sinusoidal voltage, supplied by HV generator LIFE TECH VF700. The power consumption of DCSBD plasma reactor was monitored by METEX M-460M multimeter.

The DCSBD electrode was mounted in the prototype of continuous feed reactor CONTIONE (Fig. 2). The treatment time was controlled by the speed of the take-up roll. The contact of fabric with the relatively thin layer of generated plasma (0.1–0.3 mm) was enhanced by the air-blower flow perpendicular towards the plane of plasma panel.

The DCSBD plasma panel was operated at 400 W/200 cm^2 . PP samples were in contact with plasma for 5 sec.

2.2. Chitosan coating

Immediately after the plasma treatment the PP samples were immersed into the vessel containing 2 % chitosan solution. The vessel was then placed in the waterbath shaker for 1 hour at 60 °C.

The solution was made by dissolving of 30 g chitosan powder (ALDRICH, medium mol. weight, 75–85 % deacetylated) into 1500 ml of 0.6 % (v/v) acetic acid solution (FLUKA p.a.). The choice of chitosan solution concentration is based on the results of Cernakova et al.⁶, who had found this particular concentration to be the most stable against the wash-off effect.

After drying at room temperature the fabric was washed vigorously in deionized water to remove weakly attached chitosan homopolymer and traces of acetic acid. Finally the chitosan coated samples were cut into the circular coupons of 55 mm diameter that were used during the course of all our experiments.

2.3. Weight of the coating

In order to evaluate the weight of chitosan film attached to the PP fabric following procedure was employed. Unmodi-

fied PP fabric was cut into 100 circular pieces with the diameter of 55 mm. Each circular piece was weighed on DEVNER SUMMIT SI-234A balances with the resolution of 0.1 mg. After verifying the normal (Gaussian) distribution of samples weight, arithmetic mean m_o and its standard deviation σ_o was calculated.

Circular 55 mm diameter coupons of chitosan coated samples were weighted prior each adsorption experiment. The arithmetic mean of pure PP was subtracted to obtain the mass of coating. The statistical error σ_N for the set of N samples was calculated as $\sigma_N = \sigma_o$.

2.4. Surface characterization

Scanning electron microscopy photographs of chitosan coated PP samples were done using the TESCAN VEGA TS 5136MM microscope operating in the HiVac mode.

Chemical changes on the fabric surface were explored by the FTIR spectrometer BRUKER Vertex 80v, equipped with the DRIFT module. Kubelka-Munk function was applied on the obtained spectrum.

2.5. Copper adsorption evaluation

Batch experimental conditions were employed. 20 filter coupons with the known mass of immobilized chitosan were inserted into 250 ml glass wide-mouth Erlenmeyer flask filled with the 100 ml of the water solution of $\text{Cu}(\text{NO}_3)_2 \cdot 3 \text{H}_2\text{O}$ (Fluka p.a.). The flask were placed into the waterbath shaker, where it was constantly agitated at the room temperature for given amount of time, which was usually 2–4 days.

Ion-selective electrode (ISE) measurement was used to evaluate the adsorption capacity of coated chitosan. The actual concentration of Cu^{2+} ions was evaluated by the multiple *sample addition method* using the Orion 4-Star Benchtop pH/ISE meter equipped with the Orion 9629BNWP Ionplus® Series Cupric Electrode (both from Thermo Fisher Scientific).

The sample addition method is based on adding the small known volume V_s of unknown sample C_s into the standard of large known volume V_o and concentration C_o . The change of the ISE electrode potential ΔE (mV) is used for calculating the concentration of C_s :

$$C_s = C_o \left(\frac{V_s + V_o}{V_s} 10^{\frac{\Delta E}{S}} - \frac{V_o}{V_s} \right)$$

where the S is the slope of the ISE electrode. The slope S was determined daily during the electrode calibration. The ion strength of 100 ml volume standard was always adjusted by the 2 ml of 5 M NaNO_3 . ISE measurements were carried out in the dark room, as we have experienced a significant sensitivity of Ionplus Cupric electrode to the light.

3. Results and discussion

The average mass of chitosan coating deposited on the single PP coupon (38 ± 1 mg) was 6.1 mg, which is approx. 16 wt.%. As can be seen from SEM photographs of the coated fabric, chitosan forms a thin uniform film on the surface of

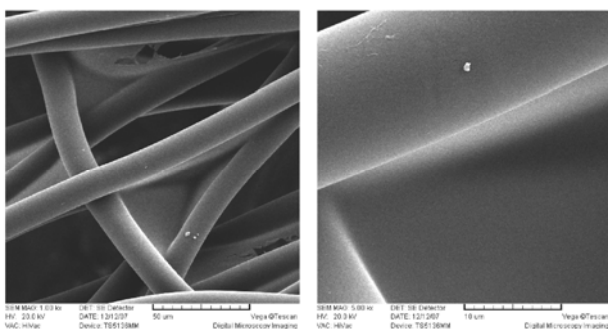


Fig. 3. SEM picture of chitosan coated PP fibers. Magnification 1000× and 5000×

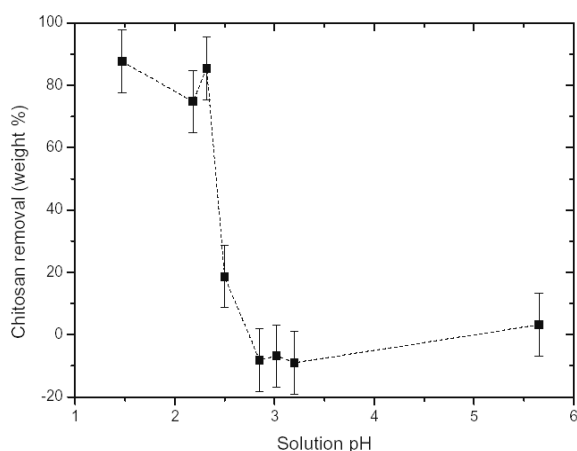


Fig. 4. Solubility of chitosan coating. The coating is insoluble down to pH 2.5 level

individual PP fibers with occasional pieces of film bridging the inter-fiber space (Fig. 3). The presence of chitosan chemical structures was further confirmed by the obtained FTIR-DRIFT spectra, where the new adsorption bands at 1150–1040 cm^{-1} (glucosidic bond) and 3450–3360 cm^{-1} (OH, NH) appeared.

The analysis of solvability of chitosan film in acidic conditions revealed that the coated chitosan is insoluble in water for the pH higher than 2.5 (Fig.4). The low pH level solutions were prepared by adding appropriate amount of HNO_3 to the deionized water. The pH level of solution measured before adding the chitosan coupons was considered.

The time evolution of adsorption process is shown in Fig. 5. Two hours after the adsorption is started, filter reaches 80 % of its final equilibrium value in the batch. It was therefore concluded, that 2 days lasting adsorption experiment offers sufficient time to reach the final equilibrium state.

To evaluate the theoretical adsorption capacity, which will be achieved in real flowing conditions, the adsorption isotherm at pH 5.5 was determined. Chitosan coated samples were immersed into the 100 ml Cu^{2+} solutions with the concentration ranging from 0.01 M to $2 \cdot 10^{-4}$ M. For the sake of the mutual comparison, the adsorption isotherm was deter-

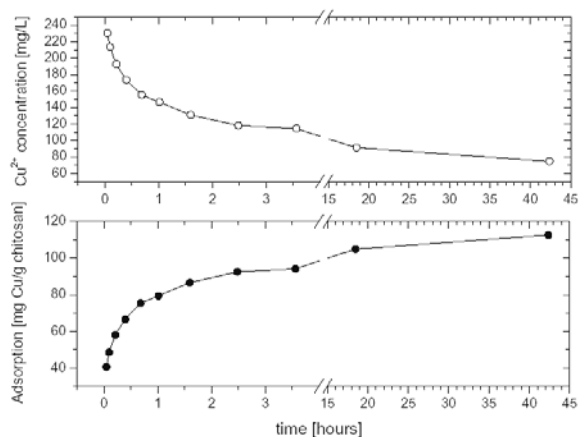


Fig. 5. Time evolution of copper removal by the chitosan filter

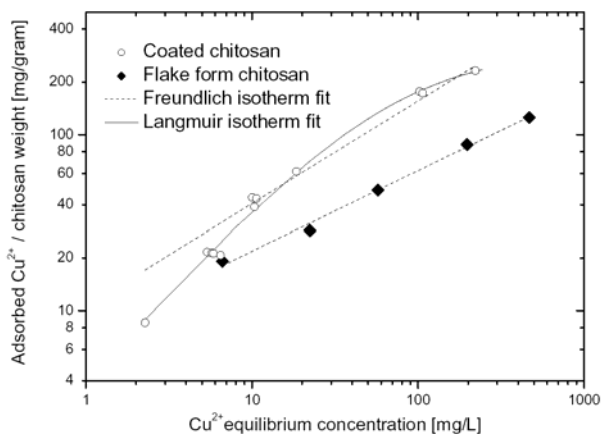


Fig. 6. Time evolution of copper removal by the chitosan filter

mined also for the chitosan in its original flake form (as it was found in the supplier package).

Fig. 6 shows the log-log plot of obtained results for both forms of chitosan. According to the literature⁷ the Freundlich adsorption isotherm is the most frequently used in discussion of adsorption from liquid solutions. The formula describing the Freundlich isotherm is

$$w = a \cdot c^b$$

where w states for the mass fraction adsorbed (the mass of solute adsorbed per unit mass of adsorbent), c is the solution's equilibrium concentration, and a , b are the empirical parameters. The straight dashed lines in Fig. 6 correspond to this isotherm. For the original flake form chitosan parameters a and b are 7.6 ± 0.7 and 0.45 ± 0.02 respectively. For the coated chitosan $a = 10.6 \pm 1.7$ and $b = 0.58 \pm 0.01$. Clearly

the adsorption capacity of chitosan coated on PP fabric is higher at least by 40 %.

Although the correlation between the Freundlich isotherm formula and data for the flake chitosan is acceptable, data obtained for the coated chitosan are better represented when the formula for Langmuir adsorption isotherm is applied:

$$\frac{w}{w_{\max}} = \frac{Kc}{1 + Kc}$$

Here w states for the mass fraction adsorbed, w_{\max} is the theoretical maximum for w , c is the solution's equilibrium concentration, and K is the Langmuir adsorption equilibrium constant. The parameters w_{\max} and K for the fit shown in Fig. 6 are $313 \pm 5 \text{ mg g}^{-1}$ and $12.8 \pm 0.5 \text{ L g}^{-1}$ respectively.

The validity of Langmuir adsorption isotherm for the coated chitosan can be explained by the better agreement with the assumption used during its mathematical derivation: (a) monolayer coverage only; (b) surface perfectly flat on microscopic scale, so the all sites are equivalent; (c) molecule adsorption ability is independent of the occupation of neighboring sites. The morphology of flake form chitosan obviously violates the (b) assumption, therefore the empirical Freundlich isotherm formula provides a better correlation with obtained data.

At the same time, the agreement of Langmuir isotherm for the coated chitosan data suggests that the mechanism of copper adsorption is occurring within the frame of Langmuir formula premises, i.e. monolayer coverage and negligible interaction between the neighboring sites.

4. Conclusion

The completed prototype of continuous DCSBD plasma treater demonstrated its viability with respect to the PP surface activation. Thin chitosan coating (16 wt.%) on the fibers of polypropylene nonwoven fabric was prepared. The film was evaluated with respect to its adsorption capacity towards copper ions. The capacity was more than 40 % times higher than the capacity of chitosan in its natural flake form. This may be attributed to better availability on the active sites on the thin flat structures of chitosan film. The adsorption behavior of chitosan filter is well described by the Langmuir adsorption isotherm. The theoretical adsorption capacity determined at pH level of 5.5 from the Langmuir isotherm is $313 \pm 5 \text{ mg g}^{-1}$ (Cu^{2+} /chitosan).

This research has been supported by the Czech Science Foundation under the contract number 202/06/P337 and by the research intent MSM:0021622411 funding by the Ministry of Education of the Czech Republic.

REFERENCES

1. Salmen K. S.: US Patent #6,140,130 (Oct.31, 2000).
2. Bailey S. E., Olin T. J.: *Water Res.* 33, 2469 (1999).
3. Babel S., Kurniawan T. A.: *J. Hazard. Mater.* B97, 219 (2003).
4. Wan M. W., Petrisor I. G.: *Carbohydrate Polymers* 55, 249 (2004).
5. Toth A., Cernakova L., Cernak M., Kunovska K.: *Holzforchung* 61, 528 (2007).
6. Cernakova L.: *Proc. of 9th HAKONE August 23-27 2004, Padova, Italy.*
7. Atkins P. W., in: *Physical Chemistry*, 5. ed. Chap. 28.12, p. 993. Oxford University Press, 1994.

INFLUENCE OF WASTE COMPOSITION ON ELECTRIC ARC ELECTRON DENSITY

GRZEGORZ RANISZEWSKI*, ZBIGNIEW KOLACINSKI, and LUKASZ SZYMANSKI

Technical University of Lodz, Department of Electrical Apparatus, Faculty of Electrical, Electronic, Computer and Control Engineering, ul. Stefanowskiego 18/22, 90-924 Lodz, Poland,
larryl@o2.pl

1. Introduction

The management of solid waste is a major problem in many parts of the world. There are many techniques for treatment wastes. At the beginning of XX century there were built incinerating plants. Now conventional methods are well known and have been applied for many years. But conventional thermal treatment do not solve the problem. Its due to oxygen presence and temperature range what leads to form more hazardous form of wastes as dioxins and furanes. Utilization carried out by means of plasma technology enable to obtain a green technology, free of hazardous components.

An electric arc as a source of plasma can be an effective tool for smelting of municipal and industrial wastes as well as medical and power plant ashes. In this work we focus an influence of compounds of utilized ashes as the most hazardous on electric arc parameters.

The arc starts to burn in the neutral gas (i.e. argon) and then melting mineral compounds of ashes as: SiO_2 , CaO , Al_2O_3 , Fe_2O_3 , MgO etc. followed by their gasification, thermal decomposition, ionization and formation of the mineral arc plasma. Determination of the mineral compounds influence on electric arc is associated with many equilibrium and thermodynamics parameters. The purpose of the paper is to establish an influence of individual components to electron density enabling following calculations.

2. Plasma for zero waste treatment

The incineration of certain wastes results in the formation of relatively highly toxic residues. The toxic leftovers (ash, slag, filter deposits, sedimentation residues) could be easily disposed in landfills assuming that they were first immobilized and converted into a non-leaching product. When the leftovers are heated to a sufficient temperature, their elements, including minerals and toxic heavy metals, melt and glassify. Even partial solidification (vitrification) of those residues requires the temperature above 1700 K, which is not available in most incinerators but easily reachable in thermal plasma reactors. Temperatures of the order of 10 000 K are typical for arc in plasma furnaces and all inorganic residues can be easily solidified. The system of plasma vitrification of ash produces a chemically stable and mechanically resistant product. After vitrification the mineral product looks like

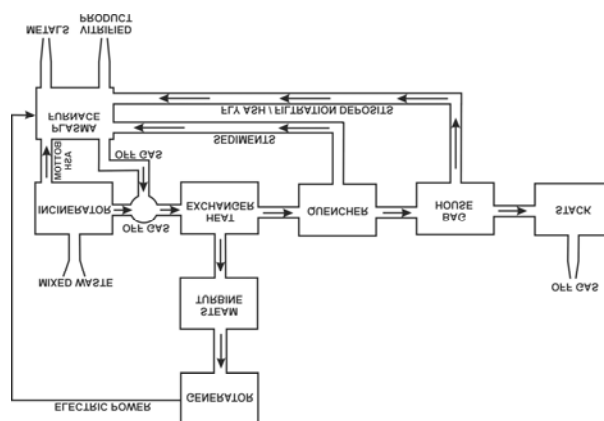


Fig. 1. Phase equilibrium of CaO

glassy, basalt structured lava (even of higher than basalt mechanical strength), and its main components are silicon, aluminum and calcium oxides in the form of chemically inactive compounds, resistant to flushing.

The DC plasma furnace was designed in the Technical University of Lodz and applied to treat the ash samples with high degree of flexibility¹.

In Fig. 1 the flow chart of classic fuel burning incinerator combined with plasma vitrification system of all solid residues is presented. The system is self-supplied in the electric power and it employs only single plasma furnace for vitrification of solids. All the post incineration residues: ash, slag, filter deposits, sedimentation residues are heated to a sufficient temperature and their minerals and toxic heavy metals, melt and glassify. This way every classic waste incineration plant can be converted to zero waste emission system. The excess of energy in the form of electricity or steam can be sold.

3. Compounds of fly ash

Fly ash is one of the residues generated in the incinerators of industrial, municipal, medical and hazardous plants as well as combustion of coal. Fly ash consist of particles containing metals as Si, Ca, Al, Fe, Mg, K. Though the majority from ashes can be used in the more far production, particularly in the building industry e.g. cement production and/or concrete products, structural fills or embankments, stabilization of waste materiale, road base or subbase materiale, flowable fill and grouting mixes, mineral filler in asphalt paving, cement in concentrate, in ceramics industry, as a filler in road pavement, in decorative materials in glass-ceramics application, as a fertilizers in soil amendmets, as a sorbent in wastewater treatment² but about 75 percent of fly ash generated is still disposed of in landfills or storage lagoons. Stored ash may contain heavy metals that are know no be harmful to healt as nickel, vanadium, arsenic, berylium cadmium, barium, chromium, copper, molybdenum, zinc, lead, selenium, uranium, thorium, radium³.

Plasma is the best medium to achieve temperatures which enable efficient decomposition of waste compounds

Table I
Chemical composition of ashes in Poland

Component	Amount [%]	
	subbituminous	lignite
SiO ₂	4,15–63,02	18,02–51,33
Al ₂ O ₃	0,81–40,43	1,03–36,78
Fe ₃ O ₄	2,08–57,85	8,14–18,42
CaO	1,10–51,50	2,26–53,10
MgO	0,10–23,80	1,40–11,32
SO ₃	0,37–30,62	1,37–19,50

Table II
Bulk chemical composition data for coal fired plants fly ashes^{6,7}

	SiO ₂	Al ₂ O ₃	Fe ₂ O ₃	CaO	MgO	Na ₂ O	K ₂ O	SO ₃
Yugoslavia	52,6	26,3	6,8	6,0	2,2	0,2	1,1	1,0
UK	50,1	28,1	11,7	1,6	1,5	0,3	0,6	–
USA	52,2	19,0	15,7	4,5	0,9	0,8	2,0	1,3
Netherlands	50,5	25,7	6,5	4,3	2,2	2,0	4,4	–
Japan	57,5	26,1	4,0	5,1	1,3	1,5	1,4	0,4
Taiwan	48,8	23,2	4,2	3,9	1,0	0,2	1,1	–
Poland	50,8	23,9	8,6	3,6	2,8	0,8	2,9	0,8
Saudi Arabia	52,3	25,2	4,6	10,0	2,2	–	–	0,8
China (Wuhan)	47,6	23,4	14,6	1,2	0,7	1,1	–	0,9
Hong Kong	50,0	37,1	3,1	3,40	0,5	0,6	–	0,7

and to neutralize toxic compounds by vitrification.

There are only few main ashes compound (Table I and 2)^{4,5}.

We used thermodynamic program CHEMSAGE to predict variety and amount of different products after heating fly ashes in a plasma arc. Our aim is to determine temperature of total decomposition of ash.

Fig. 2–5 shows phase equilibria for most numerous compounds: SiO₂, Al₂O₃, Fe₂O₃, CaO at temperature over 3000 K.

It was calculated that all compounds are in gas phase over 4000 K and that during ash components decomposition there are gas compounds as below:

Al, AlO, AlO₂, Al₂O, Al₂O₂, Al₂O₃, Al₂,
Ca, CaO, Ca₂,
Cr, Cr₂O₃, Cr₂, CrO, CrO₂, CrO₃, Cr₂O, Cr₂O₂,
Fe, FeO, FeO₂,
Mg, MgO, Mg₂,
Na, Na₂, NaO, Na₂O, Na₂O₂,
O, O₂, O₃,
SiO, SiO₂, Si, Si₃, Si₂O₂.

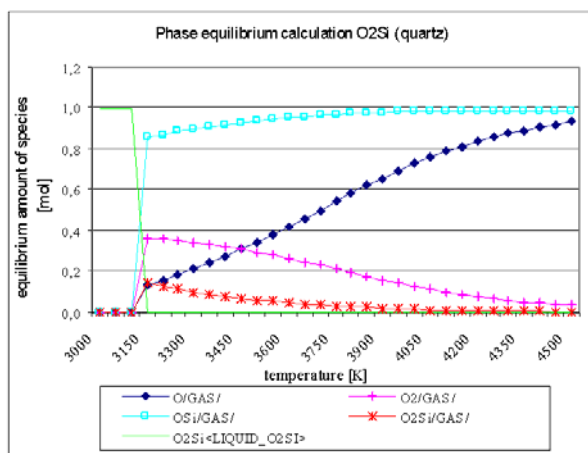


Fig. 2. Phase equilibrium of SiO₂

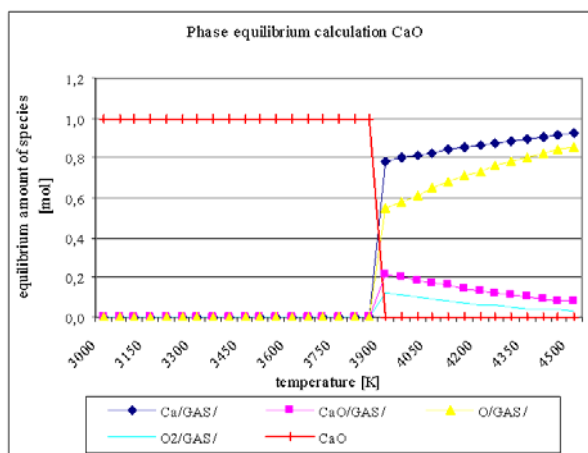


Fig. 3. Phase equilibrium of CaO

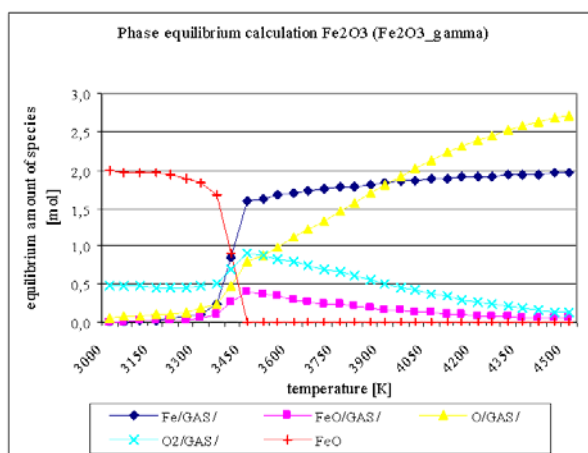
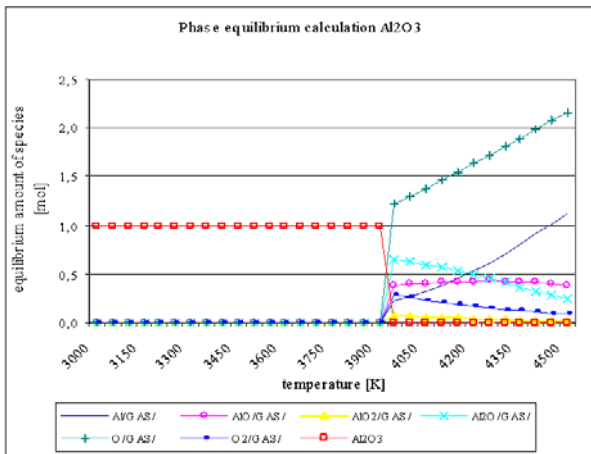


Fig. 4. Phase equilibrium of Fe₂O₃

Fig. 5. Phase equilibrium of Al_2O_3

4. Metal Arc Plasma properties

Metal arc plasma consists of atoms, ions and electrons. Argon has been used as a working gas. It was assumed that unbounded metal occurs in the argon atmosphere and that multiple ionization below 10 000 K is negligible.

Local Thermodynamic Equilibrium has been assumed to calculate arc plasma composition. To determine electron density – N_e , atoms density – N_0 , ions density – N_+ system of non-linear equation must be solved

Saha-Eggert equations, abbreviated as⁸:

$$\frac{N_e \cdot N_{Ar+}}{N_{Ar}} = 2 \cdot \frac{u_{Ar+}(T)}{u_{Ar}(T)} \cdot \frac{(2 \cdot \pi \cdot m \cdot k \cdot T)^{3/2}}{h^3} \cdot \exp\left(-\frac{E_{Ar} - \Delta E_{Ar}}{kT}\right)$$

$$\frac{N_e \cdot N_{Me+}}{N_{Me}} = 2 \cdot \frac{u_{Me+}(T)}{u_{Me}(T)} \cdot \frac{(2 \cdot \pi \cdot m \cdot k \cdot T)^{3/2}}{h^3} \cdot \exp\left(-\frac{E_{Me} - \Delta E_{Me}}{kT}\right)$$

Dalton's law:

$$p = (N_{Ar} + N_{Ar+} + N_{Me} + N_{Me+} + N_e) \cdot k \cdot T$$

Charge equilibrium in LTE conditions:

$$N_e = N_{Ar+} + N_{Me+} + N_e$$

Percentage of metal vapour in gas

$$x = \frac{N_{Me} + N_{Me+}}{N_{Me} + N_{Me+} + N_{Ar} + N_{Ar+}}$$

where:

- $u_{Ar}(T)$ partition function of argon;
- $u_{Ar+}(T)$ partition function of single ionized argon;
- $u_{Me}(T)$ partition function of metal;
- $u_{Me+}(T)$ partition function of single ionized metal;
- m electron rest mass;
- h Planck's constant;
- k Boltzmann's constant;

- E_{Ar} ionization energy for argon,
- E_{Me} ionization energy for metal,
- ΔE_{Ar} lowering of ionization energy for argon,
- ΔE_{Me} lowering of ionization energy for metal,
- T absolute temperature [K];
- $\Delta \chi$ lowering of ionization energy

The partition function for considered elements has been calculated by Drawin⁹.

5. Results

Calculation are made for mixture of metal in argon. Fig. 6 show concentration of argon plasma components with examined metal in function of temperature at the atmospheric pressure.

Different compositions of metal plasma have been considered to establish correlation between metal density and electron amounts (Fig. 6-10). On figures there are following denotation:

e – electron density;

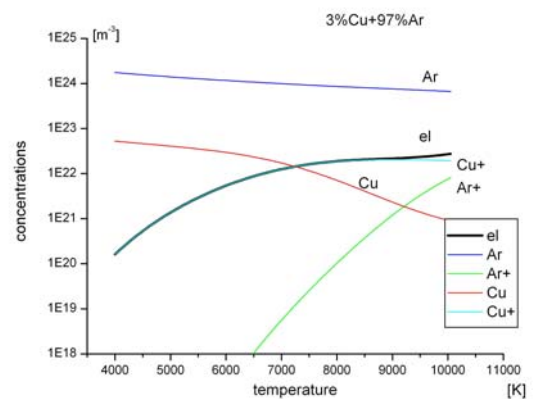


Fig. 6. Argon with 3 % of copper

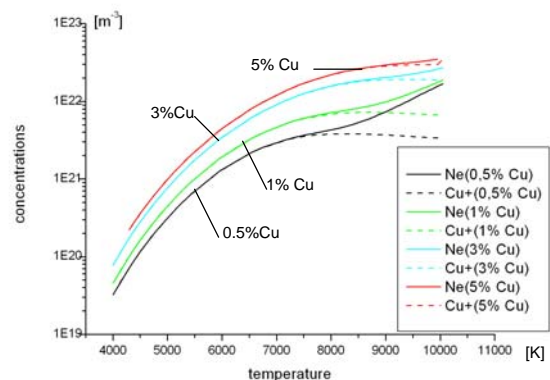


Fig. 7. Electron densities for different copper concentrations

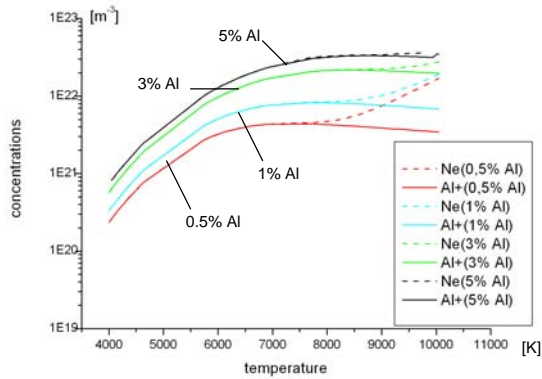


Fig. 8. Electron densities for different aluminium concentrations

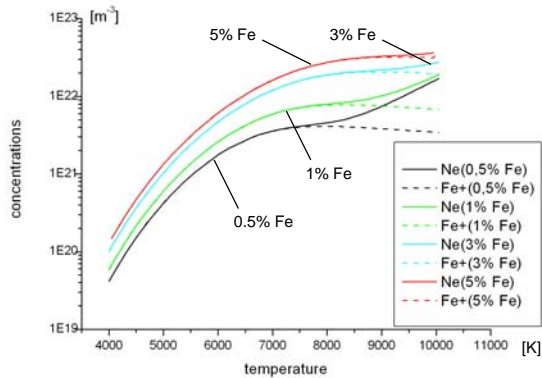


Fig. 9. Electron concentrations for different iron concentrations

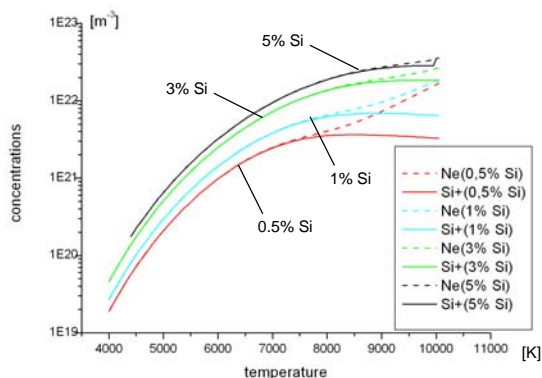


Fig. 10. Electron densities for different silicon concentrations

Ar – argon atoms density;
 Ar+ – argon atoms density;
 Cu, Al, Si, Fe – atom density of copper, aluminium, silicon and iron respectively;
 Cu+, Al+, Si+, Fe+ – ion density of copper, aluminium, silicon and iron respectively.

Calculations have been conducted for 0,5 up to 5 % metal ratio in argon plasma. For each examined compound the electron concentration mainly depends of concentration of ions of examined element. Even 1 % addition of metal determine electron densities in plasma.

6. Research chamber

An electric arc burns between two 6 mm graphite electrodes. One of the electrode is hollowed. The metal sample is placed in this hollow with addition of detecting material – copper. The distance between electrodes is 3 mm. The research chamber enable pirometry, spectroscopy and visual process registration

Fig. 11 show frame from high speed camera with 12 000

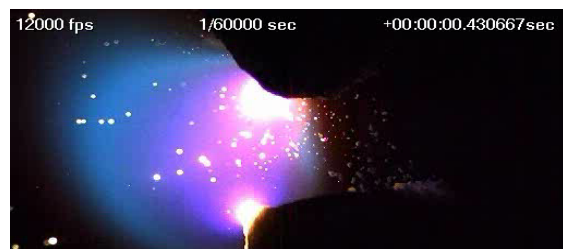


Fig. 11. Image from high speed camera

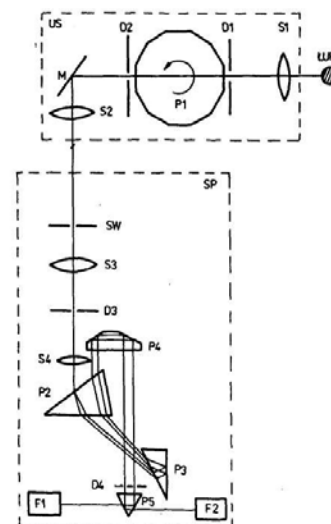


Fig. 12. Optical set-up. US – scanning device, SP – spectrograph, D – diaphragmas, P – prisms, S – lenses, ES – entrance slit, F – photomultipliers

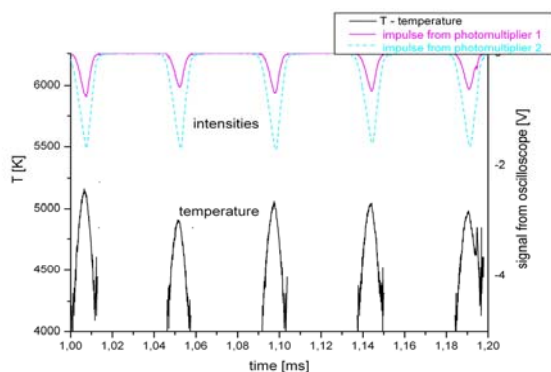


Fig. 13. Example of temperature calculation

frames per second.

The main parts of the measuring arrangement are: the optical set-up and the data collecting equipment. To measure time-dependent temperature profiles at an arc cross-section, a special scanning technique was used. The optical set-up was composed of two main units: the scanning device – US and the spectrograph – SP (Fig. 12).

The polycone prism of the scanning device unit was driven with a compressed-gas propelled turbine up to 1000 revolutions per second. It was possible to reach a scanning time of $5 \cdot 10^{-5}$ s with a scanning frequency 12 000 full profile scans/s. In this way only a single test was necessary to obtain the time variation of temperature profiles in an arc cross-section. With the use of the scanning unit the arc image focused on the entrance slit SW of the spectrograph SP was scanned. Diaphragm D4 was designed to select spectral lines characteristic for copper – 510,55 nm and 521,82 nm. Two spectral lines selected by the diaphragm D4 and splitted by the prism P5 were detected by two photomultipliers F1 and F2. Signals from photomultipliers are recorded by oscilloscope. Measurement of the plasma channel temperature are based on the relative line intensities spectroscopic technique. Fig. 13 show a part of two lines intensities recorded by oscilloscope and calculated temperature for arc burning between graphite and copper 6mm electrodes, current 20 A, voltage 60 V. Distance between electrodes 3 mm. The arc unit volume are computed from Abel's transformation.

7. Conclusion

In this paper, we have presented an effect of metal presence in argon plasma. In literature influence of electrode material was presented¹⁰. Many authors presented influence of different working gases. Double- and multiatom gases usage enable to carry much more thermal energy than in case of one atom gases^{11,12}.

Assumed that mineral additions will be injected in con-

trolled way into the arc through one of the electrode. Electric arc burns in argon as a working gas where considered compounds are melted following gasification and ionization. There are dosed into the arc channel changing series of properties. Estimate of influence for these components is connected with calculation of equilibrium and thermodynamics parameters.

Addition of chemical compounds into neutral gas in which burns an electric arc change heat transport conditions due to their thermal conductivity. Resistance and electrical conductivity is changed. In plasma stream with molecular gases there have been created a large amounts of unbounded atoms.

Electric arc stability depends on two factors: source quality parameters and resistance changes during the process. The resistance influence voltage. Additions of mineral compounds changes effective ionization potential and in effect conductance. It has been estimated that minimal addition of metal vapour strongly changes plasma composition what results by changing plasma properties. Even 0,5 % of metal vapour determine electron quantity in plasma in temperature up to 7000 K. Number of electrons influences on electric parameters and thermodynamic state. The 3 % amount of metal vapour determine electron quantity in temperature lower than 9000 K what is sufficient in the most plasma waste treatment technologies.

The scientific work has been financed by the Ministry of Science and Higher Education (MNiSW) under the programme 1754/B/T02/2007/33.

REFERENCES

- Cedzyska K., Kołaciński Z.: Polish J. Appl. Chem. No XLII, z. 2, pp. 143–149, (1998).
- Ferreira C., Ribeiro A., Ottosen L.: J. Hazardous Materials B96, 201 (2003).
- DiGioia Anthony M., Jr., Nuzzo William L.: Proceedings of the American Society of Civil Engineers, Journal of the Power Division, New York, NY, June 1972.
- <http://home.agh.edu.pl/~kepw>
- Jemiołkowski W.: *Wpływ kondycjonowania spalin trojtenkiem siarki na wartość handlową popiołu*, EC Siekierki, D/W/Siarka/WJ196/96.
- Ilic M., Cheesman C., Sollars C., Knight J.: Fuel 82, 331 2003.
- Baoguo Ma, Meng Qi, Jun Peng, Zongijn Li: Environmental International 25, 423 (1999).
- Lochte-Holtgreven W.: *Plasma diagnostics*, Amsterdam 1968.
- Drawin H. W.: *Data for plasmas in local thermodynamic equilibrium*. Gauthier-Villars, Paris 1965.
- Gleizes A., Bouaziz M., Gonzalez J. J., Razafinimanana M.: IEEE Trans. Plasma Sci. 25, No. 5 (1997).
- Krolikowski C.: *Technika łączenia obwodów elektroenergetycznych*. PWN, Warszawa 1990.
- Brzeski J.: *Chemia plazmy niskotemperaturowej*. Wydawnictwa Naukowo-Techniczne, Warszawa 1983.

STERILIZATION OF *Escherichia Coli* USING HIGH FREQUENCY ATMOSPHERIC PRESSURE PLASMA DISCHARGE

PETR SMEKAL^a, PAVEL SLAVICEK^a, MILOS KLIMA^a, and MONIKA SZOSTKOVA^b

^a Department of Physical Electronics, Faculty of Science, Masaryk University, Kotlářská 2, 611 37 Brno, ^b Department of Agrochemistry, Soil Science, Microbiology and Plant Nutrition, Faculty of Agronomy, Mendel University of Agriculture and Forestry Brno, Zemědělská 1, 613 00 Brno
petr.s.smekal@seznam.cz

Key words : sterilization process, plasma discharge, optical emission spectroscopy

1. Introduction

Sterilization is very important biomedical process because of possible disease effect of microorganisms to human body. Its potential pathogenesis presents a danger for a healthy person but most for in-patient and postoperative full weakened patients.

Sterilization process has to inactivate all microorganisms and their vegetative form too.

Sterilization by ethylene oxide is one of many low temperature techniques. Ethylene oxide could be very useful to sterilize heat sensitive materials but there is a major problem with its carcinogenicity and high absorption in plastics. Long time is needed for this physical sterilization process too¹.

Gamma rays irradiation is another low temperature sterilization method. Ionizing radiation affects DNA molecules and changes its structure that causes inactivation of a microorganism². But it is necessary to have well protected working box and well-educated staff to control this sterilization process. Gamma ray can change inner structure of sterilized objects too³.

Autoclaving is a sterilization method which uses high pressure and temperature to inactivate microorganisms. So it is very harmful for heat sensitive materials but very useful to sterilize glass, metal or ceramics.

Plasma sterilization process at atmospheric pressure eliminates many problems like high ionizing irradiation, presence of toxic substances, high temperature or long operative duration. There is a several mechanism to inactivate microorganisms. It is irradiation of DNA molecule, interaction of reactive species (oxygen and nitrogenous molecules) with biomolecules. The UV irradiation incurs structural changes of nuclear acids and other biomolecules and reactive species causes erosion of microorganisms by its extremely high reactivity⁴⁻⁶.

A bacterium *Escherichia Coli* as a model microorganism was used to determine an inactivation effect of plasma sterilization by using high frequency atmospheric pressure plasma

discharge. To confirm the sterilization attainments a special selective medium was used.

Emission spectroscopy is very effective method to obtain physical plasma characterization in a short time without affect to plasma discharge. Presence of reactive species in plasma discharge during a sterilization process was confirmed and rotational and vibrational temperature was obtained by optical emission spectroscopy. Presence of UV wave range in plasma discharge was confirmed too.

2. Experimental

To generate a plasma discharge high frequency generator CESAR 1310 with frequency 13,56 MHz, matching unit WM 1000 A and argon as a working gas was used. Gas flow was set to 2,5 slpm for all sterilization experiments. A power electrode was connected from matching unit to silica glass tube with inner diameter of 2 mm^{7,8}. Distance of power electrode from mouth of silica glass tube was different depending on working power output.

Plasma discharge was created in the glass tube and got to the strip of filter paper with an experimental sample with volume of 25 μ l. This strip was placed on the Petri dish in distance of 2 mm from mouth of silica glass tube. Translational device to scan whole sample by plasma discharge during a sterilization process was used. Fig. 1 shows experimental device for plasma sterilization.

Different plasma sterilization conditions were used. Power output of plasma sterilization device was altered. Several counts of scans were realized.

The experimental sample was made of a bacterium *Escherichia Coli* with count of 10^{10} CFU ml⁻¹. To verify a sterilization effect of plasma discharge a selective culture medium Presence-Absence broth⁹ was used.

When using a plasma sterilization device without plasma discharge (gas flow only), a control sample was made. To perform a control sample two scans was applied.

To confirm a presence of reactive species and UV wave

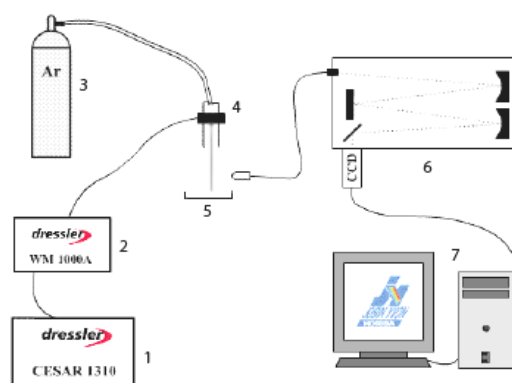


Fig. 1. Scheme of plasma sterilization device; 1) high frequency generator, 2) matching unit, 3) working gas, 4) silica glass tube with a power electrode, 5) Petri dish with an experimental sample, 6) spectrometer, 7) computer

Table I

Measured sterilization data for high frequency atmospheric pressure plasma discharge

Origin – [CFU ml ⁻¹]	Power output	Counts of scans	D	S
1,721·10 ¹⁰	without discharge	2		Yellow / With germ
1,721·10 ¹⁰		1		Red / Germfree
1,721·10 ¹⁰	45 W	2	40 mm	Red / Germfree
1,721·10 ¹⁰		3		Red / Germfree
1,721·10 ¹⁰		4		Red / Germfree
1,246·10 ¹⁰		2		Yellow / With germ
1,246·10 ¹⁰	without discharge	1		Red / Germfree
1,246·10 ¹⁰	50 W	2	50 mm	Red / Germfree
1,246·10 ¹⁰		3		Red / Germfree
1,246·10 ¹⁰		4		Red / Germfree
1,246·10 ¹⁰		2		Red / Germfree

D – distance of power electrode from mouth of silica glass tube, S – sample after plasma sterilization process, CFU/ml – Colony Form Unit / ml

range in plasma discharge used for sterilization process and get a physical plasma characterization the spectrometer Horiba Jobin-Yvon FHR 1000 with CCD camera was used. To recognize atomic molecular lines software Spectrum Analyzer 1.6 was used⁹.

To determine a rotational and vibrational temperature the optical emission spectroscopy was applied. To acquire a rotational temperature the molecular OH anion bend, Q1 branch for transition ${}^2\Sigma \rightarrow {}^2\Pi$, was used. To get a vibrational temperature the molecular N₂ bend, heads 0–2, 1–3 and 2–4, was used.

Rotational and vibrational temperature was measured in plasma sterilization device configuration with plasma discharge only and plasma discharge with Petri dish too.

During a sterilization process a plasma discharge was applied. Plasma jet scanned the strip with an experimental sample (in the various count for each experiment). Than the strip was added into the Presence-Absence broth and was cultivated at 35° C for 48 hours. The selective medium was colored to yellow in presence of bacterium and stayed red in the germfree.

3. Results and discussions

A measured data of plasma sterilization experiments and its outgrowths are encapsulated in Table I. Two power output readings were used. For every power output a several counts of scans were executed.

It is shown the high frequency plasma discharge has a positive sterilization effect to the experimental sample with a bacterium *Escherichia Coli* for all conditions of plasma discharge we used. It is shown the gas flow without a plasma discharge has no sterilization effect to the experimental bacterium sample.

Fig. 2 and Fig. 3 show that presences of reactive species, which are one of several sterilization factor of plasma sterili-

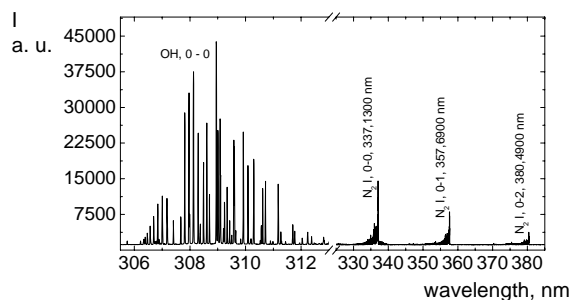


Fig. 2. N₂ and OH reactive species, power output 50 W, gas flow (Ar) 2,5 slpm

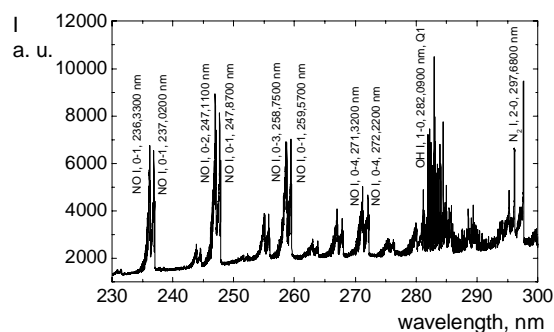


Fig. 3. NO, N₂ and OH reactive species, power output 50 W, gas flow (Ar) 2,5 slpm

zation, were confirmed. To determine a character of reactive species the software Spectrum Analyzer 1.6 was used¹⁰. The NO, N₂ and OH reactive species were located. It is recognizable that plasma discharge we used for plasma sterilization

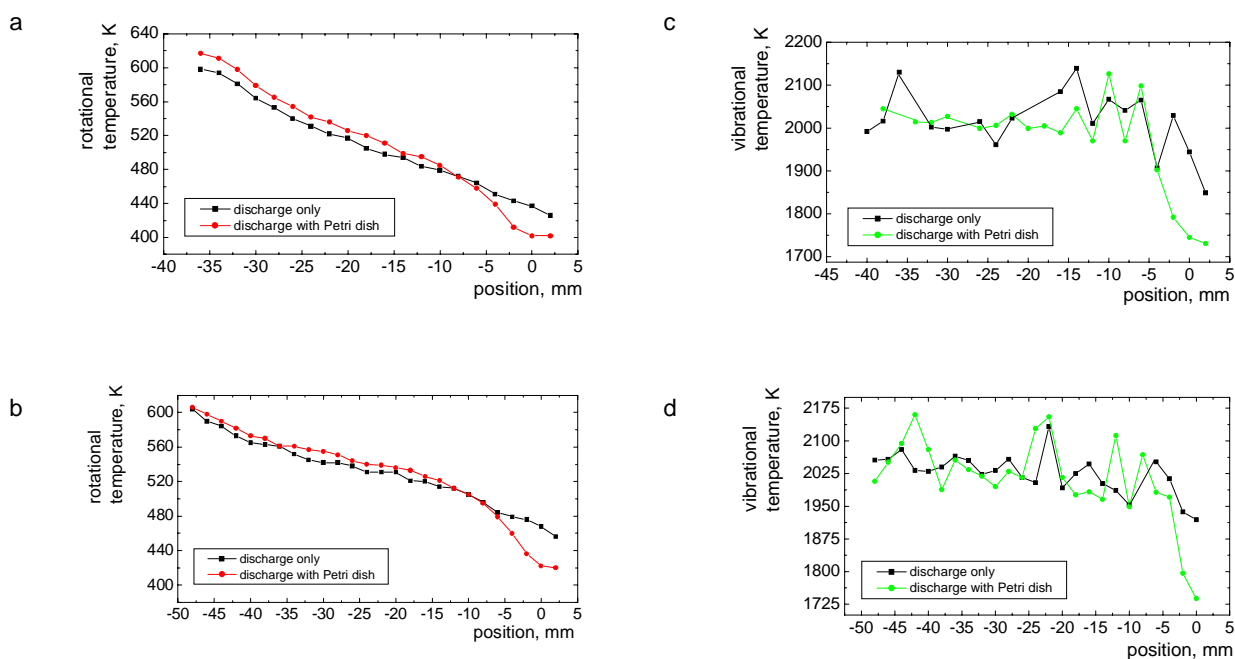


Fig. 3. Rotational and vibrational temperature of plasma discharge with (a) power output 45 W, gas flow (Ar) 2,5 slpm, (b) power output 50 W, gas flow (Ar) 2,5 slpm, (c) power output 45 W, gas flow (Ar) 2,5 slpm, (d) power output 50 W, gas flow (Ar) 2,5 slpm

contains many reactive species in wide range of its wave length.

Fig. 3 shows that plasma discharge sends out rays with wave range of 260–290 nm. This wave range come in to the UV wavelength, witch is a major sterilization effect of plasma sterilization.

UV radiation is responsible for structural changes of essential biomolecules in cells. Subsequently this changes cause malfunction of these molecules¹¹. The range of 260–265 nm is absorbed by nuclear acids (DNA, RNA) and causes the highest germicide effect of UV range of 240–280 nm and the range of 280–290 nm is absorbed by enzymes which are answerable for repairing of nuclear acids¹².

Fig. 4 shows a dependence of rotational and vibrational temperature on the position of emission spectroscopie probe. Measuring of plasma discharge with Petri dish and discharge only was taken.

It is shown the rotational temperature descends with position of probe from electrode to mouth of silica glass tube. The vibrational temperature is invariable in position of spectroscopie probe from electrode to position 4 mm into the silica glass tube.

For every power output we used it is shown that the rotational and vibrational temperature is smaller for plasma device configuration with plasma discharge and Petri dish than for configuration with discharge only in position of spectroscopie probe. This fall of temperature of plasma discharge with Petri dish is recognizable from 4 mm into the glass tube to out of this tube.

Fig. 4 demonstrates curves of rotational temperature for two power output we used for plasma sterilization experiments. It is shown to get a lower rotational temperature rather power output of 45 W than power output of 50 W is needed to set.

4. Conclusions

The high frequency atmospheric pressure plasma discharge was taken to test its potential sterilization effect on the experimental strip of filter paper with a bacterium *Escherichia Coli*.

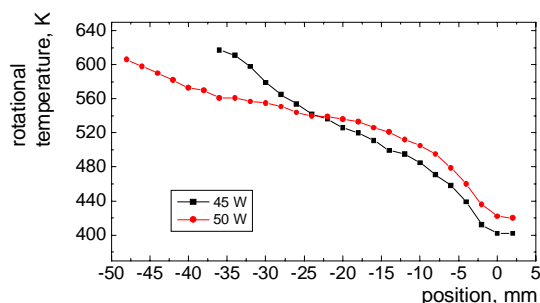


Fig. 4. Rotational temperature, power output 45, 50 W, gas flow (Ar) 2,5 slpm, plasma discharge with Petri dish

The experimental samples were germfree for all plasma sterilization conditions we used – different power output and counts of scans were set. A control sample confirmed no sterilization effect of gas flow (argon as a working gas) without a plasma discharge.

By using optical emission spectroscopy presence of major plasma sterilization effectors, reactive species and UV rays, was confirmed.

Many reactive species in wide range of plasma discharge wave length were recognized, mostly OH, NO and N₂ reactive species. UV wavelength in wave range of plasma discharge we used for plasma sterilization was detected.

From emission spectroscopy a dependence of rotational and vibrational temperature of plasma discharge on position of spectroscopy probe was acquired.

These obtained results are very important to optimize very promising alternative sterilization method, atmospheric pressure plasma sterilization. This method could substitute present-day used physical and chemical sterilization methods, which stand up to new sterilized object with special features – heat, pressure and chemical sensitivity.

This research has been supported by the grant 202/07/1207, by the Czech Science Foundation and by the research intent MSM: 0021622411 funding by the Ministry of Education of the Czech Republic.

REFERENCES

1. Chau T. T., Kao K. C., Blank G., Madrid F.: *Boimaterials* 17, 1273 (1996).
2. Lado B. H., Yousef A. E.: *Microbes and Infection* 4, 433 (2002).
3. Moreira A. J., Mansano R. D., Pinto T., Ruas R., Zambon L., Silva M., Verdonck P. B.: *Appl. Surf. Sci.* 235, 151 (2004).
4. Lee K. Y., Park B. J., Lee D. H., Hyun S. O., Chung K. H.: *Surf. Coat. Technol.* 193, 35 (2008).
5. Chichester C. O., Maxwell W. A.: *Life Sci. Space Res.* 7, 8 (1969).
6. Racek J., Holeček V.: *Chem. Listy* 93, 774 (1999).
7. Slaviček P., Janča J., Kapička V., Brablec A., Kadlecová J., Smékal P., Klíma M.: *XVI Symposium on Physics of Switching Arc*, p. 170, Brno: Faculty of Electrical Engineering and Communication, BUT 2005.
8. Slaviček P., Kapička V., Brablec A., Kadlecová J., Smékal P., Vaněk P., Klíma M.: *In Proceeding of XXVIII ICPIG*, p. 197, Praha. Institute of Plasma Physics AVCR, Praha 2007.
9. http://service.merck.de/microbiology/tedisdata/prods/4970-1_00414_0500.html#literature, downloaded at 25th April 2008.
10. Navrátil Z., Trunec D., Šmíd R., Lazar L.: *Czech J. Phys.* 56, 944 (2006).
11. Zepp R. G., Callaghan T. V., Ericsson D. J.: *J. Photochem. Photobiol., B* 46, 69 (1998).
12. Wang T., MacGregor S. J., Anderson J. G., Woolsey G.: *Water Res.* 39, 2921 (2005).

PAPER STERILIZATION BY ATMOSPHERIC PRESSURE DBD DISCHARGE

J. VRAJOVÁ^{a*}, L. CHALUPOVÁ^b, J. ČECH^b,
F. KRČMA^a, and P. ŠTAHEL^b

^a Institute of Physical and Applied Chemistry, Faculty of Chemistry, Brno University of Technology, Purkyňova 118, 612 00 Brno, ^b Department of Physical Electronics, Faculty of Science, Masaryk University, Kotlarska 2, 61137 Brno, Czech Republic
vrajova@fch.vutbr.cz

Introduction

For many centuries, paper was the main recording medium all over the world. Paper due to the influence of wide range of agents (chemical composition, climatic conditions, biological agents etc.) undergoes different degradation processes that result in alarming conditions of many historical documents. One of the problem that has to be solved is the paper biodeterioration by microbiological agents.

The microbial contamination of the paper materials is a serious problem of many archives and libraries. Among the microorganisms present in archives, the microscopic fungi, commonly known as moulds, play the most important role¹. The Czech National Library in cooperation with Czech National Archives studied the microbial contamination of old prints originated from 16th – 17th century. The presence of 78 different fungi was proved². The most visible effect of the paper biodeterioration due to the fungi are the colour stains that originated either from the presence of the fungi itself (fungi mycelium or spores) or as the result of the fungi metabolites. Other important effects are both mechanical corrosion due to the growth of fungi and enzymatic degradation. All of these processes result in the loss of the paper mass and decrease of the paper strength³.

Generally, the material sterilization can be achieved by chemical and/or physical means, such as heat, chemical solutions, gases and radiation⁴. Majority of conventional sterilization techniques are associated with some level of damage to the material or medium supporting the microorganisms. This does not present any problem, in case where material preservation is not an issue⁵. However, in case where the preservation of the material is the imperative duty, new techniques have to be developed.

In past year many studies were done in the field of plasma sterilization. For an extensive coverage on the sterilization application in low-pressure plasmas, the reader is referred to reference⁶. An overview of sterilization application in atmospheric pressure plasma was given in reference⁷ moreover the influence of the UV on sterilization process is described. In recent years, the influence of low-pressure plasma on the biodeteriorated paper and on the paper mechanical and chemical properties was studied^{8,9}.

Basically, the main inactivation factors for cells exposed to plasma are heat, UV radiation and various reactive speci-

es^{5,6,10}. Each of the single mechanisms mentioned above is germicidal, but they always occur in combinations in the gas plasma and can enforce the sterilizing effect synergistically¹⁰. The extent of the influence of each factor depends on the plasma operating parameters (applied electrical power, gas mixture, the gas pressure, etc.)⁵.

This contribution presents results of the paper sterilization using atmospheric pressure DBD. Moreover the effect of the plasma treatment on the paper morphology and colorimetric properties were studied.

Experimental

The experiments were carried out in a Plexiglass discharge reactor (Fig. 1) with the dimensions 120 × 118 × 120 mm³. The discharge burned between two plane metal electrodes, both covered with Al₂O₃ ceramics, 0.5 mm thick. Dimensions of metal electrodes were 40 × 40 mm and dimensions of Al₂O₃ ceramics covering the electrodes were 100 × 100 mm. The distance between electrodes was 4 mm in the case of nitrogen and argon plasmas and 10 mm when helium plasma was used. The sample was fixed in the middle of the discharge gap. The scheme of the experimental set-up is shown in the Fig. 2. High voltage with the frequency of 6 kHz was used for discharge generation. The plasma power density was varied from 83 m W cm⁻³ to 1080 m W cm⁻³. The working gas flow rate was 3 slm in all cases. The discharge parameters were studied by means of the optical emission spectroscopy. The spectra emitted by the discharge were recorded with the Jobin-Yvon TRIAX 550 monochromator equipped with 1200 gr mm⁻¹ and 3600 gr mm⁻¹ gratings and liquid nitrogen cooled CCD detector. The spectras were recorded in range 200–960 nm. From optical emission spectra, some plasma parameters such as vibrational and rotational temperatures were determined.

Aspergillus niger F8189, the fungi which is commonly found in libraries and archives^{1,2}, has been chosen as a bio-indicator to evaluate the plasma microbial inactivation. The fungi was obtained in Czech collection of microorganisms (Masaryk University Brno – Faculty of Science). The culture of *Aspergillus niger* was cultivated on wort agar (wort + agar powder Himedia RM 026). The spore suspension was prepared by pouring 5 ml sterile water with Tween 80 into the *Aspergillus* culture and the surface was gently scraped with a wire. The obtained spore suspension was centrifuged three times and the supernatant was discarded. The spore suspen-

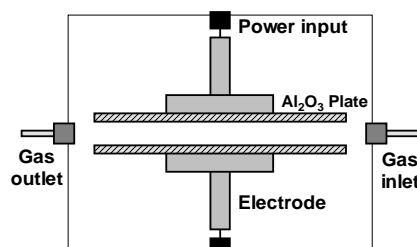


Fig. 1. Scheme of DBD reactor

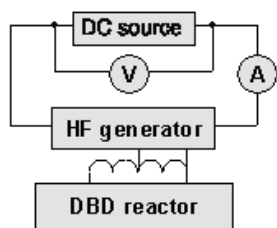


Fig. 2. Scheme of the experimental set-up

sion was diluted in sterile water with Tween 80 in order to obtain suspension containing roughly 10^6 spores/ml (Bürker cell was used for spore counting). Afterward the sterilized Whatman paper no. 1 was placed on wort agar in Petri dish and 100 μ l of the prepared spore suspension was inoculated on the paper samples. The samples were incubated for seven days at 25 °C. Before the plasma treatment, the paper samples were reached from agar medium and dried for 24 hours at 25 °C. After the plasma treatment the samples were immersed into 10 ml of sterile water with Tween 80 and placed overnight on the Horizontal Receptable Shaker in order to wash away the spores from the samples. The spore suspension was diluted and dispersed on wort agar plates. After 72 hours of incubation the number of colony forming units (cfu) was counted (Fig. 3). Quantification of the plasma treatment effect was carried out via the survival factor $S = N_t, \text{CFU}/N_{t0}$ (N_t, CFU – number of colony forming units/ N_{t0} – concentration of the spore suspension placed on wort agar).

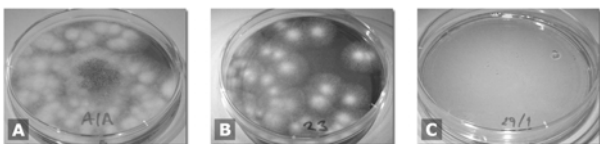


Fig. 3. Re-cultivated samples after 3 days: A/ non-treated sample, 70 cfu; B/ sample treated in Argon for 40 s, plasma power density $305.6 \text{ m W cm}^{-3}$, 41 cfu; C/ sample treated in Ar for 240 s, plasma power density $305.6 \text{ m W cm}^{-3}$, 0 cfu

Results

The plasma was studied by optical emission spectroscopy in order to understand the processes, which are present during the plasma sterilization. The OES spectra were taken through the Pyrex glass window, therefore the radiation below 300 nm was absorbed.

The rotational temperature was calculated from the intensities of rotational lines of OH 0–0 system in case of rare gasses discharges and from the structure of rotationally unresolved 0–2 vibrational band of 2nd positive system of nitrogen in the case of nitrogen discharge¹¹. The rotational temperature corresponds to temperature of neutral gas. Rotational temperatures of Ar, He and nitrogen plasmas (given in Tab. I)

Table I
Examples of rotation and vibration temperatures

Gas/power	T_{rot} [K]	T_{vibr} [K]
$\text{N}_2/ 1083 \text{ m W cm}^{-3}$	400 ± 100	2220 ± 20
$\text{He}/ 88.9 \text{ m W cm}^{-3}$	290 ± 30	2900 ± 160
$\text{He}/ 516.7 \text{ m W cm}^{-3}$	310 ± 20	3600 ± 400
$\text{Ar}/ 83.33 \text{ m W cm}^{-3}$	310 ± 10	1700 ± 200
$\text{Ar}/ 305,6 \text{ m W cm}^{-3}$	320 ± 10	2300 ± 400

are low enough to ensure the treatment of temperature sensitive samples by means of this plasmas. Vibrational temperature was calculated from the 2nd pos. system of nitrogen ($\text{C}^3\Pi_u - \text{B}^3\Pi_g$, $\Delta v = -2$ sequence). The vibrational temperature gives us information about excitation level of plasma. The thermal non-equilibrium of plasma can be seen from the values of the rotational and vibrational temperature given in Tab. I.

The effectiveness of the plasma treatment was reported as the survival factor. The effect of the plasma power input and treatment time using nitrogen plasma has been evaluated from the data shown in Fig. 4. Plasma power density was varied from 262 m W cm^{-3} to 1083 m W cm^{-3} . As it can be seen in the Fig. 4, survival factor decreases with increasing the treatment time. The most significant reduction of the survival factor was obtained within 20 s regardless of the used plasma power density or process gas (Fig. 5). Further increasing of the treatment time leads only to very slight decrease of the survival factor. This may be due to the „shadowing“ effects by spores protecting the underlying layers^{12,13}. Moreover, the porosity of the paper has to be considered. The spores may penetrate into the paper material and embed in pits and cavities¹⁴. Such penetration could preclude the interaction of plasma with the spores, thereby decreasing the efficiency of spore inactivation. Therefore further study has to be done in order to evaluate the contribution of spore concentration and material porosity to the inactivation process. The total removal of the fungi was observed using treatment time of 180 s and plasma power input 1083 m W cm^{-3} . When working with the lower plasma densities longer exposition time is necessary.

Similar results were obtained for all process gases. To compare the inactivation efficiency of nitrogen, argon and helium the plasma power density approximately 300 m W cm^{-3} was used (Fig. 5). The best results were obtained for argon plasma. When operating plasma discharge with plasma densities of 300 m W cm^{-3} the nitrogen plasma seems to be more effective in microorganism inactivation than the helium plasma. For the higher plasma power input, the helium plasma gives much better results, this can be explained by increase of the intensity of O and OH peaks. In order to obtain the same results in nitrogen/ helium as in argon approximately three times (1083 m W cm^{-3})/ two times higher plasma power input (516 m W cm^{-3}) is required.

Possible inactivation processes were provided and commented in the review paper by Moisan⁶, which included: (a) direct destruction of the genetic material of microorganism by UV radiation; (b) erosion of microorganisms, atom by atom,

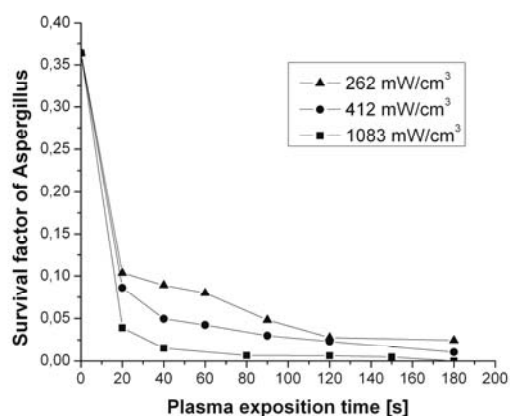


Fig. 4. Survival factor of *Aspergillus niger* vs. treatment time, nitrogen was used as a working gas, plasma power input was varied from 262 m W cm^{-3} – 1083 m W cm^{-3}

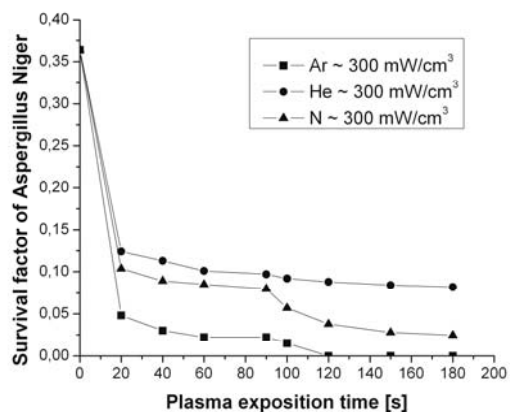


Fig. 5. Comparison of the inactivation efficiency of nitrogen, argon and helium plasma, plasma power density approximately 300 m W cm^{-3}

by intrinsic photodesorption; (c) erosion of microorganisms, atom by atom, through etching. Taking into account more recent work on low-temperature plasma inactivation at atmospheric pressure, following inactivation mechanisms should be added⁷: (d) diffusion of oxygenated species (e.g. OH) through the spore material with ensuing local damage; (e) lyses of the bacterium as a results of the rupture of its membrane due to the electrostatic forces exerted on it by accumulation of charged particles coming from the plasma (proved only Gram-negative vegetative spores).

According to Laroussi⁵, the UV radiation does not play the prominent inactivation role in atmospheric plasmas. Contrary to this statement, Boudam⁷ proved that spore inactivation, depending on operating conditions, can be achieved either under dominant UV radiation or, on the contrary, under the sole action of the reactive species.

Generally, the most efficient microbial DNA destruction

is obtained with the UV radiation in interval 220–270 nm (ref.¹⁵). Since the significant light intensity losses in our OES occurred in the wavelengths below 300 nm, we are limited to the wavelengths above 300 nm, and thus we are not able to evaluate the influence of the UV radiation on the fungi destruction.

However, the higher inactivation efficiency of argon and helium plasma could result from the presence of impurities in our process gases. The OES spectroscopy proved the presence of OH radical and atomic oxygen (Fig. 6). These species can contribute to the higher sterilization efficiency as mentioned above. Further the second positive system of molecular nitrogen was presented in both argon and helium plasma and molecular bands of ionized nitrogen in helium plasma. In nitrogen plasma, only the second positive system of nitrogen was observed in the spectra mainly due to the strong absorption of Pyrex glas below the 300 nm.

Besides the UV radiation and presence of the reactive species, the temperature can play important role during micro-organism inactivation. Sterilization by heat is one of the conventional methods used for thermally resistant material sterilization⁴. The contribution of this effect could be low because of low value of rotation temperature (see Tab. I). Except for the nitrogen plasma, the rotation temperature of argon and helium plasma is more or less the same. In the case of nitrogen plasma the temperature can contribute to the plasma sterilization process.

Furthermore the interaction of the DBD with the plain paper material was studied. The paper samples were treated under the same conditions as the samples containing *Aspergillus niger* spores. Treatment time up to 240 s was used and the total plasma power density was according to the working gas varied in the range $83.33 \text{ m W cm}^{-3}$ to 1083 m W cm^{-3} . Afterwards, the colorimetric measurements (colorimeter X-Rite 918) were done to evaluate the changes in paper whiteness and yellowness due to the plasma treatment. The whiteness of the paper decreases with increasing of both the treatment time and/or the plasma power density. Table II. compares the influence of varying plasma power density on the paper colour.

The yellowness of treated paper increased after the plasma treatment, however for argon and helium treated paper

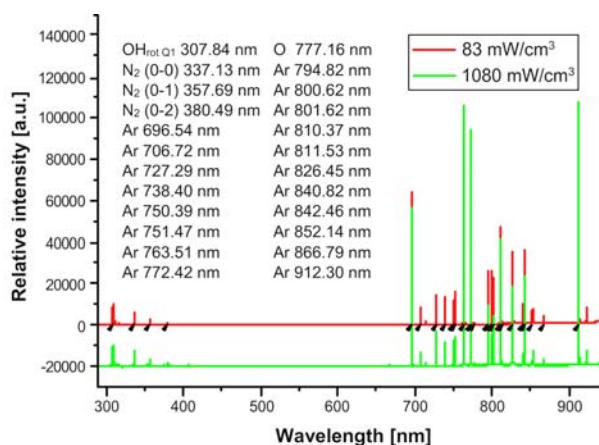


Fig. 6. OES spectrum of Argon plasma, plasma power density 83 m W cm^{-3} and 1080 m W cm^{-3}

Table II

Changes of the paper whiteness (Δ WHT) and yellowness (Δ YEL). Paper was treated in Argon for 240 s, minus = decrease, plus = increase

Power [m W cm^{-3}]	Δ WHT	Δ YEL
83.3	-3.87	+1.85
180.6	-4.53	+2.03
305.6	-7.24	+2.34

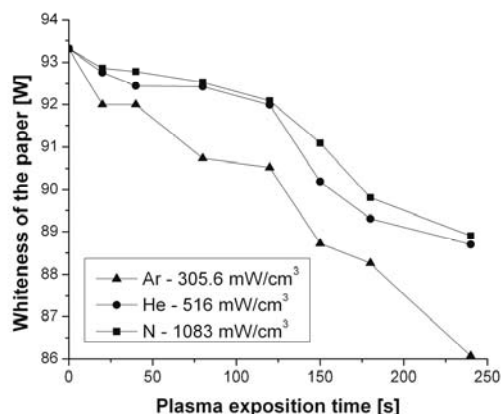


Fig. 7. The whiteness of the paper after the plasma treatment. Different plasma power input for each gas is used, in order to compare the samples treated under conditions when the sterilization efficiency was same for all gases

this change was not eye-visible. Fig. 7 compares the influence of different plasma gases on the paper whiteness. The plasma power input, when the same sterilization efficiency was obtained is used for each gas (Ar – $305.6 \text{ m W cm}^{-3}$, He – 516 m W cm^{-3} , N₂ – 1083 m W cm^{-3}). The highest change in the paper whiteness was observed for the argon plasma. According to the literature¹⁶ the paper yellowing and loss of paper strength results from the oxidation of the cellulose fibers. The presence of the atomic oxygen was proved using OES (Fig. 6). The presence of oxygen and nitrogen in OES can give us the assumption on the presence of NO_x species in the discharge, but this statement cannot be proved due to the Pyrex glass spectral cutoff below 300 nm.

Furthermore the structure of the paper was investigated using SEM microscopy. No significant changes were observed after the plasma treatment in the used range of operating conditions.

Conclusion

The DBD discharge generated at atmospheric pressure could be used as the efficient technique for the paper steriliza-

tion. The efficiency of the plasma sterilization increases with increasing treatment time and plasma power density. Minimum treatment time over 150 s is required in order to achieve satisfactory sterilization in all used plasmas. The interaction of the plasma discharge with the paper substrate causes the slight decrease of the paper whiteness and yellowness of the paper samples.

Further studies will be done in order to study the sterilization efficiency of DBD on wide spectrum of microorganisms, moreover the influence of the plasma treatment on the chemical and mechanical properties of the paper materials will be studied.

This work was supported by the Czech Science Foundation contracts No. 202/03/H162, by Grant Agency of Academy of Science of Czech Republic contract No. KAN101630651 and by the Research Intent from Ministry of Education, Youth and Sports of Czech Republic No. MSM0021622411.

REFERENCES

- Skorkovsky B., in: *Microorganisms as the agents of archival documents degradation*, Chap. 1, p. 108. TEPS, Prague, 1981.
- Odvarikova J., Bacilkova B., in: *Proceedings of 7th Symposium on Historical and Scarce Books of Bohemian, Moravian and Silesian Book Stock*, Olomouc, 1998.
- Bacilkova B.: *Bulletin STOP* 6, 2 (2004).
- Silhankova L., in: *Microbiology for the Food Industry and Biotechnology*. Victoria Publishing, a.s., Prague 1995.
- Laroussi M., Leipold F.: *Int. J. Mass Spectrom.* 233, 81 (2004)
- Moisan M., Barbeau J., Moreau S., Pelletier J., Tabrizian M., Yahia L. H.: *Int. J. Pharmaceutics* 226, 1 (2001)
- Boudam M. K., Moisan M., Saoudi B., Popovici C., Gherardi N., Massines F.: *J. Phys. D: Appl. Phys.* 39, 3494 (2006)
- Laguardi L., Vassallo E., Cappitelli F., Mesto E., Cremona A., Sorlini C., Bonizzoni G.: *Appl. Surf. Sci.* 252, 1159 (2005).
- Vohrer U., Trick I., Bernhardt J., Oehr C., Brunner H.: *Surf. Coatings Technol.* 142–144, 1069 (2001).
- Muranyi P., Wunderlich J., Heise M.: *J. Appl. Microbiology* 103, 1535 (2007)
- Janca J., Skricka L., Brablec A.: *Plasma Chem. Plasma Process.* 13, 3 (1993).
- Heise M., Neff W., Franken O., Muranyi P., Wunderlich J.: *Plasmas and Polymers* 9, 23 (2004)
- Muranyi P., Wunderlich J., Heise M.: *J. Appl. Microbiology* 103, 5 (2007).
- Rogers J. V., Sabourin C. L. K., Choi Y. W., Richter W. R., Rudnicki D. C., Riggs K. B., Taylor M. L., Chang J.: *J. Appl. Microbiology* 99, 4 (2005).
- Moisan M., Bateau J., Crevier M. C., Pelletier J., Phillip N., Saudoni B.: *Pure Appl. Chem.* 74, 349 (2002).
- Durovic M., in: *Restoration and Conservation of the Archival Documents and Books*, Chap. 2.1.5., p. 517. Paseka, Prague 2002.

J. Vrajobá^{a*}, L. Chalupová^b, J. Čech^b, F. Krčma^a, and P. Sřahel^b (^a*Institute of Physical and Applied Chemistry, Faculty of Chemistry, Brno University of Technology, Brno,* ^b*Department of Physical Electronics, Faculty of Science, Masaryk University, Brno, Czech Republic*): **Paper Sterilization by Atmospheric Pressure DBD Discharge**

In this paper, the removal of the microbial contamination from paper material using the plasma treatment at atmospheric pressure is investigated. The *Aspergillus niger* has been chosen as a bio-indicator enabling to evaluate the effect

of plasma assisted microbial inactivation. Dielectric barrier discharge (DBD) operated at atmospheric pressure was used for the paper sterilization. The working gas (nitrogen, argon and helium), plasma exposition time and the plasma power density were varied in order to see the effect of the plasma treatment on the fungi removal. After the treatment, the microbial abatement was evaluated by the standard plate count method. This proved a positive effect of the DBD plasma treatment on fungi removal. Morphological and colorimetric changes of paper substrate after plasma treatment were also investigated.

BIOMEDICAL APPLICATIONS OF ATMOSPHERIC PRESSURE PLASMA

K.-D. WELTMANN*, TH. VON WOEDTKE,
R. BRANDENBURG, and J. EHLBECK

INP Greifswald e.V., Felix.Hausdorff-Strasse 2, 17489
Greifswald, Germany
weltmann@inp-greifswald.de

Introduction

Progress in life sciences is increasingly caused by utilization of unrelated technologies and knowledge. Microelectronics, optics, or material sciences as well as nanotechnology nowadays are key technologies in modern medicine. A similar trend can be expected concerning plasma technology. Plasma medicine as an independent medical field is emerging worldwide – comparable to the development of laser technology years ago. Plasma medicine can be subdivided into three main components: plasma surface modification, plasma bio-decontamination, and – as the central field – therapeutic plasma application. The scientific basis of plasma medicine is a fundamental knowledge of the mechanisms of plasma interaction with living cells and tissue (Fig. 1).

In the areas of plasma surface modification and plasma bio-decontamination, plasma is used to treat surfaces and products to improve their bio-applicability and bio-performance, respectively, to use it for therapeutic purposes. Whereas in these fields, both low-pressure and atmospheric pressure plasmas can be used, for direct therapeutic plasma applications only atmospheric pressure plasma sources can be used.

Plasma surface modification

Plasma surface modification is a state-of-the-art technique to optimize medical implants and biological diagnostic tools^{1,2}. Own experiences include the alteration of surface energy to increase the wettability of polymer surfaces by plasma treatment³, plasma-induced chemical micropatterning for cell culture control⁴ as well as plasma-based polymer coating of implant surfaces to optimize its biocompatibility as

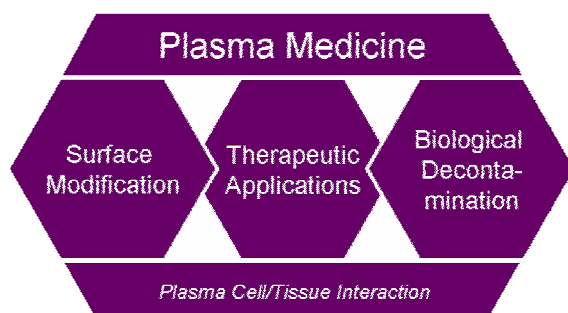


Fig. 1. Plasma medicine: scientific basis and main components

well as bio-functionality⁵. A new and very promising application is the plasma-assisted coating of surfaces to realize the controlled delivery of active substances as antibiotics or cells for therapeutic use⁶.

Plasma bio-decontamination

Plasma based antimicrobial treatments of sensitive products are in the focus of scientific research and development for several years. The technological potential of non-thermal plasmas for the antimicrobial treatment of heat sensitive materials is well known^{7,8}. One of the main advantages of processes using atmospheric pressure plasmas is the possibility to adapt it to a great extent to special product requirements⁹. There is a huge chance to use atmospheric pressure plasma sources for effective antimicrobial treatment of sensitive as well as intricate medical products like medical catheters (Fig. 2) and diagnostic devices as well as pharmaceutical packaging materials^{10–12}.

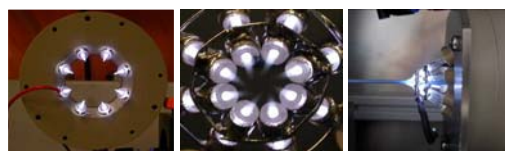


Fig. 2. Modular arrangement of Rf-driven plasma jets for catheter treatment¹¹

Therapeutic plasma application

The use of physical plasmas for bio-decontamination just as first surgical plasma applications like argon-plasma coagulation (APC)^{13,14} are mainly based on lethal plasma effects on living systems. However, there is an additional huge potential of low temperature plasma application for therapeutic fields, which will be based on non-lethal, stimulating plasma effects on living cells and tissue^{15,16}.

An extremely promising field will be the plasma-based treatment of chronic wounds. A selective antimicrobial (antiseptic) activity without damaging surrounding tissue, combined with a controlled stimulation of tissue regeneration could revolutionize wound care. Other fields are the treatment of skin diseases, tissue engineering, or tumour treatment based on specific induction of apoptotic processes. First practical applications of plasmas for wound healing have been interpreted to be very promising, but are only empirical individual case reports¹⁶. Own present studies are focussed on the verification of a selective antiseptic effect of an atmospheric pressure plasma source, i.e. the inactivation of infectious micro-organisms on living tissue like wounds without damaging side effects. Second step of this work is to investigate the chance of plasma-based stimulation of cell proliferation and tissue regeneration. This is investigated using in-vitro cell culture models to establish a scientific basis for following systematic clinical application studies. The aim of this work is to develop a plasma-based device for effective wound antiseptics combined with stimulation of wound healing (Fig. 3).

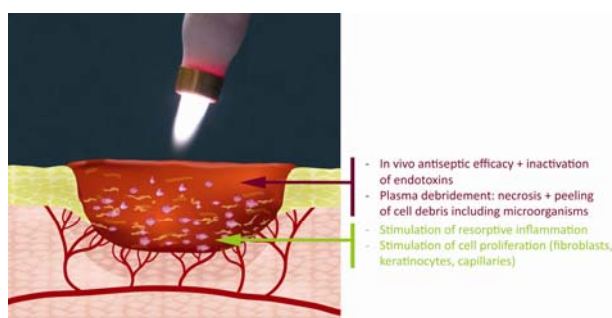


Fig. 3. Concept of multi-stage selective plasma-application for wound healing

Outlook

The main challenge to open up systematically new and promising fields of plasma application in life sciences is to understand the basic physiological and biochemical mechanisms of plasma interaction with living cells and tissue. This includes the systematic investigation of direct plasma effects on growth and vitality of cells just as indirect plasma effects on the vital environment of cells and tissue. On a solid scientific basis, new therapeutic plasma applications e.g. in dermatology, surgery, or dentistry, will be opened during the next years¹⁷.

REFERENCES

- Oehr C.: Nucl. Instr. Meth. Phys. Res., B 208, 40 (2003).
- Ohl A., Schröder K.: *Plasma assisted surface modification of biointerfaces*. In: Hippler R., Kersten H., Schmidt M., Schoenbach K. H. (ed.). *Low Temperature Plasmas*, Vol. 2. 803–820. Wiley-VCH, Weinheim 2008.
- Foest R., Kindel E., Ohl A., Stieber M., Weltmann K.-D.: *Plasma Phys. Control. Fusion* 47, B525-B536 (2005).
- Ohl A., Schröder K.: *Surf. Coat. Technol.* 116-119, 820 (1999).
- Finke B., Luethen F., Schröder K., Mueller P. D., Bergemann C., Frant M., Ohl A., Nebe J. B.: *Biomaterials* 28, 4521 (2007).
- Haddow D. B., MacNeil S., Short R. D.: *Plasma Process. Polym.* 3, 419 (2006).
- Moisan M., Barbeau J., Moreau S., Pelletier J., Tabrizian M., Yahia L'H.: *Int. J. Pharm.* 226, 1 (2001).
- Laroussi M.: *Plasma Process. Polym.* 2, 391 (2005).
- von Woedtke Th., Kramer A., Weltmann K.-D.: *Plasma Process. Polym.* 5, 534 (2008).
- Brandenburg R., Ehlbeck J., Stieber M., von Woedtke Th., Zeymer J., Schlüter O., Weltmann K.-D.: *Contrib. Plasma Phys.* 47, 72 (2007).
- Ehlbeck J., Brandenburg R., von Woedtke Th., Krohmann U., Stieber M., Weltmann K.-D.: *PLASMOSE – antimicrobial effects of modular atmospheric plasma sources*. *GMS Krankenhaushyg. Interdiszip.*, 3, Doc14; <http://www.egms.de/en/journals/dgkh/2008-3/dgkh000112.shtml> (2008).
- Weltmann K.-D., Brandenburg R., von Woedtke Th., Ehlbeck J., Foest R., Stieber M., Kindel E.: *J. Phys. D: Appl. Phys.* 41, in press (2008).
- Raiser J., Zenker M.: *J. Phys. D: Appl. Phys.* 39, 3520 (2006).
- Zenker M.: *Argon plasma coagulation*. *GMS Krankenhaushyg. Interdiszip.*, 3, Doc15; <http://www.egms.de/en/journals/dgkh/2008-3/dgkh000113.shtml> (2008).
- Stoffels E.: *Contrib. Plasma Phys.* 47, 40 (2007).
- Fridman G., Friedman G., Gutsol A., Shekter A. B., Vasilets V. N., Fridman A.: *Plasma Process. Polym.* 5, DOI: 10.1002/ppap.200700154 (2008).
- Kramer A., Lindequist U., Weltmann K.-D., Wilke C., von Woedtke Th.: *Plasma Medicine – its perspective for wound therapy*. *GMS Krankenhaushyg. Interdiszip.* 3, Doc16; <http://www.egms.de/en/journals/dgkh/2008-3/dgkh000114.shtml> (2008).

SURFACE TREATMENT BY PLASMA DISCHARGES AND THIN FILM DEPOSITION

CLEANING OF ALUMINIUM SURFACE USING DIFFUSE COPLANAR SURFACE BARRIER DISCHARGE

LUCIA BÓNOVÁ^a, ANDREJ BUČEK^{a,b}, TOMÁŠ PLECENIK^a, ANNA ZAHORANOVÁ^{a*}, and MIRKO ČERNÁK^{a,b}

^a *Dep. of Experimental Physics, Faculty of Mathematics, Physics and Informatics, Comenius University, Mlynska dolina F2, 842 48 Bratislava, Slovak Republic,* ^b *Institute of Physical Electronics, Faculty of Science, Masaryk University, Kotlarska 2, 611 37 Brno, Czech Republic*
 zahoranova@gimmel.ip.fmph.uniba.sk

Introduction

Non-thermal plasmas have recently received increased attention because of their use in „clean technology“ industrial applications¹. The fact that these plasmas can be generated in large volumes and at atmospheric pressure makes them very attractive for various industrial applications^{1–3}. However, if ambient air is used as the background gas, several serious difficulties are encountered in the plasma generation process. Amongst these are prohibitive power requirements, high gas temperatures, and disrupting instabilities. For the mentioned industrial applications the so-called „Diffuse coplanar surface barrier discharge“ (DSCBD), enabling to generate macroscopically homogeneous plasma in ambient air^{4,5} appears to be to be a very efficient solution. This novel type of discharge has already been successfully used for the treatment of the nonwoven fabrics, foils, wood, paper and glass^{6–9}.

Also in the industry producing metallic films and sheets the treatment of surfaces by non-equilibrium plasma could be solution for environmentally safe and low-cost in-line processing. For temporary corrosion protection or lubrication sheet metals are coated by organic oils. This coatings need to be removed in advance of further metal manufacturing processes. Usually, the cleaning is performed in wet alkaline or acid baths; however, these chemical treatments are problematic from environmental point of view. Therefore the non-equilibrium atmospheric-pressure plasma treatment seems to be a suitable alternative to the above-mentioned methods^{10,11}. Another advantage of such a cleaning could be better performance concerning the activation of the treated surface what is useful for further coating of the surface. The aim of our experimental study was to investigate the possibility of the use of DCSBD discharge for the surface cleaning of aluminium and to evaluate the durability (ageing effect) of such a treatment.

Experimental apparatus and method

The simple scheme of experimental apparatus is shown in the figure 1. Surface modification was carried out using the Diffuse Coplanar Surface Barrier Discharge (DCSBD) generated in air at atmospheric pressure.

The DCSBD electrode geometry consists of 38 parallel stripline silver electrodes embedded 0.5 mm below the surface of 96 % Al₂O₃ ceramics (see Fig. 2). The discharge was powered by 14 kHz sinusoidal voltage, supplied by HV generator LIFETECH VF 700. The active plasma area has the dimensions 200 × 80 mm. The thickness of the plasma layer generated on the surface of the Al₂O₃ ceramics is approximately 0.5 mm. The power supplied to the reactor was approximately 332 W. The 1 × 20 × 70 mm size samples were cut from 99.5 % aluminium metal sheet. The samples were sonicated for 6 minutes in acetone prior to the plasma cleaning. By the treatment they were attached to a plastic cart. The cart was moving trough the discharge area at a constant speed carrying the sample. The distance between sample surface and the surface of the Al₂O₃ ceramics was 0.3 mm. By changing the cart speed it is possible to change the treatment time.

In general, a good wettability of metal surface is considered a good indication that organic contamination was virtually absent from the cleaned surfaces. As a consequence, the following surface energy measurement was used as an indication of the plasma surface cleaning efficiency.

After the plasma cleaning the contact angle of one drop of distilled water (2 μl) on the treated surface was measured by the means of the Surface Energy Evaluation System (SEE System¹²; Advex Instruments s. r. o., Czech republic). Supplied See Software 6.0 firmware was used to process the

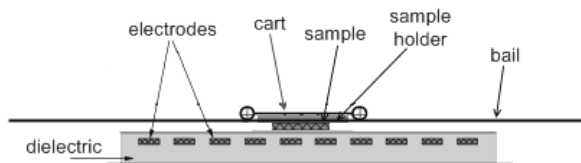


Fig. 1. Simple block scheme of experimental apparatus

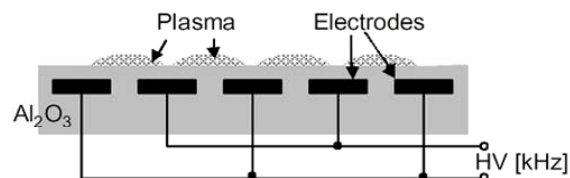


Fig. 2. Schematic drawing of the DCSBD electrode arrangement

droplet images and calculate the contact angle. Each resulting contact angle is an average of 20 measured values.

The ageing effect of the treatment was also studied. The contact angle measurement of the samples treated for a period of 3 s was done at several selected times (every hour in the interval from 0 to 8 hours and then at 24, 48 and 72 hours after the treatment). During the ageing study the samples were stored under ambient conditions. The results were compared to the untreated samples and to the treated samples stored in vacuum.

The possible changes in the morphology of the plasma-treated aluminium surfaces were investigated by the means of AFM microscopy using the Solver P47-PRO (NT-MDT Co., Russia) AFM setup. As a well defined aluminium surface the surface of Al-coated Si-wafers was used. The DCSBD plasma treatment was done in ambient air at the discharge power of 332 W. The treatment time was 3 s, the distance between the sample and the electrode surface was 0.3 mm during the treatment. By the means of AFM measurements the root mean square (RMS) roughness of the aluminium surfaces has been evaluated.

Experimental results and discussion

In the fig. 3a and 3b the shapes of water drops placed on untreated and plasma-treated sample, respectively, are shown. The discharge power was 332 W, the distance between sample and the surface of the dielectrics was 0.3 mm and the treatment time was 3 s.

In the fig. 4 the dependence of contact angle on the treatment time is shown. From the figure it is clear that after the treatment lasting for 1 s the contact angle changes dramatically. 3 s lasting treatment causes almost maximum wettability of the surface. The observed effect can be explained through the plasma induced removal of organic contamination from the treated aluminium surface¹¹ with possible increase in surface –OH groups density, which are responsible for the wettable properties of oxide surfaces.

In fig. 5 the ageing effect of the 3 s treatment is shown. The contact angles on the sample stored in ambient air are compared to the contact angle of sample stored under vacuum and the contact angle of an untreated sample. From the figure it is clear that the wettability of the treated surface decreases with the storage time. This can be assigned to the adsorption of organic compounds from the surrounding ambient on the

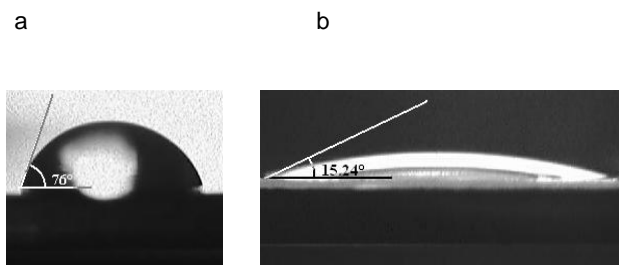


Fig. 3. Photographs (a) and (b) showing the shapes of water drops placed on an untreated aluminium surface and on the air plasma-treated aluminium surface, respectively. The discharge power was 332 W, the treatment time was 3 s

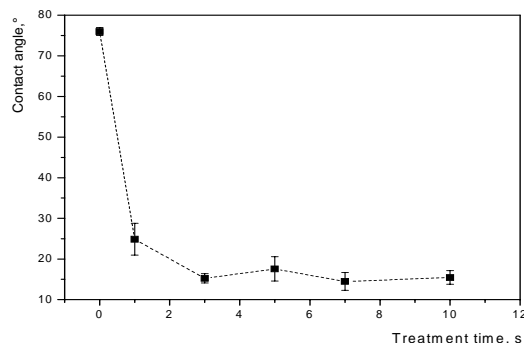


Fig. 4. Contact angle measurements on aluminium surfaces treated by the plasma generated at the discharge power of 332 W in ambient air

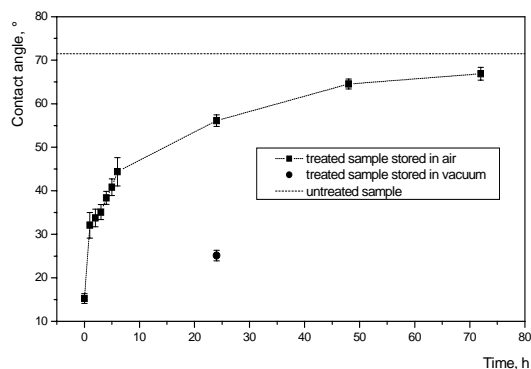
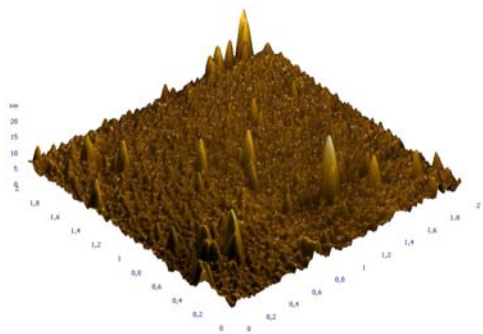


Fig. 5. Ageing effect of the ambient air plasma surface treatment. Treatment time 3 s, discharge power 332 W, stored under ambient conditions and vacuum

treated surface, which leads to the decrease in the free surface energy of the treated surface. This conclusion is supported by the result of the vacuum storage of the treated surface, where, due to the considerably lower content of the organic compounds in the surrounding ambient, the contact angle retained at lower value when compared with the surface stored in ambient air.

In the fig. 6 the AFM images of the untreated as well as the plasma-treated aluminium surfaces are shown. The comparison of the RMS values for the untreated and the plasma-treated aluminium surface revealed, that the 3 s lasting plasma treatment, which time is optimal to achieve the hydrophilisation of the surface, led to the slight increase in the roughness of the treated aluminium surface. The obtained value of the RMS roughness in the case of the untreated aluminium surface was 1.533 nm, whereas it's value in the case of the plasma-treated aluminium surface was 1.866 nm.

a



b

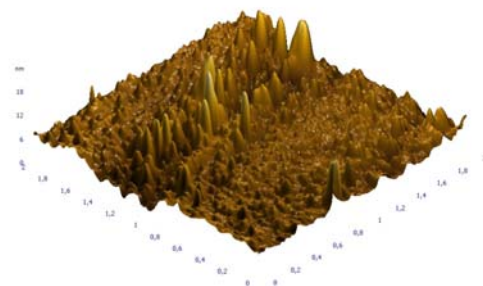


Fig. 6. AFM images of (a) untreated sample and (b) ambient air plasma treated aluminium surface. Scanned area: $2 \times 2 \mu\text{m}$

Conclusions

Presented results of the plasma activation of aluminium surface demonstrate that the DCSBD plasma is an effective tool in enhancing the wettability (Fig. 4) of the treated surface. Treatment time of 3 s is sufficient enough to turn the treated aluminium surface hydrophilic. The observed effect was assigned to the removal of the organic contamination from the treated surface with possible increase in the surface hydroxyl groups density. The ageing effect of the treatment was observed, the wettability of the treated surface decreases with the storage time. This was assigned to the adsorption of the organic compounds from the surrounding ambient on the treated surface, which assumption was supported by the result of the vacuum storage experiment.

The AFM measurements showed slight increase in the surface roughness of the aluminium surface treated by the plasma at the treatment time of 3 s.

The preliminary results indicate that this novel atmospheric-pressure plasma source may be useful for the activation of the aluminium surface.

This research has been supported by the Grant AV/4/2033/08 from Ministry of Education of the Slovak Republic, by Comenius University grant UK/401/2008, and by the research project MSM0021622411 of the Ministry of Education of the Czech Republic.

REFERENCES

1. Roth J. R.: *Industrial Plasma Engineering*, Vol. 2: Indt. Of Phys. Publishing, Bristol and Philadelphia, 2001
2. Hwang Y. J., An J. S., McCord M. G., Park S. W., Kang B. C.: *Fibers and Polymers* 4, 145 (2003).
3. Temmerman E., Akishev Y., Trushkin N., Leys C., Verschuren J.: *J. Phys. D: Appl. Phys.* 38, 505 (2005).
4. Šimor M., Ráhel' J., Vojtek P., Brablec A., Černák M.: *Appl. Phys. Lett.* 81, 2716 (2002).
5. Černák M., Ráhel' J., Kováčik D., Šimor M., Brablec A., Slaviček P.: *Contrib. Plasma Phys.* 44, 504 (2004).
6. Černáková L., Sťahel P., Kováčik D., Johansson K. Černák M.: *9th TAPPI Advanced Coating Fundamentals Symposium, Turku: Contributed Papers, Abo Akademi University, 2006.* pp. 7-17.
7. Odrášková M., Ráhel' J., Zahoranová A., Tiňo R., Černák M.: *Plasma Chem. Plasma Process.* 28, 203 (2008).
8. Černák M., Kováčik D., Buček A., Zahoranová A., Ráhel' J., Sťahel P.: *17th Symposium on Physics of Switching Arc, Proceedings: Contributed Papers, Vol. I, Nové Město na Moravě, September 10-13, 2007, Czech Republic*, pp. 49–52, Nové Město na Moravě 2007.
9. Homola T., Buček A., Zahoranová A.: *16th Annual Conference of Doctoral Students WDS '07, Part 2 : Physics of Plasmas and Ionized Media, Praha: Matfyzpress, 2007* S. 124-128. Praha 2007.
10. Shin D. H., Bang C. U., Kim J. H., Han K. H., Hong Y. C., Uhm H. S., Park D. K., Kim K. H.: *Surf. Coatings Technol.* 201, 4939 (2007).
11. Pinson S. J. M., Collins J., Thompson G. E., Alexander M. R.: *ATB Metallurgie* 43, 448 (2003).
12. <http://www.seesystems.wz.cz>

L. Bónová^a, A. Buček^{a,b}, T. Pleceník^a, A. Zahoranová^a, and M. Černák^{a,b} (^a *Dep. of Experimental Physics, Faculty of Mathematics, Physics and Informatics, Comenius University, Bratislava, Slovak Republic*, ^b *Institute of Physical Electronics, Faculty of Science, Masaryk University, Brno, Czech Republic*): **Cleaning of Aluminium Surface Using Diffuse Coplanar Surface Barrier Discharge**

A novel type of barrier discharge, the so called Diffuse Coplanar Surface Barrier Discharge (DCSBD) operating in air at atmospheric pressure, has been used to clean the surface of aluminium. The effect of plasma treatment was studied by the means of the contact angle measurements on water droplets dropped on the treated aluminium surface. The presented experimental results show an efficient cleaning of the aluminium surface even after short plasma exposure (1–3 sec). The durability of the treatment (ageing effect) was also investigated. The atomic force microscopy AFM was used for more detailed evaluation of the surface topolygy changes.

EFFECT OF THE DECAMETHYLTETRASILOXANE FILMS DEPOSITION PARAMETERS ON THEIR PROPERTIES

Z. RZANEK-BOROCH^a, K. GRADKOWSKA^a,
A. ILIK^b, and A. KOSIŃSKI^c

^a Faculty of Chemistry, Warsaw University of Technology, 00-664 Warsaw, Noakowskiego 3, Poland, ^b Faculty of Physics and Chemistry, University of Łódź, 90-236 Łódź, Pomorska 149/153, Poland, ^c Institute of Physical Chemistry Polish Academy of Sciences, 01-224 Warsaw, Kasprzaka 44-52, Poland
rzanek@ch.pw.edu.pl

Keywords: thin films, DBD, decamethyltetrasiloxane, friction coefficient

Introduction

Many critical systems in spacecraft or vacuum technology involve relative motion of contacting surfaces. Most of the applications require the use of low friction rate lubricants, taking into account the need for low power consumption and extreme reliability in a wide range of environments¹.

The increased interest in MEMS has raised the request for long-term stable micro actuators. However, the requirements on reliability, durability and local pressure will be comparable to macroscopic applications. One major problem is the lack of tribological optimized surfaces for micro parts. As a solution, microtribological coatings are used^{2–4}.

The plasma deposition of thin films with low friction coefficient have been intensively investigated in recent years^{5–7}. The most known examples are the plasma deposited DLC diamond-like coatings^{8–12}.

An increasing interest in plasma deposition of thin films under atmospheric pressure, with the use of alkylsiloxanes compounds as the precursors^{13,14,1} is observed. The interest stems not only from economic reasons, as compared with the low pressure methods used up to now, but also from the steadily increasing role of surface and demand of new utility prop-

erties of materials, as well as from the exhaustion of possibilities of the traditional technologies^{15–17}.

The goal of the investigations was to study the process of thin film deposition from decamethyltetrasiloxane (DMTOS) mixtures with argon and oxygen, which can be applied in MEMS (micro electro mechanical systems).

Experimental

The aim of the work was to determine the optimal conditions of depositing films in DBD (dielectric barrier discharge) under atmospheric pressure^{1,2}. The process was carried out for 15 minutes at 1.5 kV voltage and 3–4 kHz frequency. Decamethyltetrasiloxane (DMTOS) of C₁₀H₃₀Si₄O₃ formula was the precursor. The films were deposited on monocrystalline silicon <100> surfaces, at 100–400 °C from 0.04 % DMTOS + O₂ + Ar mixtures at overall gas flow of 12 dm³ h⁻¹ and oxygen concentration in the range of 0–1.42 %.

The obtained films were studied by:

- Composition: Infrared Spectroscopy with Fourier Transformation (FT-IR).
- Friction coefficient: Linear tribometer (designed at Łódź University, with a ¼" ball of ZrO₂ modified with Y₂O₃, under the loads of 30–90 mN. Rate of ball shift with respect to the surface studied – 10 mm min⁻¹, number of repetitions 4.
- Composition: Auger Electron Spectroscopy (AES) using a MICROLAB-350, produced by Thermo Fischer, using electron energy of 10 kV.
- Surface topography: Atomic Force Microscopy (AFM) produced by Park Scientific Instruments.
- Film thickness was measured by ellipsometry at 632.8 nm wavelength using Ellipsometr II (Applied Materials).

Results and discussion

In the studies carried out attention has been put on the effect of the surface temperature and oxygen content in the mixture on the properties of films.

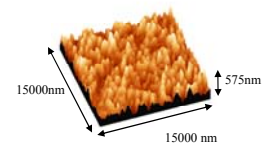
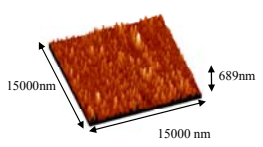
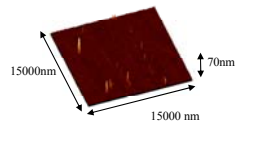
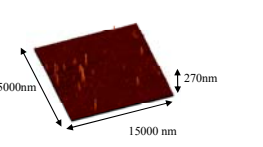
On the basis of IR studies, for mixtures 0.04 % DMTOS + O₂ + Ar comprising 0–0.18 % of oxygen it was found that with an increase in the surface temperature a decrease in the intensity of absorption bands characteristic of Si-CH₃, Si-

Table I
Characteristics of thin films deposited from the mixture of 0.04% DMTOS + Ar

Sample	Temperature [°C]	Thickness [nm]	Composition			Fiction coefficient
			C [%]	O [%]	Si [%]	
29 KR	100	85.5	42.4	18.9	38.7	0.048 ± 0,006
30KR	200	55.8	36.4	22.1	41.5	0.123 ± 0,014
32KR	300	37.0	26.7	27.3	46.0	0.262 ± 0,028
31KR	400	41.8	30.4	27.2	42.4	0.442 ± 0,044
Si						0.072 ± 0,014

Table II

Topography of the surface of films deposited at various temperatures from the 0.04 % DMTOS + 1.42 % O₂ + Ar mixture

<p>40KR</p>  <p>15000nm 15000 nm 575nm</p> <p>temp.100°C RMS=32.4 nm</p>	<p>43KR</p>  <p>15000nm 15000 nm 689nm</p> <p>temp.200°C RMS=16.6 nm</p>
<p>42KR</p>  <p>15000nm 15000 nm 70nm</p> <p>temp.300°C RMS=16.5 nm</p>	<p>41KR</p>  <p>15000nm 15000 nm 270nm</p> <p>temp.400°C RMS=2.3 nm</p>

(CH₃)₃, Si-O-Si, Si-O and Si-O-C groups occurs, as well as that of the CH_x group decays. The results of FTIR studies of films deposited from mixtures containing from 0.72 % to 1.42 % of oxygen show a decrease in the intensity of bands characteristic of Si-CH₃ and Si-(CH₃)₃ groups, as well as an increase in that of Si-O-Si linkages with an increase in the surface temperature. XPS studies of thin films deposited from the mixture of 0.04 % DMTOS + Ar (films deposited from the mixture of 0.04 % DMTOS + Ar) revealed that with an increase in the surface temperature the carbon content in the layer decreases from 42 % to about 27 % (tab. I).

Topographic studies of the surface of films showed that with a rise of the surface temperature, the roughness (RMS) of films deposited from the 0.04 % DMTOS + 1.42 % O₂ + Ar mixture decreases (tab. II).

In the case of films deposited from other mixtures no such relation was found. The value of the friction coefficient for layers deposited from 0.04 % DMTOS + Ar mixtures shows a clear increasing tendency with a rise of the surface temperature. The lowest friction coefficient of 0.048 was obtained at 100 °C. It was also found that an increase in the

Table III

Characteristics of thin films deposited from the 0.04 % DMTOS + O₂ + Ar mixture with different oxygen content

Sample	O ₂ content [%]	Thickness [nm]	Composition			Friction coefficient
			C [%]	O [%]	Si [%]	
29 KR	0	85.5	42.4	18.9	38.7	0.048 ± 0,006
34KR	0.18	176.6	36.5	21.2	42.3	0.251 ± 0,007
44KR	0.72	74.8	36.9	20.1	43.0	0.085 ± 0,010
40KR	1.42	35.8	22.6	30.1	47.3	0.225 ± 0,016
Si						0.072 ± 0,014

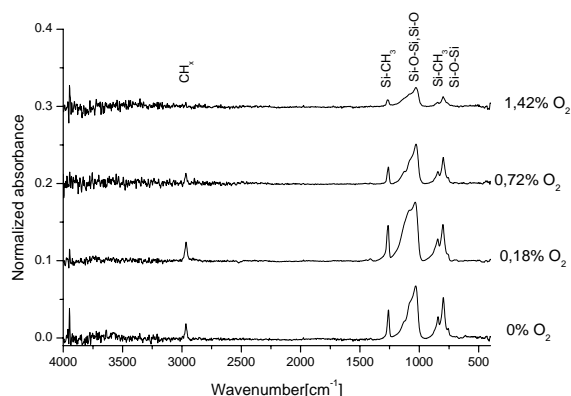


Fig. 1. FTIR spectra of films deposited at 100 °C from the 0.04 % DMTOS + O₂ + Ar mixture with different oxygen content

surface temperature as well as increase in the oxygen content in the mixture caused a decrease in the rate of the deposition of films.

Studies carried out by means of infrared spectroscopy showed differences in the composition of films deposited at 100 °C from the 0.04 % DMTOS + (0–1.42 %) O₂ + Ar mixtures (Fig. 1).

With an increase in the oxygen concentration in the mixtures, a decrease in intensity of the absorption bands characteristic of Si-O-Si and Si-O-C groups (800 cm⁻¹) as well as of Si-CH₃ and Si-(CH₃)₃ ones (1260 cm⁻¹) has been observed. For films deposited at 200 °C no relationship between the films' composition and oxygen content in the mixture was found.

XPS studies revealed that an increase in the oxygen content in the gas mixture caused a decrease in the carbon content of the film from 42 % to about 23 % and an increase in the silicon content from 39 % to 47 % (tab. III). The silicon to oxygen ratio in the films was 2:1 and was analogous as in Si-O-Si linkages, despite an increase in the oxygen concentration in the mixture from 0 % to 0.72 %. For oxygen concentration of 1.42, the Si : O ratio decreases and is equal to 1.57. The friction coefficient of these films is equal to 0.225 and is larger than that for films deposited from mixtures with (0.72 %) oxygen (0.082) and without oxygen (0.048).

In coatings 29KR and 44KR the presence of CH(CH₃)OCH(CH₃)O- linkages was observed. The pres-

Table IV
Concentration of carbon linkages in coatings with small friction coefficients

Sample	O ₂ content [%]	Binding energy [eV]	Content [at. %]	Assigned group
29KR	0	286.64	9.5	(CH ₃ CH ₂) ₂ O
		287.60	30.2	CH(CH ₃)OCH(CH ₃)OCH(CH ₃)O-
		288.92	2.7	(-CH ₂ C(O)O-)n
44KR	0.72	283.73	7.9	C
		284.69	16.1	C
		285.84	9.3	C
		287.06	3.6	CH(CH ₃)OCH(CH ₃)OCH(CH ₃)O-

Table V
Friction coefficient of layers deposited on various surfaces at 100°C, from 0.04 % DMTOS + Ar and 0.04 % DMTOS + 0.72 % O₂ + Ar mixtures

Type of surface	Friction coefficients		
	Pure surface	Film deposited from mixture	
		0.04 % DMTOS + Ar	0.04 % DMTOS 0.72 % O ₂ + Ar
Polycrystalline silicon	0.580 ± 0.031	0.160 ± 0.016	0.162 ± 0.018
Aluminum	0.499 ± 0.054	0.237 ± 0.024	0.206 ± 0.013
Silicon nitride	0.203 ± 0.016	0.181 ± 0.011	0.241 ± 0.019
Polysiloxane	0.4 – 0.75	1.151 ± 0.097	0.263 ± 0.011
Parilene	0.450 ± 0.013	0.058 ± 0.006	0.310 ± 0.022

ence of these groups in the film is probably responsible for the low friction coefficient value (Tab. IV).

Topographic studies of the films surface carried out by means of an atomic forces microscope did not show a relationship between the addition of oxygen and surface structure and roughness of the deposited films. Tribologic studies did not show a correlation between the addition of oxygen, substrate temperature and the friction coefficient value. In order to check the tribologic properties of films of selected parameters, they were deposited on other surfaces, such as polycrystalline silicon, aluminum, silicon nitride, polysiloxane and parilene (tab. V).

Conclusions

The films deposited at 100 °C from a 0.04 % DMTOS + Ar mixture had a from 2 to 8 times smaller friction coefficient than that of the surfaces used. A two-fold smaller friction coefficient was also obtained for films deposited at 100 °C from a 0.04 % DMTOS + 0.72 % O₂ + Ar mixture on an aluminum bed and from polysiloxane.

Films deposited from these mixtures have promising tribologic properties and can be utilized in micromechanics as films decreasing the friction coefficient.

This work was financially supported by Warsaw University of Technology, Poland

REFERENCES

- Gangopadhyay A. K., Vessel W. C., Tamor M. A., Willermet P. A.: *J. Tribol. Trans. ASME* 116, 454 (1994).
- Bandorf R., Lüthje H., Wortmann A., Staedler T., Wittorf R.: *Surf. Coat. Technol.* 174, 461 (2003).
- Gatzen H.: *Proc. Actuator, Bremen*, 363 (2000).
- Bandorf R.: *Proc. Micro System Technologies, Düsseldorf*, 243 (2001).
- Ayala P., Maia da Costa M. E. H., Prioli R., Freire Jr F. L.: *Surf. Coat. Technol.* 182, 335 (2004).
- Freire Jr. F. L., Maia da Costa M. E. H., Jacobsohn L. G., Franceschini D. F.: *Diamond Relat. Mater.* 10, 125 (2001).
- Ko-Shao Chen, Mu-Rong Yang, Shao Ta Hsu: *Mater. Chem. Phys.* 61, 214 (1999).
- Takadom J., Rauch J. Y., Cattenot J. M., Martin N.: *Surf. Coat. Technol.* 174-175, 427 (2003).
- Freyman C. A., Chen Yanfeng, Chung Yip-Wah: *Surf. Coat. Technol.* 201, 164 (2006).
- Tanaka A., Nishibori T., Suzuki M., Maekawa K.: *Diamond Relat. Mater.* 2003, 12, (2006).
- Yu G. Q., Tay B. K., Sun Z., Pan L. K.: *Appl. Surf. Sci.* 219, 228 (2003).
- Donnet C.: *Surf. Coat. Technol.* 100-101, 180 (1998).
- Schmidt-Szałowski K., Rżanek-Borocho Z., Sentek J., Rymuza Z., Kusznierevicz Z., Misiak M.: *Plasmas and Polymers* 5, 173 (2000).

14. Schmidt-Szałowski K., Rżanek-Boroch Z., Sentek J., Rymuza Z., Kusznierevich Z., Misiak M.: *Hakone VII* vol. 2, 434 (2000).
15. Rymuza Z., Misiak M., Rżanek-Boroch Z., Janowska J.: *J. Thin Solid Films* 466, 156 (2004).
16. Nakamura T., Ohana T., Suzuki M., Ishihara M., Tanaka A., Koga Y.: *Surf. Sci.* 580, 101 (2005).
17. Rżanek-Boroch Z., Jóźwik K., Ilik A., Kosiński A.: *Przemysł Chemiczny* 8/9, 748 (2006).

Z. Rżanek-Boroch^a, K. Gradkowska^a, A. Ilik^b, and A. Kosiński^c (^a*Faculty of Chemistry, Warsaw University of Technology, Warsaw,* ^b*Faculty of Physics and Chemistry, University of Łódź, Łódź,* ^c*Institute of Physical Chemistry Polish Academy of Sciences, Warsaw, Poland*): **Effect of the Decamethyltetrasiloxane Films Deposition Parameters On Their Properties**

In the barrier discharge under atmospheric pressure, thin surface films were obtained from decamethyltetrasiloxane (DMTOS) as a precursor. The experiments were carried out in a laboratory reactor of controlled surface temperature (100–400 °C), at 3.3 kHz frequency. The films were deposited on surfaces of monocrystalline silicon <100> from mixtures of 0.04 % DMTOS + O₂ + Ar; oxygen concentration in the range of 0–1.42 %. The films obtained at 100 °C from mixtures of 0.04 % DMTOS + Ar, 0.04 % DMTOS + 0.72 % O₂ + Ar showed a smaller friction coefficient than that of silicon, and, therefore, they were applied as self-lubricating films on other surfaces used in MEMS .

ATMOSPHERIC PRESSURE NON-EQUILIBRIUM PLASMA TREATMENT OF GLASS SURFACE

ANDREJ BUČEK^{a*}, TOMÁŠ HOMOLA^a,
MONIKA ARANYOSIOVÁ^b, DUŠAN VELIČ^b,
TOMÁŠ PLECENIK^a, JOSEF HAVEL^c, PAVEL
ŠTAHEL^c, and ANNA ZAHORANOVÁ^a

^aDep. of Experimental Physics, Faculty of Mathematics, Physics and Informatics, Comenius University, Mlynska dolina F2, 842 48 Bratislava, Slovak Republic, ^bInternational Laser Centre, Ilkovicova 3, 812 19 Bratislava, Slovak Republic, ^cInstitute of Physical Electronics, Faculty of Science, Masaryk University, Kotlarska 2, 611 37 Brno, Czech Republic
bucek@gimmel.ip.fmph.uniba.sk

Introduction

Glass surface plays important role in nowadays technological practice concerning, for example, automotive and structural glass manufacturing, hard disk manufacturing¹ and applications in the field of microbiology. In the mentioned applications sufficient cleanliness of the glass surface is requested. At ambient conditions the glass surface is contaminated by adsorbed hydrocarbons and, for example, dust particles^{2,3}. Such a contamination may result, for example, in lesser adhesion between bulk glass and the material bonded to it. This can result in delamination of various functional films created on the glass surface. Therefore it is important to ensure certain level of glass surface cleanliness according to specifications of the corresponding technological process. There are several cleaning methods available: dust particles can be blown, rubbed or washed away, for example by sonicating in organic solvents as acetone and various alcohols³. To remove organic contamination various wet cleaning procedures can be chosen, UV and ozone cleaning³ and heating of the glass surface to high temperature⁴. Most often the wet cleaning procedures are used which comprise cleaning by the use of organic solvents and/or strong acids and bases⁵. However, large volumes of aggressive and toxic chemicals used in this case are disadvantageous². Environmental, safety and economical issues promote new method of glass surface cleaning – the plasma cleaning^{6–8}. Advantages of the plasma cleaning are the lower production of hazardous waste and the shorter treatment times. Results of the glass surface plasma cleaning are furthermore, to some extent, applicable in the area of silicon surface treatment due to the fact, that the glass surface and the native/thermal silicon oxide surfaces are practically the same². In this paper results of plasma cleaning of glass surface by a novel type of barrier discharge, Diffuse Coplanar Surface Barrier Discharge (DCSBD), are presented. Treated glass surfaces were characterised by the means of contact angle measurements, AFM, SIMS and MALDI TOF MS analyses.

Experimental part

As the plasma source, the so called Diffuse Coplanar Surface Barrier Discharge (DCSBD) was used. This type of discharge produces a thin layer (~0.5 mm) of atmospheric-pressure non-equilibrium plasma even in strongly electronegative gases (e.g. pure oxygen) without any admixture of helium^{9,10}. The plasma layer is produced on the surface of flat alumina slab, which serves as the dielectric barrier in the DCSBD electrode system. Samples to be treated are attached on a movable sample holder, which moves them over the surface of the alumina slab during the treatment to ensure homogeneity of the treatment (Fig. 1). The distance between the surface of the sample and the surface of the slab was set to 0.3 mm. The whole setup is installed in a plexiglass reactor which allows to perform the treatments in various working gas mixtures.

Contact angle measurements were carried out on See System surface energy evaluation system (Advex Instruments s. r. o., Czech republic). Distilled water was used as the measuring liquid. Microscope slides with dimensions 76 × 26 mm were used as the glass substrates. They were pre-cleaned by sonicating for 5 min in acetone prior to the plasma treatment. The treatment has been carried out in three various working gases – ambient air, pure nitrogen and pure oxygen – at the discharge power of 300 W, at various treatment times. To investigate the ageing effect of the surface treatment, air plasma treated samples (355 W, treatment time 3 s, samples weren't moved during the treatment) were stored under ambient conditions and the water contact angle has been periodically measured.

In order to get the information about the surface contamination changes, SIMS and MALDI TOF MS analyses have been carried out on the treated substrates. SIMS analysis was carried out on TOF SIMS IV setup (ION-TOF, Germany). The samples with dimensions 1 × 1 cm were cut from microscope slides. The analysis was carried out on as-received samples, samples sonicated for 5 min in acetone and samples sonicated for 5 min in acetone and subsequently air plasma treated at 290 W discharge power for 5 s. The parameters of the SIMS analysis were as follows: static SIMS; primary ions: Ga; mode: Hc-bunched; primary ion dose density: 5 · 10¹² cm⁻²; analysed area: 200 × 200 mm².

MALDI TOF MS analysis was carried out on AXIMA – CFR setup (Kratos Analytical, UK). Microscope cover slides with dimensions 15 × 15 mm were used as the samples. The samples were sonicated for 5 min in acetone and subsequently dried out by a stream of air at ambient temperature. Plasma treated sample was subsequently treated for 30 s by DCSBD

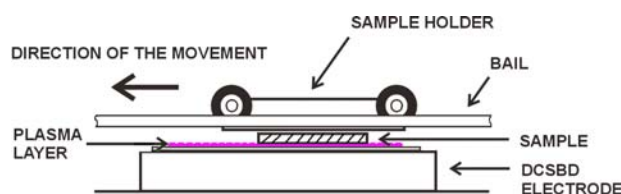


Fig. 1. The sample treatment scheme

plasma generated in ambient air at the discharge power of 524 W. The parameters of the MALDI TOF MS analysis were as follows: nitrogen laser with $\lambda = 337$ nm was used; laser power: 170; mode: linear, positive; matrix: 3-hydroxypicolinic acid (OHP).

In order to analyse topographical changes in the plasma treated glass surfaces, AFM measurements using Solver P47-PRO setup (NT-MDT Co., Russia) have been carried out. The samples with dimensions 1×1 cm were cut from microscope slides. They were subsequently sonicated for 12 min in acetone, 12 min in isopropylalcohol and 12 min in distilled water and finally dried off by the stream of pure nitrogen. The plasma treatment was done at the discharge power of 390 W in ambient air, at various treatment times. Overall topography and the RMS roughness were investigated.

Results and discussion

In Fig. 2 results of the contact angle measurements are shown. From the figure it is clear it was possible to make the samples hydrophilic, even at the 1 s treatment time. Generally, the contact angle values decrease with increasing treatment time. The increase in the wettability of the plasma treated glass surfaces is, probably, due to the removing of the organic contamination from these surfaces. The better performance of the ambient air plasma could be a combination of the above mentioned process and a possible increase in the surface hydroxyl –OH groups density, which are responsible for the hydrophilic properties of the glass surface¹¹, due to the presence of water vapour in the working gas⁸.

The energy consumption to achieve such a result was estimated to $\sim 5 \cdot 10^3$ W s m^{-2} of the glass activated; compared to the performance of the so called *plasma jet* systems with energy consumption estimated¹² to $\sim 5 \cdot 10^5$ W s m^{-2} there is two-order difference in the energy consumption in favor of the DCSBD system.

In Fig. 3 the ageing effect of the air plasma treatment is

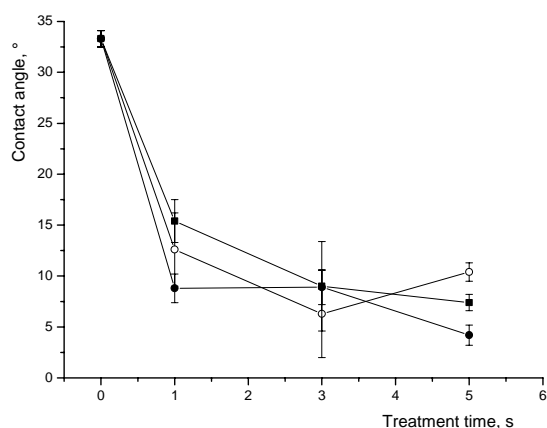


Fig. 2. Contact angle measurements on glass samples treated by the plasma generated at the discharge power of 300 W in various working gases: ● – ambient air, ○ – pure nitrogen, ■ – pure oxygen

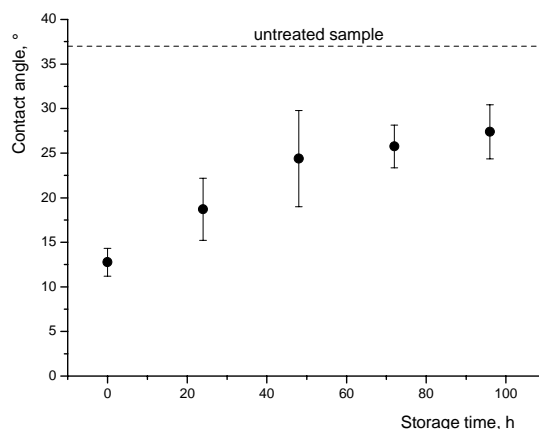


Fig. 3. Ageing effect of the air plasma surface treatment. Treatment time 3 s, discharge power 355 W, stored under ambient conditions

shown. It is clear, that values of the contact angles increase with the increasing storage time, which could be subscribed to the deposition of organic contamination on the glass surface from the surrounding ambient.

The SIMS analysis of air plasma treated glass surfaces showed overall decrease of organic surface contamination, which is indicated by the increase of the intensity of the Si^+ peak, as the basic substance of the glass, and decrease of the peaks of organic fragments $413u^+$, $441u^+$, $763u^+$, $255u^-$, $283u^-$ and $405u^-$ (Tab. I). On the other hand, however, increase in the intensity of the peaks $149u^+$, $430u^-$ and $446u^-$ was detected, probably due to the polymerization of shorter organic fragments (Tab. I). Generally, washing of the samples with acetone greatly reduced the overall contamination of the surfaces, while subsequent plasma treatment led to further reduction of the contamination, which is in good agreement with the results of the contact angle measurements.

Table I
Intensity values (in cts) of ionic peaks measured by SIMS (u denotes atomic mass unit)

Sample	Ionic specie				
	Si^+	$149u^+$	$413u^+$	$441u^+$	$763u^+$
as-received	1278935	20648	12765	1033	–
acetone washed	2612296	85859	1725	183	58
plasma treated	3041832	254390	355	–	25

Sample	Ionic specie				
	$255u^-$	$283u^-$	$405u^-$	$430u^-$	$446u^-$
as-received	23586	4944	426	–	141
acetone washed	2229	596	71	–	–
plasma treated	188	365	–	561	403

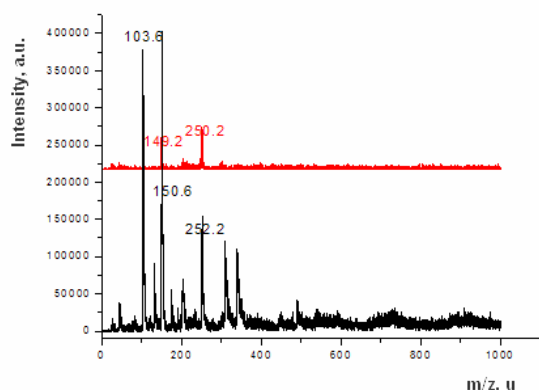


Fig. 4. MALDI TOF MS spectra acquired on untreated (black one) and plasma treated (ambient air, 30 s treatment time, 524 W discharge power – red one) glass surfaces. Note the spectrum for the plasma treated surface has been shifted for better clarity

Results of the MALDI TOF MS analysis are shown in Fig. 4. From the figure it is clear, that air plasma treatment led to the decrease of the organic contamination on the glass surface, as indicated by the 13-fold decrease in the amplitude of the signal for the plasma treated sample in comparison with the untreated sample (note the spectrum for the plasma treated sample has been shifted for better clarity, i.e. its zero was set over 200 000 in the figure). This result is again in good agreement with the results of the contact angle measurements and the SIMS analysis.

In Tab. II are listed the results of the RMS surface roughness AFM measurements conducted on the plasma treated glass surfaces. From the data it is clear, that a distinct change in the RMS roughness appears at the treatment times longer than 20 s. As for the hydrophilic surface treatment of glass the treatment times less than 5 s are sufficient (Fig. 2), the changes in surface roughness play no role in this case. In Fig. 5 are depicted the AFM images of the glass surface untreated, plasma treated for 20 s and plasma treated for 60 s.

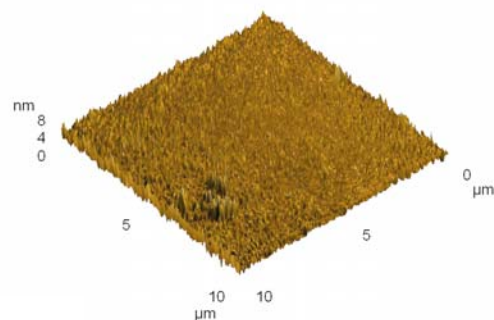
Conclusions

A novel type of barrier discharge, the so called Diffuse Coplanar Surface Barrier Discharge (DCSBD), was used for the surface treatment of glass. Even short treatment times, on

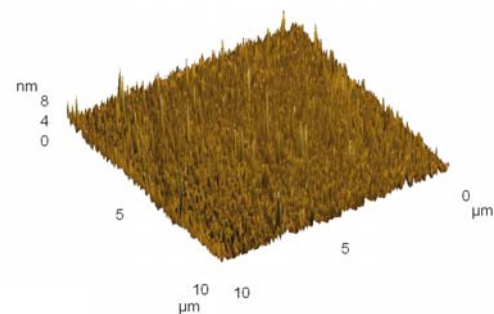
Table II
RMS roughnesses of the plasma treated glass surfaces

	Treatment time [s]					
	0	2	5	10	20	60
RMS roughness [nm]	1.065	0.796	1.729	0.809	1.13	11.63

a



b



c

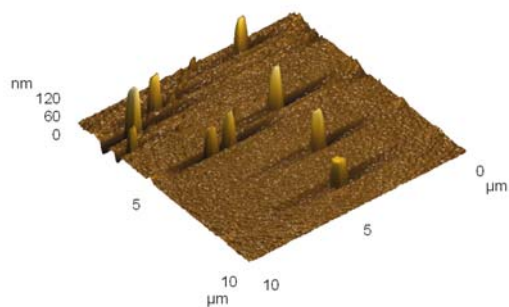


Fig. 5. AFM images of the air plasma treated glass surfaces. The discharge power was 390 W, the treatment time was: a) 0 s, b) 20 s and c) 60 s

the order of seconds, were sufficient to make treated glass surfaces hydrophilic. By the means of the SIMS and MALDI TOF MS analyses it was shown, that the removing of the organic contamination from the treated surfaces by the action of DCSBD plasma plays important role in the improvement of the wettability of the glass surface. The AFM measurements showed no significant changes in the surface roughness of the glass substrates treated by the plasma at the treatment times of 20 s and less. The energy consumption of the DCSBD system

was estimated to $\sim 5 \cdot 10^3 \text{ W s m}^{-2}$ of the glass activated, which is 2 order less than the energy consumption of the competing plasma jet systems.

This research has been supported by the Slovak Scientific Grant Agency, Project No. VEGA 1/4014/07, by the Slovak Research and Development Agency, Project No. APVV-0491-07, by the research project MSM0021622411 of the Ministry of Education of the Czech Republic and by the research project KAN 101630651 of the Czech Academy of Science.

REFERENCES

- Ochs D., Schroeder J., Cord B., Scherer J.: Surf. Coat. Technol. 142-144, 767 (2001).
- Plöchl A., Kräuter G.: Mat. Sci. Eng. R25, 1 (1999).
- http://liqcryst.chemie.uni-hamburg.de/lcionline /training/train_01/topics/2DSPT1.htm
- Gonzales-Benito J., Cabalenas J. C., Aznar A. J., Vigil M. R., Bravo J., Baselga J.: J. Appl. Polymer Sci. 62, 375 (1996).
- Lee D.-J., Ju B.-K., Jang J., Lee K.-B., Oh M.-H.: J. Micromech. Microeng. 9, 313 (1999).
- Wang CH., He X.: Appl. Surf. Sci. 252, 8348 (2006).
- Lim K.-B., Lee D.-CH.: Surf. Interface Anal. 36, 254 (2004).
- Larson B. J., Helgren J. M., Manolache S. O., Lau A. Y., Lagally M. G., Denes F. S.: Biosens. Bioelectron. 21, 796 (2005).
- Simor M., Rahel J., Vojtek P., Cernak M., Brablec A.: Appl. Phys. Lett. 81, 2716 (2002).
- Cernak M., Rahel J., Kovacik D., Simor M., Brablec A., Slavicek P.: Contrib. Plasma Phys. 44, 492 (2004).
- Wood B. J., Lamb R. N., Raston C. L.: Surf. Interface Anal. 23, 680 (1995).
- Ogawa H., Yamamoto H., Teranishi T., Kobayashi H., Kuramoto Sh.: Partially treated water-repellent glass sheet. United States Patent US 6926946, 18 September 2003.

INFLUENCE OF THE OPERATIONAL PARAMETERS ON THE WETTABILITY OF THE DLC FILMS DEPOSITED BY TVA METHOD

RODICA VLADOIU*, VICTOR CIUPINA,
VIRGINIA DINCA, and GEAVIT MUSA

Department of Physics, Ovidius University, Constanta,
900527, Romania
rvladoiu@univ-ovidius.ro

1. Introduction

Wetting of solid substrates by liquids is a fundamental phenomenon with relevance to both the technological and natural worlds. Applications include the spreading behaviour of liquids on coatings, as well as flows in oil reservoirs and chemical reactors.

For solid surfaces, the concept of wettability is defined by mean of surface energy. The surface free energy is the extra energy needed to form a material surface exposed to gas or vacuum. The surface energy of the films is an important factor due to the fact that it can give some clues to the surface properties of the thin film could be crucial for applications of various branches of industry.

Surface modification can change surface chemical composition and structure and the surface free energy. The exact knowledge of the surface free energy of films is essential for optimizing deposition parameters and coatings processes.

A common way of estimating solid surface energies is to measure the contact angle that a liquid makes with its surface. The contact angle measurements can be performed by establishing the tangent angle of a liquid drop with a solid surface. An imaging system (SEE SYSTEM) was used to measure contact angle of testing liquids droplets on the deposited films.

This measurement is considered to be a relatively simple, useful and sensitive tool for assessing hydrophobicity or hydrophilicity of a surface¹.

This technique is generally applied only to low energy solid surfaces, as most available liquids as water and ethylene glycol have relatively low surface tensions and wet solids with higher surface energy. In the contact angle measurement process, the selection of appropriate test liquids is sometimes sophisticated².

If the energy required to create the solid-liquid (γ_{sl}) interface is greater than that required for creation of a solid-vapour (γ_{sv}) interface, then the critical angle will be greater than 90° . In other words, the liquid will bead up on the surface to minimize the solid-liquid interfacial area.

For DLC films deposited on different substrates the evaluation of the surface energy with contact angle measurement using different liquids represents an optimum method³. The diversity of methods used for the deposition of diamond-like carbon films provides the flexibility to tailor their properties according to specific needs and potential applications.

The aim of this paper is to analyse the surface free en-

ergy by meaning of the contact angle of the nanostructured carbon thin films deposited by an original method: Thermionic Vacuum Arc (TVA). By variations of plasma treatment conditions it is possible either to increase or decrease the wettability of the surface

2. Experimental set-up

The deposition of the DLC thin films was carried out by the Thermionic Vacuum Arc (TVA) method. Because this system can heat any material at relevant temperature it is one of the most adequate deposition technologies for evaporate and condensate on a substrate high melting point materials. Moreover, it has been already reported to be a very suitable method for deposition of high purity carbon thin films with compact structure and extremely smooth, just convenient for nanostructured film synthesis⁴.

Thermionic Vacuum Arc (TVA) deposition method consists from an externally heated cathode surrounded by a Wehnelt cylinder. The vapors are obtained by heating the material with thermo electrons generated by the externally heated filament of a circular form placed above the anode. The anode used was a graphite rod⁵.

The cathode and the vacuum chamber are grounded, so the carbon plasma has a potential against the chamber wall equal with the cathode potential fall. On the substrate are deposited, with the evaporated neutral atoms, the incident energetic ions.

The cathode can be mounted in various positions against the anode. The highest density of plasma vapors is obtained above the anode. Due to the potential differences between the plasma potential and the walls, the ions are accelerated to the chamber walls.

Practically, the deposition takes part in the vapors of the anode materials, the deposited film containing only the ions of this material and therefore the energy of ions could achieve values up to 500 V. In this way the carbon film is bombarded during its deposition by carbon ions with established value of energy.

In Fig. 1 is presented the experimental setup. The symmetry of the cathode – anode arrangement allows

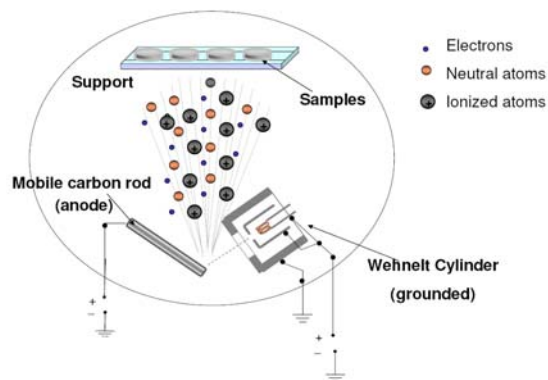


Fig. 1. Experimental setup of the Thermionic Vacuum Arc (TVA) system

Table I
Experimental parameters for the deposition of the DLC films on samples

Sample no.	B3	B5	B7	B8	B10	B11	B12
d [cm]	20	29	28	30	31	35	35
I _f [A]	50	50	51	50	45	53	45

a perpendicular bombardment of the electron beam on the anode surface.

Due to the high energy dissipated in the unit volume plasma, the material is strongly dispersed and completely droplets free. The obtained thin film was very smooth and in some experimental conditions had a nano-scale structure.

In Table I are presented the main experimental parameters involved in this study: the distance between samples and the point of the ignition of the discharge (**d**) and the intensity of the heating current of the filament (**I_f**). The voltage applied ranged between 2 kV to 4 kV.

The variation of the contact angle measurements with ion energy is believed to be correlated to the topography of the films^{7–9}.

An imaging system (SEE SYSTEM) was used to measure contact angle and shape of testing liquids droplets for the prepared samples. This system mainly consist of a device with a adjustable view-station sample support and a CCD camera, which observe a liquid drop on the studied surface and a computer software that calculates the contact angle, the total free surface energy and her components¹⁰.

For making the measurements, samples were placed on the top of a miniature height adjustable view-station in front of the CCD camera. Static contact angles were measured in the horizontal direction.

The drops of 0.5 µl volumes was released on the thin film surface in 10–15 locations and the data were averaged. Small droplets of constant volume were used for the measurements in order to minimize gravitational effects.

During the measurements the room temperature was 22–25 °C and the contact angle for spread liquid droplets was determined from the side view.

For determination of the free surface energy some mathematical formulas were used, for equations of states models (Kwok-Neumann model, Li-Neumann model, Wu model) and for OWENS-WENDT method.

Because plenty of samples have to be analyzed for determination of the surface energy the results can differ from sample to sample and in consequence the statistical free energy distributions could be undesirably distorted by the non-uniformity of the samples. Therefore we snapped the drops of various liquids on one sample only and we determinate the contact angle from these snaps.

The operator selects the points of the interface with a normal error distribution, being discredited due to the finite resolution of the analyzed bitmap. The generated values of contact angles were analyzed with the two-liquid equations of states models and with OWENS-WENDT method and compared¹¹.

The accuracy of the values obtained is essentially influenced by the test liquids selected. On the one hand an in-

fluence on the surface by the test liquid by partial etching or dissolving must be ruled out. On the other hand, the surface tension of the test liquid must not be changed by soluble substances possibly existing on the solid surface. If one or both of the described processes take place, this manifests itself by a strong variation of the measured contact angles in spite of a visually homogeneous surface, and by a poor reproducibility of the results.

3. Results and discussions

The contact angle method uses the ability of a liquid to flow in response to the tension generated by the differences in surface energies at the solid – liquid contact line.

Typical images frames acquired by the image analysis system described above are displayed in Fig. 2. The figure shows a printout of the sample of experimental measurement for ethylene glycol and water spreading on polycarbonate substrate. Selection of several points of solid–liquid and liquid–vapor interface makes possible to fit the drop profile and to calculate the tangent angle of the drop with the solid surface. The contact angle for spreading of liquid droplets was determined from the side view. These data were digitalised and measured using the SEE SYSTEM software.

The equilibrium contact angle was given by Young when a drop of liquid lies on a solid surface. Young's equation is^{12,13}:

$$\gamma_{sv} - \gamma_{sl} = \gamma_{lv} \cos\theta \quad (1)$$

where γ_{SL} , γ_{SV} , and γ_{LV} are solid-liquid, solid-vapour and respectively liquid-vapour interfacial tensions which measure the free energy, θ is the equilibrium contact angle.

The OWENS-WENDT method requires the use of at least two test liquids with known surface tension and its polar and dispersive contributions. Each additional liquid will increase the accuracy of the estimation¹⁴.

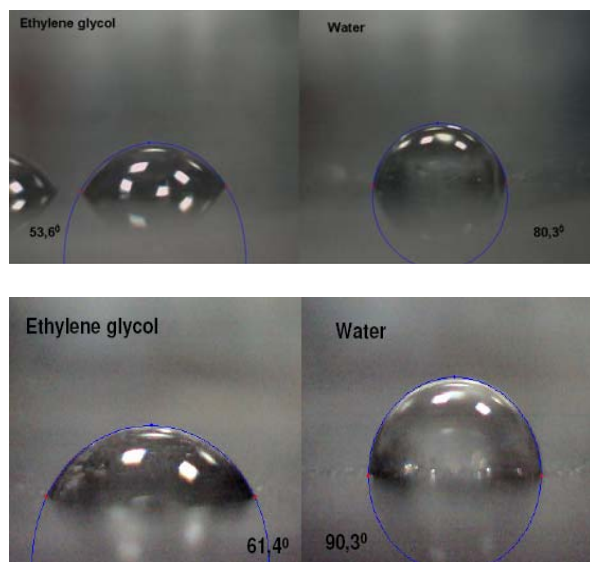


Fig. 2. Pictures of the droplets on sample B3 (up) and samples B12 (down)

The formula for equation of states proposed by Kwok-Neumann in combination with the Young's equation gives:

$$\cos\theta = -1 + 2 (\gamma_{sv}/\gamma_{lv})^{1/2} [1 - 0,0001057(\gamma_{lv} - \gamma_{sl})^2] \quad (2)$$

The equation derived by Li and Neumann combined with Young's equation yields:

$$\cos\theta = -1 + 2 (\gamma_{sv}/\gamma_{lv})^{1/2} \exp(-0,0001057(\gamma_{lv} - \gamma_{sl})^2) \quad (3)$$

Wu suggested for equation of state the following expression:

$$\gamma_c = \frac{\gamma_l(1 + \cos\theta)^2}{4} \quad (4)$$

where γ_c is function of interaction parameter on the surface free energy.

The equation proposed by Owens and Wendt is an extension of the equation give by Fowkes and propose a division of the total surface energy in two components: the dispersive force component γ^d and hydrogen bonding component γ^p .

$$\gamma_{sl} = \gamma_s + \gamma_l - 2\left(\sqrt{\gamma_s^d \gamma_l^d} + \sqrt{\gamma_s^p \gamma_l^p}\right) \quad (5)$$

Combining this equation with Dupre's formula the following term is obtained⁹:

$$(1 + \cos\theta)\gamma_l = 2\left(\sqrt{\gamma_s^d \gamma_l^d} + \sqrt{\gamma_s^p \gamma_l^p}\right) \quad (6)$$

In Table II are presented the values obtained for the contact angle in the case of the two liquids used for measurements: water and ethylene glycol.

The data in the table shows clearly that there are differences in the contact angles between the treated films that were closer of the ignition of plasma and the films obtained at a bigger distance from the plasma.

The obtained values of the contact angle, in the case of water as testing liquid, vary from 77.44° to 90.34° and a constant increase is observed for samples B8, B10, B11 and B12.

Using ethylene glycol as liquid test the obtained values are between 51.27° and 61.42° and the samples B11 and B12 present 5 respectively 6 degrees visible increased compared with the previous samples.

In Fig. 3 the total film surface energy calculated with the

Table II
Contact angle values for DLC films

Sample no.	Contact angle water [°]	Error	Contact angle ethylene glycol [°]	Error
B3	80.67	0.40	53.93	1.46
B5	77.68	0.28	55.28	0.39
B7	79.46	0.34	51.53	0.32
B8	77.44	0.36	51.27	0.32
B10	83.25	0.20	54.62	0.18
B11	85.37	0.52	60.39	0.41
B12	90.34	0.27	61.42	0.33

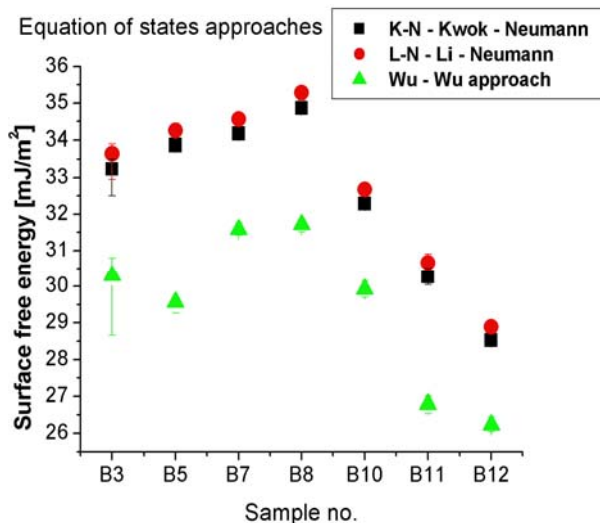


Fig. 3. Equations of states approaches

two liquids by mean of equations of states approaches are presented.

As can be noticed in Fig. 4 the total free surface energy of the thin film present, for Kwok-Neumann and Li-Neumann methods, have the same increased linear pattern for the first four samples with values of the surface energy from 33.23 to 34.86 mJ m^{-2} (K-N method) and 33.63 to 35.28 mJ m^{-2} (Li-N method).

For the last three samples a decreased is observed from 32.28 to 28.53 mJ m^{-2} (KN method) and 32.67 to 28.89 mJ m^{-2} (LiN method), the values of the surface energy for the two equation of state mentioned above are almost the same.

A similar distribution is observed for the Wu approach, with smaller values of the surface energy from 31.58 to 26.23 mJ m^{-2} .

In Fig. 4 are represented the variation of total surface energy g_{total} , of the dispersive component g_{LW} and the polar component g_{AB} obtained by mean of Owens Wendt model.

The total surface energy and LW component (g_{LW}) present the same variation of the surface energy and values are between 27.86 – 32.55 mJ m^{-2} for g_{total} and 17.85 – 27.99 mJ m^{-2} for LW component of the energy. The g_{AB} component describe a plot variation whit values from 26.23 to 31.71 mJ m^{-2} .

4. Conclusions

The SEE SYSTEM device and software offers an easy way to determine the surface energy of thin films deposited on different substrates.

The contact angle measurements of the samples deposited by TVA method have shown reproducible results ranging from 90.34 to 77.44 degrees for water and 51.27 to 61.42 degree for ethylene glycol which implies low ion energies of surface energy values. In this way, it was proved a hydrophobic character of these films.

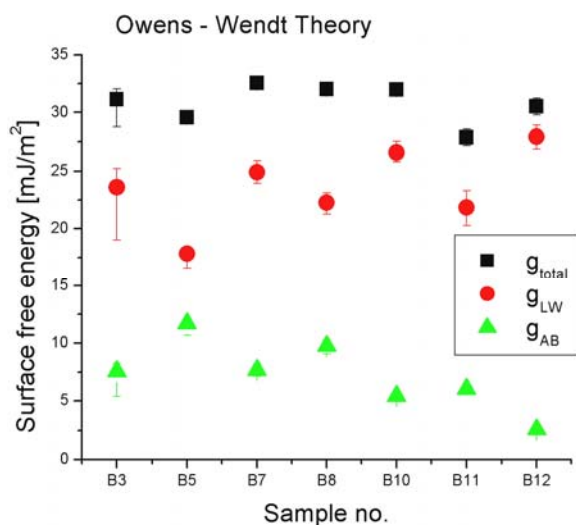


Fig. 4. Plot of the surface free energy obtained with Owens-Wendt method

The highest value of the surface free energy has been obtained in the case of sample B8 for Li-Neumann equation of states approaches. Contact angle can reflect the wettability of materials, and it is influenced by many aspects such as surface characters, roughness and temperature.

This work was supported by Romanian Ministry of Education and Research under project CEx 2 - DII - 62/2006.

REFERENCES

- Derrick O. Njobuenwu, Esio O. Oboho, Rhoda H. Gumus: Leonardo Electronic J. Of Practice and Technologies, 6, 29 (2007).
- Endrino J. L., Marco J. F., Poolcharuansin P., Phani A. R., Allen M., Albella J. M., Anders A.: Appl. Surf. Sci. 254, 5323 (2008).
- Mathew Mate C.: *Tribology on the small scale – a bottom up approach to friction, lubrication and wear*. Oxford University Press, 2008.
- Vladoiu R., Ciupina V., Lungu C. P., Bursikova V., Musa G.: J. Optoelectron. Adv. Mater. 8, 71 (2006).
- Vladoiu R., Musa G., Mustata I.: J. Optoelectron. Adv. Mater. 5, 325 (2003).
- Musa G., Mustata I., Ciupina V., Vlădoiu R., Prodan G., Vasile E., Ehrich H.: Diamond Relat. Mater. 13, 1398 (2004).
- Surdu-Bob C., Vladoiu R., Badulescu M., Musa G.: Diamond Relat. Mater. 17, 1625 (2008).
- Martin P. J.: Thin Solid Films 394, 1 (2001).
- Helmersson U.: Thin Solid Films 513, 1 (2006).
- Tang Li-Qin, Wang Yue-Yan, Yin Lu: J. of US-China Medical Science, USA, 4, 43 (2007).
- Bursikova V., St'ahel P., Navratil Z., Bursik J., Janca J.: *Surface energy evaluation of plasma treated materials by contact angle measurement*. (2004).
- Young T.: Phil. Trans. R. Soc. London 9, 255 (1805).
- Navratil Z., Bursikova V., Stahel P., Sira M., Zverina P.: Czech. J. Phys. 54, Suppl. C, 877 (2004).
- Daniel H. C., Chuua K. B., Teo K., Tsai T. H., Milne W. I., Sheej D., Tay B. K., Schneider D.: Appl. Surf. Sci. 221, 455 (2004).

APPLICATION OF PLASMA-INDUCED GRAFTING FOR MODIFICATION OF ALKALINE BATTERY SEPARATOR

IRENA GANCARZ*^a, JERZY KUNICKI^b,
and ALEKSANDER CISZEWSKI^c

^a Chemistry Department, Wrocław University of Technology, Wybrzeże Wyspińskiego 27, 50-370 Wrocław, ^b Central Laboratory of Batteries and Cells, Forteczna 12, 61-362 Poznań, ^c Institute of Chemistry and Technical Electrochemistry, Poznań University of Technology, Piotrowo 3, 60-965 Poznań, Poland
irena.gancarz@pwr.wroc.pl

Key words: porous polypropylene membrane, acrylic acid, plasma-induced grafting, high power nickel-cadmium battery

Introduction

The performance and cycle life of each battery are significantly affected by the type of separator used in these batteries. The separator is placed between the positive and negative electrodes to prevent physical contact between them while enabling free ion flow. There are many requirements for a material to be a good separator, such as high chemical stability, small thickness, appropriate porosity and pore size, mechanical strength, dimensional stability and wettability¹. Porous polypropylene membrane (i.e. Celgard) fulfills most of these requirements except wettability. Polyolefines are hydrophobic polymers and modification is necessary to gain some hydrophilicity to make them suitable as separators. Commonly used methods include applying surfactants or priming the membranes with certain solvents. Such treatment however improves the wettability only temporarily, since the surfactant is subjected to washing away by the liquid electrolyte upon cycling and storage¹. In the last decade application of low-temperature plasma for hydrophilization of polymer surfaces has grown rapidly. From all plasma techniques – plasma modification, polymerization, etching and plasma-induced grafting – the last-named seems to be the most suitable for it can give permanently hydrophilic surfaces. In the literature one can find some remarks on the electrochemical properties of polyolefin membranes grafted with poly(acrylic acid)². Published results are however scarce and give no information on their usage in alkaline power sources. Our preliminary results⁴ have clearly shown that this might be the way to improve the properties of battery separators, hence also performance and reliability of alkaline batteries. In the present work, we covalently attached poly(acrylic acid) to the surface of the porous polypropylene using two different types of plasma apparatus. We have tried to learn how the plasma parameters influence the degree of grafting and we have checked the suitability of such material as an alkaline battery separator.

Experimental

Materials and equipment

Celgard 2500 (Daicel Chemical Industries, Ltd) microporous PP membrane was used as the substrate for grafting. Its pore size was $0,05 \times 20 \mu\text{m}$, porosity 45 % and thickness – 25.4 μm . Acrylic acid (AAc, Aldrich Chem. Co., Ltd) was vacuum distilled prior to use.

Two different types of plasma apparatus were used:

- plasma generator of 75 kHz frequency (Dora, Wrocław, Poland), with modulation of 300 kHz, regulated power and regulated distance between two electrodes; the sample could be attached to both electrodes.
- microwave plasma generator of 2.45 GHz frequency with power regulated from 0 to 1000 W (Ertec, Wrocław, Poland). Plasma was generated in the quartz tube at the top of a thick-walled glass reaction chamber and the sample was put in the post-discharge area on a table of which the distance from the lower edge of the plasma could be regulated.

Grafting procedure

Before plasma treatment the reactors were evacuated to a pressure below 10^{-3} mbar. Argon flow was adjusted to the desired value and the plasma was ignited at the desired power level for the predetermined time.

After two-sided plasma treatment, membranes were immersed in the AAc solution (water : acetic acid : AAc = 1:1:0.5 volume ratio) and exposed to UV radiation for a definite time. The sample was then intensively washed with water to remove homopolymer and dried in air. The degree of grafting (moles of AAc/PP weight) and the amount of homopolymer were determined gravimetrically.

Surface characterization

Measurement of contact angle

To get a nonporous sample of the same material as porous examples pieces of porous membranes were put into a laboratory press (190 °C, 50 kG, 2 min). The static contact angles of water and diiodomethane were measured on the nonporous samples by means of a goniometer PG-X (Fibro System AB). At least 20 readings were made on each film. The surface tension and its polar and dispersive components were calculated according to harmonic averaging⁴. The polar and dispersive components of surface tension for testing liquids were taken according to Kuznetsov⁵. Sample polarity was defined as a percent ratio of the polar component of surface tension and total surface tension. The dynamic contact angle of water was determined on the porous samples.

Fourier Transform Infrared Spectroscopy

Spectra were obtained using a Perkin-Elmer System 2000 spectrometer with horizontal ATR device (Ge, 45°). Sixty four scans were taken with 4 cm^{-1} resolution.

Scanning Electron Microscopy

The surface and cross-section of samples were observed using a JSM-5800 LV, JEOL device working at 25 kV.

Measurement of ionic conductivity

The electrolytic resistance (area resistance) of the membrane was determined by two successive measurements of potential difference between the reference electrodes; the first one without membrane (E), and the second one with the membrane (E'). In all measurements concentrated KOH solution (29 % solution, $d = 1.28 \text{ g cm}^{-3}$) was used. The electrolytic area resistance R of the membrane was determined from the following equation⁶: $R = (E' - E)S / I$, where S is the membrane surface area exposed to the electric field.

Results and discussion

Choice of materials and methods

The main goal of the present work was permanent hydrophilization of porous polypropylene to make it usable as a battery separator. Polypropylene is very hydrophobic polymer with surface tension about 30 mN m^{-1} and very low ($\sim 2 \text{ mN m}^{-1}$) its polar component.

Plasma is known as a modern, clean, environmentally friendly and very efficacious technique of modification of polymer surfaces. There are several ways of using plasma to change surface characteristics – plasma polymerization, plasma modification and plasma-initiated grafting. The first technique creates a layer of polymer-like materials on the surface. This however rarely resembles the compound taken for the treatment. Plasma polymerization of acrylic acid on the polypropylene surface did not give the expected results³. Modification of the surface by plasma of such gases as air, argon, nitrogen, oxygen increases the surface tension rapidly but the attained results diminish or even disappear with time. The third method uses plasma only to produce on the polymer surface the radicals that are able to polymerize a monomer in the conventional way. We applied the third technique and decided to use the acrylic acid as a grafting monomer for it is a low-boiling, water-soluble, very reactive compound which provide the surface with many hydrophilic carboxylic groups.

The schematic path of the membrane modification process is shown in Fig. 1.

Argon plasma is known to introduce on the surface a lot of radicals that are rapidly modified by contact with air into various functional groups, among others also peroxides and hydroxyperoxides. These, decomposed by UV light in the monomer solution, initiate its polymerization and hence create grafting chains on the polymer surface.

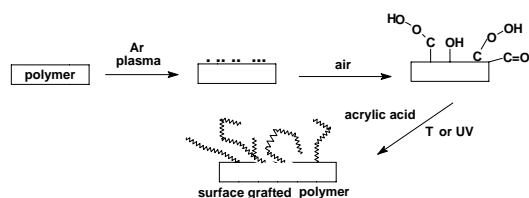


Fig. 1. The scheme of plasma initiated grafting of acrylic acid onto the polymer surface

Plasma devices and plasma parameters

Two types of plasma apparatus differing in plasma frequency were accessible to modify the PP surface. The one

Table I
Grafting results for various parameters of KHz frequency plasma

Parameter	Value	Grafting degree, mmol g ⁻¹	Amount of homo-polymer, %	Electrolytic area resistance, mΩ cm ²
Plasma power, mW	55	6.25	4.2	61
	75	4.26	10.0	20
	88	2.89	–	27
	105	2.12	10.5	142
Argon pressure, torr	0.09	4.58	7	152
	0.2	3.89	14	31
	0.5	2.12	–	142
Distance between electrodes cm	28	4.44	8.4	49
	35	5.69	5.6	40
	45	10.7	4.1	48
Treatment time, min	0.5	7.64	4.0	53
	1	8.47	3.7	40
	2	5.14	5.2	57
	3	6.25	4.2	61

Table II
Grafting results for various parameters of GHz frequency plasma

Parameter	Value	Grafting degree, mmol g ⁻¹	Amount of homo-polymer, %	Electrolytic area resistance, mΩ cm ²
Plasma power, W	260	10.1	8.1	77
	220	9.72	9	106
	180	13.4	9.8	41
	130	15.7	12.0	22
Argon pressure, torr	0.15	10.0	8.7	70
	0.24	11.2	8.1	64
	0.35	10.9	9.5	61
Sample-to-plasma distance, cm	0.5	13.4	9.8	41
	9	11.1	9	53
	11	10.0	8.7	70
	13	3.47	4.4	80
Treatment time, min	0.5	11.2	8.1	64
	1	6.39	8.5	59
	1.5	10.8	12.1	67
	2	12.2	7.6	46

operated in the kilohertz range with regulation of the distance between the electrodes while the other worked in the gigahertz frequency range and the sample was put in the afterglow area. The parameters we have changed trying to optimize plasma conditions were the argon pressure, the plasma power, the distance between the electrodes (for KHz device) or sample-to-plasma edge distance (for GHz) and the treatment time. The experiments in each set of parameters were repeated a few times and average values were taken. As the important results the grafting degree and electrolytic area resistance of the membrane were taken.

Some results obtained in KHz and GHz frequency plasmas are shown in Table I and Table II respectively.

It is obvious that the plasma parameters influence the grafting results but the correlations obtained are not straightforward. Optimization of plasma treatment conditions seems to be very difficult in this case.

Comparing the results with the two kinds of plasma used we can say that these obtained in the average conditions of microwave plasma yielded a higher degree of grafting and a higher amount of homopolymer in the solution. However both plasmas created sufficient amounts of radicals to assure a significant degree of grafting that decreases the area resistance from 130 000 $\text{m}\Omega \text{cm}^2$ to as small a value as about 20 $\text{m}\Omega \text{cm}^2$.

Most important for us was the correlation between the

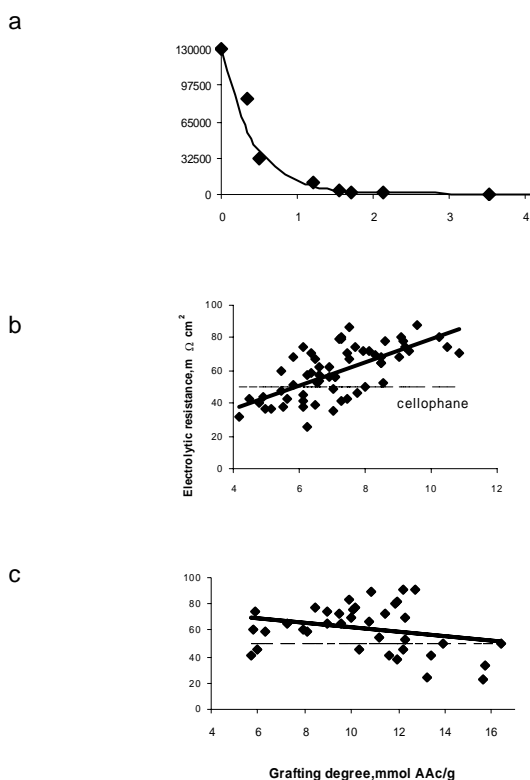


Fig. 2. Dependence of electrolytic resistance of modified porous PP membrane on acrylic acid degree of grafting; both plasmas in low grafting degree region (a) treatment with 75 kHz (b) and 2.45 GHz (c) plasmas

degree of grafting and the ionic conductivity. At low degrees of grafting the resistance decreases dramatically with the amount of grafted AAc (Fig. 2a). The situation changes when the degree of grafting becomes greater than 4 mmol g^{-1} . In that case for microwave plasma we observed slow continuation of that process – lowering of the resistance with the progress of grafting (Fig. 2c), while for KHz-plasma – a slow change of resistance for the worse was noticed (Fig. 2b).

The results obtained are highly scattered, which might be due to uneven action of the plasma or the method of measuring the resistance (in one point). Molecular weight of grafted chains and change of pores size may also influence the resistance results.

Characterization of AAc grafted membranes

The chosen modified membranes as well as the virgin polypropylene membrane were investigated with the help of accessible methods such as contact angle measurements, FTIR-ATR and SEM.

Table III presents the values of contact angles of water and methylene iodide, and the calculated values of surface tension and polarity for PP and samples after argon plasma treatment in average conditions.

As was expected, both plasmas cause a great increase of polypropylene surface tension, especially its polar component. KHz-plasma seems to affect the PP surface more but at this same time the degree of grafting obtained in these conditions is lower than for GHz plasma ($\sim 5 \text{ mmol g}^{-1}$ versus $\sim 10 \text{ mmol g}^{-1}$).

On the porous samples the dynamic contact angle of water was determined. Examples of observed curves are shown in Fig. 3.

The straight line obtained for virgin, porous membrane proves its highly hydrophobic character that prevents the hydrophobic liquid from soaking into the pores. For the sample after plasma treatment we have observed small decrease of the contact angle (usually 3–5 degrees) in the first two seconds and then the contact angle kept a constant value. The shape of the curve is always the same, however its position on the contact angle scale is different (due to various contact angle values at the start). The reason might be uneven plasma treatment on the whole sample surface.

For samples grafted with acrylic acid we have observed two kinds of curves. The one (curve 1 in the Fig. 3) shows the slow decrease of the water drop contact angle with time. This change is bigger than in case of the plasma-modified surface

Table III
Values of contact angle, surface tension and polarity of the chosen samples

Sample symbol	Contact angle		Surface tension, mN m^{-1}	Polarity, %
	H_2O	CH_2I_2		
PP	90	53	32.8	6.4
PP-KHz plasma	17	41	76.8	48.4
PP-GHz plasma	60	26	52.1	24.0

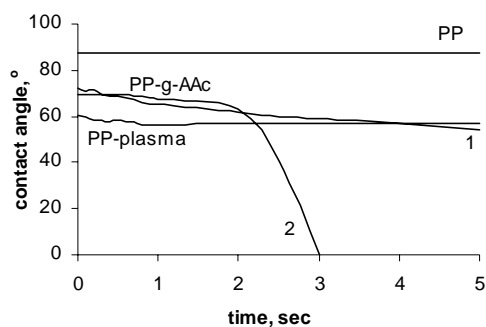


Fig. 3. Dynamic contact angle of water on the surface of virgin PP membrane (PP), PP after microwave plasma treatment (PP-plasma) and PP grafted with acrylic acid (PP-g-AAC, degree of grafting 9.4 mmol AAC/g)

and in the particular case shown in Fig. 3 equals 18 degrees after 5 sec. The other drops (curve 2 in Fig. 3) put on the grafted surface changed their volume very slowly at the beginning and disappeared completely after 3 sec.

The presence of poly(acrylic acid) on the polypropylene surface was confirmed by FTIR-ATR spectroscopy (Fig. 4). The sample was washed with KOH before the experiment to be sure that no homopolymer was left on the surface. Two new bands characteristic for carboxylic ions – the strong one from antisymmetric valence oscillation at 1554 cm^{-1} and the other, weaker, from symmetric valence oscillation at 1399 cm^{-1} were observed in the spectrum. We can see also the small band at 1705 cm^{-1} characteristic for carboxylic acid, being the proof that not all carboxylic groups were neutralized.

The macroscopic surface changes that have taken place during the grafting process are seen in SEM pictures of sample surface (Fig. 5) and cross-section (Fig. 6).

With the increasing degree of grafting the layer of polymer seems to cover the bigger sample area. For the sample with the highest grafting degree (Fig. 5d) hardly any pores structure is seen.

The cross-section pictures (Fig. 6) of the above samples prove that grafting takes place not only on the surface but also in the pores of the membrane. Membrane become significantly thicker – estimated thickness increases from $25\text{ }\mu\text{m}$ for unmodified membrane to 29, 32 and $35.5\text{ }\mu\text{m}$ for sample b, c

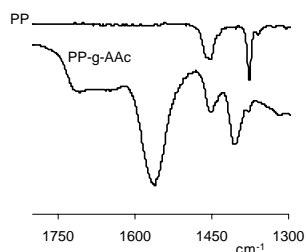


Fig. 4. FTIR-ATR spectra of the virgin (PP) and grafted (PP-g-AAC) polypropylene membrane

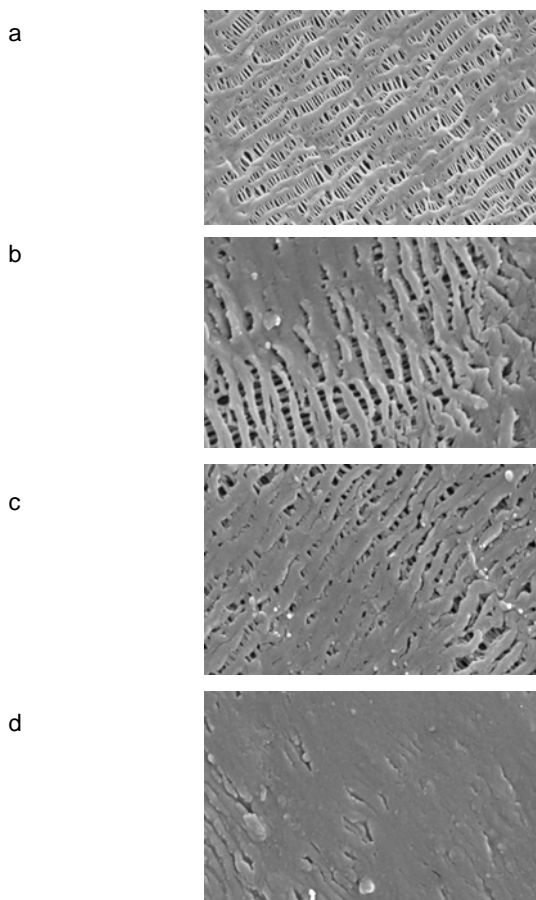


Fig. 5. SEM pictures of surface of virgin (a) and grafted (b,c,d) PP membrane of grafting degree 2.3, 9.7 and 16.2 mmol g^{-1} respectively. Magnification - 6000

and d, respectively. For the sample with the highest grafting degree the whole volume of pores is filled with grafted material.

The nonuniform, mosaic structure of the surface and various degrees of pore filling might also explain the various shapes of the dynamic angle curves observed for modified samples.

Usefulness of modified membranes as separators for high-power Ni-Cd batteries

As was mentioned earlier the porous polypropylene membranes fulfill all but one – wettability – requirements for good separators in alkaline batteries. Plasma-initiated grafting of acrylic acid appeared to be an excellent way to permanently eliminate this disadvantage. From the figs. 2b and 2c one can see that in spite of the wide range of parameters and results obtained in our experiments we obtained membranes of resistance values sufficient for use in alkaline batteries (less than $100\text{ }\Omega\text{W cm}^2$). In many cases they have better properties (lower resistance) than those commonly used, made of regenerated cellulose.

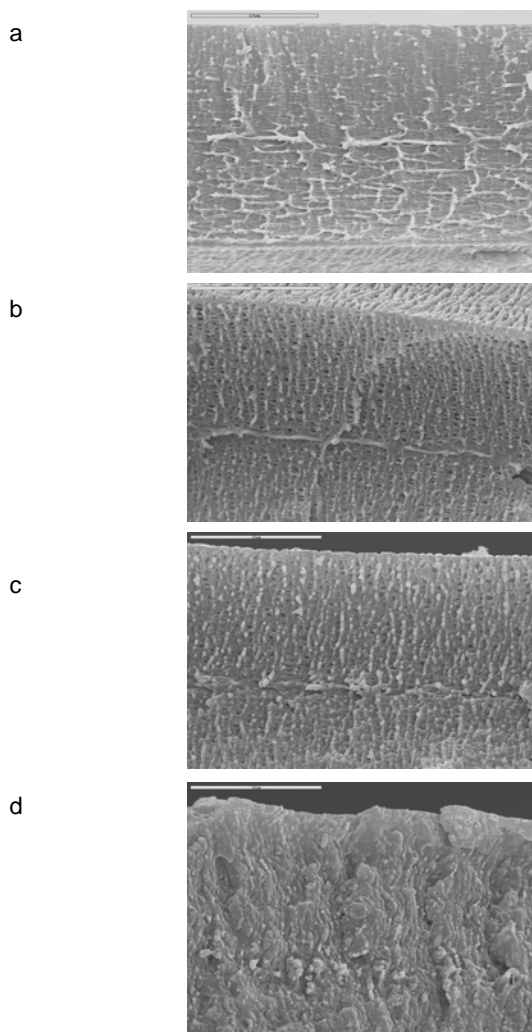


Fig. 6. SEM pictures of cross-section of virgin (a) and grafted (b,c,d) PP membrane of degree of grafting 2.3, 9.7 and 16.2 mmol g⁻¹ respectively. Magnification - 5000

These membranes did not change their characteristics with time (Fig. 7). After three months, the area resistance (41 mΩ cm²) is practically the same as at the beginning (40 mΩ cm²).

The stability of the tested membrane during charge-discharge cycles was performed for high current density (Fig. 8). The increase of electrolytic area resistance during this operation is very low, from 20 to 33 mΩ cm², and proves that the modified membrane is stable and its modification is permanent.

The dependencies shown in Fig. 7 and 8 are typical for all modified samples of low resistance. More detailed experiments concerning this new kind of separators are described in the paper⁷.

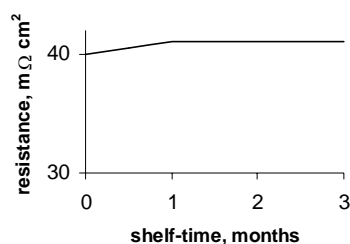


Fig. 7. Dependence of electrolytic area resistance of AAc-grafted-PP on time

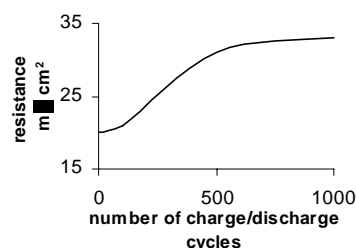


Fig. 8. Dependence of electrolytic area resistance of AAc-grafted-PP on the number of charge/discharge cycles. Current density: 150 mA cm⁻²

Conclusions

Argon plasma generated in the both kinds of apparatus used (KHz, GHz) appeared to be a very efficient source of radical polymerization initiator placed on the porous polypropylene membrane. Graft polymerization of acrylic acid on plasma-modified membrane gives a material suitable for use as separators in high-power alkaline batteries. The grafted poly(acrylic acid) is present both on the surface and inside the pores of the membrane.

Though some properties of the material after modification are not very well reproduced from one experiment to another, even using the same parameters, one can easily obtain a degree of grafting from 4 to 16 mmol g⁻¹ that assures the desired electrochemical properties of the membrane over a very wide range of plasma parameters.

REFERENCES

1. Zhang S. S.: *J. Power Sources* 164, 351 (2007).
2. Choi E. Y., Moon S. H.: *J. Appl. Polym. Sci* 105, 2314 (2007).
3. Ciszewski A., Gancarz I., Kunicki J., Bryjak M.: *Surf. Coat. Technol.* 201, 3676 (2006).
4. Wu S.: *Polymer interface and adhesion*. Dekker, New York 1982.
5. Kuznietsov A. Yu., Bagryansky V. A., Petrov A. K.: *J.*

- Appl. Polym. Sci. 47, 1175 (1993).
6. Falk S. U., Salkind A. J.: *Alkaline storage batteries*. John Wiley & Sons, Inc., New York 1969.
 7. Ciszewski A., Kunicki J., Gancarz I.: *Electrochim. Acta* 52, 5207 (2007).

Gancarz I., Kunicki J., and Ciszewski A. (^a*Chemistry Department, Wrocław University of Technology, Wrocław,* ^b*Central Laboratory of Batteries and Cells, Poznań,* ^c*Institute of Chemistry and Technical Electrochemistry, Poznań University of Technology, Poznań, Poland*): **Application of Plasma-Induced Grafting for Modification of Alkaline Battery Separator**

The commercial porous polypropylene Celgard 2500 was modified by plasma (KHz and GHz frequency) treatment with subsequent grafting with acrylic acid. Dependence of some plasma parameters on the membrane properties was investigated. The results obtained are highly scattered and choice of the best plasma parameters seems to be very difficult. Static and dynamic water contact angles were measured to observe the changes in surface properties. The presence of poly(acrylic acid) on the PP surface was confirmed by FTIR-ATR. SEM analysis has shown that grafting takes place not only on the membrane surface but also inside the pores. In spite of the wide range of the degree of grafting we obtained membranes of resistance values lower than 100 mΩ cm² which makes them acceptable for use in alkaline batteries. The modified membranes do not change their electrolytic area resistance with time and withstand severe charge-discharge treatment.

SORPTION PROPERTIES OF WOOL FIBRES AFTER PLASMA TREATMENT

RADKA CHVALINOVÁ and JAKUB WIENER

Department of Textile Chemistry, Textile Faculty, Technical University of Liberec, Studentská 2, 461 17 Liberec, Czech Republic

radka.chvalinova@tul.cz, jakub.wiener@tul.cz

Introduction

The wool fibre exhibits a typical core – shell structure consisting of an inner protein core, cortex, and surface shell, cuticle¹ (see Fig. 1). The cuticle consists of several layers (see Fig. 2).

The upper layer, epicuticle, contains lipoproteins. Lipoid part of lipoproteins is bound by the sulfoester bond with proteinous part (see Fig. 3). Covalent bonds of branched chain fatty acids implicate hydrophobic character of wool fibres. The lipoproteins are connected with upper layer of exocuticle. Exocuticle is cross-linked by disulfide links (see Fig. 4).

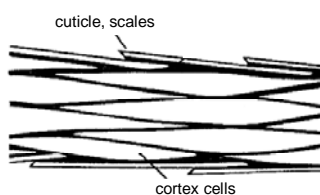


Fig. 1. Structure of wool fibres³

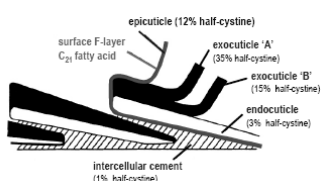


Fig. 2. Schema of cuticle⁴

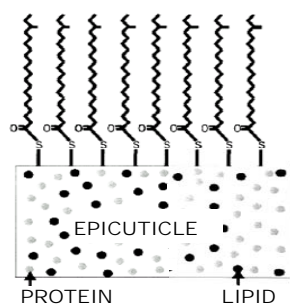


Fig. 3. Lipoproteins in epicuticle

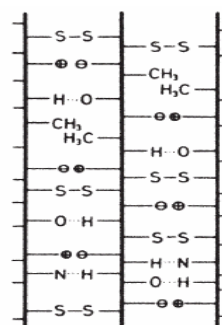


Fig. 4. Stary's wool fiber model⁶

The hydrophobic nature of the cuticle and the high cross-linking density in the outermost fibre surface creates a nature diffusion barrier², which influences sorption properties complicates wool finishing processes, such as printing, dyeing or shrink-proofing. Surface modification plays an important role for many chemical finishing processes in textile industry.

The required surface modification is mainly accomplished by wet chemical processes using special auxiliaries which attack the cuticle by hard chemicals as for example NaClO^{3,4}.

Experiments

The effects of atmospheric pressure plasma treatment on wool fabric were tested in this study.

A Diffuse Coplanar Surface Barrier Discharge (DCSBD) has been used (see Fig. 5).

The operating frequency was 15 kHz, the power input 300 W. Wool fabric has been exposed by different times. Pure wool fabric has been exposed to different intensive plasma-treatment (different exposure times at constant conditions).

A conventionally-finished, plain-weave pure wool fabric (222 g m⁻² manufactured from yarn of 2×19 tex) was used.

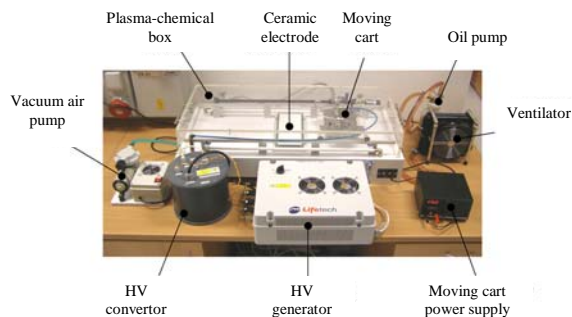


Fig. 5. Used equipment DCSBD

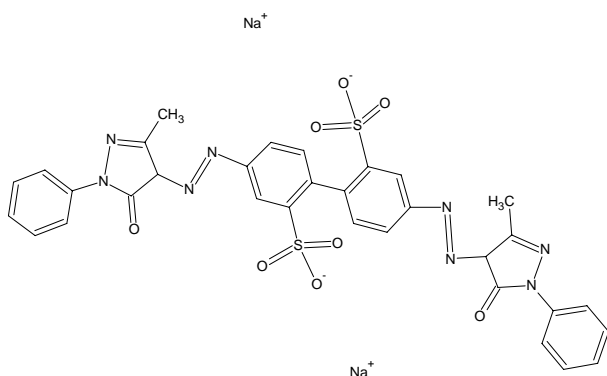


Fig. 6. The chemical structure of acid dye with Colour Index Acid Yellow 42

Dyeing of wool fabrics

Wool samples were pretreated by plasma for time 10, 20, 30, 50 and 100 seconds.

Untreated and plasma treated wool materials were dyed isothermal by acid dye (Colour Index Acid Yellow 42 – see Fig. 6) in weak acid solution (pH 6) at the temperature 60 °C (respectively 80 °C) for 2, 10 and similarly for 60 minutes. The dye bath contained 2 % dye of sample weight. After dyeing, the dyed fabrics were rinsed with cold water for 5 minutes.

Dry dyed materials were measured by spectrophotometer Datacolor 3890 (Datacolor, Switzerland). As results of measurement were achieved remission values. The remissions R were by the using of well known Kubelka-Munk equation recalculated to the K/S values.

Printing of wool fabrics

Wool fabrics (untreated and plasma treated for 10, 50, 100 seconds) were printed by a printing paste (pH 6) with acid dye (C. I. Acid Yellow 42). Printed wool fabrics were fixed for 1, 3, 6 and 10 minutes at 60 °C. Samples were by this fixation wet – evaporation of water was eliminated. Along the aftertreatment were realized the rinsing with cold water for 5 minutes, the soaping at 40 °C with 2 g l⁻¹ Synta-



Fig. 7. Environmental scanning electron microscope Vega TS 5130

pon ABA for 10 minutes and the last rinsing with cold water for 5 minutes. The dyed wool materials were measured by spectrophotometer Datacolor 3890.

Visualization of surface structure

The structure and the appearance of fibres surfaces were observed with using of Scanning Electron Microscopy (SEM) on device VEGA (see Fig. 7). All the samples were coating by Gold before SEM testing.

The structure of surface was observed by the means of microscopic method Atomic Force Microscopy (AFM). AFM is the method used for characterization of prepared sub-micron optical elements.

The method to describe changes of chemical bonds and formation of new chemical groups after the plasma treatment was used Fourier Transform Infrared Spectroscopy (FTIR) Spectrometer One (Perkin Elmer – ATR technique on ZnSe crystals).

Next it was used method X-ray Photoelectron Spectroscopy (XPS). The XPS technique is highly surface specific due to the short range of the photoelectrons that are excited from the solid. The energy of the photoelectrons leaving the sample gives a spectrum with a series of photoelectron peaks. The binding energy of the peaks is characteristic of each element. The measurements were preceded with the using apparatus ESCA PROBE P (Omicron Nanotechnology Ltd) in ultra-high vacuum (under pressure order 10⁻¹⁰ mbar). X-rays emitter is aluminium electrode (used energy 1486.7eV). Measured spectra were analysed by way of CasaXPS programme.

Results

Results of wool dyeing

The K/S values are the observed shade-area directly proportional to dye concentration in fibres. In Fig. 8 there are marked differences in sorption properties untreated and plasma treated wool dyed at 60 °C. The dye concentration increases with dye time and plasma treatment intensity. The plasma treatment for 10 second is exactly insufficient. The best dye sorption is obtained by plasma treated wool fabric for longest time (100 second).

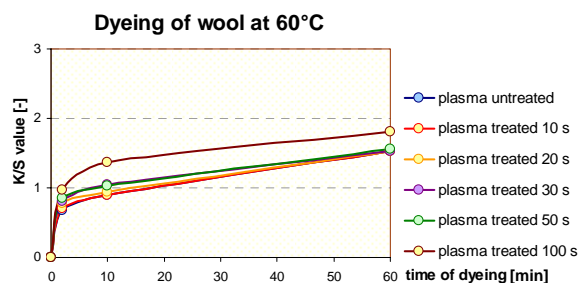


Fig. 8. The influence of dyeing time on K/S values. Dyed at 60 °C

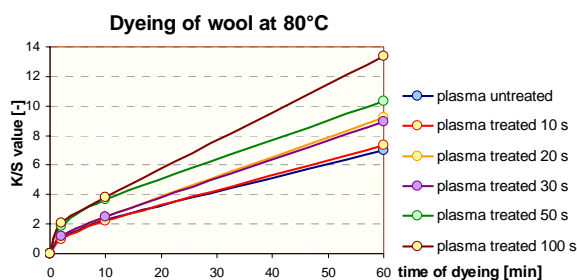


Fig. 9. The influence of dyeing time on K/S values. Dyed at 80 °C

Results of wool printing

Fig. 9 shows faster dye sorption and higher K/S values for dyeing of wool at 80 °C. The plasma treatment time 10 seconds doesn't return sufficient results. These K/S values are the same as K/S values of untreated wool. The plasma treated wool fabric for 100 seconds sorbs double more dye than untreated wool fabric. The similar results were stated in printing experiments.

The untreated wool fabric absorbs double under dye concentration than wool fabric which was plasma treated for

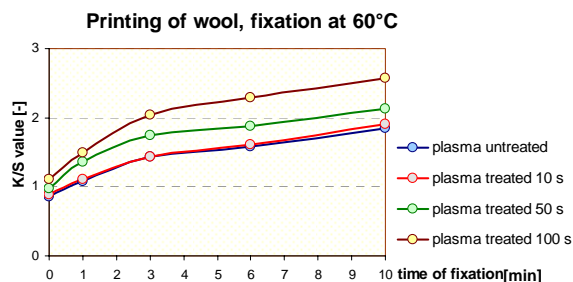


Fig. 10. The influence of fixation time on K/S values. Fixed at 60 °C

100 second (see Fig. 10).

Visualization of surface structure – results

SEM was used for visualization of surface structure wool fibers – epicuticle.

They were observed changes of surface wool scales. In Fig. 11–14 we can see invasion of structure of wool scales and breaking off their parts by the influence of plasma treatment.

By the using of method AFM, it visualized disturbs of epicuticle scales by plasma treatment.

In Fig. 15 and fig. 16 we can see evident differences between surfaces untreated and plasma treated wool fibres.

By means of the FTIR were proved minor changes of wool chemical structure (see Fig. 17).

From results of the XPS it is obvious that it achieved

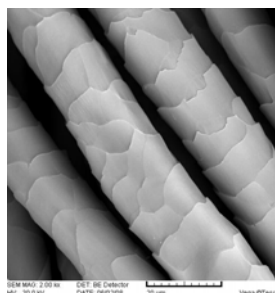


Fig. 11. Untreated wool

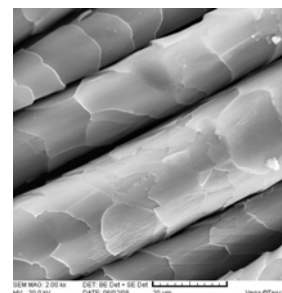


Fig. 12. Plasma treated wool for 10 s

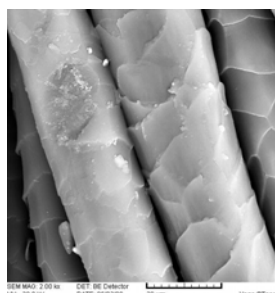


Fig. 13. Plasma treated wool for 50 s

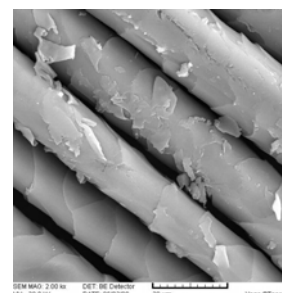


Fig. 14. Plasma treated wool for 100 s

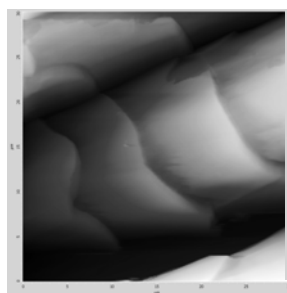


Fig. 15. Untreated wool fibres

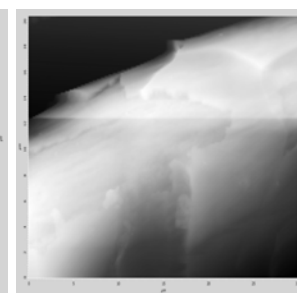


Fig. 16. Plasma treated wool fibres for 100 s

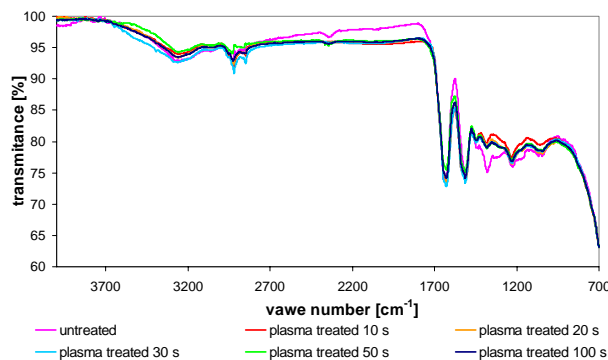


Fig. 17. FT-IR spectrum of wool fibers

Table I
Relative chemical composition ratios determined by XPS for wool fabric

Condition	Chemical composition [%]		
	C1s	O1s	N1s
Untreated wool	76,2	13,7	8,0
Plasma treated 10 s	67,6	19,3	9,4
Plasma treated 100 s	57,6	32,1	8,1

Table II
Relative atomic ratios determined by XPS for wool fabric

Condition	Atomic ratio [%]	
	O/C	N/C
Untreated wool	18,0	10,5
Plasma treated 10 s	28,5	14,0
Plasma treated 100 s	55,6	14,1

changes of chemical structure on surface epicuticle. The concentrations of oxygen increased after plasma treatment of wool fabric. The concentrations of nitrogen increased for 10 second plasma treatment and decreased for 100 seconds plasma treated wool fabric (see Table I).

There were stated the relative atomic ratios O/C and N/C. It was found the increasing the relative atomic ratios O/C and N/C.

Surface oxidation is possible due to the existence of reactive species from the plasma. In Fig. 16–18 are showed surveillance spectrums untreated and plasma treated wool fibres.

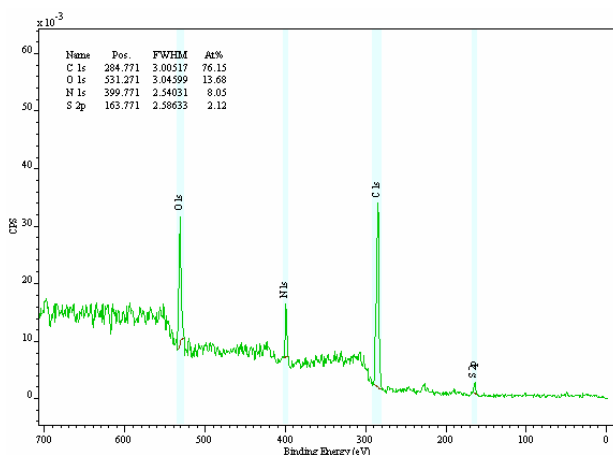


Fig. 18. Surveillance spectrum of untreated wool

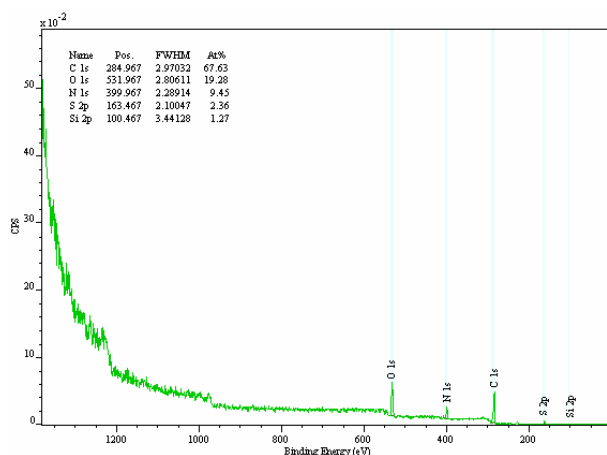


Fig. 19. Surveillance spectrum of plasma treated wool for 10 s

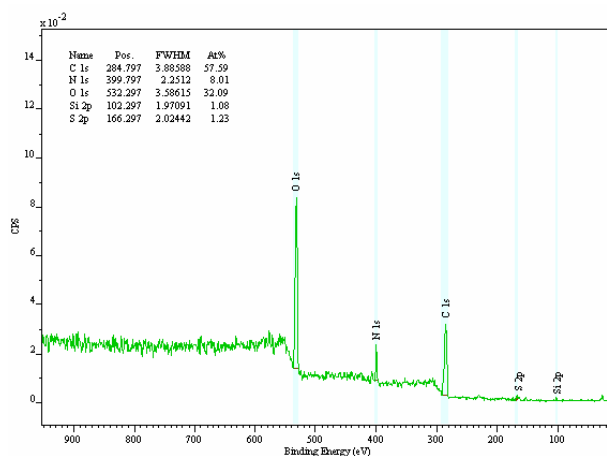


Fig. 20. Surveillance spectrum of plasma treated wool for 100 s

Conclusion

Experiments showed invasion of surface layer of cuticle by plasma. Plasma treatment wool adsorbs dye more intensive at lower temperature. Plasma treatment of wool can in future replace wet pre-treatment processes for wool dyeing and wool printing. The pre-treatment of wool with atmospheric plasma give an appropriate environmentally acceptable alternative to conventional treatments.

This research has been supported by KAN 101630651.

REFERENCES

1. Naebe M., Rippon J. A., Brady P. R., Wang X. G., Brackl N., Riessenl G. Van, Cookson P. G.: *6th International Conference - TEXSCI 07, 2007.*
2. Thomas T., (Shishoo R., ed.), p. 228. Woodhead Publish-

- ing Limited, Cambridge 2007.
3. Lewis D. M.: *Wool dyeing*, Society of Dyers and Colourists, Leeds 1992.
 4. Feldtman H. D., Leeder J. D., Rippon J. A, (R. Postle, S. Kawabata, M. Niwa, ed.) Osaka: Text. Mach. Soc. Japan, 1983, 125.
 5. Jones N.: *Hair Structure Anatomy and Comparative Anatomy*, 98. Elsevier Science, New York 2001.
 6. Rouette H. K.: *Encyclopedia of Textile Finishing*, Springer, New York 2001.
 7. Höcker H.: Int. Text. Bull. Veredlung 41, 18 (1995).

R. Chvalinová and J. Wiener (*Department of Textile Chemistry, Textile Faculty, Technical University of Liberec, Liberec, Czech Republic*): **Sorption Properties of Wool Fibres after Plasma Treatment**

The effects of atmospheric pressure plasma treatment on wool fabric were tested in this study. A Diffuse Coplanar Surface Barrier Discharge (DCSBD) has been used. The operating frequency was 15 kHz, the power input 300 W. Wool fabric has been exposed by different times.

Changes of fibres surface were characterized by means of XPS, FTIR spectroscopy and AFM methods. With the maximal experimental attention was observed dye sorption. Wool fabrics were dyed in dye bath by common used acid hydrophilic dyestuffs. As criterions dye sorption on wool were stated dyeing rate and dye uptake on wool fibres. Printing of wool by acid dyestuffs was carried out as well.

PREPARATION AND CHARACTERISATION OF CARBON FILMS PREPARED FROM HMDSZ/METHANE/NITROGEN OR HYDROGEN MIXTURE USING PECVD

LUKÁŠ KELAR^a, VILMA BURŠÍKOVÁ^{a*},
PAVEL ŠTAHEL^a, ZDENĚK BOCHNÍČEK^a,
VRATISLAV PEŘINA^b, and JIŘÍ BURŠÍK^c

^a Department of Physical Electronics, Masaryk University, Kotlářská 2, CZ-61137 Brno, ^b Institute of Nuclear Physics, Academy of Sciences of the Czech Republic, 25068 Rež near Prague, ^c Institute of Physics of Materials, Academy of Sciences of the Czech Republic, Žitkova 22, 616 62 Brno
vilmab@physics.muni.cz

1. Introduction

Recently, there is a great industrial interest in the development of thin film deposition techniques improving the wear and scratch – resistance of plastics such as polycarbonate. Polycarbonate (PC) substrates in contrary to glasses offer the additional advantages of lower cost, less chance of damage due to breakage, longer durability, manufacturing of lightweight products suitable for many applications in the growing market of large area displays, as well as a number of new product opportunities, such as compact disks, pagers, cell phones and plastic electronics. PC is thermally stable in temperature range from $-100\text{ }^{\circ}\text{C}$ to $+120\text{ }^{\circ}\text{C}$. However, its use is limited to relatively non-abrasive and chemical free environments, because of its low hardness, low scratch resistance and high susceptibility to aggressive chemical environments.

There are a rather limited number of methods for improving the scratch – resistance of plastics such as polycarbonate. Plasma-chemical methods are generally using radio-frequency discharges in mixture of hard-coating precursors for deposition of a very thin film directly on a PC substrate. However, hard-coatings such as amorphous diamond-like carbon (a-C:H or DLC) deposited directly onto plastics such as polycarbonate have performance problems when the system is subjected to stresses produced by mechanical or thermal effects. These problems are due to the difference in property characteristics of inorganic and plastic materials. There is a continuing interest in improving methods for forming hard-coatings having still greater abrasion resistance while also exhibiting improvements in various other physical properties^{1–3}. It is therefore an object of the present work to provide a method for deposition of smooth, hard, optically transparent thin films over the polycarbonate substrates having a high level of abrasion resistance, with improved resistance to cracking under exposure to thermal and mechanical stresses. DLC films have all the properties needed for excellent barrier coatings including high hardness, low friction coefficient, excellent chemical and thermal stability and transparency in the visible spectrum.

The intense ion bombardment of the surface of the growing film results in increased film hardness, however also in high intrinsic residual stress between the substrate and the film. Unfortunately, the high internal stress of these films limits their adhesion and thickness. Silicon and nitrogen incorporated diamond-like carbon films have a great potential for solving some of the major drawbacks of pure DLC films, because they present reduced residual internal stress, high hardness, high deposition rates and good adhesion to PC^{4,5}. In the present work hexamethyldisilazane (HMDSZ) was used to modify the properties of DLC coatings.

2. Experiment

The deposition reactor used consisted of glass cylinder 310 mm in diameter, 210 mm height, closed by two stainless steel flanges^{4,5}. The diameter of the graphite electrodes was 150 mm and distance between them was 55 mm. Bottom electrode was capacitively coupled to the r.f. generator working on frequency 13.56 MHz. The vacuum system consisted of rotary pump and diffusion pump. The working pressure depended on the gas mixture used and was kept around 17 Pa. Minimum pressure achieved by diffusion pump was 0.1 Pa. The flow rate of the hydrogen was kept at 0.7 sccm, the flow rate of the HMDSZ ranged from 0 to 0.4 sccm. The applied power was 50 W. The negative self-bias voltage changed from -100 to -250 V.

The samples were prepared onto crystalline silicon, glass and polycarbonate (Marlon FX) substrates placed on the cathode of the reactor.

A Fischerscope H100 depth sensing indentation (DSI) tester was used to study the indentation response of DLC films on PC substrates. Several different testing conditions were used in order to find the optimum procedure allowing the suppression of the influence of the time dependent indentation response of PC substrate. The loading period of 20 s was followed by a hold time of 5 s, an unloading period of 5 s and finished after holding the minimum load for 5 s. The tests were made for several different indentation loads in order to study the composite mechanical properties of the film/substrate system from near surface up to film-substrate interface. The applied load varied from 1 to 100 mN. Each test was repeated at least 9 times in order to minimize the experimental errors.

The optical measurements were done with Horiba Jobin Yvon ellipsometer in the spectral range from 190 to 2100 nm at the incidence angles from 55° to 75° .

The internal stress was calculated from measurements of a bending curvature of single crystal silicon (111) strips coated with the studied films using the Stoney formula. The samples were subjected to heating with heating rate of 2 K min^{-1} . The temperature dependence of the bending curvature was determined using X-ray diffraction technique for both heating and cooling process.

The films on silicon substrates were annealed in the laboratory furnace Classic Clare 4.0. The furnace chamber was evacuated by turbomolecular pump down to minimum pressure of about 10^{-5} Pa. The studied samples were subjected to heating with constant heating rates in the range from 2 to 10 K min^{-1} . The mass spectrometer Pfeiffer Vacuum Prisma

80 was set in order to follow the evolution in time of 8 specific masses. These specific masses are associated to the ions originated from desorbed gas mixture.

3. Results and discussion

A large set of films was prepared in order to find the optimum amount of HMDSZ in CH_4/H_2 deposition mixture enabling to prepare hard film with enhanced adhesion and minimised compressive stress. The dependence of the deposition rate on HMDSZ flow rate is shown in Fig. 1.

The film prepared in optimum conditions (0,4 sccm HMDSZ, 0,7 sccm H_2 , 2,7 sccm CH_4 , 17 Pa, 50 W, $U_{\text{bias}} = -215$ V) exhibited very interesting properties on PC substrate. The bulk concentrations of carbon, hydrogen, silicon and oxygen atoms, composing the prepared films were obtained by combination RBS and ERDA. The film with optimum mechanical properties consisted 65 at% of carbon, 18 at% of

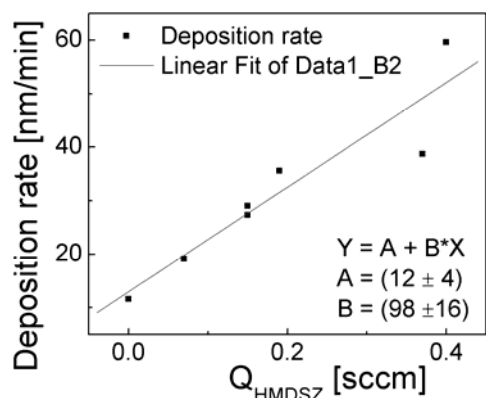


Fig. 1. The dependence of the deposition rate on the HMDSZ flow rate obtained in case of films on silicon substrates

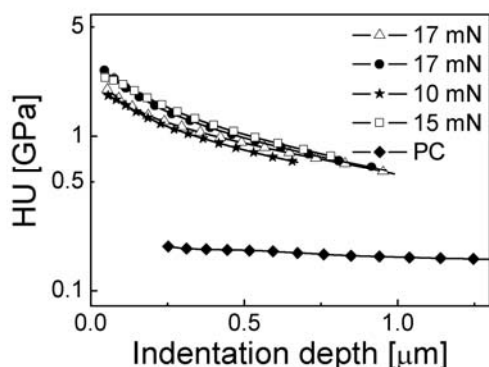


Fig. 2. Dependence of the universal hardness H_U on the indentation depth for sample LD2

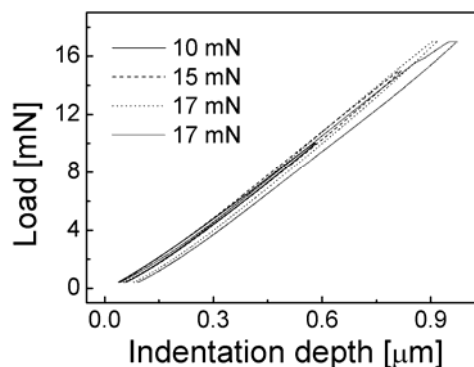


Fig. 3. Indentation loading and unloading curves obtained on sample LD2 for three different loads

hydrogen, 8 at% of silicon, 5 at% of silicon and 4 at% of oxygen.

The mechanical behaviour was studied by DSI method enabling the determination of the so-called universal hardness H_U , which is the measure of the indentation resistance against plastic and elastic deformation. The comparison of the universal dependence on the indentation depth for uncoated and coated PC in Fig. 2 shows, that H_U at the surface was increased of one order of magnitude by the help of the protective film.

There are some specific problems with interpretation of nanoindentation dates related to system of viscoelastoplastic substrate and hard film. Except elastic and plastic response these types of film/substrate systems exhibit a considerable time dependent plastic deformation, and may show also time dependent reversible (anelastic) behaviour. The prints done with low loads can heal out.

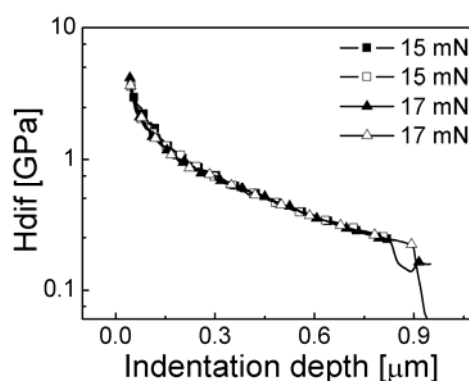


Fig. 4. Dependence of the differential hardness H_{dif} on the indentation depth obtained on sample LD2 for two different maximum loads. The cracking of the film at the film-substrate interface was not observed up to 17 mN of testing loads and indentation depths of 0.9 mm. The sample showed high resistance against indentation induced cracking and delamination

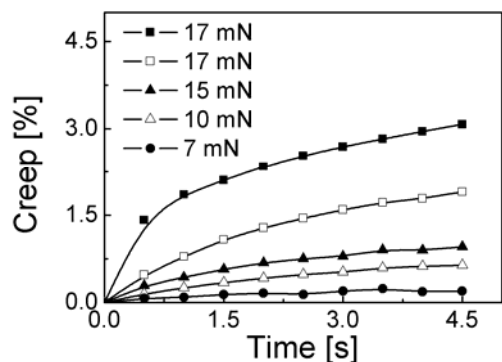


Fig. 5. Results obtained on study of indentation creep (time dependent plastic deformation at constant load) at several different loads. The creep deformation was minimum at low loads when the creep behaviour of the film was dominant. With increasing load the effect of PC substrate became significant and the creep deformation increased

This effect was observed also in the case of our hard and elastic film on polycarbonate substrate, with prevalent viscoplastic properties.

It is illustrated in Fig. 3, where the loading and unloading hysteresis obtained on the studied LD2 sample shows almost complete elastic deformation for loads up to 17 mN and indentation depths up to 900 nm. This depth almost corresponds with the thickness of the prepared film. Hence the system of HMDSZ modified DLC film on PC substrate exhibited the so-called “plate-bending model”^{6,7}, i.e. the hard film on plastic substrate acted as a hard, elastic membrane with extremely high fracture toughness. Due to anelastic behaviour of sample LD2 the indentation prints made with loads lower

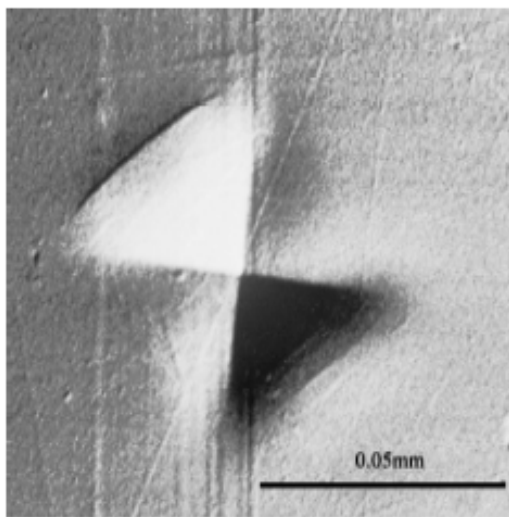


Fig. 6. SEM image illustrating the high indentation resistance of the film against indentation induced cracking and delamination. The image shows indentation print after test with maximum load of 500 mN. The indentation depth several times exceeded the film thickness

than 30 mN disappeared after a short time, i.e. they were healed out.

The DSI method is a very powerful technique. It enables also the determination of the film fracture toughness and the interfacial fracture toughness^{4–8}. If the studied sample undergoes some fracture events, part of the irreversibly dissipated energy is related to the creation and propagation of cracks and may be used for calculation of the fracture toughness.

Moreover, the differential hardness H_{dif} ($H_{dif} = k\partial L/\partial(h^2)$, here L is the load, k is a constant value dependent on the indenter geometry and h is the indentation depth) dependence on the indentation depth may be used to visualise the crack creation or the penetration through film/substrate interface. The differential hardness H_{dif} represents the ratio of the instantaneous load increase to the corresponding change in the square of the indentation depth (i.e. change in contact area of the indenter and the tested material). Therefore, the abrupt changes appear on the depth dependence of H_{dif} as abrupt jumps. In Fig. 5 the depth dependence of H_{dif} for studied film/substrate system is shown. According to this graph the indentation induced failures at the interface begun to create mostly at maximum load of 17 mN and at indentation depth of approximately 900 nm. Achieving this depth, which corresponded with the film thickness, the strong influence of the PC substrate on measured values started.

The maximum load may be kept constant during a certain time period and from the time dependence of the indentation depth it is possible to evaluate the indentation creep resistance of the tested material. In Fig. 6 the results of indentation creep are shown for three different indentation loads. The increase in creep strain for higher loads was caused by the increasing influence of the PC substrate. In Fig. 6 the SEM image of the indentation print made with load of 500 mN is shown. The SEM image demonstrates the high resistance of the sample against indentation induced cracking and delamination.

The thermal stability of films deposited on single crystal silicon substrate was studied using thermal desorption spectroscopy and X-ray diffraction technique.

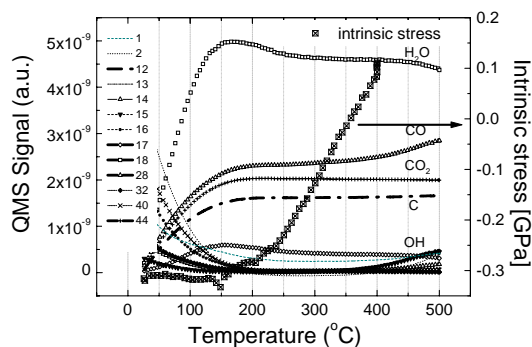


Fig. 7. Comparison of the thermal desorption spectroscopy results with the intrinsic stress dependence on the temperature for sample prepared from HMDSZ/methane/nitrogen mixture

The compressive stress of the as-deposited films was relatively low, it was around -0.3 GPa. The compressive stress decreased during heating and reached the zero value for temperatures around 300 °C. The decrease in compressive stress with temperature was accompanied with desorption of water, OH, CO and CO₂. The maximum in water desorption at around 300 °C corresponds to the start of the decrease in compressive stress. Further heating caused increase in tensile stress (see Fig. 7). The tensile stress of $\sigma = 0.1$ GPa remained in films even after cooling down to room temperature. The films were not deteriorated after heating, however during indentation testing showed less resistance against indentation induced cracking, than as-deposited films or films heated up to 300 °C.

4. Conclusion

We have deposited a large set of diamond like carbon films with incorporation of silicon, oxygen and nitrogen. The optimum deposition condition for deposition of smooth, hard, wear resistant thin films suitable for protection of the polycarbonate substrates were found. The film prepared under optimum conditions exhibited excellent fracture resistance and low intrinsic stress. The prepared films have all the properties needed for excellent protective coatings including high hardness, low friction coefficient, excellent chemical and thermal stability and transparency in the visible spectrum.

This research has been supported by Ministry of Education, Youths and Sports of the Czech Republic under project MSM0021622411 and by the grant of Czech Science Foundation No. 202/07/1669.

REFERENCES

1. Damasceno J. C., Camargo S. S., Cremona M.: *Thin Solid Films* 420–421, 195 (2002).
2. Damasceno J. C., Camargo S. S., Cremona M.: *Thin Solid Films* 433, 199 (2003).
3. Martinu L.: *Plasma Processing fo Polymers*, p. 247. Kluwer Academic Publishers, 1997.
4. Zajíčková L., Buršíková V., Peřina V., Macková A., Janča J.: *Surf. Coat. Technol.* 174–175, 281 (2003).
5. Buršíková V., Sládek P., Sřahel P., Buršík J.: *J. Non-Cryst. Solids* 352, 1242 (2006)
6. McGurk M. R., Chandler H. W., Twigg P. C., Page T. F.: *Surf. Coat. Technol.* 68/69, 576 (1994).
7. Gerberich W. W., Strojny A., Yoder K., Cheng L.-S.: *J. Mater. Res.* 14, 2210 (1999).
8. McGurk M. R., Page T. F.: *Surf. Coat. Technol.* 92, 87 (1997).

CHARACTERIZATION OF NANO-STRUCTURED CARBON-METAL BILAYERS DEPOSITED BY THERMIONIC VACUUM ARC (TVA) TECHNOLOGY

R. VLADOIU^{a*}, V. CIUPINA^a, C. P. LUNGU^b,
O. I. POMPILIAN^b, P. CHIRU^b,
A. M. LUNGU^b, G. PRODAN^a, A. MANDES^a,
and G. MUSA^a

^a Dep. of Physics, Ovidius University, Constanta 900527,

^b National Institute for Laser, Plasma and Radiation Physics,
PO Box MG-36, 077125, Bucharest Romania
rvladoiu@univ-ovidius.ro

Introduction

Composed of alternating layers of two different materials as thin as a few atoms, multilayers – an unique class of materials – offer extraordinary strength, hardness, heat-resistance, and unexpected new properties.

Multilayers are part of a larger, established scientific field of so-called designer or „nanostructured“ materials that represent the current limits of materials engineering and that are currently impacting numerous research programs.

Nanostructured materials may be defined as those materials whose structural elements – clusters, crystallites or molecules – have dimensions in the 1 to 100 nm range. The explosion in both academic and industrial interest in these materials over the past decade arises from the remarkable variations in fundamental electrical, optical and magnetic properties that occur as one progresses from an „infinitely extended“ solid to a particle of material consisting of a countable number of atoms¹.

The continuous development of technology is based on new materials with improved properties used in highly performing devices. One of the most interesting materials nowadays is metal-carbon film².

In recent years, multilayers composed of C coating with very thin buffer layers metals like Ag or Cu become a major area of interest, especially for tribological applications. An important amount of work is presently dedicated to studying synthesis of high quality carbon films using different methods like: magnetron sputtering, Thermionic Vacuum Arc (TVA) chemical and plasma vapor deposition (CVD and PACVD, respectively), electron cyclotron resonance (ECR), filtered cathodic vacuum arc (FCVA), ion beam sputtering, pulsed laser deposition (PLD), ion Beam sputtering etc³.

Among them, thin film deposition process by Thermionic Vacuum Arc (TVA) might become one of the most suitable technologies to significantly improve the quality of the surfaces covered with films in which the coating is bombarded by high energy ions of even depositing materials^{4,5}.

The aim of this paper is to analyze the nanostructured

carbon-metal bilayers deposited by Thermionic Vacuum Arc (TVA) technology in a special two electron gun configuration^{6,7}.

Experimental setup

The two electron gun TVA configuration consists of two independent systems that generate incident electron beams on the specific anode material (carbon and metal), each gun being connected to a high power supply. By using the TVA method, the metal deposition takes place in high or ultrahigh vacuum conditions, without the presence of any gas, excepting the vapors of the material evaporated at the anode. This method allows the simultaneous deposition of different materials, providing the possibility of obtaining multi-component thin films, in this particular case the C-Ar or C-Cu composites. (Fig. 1) The electron guns are symmetrically arranged with respect to the substrate – glass and stainless steel – mounted at a distance of 400 mm on the central line.

The intensity of the heating current of the filament was $I_f = 48$ A. at a deposition rate of 3 \AA s^{-1} . The pressure during the discharge process was about $1.5 \cdot 10^{-6} - 7.5 \cdot 10^{-6}$ Torr.

In the case of C-Ag experimental arrangement were used as anodes a carbon rod of 12 mm diameter and TiB₂ crucible containing Ag pebbles, respectively. On sample holder was set 5 discs of smooth stainless steel (255 mm diameter, 3 mm lengths), 8 samples of lima glass and 5 samples of optical glass discs (25 mm diameter, 1mm length). The sample holder was heated at a temperature of 200 °C, without being rotated.

The thickness of the film during deposition was performed by a FTM 7 device.

First, an intermediate layer of 300 nm Ag thickness was deposited and after, the process was continued with C and Ag deposited simultaneously. After the deposition FTM 7 indicated a thickness of the film around $2 \mu\text{m C/Ag} + 300 \text{ nm Ag}$. For Ag deposition we used a Heizenger power supply provided with a balast resistance of $R = 272 \Omega$.

In Table I are presented the values of working parameters used during deposition of C-Ag.

Fig. 2 presents the distribution of the samples on the

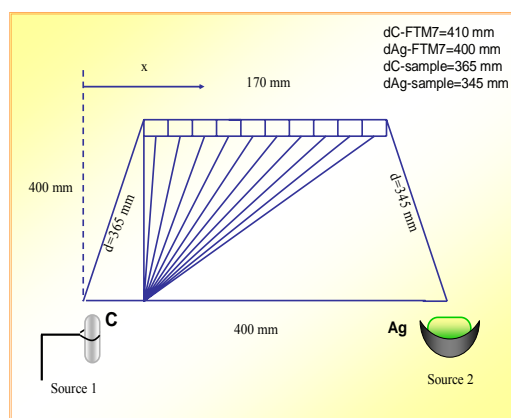


Fig. 1. Experimental set-up of the sample

Table I
Working parameters for C-Ag composites

$I_{fAg} = 37.6 \text{ A}$		$I_{fC} = 49.5 \text{ A}$	
$I_a [\text{A}]$	$U [\text{V}]$	$I_a [\text{A}]$	$U [\text{V}]$
0.732	510	1.3	977
0.668	610	1.4	697
0.810	460	1.2	1966
0.812	770	1.4	913
0.808	720	1.4	169
0.813	700	1.4	1302

holder.

In the case of C-Cu deposition we used for anode a carbon rod and a crucible containing Cu. Deposition was made on different substrates of various materials (5 pieces of stainless steel discs, 5 pieces of optical glass and 8 pieces of lima glass) as it is shown in Fig. 3 the distance between the FTM device and carbon rod was $d_{Cu-FTM7} = 410 \text{ mm}$, the same as the value for distance to the crucible with Cu.

Other distances maintained in this experimental arrangement were: $d_{C-sample} = 350 \text{ mm}$ (between the sample and C source); $d_{Cu-sample} = 330 \text{ mm}$ (between the sample and Cu

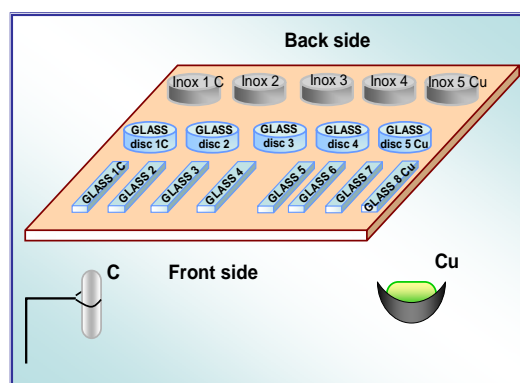


Fig. 3. Sample position on holder for C-Cu discharge

source) and $d_{C-Cu} = 140 \text{ mm}$ (the distance between the anodes).

In Table III are listed the working parameters for C-Cu obtained during the deposition time.

The holder sample was heated at $200 \text{ }^\circ\text{C}$ and it was not rotated.

As in the previous case, we have deposited first an intermediate layer of 300 nm Cu thickness, and after that we started the simultaneous process of deposition for C and Cu.

After the total time of deposition 3500 seconds FTM device indicated a thickness of the film around $2 \text{ } \mu\text{m}$ C/Cu + 300 nm Cu.

Surface free energy of films was analyzed by means of the contact angle measurement, using performed analysis software See System and Optical Emission Spectroscopy (OES) has been also carried out. Tribological behavior of the C-Ag and C-Cu films was investigated by CSM Ball-on-Disc Tribometer with 10 cm s^{-1} sliding speed at 1 N Load.

Results and discussion

The elementary composition of the obtained carbon multilayers were investigated by mean of Optical emission spectroscopy (OES) and by mean of Surface Energy Evaluation System (See System).

In Fig. 4 there are presented the OES investigation for C-Ag and C-Cu bilayers.

Fig. 5a shows the frictional behavior of the C-Ag films prepared by TVA method. One can observe a maximum coefficient of friction when the Ag concentration in the carbon matrix was in the range of 15%. Lower content of Ag leads to a decreasing of the coefficient of friction, but the adherence of the film was low. Higher adherence of the C-Ag films was obtained at higher concentration of the Ag, a minimum coefficient of friction being achieved at about 35% atomic percent concentration of Ag in C matrix. In the case of C-Cu composite the Cu concentration was 25% for higher value of friction coefficients (Fig. 5b) (ref.⁸).

The determination of surface free energy of solid is of a great importance in a wide range of problems in applied science. Usually the evaluation of the surface free energy is performed by mean of the contact angle. The contact angle of a liquid drop on a solid surface is defined by mechanical equi-

Table III
Working parameters for C-Cu nanocomposites

$I_{fC} = 33 \cdot 1.5 = 45 \text{ A}$ $P_{lucru} = 1.5 \cdot 10^{-5} \text{ Torr}$		$I_{fCu} = 42 \text{ A}$ $P_{lucru} = 7.5 \cdot 10^{-6} \text{ Torr}$	
$I_a [\text{A}]$	$U [\text{V}]$	$I_a [\text{A}]$	$U [\text{V}]$
1	1299	0.506	1130
1.2	347	0.749	1030
1.2	340	0.753	900
1.2	335	0.753	870
1.3	574	0.902	950

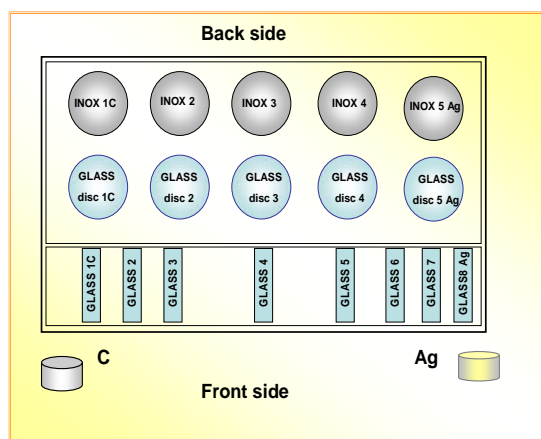


Fig. 2. Sample position on holder for C-Ag discharge

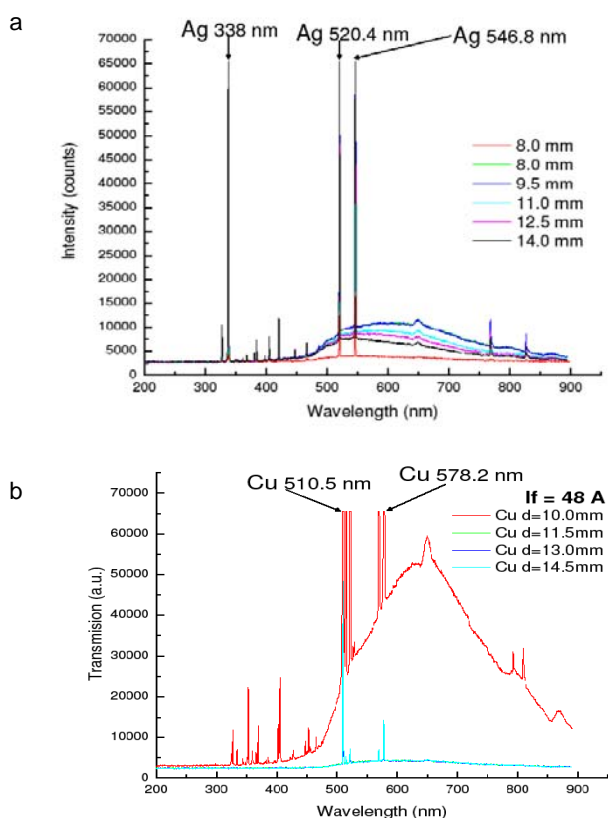


Fig. 4. a) Optical emission spectroscopy (OES) for C-Ag and b) C-Cu layers at different interelectrode distance

librium of the drop under the action of three interfacial tensions solid/vapour, solid/liquid and liquid/vapour.

The contact angles and free surface energy were determined by means of Surface Energy Evaluation System (See System). It is based on the usage of a CCD camera, which observes a liquid drop on the studied surface. Recorded pictures are analyzed manually by the user, which is substantial for the full control of the contact angle determination. Selection of several points of solid–liquid and liquid–vapor interface makes possible to fit the drop profile and to calculate the tangent angle of the drop with the solid surface. In order to obtain as precise results as possible, the profile of the drop should be fitted with more than three basic points: two on the liquid – solid interface – the base line – and one on the drop contour. In this way the errors can be minimized⁹.

The surface energy evaluation system was made on the basis of state equations Kwok-Neumann equation (Table V), Li-Neumann equation (Table VI), Wu equation (Table VII). Analyses obtained by contact angle measurements method, showed for C-Cu low values for surface free energy, and for C-Ag double surface free energy values, in both cases proving the hydrophobic character of these films.

As it can be noticed from Fig. 6, the comparison revealed that in the case of samples obtained for C-Cu the contact angle has lower values than in the case of sample obtained for C-Ag for ethylene glycol as testing liquid, while for water the values are the same.

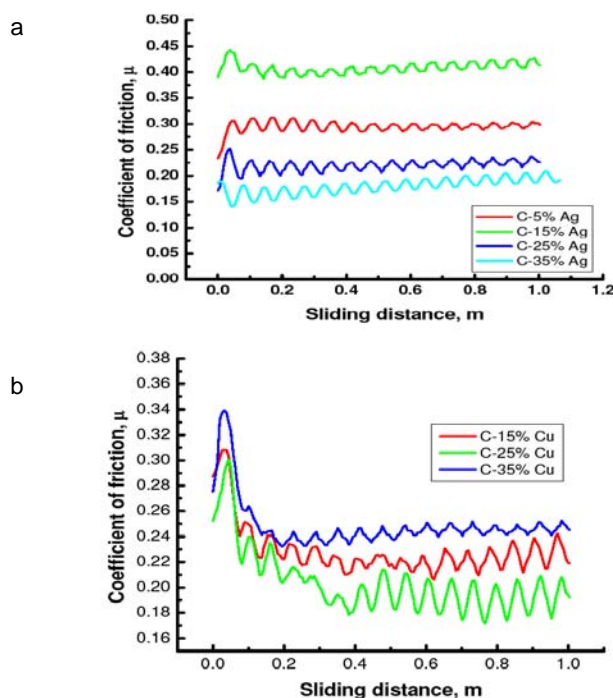


Fig. 5. a) Tribological behaviour of the C-Ag films; b) tribological behaviour of the C-Cu films

Table V
Kwok-Neumann Equation of State model

Sample no.	g water [mJ m ⁻²]	g ethylene glycol [mJ m ⁻²]	Kwok- Neumann model Mean
C-Cu	6,32	15,21	10,77
C-Ag	17,00	24,59	20,79

Table VI
Li-Neumann Equation of State model

Sample no.	g water [mJ m ⁻²]	g ethylene glycol [mJ m ⁻²]	Li-Neumann model Mean
C-Cu	5,55	15,56	10,55
C-Ag	16,78	24,94	20,86

Table VII
Wu-Equation of State model

Sample no.	water [mJ m ⁻²]	ethylene glycol [mJ m ⁻²]
C-Cu	1,79	11,96
C-Ag	7,66	21,83

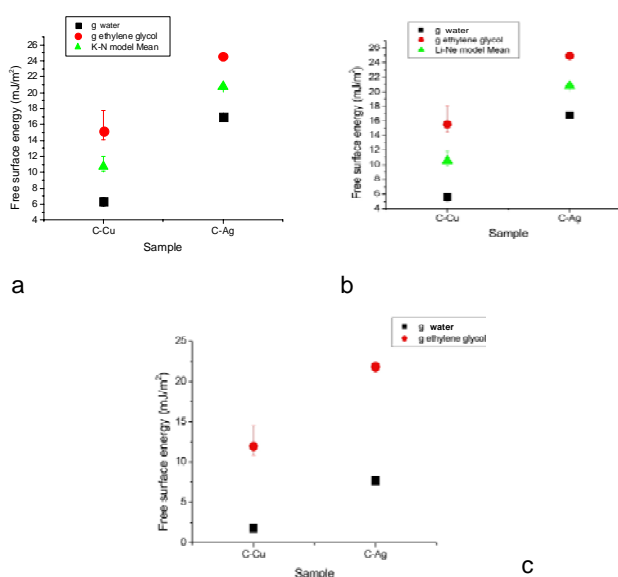


Fig. 6. Comparative view of free surface energy obtained for Kwok-Neumann Equation of State model (a); Li-Neumann Equation of State model (b) and Wu-Equation of State model (c)

Fig. 7 presents the feature of the drops as photos captured during the measurements with two testing liquids: water and ethylene glycol for C-Cu and in the Fig. 8 for C-Ag bilayers.

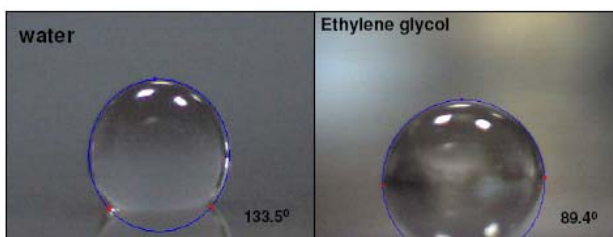


Fig. 7. Pictures of the drops captured during the free surface determination for C-Cu bilayers

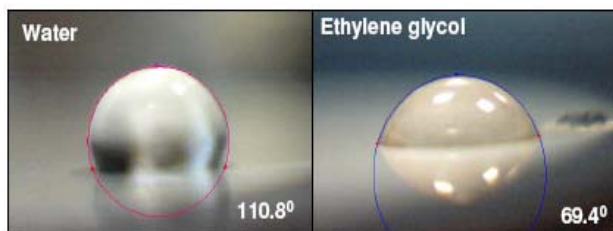


Fig. 8. Pictures of the drops captured during the free surface energy measurement for C-Ag bilayers

Conclusions

Thermionic Vacuum Arc (TVA) method represents a very suitable procedure for obtaining multilayers films of a controlled quality. The carbon – metal bilayers deposited by TVA in two electron gun configuration was investigated in terms of tribological behavior, surface free energy and OES. The higher coefficient of friction has been obtained for 15 % Ag in C-Ag films and for 25 % Cu in the case of C-Cu films.

The surface free energies obtained for C-Cu sample were lower than in the case of C-Ag sample in all studied models. These results proved a good hydrophobic character for these bilayers.

This work was supported by Romanian Ministry of Education and Research, under project CEx 62/2006 and project CEx 237/2006.

REFERENCES

- Lu X., Li M., Tang X., Lee J.: Surf. Coat. Technol. 201, 1679 (2006).
- Lungu C. P., Mustata I., Lungu A.M., Brinza O., Zaroschi V., Kuncser V., Filoti G., Ion L.: J. Optoelectron. Adv. Mater. 5, 2507 (2005).
- Lungu C. P., Mustata I., Lungu A.M., Brinza O., Moldovan C., Rotaru C., Iosub R., Sava F., Popescu M., Vladioiu R., Ciupina V., Prodan G., Apretroaei N.: J. Optoelectron. Adv. Mater. 8, 74 (2006).
- Musa G., Mustata I., Ciupina V., Vladioiu R., Prodan G., Vasile E., Ehrich H.: Diamond Relat. Mater. 13, 1398 (2004).
- Musa G., Mustata I., Ciupina V., Vladioiu R., Prodan G., Lungu C. P., Ehrich H.: J. Optoelectron. Adv. Mater. 7, 2485 (2005).
- Vladioiu R., Ciupina V., Surdu-Bob C., Lungu C.P., Janik J., Skalny J. D., Bursikova V., Bursik J., Musa G.: J. Optoelectron. Adv. Mater. 9, 4862 (2007).
- Surdu-Bob C., Vladioiu R., Badulescu M., Musa G.: Diamond Relat. Mater. 17, 1625 (2008).
- Mathew Mate C.: *Tribology on the small scale*, Oxford University Press 2008.
- Bursikova V., St'ahel P., Navratil Z., Bursik J., Janca J.: *Surface energy evaluation of plasma treated materials by contact angle measurement*, (2004).
- Lieberman M. A., Lichtenberg A. J.: *Principle of plasma discharges and Material Processing*, John Wiley & Sons, N. Y. 1995.
- Donnet C., Erdemir A.: *Tribology of Diamond Like Carbon films*, Springer, 2008.

PLASMA IN TEXTILE TREATMENT

PETR NASADIL* and PETR BENEŠOVSKÝ

Textile Testing Institute, Vaclavska 6, 658 41 Brno, Czech Republic; www.tzu.cz
nasadil@tzu.cz

Introduction

Plasma modification of textiles represents great opportunity for improvement of older, energetically demanding, slow and sometimes not very eco-friendly treatment technologies. Application of plasma is ecological and friendly for production costs due to energy savings and reduction of processing times. Compared to other scientific works describing increase of hydrophilicity of hemp, wool or polypropylene textiles or decrease of felting shrinkage of wool^{1,2}, our activities were focused mainly on effects important for manufacturers and their interest in plasma applications as a new advantageous technology.

In this work we present possibilities of utilizing plasma pre-treatment in three different textile-processing areas. At first, the possibility of dyeing of plasma pre-treated cotton at temperatures lower as usual was tested. In the second experiment, the recent method of textile printing – inkjet print, normally suitable mainly for cotton substrates, was tested on very hard-to-print polypropylene with plasma pre-treatment. Finally the last experiment proved that plasma is capable to photo catalytically activate TiO₂, applied on textile substrate, which is subsequently able to inhibit bacteria growth on surface.

The main reason for using plasma pre-treatment is saving of quite considerable amounts of energy during dyeing process. Normally, cellulose textiles like cotton have to be heated to 100 °C and this level has to be held for ca 30 min. Hydrophilicity increased by plasma should lead to good results using lower dyeing temperatures and/or shorter processing times. Therefore interesting power savings are possible.

Polypropylene is known as very hard-to-print and hard-to-dye material. Use of conventional printing technologies is difficult and limited.

Inkjet printing is novel method of textile printing, utilizing printers similar to office inkjet ones. In the present, these types of printers are capable to print only onto hydrophilic substrates, i.e. textiles with high content of cotton. Plasma pre-treatment of polypropylene should increase colourfastness of inks and their better fixation on polypropylene fibres.

Photocatalytic properties of TiO₂ activated by UVA irradiation or by visible light are well known³. In presented experiment, the activation of TiO₂ by plasma is studied and expressed in unconventional manner – by antibacterial activity of textile sample with colloidal TiO₂ application. Antibacterial attributes were tested according to ASTM E2149-1 standard.

In all experiments the comparison between plasma treated and untreated samples was made in order to show effect of plasma modification.

Experimental

All experiments were carried on using laboratory coplanar low temperature atmospheric plasma discharge with power of 400 W. Exposition time was in all cases 5 s. Samples were processed immediately after plasma pre-treatment (except of inkjet printing experiments, where transport to printer took approximately 30 minutes).

For experiments with dyeing white woven cotton fabric was used. As a dye, industrial saturn navy blue was used. Samples were processed in laboratory dyeing device AHIBA. Washing of samples was performed in laboratory washing machine.

Inkjet prints were performed on knitted, 100% polypropylene white t-shirt (producer Klimatex, Czech Republic), utilizing standard small inkjet printer and commercial inks, used in external graphic studio. Washing of samples was performed in laboratory washing machine Wascator FOM71MP-Lab.

TiO₂ (anatase) nanoform colloidal solution (containing 0,8 % of TiO₂) was purchased from TitanPE Ltd., China. *Klebsiella Pneumoniae* (Czech Collection of Microorganisms strain) was used for antibacterial testing.

For determination of colour differences between plasma-treated and untreated samples EN ISO 105-A02 was used. Domestic laundering was carried-on according to standard EN ISO 6330.

Differences between inkjet-printed samples before/after home laundering were specified by eye observation.

Determination of antibacterial activities of plasma-treated/untreated samples was carried on according to ASTM E2149-1 standard.

1.) Dyeing of plasma pre-treated cotton woven fabrics:

Three different temperature modes were used for dyeing process (see Fig. 1):

- mode A: maximal temperature of 100 °C
- mode B: maximal temperature of 80 °C
- mode C: maximal temperature of 60 °C

Two samples (woven cotton fabric, weight 10 g, dimension ca 28 × 23 cm) were prepared for every temperature

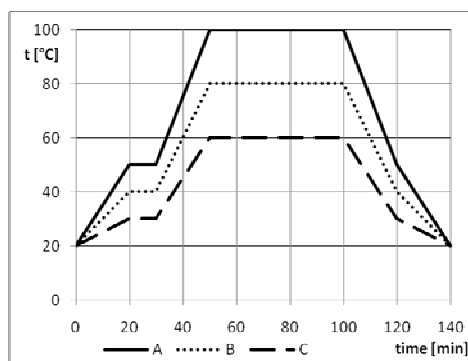


Fig. 1. Temperature modes of dyeing

mode; first one without plasma pre-treatment, second one with plasma pre-treatment (in Fig. 3–6 marked with *). Dyeing bath (distilled water) volume for every sample was 400 ml, with 0,05 g of Saturn navy blue dye itself. Dyeing was carried out using laboratory dyeing apparatus AHIBA NUANCE Top Speed II.

Plasma pre-treated samples were inserted into dyeing bath and dyed immediately after plasma surface modification (400 W, exposition time 5 s). After dyeing, all samples were dried at room temperature.

Colour fastness of samples was evaluated after five washing cycles using standard washing machine WASCA-TOR FOM71MP-Lab (30 °C, 3 g l⁻¹ of ECE detergent).

2.) Inkjet print on plasma pre-treated polypropylene knitted fabric:

For this experiment two samples were prepared; with and without plasma pre-treatment. Plasma modified sample was exposed to plasma ca 30 minutes prior to the main print. The same test picture (see Fig. 2.), consisting of different print elements like photo, text, vector graphic etc. was printed on both samples.

After printing, dyes were thermally fixed on both samples for 30 seconds under 100 °C.

Colour fastness of samples was evaluated after five washing cycles using standard washing machine WASCA-TOR FOM71MP-Lab (30 °C, 3 g l⁻¹ of ECE detergent).

3.) Photocatalytic activation of TiO₂ on textile by means of plasma:

Two cotton woven samples were prepared; first without plasma activation and second by plasma pre-treated. Colloidal TiO₂ was applied on samples using laboratory dyeing device AHIBA NUANCE Top Speed II. Samples were rinsed and then for 1 minute dried using 160 °C iron. Afterwards, first sample was exposed to plasma (exposition time 5 s), while second wasn't. Both samples were tested for antibacterial activity according to ASTM E2149-1 standard. Difference in antibacterial activity of plasma-treated and untreated sample as well as duration of antibacterial effect over time were



Fig. 2. Test picture for inkjet print

checked.

According this standard nutrient broth with specified concentration of selected bacteria (*Klebsiella Pneumoniae*) was prepared. Then the specified weight of sample was inserted into broth solution and agitated. After desired times small amount of solution was taken and poured into agar plates. On the plate, colonies of microorganisms were grown after specified time and then counted (CFU – colony forming unit). High number of CFU represents small antibacterial effect of sample. For comparison, the “blank” broth solution without any sample (represents untreated textile sample) was processed in the same way. Results are expressed as proportional reduction of bacteria on tested sample against this blank sample.

Results and discussions

1.) Dyeing of plasma pre-treated cotton woven fabrics

Experimental results of dyeing are in Fig. 3. After all three dyeing modes the plasma pre-treated samples show brighter and deeper colour shade. Fig. 4–6 show appearance of samples after first, third and fifth washing cycle, respectively.

Difference between treated and untreated samples is clearly visible. Plasma pre-treated samples show deeper colour shade than untreated samples. Biggest differences can be seen after dyeing. After several washing cycles the difference decreases. It means that used plasma helps the textile to absorb more dye from dyeing bath, but has only small impact on colourfastness of textile material (colourfastness is in this case more significant than dyeing technology).

Samples with plasma treatment are marked “* ”.

2.) Inkjet print on plasma pre-treated polypropylene woven fabric

Results before and after two washing cycles are presented in Fig. 7 and 8, respectively.

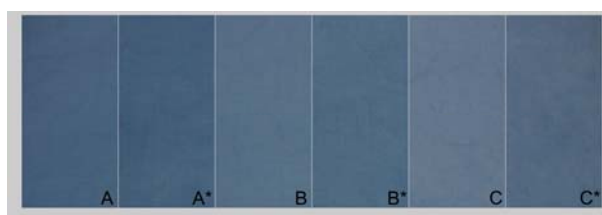


Fig. 3. Samples after dyeing

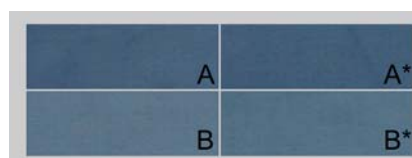


Fig. 4. Samples after first washing cycle

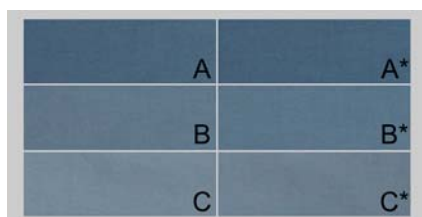


Fig. 5. Samples after third washing cycle

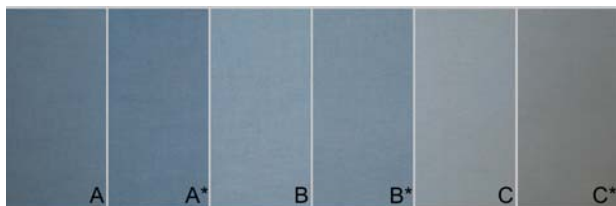


Fig. 6. Samples after fifth washing cycle



Fig. 7. Inkjet prints on PP before washing

Even before washing, the plasma pre-treated sample show much brighter colour shades. After two washing cycles the difference between treated and untreated sample is obvious. It means that plasma is able to bring added value to inkjet printing on polypropylene so that it participates on hydrophilization of substrate and partially in sorption of inks on samples. Results are very positive and this topic will be subject of further research.

Table I summarizes numerical expression of colour fastness results according to EN ISO 105-A02 standard, measured on colour rectangles, positioned above the photograph in tested picture. In four from six measurements treated sample exhibits better colourfastness than untreated.

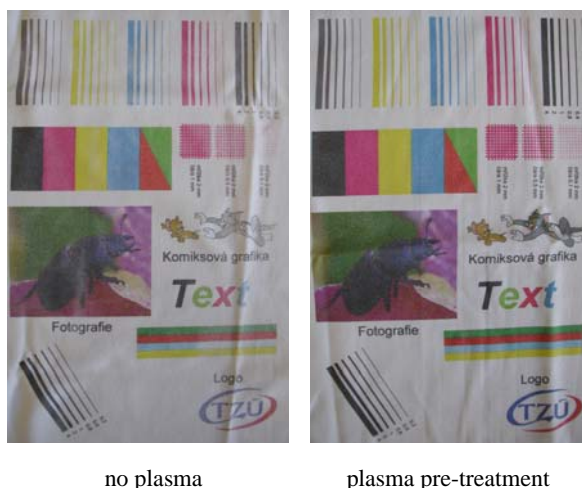


Fig. 8. Inkjet prints on PP after two washing cycles

Table I

Colourfastness level of samples (1- bad colourfastness, 5- very good colourfastness)

Colour in sample	Treated sample	Untreated sample
black	4	2
violet	3	4
yellow	2–3	1–2
blue	2	1–2
red	4	1
green	2–3	2–3

Table II

Antibacterial activity of TiO₂ doped sample in time

Time [hours]	Tested sample [CFU]	“Blank” sample [CFU]	Reduction [%]
0	86	262	67
1	4	148	97
2	6	172	96
3	38	237	84
5	153	400	62

3.) Photo catalytic activation of TiO₂ on textile by means of plasma

Results of antibacterial tests are summarized in Table II. Time dependence of proportional reduction is shown in Fig. 9.

Results show good antibacterial effect and confirm that plasma is able to activate TiO₂ (note: TiO₂ without activation has no antibacterial, nor photocatalytic properties) for antibacterial effectiveness. Activated TiO₂ can inhibit bacteria

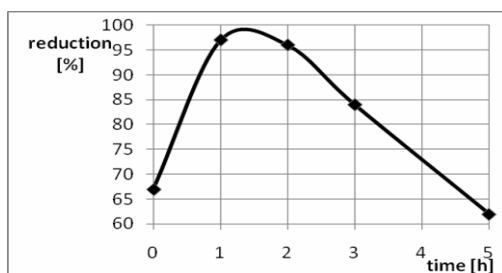


Fig. 9. Reduction of *Klebsiella Pneumoniae* in time

growth more than 5 hours after activation, even if it's placed in dark.

Conclusion

All three experiments showed more or less positive results, proving effect of plasma treatment on processes of dyeing and printing as well as ability to photo catalytically activate TiO_2 on textile substrate in very short time. All those effects should lead to innovative and energy-saving modifications of traditional textile processing. Novel technologies mainly for inkjet textile printing and photo catalytic activation of TiO_2 can extend nowadays possibilities and help producers to offer new or innovative products. All three reported themes are subject to further research.

This work is supported by The Academy of Sciences of The Czech Republic under project number KAN101630651.

REFERENCES

1. Radetic M., Jovancic P., Puac N., Petrovic Z. Lj.: J. Phys. Conference Series 71, 012017 (2007).
2. Höcker H.: Plasma Treatment of Textile Fibers, www.fibre2fashion.com.
3. Kühn K. P., Chaberny I. F., Massholder K., Stickler M., Benz V. W., Sonntag H. G., Erdinger L.: Chemosphere 53, 71 (2003).

P. Nasadil* and P. Benešovský (*Textile Testing Institute, Brno, Czech Republic*): **Plasma in Textile Treatment**

The paper deals with three different initial experiments focused on treatment of different textile materials (polypropylene and cotton) by low temperature atmospheric air plasma and its effects. Main idea was to prove positive influence of plasma applications to manufacturers and increase of market value of textile articles by improved dyeing, affinity to prints and antimicrobial effect.

Modified parameters of textiles were tested according to EN standards as standardized tests are important and known by textile producers and also by end-users of textile products. Change of colour characteristics and dyeing effects after plasma pre-treatment, effects of plasma on appearance of inkjet prints and photo activation effect of plasma on TiO_2 treated cotton – as ecological antibacterial activity are reported.

STUDY OF POLYPROPYLENE NON-WOVEN FABRICS TREATMENT IN UNDERWATER ELECTRICAL DIAPHRAGM DISCHARGE

GABRIELA NEAGOE^{a*}, ANTONÍN BRABLEC^a,
JOZEF RÁHEL^{a,b}, PAVEL SLAVÍČEK^a,
and MIROSLAV ZAHORAN^b

^aDep. of Physical Electronics, Faculty of Science, Masaryk University, Kotlářská 2, 61137 Brno, Czech Republic, ^bDep. of Experimental Physics, Comenius University, Mlynská dolina F2, 84248 Bratislava, Slovak Republic
gabriela.pirpiliu@yahoo.com

Introduction

Plasma treatment has an explosive increase in interest and use in industrial applications as for example in medical, biomedical, automobile, electronics, semiconductor and textile industry. A lot of intensive basic research has been performed in the last years, also in the field of textiles and technical textiles. This has resulted in an increasing knowledge of the possibilities of this process regarding demands as wettability, dyeability, printability, coating and washability of conventional and technical textile. All day problems of wettability and adhesion, together with the environmental driven forces have increased the interest of industry today. This delivers new materials with new possibilities, which opens perspectives to resolve production or even develop complete new applications.

Production problems are mainly caused by the substitution of the base material to new materials for example polymers, which have not the correct surface behavior for further processing.

Plasma treatment of textiles is becoming more and more popular as a surface modification technique. Plasma treatment changes the outermost layer of a material without interfering with the bulk properties. Textiles are several millimeters thick and need to be treated homogeneously throughout the entire thickness. It is known that hydroxyl radicals generated in low-pressure H₂O plasma may be used to incorporate hydroxyl functionality onto a polymer surface to increase their surface energy and reactivity. Underwater pulse diaphragm discharge is an effective tool in the production of hydrated electrons and hydroxyl radicals, which can be used for material surface modification (bondability, hydrophilicity, surface energy).

Preliminary results on physical characteristics of pulsed underwater diaphragm electrical discharge^{1,2} have shown that the discharges burning in tap water, water-chelaton solutions, and some other water based solutions can be used as a potential atmospheric-pressure H₂O – plasma source for surface activation of various materials in the form of fabrics, films, fibers, etc. The discharge burning at atmospheric pressure can substitute low-pressure plasma sources^{3–6} when atmospheric pressure on-line surface treatments of polymer products with the low added value in large amounts are required.

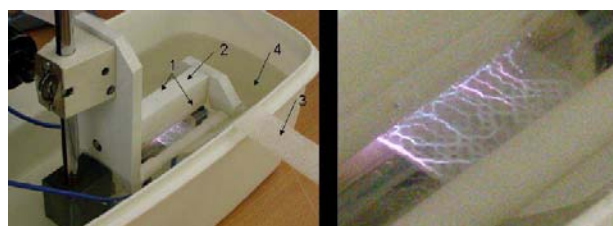


Fig. 1. Experimental arrangement (left) for underwater diaphragm discharge: 1 – electrodes; 2 – diaphragm; 3 – polypropylene nonwoven fabric; 4 – water-based solution. A detail of the discharge treating the textile is also shown (right)

Underwater pulsed corona discharges generated in liquid water matrix at atmospheric pressure have been demonstrated to be effective in the production of hydrated electrons and hydroxyl radicals^{7–11,13,14}. Following the pioneering work of Clements et al.⁷ on pulsed streamer corona generated using point-to-plane geometry of electrodes in water, various types of underwater electrical discharges producing hydrated electrons and hydroxyl radicals in liquid water-based media have been tested for the removal of low levels of non biodegradable organic pollutants from ground water and industrial waste water¹⁴. Very few results, however, have been published on interactions of the active species generated in pulsed electrical discharges in water with polymer materials^{1,15,16}. Few applications are helpful for fixing metallic atoms on the polypropylene (PP) surface for metal coating.

In contrast to other types of underwater electrical discharges, in diaphragm electrical discharge the discharged plasma is in a direct contact with the metallic electrodes.

While in ref.¹ and ref.² the common features and chemical effects including promising application of this discharge for surface treatment of polymer materials are presented and discussed, the main object of the present paper is to report a more detailed study of the discharge physical properties. Using optical emission spectroscopy the electron number densities have been determined from broadening of hydrogen lines (H_{α}) vs. solution conductivity, frequency of high voltage pulses, speed of fiber movement for fixed applied voltage, length of the slit in dielectric diaphragm, and the diaphragm thickness.

Experiment

The H₂O-plasma treatment was performed using a diaphragm discharge apparatus illustrated by Fig. 1. The discharge was generated in a narrow slit of 0.1×1 mm positioned between two metallic electrodes at 2 cm mutual distance. Both electrodes and the slit (diaphragm) were immersed in water medium. Polypropylene nonwoven fabrics of 50 gsm and 30 mm width was fed trough the slit with an adjustable speed. The electrodes were connected to a pulsed HV power supply based on the double rotating spark gap. The maximum peak voltage was 40 kV DC. The maximum repetitive rate of pulses was 60 Hz. The duration of the electrical pulses was given by the water conductivity. Different water based media were used in this study: deionized water, Cu²⁺ solution with the concentration $C = 0.0075$ M of Cu(NO₃)₂ · 3 H₂O; and

CO₂ saturated mineral water. Similar experiment was already realized in ref.².

Results and discussion

Initially the plasma starts within the air bubbles trapped inside the porous structure of nonwovens. After the air voids are filled with water a different discharge breakdown mechanism takes place. The high intensity electrical current flowing through the narrow slit is capable of initiating the water vaporization. The discharge starts in the water vapour bubbles created by that vaporization. The discharge manifests itself as thin plasma filaments propagating along the textile surface up to the distance where the metallic electrodes are positioned. The length of propagation is given by the conductivity of water solution and amplitude of the applied voltage.

Typical profiles of H_α are shown in Fig. 2a. To determine electron temperature and density the standard Griem's table (which takes into account the impact broadening by electron and quasi-static broadening by ions) of H_α line

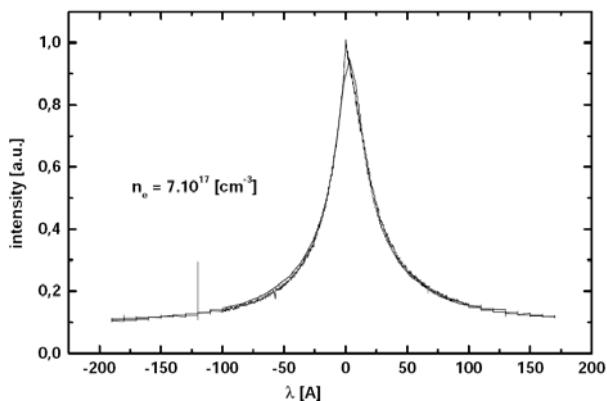


Fig. 2a. The typical H_α line profile fitted with a model based on Stark broadening

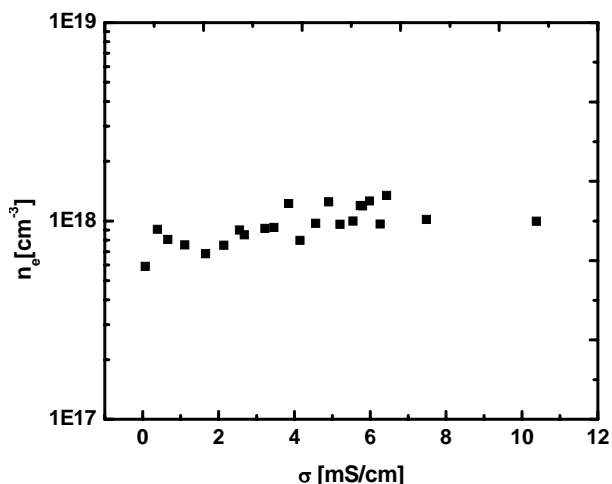


Fig. 2b. The typical dependence of electron number density vs. conductivity for different Cu²⁺ solutions

profile¹⁷ and the procedure for data processing presented in ref.¹ were used. Note, that all profiles were symmetrical. In our case (rectangular discharge slit) the electron density changes from $1 \cdot 10^{22} \text{ m}^{-3}$ to $2 \cdot 10^{24} \text{ m}^{-3}$ while the electron temperature was practically constant $\approx 4 \cdot 10^4 \text{ K}$ in all experimental conditions studied. The same results were obtained as in the previous experiments (for diaphragm discharge). This is an interesting phenomenon and it means that comparable high density of electrons can be reached in the rectangular configuration. The error of the measured electron density was less than 5%. The error of electron temperature was much higher, which is due to the weak dependence of the line profile on the electron temperature.

In Fig. 2b, the change of electron number density vs. conductivity of Cu²⁺ solution is presented. Taking into account the possible dispersion in the electron number density (for example, the corresponding error is always about 5%), it

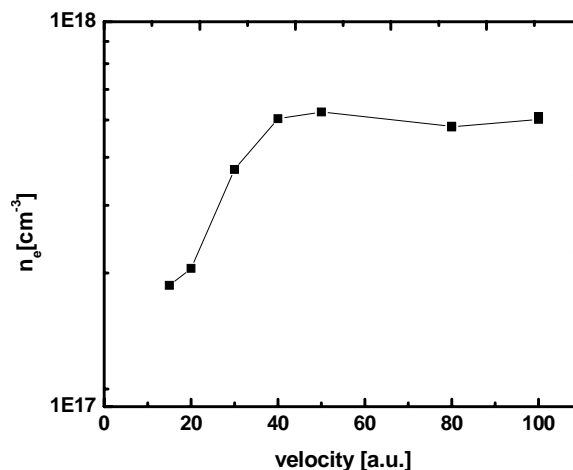


Fig. 3a. The electron number density (n_e) vs. speed of the polypropylene nonwoven fabrics through the discharge for deionized water

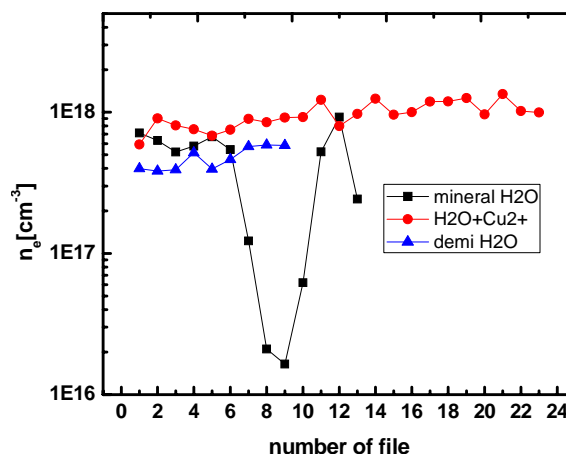


Fig. 3b. Dispersion of n_e for different solutions during time interval of more than 1 hour is presented

seems that the conductivity does not influence significantly the electron number density in the specified conductivity range.

In Fig. 3a, there is shown that the electron number density remains constant while the statistics presented in Fig. 3b demonstrate an interesting effect of CO₂ bubbles – the unexpected decrease of n_e in several cases. This phenomenon was also manifested on character of the discharge (suddenly, the intensity was higher, its colour became different). However,

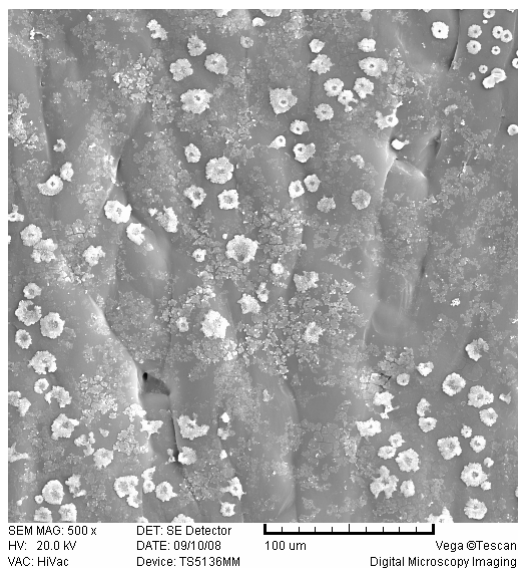


Fig. 4a. SEM micrographs of textile surface treated twice in water solution of Cu²⁺ without washing

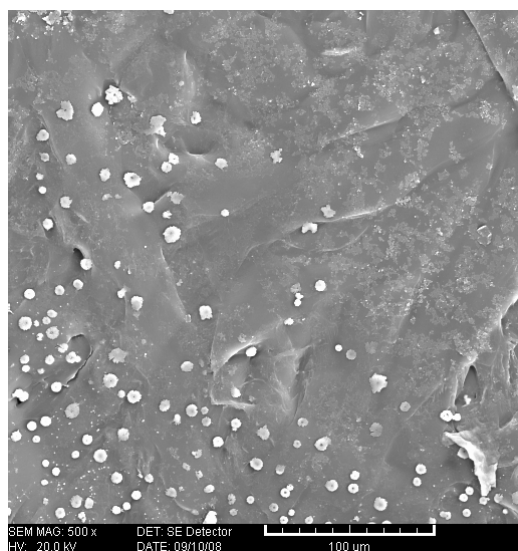


Fig. 4b. SEM micrographs of textile surface. The textile was washed with detergent in Ultrasonic Bath for 15 minutes after double treatment

in this moment this is only a stochastic effect.

A practical application of diaphragm plasma treatment of PP is shown in Fig. 4a,b.

The textile was treated in water solution of Cu²⁺ in the same conditions as described above. The treatment was repeated after 1 minute on the same sample. Furthermore, we washed the sample in a detergent solution in Ultrasonic Bath for 15 minutes to see how much of copper attached to the textile material. The SEM photographs reveal a presence of copper microcrystals attached to the PP fabrics (Fig. 4a). More than 60 % of these crystals were still attached even after intense washing (Fig. 4b). This implies a strong chemical interaction between the crystals and PP. The chemical (copper) nature of crystal was confirmed by the EDX analysis of the sample. At this moment we are not able to confirm if the crystals are made from Cu only.

Conclusion

The determination of n_e in case of selected quantities at optimized parameters show that their values do not influence significantly electron density and its fluctuation is almost covered with the confidence interval. It was found that the effect of CO₂ bubbles as well as the role of Cu²⁺ solution (or other metallic atoms) can bring interesting application. Further research is necessary in order to fully understand the influence of the double treatment and washing on the PP fiber and to compare these results with the case of single treatment applied to the PP fiber. By performing diaphragm plasma in the water solution of copper salt we were able to immobilize copper crystals on the PP surface.

This research has been supported by the Czech Science Foundation under the contract numbers KAN101630651 and 202/06/P337 and by the research intent MSM:0021622411 funding by the Ministry of Education of the Czech Republic.

REFERENCES

1. Brablec A., Slavicek P., Stahel P., Cizmar T., Trunec D., Simor M., Cernak M.: Czech. J. Phys. 52 Suppl. D491 (2002).
2. Simor M., Krump H., Hudec I., Rahel J., Brablec A., Cernak M.: Acta Physica Slovaca 54, 43 (2004).
3. Chan C. M., Ko T. M., Hiraoka H.: Surf. Sci. Reports 24, 1 (1996).
4. Okazaki S. : E.C. Chemical Co.,Ltd., JP 34425092 (1992).
5. Chou N. J. : US5, 019, 210 (1991).
6. Hayat U.: GB 9124467 (1993).
7. Clements J. S., Sato M., Davis R. H.: IEEE Trans. Ind. Appl. IA-23, 224 (1987).
8. Slobodskoi S. A. : Vopr. Technol. Ulavlivanja i Pererab. Prod. Koksovania 71 (1978).
9. Sharma A. K., Locke B. R., Arce P., Finney W. C.: Hazardous Waste & Hazardous Materials 10, 209 (1993).
10. Grimonpre D. R., Sharma A. K., Finney W. C., Locke B. R.: Chem. Eng. J. 82, 189 (2001).
11. Lukes P.: *Ph.D. Thesis*, Prague 2001.
12. Sunka P., Clupek M., Lukes P., Simek M., Schmidt J., Cernak M.: Plasma Sources Sci. Technol. 8, 258 (1999).

13. Sunka P., Babicky V., Clupek M., Kolacek K., Lukes P., Ripa M., Cernak M.: *In Proc. of 18th Symp. Plasma Physics and Technology, Prague, 1977*, 144 (1997).
14. Sunka P.: *Phys. Plasmas* 8, 587 (2002).
15. Mikula M., Panak J., Dvonka V.: *Plasma Sources Sci. Technol.* 6, 179 (1997).
16. Simor M., Cernak M., Krump H., Hudec J., Stefecka M.: *In Proc. of XXV Int. Conf. on Phenomena in Ionised Gases 4, Nagoya, 2001*. 63 (2001).
17. Griem H. R.: *Spectral line broadening by plasmas*. Academia Press, New York 1974.

G. Neagoe^{a,*}, A. Brablec^a, J. Ráhel^{a,b}, P. Slavíček^a, and M. Zahoran^b (^a *Dep. of Physical Electronics, Faculty of Science, Masaryk University, Brno, Czech Republic*, ^b *Dep. of Experimental Physics, Comenius University, Bratislava, Slovak Republic*): **Study of Polypropylene Nonwoven Fabrics Treatment in Underwater Electrical Diaphragm Discharge**

During the last two decades functionalization of polymer surfaces has been recognized as a valuable tool to improve their adhesion properties. Underwater pulse diaphragm discharge is an effective tool in the production of hydrated electrons and hydroxyl radicals, which can be used for material surface modification (bondability, hydrophilicity, surface energy). For efficient material treatment it is necessary to identify operational key parameters controlling the discharge plasma characteristics and to establish some appropriate diagnostic methods and models for plasma characterization. The plasma parameters – electron number density, temperature of electrons, excitation temperature, have been measured by optical emission spectroscopy completed by the voltage, and current measurement. The sampling optical fiber was installed directly in the slit to minimize the water absorption of light emission. The electron number density will be estimated preferable from spectral line profile of H_α. Our contribution will summarize the results of our experiments.

TREATMENT OF SURFACTANTS IN THE FOAMING COLUMN

JOANNA PAWLAT*^a, SATOSHI IHARA^b,
KAROL HENSEL^c, and CHOBEI YAMABE^b

^a Graduate School of IPS, Waseda University, 808-0135 Fu-kuoka ken, Kitakyushu-shi, Wakamatsu-ku, 2-7 Hibikino, Japan, ^b School of Science and Engineering, Saga University, 840-8502 Saga ken, Saga-shi, 1 Honjo-machi, Japan, ^c Department of Astronomy, Earth Physics and Meteorology, Comenius University, Bratislava, Slovakia, askmik@hotmail.com

Introduction

Nowadays, the processes where the interaction between gas and liquid occurs are very popular in the chemical engineering technology. Prevalence of them in the industry makes even slight improving of parameters of work very desirable. Foaming system was introduced a long time ago as the way of increasing the efficacy. Presently, it can be one of options for cleaning the large amounts of the polluted exhaust gas because the heat and mass exchange is especially efficient in the two-phase systems like a dynamic foam environment.

Several kinds of foam, with totally different properties and hydraulic parameters exist. The most famous are foams created using surfactants, three-state foams and unstable foams generated using only kinetic energy of the gas flow. It must be emphasized that foams created without any surfactants are the most desirable from the environmental point of view. The experiments using this kind of foam, generated from gases and pure water only were reported in the previous works^{1–3}.

On the further stages of the research the possibility of foaming system application for the dusty, polluted gas or the treatment of special kind of wastewater will be investigated. Some of contaminants show the surface-active character, they can change and extremely enhance the foaming properties of the purified solution.

Foams

Foams are unstable colloidal mixtures, which contain prevailing part of gas by volume. The initial distribution of liquid in foam depends on the manner in which the foam was produced. Foams can be divided into two categories, homogenous and pneumatic forms, depending on the method of generation⁴. *Static foams* (also called homogenous, stable or standing foams) are produced by vigorous agitation of solutions. The initial distribution of liquid is homogenous. *Pneumatic foams* (also called dynamic foams) are produced by bubbling of gas through the solution, as the bubbling proceeds, foam increases its length (until the gas supply is shut off) and the profile of liquid fraction develops. Such foam is drier at the top (liquid fraction is lower) and wetter in the lower part. Pneumatic foams are always in contact with the

foaming solution (in the static foams there is a time lag before some liquid appears in the bottom of the column). They also have some steady state height and the same amount of foam is produced as destroyed.

Pure liquids cannot foam unless the foaming agent (surfactant) is added in the case of typical static foams. The shaking of the sample of the water can become its purity test. Pneumatic foam can be created by a pure liquid using the kinetic energy of flowing gas. Foam can be easily created using dispersion technique – shaking or whipping the liquid with gas, which is immiscible in that liquid. The general ways to create foam are whipping, injection, sparging, shaking, aspiration or compressed air foams generation^{5,6}.

Properties of foam depend on composition of the solution, eventual surfactant, eventual contaminants, foam formation, and foam maintenance (temperature, pressure, etc.). General rules concerning the flow and apparatus-construction limits for foam environment creation are: a) linear velocity of substrate gas for whole apparatus cross-section (V_C): 0.1–4.0 m s⁻¹, b) gas velocity in the diffuser hole (V_D): 10–20 m s⁻¹, c) diffuser's perforation level: 5–20 % of whole shelf area^{7,8}. Foaming leads to the intensification of the processes between gas and liquid phase, especially those, this proceed on the inter-phase surfaces. The contact area is much larger than in typical bubbling process⁹. The three zones above the diffuser's shelves in the apparatus can be distinguished:

- the lowest one: bubbling in the thin liquid layer,
- middle: foam zone,
- upper: splash zone.

Experimental set-up

The main reactor vessel of the foaming system is depicted in Figs. 1. It consists of a cylindrical, polyacrylate column of 50 mm diameter. A ceramic diffuser made of Al₂O₃ was placed perpendicularly to the flow direction of media.

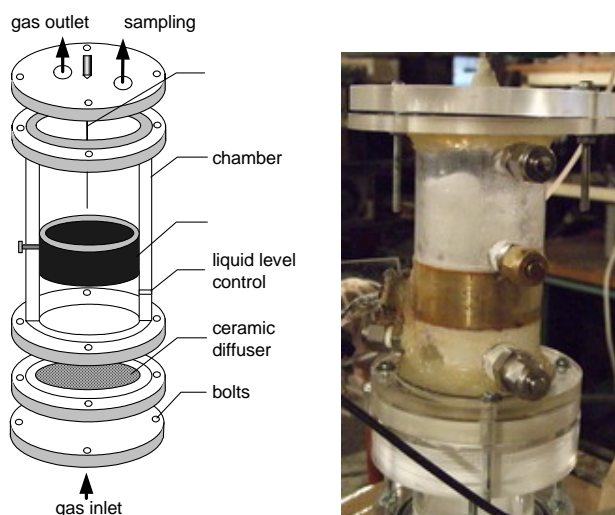


Fig. 1. Scheme of foaming vessel and its photograph during the foaming process

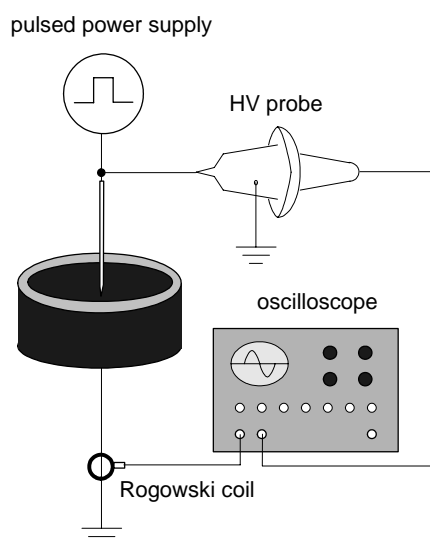


Fig. 2. Experimental apparatus

The central high voltage (HV) electrode of 1.5 mm diameter was placed inside the cylindrical, grounded electrode (40 mm of diameter, 30 mm of height) in homogenous foam zone, above the diffuser.

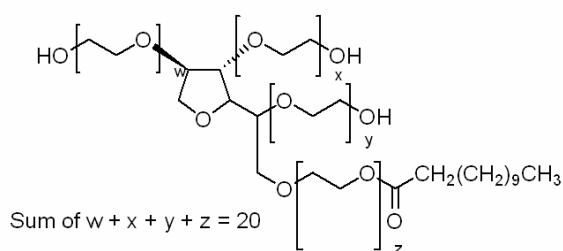
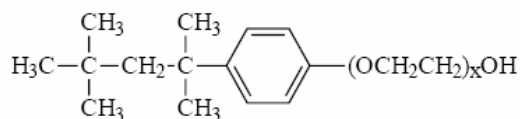
The electrical circuit is shown in Fig. 2. Blumlein type pulsed power source consisted of coaxial cables (RG-8U) for charging energy, triggered spark gap switch and switch triggering system. The pulse width of output voltage depended on the length of coaxial cable. In the performed experiments the pulse width of voltage was 50 ns, which corresponded to the cable length of 5 m. Surfactant-supported foam was uniform, with 1–2 mm diameter bubbles.

Results and discussion

Many kinds of the surface-active foaming materials can be distinguished. They can be particles of dust, liquid crystals, polymers or specific cations or anions from inorganic salts. Some of them can cause foaming in very low concentrations, even 10^{-9} M (ref.¹⁰). Large-molecule, nonionic surfactants do not dissociate into ions in aqueous solutions. They have plenty domestic, medical and industrial applications as mild and non-denaturing detergents. Showing excellent chemical stability, are good solvents of moderate foaming properties but they also have a tendency to bioaccumulation and can be harmful for aquatic organisms.

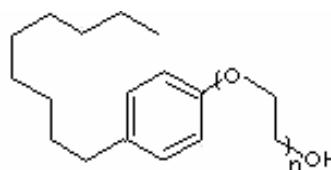
Tween® 20 (polyoxyethylene sorbitan monolaurate), which chemical structure is presented in Fig. 3, is yellow, viscous liquid miscible with water and used in the biotechnology, textile production and food industry.

Triton X-100 (polyoxyethylene octyl phenyl ether) is very stable non-ionic detergent soluble in water, benzene, toluene, xylene, trichloroethylene, ethylene glycol, ethyl ether, ethanol, isopropanol, and ethylene dichloride. At 10 % (v/v) in water, it gives a clear to slightly hazy solution, from clear to slightly yellow in appearance¹¹. It absorbs in UV region at 280 nm. Triton X-100 is relatively non-toxic and

Fig. 3. Chemical structure of Tween® 20 (ref.¹¹)

$$x = 9-10$$

Fig. 4. Chemical structure of TRITON-100

Fig. 5. Chemical structure of Polyoxyethylene Nonylphenyl Ether (P5NPE)¹³

widely used in biochemical procedures. Its chemical structure is presented in Fig. 4.

Polyoxyethylene (5) nonyl phenyl ether (P5NPE, NE), (Fig. 5) is the large molecule nonionic surfactant playing important role in nanotechnology and biochemistry, but it also occurs to be a skin sensitizer, sometimes causing allergies¹².

For the experiment, 0.025 % water solution of Tween® 20, P5NPE, and Triton X-100 were prepared. 50 ml of the solutions were dosed into the foaming apparatus. Oxygen gas flow rate was fixed to 1.0 l min^{-1} . Change of COD (Chemical Oxygen Demand) during the treatment by the electrical discharge in foam was monitored for each pollutant. COD was measured using HACH spectrometer and COD 2720 method at 620 nm wavelength. The average energy per pulse ranged from 2 to 4 mJ. After 20 minutes of treatment at 30 Hz and 17 kV discharge voltage, 53 %, 87 %, 58 % COD removal efficiencies for Tween® 20, P5NPE, and Triton X-100 were achieved, respectively. The experimental data are summarized in Fig. 6.

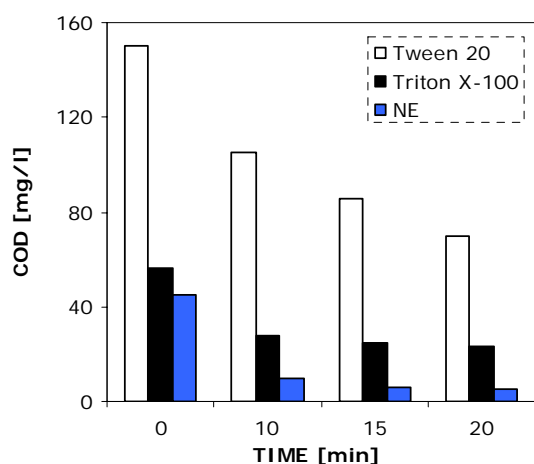


Fig. 6. Change of COD in dependence on the treatment time

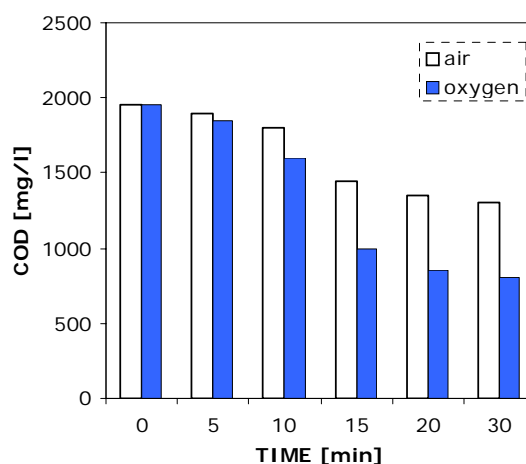


Fig. 8. Removal of COD in SDS solution and ethyl violet residues in dependence on the substrate gas

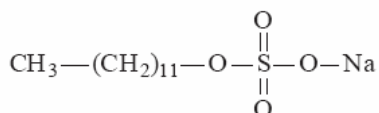


Fig. 7. Chemical structure of dodecyl sodium sulfate

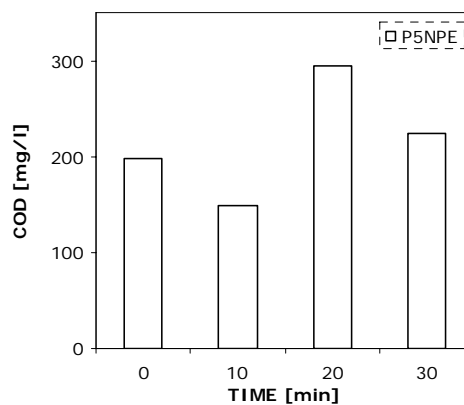


Fig. 9. COD in dependence on the treatment time at low pulse energy (P5NPE)

Dodecyl sodium sulfate (SDS, Lauryl sulfate sodium salt, Fig. 7) is a white powder soluble in water giving colorless liquid. This anionic detergent is widely used in molecular biology, drug and food industry, ceramics, and in methane hydrate formation^{14–16}.

In the experiment with SDS, 58 % reduction of COD was observed after 30 min of treatment of 15 ml solution of SDS surfactant (0.05 g l^{-1}) and residues of cationic dye: ethyl violet (Fig. 8) at 0.3 l min^{-1} oxygen flow. EV is highly pH-sensitive dye, which reacts mostly via OH reaction route.

For the lower pulse energies after the COD reduction in the first 10 minutes, the rapid increase of COD, sometimes exceeding the primary untreated value was observed. For instance, in the case of P5NPE solution, 30 minutes treatment time led to 13 % increase in COD comparing the initial value (Fig. 9).

After initial decrease in COD, what may suggest breaking the large molecule compound, further application of the electrical discharge promoted the unwanted reaction paths and formation of some other large-molecule species. In such condition, attempt of SDS and EV residues solution treatment due to complicated chemical structure of both compounds caused rapid increase of COD even by 30 times during the first 10 minutes and then slow decrease of this value, which after 30 minutes was still 15 times higher than untreated one.

In all observed cases, there was a visible decrease in the foamability of the treated solutions and in the last 5 minutes of treatment the bubbling prevailed over the foaming phenomenon.

Conclusions

Various active species as ozone, hydrogen peroxide and OH radicals were formed during the electrical discharge in the foaming column.

Treatment of pollutants and oxidants' formation was performed in the same reaction zone in the apparatus.

53 %, 87 %, 58 %, 58 % COD removal efficiency was achieved for Tween® 20, P5NPE, Triton X-100 and SDS, respectively. However, decreasing of the pulse energy led to the increase in COD of the solutions.

REFERENCES

1. Pawłat J., Hensel K., Yamabe C.: Czech. J. Phys. 54, C964 (2004).
2. Pawłat J., Hensel K., Ihara S.: Acta Phys. Slovaca 55(5), 479 (2005).
3. Pawłat J., Hensel K., Ihara S.: Czech. J. Phys. 56, B1174 (2006).
4. Bhakta A., Ruckenstein E.: Adv. Colloid Interface Sci. 70, 1 (1997).
5. Magrabi A., Długogorski B., Jameson G.: Chem. Eng. Sci. 54, 4007 (1999).
6. Patino J., Delgado M., Fernandez J.: Colloids Surf., A 99, 65 (1995).
7. Hobler T.: *Dyfuzyjny ruch masy i absorbera*, WNT, Warszawa 1976.
8. Bistrón S., Sarre P., Szymonik B.: Chemik 3, 81 (1978).
9. Pozin M., Muchlenow I., Tarat E.: *Pianowe oczyszczalniki gazu, wymienniki ciepła i absorbera*, WNT, Warszawa 1962.
10. Pugh R.: Adv. Colloid Interface Sci. 64, 67 (1996).
11. www.sigmaaldrich.com.
12. Kabasawa Y., Kanzaki T.: Contact Dermatitis 20 (5), 378 (1989).
13. <http://chemicalland21.com>.
14. Watanabe K., Imai S., Mori Y.: Jap. Chem. Eng. Sci. 60 (17), 4846 (2005).
15. Vladimirova T., Morgunova E.: J. Chem. Soc., Faraday Trans. 91, 681 (1995).
16. Dutta R., Chowdhury R., Bhat S., Gokturk S., Tuncay M.: J. Surf. Detergents 6 (4), 325 (2003).

USE OF COLD PLASMA FOR TRANSFORMATION OF IRON NANOPARTICLES

KLARA SAFAROVA*^a, MIROSLAV MASHLAN^a, ROMAN KUBINEK^b, and JIRI PECHOUSEK^a

^a Centre for Nanomaterial Research, Palacky University, Slechtitelu 11, 783 71 Olomouc, ^b Department of Experimental Physics, Faculty of Science, Palacky University, tř. 17. listopadu 50, 772 07 Olomouc
klara.safarova@upol.cz

1. Introduction

Plasma is called the fourth state of the matter. Plasma contains a certain portion of free electrons and the atoms are partly ionized. The presence of negative and positive carriers of the charge makes plasma¹ electrically conductive and distinguishes it from gaseous state.

The plasma that contains a very small part of the ionized particles (approximately 1 %) is named cold (nonthermal) plasma. The cold plasma is generated in a high-voltage electric field, and although the velocity of electrons is strongly dependent to the temperature up to a few thousands degrees of Celsius, their effect on the plasma temperature is low and final plasma temperature is close to the temperature of the surrounding.

Cold plasma plays an important role in a variety of technologies, i.e. particularly plasma activation serves to alter or improve adhesion properties of surfaces prior to coating, painting, etc. Cold plasma systems have become also a very important tool for nanotechnology processing including semiconductors, thin films and the production of polymers and the modification of the materials.

In this paper, the cold plasma has been used to initialize an oxidation process of iron nanoparticles.

2. Materials and methods

Iron nanoparticles, used as a precursor, were prepared by a spark discharge^{2,3}. The carbon shell protects these iron nanoparticles from spontaneous oxidation. The oxidation process has been performed in a laboratory cold plasma-chemical reactor. The iron nanoparticles were placed on an electrode for 20 seconds of the exposition time and the reactor was activated with maximal power. The iron nanoparticle precursor and final iron oxide product were characterized by TEM⁴, BET⁵, XRD and Mössbauer spectroscopy⁶.

2.1. Transmission Electron Microscopy (TEM)

Transmission Electron Microscope JEOL 2010 F – type high contrast (HC) was used to determine the size and morphological properties of the initial iron nanoparticles and final

nanoparticles. Accelerating voltage of 200 kV and magnifications from 100000 to 400000 times were used in these measurements.

The preparation of the sample is the key moment in the TEM application. The nanopowder was added into the ethanol and exposed to ultrasonic waves. Then, one drop of the suspension was placed on a 300 mesh copper grip, which was coated with holey carbon film. Finally, the sample was dehydrated at room temperature.

The local electron diffraction was used for a determination of the phase composition of the nanoparticles.

2.2. BET method

A specific surface area of the dispersive or porous materials can be determined by the BET method. The BET (Brunauer-Emmett-Teller) method is based on the measuring the adsorbed gas quantity. The adsorption-desorption isotherm was obtained by nitrogen adsorption using a Sorptomatic 1990 (ThermoFinnigan) surface area analyzer. The specific surface area of this sample was determined by the multipoint BET3 method in the p/p_0 range between 0 and 0.5. Sample was de-gassed at room temperature with a pressure of 10^{-6} for 24 h.

2.3. Mössbauer Spectroscopy

Mössbauer spectroscopy was applied to determinate the iron phase composition of initial and final materials. ⁵⁷Fe Mössbauer spectra were measured by a standard transmission method in a constant acceleration mode with a ⁵⁷Co (Rh) radioactive source. The spectra were collected at room temperature. The values of the isomer shift are related to α -Fe at room temperature. For computer processing of the spectra, a NORMOS package was used yielding the values of the relative spectrum area RA and the values of the hyperfine parameters including the hyperfine magnetic field B, isomer shift δ_{Fe} , quadrupole splitting Δ and quadrupole shift ϵ .

2.4. X-ray powder diffraction (XRD)

XRD was also used for a determination of the phase composition of the samples. An X'Pert PRO instrument with a Co K α radiation was employed for the XRD analyses. The phase composition of the samples was evaluated using an X'Pert HighScorePlus software package (PANalytical®) and the JCPDS PDF-4 database.

3. Results and Discussion

At first, the initial iron nanoparticles were characterized. TEM gave information about the size and morphology of the iron nanoparticles as well as the thickness of the carbon preservation shell has been estimated.

We can see that the iron nanoparticles form agglomerates (see Fig. 1). A more detailed Fig. 2 shows that they have a ball-shaped profile and their sizes vary from 15 to 100 nm. Individual particles are covered with a carbon preservation envelope. Its thickness is estimated to 8 nm. The fact that the core and the shell of the nanoparticles are composed of iron

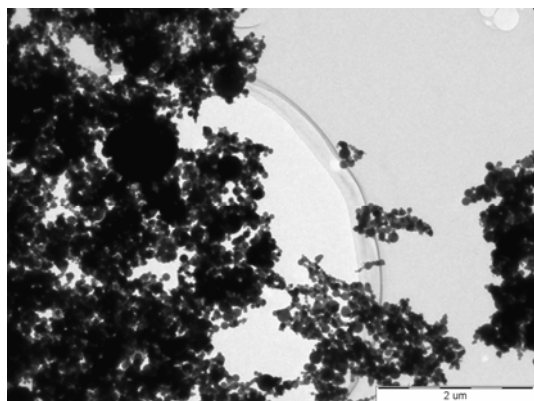


Fig. 1. TEM picture of the initial iron nanoparticles

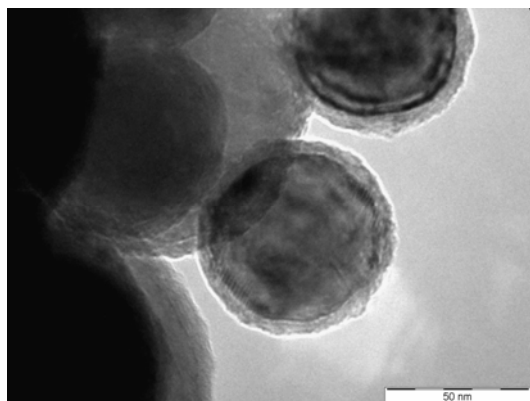


Fig. 2. Detailed TEM picture of the iron nanoparticles covered by a carbon preservation shell

and carbon, respectively, has been confirmed by local electron diffraction.

From the adsorption-desorption isotherm (dependence of the V_{ads} on p/p_0) (Fig. 3), it was determined, that this material is nonporous with the surface area of $7.3 \text{ m}^2 \text{ g}^{-1}$.

RT Mössbauer spectrum (see Fig. 4) contains one sextet with $\delta_{\text{Fe}} = 0 \text{ mm s}^{-1}$, $\varepsilon = 0 \text{ mm s}^{-1}$ and $B = 33 \text{ T}$, well corresponding to alpha iron.

XRD (Fig. 5) pattern confirms that the initial material does not include any other iron-bearing phase.

The changes of the phase composition as well as changes of the morphology particles were observed after oxidation initialized by a cold plasma.

RT Mössbauer spectrum of the final product (see Fig. 6) consists of $\alpha\text{-Fe}$ sextet ($\delta_{\text{Fe}} = 0 \text{ mm s}^{-1}$, $\varepsilon = 0 \text{ mm s}^{-1}$, $B = 33.0 \text{ T}$, $\text{RA} = 24 \%$), $\alpha\text{-Fe}_2\text{O}_3$ sextet ($\delta_{\text{Fe}} = 0.37 \text{ mm s}^{-1}$, $\varepsilon = -0.16 \text{ mm s}^{-1}$, $B = 51.6 \text{ T}$, $\text{RA} = 46 \%$), two sextets of Fe_3O_4 ($\delta_{\text{Fe}} = 0.27 \text{ mm s}^{-1}$, $\varepsilon = 0 \text{ mm s}^{-1}$, $B = 49.2 \text{ T}$, $\text{RA} = 14 \%$ and $\delta_{\text{Fe}} = 0.66 \text{ mm s}^{-1}$, $\varepsilon = 0 \text{ mm s}^{-1}$, $B = 45.7 \text{ T}$, $\text{RA} = 12 \%$) and FeO doublet ($\delta_{\text{Fe}} = 0.93 \text{ mm s}^{-1}$, $\Delta = 0.73 \text{ mm s}^{-1}$, $\text{RA} = 4 \%$).

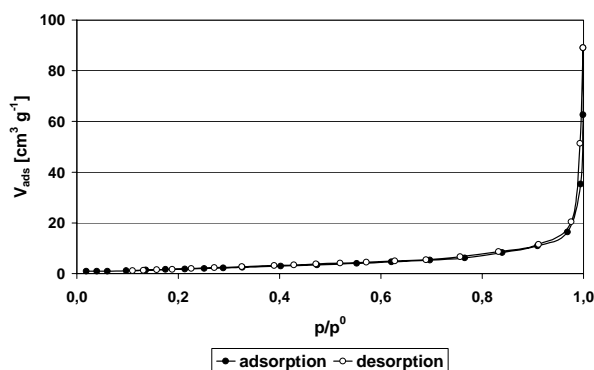


Fig. 3. Adsorption-desorption isotherm of the iron nanoparticles covered by a carbon preservation shell

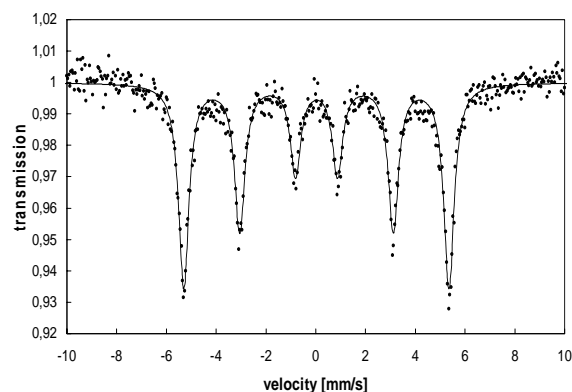


Fig. 4. The RT Mössbauer spectra of the iron nanoparticles

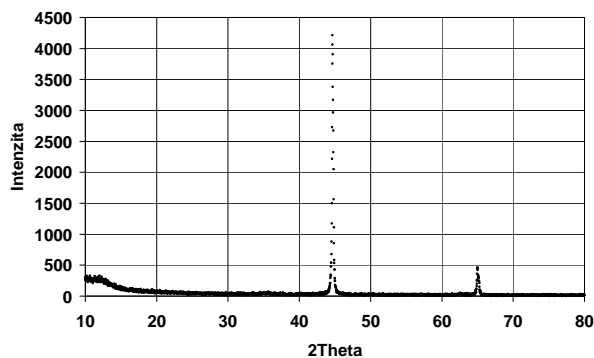


Fig. 5. XRD pattern of iron nanoparticles

The presence of all the iron phases identified by Mössbauer spectroscopy was confirmed also by XRD (see Fig. 7).

TEM shows that the sizes of the nanoparticles of final

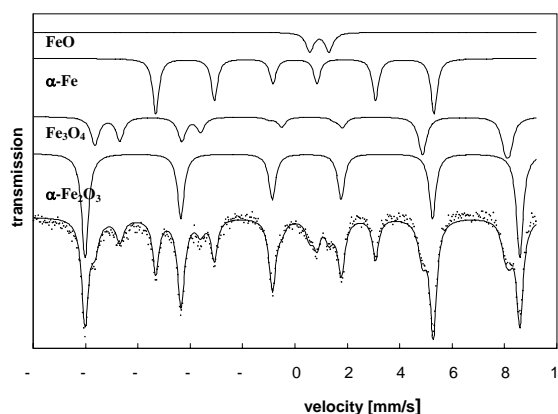


Fig. 6. RT Mössbauer spectrum of the final product

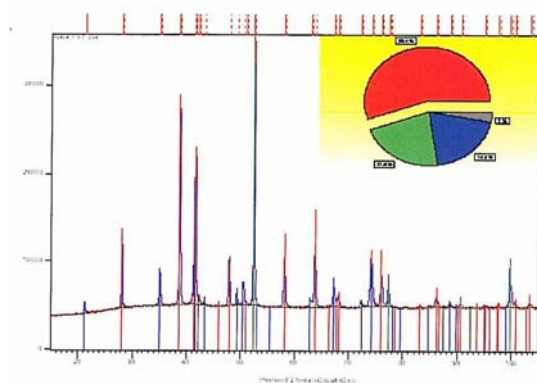


Fig. 7. XRD and pattern list of the final product

product are the same as the sizes of the nanoparticles of the initial system, but some nanoparticles have changed the ball-shaped form (see Fig. 8). At the same time, we can see that the carbon preservation cover is disturbed and nanoparticles form certain clusters (see Fig. 9). The local electron diffraction shows on one hand that the core of the carbon preserved nanoparticles contains iron. On other hand, the core of the nanoparticles with the disturbed carbon shell contains iron oxide.

4. Conclusion

The initialization of oxidation process of iron nanoparticles by the cold plasma was studied. It is obvious that the cold plasma disturbs the carbon preservation shell of the nanoparticles and these nanoparticles are continuously oxidizing. α - Fe_2O_3 (hematite), Fe_3O_4 (magnetite) and FeO (wüstite) were identified in the final product. On one hand, the nanoparticles with disturbed carbon cover oxidize, but on other hand, they

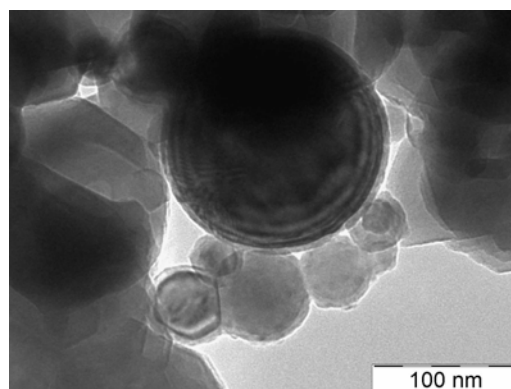


Fig. 8. TEM pictures of the nanoparticles of the final product

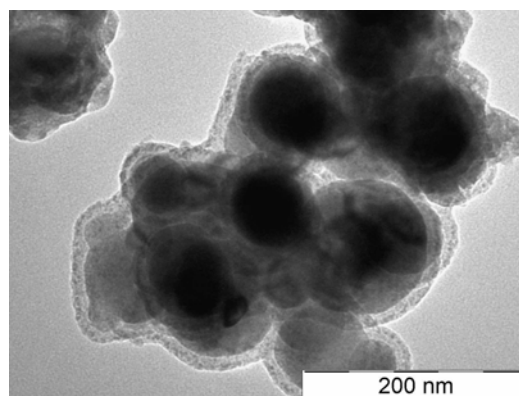


Fig. 9. Clustering of the nanoparticles with the disturbed carbon cover

arrange into irregular clusters in which iron and iron oxide were observed. It thus seems that there exists a possibility to control the process of oxidation of iron nanoparticles via using a different power of the cold plasma source and different exposition time. This potentiality will be a subject of the next study.

Financial support from The Ministry of Education, Youth and Sports of the Czech Republic under the research project IM0512 and Czech Academy of Science under research project KAN101630651 are gratefully acknowledged.

REFERENCES

- Ostrikov K.: Rev. Mod. Phys. 77, 489 (2005).
- Hyuncheol O., Junho J., Jaehee J., Sangsoo K.: Mater. Sci. Forum. 544-545, 143 (2007).
- Kuo-Hsiung Tseng, Chih-Yu Liao, Jen-Chuen Huang, Der Chi Tien, Tsing-Tshih Tsung: Mat. Lett. 62, 3341 (2008).
- Williams D. B., Carter C. B.: *Transmission Electron Microscopy: A textbook for Materials Science Basics, Diffraction, Imaging, Spectrometry*, Kluwer Acad. Pub, Norwell 1996.

5. Walton K. S., Snurr R. Q.: *J. Am. Chem. Soc.* 129, 8552 (2007).
6. Maddock A. G.: *Mössbauer Spectroscopy: Principles and Applications of the Techniques*, Horwood Publishing, Chichester 1997.

K. Safarova*^a, **M. Mashlan**^a, **R. Kubinek**^b,
and J. Pechousek^a (^a*Centre for Nanomaterial Research, Palacky University, Olomouc*, ^b*Department of Experimental Physics, Faculty of Science, Palacky University, Olomouc*):
Use of Cold Plasma for Transformation of Iron Nanoparticles

The pure iron nanoparticles, prepared by a spark discharge were transformed (oxidized) using a cold plasma effect. Structural and size properties of the initial iron nanoparticles as well as final product of iron oxide nanoparticles were characterized using TEM, XRD, BET and Mössbauer spectroscopy.

DEPOSITION OF GAS - TIGHT COATINGS ON PLASTIC FILMS BY PULSED DIELECTRIC-BARRIER DISCHARGES

J. SENTEK, Z. RŻANEK-BOROCH,
M. BRYKAŁA, and K. SCHMIDT-SZAŁOWSKI*

Faculty of Chemistry, Warsaw University of Technology, ul.
Noakowskiego 3, 00-662 Warszawa, Poland
kss@ch.pw.edu.pl

Keywords: Packaging film, permeability reduction, barrier discharges, TEOS

Introduction

A number of experimental studies have been carried out in order to improve the barrier properties of the packaging materials, first of all, their tightness with respect to gases, organic vapors, and water vapor. In the opinion of numerous authors, plasma enhanced chemical vapor deposition (PE-CVD) may be the most suitable technique for manufacturing of thin tight coatings (e.g. from SiO_x) reducing the polymer films permeability¹⁻⁶. Pulsed dielectric barrier discharges (PDBD) at atmospheric pressure are one of the new ideas in this field⁷⁻¹⁰. Organic compounds of silicon, e.g. tetraethoxysilane (TEOS), tetramethoxysilane (TMOS), hexamethyldisiloxane (HMDSO) and some other, are known as advantageous starting materials for PE-CVD of thin SiO_x coatings. However, because of the complex structure of these compounds, their chemical transformations in plasmas are frequently not complete, and thus, the coatings deposited from TEOS, TMOS, HMDSO often contain some "organic" fragments ($\text{Si}-(\text{CH}_3)_n$, Si-C, Si-CO, etc.), besides the SiO_x structure. As known, oxygen and other oxidants strongly influence the process of the coating deposition. Oxygen and oxygen containing radicals take part in the reactions proceeding in the plasma zone resulting in acceleration of the gas reactions, as well as the transformation of the solid organo-silicon product deposited on the substrate surface. The coatings, when produced in the presence of oxygen contain generally more distinct O-Si-O structures and lower content of organic residues^{9,11-13}.

Experimental set-up

For the present study of thin coating deposition on packaging plastic films, pulsed dielectric-barrier discharges (PDBD) were used. A new laboratory reactor was tested^{13,14} with a rotating cylindrical internal electrode and the cylindrical glass body playing the role of a dielectric barrier (Fig. 1).

A strip of aluminum sheet 0.05 mm thick and 15 mm wide attached to the external surface of the glass body in parallel to the axis is used as the high voltage electrode. A sample of the examined plastic film adheres to the surface of the

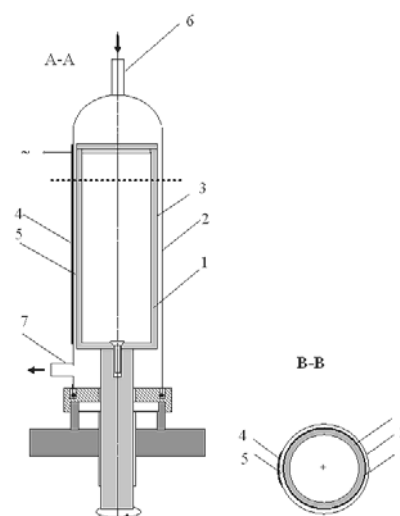


Fig. 1. The reactor: vertical section A-A and horizontal section B-B. 1 – rotating electrode, 2 – glass body, 3 – PE film, 4 – HV electrode, 5 – discharge gap (1.5 mm), 6, 7 – inlet and outlet pipes

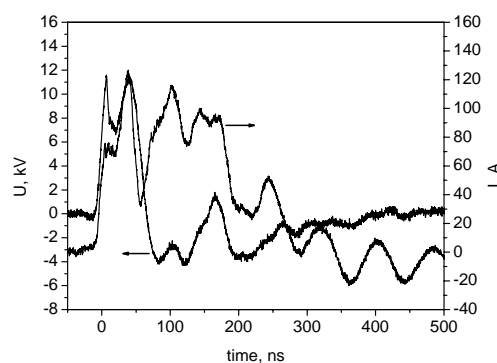


Fig. 2. Pulse voltage and current courses

rotating electrode and the PDBD zone is located in the part of the gap in the nearness of the metal foil being the external electrode. The sample attached to the rotating electrode moves through the discharge zone with a stable velocity (3 s for one turn), and the real time of the discharge action may be controlled by changing the HV electrode width, as well as the overall discharge duration. The gap distance between the film attached to the rotating electrode surface and the internal surface of the glass body is about 1.5 mm. The plasma treating and deposition were conducted at ambient temperature using an electrical supplying system generating the voltage pulses of about 60 ns duration up to 15 kV. The voltage and current were registered by the Tektronix TDS 3032 oscilloscope and the pulse power was computed from those measurements (Fig. 2).

For example, when the pulse frequency was kept at the level of 400 Hz the energy of the individual pulse was assessed as 79 mJ with 6.5 μC load transferred.

Coating deposition

Coatings were deposited on polyethylene (PE) films 19 μm thick keeping the stable pulsed discharges frequency of 400 Hz. Tetraethoxysilane (TEOS) was used as a precursor being a component of the feed gas mixtures with helium or with helium and oxygen. The flow rate of helium gas was 10 NI h^{-1} and the residence time in the gap volume was about 18 s. The TEOS vapors were added to the gas stream at the rate of 0.6 mmol h^{-1} by evaporation of the liquid at constant temperature and the concentration of TEOS was kept at 0.13 mol.%. Four kinds of the feed gases have been tested: (i) He, (ii) TEOS + He, (iii) TEOS + He + 5 % O_2 , (iv) TEOS + He + 10 % O_2 for the real durations of the plasma action from 2.2 to 44 s. The mass of coatings was determined gravimetrically for long duration of the deposition and the rates were calculated basing on those measurements. The maximum deposition rate (1.8 $\text{g cm}^{-1} \text{min}$) was observed using the gas mixture (iii).

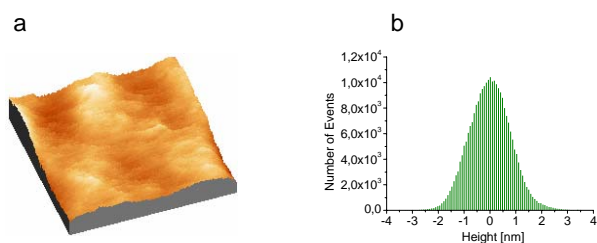


Fig. 3. AFM image of the virgin PE film. a – 3D image, b – Height deviation distribution (referred to the mean plane); $R_q = 0.80 \text{ nm}$, $Z = 7.8 \text{ nm}$

Coating topography and elemental composition

The surface topography was studied using atomic force microscope (AFM) NanoScope IIIA Digital Instruments Veeco Group. The coating surface topography was characterized by R_q – RMS average of height deviation from mean data plane, and Z – maximum vertical distance between the highest and lowest data points.

It was found that the roughness of the film surfaces increased after plasma treatment in all of the gas mixtures

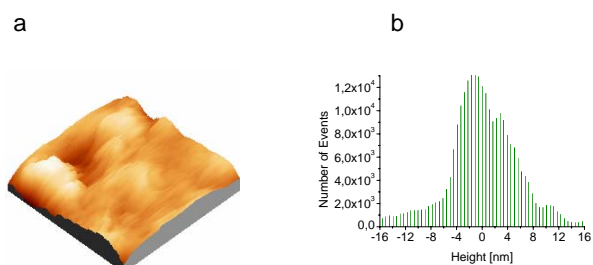


Fig. 4. AFM image of the PE film treated with helium plasma during 2.2 s. a – 3D image, b – Height deviation distribution (referred to the mean plane); $R_q = 6.15 \text{ nm}$, $Z = 55.9 \text{ nm}$

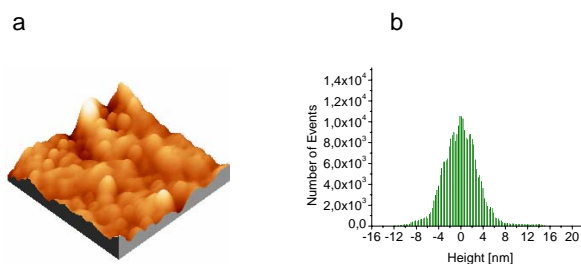


Fig. 5. AFM image of the coating deposited from TEOS+He during 2.2 s. a – 3D image, b – Height deviation distribution (referred to the mean plane); $R_q = 3.26 \text{ nm}$, $Z = 27.5 \text{ nm}$

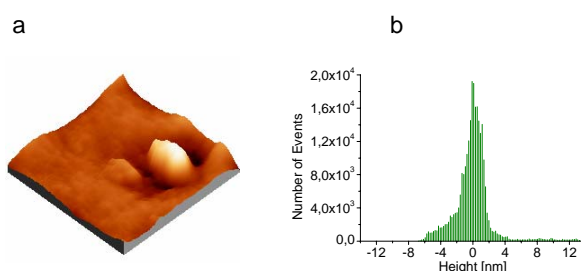


Fig. 6. AFM image of the coating deposited from TEOS + He + 5 % O_2 during 2.2 s. a – 3D image, b – Height deviation distribution (referred to the mean plane); $R_q = 2.40 \text{ nm}$, $Z = 20.9 \text{ nm}$

tested, the maximum roughness, however, revealed the film treated with helium plasma with $R_q = 6.15 \text{ nm}$ and $Z = 55.9 \text{ nm}$ (Fig. 4). Minor roughness of the films was observed after coating deposition from the mixtures (ii) TEOS + He and (iii) TEOS + He + 5 % O_2 . For the latter one, $R_q = 2.40 \text{ nm}$ and $Z = 20.9 \text{ nm}$, being, however, larger than those of the virgin film.

The coating elemental composition was determined by

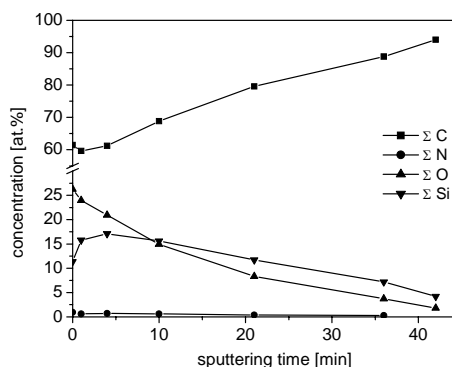


Fig. 7. Element concentrations across the coating deposited from TEOS + He during 22 s

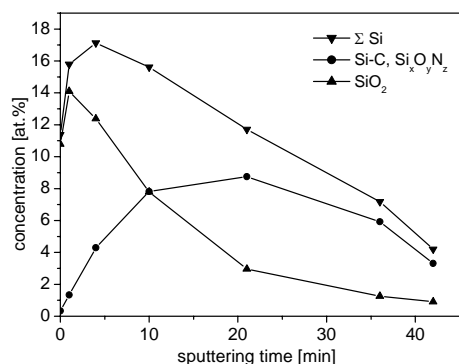


Fig. 8. Different forms of silicon in the coating shown in Fig. 7

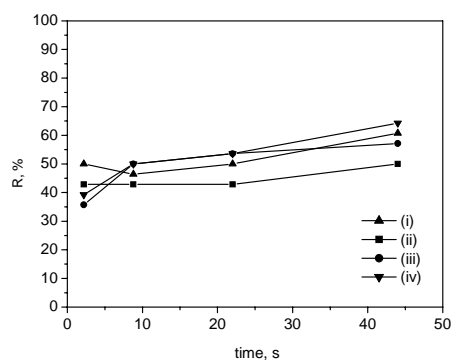


Fig. 9. Residual permeability R of PE films plasma treated in different gases: (i), (ii), (iii), and (iv) during 2.2 to 44 s

X-ray photoelectron spectroscopy (XPS) using a VG Scientific ESCALAB-210 spectrometer with a $AlK\alpha$ X-ray source (1486.6 eV). The changes in the content of individual elements across the layers could be observed due to the coating sputtering with an argon ion gun AG-21 during 40 min (Figs. 7 and 8).

Silicon, oxygen and carbon were found the main components of the coatings and their contents changed with the coating depth (hydrogen was not determined). Various forms of silicon bonds were recorded in the XPS spectra, mainly SiC and SiO₂.

The content of SiO₂ was in maximum at the surface layer of the coatings (with the molar ratio O/Si nearly 2), however, in the deeper layers, the O/Si ratio was lowered to nearly 1. High carbon contents (exceeding 60 %) that was found over the whole coatings could be assigned to the organic residues (from the precursor), however, the effect of the penetration of substrate (PE) structure fragments into coatings seems to be essential. The latter conclusion may be derived from the carbon distribution across the coatings.

Coating permeability

The permeability of oxygen through the foils was determined by measurement of the oxygen diffusion rate at 30°C using an interferometer for the gas analysis. The residual permeability R of the films was defined as:

$$R = \frac{P_i}{P_0} \cdot 100\%$$

where: P_i – permeability after treatment, P_0 – permeability of the original foil equal to $60 \cdot 10^{-10} \text{ cm}^3 \text{ O}_2 / \text{cm}^2 \text{ s cm Hg}$.

It was found that using helium gas, the residual permeability R was near 50 % for the treatment times up to 22 s (Fig. 9).

Testing the gases containing TEOS, the lowest R (35 %) was observed for the feed gas (iii) with the shortest treatment duration (2.2 s). When the deposition was prolonged, however, the permeability reduction tended to decrease. Different circumstances may be responsible for that:

- pinholes and other damages produced by the discharge channels
- micro-cracks occurring owing to low mechanical strength and weak adhesion to the substrate
- high porosity of the coating and high roughness (Figs. 4–6).

As can be seen from the Fig. 2, the discharge is rather of homogeneous character with no traces of stronger individual microdischarge channels being able to produce pinholes. On the other hand, in microscopic images of the coatings only few pinholes or other damages were found. The micro-cracks may result in higher permeability of thick coatings (as was seen in the SEM image). For the thin layers, however, the probability of micro-cracks formation is rather low. Thus, the probable reasons for the residue permeability of the coating were their porosity and roughness. The low conversion of the complex organo-silicon deposit on the surface into a continuous and tight SiO_x structure may facilitate the oxygen diffusion across the coating. On the other hand, because of high roughness of the deposit layer, there may be a great number of local valleys and micro-caverns enabling the gas penetration.

This work was financially supported by the Warsaw University of Technology, Warszawa, Poland.

REFERENCES

1. Czeremuszkin G., Latreche M., Wertheimer M. R., da Siva Sobrinho A. D.: *Plasmas Polymers* 6, 107 (2001).
2. Creatore M., Palumbo F., and d'Agostino R.: *Pure Appl. Chem.* 74, 407 (2002).
3. Foest R., Adler F., Sigener F., Schmidt M.: *Surf. Coat. Technol.* 163-164C, 305 (2003).
4. Madocks J., Rewhinkle J., Barton L.: *Mater. Sci. Eng. B* 119, 268 (2005).
5. Sentek J., Olińska K., Deptuła H.: *Polish J. Appl. Chem.* 49, 153 (2005).
6. Hopfe V., Sheel D.W.: *IEEE Trans. Plasma Sci.* 35, 204 (2007).
7. Ken Okazaki and Tomohiro Nozaki.: *Pure Appl. Chem.* 74, 447 (2002).
8. Opalińska T., Ulejczyk B., Karpiński L., Schmidt-

- Szałowski K.: Polish J. Chem. Technol. 4, 30 (2002).
9. Ulejczyk B., Ekwińska M. A., Opalińska T., Karpiński L., Rymuza Z., Scholz M., Żukowska E., Schmidt-Szałowski K.: Czechoslovak J. Phys. B 56, 1383 (2006).
 10. Wróbel A. M., Walkiewicz-Pietrzykowska A., Wickramanayaka S., Hatanaka Y.: J. Electrochem. Soc. 145, 2866 (1998).
 11. Zajickova L., Brusickova V., Kucerova Z., Franclova J., Stahel P., Perina V., Mackova A.: J. Phys. Chem. Solids 68, 1255 (2007).
 12. Shujun Yang, Hong Yin: Plasma Chem. Plasma Process 27, 23 (2007).
 13. Sentek J., Krawczyk K., Kuś M., Schmidt-Szałowski K.: Polish J. Chem. 79, 1539 (2005).
 14. Sentek J., Kuś M., Schmidt-Szałowski K.: Przem. Chem. 85, 258 (2006).

J. Sentek, Z. Rżanek-Boroch, M. Brykała, and K. Schmidt-Szałowski* (*Faculty of Chemistry, Warsaw University of Technology, Warszawa, Poland*): **Deposition of Gas-Tight Coatings on Plastic Films by Pulsed Dielectric-Barrier Discharges**

Organosilicon coatings deposition from tetraethoxysilane (TEOS) was conducted in pulsed dielectric barrier discharges (PDBD) for packaging polyethylene (PE) films tightening. A laboratory reactor was tested with a rotating cylindrical internal electrode bearing the PE film and with the cylindrical glass body being a dielectric barrier. The oxygen permeability of the films was examined after plasma treatment with different gases: (i) He, (ii) TEOS + He, (iii) TEOS + He + 5 % O₂, (iv) TEOS + He + 10 % O₂. For the film surface topography observations, atomic force microscopy (AFM) was used. The coating composition was examined by X-ray photoelectron spectroscopy (XPS). It was found that under PDBD conditions both the treatment in helium plasma and the coating deposition from different TEOS+carrier-gas mixtures reduce the oxygen permeability of PE films.

INFLUENCE OF N₂ AND CH₄ ON DEPOSITON RATE OF BORON BASED THIN FILMS PREPARED BY MAGNETRON SPUTTERING

M. ELIÁŠ, P. SOUČEK, and P. VAŠINA*

*Department of Physical Electronics, Faculty of Science, Masaryk University, Kotlářská 2, 611 37 Brno, Czech Republic
vasina@physics.muni.cz*

Key words: hybrid PVD-PECVD, BCN, BN, thin films

Introduction

Deposition of thin films by reactive magnetron sputtering is nowadays largely used process to prepare wide range of compound thin films¹. Oxygen or nitrogen gas is routinely added to the deposition process in order to let grow oxide or nitride thin films. Recently a hybrid PVD-PECVD process has been successfully used for preparation of n-TiC/a-C:H thin films²⁻⁴. In this deposition process, a gaseous hydrocarbon is used as a source of carbon instead of its conventional sputtering from the magnetron target. Generally, adding any reactive gas to the deposition chamber may result in processing stability problems⁵⁻⁷. It is well known, that reactive magnetron sputtering using nitrogen or oxygen being controlled by flow of the reactive gas exhibits hysteresis behavior. Increasing the flow of the reactive gas results firstly in an enhanced gettinger of the reactive gas in the growing thin film however the compound fraction on the target remains low – the process runs in so called metallic mode^{8,9}. When the growing thin film reaches its gettinger capacity, the target erosion rate steeply drops. In this case, it is told that the transition from the metallic to the compound mode takes place. The deposition rate generally increases with low amount of nitrogen or oxygen admixture due to the incorporation of the oxygen and nitrogen into the growing thin film and decreases for higher reactive gas supplies due to the progressive target poisoning resulting in reduced sputtering rate.

In principle the process using the admixture of the hydrocarbon should be very similar to the one which uses the nitrogen or the oxygen gas. Instead of covering of the magnetron cathode by hardly sputtered compound (nitride or oxide), it can get covered by a carbon film, which is hard to sputter too. The very important question arises concerning the carbon incorporation into the growing thin film because the situation on the substrate plays an important role in determining of the behavior of the whole deposition process. Moreover, it should be very important to know whether the carbon incorporating in the growing thin film originates from the gas phase or from hardly sputtered thin film on the cathode. The first attempt to answer these questions is to study the trends in the deposition rate when nitrogen and/or hydrocarbon is added into the deposition chamber followed by FTIR spectroscopy of prepared thin films.

Experimental set-up

The drawing of the experimental device is shown in Fig. 1. The experiment is performed using the industrial sputtering deposition system Alcatel SCM 650. A cylindrical vacuum chamber, 65 cm in diameter and 35 cm in height, is equipped by a set of four well balanced magnetrons – two are located on the top and two at the bottom of the deposition chamber (see the sketch of the magnetic field in Fig. 2). Rotating substrate holder is placed between them. The boron target of 20 cm in diameter is mounted on the top magnetron. RF power to the target is supplied by 1.2 kW 13,56 MHz RF power generator, the substrate can be biased by 500 W of 13,56 MHz RF power resulting in a formation of non-magnetized RF plasma near the substrate. Prior to each deposition, the chamber is evacuated by a turbo molecular pump backed by a rotary pump. The turbo molecular pump is throttled during the experiment to obtain desired pumping speed. Argon and reactive gases – nitrogen and methane – are dosed using a thermal mass flow regulator; the pressure is registered by a precise MKS baratron.

The deposition itself goes in several steps. After the vacuum vessel gets sufficiently pumped during several hours, Ar gas is introduced into the deposition chamber to the pressure of 3.0 Pa, the shutter between the target and the substrate is closed and the target gets cleaned by ion bombardment induced by 1 kW of RF power applied on the target during 30 minutes. After that, the substrates is cleaned applying 0,5 kW during 30 minutes. Now, after setting the experimental conditions for the depositions (Ar is introduced into the chamber to a pressure of 1.2 Pa simultaneously with reactive gases, RF power is applied on the magnetron cathode and on the substrate etc.), the deposition starts opening the shutter between the target and the substrate. After desired time, the RF powers are stopped, gas inlets are closed and the substrate cool down under vacuum.

Shortly after the substrate is removed from the deposition chamber, the film thickness is determined from the re-

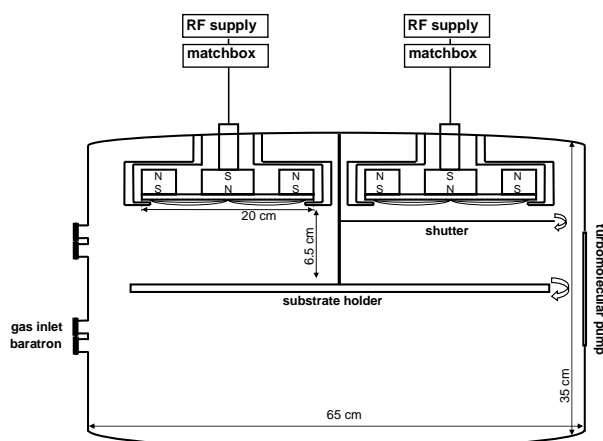


Fig. 1. Experimental set-up

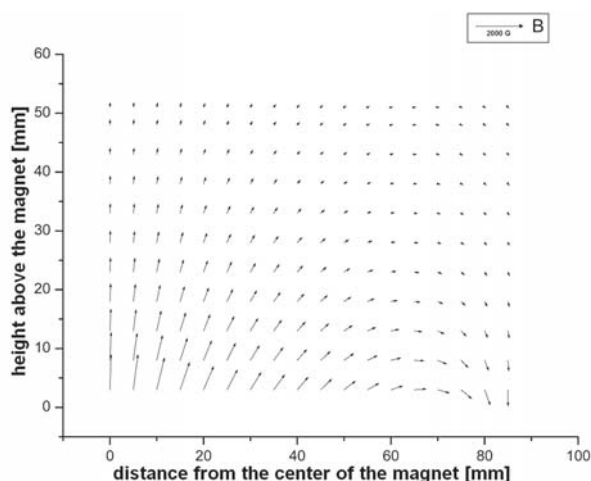


Fig. 2. Sketch of the magnetic field configuration

flectometry measurement (UV-VIS Perkin Elmer Lambda 45 spectrophotometer) using the model from Franta et al¹⁰. An example of measured data and fitted curve is shown in Fig. 3. The infra-red spectra of the deposited film are obtained using FTIR spectrometer Bruker Vertex 80v.

Results and discussion

Table I shows the set of experimentally derived deposition rates of thin films prepared by the sputtering of the boron target in the reactive atmosphere containing nitrogen and/or methane. The experiment is performed either for the substrate holder let at the floating potential (v_{d0}) or for the substrate holder biased by the power of 500 W supplied by the 13,56 MHz generator (v_{d500}) resulting in non-magnetized plasma formation near the substrate and self-bias on then substrate of about -100 V.

Let's discuss the results obtained with the substrate at the floating potential now. Addition of the nitrogen gas into the deposition chamber results first in an increase of the deposition rate followed by a decrease. Precisely, adding 1,5 sccm of N_2 increases deposition rate from 11 nm min^{-1} to 24 nm min^{-1} ; subsequent increase of N_2 supply to 3 sccm leads to the deposition rate of 11 nm min^{-1} . Such behavior is typical for reactive magnetron sputtering deposition process. When methane is added into the deposition process, either together with N_2 or only with Ar, deposition rate changes only a little.

However different situation appears when 500 W of RF is applied on the substrate (DC self-bias ~ -100 V, additional plasma near the substrate). In these conditions, the re-sputtering of the pure boron thin film exceeds the deposition and no deposit is obtained without N_2 and/or CH_4 admixture. When 1.5 sccm of the N_2 is added, thin films grow with the deposition rate of 19 nm min^{-1} , adding 3 sccm of N_2 results in deposition rate of 9 nm min^{-1} . Again, the typical behavior of the reactive deposition process – an increase of the deposition

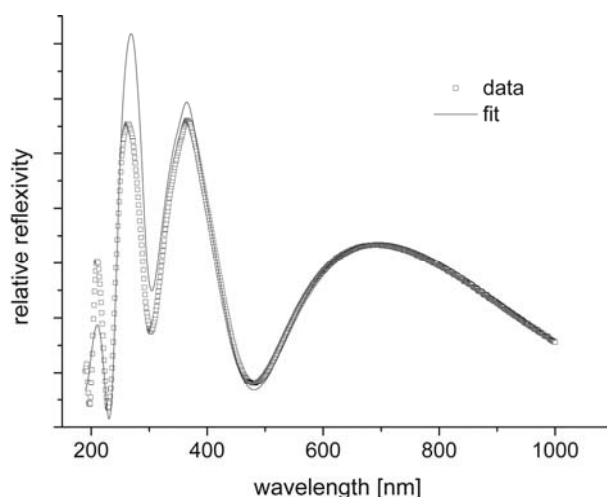


Fig. 3. Example of measured spectral dependency of the reflectivity and the fit used to determine the film thickness

Table I

Deposition rate of boron based thin films prepared by the sputtering of boron target in atmosphere containing nitrogen and/or methane

Q_{N_2} [sccm]	Q_{CH_4} [sccm]	v_{d0} [nm min^{-1}]	v_{d500} [nm min^{-1}]
0	0	11	0
1.5	0	24	19
3	0	11	9
0	1.5	11	3
1.5	0.5	–	26
1.5	1.5	24	7

rate followed by a decrease – is obtained. Keeping all of the experimental conditions which do not lead to deposition of boron thin films the same and adding 1.5 sccm of the methane; a deposit is obtained. The deposition rate in this case was 3 nm min^{-1} . For 1.5 sccm of nitrogen supplied simultaneously with methane the significant increase of deposition rate – from 19 nm min^{-1} (without CH_4) to 26 nm min^{-1} (with 0,5 sccm of CH_4) – is observed. Adding of 1.5 sccm of N_2 together with 1.5 sccm of CH_4 results in deposition rate of 7 nm min^{-1} , which is significantly lower than 19 nm min^{-1} obtained only by using 1.5 sccm of N_2 .

The presence of carbon in the deposits is proved by the FTIR spectroscopy where peaks corresponding to h-BN, c-BN, CC and CH are clearly identified (see Fig. 4) not only for the samples prepared with biased substrate, but also in the case of unbiased substrate, where the deposition rate does not depend significantly on the methane supply. Adding the methane results is lowering of the BH peak indicating that the boron content in the thin films prepared with methane admixture is lowered. Surprisingly, no peak corresponding to BC or CN is identified. The lack of CN peaks in the infra-red spectra

shows that the nitrogen in the growing thin film is banded mainly on boron. Previous results show that the carbon from the gaseous hydrocarbon added into the deposition chamber incorporates in the growing thin film.

When no RF power is applied on the substrate, the carbon detected in the growing thin film can originate from methane partially or fully dissociated in the magnetized plasma or from the sputtering of the carbon layer being very probably formed on the magnetron target. From the infra-red spectroscopy results, it can be deduced that peaks corresponding to carbon rise in favor of peaks corresponding to boron. However the reflectometry measurements show that the deposition rate does not change significantly. It indicates that adding methane, boron is in the thin film partially replaced by carbon. Since the sputtering rate of carbon is twice lower than the sputtering rate of boron, a certain amount of carbon being incorporated into the growing thin film should originate from the magnetized plasma too. The reduction of the boron in the growing thin film indicates that there is a carbon thin film being formed on the boron target. The carbon to boron ratio at the magnetron target is given by the balance of the carbon flux from the magnetized plasma to the target and from the flux of carbon atoms, out sputtered from the target. The composition of the thin film on the substrate should be given by the flux of carbon and boron atoms out sputtered from the target and by the flux of carbon atoms origination from the magnetized plasma.

Applying the 500 W of RF power on the substrate results in formation of the RF plasma near the substrate where methane can be dissociated. It increases the flux of carbon atoms on the substrate with respect to the previous case where the substrate has been left floating. Moreover, the growing thin film is bombarded by Ar ions accelerated to energy of ~ 100 eV sufficiently high to produce sputtering of the growing thin film. The boron to carbon ratio in the growing thin film should be given not only by the flux of carbon and boron atoms out sputtered from target and by the flux of carbon originating from the magnetized plasma and from the non-

magnetized RF plasma near the substrate but also by the carbon and boron losses due to the sputtering of the growing thin film.

The deposition process where methane is added simultaneously with nitrogen behaves very similarly to the reactive magnetron sputtering with two reactive gases. Adding small amount of methane increases the deposition rate of the growing thin film, however substantial increase of the methane supply results in significant reduction of the deposition rate. Adding small amount of methane, the carbon is incorporated into the growing thin film but the boron target remains relatively carbon free ensuring high boron sputtering and consequently high nitrogen banding in the thin film. Increasing the supply of the methane the target gets covered by a carbon layer resulting in lower boron sputtering and consequently lower fraction of boron and nitrogen in the growing thin film and the deposition rate drops.

Conclusion

In this paper the preliminary results concerning properties and deposition rates of thin films prepared by hybrid PVD-PECVD process. The infra red spectroscopy of deposits obtained introducing methane into the deposition chamber clearly proves the carbon incorporation into the growing thin film. Trends in deposition rates indicate that there are probably three sources of carbon atoms incorporating the growing thin film. It can originate from the methane partially or fully dissociated either by the magnetized plasma or from the non-magnetized plasma ignited near the substrate. Third source of the carbon is the sputtering of the carbon layer being formed on the magnetron target. Adding nitrogen and methane simultaneously, the process behaves very similarly to the reactive sputtering deposition process with two reactive gases.

This research has been supported by the MSM contract 0021622411 and by GACR contract 202/08/P038.

REFERENCES

1. Depla D., Mahieu S. (ed.): *Reactive Sputter Deposition*, Springer Series in Material Science 109 (2008).
2. Berg S., Nyberg T.: *Thin Solid Films* 476, 215 (2005).
3. Vašina P., Hytková T., Eliáš M.: submitted to *Plasma Source Science Technology* (2008).
4. Kubart T., Kappertz O., Nyberg T., Berg S.: *Thin Solid Films* 515, 421 (2006).
5. Nyberg T., Berg S., Helmersson U., Hartig K.: *Appl. Phys. Lett.* 86, 164106 (2005).
6. Berg S., Blom H-O., Larsson T., Nender C.: *J. Vac. Sci. Technol., A* 5(2), 202 (1987).
7. Hytková T., Vašina P., Eliáš M.: submitted to *Chemické listy* (2008).
8. Pei Y. T., Galvan D., de Hosson J. Tm. M: *Acta Materialia* 53, 4505 (2005).
9. Galvan D., Pei Y. T., de Hosson J. Tm. M : *J. Vac. Sci. Technol., A* 24(4), 1441 (2006).
10. Franta D., Nečas D., Zajíčková L.: *Optics Express* 15, 16230 (2007).

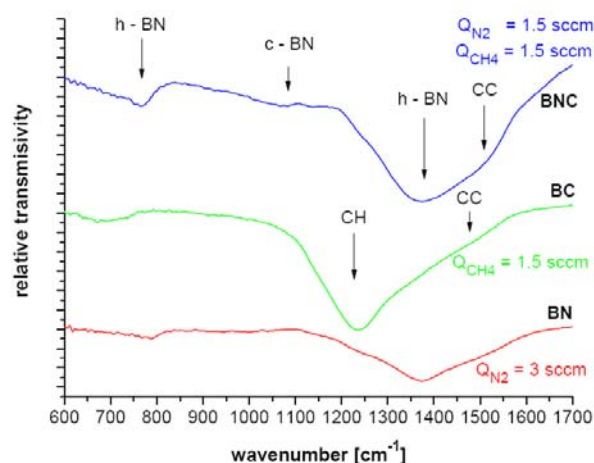


Fig. 4. Infra red spectra of thin films prepared with floating substrate

M. Eliáš, P. Souček, and P. Vašina* (*Department of Physical Electronics, Faculty of Science, Masaryk University, Brno, Czech Republic*): **Influence of N₂ and CH₄ on Deposition Rate of Boron Based Thin Films Prepared by Magnetron Sputtering**

The goal of this paper is to present preliminary results concerning properties and deposition rates of thin films prepared by hybrid PVD-PECVD process. In this hybrid deposition process a gaseous hydrocarbon is used as a source of carbon instead of its conventional sputtering from the magnetron target. The influence of the reactive gas admixture on the deposition rate of growing films is investigated. Comparative study using two different gases – nitrogen and methane – is performed. Both gases are added also simultaneously. Interesting findings on carbon incorporation into the growing thin film are obtained from FTIR spectroscopy of the deposits. Moreover, from trends in the deposition rate, some statements concerning behavior of the hybrid PVD-PECVD process are derived.

DEPOSITION OF THIN FILMS IN ATMOSPHERIC PRESSURE GLOW DISCHARGE IN $N_2 + HMDSO + O_2$ ATMOSPHERE

FILIP STUDNIČKA*, DAVID TRUNEC, PAVEL ŠTAHEL, VILMA BURŠÍKOVÁ, and LUKÁŠ KELAR

Department of Physical Electronics, Masaryk University, Kotlářská 2, CZ-61137 Brno, Czech Republic
trunec@physics.muni.cz

1. Introduction

Dielectric barrier discharge (DBD) can be used to change properties of materials, such as adhesion, hardness, etc. We can deposit thin films on the material in order to achieve protective layers or to make some liquids more adhesive to the material. The main disadvantage of DBD is that it is in the filamentary state under normal conditions. It was found, that under certain conditions DBD becomes homogeneous. This discharge is called atmospheric pressure glow discharge (APGD). The deposition in the atmospheric pressure has a great advantage in economy of the deposition, because we don't need expensive vacuum technologies and we can make a lot of depositions in a short amount of time. One of the disadvantages is, that it is quite difficult to achieve depositions in large area¹. Sawada² reported the organosilicon thin films deposition in APGD in helium with the admixture of tetraethoxysilane (TEOS) or hexamethyldisiloxane (HMDSO) and oxygen. Prat³ reported the fluoro-polymer film deposition in helium APGD with admixture of hexafluoropropylene or tetrafluorethylene. Gherardi⁴ used N_2 - SiH_4 - N_2O APGD for SiO_2 deposition. Foest⁵ used APGD in helium with admixture of HMDSO for organosilicon thin film deposition. The APGD can be easily generated in various pure gases⁶⁻⁹. However we used nitrogen because it is the most suitable gas from the technological point of view.

We studied the influence of hexamethyldisiloxane ($C_6H_{18}Si_2O$ – HMDSO) and O_2 mixture on the discharge properties, so we can achieve APGD. The properties of discharge were studied by electric measurement. The properties of films were studied by depth sensing indentation technique using the Fischerscope H100 tester and AFM. We also studied new ring-type of electrode, which has an unique exhaustion pipe in the center, so we can have better control of the amount of the HMDSO flowing under the electrode. As a deposition substrate we used 350 mm thick silicon wafers with a diameter of 10 cm and (dimensions 160×65 mm) glass plates with thickness of 1 mm. The films had uniform thickness and under optimum conditions exhibited higher hardness than the material on which the films were deposited.

2. Experiment

The experiments were carried out in a plasma reactor of dimensions 500×500×500 mm. The schematic drawing of the reactor is shown in the Fig. 1. Electrode system is created from two metal electrodes. The bottom electrode was rectangular with dimensions 150×60 mm; on this electrode the substrates were placed. As an upper electrode two types of electrode were used. First type of electrode with dimensions 15×30 mm was covered by Petri dish with diameter of 50 mm. The metal electrode was glued to Petri dish by the ceramic glue. Second type of electrode (ring-type) created the ring with diameter 30 mm with the hole of 15 mm diameter in the middle of the electrode (see Fig. 2.). The ring metal electrode was covered with 0,5 mm thick Pyrex^o glass. The distance between the substrate and the upper electrode varied from 0.6 to 1.2 mm. The upper electrode was movable in the horizontal direction (see Fig. 1). The bottom electrode was electrically heated up from 50 to 150 °C.

The DC laboratory source powered AC high voltage sin. source Lifetech connected to the discharge electrodes. High voltage source worked in the resonance mode with the frequency around 6 kHz. Electric properties of the discharge were measured using oscilloscope HP 54820A equipped with high voltage probe and Rogowski coil. In the reactor there were three gas bushings. First gas bushing was used for the

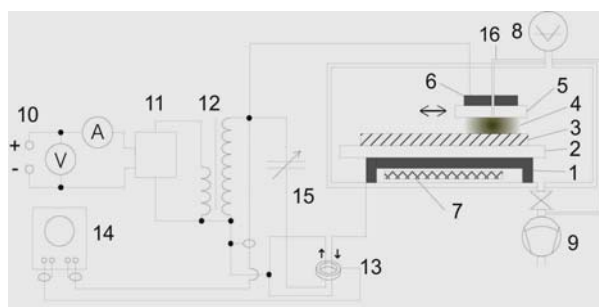


Fig. 1. **Schema of the reactor.** 1 – bottom electrode, 2 – bottom dielectric, 3 – substrate, 4 – discharge, 5 – upper dielectric, 6 – upper electrode, 7 – heating, 8 – input of gases, 9 – vacuum pump, 10 – DC source, 11 – AC source, 12 – transformer, 13 – Rogowski coil, 14 – oscilloscope, 15 – tunable capacitor, 16 – exhaustion pipe

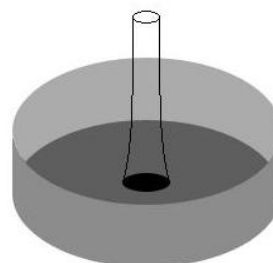


Fig. 2. **The ring-type electrode.** The darkest gray represents metal ring

input of nitrogen with/without monomer admixture, second one was connected to pumping system and the last one was connected to the exhaust pipe in the ring-type electrode.

In this work the influence of flow rate of buffer gas or monomer and influence of the substrate temperature was investigated. We also studied influence of geometry and different type of electrodes on the quality of deposited films.

In the case of first type of the electrode (Petri dish electrode), it was problematic to achieve homogenous and as well as controlled distribution of admixtures under the whole surface of the electrode. Special ring-type electrode enabled us to control easily the amount of the monomer and also buffer gas in discharge space.

Using this type of the electrode the distribution of gas is homogenous and deposited films had uniform thickness (except for the little spot under the exhaustion pipe).

The monomer vapors (in our case HMDSO) were carried with the carrier gas (in our case nitrogen or synthetic air) with flow rate varying from 5 to 30 sccm bubbled through the monomer. The relation between the amount of carrier gas and amount of HMDSO is expressed:

$$\text{HMDSO [g/h]} = 0.01752 + 0.02467 \times \text{CARRIER [slpm]}.$$

Use of the synthetic air as a carrier gas containing mainly nitrogen ($\approx 80\%$) and oxygen ($\approx 20\%$) enabled us to sensitively control oxygen content.

Before starting the experiment, the substrate was cleaned in mixture of 50% isopropylalcohol and 50% cyclohexane bath followed with the ethanol bath.

Before deposition the reactor was pumped down to 20 Pa to obtain the same before deposition conditions. Then the reactor was filled with the nitrogen to the pressure 99.8 kPa. The flow rate of nitrogen was 6 slpm in all experiments. After that the resonance frequency was set up (generally about 6 kHz). Before the deposition the substrate was cleaned and activated with plasma treatment in APGD with power density 30 W cm^{-3} . After that the nitrogen was mixed with the HMDSO + carrier gas and the reactor was run through with this mixture for about 30 minutes to achieve homogenous distribution of gases in the reactor. If the ring-type electrode was used then the exhaustion rate was possible to set up. Then the temperature was increased to the desired value and the deposition started. In this paper only depositions in static mode are presented. Upper electrode did not move

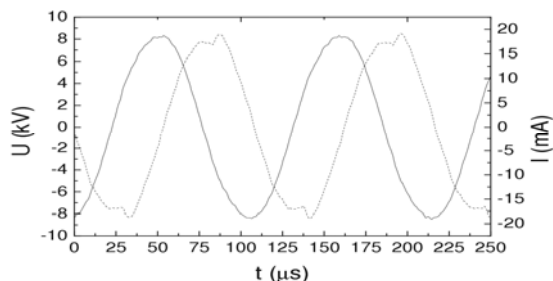


Fig. 3. Typical APGD current-voltage characteristic. The discharge current consists of two parts—the sinusoidal capacitive current part and the small peak of APGD discharge current

and deposition time was always 25 minutes. The difference between filamentary DBD and APGD was determined from the oscilloscope current-voltage measurement; the typical current-voltage characteristic is shown in the Fig. 3. The power varied from 30 to 150 W cm^{-3} , the peak-to-peak AC voltage varied from 8 to 22 kV, the flow rate of synthetic air from 5 to 30 sccm and the temperature from 50 to $200 \text{ }^\circ\text{C}$.

3. Results and discussion

All experiments were performed in APGD mode. If filamentary DBD appeared, the deposition conditions were changed to obtain homogenous mode (e.g. lowering the power, lowering the flow rate of admixtures, lowering the exhaustion rate). Exhaustion rate higher than 500 sccm or flow rate of synthetic air higher than 30 sccm can cause the discharge to be filamentary. The films deposited with the admixture of O_2 exhibited better hardness properties because the oxygen works as an oxidation reagent. The films deposited with Petri dish electrode showed good hardness properties but weren't homogenous under the whole surface of the electrode. That is because the monomer vapors were able to reach the center of the APGD and were consumed under the edge of the electrode perimeter. In opposite the films deposited with ring-type electrode were perfectly homogenous.

After several experiments with electrodes made from Petri dish electrode we obtained the conditions for hard glass like coatings (see Table I, sample 8081303). The deposition rate in the edge of the electrode of the films was extremely fast, so films were after 25 minutes of deposition so thick that internal stress in film caused delamination from the substrate as is shown in the Fig. 4–7. Deposited films exhibited high hardness however in the case of Petri-dish electrode the deposition proceeded only under the electrode edge and films were not completely homogenous. With the ring-type electrode we obtained films with similar mechanical properties but with

Table I
Deposition conditions

Sample no.	Synth. air [sccm]	Exh. [sccm]	Temp. [$^\circ\text{C}$]	Power dens. [W cm^{-3}]
8081303	6	0	100	134
8082601	6	0	100	41
8082602	6	0	100	24
8082805	6	250	100	59
8082807	15	50	100	53
8082701	10	200	100	36
8082702	6	100	100	53
8082703	10	100	100	53
8082704	10	200	100	53
8082705	6	500	100	25
8082706	6	200	100	25
8090101	30	500	150	53
8090102	30	500	150	62

Table II
Some results from depth sensing indentation measuring

Sample no.	Max. load [mN]	HU [GPa]	HU _{pl} [GPa]	Y [GPa]	Electrode
8081303	15	3.36	7.08	74.49	petri dish
8081303	5	3.32	6.73	78.55	petri dish
8082602	5	3.23	6.67	72.98	ring-type
8082601	5	0.92	1.33	26.63	ring-type
8082807	7	1.16	1.80	30.75	ring-type
8082805	7	1.03	1.60	28.39	ring-type
8082701	10	1.76	2.98	44.33	ring-type
8082702	10	1.82	3.05	45.55	ring-type
8082703	10	1.35	1.86	42.27	ring-type
8082704	10	1.03	1.63	27.77	ring-type
8090101	50	3.02	6.07	68.20	ring-type
8090101	10	2.62	5.16	60.18	ring-type
8090101	7	2.47	4.83	57.09	ring-type
8090101	5	2.23	4.63	49.73	ring-type
8090102	50	3.34	6.95	74.72	ring-type
8090102	10	2.97	5.84	68.09	ring-type
8090102	7	2.84	5.49	65.91	ring-type
8090102	5	2.73	5.30	63.25	ring-type
8082705	50	3.04	7.75	60.90	ring-type
8082705	10	3.37	8.39	69.61	ring-type
8082705	7	3.27	8.46	66.93	ring-type
8082705	5	3.65	10.55	74.70	ring-type
8082706	50	3.59	7.95	77.97	ring-type
8082706	10	3.56	8.23	76.45	ring-type
8082706	7	3.47	8.02	74.65	ring-type
8082706	5	3.31	7.57	71.51	ring-type

uniform thickness (see Table I, II, sample no. 8082602).

Film deposition conditions are shown in the Table I. Mechanical properties obtained from depth sensing indentation tests are summarized in Table II.

- the sample 8081303 has Young's module around 76 GPa, this value is nearly glass-like (glass is about 70 GPa),
- the sample 8082602 has Young's module around 73 GPa,
- the sample 8090101 is quite weak, because Young's module much differs for load 5 and 7 mN,
- the samples 80827[05-06] are really hard, nearly glass-like, their Young modules are even higher then the Young module of the substrate,
- the other samples are quite thin, we can tell this from the rising HU which corresponds to higher load, thus the properties of the substrate are influencing the measured characteristics,
- the hardness of the prepared films was in the range from 1.3 to 10.5 GPa,

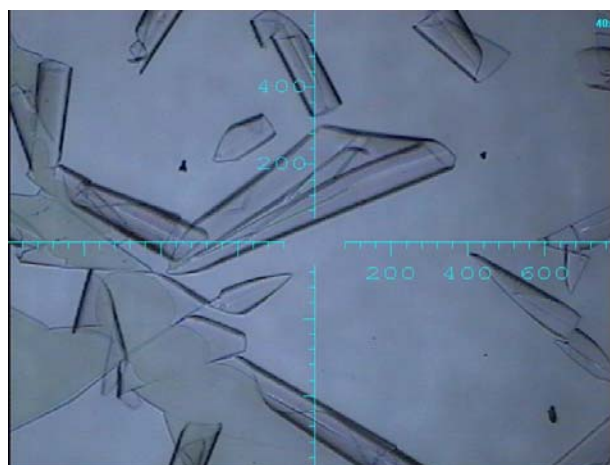


Fig. 4. Delaminated film from sample 8082602 – tension stress

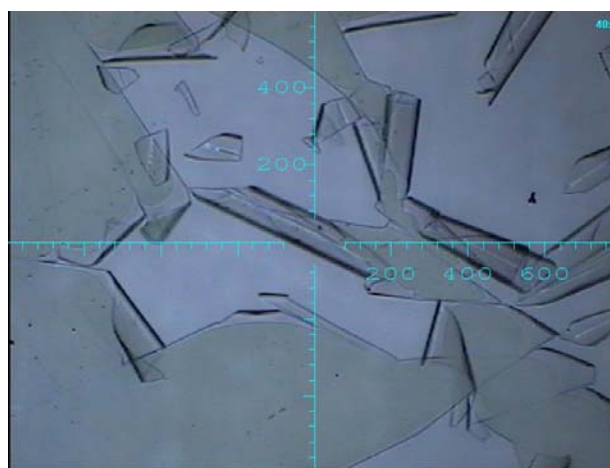


Fig. 5. Delaminated film from sample 8082602 – tensile stress

- the samples 8082701-04 are quite thick but exhibit relatively low HU_{pl},
- not only HU_{pl} but also HU and Young module are important in the characterization of the films. If the film is hard but not elastic, it would be fragile and if the system film/substrate will be under stress, the film could easily peel off.

From the pictures of delaminated films it is possible to study internal stress of films. I will now concentrate on the two films 8081303 and 8082602 which delaminated from the substrate.

Delamination of film from the substrate is caused by the internal stress. The sample 8082602 delaminated because of the tensile stress (see Fig. 4, 5) and the sample 8081303 delaminated because of the compressive stress (see Fig. 6, 7).

The rolls on the Fig. 4, 5 are signaling the tension stress in the film with low adhesion. The film is trying to shrink what leads to film cracking and thanks to the low adhesion the film delaminates from the substrate and creates rolls.

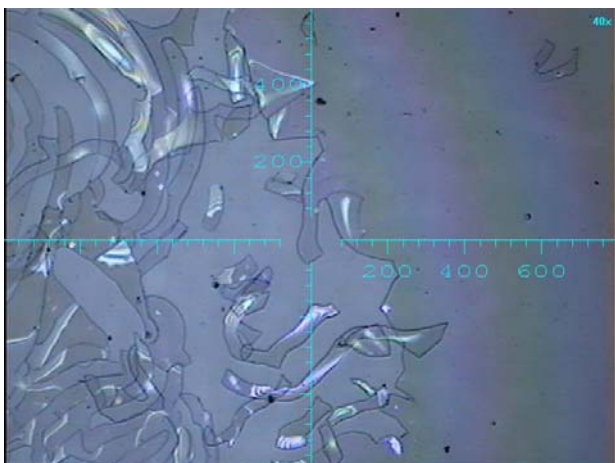


Fig. 6. Delaminated film from sample 8081303 – pressure stress

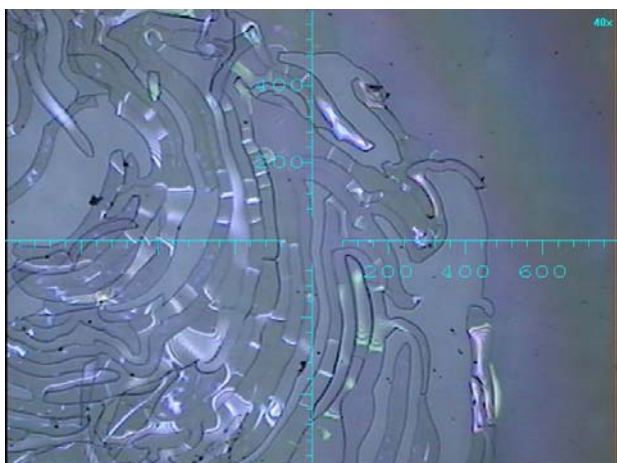


Fig. 7. Delaminated film from sample 8081303 – compressive stress

The corrugation on the Fig. 6, 7 shows the pressure stress in the film with low adhesion. The film is trying to stretch. If this film would be soft, then the film only corrugates. Since this film is really hard, then after corrugation it cracks, after gaining enough curvature.

It is evident, that deposition conditions influence not only hardness (both films 8081303 and 8082602 had at about same hardness) but also different type of internal stress. By this technique it is possible to prepare films either with tension or pressure stress. To obtain samples without cracks it is necessary to optimize plasma treatment before deposition to obtain better adhesion of the prepared films to the substrate.

On the Fig. 8 there are indentations with max. load 100 mN. The indenter was deep in the substrate at this load, but it is obvious that there are no cracks or delamination around the indentations. That means the films are not fragile and the adhesion to the substrate is really good.

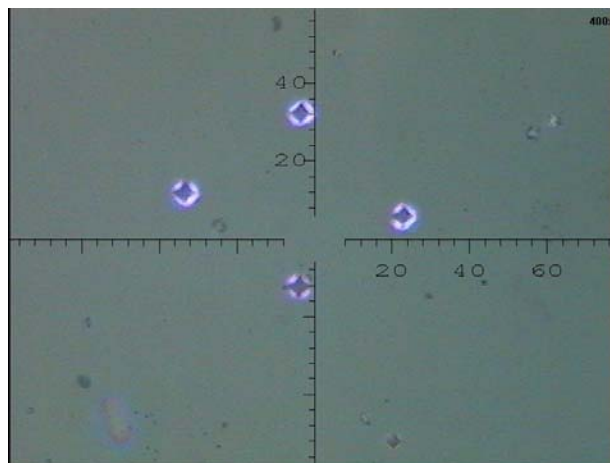


Fig. 8. Four indentation prints carried out with indentation load of 100 mN and one with 50 mN on the sample 8090101

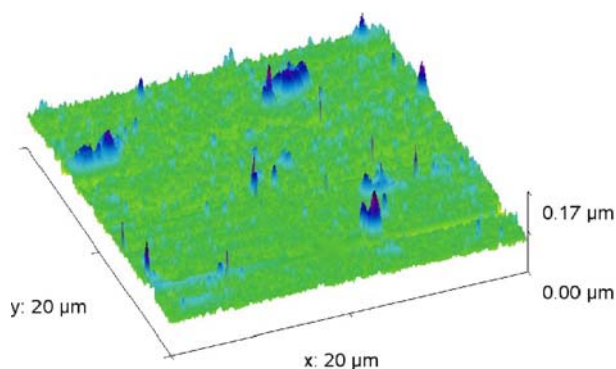


Fig. 9. AFM picture of film from the APGD

The AFM picture of the film deposited in APGD is on the Fig. 9. As you can see, the film is smooth and homogeneous except for some sharp objects, which occur seldom even on APGD made films.

4. Conclusion

Deposition of thin glass-like films in atmospheric pressure glow discharge from nitrogen + HMDSO + oxygen atmosphere is shown in this paper. The effect of different oxygen and HMDSO flow rates, temperature, power density and different type of electrodes on the film properties was investigated. Under special conditions it is possible to deposit glass-like films with HU_{pl} over 6 GPa, Young's module over 70 GPa with tensile or compressive stress. We also presented the new ring-type of electrode with exhaustion pipe in the center enabling us to obtain homogenous film deposition. With the ring-type electrode we were able to deposit glass-like films with good adhesion to the substrate and uniform thickness.

This research has been supported by the grant of Czech Science Foundation no. 202/06/1473. I would also like to thank Mr. Milan Kunovský for great technical support.

REFERENCES

1. Trunec D., Navrátil Z., Sťahel P., Zajíčková L., Buršíková V., Čech J.: *J. Phys. D: Appl. Phys.* 37, 2112 (2004).
2. Sawada Y., Ogawa S., Kogoma M.: *J. Phys. D: Appl. Phys.* 28, 1661 (1995).
3. Prat R., Koh Y. J., Babukutty Y., Kogoma M., Okazaki S., Kodama M.: *Polymer* 41, 7355 (2000).
4. Gherardi N., Martin S., Massines F.: *J. Phys. D: Appl. Phys.* 33, L104 (2000).
5. Foest R., Adler F., Sigenege F., Schmidt M.: *Surf. Coat. Technol.* 163-164, 323 (2003).
6. Kanazawa S., Kogoma M., Moriwaki T., Okazaki S.: *J. Phys. D: Appl. Phys.* 21, 838 (1988).
7. Gherardi N., Gouda G., Gat E., Ricard A., Massines F.: *Plasma Sources Sci. Technol.* 9, 340 (2000).
8. Trunec D., Brablec A., Buchta J.: *J. Phys. D: Appl. Phys.* 34, 1697 (2001).
9. Brandenburg R., Kozlov K. V., Massines F., Michel P., Wagner H.-E.: *Proc. HAKONE VII (Greifswald)*, 2000.

USING OF DSCBD PLASMA FOR TREATMENT OF KEVLAR AND NOMEX FIBERS

MARIE ŠTĚPÁNKOVÁ^{*a}, JANA ŠAŠKOVÁ^a,
JAN GRÉGR^b, and JAKUB WIENER^a

^a Department of Textile Chemistry, Textile Faculty, Technical University of Liberec, Studentská 2, 461 17 Liberec,

^b Department of Chemistry, Faculty of Education, Technical University of Liberec, Studentská 2, 461 17 Liberec

*marfousek@seznam.cz

Introduction

Aramids are a family of nylons, including Nomex and Kevlar. Chemical structure of Nomex and Kevlar fibers can be described by the common formula in Fig. 1 a 2.

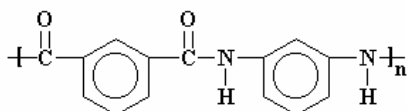


Fig. 1. Structure of Nomex fiber

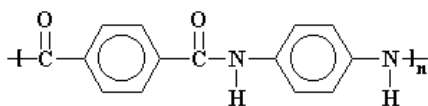


Fig. 2. Structure of Kevlar fiber

In Kevlar the aromatic groups are all linked into the backbone chain through the 1 and 4 positions (called para-linkage). Kevlar has high strength, high modulus (stiffness), toughness and thermal stability. Also it is resistant to many of the chemicals and solvents. It has high physical resistance, like high break and tear resistance and also presents high durability through for example high abrasion resistance.

Nomex has meta-phenylene groups, that is the amide groups are attached to the phenyl ring at the 1 and 3 positions. Nomex is inherently flame resistant and presents a high resistance to chemicals and does not dissolve easily, but is prone to hydrolysis. One way to prevent hydrolysis is using a diffuse barrier discharge¹. After this treatment, Nomex fiber is absolutely resistant to 85 % H₂SO₄.

Their applications are focused on the technical sphere. They are usually used in tyre reinforcement, ballistics applications, ropes and cables, and in protective apparel where high strength, and thermal, puncture, and cut resistance are required².

For some applications it is necessary to improve surface properties. One of possible way is plasma treatment – subject of this study.

Plasma treatment is probably the most versatile surface treatment technique. Different types of gases (argon, oxygen, nitrogen) can produce the unique surface properties required by various applications. The advantage of plasma treatment is the fact that plasma treatment usually changes surface properties of polymers without interfering the bulk properties³.

To modify polymer surface it is possible to employ oxygen or nitrogen-containing plasma. A variety of oxygen functional groups (e.g. C–O, C=O, O–C=O, C–O–O) we can obtain from oxygen-containing plasma. Due to plasma treatment it can be improve wettability, printability and biocompatibility of polymer surfaces³.

Experimental

Materials

The fibers used in this experiment were Kevlar and Nomex. Before plasma treatment, all fibers were washed twice with isopropyl alcohol for 2 min and dried in oven at 50 °C for 1 hour. Than samples were let in a fume chamber for 24 hours.

Plasma treatment

An atmospheric pressure plasma source of Diffuse Coplanar Surface Barrier Discharge (DCSBD) was employed for the plasma treatment of samples. To initiate plasma, atmospheric air and nitrogen were chosen as working gases. Model of used equipment is DCSBD A4-LIN (Fig. 3), which means that is device with linear displace. The discharge power was 300 W and frequency 15 kHz. Fibers of Kevlar and Nomex were treated by plasma for 30 sec, 2 and 5 min.

SEM morphological study

Surface morphology of fibers was investigated using scanning electron microscopy (SEM). It was performed in TS5130 VEGA TESCAN at magnification of 1.5·10⁵ and

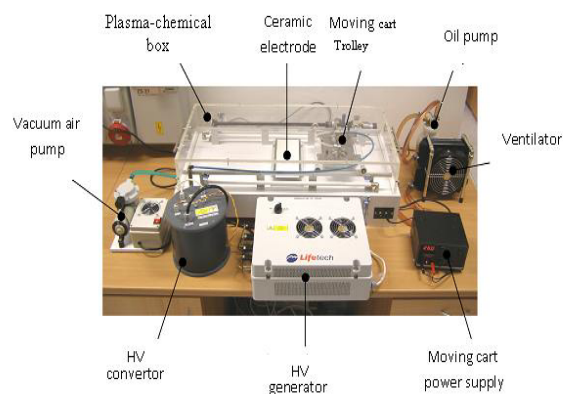


Fig. 3. The photo of plasma source of DCSBD

a voltage of 30 kV.

Before SEM analysis, all the samples were coated by platinum with model of PRONEN SCD 030. Conditions of coating were 120 s, electric current 115 mA at vacuum.

FTIR analysis

A FTIR spectrophotometer (model One, Perkin Elmer – ATR technique on ZnSe crystals) was used to analyze the functional groups of the surface pure and plasma treated fibers. Thickness of analysed surface layer is in the micron range.

XPS surface chemical analysis

The X-ray photoelectron spectroscopy (XPS) experiment was performed using ESCA PROBE P photoelectron spectrometer (Omicron Nanotechnology Ltd) equipped with Al anode (1486,7 eV) X-ray source. The base pressure in the sample chamber was controlled in the range of 10^{-10} mbar. Thickness of analysed surface layer is in the range from 5 to 10 nm.

Measured spectra were analysed by way of CasaXPS programme. Deconvolution analysis of the C1s peaks was performed to determine changes of functional groups.

Results and discussion

SEM results

Fig. 4a-d show the SEM micrographs of untreated and plasma-treated Kevlar fibers. It can be observed that no ripple-like structure has been shown on fibers after the plasma treatment neither in the air nor nitrogen.

Some irregularities on Nomex fiber can be proceed from manufacturing process. After air-plasma or nitrogen plasma treatment, no ripple-like structures can be obtained as shown Fig. 5a-c. Plasma treated Nomex fiber has a rougher surface than untreated fiber.

On these fibers the etching action of ions is weaker than on other polymers. It is due to high crystallinity of fibers and rigidity of polymer chains.

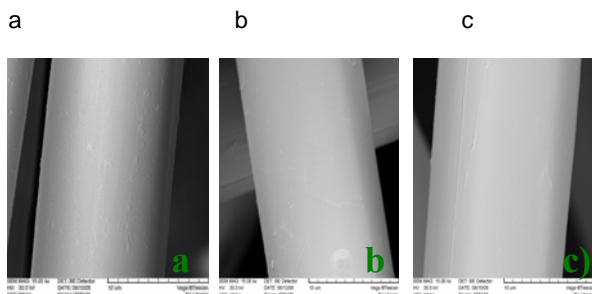


Fig. 4. SEM micrographs of Kevlar fiber: a) untreated, b) air-plasma treated after 5 min, c) nitrogen-plasma treated after 5 min

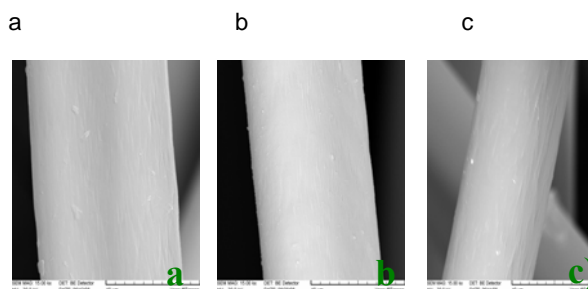


Fig. 5. SEM micrographs of Nomex fiber: a) untreated, b) air-plasma treated after 5 min, c) nitrogen-plasma treated after 5 min

FTIR analysis

No significant changes in IR spectra of Kevlar fibers were observed for air-plasma and nitrogen-plasma treatment (Fig. 6, 7).

We can observe on slight changes in IR spectra of Nomex fiber after plasma treatment (Fig. 8, 9). These changes were found in C=O groups at 1740 cm^{-1} and O=C–O– groups at 1124 cm^{-1} .

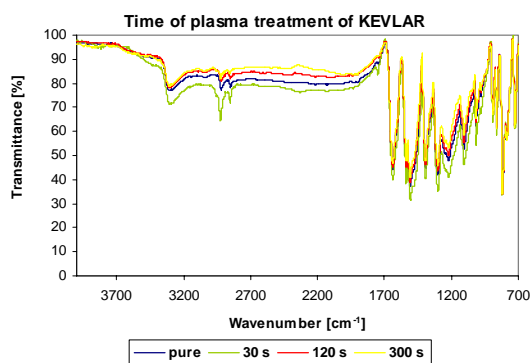


Fig. 6. FTIR spectra of Kevlar fiber after air-plasma

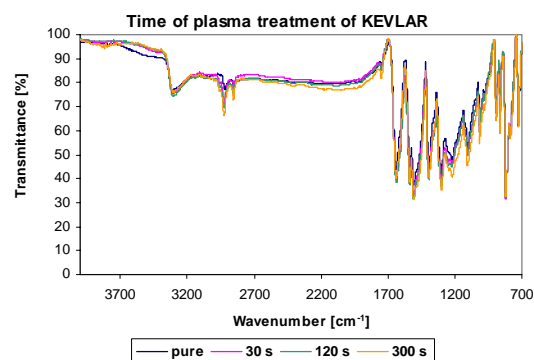


Fig. 7. FTIR spectra of Kevlar fiber after nitrogen-plasma

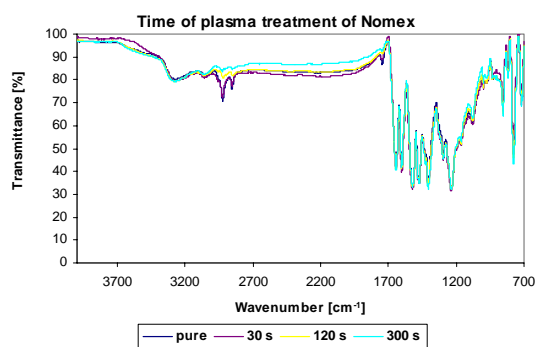


Fig. 8. FTIR spectra of Nomex fiber after air-plasma

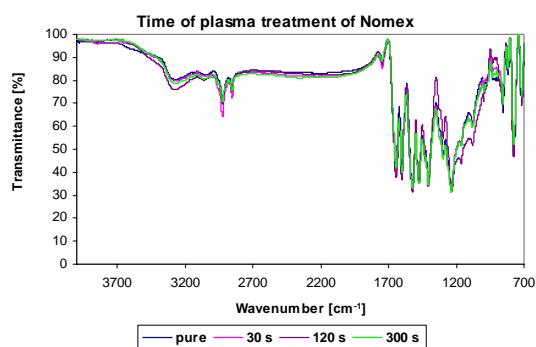


Fig. 9. FTIR spectra of Nomex fiber after nitrogen-plasma

XPS results

XPS analysis was performed to estimate changes in chemical composition of the fiber surfaces. For chemical analysis, where carbon bonds are determined by virtue of curve-fitted spectra, we used these values of carbon energy C 1s obtained on account of literary references^{4–6}. The aramid fiber surface after plasma treatments has potential carbon-containing components with binding energies of 284,7 eV (C–C), 286,3 eV (C–O/C–N), 287,5 eV (C=O), 289 eV (C=OOH).

Obtained results are summarized in Tab. I and II. After plasma treatment, the concentrations of oxygen significantly increased for all plasma treated samples. Also we can see a significant reduction in concentration of carbon. It is a typical effect for plasma treated polymers⁷. It is caused by the active species in plasma due to the chain scission mechanisms.

We can conclude that the air-plasma and nitrogen plasma treatment of fibers of Kevlar and Nomex leads to changes in chemical states of carbon and oxygen.

In order to examine changes of functional groups deconvolution analysis of the C1s peaks was performed (tab. III, IV). We can find that ketone groups concentration at Kevlar and Nomex fibers surfaces increased for almost all samples after plasma treatment.

Table I

Relative chemical composition and atomic ratios determined by XPS for fiber of Kevlar and Nomex after air-plasma treatment

Condition	Chemical composition [%]			Atomic ratio [%]	
	C1s	O1s	N1s	O/C	N/C
Kevlar untreated	81,29	13,69	5,02	16,84	6,18
plasma – 30 s	72,20	23,71	4,09	32,84	5,66
plasma – 120 s	71,25	22,89	5,85	32,13	8,21
plasma – 300 s	71,31	24,55	4,15	34,43	5,82
Nomex untreated	79,25	14,74	5,22	18,60	6,59
plasma – 30 s	71,21	22,87	4,36	32,12	6,12
plasma – 120 s	66,23	27,61	6,15	41,69	9,29
plasma – 300 s	66,46	27,41	5,01	41,24	7,54

Table II

Relative chemical composition and atomic ratios determined by XPS for fibers Kevlar and Nomex after nitrogen-plasma treatment

Condition	Chemical composition [%]			Atomic ratio [%]	
	C1s	O1s	N1s	O/C	N/C
Kevlar untreated	81,29	13,69	5,02	16,84	6,18
plasma – 30 s	79,34	15,76	4,90	19,86	6,18
plasma – 120 s	74,75	20,20	5,04	27,02	6,74
plasma – 300 s	72,10	21,69	6,21	30,08	8,61
Nomex untreated	79,25	14,74	5,22	18,60	6,59
plasma – 30 s	80,02	15,05	4,93	19,37	6,16
plasma – 120 s	75,72	17,23	7,06	22,75	9,32
plasma – 300 s	73,75	18,40	7,13	24,95	9,67

Table III

Results of analysis of C1s peaks for fibers of Kevlar and Nomex after air-plasma treatment

Condition	Relative area corresponding to different chemical bonds [%]			
	C-C,H	C=O	C-O-	C=OOH
Kevlar untreated	74,92	7,46	15,37	2,26
plasma – 30 s	75,44	12,12	12,44	–
plasma – 120 s	74,37	9,76	15,86	–
plasma – 300 s	78,19	12,70	9,11	–
Nomex untreated	85,36	6,52	8,12	–
plasma – 30 s	77,76	9,71	12,53	–
plasma – 120 s	70,64	11,39	12,71	5,26
plasma – 300 s	67,25	14,78	15,35	2,63

Table IV
Results of analysis of C1s peaks for fibers of Kevlar and Nomex after nitrogen-plasma treatment

Condition	Relative area corresponding to different chemical bonds [%]			
	C-C,H	C=O	C-O-	C=OOH
Kevlar untreated	74,92	7,46	15,37	2,26
plasma – 30 s	83,81	5,25	10,94	–
plasma – 120 s	85,19	3,63	11,18	–
plasma – 300 s	84,97	5,08	9,95	–
Nomex untreated	85,36	6,52	8,12	–
plasma – 30 s	76,57	4,64	18,83	–
plasma – 120 s	82,59	9,23	8,18	–
plasma – 300 s	79,13	6,51	14,36	–

Carboxyl groups of Kevlar fiber disappear after air-plasma and nitrogen plasma. It was found that content of carboxyl groups of Nomex fiber increased after longer times of plasma treatment in the air.

Conclusion

There are presented results of surface properties of Kevlar and Nomex fibers before and after plasma treatment in the air and in nitrogen.

No ripple-like structure is formed on surface of fibers of Kevlar and Nomex due to weaker etching action of DCSBD plasma in comparison with rigidity of polymer chains on these fibers.

Plasma treatment causes changes in chemical state of carbon and oxygen. While content of carbon decrease, content

of oxygen significantly increased after plasma treatment of fibers of Kevlar and Nomex. This oxidation process was realised only in the surface layers of fibers. According this theory changes of surface were estimated only by XPS.

This research has been supported by KAN 101630651.

REFERENCES

- Höcker H.: Pure Appl. Chem. 74, 423 (2002).
- Su F., Zhang Z., Guo F., Song H., Liu W.: Wear 261, 293 (2006).
- Chan C.-M.: Surf. Sci. Rep. 24, 1 (1996).
- Dark D., Cromarty B., Dilks A.: J. Pol. Sci. 16, 3173 (1978).
- Iganaki N., Tasaka S., Kawai H.: J. Appl. Pol. Sci. 64, 831 (1997).
- Wang Q., Ait-Kadi A., Kaliaguine S.: J. Appl. Pol. Sci. 45, 1023 (1992).
- Pappas D., Bujanda A., Demaree J.: J. Appl. Pol. Sci. 45, 1023 (1992).

M. Štěpánková^{a,*}, J. Šašková^a, J. Grégr^b, and J. Wiener^a (^aDepartment of Textile Chemistry, Textile Faculty, Technical University of Liberec, ^bDepartment of Chemistry, Faculty of Education, Technical University of Liberec): **Using of DCSBD Plasma for Treatment of Kevlar and Nomex Fibers**

In this study the influence of plasma treatment on fibers of Kevlar and Nomex is discussed. These fibers were treated by means of the plasma source of Diffuse Coplanar Surface Barrier Discharge (DCSBD) at different conditions. The change in chemical compositions of pure, air-plasma and nitrogen-plasma treated Nomex and Kevlar fibers were analyzed by means of X-ray photoelectron spectroscopy and Fourier transform infrared spectroscopy. The morphologies of surface of the pure and air-plasma and nitrogen-plasma treated Kevlar and nomex fibers were analyzed by means of scanning electron microscopy.

DEPOSITION OF THIN FILMS IN ATMOSPHERIC PRESSURE HOMOGENOUS DISCHARGE IN $N_2 + HMDSO + O_2$ ATMOSPHERE

FILIP STUDNIČKA*, DAVID TRUNEC, PAVEL ŠTAHEL, VILMA BURŠÍKOVÁ, and LUKÁŠ KELAR

Department of Physical Electronics, Masaryk University,
Kotlářská 2, CZ-61137 Brno, Czech Republic,
trunec@physics.muni.cz

1. Introduction

Dielectric barrier discharge (DBD) can be used to change properties of materials, such as adhesion, hardness, etc. Thin films can be deposited on the material in order to achieve protective layers or to make the surface of the material more adhesive to some liquids. The main disadvantage of DBD is that it is in the filamentary state under normal conditions. It was found that under certain conditions DBD becomes homogenous. The deposition in the atmospheric pressure has a great advantage in economy of the deposition, because there is no need for expensive vacuum technologies and more depositions can be made in shorter time in comparison to low pressure deposition. One of the disadvantages is that it is quite difficult to achieve depositions in large area¹. Sawada² reported the organosilicon thin films deposition in atmospheric pressure glow discharge in helium with the admixture of tetraethoxysilane (TEOS) or hexamethyldisiloxane (HMDSO) and oxygen. Prat³ reported the fluoro-polymer film deposition in helium APGD with admixture of hexafluoropropylene or tetrafluoroethylene. Gherardi⁴ used $N_2-SiH_4-N_2O$ discharge for SiO_2 deposition. Foest⁵ used APGD in helium with admixture of HMDSO for organosilicon thin film deposition. The atmospheric pressure homogenous discharge can be easily generated in various pure gases^{6–9}. However we used nitrogen because it is the most suitable gas from the technological point of view.

We studied the influence of HMDSO and O_2 mixture on the discharge properties, so we can achieve homogenous discharge. The properties of discharge were studied by electric measurement. The properties of films were studied by depth sensing indentation technique using the Fischerscope H100 tester and AFM. We also studied new ring-type of electrode, which has a special exhaustion pipe in the center, so we can have better control of the amount of the HMDSO flowing under the electrode. As a deposition substrate we used 350 mm thick silicon wafers with a diameter of 10 cm and glass plates (dimensions 160×65 mm) with thickness of 1 mm. The films had uniform thickness and under optimum conditions exhibited higher hardness than the substrate.

2. Experiment

The experiments were carried out in a plasma reactor of dimensions 500 × 500 × 500 mm. The schematic drawing of the reactor is shown in the Figure 1. Electrode system is created from two metal electrodes. The bottom electrode was rectangular with dimensions 150 × 60 mm; on this electrode the substrates were placed. As an upper electrode two types of electrode were used. First type of electrode with dimensions 15 × 30 mm was covered by Petri dish with diameter of 50 mm. The metal electrode was glued to Petri dish by the ceramic glue. Second type of electrode (ring-type) created the ring with diameter 30 mm with the hole of 15 mm diameter in the middle of the electrode (see Fig. 2). The ring metal electrode was covered with 0.5 mm thick Pyrex[®] glass. The distance between the substrate and the upper electrode varied from 0.6 to 1.2 mm. The upper electrode was movable in the horizontal direction (see Fig. 1). The bottom electrode was electrically heated up from 50 to 150 °C.

The DC laboratory source powered AC high voltage sinusoidal source Lifetech connected to the discharge electrodes. High voltage source worked in the resonance mode with the frequency around 6 kHz. Electric properties of the discharge were measured using oscilloscope HP 54820A equipped with high voltage probe and Rogowski coil. One gas inlet and two gas outlets were in the reactor. Gas inlet was used for the input of nitrogen with/without monomer admixture, first gas outlet was connected to pumping system and second gas outlet was connected to the exhaust pipe in the ring-type electrode.

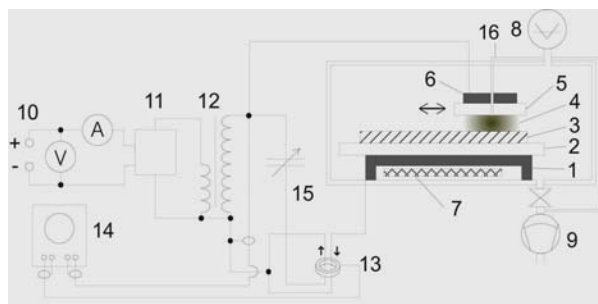


Fig. 1. **Schema of the reactor.** 1 – bottom electrode, 2 – bottom dielectric, 3 – substrate, 4 – discharge, 5 – upper dielectric, 6 – upper electrode, 7 – heating, 8 – input of gases, 9 – vacuum pump, 10 – DC source, 11 – AC source, 12 – transformer, 13 – Rogowski coil, 14 – oscilloscope, 15 – tunable capacitor, 16 – exhaustion pipe

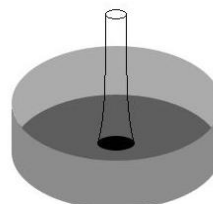


Fig. 2. **The ring-type electrode.** The darkest gray represents metal ring

In this work the influence of flow rate of buffer gas or monomer and influence of the substrate temperature was investigated. We also studied influence of geometry and different type of electrodes on the quality of deposited films.

In the case of first type of the electrode (Petri dish electrode), it was problematic to achieve homogenous and as well as controlled distribution of admixtures under the whole surface of the electrode. Second type of electrode, the ring-type electrode, enabled us to control easily the amount of the monomer and also buffer gas in discharge space.

Using this type of the electrode the distribution of gas is homogenous and deposited films had uniform thickness (except for the little spot under the exhaustion pipe).

The monomer vapors (in our case HMDSO) were carried with the carrier gas (in our case nitrogen or synthetic air) with flow rate varying from 5 to 30 sccm bubbled through the monomer. The relation between the amount of carrier gas and amount of HMDSO is expressed:

$$\text{HMDSO [g/h]} = 0.01752 + 0.02467 \times \text{CARRIER [slpm]}.$$

Use of the synthetic air as a carrier gas containing mainly nitrogen ($\approx 80\%$) and oxygen ($\approx 20\%$) enabled us to control sensitively oxygen content.

Before starting the experiment, the substrate was cleaned in mixture of 50 % isopropylalcohol and 50 % cyclohexane bath followed with the ethanol bath.

Before deposition the reactor was pumped down to 20 Pa to obtain the identical conditions before deposition. Then the reactor was filled with the nitrogen to the pressure 99.8 kPa. The flow rate of nitrogen was 6 slpm in all experiments. After that the resonance frequency was set up (generally about 6 kHz). Before the deposition the substrate was cleaned and activated with plasma treatment in the discharge with power density 30 W cm^{-3} . After that the nitrogen was mixed with the HMDSO + carrier gas and the reactor was run through with this mixture for about 30 minutes to achieve homogenous distribution of gases in the reactor. If the ring-type electrode was used then the exhaustion rate was set up. Then the temperature was increased to the desired value and the deposition started. In this paper only depositions in static mode are presented. Upper electrode did not move and deposition time was always 25 minutes. The

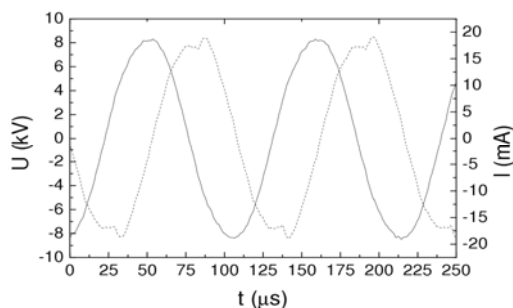


Fig. 3. Typical APGD current-voltage characteristic. The discharge current consists of two parts—the sinusoidal capacitive current part and the small peak of APGD discharge current

difference between filamentary DBD and homogenous discharge was determined from the oscilloscope current-voltage measurement.

The typical current-voltage characteristic is shown in the Figure 3. The power varied from 30 to 150 W cm^{-3} , the peak-to-peak AC voltage varied from 8 to 22 kV, the flow rate of synthetic air from 5 to 30 sccm and the temperature from 50 to 200°C .

3. Results and discussion

All experiments were performed in APGD mode. If filamentary DBD appeared, the deposition conditions were changed to obtain homogenous mode (e.g. lowering the power, lowering the flow rate of admixtures, lowering the exhaustion rate). Exhaustion rate higher than 500 sccm or flow rate of synthetic air higher than 30 sccm can cause the discharge to be filamentary. The films deposited with the admixture of O_2 exhibited higher hardness because the oxygen works as an oxidation reagent. The films deposited with Petri dish electrode showed good hardness properties but were not homogenous under the whole surface of the electrode. That is because the monomer vapors were able to reach the center of the APGD and were consumed under the edge of the electrode perimeter. In opposite the films deposited with ring-type electrode were perfectly homogenous.

After several experiments with electrodes made from Petri dish electrode we obtained the deposition conditions for hard glass like coatings (see Table I, sample 8081303). The deposition rate in the edge of the electrode of the films was extremely fast, so films were after 25 minutes of deposition so thick that internal stress in film caused delamination from the substrate as is shown in the Fig. 4–7. Deposited films exhibited high hardness however in the case of Petri-dish electrode the deposition proceeded only under the electrode edge and films were not completely homogenous. With

Table I
Deposition conditions

Sample no.	Synth. air [sccm]	Exh. [sccm]	Temp. [$^\circ\text{C}$]	Power dens. [W cm^{-3}]
8081303	6	0	100	134
8082601	6	0	100	41
8082602	6	0	100	24
8082805	6	250	100	59
8082807	15	50	100	53
8082701	10	200	100	36
8082702	6	100	100	53
8082703	10	100	100	53
8082704	10	200	100	53
8082705	6	500	100	25
8082706	6	200	100	25
8090101	30	500	150	53
8090102	30	500	150	62

Table II
Some results from depth sensing indentation measuring

Sample no.	Max. load [mN]	HU [GPa]	HU _{pl} [GPa]	Y [GPa]	Electrode
8081303	15	3.36	7.08	74.49	petri dish
8081303	5	3.32	6.73	78.55	petri dish
8082602	5	3.23	6.67	72.98	ring-type
8082601	5	0.92	1.33	26.63	ring-type
8082807	7	1.16	1.80	30.75	ring-type
8082805	7	1.03	1.60	28.39	ring-type
8082701	10	1.76	2.98	44.33	ring-type
8082702	10	1.82	3.05	45.55	ring-type
8082703	10	1.35	1.86	42.27	ring-type
8082704	10	1.03	1.63	27.77	ring-type
8090101	50	3.02	6.07	68.20	ring-type
8090101	10	2.62	5.16	60.18	ring-type
8090101	7	2.47	4.83	57.09	ring-type
8090101	5	2.23	4.63	49.73	ring-type
8090102	50	3.34	6.95	74.72	ring-type
8090102	10	2.97	5.84	68.09	ring-type
8090102	7	2.84	5.49	65.91	ring-type
8090102	5	2.73	5.30	63.25	ring-type
8082705	50	3.04	7.75	60.90	ring-type
8082705	10	3.37	8.39	69.61	ring-type
8082705	7	3.27	8.46	66.93	ring-type
8082705	5	3.65	10.55	74.70	ring-type
8082706	50	3.59	7.95	77.97	ring-type
8082706	10	3.56	8.23	76.45	ring-type
8082706	7	3.47	8.02	74.65	ring-type
8082706	5	3.31	7.57	71.51	ring-type

the ring-type electrode we obtained films with similar mechanical properties but with uniform thickness (see Table I, II, sample no. 8082602).

Film deposition conditions are shown in the Table I. Mechanical properties obtained from depth sensing indentation tests are summarized in Table II.

- the sample 8081303 has Young's module around 76 GPa, this value is nearly glass-like (glass is about 70 GPa),
- the sample 8082602 has Young's module around 73 GPa,
- the sample 8090101 is quite weak, because Young's module much differs for load 5 and 7 mN,
- the samples 80827[05-06] are really hard, nearly glass-like, their Young modules are even higher then the Young module of the substrate,
- the other samples are quite thin, we can tell this from the rising HU which corresponds to higher load, thus the properties of the substrate are influencing the measured characteristics,
- the hardness of the prepared films was in the range from

1.3 to 10.5 GPa,

- the samples 8082701-04 are quite thick but exhibit relatively low plastic hardness (HU_{pl}),
- not only HU_{pl} but also universal hardness (HU) and Young module are important in the characterization of the films. If the film is hard but not elastic, it would be fragile and if the system film/substrate will be under stress, the film could easily peel off.

It is possible to study internal stress of films from the pictures of delaminated films. I will now concentrate on the two films 8081303 and 8082602 which delaminated from the substrate.

Delamination of film from the substrate is caused by the internal stress. The sample 8082602 delaminated because of the tensile stress (see Fig. 4, 5) and the sample 8081303 delaminated because of the compressive stress (see Fig. 6, 7).

The rolls on the Fig. 4, 5 are signaling the tension stress in the film with low adhesion. The film is trying to shrink what leads to film cracking and thanks to the low

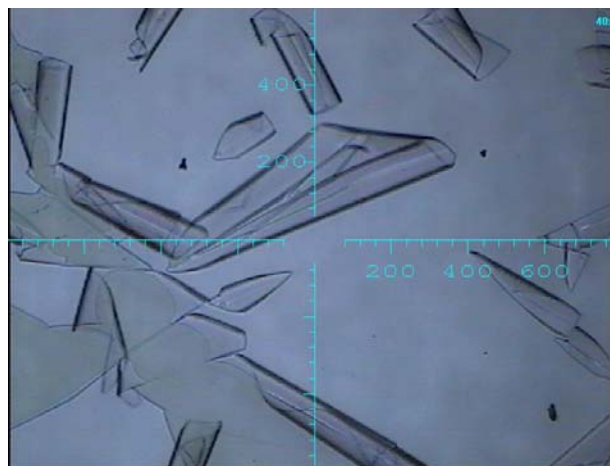


Fig. 4. Delaminated film from sample 8082602 – tensile stress

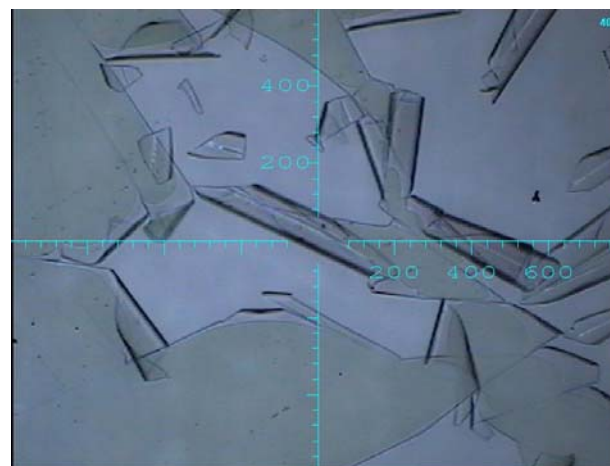


Fig. 5. Delaminated film from sample 8082602 – tensile stress

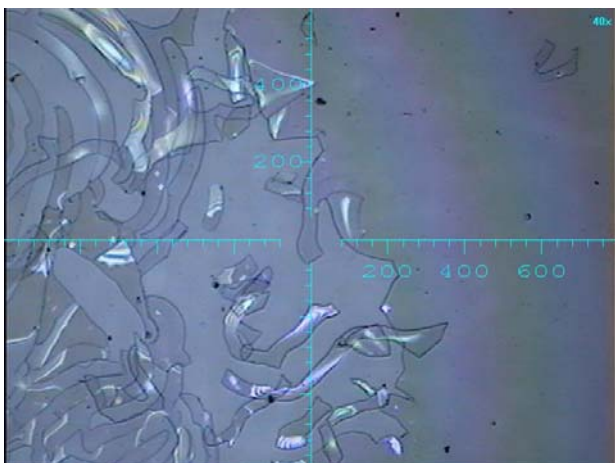


Fig. 6. Delaminated film from sample 8081303 – compressive stress

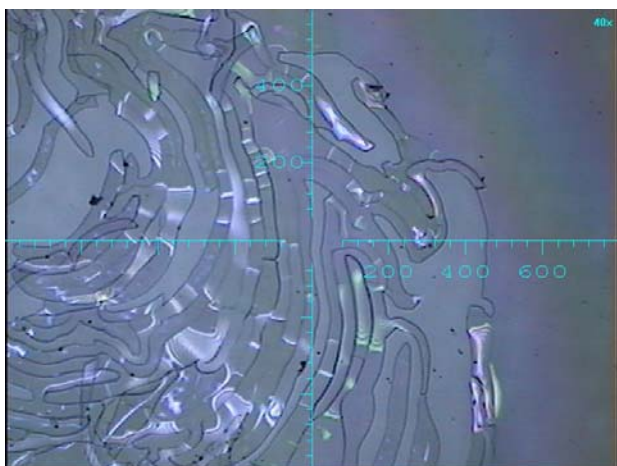


Fig. 7. Delaminated film from sample 8081303 – compressive stress

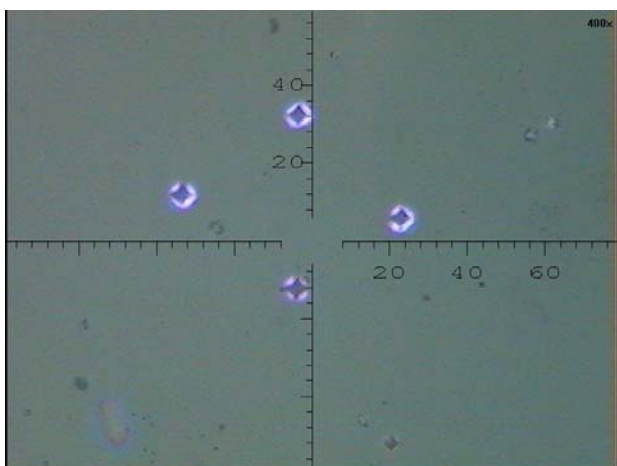


Fig. 8. Four indentation prints carried out with indentation load of 100 mN and one with 50 mN on the sample 8090101

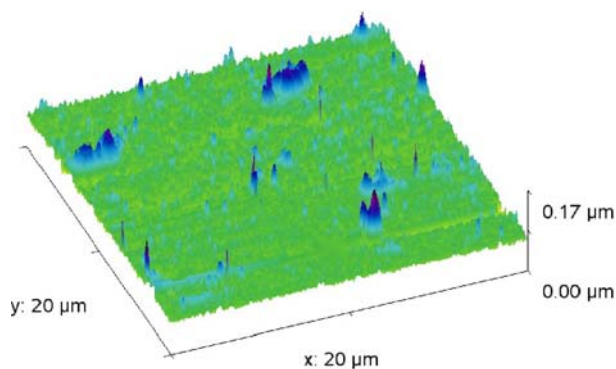


Fig. 9. AFM picture of film from the atmospheric pressure homogeneous discharge

adhesion the film delaminates from the substrate and creates rolls.

The corrugation on the Fig. 6, 7 shows the pressure stress in the film with low adhesion. The film is trying to stretch. If this film would be soft, then the film only corrugates. Since this film is really hard, then after corrugation it cracks, after gaining enough curvature.

It is evident, that deposition conditions influence not only hardness (both films 8081303 and 8082602 had at about same hardness) but also different type of internal stress. By this technique it is possible to prepare films either with tension or pressure stress. To obtain samples without cracks it is necessary to optimize plasma treatment before deposition to obtain better adhesion of the prepared films to the substrate.

On the Fig. 8 there are indentations with max. load 100 mN. The indenter was deep in the substrate at this load, but it is obvious that there are no cracks or delamination around the indentations. That means the films are not fragile and the adhesion to the substrate is really good.

The AFM picture of the film deposited in atmospheric pressure homogeneous discharge is on the Fig. 9. The film is smooth and homogeneous except for some sharp objects, which occur seldom even on homogeneous discharge made films.

4. Conclusion

Deposition of thin glass-like films in atmospheric pressure homogeneous discharge from nitrogen + HMDSO + oxygen atmosphere is shown in this paper. The effect of different oxygen and HMDSO flow rates, temperature, power density and different type of electrodes on the film properties was investigated. Under special conditions it is possible to deposit glass-like films with HU_{pl} over 8 GPa, Young's module over 70 GPa with tensile or compressive stress. The new ring-type of electrode with exhaustion pipe in the center was presented. The ring-type electrode enabled us to obtain homogeneous film deposition and it was possible to deposit glass-like films with good adhesion to the substrate and uniform thickness.

This research has been supported by the grant of Czech Science Foundation no. 202/06/1473. I would also like to thank Mr. Milan Kunovský for great technical support.

REFERENCES

1. Trunec D., Navrátil Z., Šťáhel P., Zajíčková L., Buršíková V. and Čech J.: J. Phys. D: Appl. Phys. 37, 2112 (2004).
2. Sawada Y., Ogawa S. and Kogoma M.: J. Phys. D: Appl. Phys. 28, 1661 (1995).
3. Prat R., Koh Y. J., Babukutty Y., Kogoma M., Okazaki S., Kodama M.: Polymer 41, 7355 (2000).
4. Gherardi N., Martin S., Massines F. : J. Phys. D: Appl. Phys. 33, L104 (2000).
5. Foest R., Adler F., Sigener F., Schmidt M.: Surf. Coat. Technol. 163-164, 323 (2003).
6. Kanazawa S., Kogoma M., Moriwaki T., Okazaki S.: J. Phys. D: Appl. Phys. 21, 838 (1988).
7. Gherardi N., Gouda G., Gat E., Ricard A., Massines F.: Plasma Sources Sci. Technol. 9, 340 (2000).
8. Trunec D., Brablec A., Buchta J.: J. Phys. D: Appl. Phys. 34, 1697 (2001).
9. Brandenburg R., Kozlov K. V., Massines F., Michel P., Wagner H.-E.: Proc. HAKONE VII (Greifswald), 2000.

ORGANIC POLLUTANTS TREATMENT IN GAS PHASE BY USING ELECTRON BEAM GENERATED NON-THERMAL PLASMA REACTOR

YONGXIA SUN*, A.G.CHMIELEWSKI, S. BULKA, and Z. ZIMEK

*Institute of Nuclear Chemistry and Technology, Dorodna 16, 03-195 Warsaw, Poland
yongxia@ichtj.waw.pl*

Key words: 4-chlorotoluene, 1,4-dichlorobenzene, gas phase treatment, non-thermal plasma

Contents

1. Introduction
2. Experimental
 - 2.1. Preparation model gas containing 4-chlorotoluene
 - 2.2. An accelerator applied for generating plasma generation in the reactor
 - 2.3. Analytical methods
 - 2.4. Dose dependence of removal efficiency or decomposition efficiency
3. Results and discussion
 - 3.1. 4-Chlorotoluene decomposition
 - 3.2. Gaseous products
 - 3.3. Mechanism of 4-chlorotoluene decomposition
 - 3.3.1. Positive charge and negative charge transfer reaction pathways
 - 3.3.2. OH radicals decomposition pathway
 - 3.4. 4-chlorotoluene and 1,4-dichlorobenzene decomposition comparison
4. Conclusions

Introduction

Chlorinated organic compounds, which are emitted from fossil-fuel power stations¹, waste incinerators², chemical factories, etc. are very harmful to the environment and human health. Recent studies reported that chlorinated benzenes or phenols are suspected as precursors for dioxins emission³. In Poland⁴, dioxins emission from some medical waste incinerators was very high, their concentration in stack gas was up to 32 ng TEQ/m³ [Total toxic equivalency (TEQ), it is a term which describes all the products summed to give a single 2,3,7,8-TCDD equivalent]. Dioxins are relatively chemical inert and demonstrate long life time in environment, therefore they are called persistent organic pollutants (POPs). They are transported by air and are deposited on the surfaces of the soil, water and plants. They can accumulate in the fat of food-

producing animals and are transferred into fish, meat, eggs, and dairy products⁵.

Chlorinated aromatic organic compounds (Cl-AOCs) removal from gas phase has been studied in the recent years. In general, there are two ways to realize Cl-AOCs removal, one is reduction Cl-AOCs to their parent hydrocarbons by using metal catalysts^{6–8}, the other is oxidation Cl-AOCs to the corresponding aldehydes and other oxidation products⁹. Electron beam (EB) process is a promising technology for removal of trace low concentration organic compounds contained in gas mixture by oxidation process. Decomposition of aliphatic chlorinated compounds¹⁰ and aromatic hydrocarbons^{11,12}, such as benzene, toluene, xylene etc., have been extensively studied by using this technology and promising results were achieved.

Dioxin's treatment using EB technology was reported, over 90% dioxins was removed from the waste off gases^{13,14}.

Decomposition of chlorobenzene^{15,16} in gas phase by using electron beam technology have been studied, aliphatic oxygenates were found as gaseous products of chlorobenzene degradation¹⁶.

No work has been reported concerning 4-chlorotoluene (4-CTO) removal in gas phase. Dechlorination of chlorotoluene in aqueous solution were studied, toluene¹⁷ and benzene¹⁸ were reported as dechlorination products.

Since the Stockholm Convention on POPs entered into force on 17 May 2004, dioxins emission from off-gases were monitored and their concentration should be lower than 0.1ng-TEQ/m³. In this work, we studied destruction of 4-chlorotoluene in air mixture under electron beam generated plasma reactor, its decomposition efficiency was compared with 1,4-dichlorobenzene(1,4-DCB), the decomposition products of 4-chlorotoluene were identified in the aim of obtain better knowledge to diminish dioxins formation in the waste incineration process using this technology.

Experimental

2.1. Preparation model gas containing 4-chlorotoluene

The set up for preparation model gas of 4-chlorotoluene was similar to that described in our previous work¹⁹. 4-Chlorotoluene model gas was prepared by bubbling synthesized air ($\geq 99.995\%$ purity; 21% O₂, N₂ as balance gas; CO₂ ≤ 1 ppm, BOC gas company, Poland) into liquid 4-chlorotoluene (4-chlorotoluene, Purity 98% without further purification, provided by Sigma-Aldrich company, Germany). A temperature of 4-chlorotoluene was set to be 21 °C with a water bath (type LW, manufactured by WSL Bytom company, Poland). The concentration of 4-chlorotoluene in the model gas was adjusted by controlling air flow rate by means of valve and rotameters. The model gas of 4-chlorotoluene was introduced into four connected Pyrex glass reactors by parallel connection. When concentration in glass reactors became constant, the glass reactors were sealed with the stopcocks. The water concentrations in the model gas mixture were measured by a HM141 humidity and temperature indicator (Vaisala company, Finland). Water concentration in gas mixture was 56 ppm. Experiments were carried out at ambient temperature condition and 1 bar atmospheric pressure.

2.2. An accelerator applied for generating plasma generation in the reactor

A pulsed electron beam accelerator ILU-6 (2.0 MeV max, 20 kW max) was used to generate plasma inside glass reactors. Irradiation set up can be referred to our previous work¹⁹. Pyrex glass reactors were put under scan horn of the accelerator for irradiation. Irradiation conditions were described as follows: 2 Hz (pulse repetition rate), 2 MeV (energy) and 60 mA (pulse current). The absorbed dose (kGy, 1 kGy = 1 kJ kg⁻¹) inside glass reactors was measured by a cellulose triacetate film dosimeter.

2.3. Analytical methods

Concentrations of 4-chlorotoluene (4-CTO) before and after irradiation contained in reaction vessels were measured by a gas chromatography (GC-17A, Shimadzu Corporation, Japan) equipped with a flame ionizing detector (GC-FID). A capillary column (SupercowaxTM-10, 30 m × 0.32 mm × 0.25 μm, Supelco Company, USA) was used. Stock solutions of 4-chlorotoluene (200 μg ml⁻¹ in methanol, AccuStandard company, USA) were used for preparation calibration curve. Analytical conditions of 4-chlorotoluene were given as follows: column temperature was kept at 40 °C for 1 min, then increased to 160 °C at 20 °C min⁻¹; flow rate of He as carrier gas was 47 mL min⁻¹; injector temperature was 100 °C and detector temperature was 250 °C; Injection mode was split, split ratio was 40:1. The injection volume of 4-chlorotoluene air mixture was 1 mL.

By-products analysis after electron beam irradiation was carried out in this work. Organic compounds contained in reaction vessels (before and after irradiation) were adsorbed by coconut charcoal adsorbents (SKC Inc, USA) and then were desorbed by 5 ml ethyl acetate (HPLC purity, provided by J.K.Baker, USA). The solid-free extract solution was obtained by using syringe filters and then was concentrated to approximately 0.3 ml by using a micro-extractor under continuously blowing high purity N₂ (99.995 % purity, BOC gas company, Poland). A Gas Chromatography equipped with

a mass detector (GCMS-QP 5050A, Shimadzu Corporation, Japan) was used to identify by-products, a HP-5MS column (30 m × 0.25 mm × 0.25 μm, Agilent technologies Incorporation, USA) was used. The oven was held at 40 °C for 1 minute, then programmed at 20 °C min⁻¹ to 290 °C, held for 1 minute. Total flow rate of carrier gas helium was set to be 15 mL min⁻¹. Injector temperature was 280 °C and detector temperature was 280 °C. The injection volume of the concentrated extract solution was 1 μL with split mode, split ratio was 12:1. Electron impact ionization mode of MS was applied, 70 eV energy was used.

2.4. Dose dependence of removal efficiency or decomposition efficiency

In electron beam process, it is very important to consider energy consumption for degradation of pollutants, how much energy (unit: kJ) is consumed/absorbed to decompose amount of pollutants in the base gas (unit: kg). Energy absorbed by per amount of gas is defined as a term of dose, unit is kGy.

$$1 \text{ kGy} = 1 \text{ kJ kg}^{-1}.$$

Removal efficiency or decomposition efficiency of organic pollutants is defined as R: $R = (C_0 - C_i) / C_0$

where C_0 is initial concentration of organic pollutants, unit: ppm (v/v); C_i is concentration of organic pollutants at i kGy absorbed dose, unit: ppm (v/v).

Results and discussion

3.1. 4-Chlorotoluene decomposition

Decomposition of 4-chlorotoluene at different initial concentrations versus dose in an air mixture was studied in an electron beam generated non-thermal plasma reactor and results are presented in fig. 1. Water vapor concentration in an air mixture was 58 ppm (v/v). It can be seen that concentration of 4-chlorotoluene decreases with the absorbed energy increasing for the initial concentration of 4-chlorotoluene being 15.39 ppm, 51.93 ppm and 95.30 ppm, respectively. About 46.8 % 4-chlorotoluene is decomposed at 15 kGy for the initial concentration of 4-chlorotoluene being 95.30 ppm, and 69.39 % 4-chlorotoluene is decomposed at 15 kGy for the initial concentration of 4-chlorotoluene being 15.39 ppm.

3.2. Gaseous products

A GC-MS spectrum of gas mixture of 4-chlorotoluene with air after electron beam irradiation is presented in fig. 2. A compound eluted at retention time (RT) 7.590 min of the GC-MS spectrum, which was eluted at the same retention time of GC-MS spectrum obtained for 4-chlorotoluene/air mixture before irradiation, was identified as 4-chlorotoluene, its mass spectrum is shown in fig. 3. Two compounds eluted at retention time 4.91 min and 12.502 min, respectively, were identified by our carefully comparing their mass spectrums with reference mass spectrums provided by WILEY7N2 library. The mass spectrums of these two compounds and their reference mass spectrums are presented in fig. 4a, 4b & 5a, 5b, respectively. They are chlorobenzene (C₆H₅Cl, RT = 4.910 min) and 4-chlorobenzaldehyde (C₆H₄CHO,

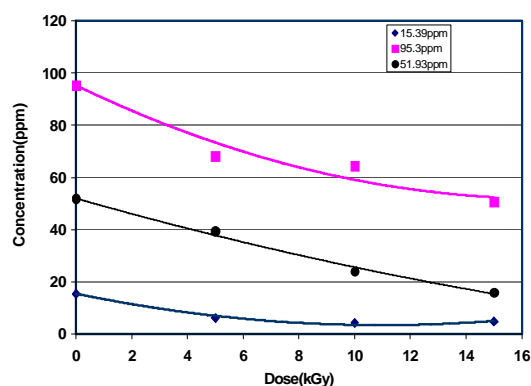


Fig. 1. 4-Chlorotoluene decomposition in air mixture in an electron beam generated non-thermal reactor

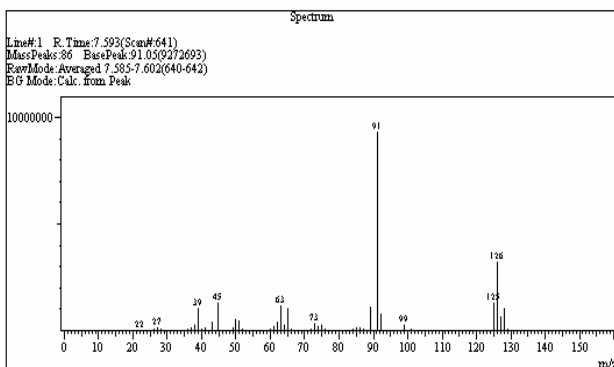


Fig. 2. A GC-MS spectrum of 4-chlorotoluene/air mixture after EB-irradiation

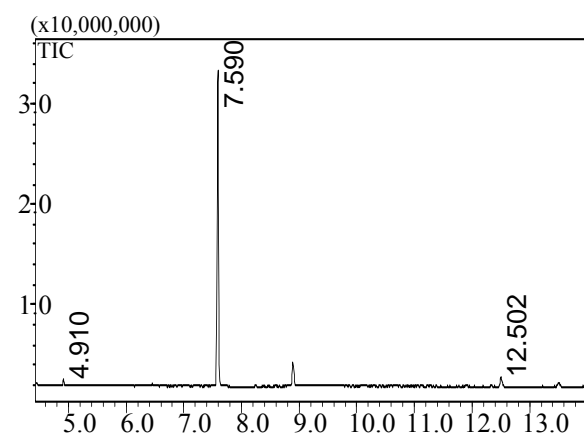
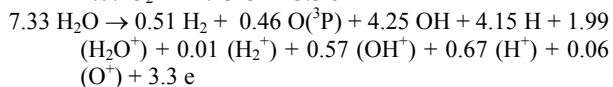
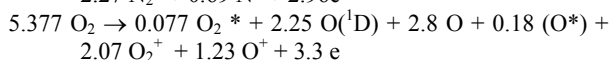
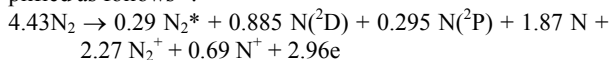


Fig. 3. A mass spectrum of 4-chlorotoluene which eluted at 7.59 min retention time

RT = 12.502 min), respectively. There is one unknown compound eluted at 8.9 min.

3.3. Mechanism of 4-chlorotoluene decomposition

When fast electrons from electron beams are absorbed in the carrier gas, they cause ionization and excitation process of nitrogen, oxygen and H₂O molecules in the carrier gas and generate non-thermal plasma reactor. Primary species and secondary electrons are formed. The secondary electrons are thermalized fast within 1 ns in air at 1 bar pressure. The G-values (molecules /100eV) of main primary species are simplified as follows²⁰:



These primary species and thermalized secondary electrons formed initiate and cause decomposition of 4-chloro-

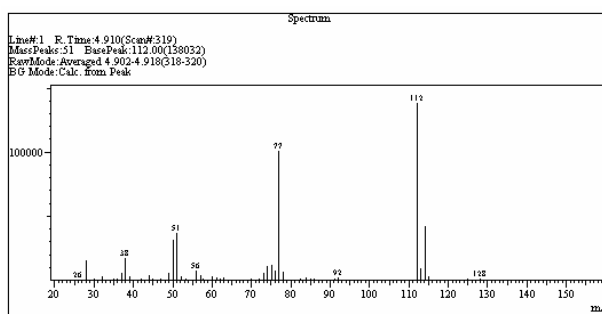


Fig. 4a. A mass spectrum of the compound which eluted at 4.910 min retention time

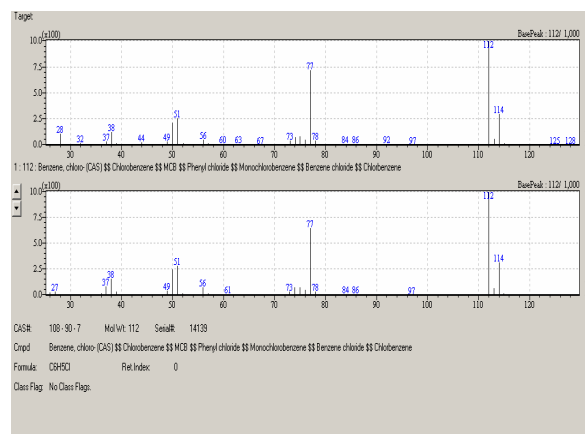
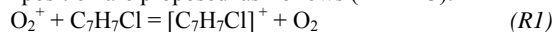


Fig. 4b. A mass spectrum of the compound which eluted at 4.910 min retention time and its reference mass spectrum of chlorobenzene (C₆H₅Cl)

toluene. In our previous work we carried out computer simulation of decomposition 1,4-dichlorobenzene in air mixture in an electron beam generated non-thermal reactor²¹ and learnt that two reaction pathways are play main roles for 1,4-DCB decomposition. Because chemical structure of 4-chlorotoluene (C₆H₄CH₃) is very similar to 1,4-DCB (C₆H₄Cl₂), decomposition mechanism of 4-chlorotoluene can be referred to 1,4-DCB, two main reaction pathways are given below (3.3.1.–3.3.2.).

3.3.1. Positive charge and negative charge transfer reaction pathways

As described above, when the carrier gas air is ionized by electron beam, positive ions (such as N₂⁺, O₂⁺ etc.) and secondary electrons etc. are formed. These positives ions transfer energy rapidly to the species with the lowest ionization energy (IE)²². The IE of 4-chlorotoluene is 8.69 ± 0.03 eV, it is smaller than the IE of N₂⁺, O₂⁺ etc.. Some important positive charge transfer reactions causing 4-chlorotoluene decomposition are proposed as follows (R1 ~ R3):



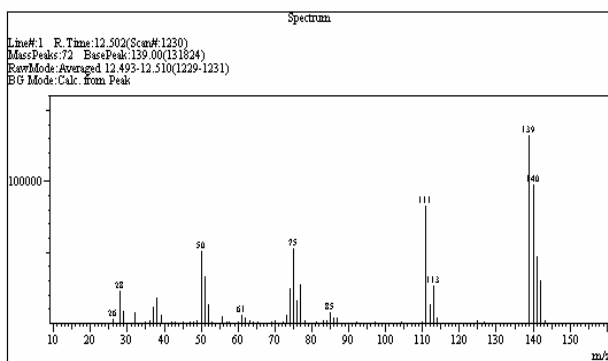


Fig. 5a. A mass spectrum of the compound which eluted at 12.502 min retention time

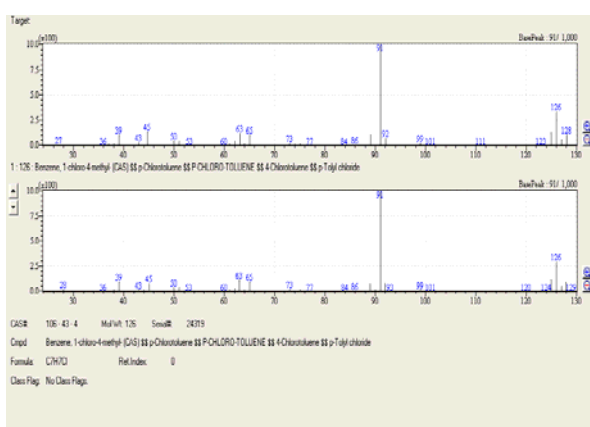
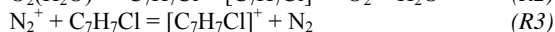
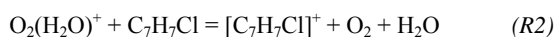
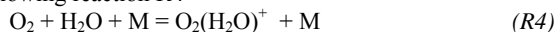


Fig. 5b. A mass spectrum of the compound which eluted at 12.502 min retention time and its reference mass spectrum of 4-chlorobenzaldehyde (C_6H_4CHO)

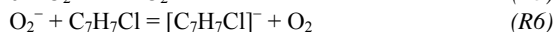


where $O_2(H_2O)^+$ in reaction R2 might be formed by a following reaction R4

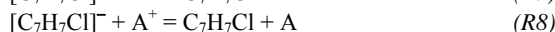
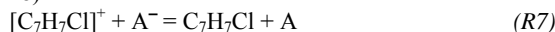


M is any specie in the gas phase.

Negative charge transfer reactions causing 4-chlorotoluene decomposition are given below (R5, R6):



$[C_7H_7Cl]^+$ and $[C_7H_7Cl]^-$ formed from above reactions might go neutralization through ionic recombination reactions (R7, R8)

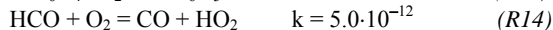
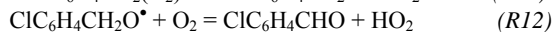
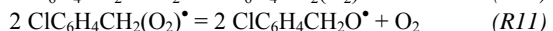
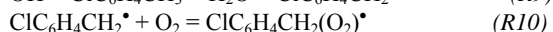
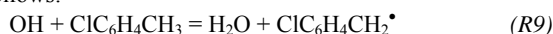


A^- , A^+ are any negative ions and positives ions in the gas phase, respectively.

3.3.2. OH radicals decomposition pathway

Based on our previous work²¹, we learn that OH radical decomposition reaction pathway plays main role for 1,4-DCB decomposition. During irradiation of low-humidity air with

4-chlorotoluene mixtures, OH radicals are formed. The reaction of OH radicals with 4-chlorotoluene at room temperature, 1 bar pressure is possible H atom elimination reaction²³ from $-CH_3$ group of 4-chlorotoluene based on by-products which were identified by the GC-MS analysis. From information of by-products identified, we learn only $-CH_3$ function group of 4-chlorotoluene involving in reaction with OH radical. The $C_6H_4CH_2^*$ radical produced in reaction (R9) may be decomposed by the reaction with oxygen molecules in the carrier gas as follows:



4-chlorobenzaldehyde (C_6H_4CHO) and chlorobenzene (C_6H_5Cl), which were identified as by-products in the experimental work, are might be formed from reactions R12 and R13, respectively.

In fact, mechanism of 4-chlorotoluene decomposition is very complicated, many reactions are involved, we just listed most important reactions we supposed.

3.4. 4-Chlorotoluene and 1,4-dichlorobenzene decomposition comparison

In order to find out whether functional group has influence on decomposition efficiency of aromatic compounds or not, we compared decomposition of 4-chlorotoluene ($C_6H_4CH_3$) with decomposition of 1,4-dichlorobenzene ($C_6H_4Cl_2$) in air mixture in an electron beam generated non-thermal plasma reactor. The experimental results are presented in fig. 6. It is found that decomposition efficiency of these two compounds is almost same at the same absorbed dose for the same range initial concentration of 4-chlorotoluene and 1,4-dichlorobenzene. Here should mention that water vapor concentration in 1,4-dichlorobenzene/air mixture was 170 ppm, this value is higher than 58 ppm water vapor in 4-chlorotoluene/air mixture.

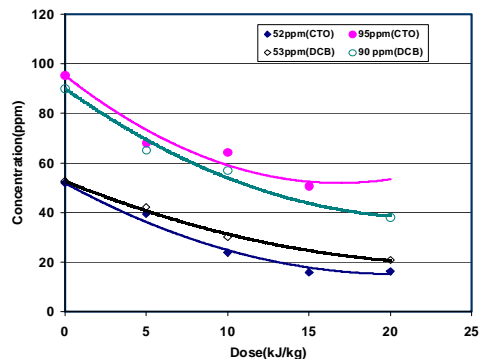


Fig. 6. Decomposition efficiency comparison between 4-chlorotoluene and 1,4-dichlorobenzene

Conclusions

4-Chlorotoluene in air can be decomposed in an electron beam generated non-thermal plasma reactor, decomposition efficiency of 4-chlorotoluene is similar to 1,4-dichlorobenzene, about 46.8 % 4-chlorotoluene is decomposed at 15 kGy for the initial concentration of 4-chlorotoluene being 95.30 ppm. Chlorobenzene and 4-chlorobenzaldehyde are identified as by-products.

This work is financed by Ministry of Science and Higher Education under the program No. CHINY/250/2006.

REFERENCES

1. Fernández-Martínez G., López-Mahía P., Muniategui-Lorenzo S., Prada-Rodríguez D., Fernández-Fernández E.: *Atmos. Environ.* **35**, 5823 (2001).
2. Jay K., Stieglitz L.: *Chemosphere* **30**, 1249 (1995).
3. McKay G.: *Chem. Eng. J.* **86**, 343 (2002).
4. Grochowalski A.: *Chemosphere* **37**, 2279 (1998).
5. Malisch R., Dilara P.: *Chemosphere* **67**, S79 (2007).
6. LaPierre R. B., Wu D., Kranich W. L., Weiss A.H.: *J. Catal.* **52**, 59 (1978).
7. Coq B., Ferrat G., Figueras F.: *J. Catal.* **101**, 434 (1986).
8. Gopinath R., Lingaiah N., Seshu B. N., Suryanarayana I., Sai Prasad P. S., Obuchi A.: *J. Mol. Catal., A Chem.* **223**, 289 (2004).
9. Martin A., Bentrup U., Wolf G.-U.: *Applied catalysis A: General* **227**, 131 (2002).
10. Chmielewski A. G., Sun Y., Bułka S., Zimek Z.: *Radiat. Phys. Chem.* **76**, 1795 (2007).
11. Kim J. C.: *Radiat. Phys. Chem.* **65**, 429 (2002).
12. Hirota K., Sakai H., Washio M., Kojima T.: *Ind. Eng. Chem. Res.* **43**, 1185 (2004).
13. Hirota H., Hakoda T., Taguchi M., Takigami M., Kim H., Kojima T.: *Environ. Sci. Technol.* **37**, 3164 (2003).
14. Paur H.-R., Baumann W., Mätzing H., Jay K.: *Radiat. Phys. Chem.* **52**, 355 (1998).
15. Han D.-H., Stuchinskaya T., Won Y.-S., Park W.-S., Lim J.-K.: *Radiat. Phys. Chem.* **67**, 51 (2003).
16. Hirota K., Hakoda T., Arai H., Hashimoto S.: *Radiat. Phys. Chem.* **57**, 63 (2000).
17. Janiak T.: *Appl. Catal. A, General* **335**, 7 (2008).
18. Haines B. M., Gland J. L.: *Surf. Sci.* **602**, 1871 (2008).
19. Sun Y., Chmielewski A. G., Bułka S., Zimek Z.: *Plasma Chem. Plasma Process* **26**, 347 (2006).
20. Mätzing H., in: *Advances in chemical physics volume LXXX*, p. 315. John Wiley & Sons, Inc., USA 1991.
21. Sun Y., Chmielewski A. G., Bułka S., Zimek Z., Nichipor H.: *Radiat. Phys. Chem.* **76**, 1132 (2007).
22. Slater R. C., Douglas-Hamilton D. H.: *J. Appl. Phys.* **52**, 5820 (1981).
23. Atkinson R.: *Chem. Rev.* **85**, 69 (1985).

SURFACE MORPHOLOGY OF AMORPHOUS HYDROCARBON THIN FILMS DEPOSITED IN PULSED RADIOFREQUENCY DISCHARGE

MIROSLAV VALTR^{a*}, PETR KLAPETEK^a,
VILMA BURŠÍKOVÁ^b, IVAN OHLÍDAL^b,
and DANIEL FRANTA^b

^a Department of Nanometrology, Czech Metrology Institute, Okružní 31, 63800 Brno, ^b Department of Physical Electronics, Faculty of Science, Masaryk University, Kotlářská 2, 61137 Brno, Czech Republic
mvaltr@cmi.cz

Introduction

Amorphous hydrocarbon thin films are still very attractive materials for many scientists. They are used in wide range of applications like optical devices, integrated digital circuits, micro-electromechanical devices, biomedical coatings, etc. One of common techniques of preparation of such films is the plasma enhanced chemical vapor deposition¹ (PECVD). The properties of resulted thin films are strongly dependent on deposition parameters. Usually, continuous mode of operation is used in the deposition process, but running the deposition in pulsed mode offers another possibility to vary the material properties². One of the aspects of deposited thin film is the surface morphology, which can play a crucial role in industrial applications of the films. The aim of this work is therefore the investigation of surface parameters like roughness and autocorrelation length of films deposited in pulsed discharge.

Experimental details

Thin films were deposited in pulsed radiofrequency discharge by PECVD technique. The reactor consisted of a horizontally mounted SIMAX glass tube and was closed by two aluminum electrodes. Distance of the electrodes was 186 mm and inner diameter of the tube was 77 mm. Scheme of the apparatus can be found in Fig. 1. Power was delivered via matching unit from Dressler CESARTM 133 generator operating at 13.56 MHz. Duty cycle and frequency of the cycles were set to 10 % and 1 Hz, respectively. Delivered power during the on-time was 10 W (generator was off during the off-time). Films were deposited in argon-acetylene (C₂H₂) gas mixture. Gases were led into the reactor through drilled powered electrode. Gas flows were controlled by Hastings flowmeters. Flowrate of Ar and C₂H₂ gas was 4 sccm and 1 sccm, respectively. The reactor was pumped through drilled grounded electrode with a rotary pump. Total pressure was measured using Leybold CERAVAC diaphragm gauge. Minimum pressure reached in the apparatus was in the range 1.5–1.8 Pa. Total pressure in the apparatus was in the range from 38.8 Pa to 39.8 Pa (measured immediately before depo-

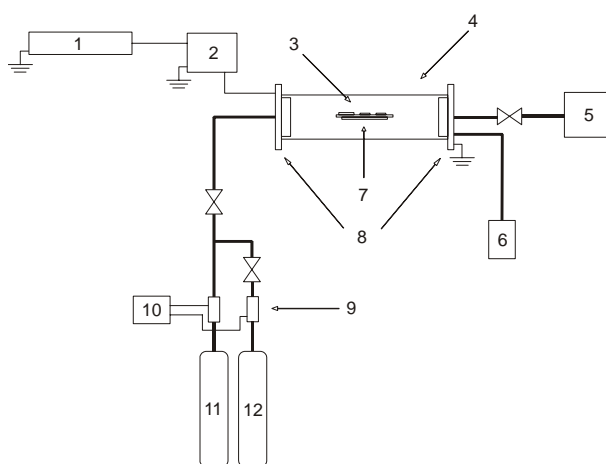


Fig. 1. Schematic view of the apparatus. 1 – power source, 2 – matching unit, 3 – samples, 4 – SIMAX glass tube, 5 – rotary pump, 6 – pressure gauge, 7 – glass sample holders, 8 – Al electrodes, 9 – flowmeters, 10 – control unit, 11 – Ar cylinder, 12 – acetylene cylinder

sition started). Substrates were made from silicon single crystal wafer and had a rectangular shape with dimensions 10 × 15 mm. Silicon substrates were located on a glass holder in the middle of the reactor (see Fig. 1). Prior to every deposition a cleaning of substrate surface in Ar in continuous mode was performed. During this procedure, the delivered power was 5 W and the discharge runned for 5 minutes.

Surface properties were evaluated on a series of samples where total deposition time (also the off-time of the period is counted in) was varied while the rest of the deposition parameters remained fixed at values already mentioned. The total deposition time was changed from 5 to 35 minutes with step of 5 minutes. Thus, the change of surface morphology of thin films with total deposition time was studied.

Film morphology was examined using Topometrix Accurex IIL atomic force microscope (AFM) with silicon nitride contact probes. Scan size was 20 × 20 μm and the resolution in both axes was 500 points. Data were analyzed with open-source program Gwyddion³. Scans were taken in the center of the sample as well as in the 3 mm distance from the shorter edge of the sample.

Surface characterization

We will assume that the film surface is randomly (statistically) rough and that the roughness is homogeneous. Furthermore, we will assume that the surface height in a given point x,y can be described by a random function $\zeta(x,y)$ that has given statistical properties.

The heights of surface irregularities are characterized by the root mean square (RMS) value (standard deviation) σ defined as follows:

$$\sigma^2 = \int_{-\infty}^{\infty} (z - \bar{z})^2 w(z) dz, \quad (1)$$

where z, \bar{z} and $w(z)$ denote a certain value, mean value and one-dimensional distribution of the probability density of the random function $\zeta(x, y)$, respectively (x and y are the Cartesian coordinates in the mean plane of the rough surface. The quantity σ is called the RMS value of the heights.

Another significant statistical quantity is the autocorrelation function G defined by this relation:

$$G(\tau_x, \tau_y) = \int_{-\infty}^{\infty} \int_{-\infty}^{\infty} z_1 z_2 w(z_1, z_2, \tau_x, \tau_y) dz_1 dz_2, \quad (2)$$

where symbols z_1 and/or z_2 and $w(z_1, z_2, \tau_x, \tau_y)$ denote certain value of $\zeta(x, y)$ in the point $[x_1, y_1]$ and/or the point $[x_2, y_2]$ and the two-dimensional distribution of probability density of $\zeta(x, y)$, respectively. The symbols τ_x and τ_y are given as follows: $\tau_x = x_2 - x_1$ and $\tau_y = y_2 - y_1$.

In practice, however, the autocorrelation function is not widely used. Instead of it the power spectral density function (PSDF) is often calculated from the AFM scans. The two-dimensional PSDF, $W_2(K_x, K_y)$, can be written in terms of Fourier transform of the autocorrelation function

$$W_2(K_x, K_y) = \frac{1}{4\pi^2} \int_{-\infty}^{\infty} \int_{-\infty}^{\infty} G(\tau_x, \tau_y) e^{-i(K_x \tau_x + K_y \tau_y)} d\tau_x d\tau_y, \quad (3)$$

where K_x and K_y denote x - and y -component of the wave vector of harmonic component of the certain spatial frequency of roughness. Within the AFM measurements we usually evaluate the one-dimensional PSDF determined only from profiles in the fast scanning axis because these are less affected by the low frequency noise and thermal drift of the sample. This function is defined in the following way

$$W(K_x) = \int_{-\infty}^{\infty} W_2(K_x, K_y) dK_y, \quad (4)$$

The one-dimensional autocorrelation function is often supposed as being Gaussian, i.e. given by the following relation

$$G(\tau_x) = \sigma^2 e^{-\tau_x^2/T^2}. \quad (5)$$

This results in one-dimensional PSDF given by relation

$$W(K_x) = \frac{\sigma^2 T}{2\sqrt{\pi}} e^{-K_x^2 T^2/4}, \quad (6)$$

where T is the autocorrelation length and characterizes lateral dimension of the irregularities of the randomly rough surface in its mean plane.

The AFM data are usually represented as a two-dimensional data field of size $N \times M$, where N and/or M represents the number of rows and/or columns within the datafield. Hence, the one-dimensional PSDF can be evaluated by means of the Fast Fourier transform as follows:

$$W(K_x) = \frac{2\pi}{NMh} \sum_{j=0}^M \left| \hat{P}_j(K_x) \right|^2, \quad (7)$$

where h is the distance between two adjacent datapoints and $\hat{P}_j(K_x)$ is the Fourier coefficient of the j -th row, i.e.

$$\hat{P}_j(K_x) = \frac{h}{2\pi} \sum_{k=0}^N z_{kj} e^{-iK_x kh}. \quad (8)$$

For more details about statistical description of rough surfaces see^{4,5}.

The surface properties of thin films were characterized by two parameters – RMS value of the heights, σ , and by the autocorrelation length T . These parameters were obtained by fitting one-dimensional PSDF calculated according to eqs. (7) and (8) with theoretical dependence given by eq. (6). The data in the procedure were treated by least-squares method (LSM). The LSM used was based on the Marquardt-Levenberg algorithm⁶.

Results and discussion

As already mentioned in previous section, surface parameters of thin films were obtained by evaluating the one-dimensional PSDF. In Fig. 2 can be found a comparison of PSDF calculated from AFM data of a selected sample together with best fit. Note that sharp peak at cca $39 \mu\text{m}^{-1}$ was filtered using one-dimensional FFT filtering. This peak (and also peaks on other space frequencies) arises from the noise of the electronics of the AFM microscope. The obtained values of σ and T in this case were as follows: $\sigma = 5.50 \pm 0.05 \text{ nm}$ and $T = 137 \pm 3 \text{ nm}$. Note that theoretical dependence according to eq. (6) fits very well with the experimental data. Therefore, it can be concluded that the assumption of Gaussian form of the autocorrelation function given by eq. (5) is substantiated.

The dependences of RMS values of heights σ and autocorrelation length T on total deposition time are carried out in Fig. 3 and 4. Note that data were collected in the center of the sample (in graph denoted as center) as well as in the 3 mm distance from the shorter edge of the sample (in graph denoted as edge).

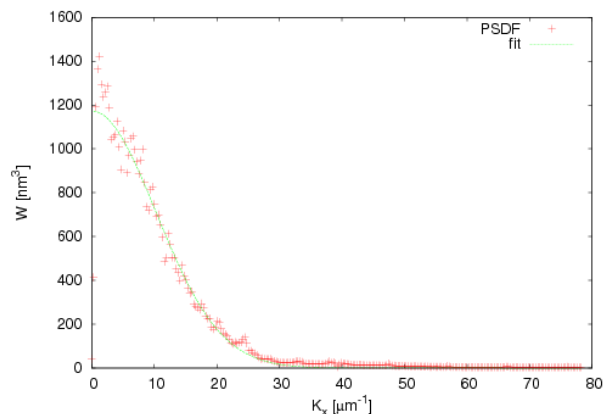


Fig. 2. Comparison of 1D PSDF calculated from AFM data of a selected sample with corresponding best fit

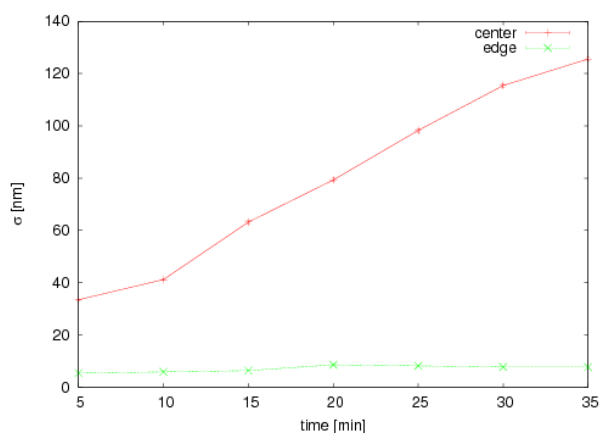


Fig. 3. Root mean square values of the heights of sample surface irregularities. The AFM data were taken in the center of the sample and also in the 3 mm distance from the edge

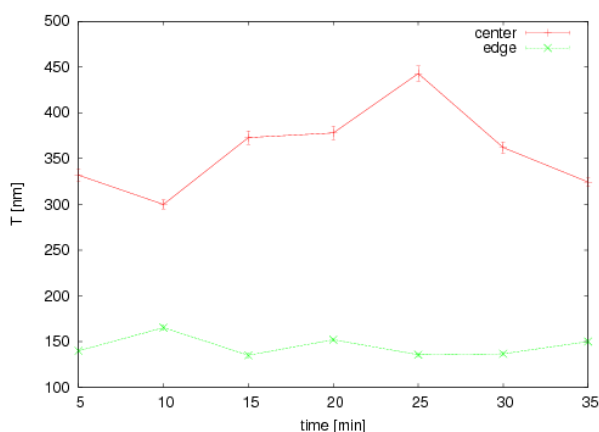


Fig. 4. Plot of the autocorrelation length resulted from best fits of the AFM data collected in the center and near the edge of the respective sample. On the abscissa is the total deposition time

It is worth to mention that the samples were oriented in such a way that the side where “edge” data were collected was headed towards powered electrode. Looking at Fig. 3, one can immediately see that in the center of the sample the surface roughness increases linearly, starting at 33.5 ± 0.3 nm. If the total deposition time reaches 35 minutes the roughness increases even up to 125.6 ± 0.9 nm. However, near the edge of the respective sample the roughness remains nearly constant and varies in the range from 5.50 ± 0.05 nm to 8.63 ± 0.04 nm. Increase of surface roughness of thin film with deposition time was reported in work by Lue et al⁷, where also a tubular type reactor was used for deposition. This would be in agreement with the development of surface roughness in the center of the sample. However, near the edge the surface roughness exhibits behavior usually seen on films deposited in bell jar type of reactors, i.e. roughness is only slightly dependent on film thickness and values of the roughness are on the order of units of nanometers^{8,9} or even on sub-nanometer scale¹⁰. Normally, very good film uniformity over large area reactors is reported¹¹. Nevertheless, the film uniformity can be strongly

affected by the design of electrode, gas inlet and pumping¹². Hence, non-uniformity of thin films deposited within this work may come from reactor design and sample position within the reactor. Of course, the deposition parameters play also an important role in the deposition process. For instance we observed that the roughness in the center of the sample is significantly reduced by lowering the peak power to 5 W.

Different are also values of autocorrelation length T in the center and near the edge of the sample as can be deduced from Fig. 4. However, in this case there is no evident dependency on the total deposition time. Mean value of the autocorrelation length in the center of the sample is 359 nm and in the 3 mm distance from the edge of the sample the respective value is 145 nm.

In Figs. 5 and 6 can be seen AFM images of the thickest sample, where total deposition time took 35 minutes. The scans were taken again near the edge (Fig. 5) and in the center (Fig. 6) of the sample. Note that there is a difference of one order of magnitude in the z-scale. The resulting RMS values

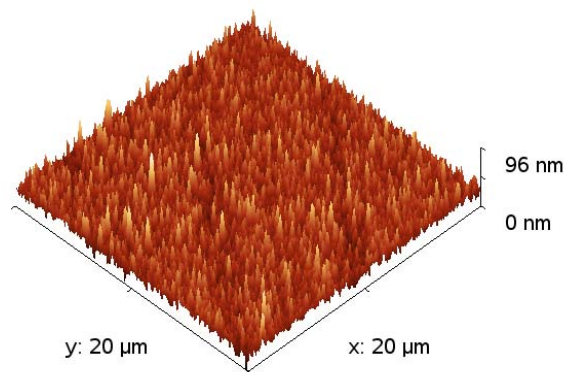


Fig. 5. AFM image taken in the 3 mm distance from the edge of the thickest sample (35 min). RMS roughness and autocorrelation length are $\sigma = 7.72 \pm 0.04$ nm and $T = 150 \pm 2$ nm, respectively

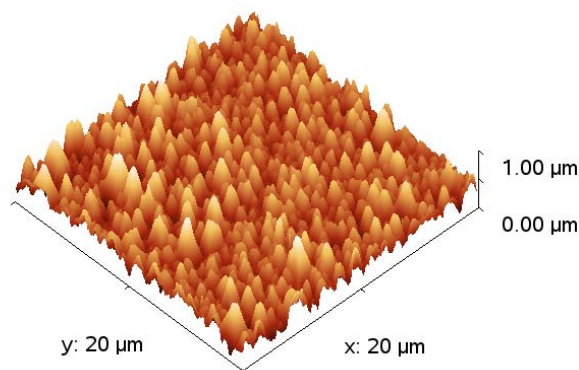


Fig. 6. AFM image taken in the center of the thickest sample. RMS value of roughness and autocorrelation length are as follows: $\sigma = 125.6 \pm 0.9$ nm and $T = 324 \pm 5$ nm

of roughness differ accordingly. While near the edge of the sample the respective value is only $\sigma = 7.72 \pm 0,04$ nm in the center of the sample the value is more than 16 times higher, i.e. $\sigma = 125.6 \pm 0,9$ nm. A difference can be observed also in the autocorrelation length. The value obtained near the edge of the sample is $T = 150 \pm 2$ nm. In the center the respective value is $T = 324 \pm 5$ nm. The autocorrelation length is a measure of lateral dimension of the irregularities of the rough surface. Hence, the increase of this quantity reflects the increase of the particle size deposited on the top of the sample.

Conclusion

We studied in this work surface morphology of thin amorphous hydrocarbon films by means of atomic force microscope. The AFM data were collected in two regions on the sample. We observed a significant difference in roughness parameters between these regions with increasing total deposition time. RMS values of the heights near the edge of the sample did not exhibit any significant change with the total deposition time and in the mean are equal to approximately 7 nm. However, RMS values of the heights in the center of the sample increased linearly with the total deposition time and reached values up to 125.6 nm. The values of autocorrelation length were independent on total deposition time, but there was a difference in absolute values. The mean value of this parameter near the edge of the sample was 145 nm, while in the center of the sample the respective value was 359 nm. The suggested reason for this surface non-uniformity is the reactor design. However, it is necessary to mention that the deposition conditions also play an important role in the film deposition process and that this difference could be at least partially ascribed to particular deposition conditions.

This work was supported by the Grant Agency of the Czech Academy of Sciences, grant no. KAN311610701 and by the Ministry of Education, Youth and Sports under the contract MSM0021622411.

REFERENCES

1. Szymanowski H., Sobczyk A., Gazicki-Lipman M., Jakubowski W., Klimek L.: *Surf. Coat. Technol.* 200, 1036 (2005).
2. Bapin E., Rudolf von Rohr P.: *Surf. Coat. Technol.* 142-144, 649 (2001).
3. <http://gwyddion.net/>
4. Klapetek P.: *PhD Thesis*, Masaryk University, Faculty of Science, Brno, 2003.
5. Ohlídal I., Franta D., in: *Progress in Optics XLI*, p. 181. North-Holland, Amsterdam 2000.
6. Marquardt W. D.: *J. Soc. Ind. Appl. Math.* 11, 431 (1963).
7. Lue S. J., Hsiaw S. Y., Wei T. C.: *J. Membr. Sci.* 305, 226 (2007).
8. Huang L. Y., Lu J., Xu K. W.: *Mater. Sci. Eng., A* 373, 45 (2004).
9. Guo C. T.: *Thin Solid Films* 516, 4053 (2008).
10. Hirakuri K. K., Minorikawa T., Friedbacher G., Grasserbauer M.: *Thin Solid Films* 302, 5 (1997).
11. Sansonnens L., Bonkowski J., Mousel S., Schmitt J. P. M., Cassagne V.: *Thin Solid Films* 427, 21 (2003).
12. Rech B., Roschek T., Repmann T., Müller J., Schmitz R., Appenzeller W.: *Thin Solid Films* 427, 157 (2003).

CONTENTS

Plasma sources, plasma reactors

<i>T. Czapka, W. Mielcarek, J. Warycha, K. Prociow, B. Mazurek</i>	Odors control with non-thermal plasma reactor	s1314
<i>K. Hensel, S. Sato, A. Mizuno</i>	Electrical discharge in honeycomb monolith	s1318
<i>M. Jasiński, Ł. Kroplewski, Z. Zakrzewski, J. Mizeraczyk</i>	Atmospheric pressure microwave microplasma sources	s1322
<i>V. Jirásek, J. Schmiedberger, M. Čenský, I. Picková, J. Kodymová, O. Špalek</i>	Plasmachemical generation of atomic iodine for iodine lasers pumped by singlet oxygen	s1327
<i>M. Jasiński, M. Dors, H. Nowakowska, J. Mizeraczyk</i>	Hydrogen production via methane reforming using various microwave plasma sources	s1332
<i>P. Slavicek, M. Klima, D. Skacelova, E. Kedronova, A. Brablec, V. Aubrecht</i>	RF discharge at atmospheric pressure – diagnostics and applications	s1338

Diagnostics of plasma processes and modelling

<i>M. Bartlova, V. Aubrecht</i>	Approximate calculations of continuous spectra of diatomic molecules	s1341
<i>J. Čech, P. Štáhel, Z. Navrátil, M. Černák</i>	Space and time resolved optical emission spectroscopy of diffuse coplanar barrier discharge in nitrogen	s1348
<i>R. Vladoiu, M. Contulov, G. Musa</i>	Double monochrome signal (double m-effect) in pulsed Ne-Ar-H ₂ mixture discharges	s1352
<i>P. Dvořák, Z. Moravec</i>	Dependence of higher harmonic frequencies measured in capacitively coupled plasma on the matching unit parameters	s1356
<i>T. Ficker</i>	Population statistics of electron avalanches and streamers	s1360
<i>J. Gregor, I. Jakubová, T. Mendl, J. Šenk</i>	Structure of hot mixture free jet at the arc-heater output	s1364
<i>I. Halamova, Z. Stara, F. Krema</i>	Interaction of electrical discharge with water solutions of humic matters	s1368
<i>A. Hrdlička, L. Prokeš, K. Novotný, V. Konečná, V. Kanický, V. Otruba</i>	Spatially resolved laser induced breakdown spectroscopy in orthogonal double pulse configuration and laser ablation inductively coupled plasma mass spectrometry of archaeological findings	s1372
<i>T. Hytková, P. Vašina, M. Eliáš</i>	Advanced modeling of reactive sputtering process with non-linear discharge Current density	s1376
<i>M. Meško, P. Vašina, J. Muňoz Espadero, V. Kudrle, A. Tálský, J. Janča</i>	Determination of N ₂ (A) population from optical emission spectra	s1380
<i>S. Lazović, N. Puač, G. Malović, A. Đorđević, Z. Lj. Petrović</i>	Diagnostic of plasma needle properties by using mass spectrometry	s1383
<i>V. Mazánková, F. Krčma</i>	Influence of oxygen traces on recombination processes in nitrogen post-discharge	s1388

<i>E. M. Peña-Méndez, J. R. Hernández-Fernaud, R. Nagender, J. Houška, J. Havel</i>	The chemistry of gold clusters in plasma generated with MALDI, laser desorption ionisation and laser ablation from various precursors	s1394
<i>K. Novotný, F. Lutzký, M. Galiová, J. Kaiser, R. Malina, V. Kanický, V. Otruba</i>	Double pulse laser ablation and plasma: time resolved spectral measurements	s1399
<i>I. Prysiazhnevych, V. Chernyak, S. Olzewski, V. Yukhymenko</i>	Plasma properties of transverse blowing arc under atmospheric pressure	s1403
<i>J. Gregor, I. Jakubová, J. Šenk</i>	Analysis of energy and mass flows in an arc heater with intensively blown electric arc	s1408
<i>M. Stano, E. Safonov, M. Kučera, Š. Matejíček</i>	Ion mobility spectrometry study of negative corona discharge in oxygen/nitrogen mixtures	s1414

Plasma in medicine, biology and environmental protection

<i>E. Azizov, A. Emelyanov, N. Rodionov, V. Yagnov</i>	Environmentally friendly method of water decontamination	s1418
<i>F. Krčma, J. Vyhnalíková, L. Poláchová, H. Grossmannová, Z. Stará</i>	VOC decomposition in surface discharge	s1424
<i>L. Leštinská, V. Martišoviš, M. Zahoran, Z. Machala</i>	Atmospheric pressure MW plasma for waste carbon treatment	s1428
<i>J. Ráhel', V. Procházka, M. Zahoran, D. Erben</i>	Removal of copper metal ions from aqueous solutions by plasma made chitosan filter	s1432
<i>G. Raniszewski, Z. Kolacinski, L. Szymanski</i>	Influence of waste composition on electric arc electron density	s1436
<i>P. Smekal, P. Slavicek, M. Klíma, M. Szostkova</i>	Sterilization of <i>Escherichia coli</i> using high frequency atmospheric pressure plasma discharge	s1441
<i>J. Vrajová, L. Chalupová, J. Čech, F. Krčma, P. Stáhel</i>	Paper sterilization by atmospheric pressure DBD discharge	s1445
<i>K.-D. Weltmann, Th. von Woedtke, R. Brandenburg, J. Ehlbeck</i>	Biomedical applications of atmospheric pressure plasma	s1450

Surface treatment by plasma discharges and thin films

<i>L. Bónová, A. Buček, T. Plecenik, A. Zahoranová, M. Černák</i>	Cleaning of aluminium surface using diffuse coplanar surface barrier discharge	s1452
<i>Z. Ržanek-Boroch, K. Gradkowska, A. Ilik, A. Kosiński^c</i>	Effect of the decamethyltetrasiloxane films deposition parameters on their properties	s1455
<i>A. Buček, T. Homola, M. Aranyosiová, D. Velič, T. Plecenik, J. Havel, P. Sťahel, A. Zahoranová</i>	Atmospheric pressure non-equilibrium plasma treatment of glass surface	s1459

<i>R. Vladoiu, V. Ciupina, V. Dinca, G. Musa</i>	Influence of the operational parameters on the wettability of the DLC films deposited by TVA method	s1463
<i>I. Gancarz, J. Kunicki, A. Ciszewski</i>	Application of plasma-induced grafting for modification of alkaline battery separator	s1467
<i>R. Chvalinová, J. Wiener</i>	Sorption properties of wool fibres after plasma treatment	s1473
<i>L. Kelar, V. Buršíková, P. Šťáhel, Z. Bochníček, V. Peřina, J. Buršík</i>	Preparation and characterisation of carbon films prepared from HMDSZ/ methane/nitrogen or hydrogen mixture using PECVD	s1478
<i>R. Vladoiu, V. Ciupina, C. P. Lungu, O. I. Pompilian, P. Chiru, A. M. Lungu, G. Prodan, A. Mandes, G. Musa</i>	Characterization of nano-structured carbon-metal bilayers deposited by thermionic vacuum ARC (TVA) technology	s1482
<i>P. Nasadil, P. Benešovsky</i>	Plasma in textile treatment	s1486
<i>G. Neagoe, A. Brablec, J. Ráhel, P. Slaviček, M. Zahoran</i>	Study of polypropylene nonwoven fabrics treatment in underwater electrical diaphragm discharge	s1490
<i>J. Pawlat, S. Ihara, K. Hensel, C. Yamabe</i>	Treatment of surfactants in the foaming column	s1494
<i>K. Safarova, M. Mashlan, R. Kubinek, J. Pechousek</i>	Use of cold plasma for transformation of iron nanoparticles	s1498
<i>J. Sentek, Z. Ržánek-Boroch, M. Brykala, K. Schmidt- Szałowski</i>	Deposition of gas - tight coatings on plastic films by pulsed dielectric-barrier discharges	s1502
<i>M. Eliáš, P. Souček, P. Vašina</i>	Influence of N ₂ and CH ₄ on depositon rate of boron based thin films prepared by magnetron sputtering	s1506
<i>F. Studnička, D. Trunec, P. Šťáhel, V. Buršíková, L. Kelar</i>	Deposition of thin films in atmospheric pressure glow discharge in N ₂ + HMDSO + O ₂ atmosphere	s1510
<i>M. Štěpánková, J. Šásková, J. Grégr, J. Wiener</i>	Using of DSCBD plasma for treatment of Kevlar and Nomex fibers	s1515
<i>F. Studnička, D. Trunec, P. Šťáhel, V. Buršíková, L. Kelar</i>	Deposition of thin films in atmospheric pressure homogenous discharge in N ₂ + HMDSO + O ₂ atmosphere	s1519
<i>Y. Sun, A. G. Chmielewski, S. Bułka, Z. Zimek</i>	Organic pollutants treatment in gas phase by using electron beam generated non-thermal plasma reactor	s1524
<i>M. Valtr, P. Klapetek, V. Buršíková, I. Ohlídal, D. Franta</i>	Surface morphology of amorphous hydrocarbon thin films deposited in pulsed radiofrequency discharge	s1529

AUTHOR INDEX

- Aranyosiová M. s1459
Aubrecht V. s1338, s1341
Azizov E. s1418
- Bartlova M. s1341
Benešovsky P. s1486
Bochníček Z. s1478
Bónová L. s1452
Brablec A. s1338, s1490
Brandenburg R. s1450
Brykała M. s1502
Buček A. s1452, s1459
Buřka S. s1524
Buršík J. s1478
Buršíková V. s1478, s1510, s1519, s1529
- Ciszewski A. s1467
Ciupina V. s1463, s1482
Contulov M. s1352
Czapka T. s1314
- Čech J. s1348, s1445
Čenský M. s1327
Černák M. s1348, s1452
- Dinca V. s1463
Đorđević A. s1383
Dors M. s1332
Dvořák P. s1356
- Ehlbeck J. s1450
Eliáš M. s1506, s1376
Emelyanov A. s1418
Erben D. s1432
- Ficker T. s1360
Franta D. s1529
- Galiová M. s1399
Gancarz I. s1467
Gradkowska K. s1455
Gregor J. s1364, s1408
Grégr J. s1515
Grossmannová H. s1424
- Halamova I. s1368
Havel J. s1459, s1394
Hensel K. s1318, s1494
Hernández-Fernaund J. R. s1394
Homola T. s1459
Houška J. s1394
Hrdlička A. s1372
- Hytková T. s1376
- Chalupová L. s1445
Chernyak V. s1403
Chiru P. s1482
Chmielewski A. G. s1524
Chvalinová R. s1473
- Ihara S. s1494
Ilik A. s1455
- Jakubová I. s1364, s1408
Janča J. s1380
Jasiński M. s1322, s1332
Jirásek V. s1327
- Kaiser J. s1399
Kanický V. s1372, s1399
Kedronova E. s1338
Kelar L. s1478, s1510, s1519
Klapetek P. s1529
Klima M. s1338, s1441
Kodymová J. s1327
Kolacinski Z. s1436
Konečná V. s1372
Kosiński A. s1455
Krčma F. s1368, s1424, s1445, s1388
Kropiewski Ł. s1322
Kubinek R. s1498
Kučera M. s1414
Kudrle V. s1380
Kunicki J. s1467
- Lazović S. s1383
Leštinská L. s1428
Lungu A. M. s1482
Lungu C. P. s1482
Lutzký F. s1399
- Machala Z. s1428
Malina R. s1399
Malović G. s1383
Mandes A. s1482
Martišovič V. s1428
Mashlan M. s1498
Matejíček Š. s1414
Mazánková V. s1388
Mazurek B. s1314
Mendl T. s1364
Meško M. s1380
Mielcarek W. s1314
Mizeraczyk J. s1322, s1332
- Mizuno A. s1318
Moravec Z. s1356
Muñoz Espadero J. s1380
Musa G. s1352, s1463, s1482
- Nagender R. s1394
Nasadil P. s1486
Navrátil Z. s1348
Neagoe G. s1490
Novotný K. s1372, s1399
Nowakowska H. s1332
- Ohlídal I. s1529
Olzewski S. s1403
Otruba V. s1372, s1399
- Pawlat J. s1494
Pechousek J. s1498
Peña-Méndez E. M. s1394
Peřina V. s1478
Petrović Z. Lj. s1383
Picková I. s1327
Plecenik T. s1452, s1459
Poláchová L. s1424
Pompilian O. I. s1482
Prociow K. s1314
Prodan G. s1482
Procházka V. s1432
Prokeš L. s1372
Prysiazhnevych I. s1403
Puač N. s1383
- Ráhel J. s1432, s1490
Raniszewski G. s1436
Rodionov N. s1418
Ržanek-Boroch Z. s1502
Ržanek-Boroch Z. s1455
- Safarova K. s1498
Safonov E. s1414
Sato S. s1318
Sentek J. s1502
Schmidt-Szałowski K. s1502
Schmiedberger J. s1327
Skacelova D. s1338
Slavicek P. s1338, s1441, s1490
Smekal P. s1441
Souček P. s1506
Sřahel P. s1348, s1445, s1459, s1478, s1510, s1519
Stano M. s1414
Stara Z. s1368
Stará Z. s1424

Studnička F. s1510, s1519
Sun Y. s1524
Szostkova M. s1441
Szymanski L. s1436 s1436

Šašková J. s1515
Šenk J. s1364, s1408
Špalek O. s1327
Štěpánková M. s1515

Tálský A. s1380
Trunec D. s1510, s1519

Valtr M. s1529
Vašina P. s1376, s1380, s1506
Velič D. s1459
Vladoiu R. s1352, s1482, s1463
von Woedtke Th. s1450
Vrajová J. s1445
Vyhnalíková J. s1424

Warycha J. s1314
Weltmann K.-D. s1450
Wiener J. s1473, s1515

Yagnov V. s1418
Yamabe C. s1494
Yukhymenko V. s1403

Zahoran M. s1428, s1432, s1490
Zahoranová A. s1452, s1459
Zakrzewski Z. s1322
Zimek Z. s1524

CONTENTS

Plasma sources, plasma reactors	s1314
Diagnostics of plasma processes and modelling	s1341
Plasma in medicine, biology and environmental protection	s1418
Surface treatment by plasma discharges and thin film deposition	s1452

CHEMICKÉ LISTY • ročník/volume 102 (S), čís./no. Symposia • LISTY CHEMICKÉ, roč./vol. 132, ČASOPIS PRO PRŮMYSL CHEMICKÝ, roč./vol. 118 • ISSN 0009-2770, ISSN 1213-7103 (e-verze), ISSN 1803-2389 (CD-ROM verze) • evidenční číslo MK ČR E 321 • Vydává Česká společnost chemická jako časopis Asociace českých chemických společností ve spolupráci s VŠCHT v Praze, s ČSPCH a ÚOCHB AV ČR za finanční podpory Nadace Český literární fond a kolektivních členů ČSCH • IČO 444715 • Published by the Czech Chemical Society • VEDOUCÍ REDAKTOR/EDITOR-IN-CHIEF: B. Kratochvíl • REDAKTOŘI/ EDITORS: J. Barek, Z. Bělohav, P. Drašar, J. Hettflejš, P. Holý, J. Horák, P. Chuchvalec, J. Podešva, P. Rauch, J. Volke; Bulletin: I. Valterová; Webové stránky: R. Liboska, P. Zámotný • ZAHRANIČNÍ A OBLASTNÍ REDAKTOŘI/FOREIGN AND REGIONAL EDITORS: F. Švec (USA), V. Větvička (USA), L. Opletal (Hradec Králové), P. Tarkowski (Olomouc) • KONZULTANT/CONSULTANT: J. Kahovec • VÝKONNÁ REDAKTORKA/ EDITORIAL ASSISTANT: R. Řápková • REDAKČNÍ RADA/ADVISORY BOARD: E. Borsig, M. Černá, L. Červený, E. Dibuszová, J. Hanika, Z. Havlas, I. Kadlecová, J. Káš, J. Koubek, T. Míšek, J. Pacák, V. Pačes, O. Paleta, V. Růžička, I. Stibor, V. Šimánek, R. Zahradník • ADRESA PRO ZASÍLÁNÍ PŘÍSPĚVKŮ/MANUSCRIPTS IN CZECH, SLOVAK OR ENGLISH CAN BE SENT TO: Chemické listy, Novotného lávka 5, 116 68 Praha 1; tel./phone +420 221 082 370, fax +420 222 220 184, e-mail: chem.listy@csvts.cz • INFORMACE O PŘEDPLATNÉM, OBJEDNÁVKY, PRODEJ JEDNOTLIVÝCH ČÍSEL A INZERCE/INFORMATION ADS: Sekretariát ČSCH, Novotného lávka 5, 116 68 Praha 1; tel/fax +420 222 220 184, e-mail: chem.spol@csvts.cz, chem.ekonom@csvts.cz • PLNÁ VERZE NA INTERNETU/FULL VERSION ON URL: <http://www.chemicke-listy.cz> • Redakce čísla Symposia (ISSUE EDITOR) A. Brablec, P. Vašina, O. Jašek, D. Trunec • TISK: České Tiskárny, s.r.o., Generála Syobody 335, 533 51 Pardubice - Rosice nad Labem; SAZBA, ZLOM: ČSCH, Chemické listy • Copyright © 2008 Chemické listy/Česká společnost chemická • DISTRIBUTION ABROAD: KUBON & SAGNER, POB 34 01 08, D-80328 Munich, FRG; Annual subscription for 2007 (12 issues) 225 EUR • This journal has been registered with the Copyright Clearance Center, 2322 Rosewood Drive, Danvers, MA 01923, USA, where the consent and conditions can be obtained for copying the articles for personal or internal use • Dáno do tisku 10.11.2008.